UNIVERSITY OF CALIFORNIA, SAN DIEGO

Three-dimensional nonlinear seismic response of large-scale ground-structure systems

A dissertation submitted in partial satisfaction of the requirements for the degree of

Doctor of Philosophy

in

Structural Engineering

by

Kyung Tae Kim

Committee in charge:

Professor Ahmed Elgamal, Chair
Professor Vlado Lubarda
Professor J. Enrique Luco
Professor Bernard Minster
Professor Benson Shing

2014

The Dissertation of Kyung Tae Kim is approved, and it is acceptable in quality and form for publication on microfilm and electronically:

Chair

University of California, San Diego

2014

DEDICATION

To my family members,

my wife, Park Jiyoon

my sons, Hyunwoo Dylan, Dahmwoo Brian

my parents,

and

my parents-in-law

EPIGRAPH

A person who never made a mistake never tried anything new.

-Albert Einstein

TABLE OF CONTENTS

LIST OF FIGURES

LIST OF TABLES

ACKNOWLEDGEMENTS

I would like to thank my advisor, Professor Ahmed Elgamal, for his tireless dedication in support of my Ph.D. research at the University of California, San Diego. His persistence and encouragement have challenged to me to grow beyond what I thought possible. For his support I express my most sincere gratitude and deepest appreciation.

I would also like to thank my committee members, Professor J. Enrique Luco, Professor Vlado Lubarda, Professor Bernard Minster, and Professor Benson Shing for the contribution of their time, guidance, and experience towards my research efforts.

This research is partially supported by the U.S. National Science Foundation (NSF) under grant OCI-0749227. Through a NSF allocation of advanced computing resources, the numerical simulations were performed on Ranger at the Texas Advanced Computing Center (TACC). This support is gratefully acknowledged.

Among many people who I have been able to rely on for help with technical questions and challenges, Professor Jacobo Bielak of Carnegie Mellon University has provided valuable feedback about the Domain Reduction Method (DRM). Dr. George Petropoulos has provided the DRM input motion and helped with its numerical implementation on the parallel computing machine at TACC. Dr. Jinchi Lu has provided assistance with a large number of OpenSees serial and parallel implementation challenges. Dr Frank McKenna has helped to make and update OpenSees versions so as to keep up with the changing computational environments of the employed parallel processing systems.

Chapters 1, 2, 3, 4, and 5 contain, in part, material published in the Earthquake Geotechnical Engineering Design (Geotechnical, Geological and Earthquake Engineering, Vol. 28, Springer) titled “Seismic Response of a Large-Scale Highway Interchange System” with authors, Kyung Tae Kim, Ahmed Elgamal, George Petropoulos, Aysegul Askan, Jacobo Bielak, and Gregory L. Fenves (2014). The dissertation author is the first author of this paper.

Finally, I would like to express my sincere appreciation to my family with an excellent foundation of support, encouragement, and endless love which has allowed me to successfully pursue my goals.

VITA

2005	Bachelor of Science, Dongguk Univeristy, South Korea
2008	Master of Science, University of California, Davis
2008 – 2014	Graduate Research Assistant, University of California, San Diego
2014	Doctor of Philosophy, University of California, San Diego

ABSTRACT OF THE DISSERTATION

Three-dimensional nonlinear seismic response of large-scale ground-structure systems

by

Kyung Tae Kim

Doctor of Philosophy in Structural Engineering

University of California, San Diego, 2014

Professor Ahmed Elgamal, Chair

Effort is geared towards development of large-scale nonlinear ground-structure seismic response simulations. Mechanisms to allow for modeling of transmitting boundaries are incorporated, mainly relying on the Domain Reduction Method (DRM) approach. Parallel computing is employed to permit the execution of these large-scale simulations. A range of geometric configurations are addressed in order to explore various aspects of the involved seismic response characteristics.

The OpenSees computational platform is employed throughout. To accommodate nonlinear response and soil/structure element stiffness considerations, an implicit time integration scheme is adopted. This scheme poses severe limitations on the number of

parallel computing processors that can be used with reasonable efficiency (due to the required taxing communications between the different processors). Within the available constraints on time and computing resources, and the necessary additional OpenSees parallel-implementation machine-specific adaptions, the conducted DRM investigations mostly employed a soil domain 3D 8-node brick element of a 20 m side length (with about 150,000 such elements in the mesh). Consequently, severe limitations are imposed on the frequency content of the propagated seismic waves and the resulting system response. Future extensions in this direction of research can build solidly on the developments in this report and provide more accurate higher frequency system response.

Significant attention is given to the simulation of a large-scale highway interchange system under seismic loading. A three-dimensional (3D) Finite Element model of an existing bridge interchange at the intersection of Interstates 10 and 215 (San Bernardino, CA) is developed. This interchange consists of three connectors at different bridge superstructure elevations. Initial focus is placed on modeling the three bridges, evaluation of vibration properties, and validation of one of the bridge models (North-West connector, NW) based on available earlier recorded earthquake response.

A strategy to incorporate the above bridge structural models into a bridge-foundation-ground system (BFGS) is implemented based on the Domain Reduction Method (DRM) as developed by Bielak and his co-workers. A numerical implementation of this DRM by Petropolous and Fenves is employed and adapted as the soil domain. In this implementation, seismic waves are propagated from a realistic fault rupture scenario in southern California. As such, the BFGS can include the three-bridge interchange subjected to a 3D seismic excitation scenario. Within this numerical analysis framework,

the effect of foundation soils of different stiffness and strength are investigated. The results are compared to the more conventional bridge model response under uniform as well as multi-support base excitation.

In addition to this DRM-based implementation, a nonlinear ground-bridge model based on the actual local soil conditions at the interchange is investigated (with the NW only as the super-structure). Efforts include implementation and validation of a classical transmitting boundary at the base of the soil domain. Using this formulation, the BFGS response is compared and validated with earthquake recorded response at the bridge and local site. Under a potential site specific strong ground motion, computed force demands from the employed linear column models are compared to the strength as defined by a representative nonlinear column formulation.

Finally, the seismic response of a large rigid structure with different embedment depths is assessed. Dynamic interaction between the structure and the surrounding soil is studied based on changes in soil elastic properties, depth of embedment, and characteristics of input excitation.

Chapter 1

Introduction

This report is concerned with large-scale numerical simulation for Soil-Structure-Interaction (SSI) applications. Employing advanced techniques for handling seismic wave propagation, much effort is dedicated to the SSI-based seismic response of a large bridge interchange and its individual bridge components. In an additional effort, some basic characteristics related to the response of large embedded and partially-embedded rigid structures are highlighted.

In this chapter, some of the relevant existing literature on numerical simulation techniques for seismic ground response and influence on soil-structure-interaction (SSI) effects are discussed. Emphasis is placed on a three-dimensional (3D) ground model subjected to incident waves directly propagated from an earthquake source. A number of related SSI efforts pertaining to bridge structures are also summarized. The objectives and scope of this research are outlined. Finally, a layout of the material presented in this reported is presented.

1.1 Literature review

1.1.1 Modeling of Seismic Wave Propagation

Over the years, numerical modeling methods for seismic wave propagation considering earthquake source, propagation path, and elastic/inelastic local site effects have been advancing considerably. Boundary element and discrete wave-number methods have been used for relatively simple geometry and geological conditions (with ground systems of moderate size). Finite difference methods (Olsen, 2001; Graves, 1993) and finite element (FE) methods (Aagard et al., 2001; Bao et al., 2001) have been used to address large size problems, such as realistic basin models with heterogeneous materials.

FE methods allow for modification of the mesh size to accommodate the involved wavelengths of the propagating waves. Ground motion due to the causative fault, its propagation path, and ground response within the region of interest can be calculated simultaneously in a single computational simulation. However, when the seismic source is far from the region of interest, a tremendously large spatial domain is involved, which results in significant inefficiency.

In order to further address this challenge, Bielak and his coworkers (Bielak and Christiano, 1984; Cremonini et al., 1988) developed an effective FE-based procedure. In this procedure, the large size problem is divided into two sequential parts. First, ground motions are calculated from a background configuration (including a specific earthquake source) in which the localized specific geological features of interest are removed. In this step, the computational grid size is dictated by the softest material in the background model, so as to represent the desired frequency range of interest. The resulting ground

motion is used to compute equivalent earthquake forces for the second step. These forces are applied to a localized computational domain (subdomain in the first step) that represents the region of interest (ROI). If an overlying super-structure is present in the ROI, the required computations are conducted only in this second step.

Within this framework, the Domain Reduction Method (DRM) was developed (Bielak et al., 2003a). This method allows efficiently for modeling 3D wave fields due to an arbitrary earthquake source in highly heterogeneous geological systems (with large localized impedance contrasts and arbitrary shapes). Further details concerning the DRM will be discussed in the following section.

Based on the DRM, Petropolous (2008) developed a FE high-performance algorithm and related software for handling the seismic response of large-size soil domains on parallel computers. In this implementation, a mixed time integration procedure was employed. In the regions dominated by wave propagation from the earthquake source, explicit time integration with diagonal mass matrices was adopted (without factorization of the dynamic stiffness matrices). To analyze super-structures, implicit time integration was required. This mixed time integration scheme was extended to solve nonlinear systems in the implicit partition, combined with Newton-Raphson iterations. Using this approach, numerical simulations were conducted (Petropolous, 2008) for large-size ground models subjected to near-fault ground motion resulting from a realistic fault rupture scenario. Relevant details of the employed ground model and the corresponding response (Petropoulos 2008) are discussed in Chapter 2.

1.1.2 Domain Reduction Method (DRM)

The DRM (Bielak et al., 2003a) is a modular two-step FE methodology for modeling earthquake ground motion in highly heterogeneous localized regions with significant contrasts in wavelengths. This method treats a semi-infinite seismic region including the fault system, the wave propagation path, and the localized geological features in 3D. Since the localized region of interest requires higher frequency resolution than the large scale wave propagation path, the DRM separates the analysis into two sub-problems. In the first problem, wave propagation of the seismic excitation resulting from the fault system to the region of interest (ROI) is computed. The second sub-problem provides a detailed analysis of the smaller subdomain encompassing the ROI under the equivalent excitation resulting from the first problem (Bielak et al., 2003a). Recently, using this approach, the effects of soil-structure interaction (SSI) on the response of yielding single-story structures embedded in an elastic half-space were discussed (Jaremprasert et al. 2013).

In the DRM, the original semi-infinite region (Figure 1.1) is truncated by outer boundary Γ^+ so as to model this region as a finite domain. The interface layer Γ divides the region into two parts, Ω (which contains the ROI) and Ω^+ (semi-infinite half-space including the fault system). In order to focus on response of the smaller region Ω, the equivalent excitation prescribed as a kinematic source resulting from the Ω^+ is applied to the domain Ω.

Ground motion in Ω and Ω+ are governed by Navier's equations of elastodynamics. Discretized spatially in the FE technique, the equations can be expressed in partitioned form as (Bielak et al., 2003a):

$$\begin{bmatrix} M_{ii}^{\Omega} & M_{ib}^{\Omega} \\ M_{bi}^{\Omega} & M_{bb}^{\Omega} \end{bmatrix} \begin{Bmatrix} \ddot{u}_i \\ \ddot{u}_b \end{Bmatrix} + \begin{bmatrix} C_{ii}^{\Omega} & C_{ib}^{\Omega} \\ C_{bi}^{\Omega} & C_{bb}^{\Omega} \end{bmatrix} \begin{Bmatrix} \dot{u}_i \\ \dot{u}_b \end{Bmatrix} + \begin{bmatrix} K_{ii}^{\Omega} & K_{ib}^{\Omega} \\ K_{bi}^{\Omega} & K_{bb}^{\Omega} \end{bmatrix} \begin{Bmatrix} u_b \\ u_e \end{Bmatrix} = \begin{Bmatrix} 0 \\ P_b \end{Bmatrix}, in\ \Omega \qquad (1.1)$$

$$\begin{bmatrix} M_{bb}^{\Omega^+} & M_{be}^{\Omega^+} \\ M_{eb}^{\Omega^+} & M_{ee}^{\Omega^+} \end{bmatrix} \begin{Bmatrix} \ddot{u}_b \\ \ddot{u}_e \end{Bmatrix} + \begin{bmatrix} C_{bb}^{\Omega^+} & C_{be}^{\Omega^+} \\ C_{eb}^{\Omega^+} & C_{ee}^{\Omega^+} \end{bmatrix} \begin{Bmatrix} \dot{u}_b \\ \dot{u}_e \end{Bmatrix} + \begin{bmatrix} K_{bb}^{\Omega^+} & K_{be}^{\Omega^+} \\ K_{eb}^{\Omega^+} & K_{ee}^{\Omega^+} \end{bmatrix} \begin{Bmatrix} u_b \\ u_e \end{Bmatrix} = \begin{Bmatrix} -P_b \\ P_e \end{Bmatrix}, in\ \Omega^+ \quad (1.2)$$

In these equations, *M*, *C*, and *K* denote the mass, damping, and stiffness matrices respectively. The subscripts *i*, *e*, and *b* represent nodes in the interior, exterior, and boundary, respectively (Figure 1.1). The superscripts Ω and Ω^+ refer to the domains over which the matrices are defined. By adding Eq. (1.1) and Eq. (1,2), the equation of motion for the total domain is written as (Bielak et al., 2003a):

$$\begin{bmatrix} M_{ii}^{\Omega} & M_{ib}^{\Omega} & 0 \\ M_{bi}^{\Omega} & M_{bb}^{\Omega} + M_{bb}^{\Omega^+} & M_{be}^{\Omega^+} \\ 0 & M_{eb}^{\Omega^+} & M_{ee}^{\Omega^+} \end{bmatrix} \begin{Bmatrix} \ddot{u}_i \\ \ddot{u}_b \\ \ddot{u}_e \end{Bmatrix} + \begin{bmatrix} C_{ii}^{\Omega} & C_{ib}^{\Omega} & 0 \\ C_{bi}^{\Omega} & C_{bb}^{\Omega} + C_{bb}^{\Omega^+} & C_{be}^{\Omega^+} \\ 0 & C_{eb}^{\Omega^+} & C_{ee}^{\Omega^+} \end{bmatrix} \begin{Bmatrix} \dot{u}_i \\ \dot{u}_b \\ \dot{u}_e \end{Bmatrix} +$$

$$\begin{bmatrix} K_{ii}^{\Omega} & K_{ib}^{\Omega} & 0 \\ K_{bi}^{\Omega} & K_{bb}^{\Omega} + K_{bb}^{\Omega^+} & K_{be}^{\Omega^+} \\ 0 & K_{eb}^{\Omega^+} & K_{ee}^{\Omega^+} \end{bmatrix} \begin{Bmatrix} u_i \\ u_b \\ u_e \end{Bmatrix} = \begin{Bmatrix} 0 \\ 0 \\ P_e \end{Bmatrix} \qquad (1.3)$$

In order to transfer the seismic excitation from the fault to the ROI, an auxiliary problem is defined in which the exterior region, material, and causative fault are identical to those of the original problem. The defined domain (denoted as Ω_o in Figure 1.2) is a simple

background domain (Ω_o and Ω^+) without the localized geological features (to permit an easier solution for the overall system). As such, the auxiliary problem can be rewritten as (Bielak et al., 2003a):

$$\begin{bmatrix} M_{bb}^{\Omega^+} & M_{be}^{\Omega^+} \\ M_{eb}^{\Omega^+} & M_{ee}^{\Omega^+} \end{bmatrix} \begin{Bmatrix} \ddot{u}_b^0 \\ \ddot{u}_e^0 \end{Bmatrix} + \begin{bmatrix} C_{bb}^{\Omega^+} & C_{be}^{\Omega^+} \\ C_{eb}^{\Omega^+} & C_{ee}^{\Omega^+} \end{bmatrix} \begin{Bmatrix} \dot{u}_b^0 \\ \dot{u}_e^0 \end{Bmatrix} + \begin{bmatrix} K_{bb}^{\Omega^+} & K_{be}^{\Omega^+} \\ K_{eb}^{\Omega^+} & K_{ee}^{\Omega^+} \end{bmatrix} \begin{Bmatrix} u_b^0 \\ u_e^0 \end{Bmatrix} = \begin{Bmatrix} -P_b^0 \\ P_e \end{Bmatrix} \quad (1.4)$$

The partitioned mass, damping, and stiffness matrices and the effective force P_e are identical to those in Eq. (1.3). The force P_e in terms of the free field is expressed as (Bielak et al., 2003a):

$$P_e = M_{eb}^{\Omega^+} \ddot{u}_b^0 + M_{ee}^{\Omega^+} \ddot{u}_e^0 + C_{eb}^{\Omega^+} \dot{u}_b^0 + C_{ee}^{\Omega^+} \dot{u}_e^0 + K_{eb}^{\Omega^+} u_b^0 + K_{ee}^{\Omega^+} u_e^0 \quad (1.5)$$

By substituting Eq. (1.5) into Eq. (1.3), the displacements, u_i, u_b, and u_e can be solved for the complete domain. Since the free field displacement u_e^0 is required to be stored throughout the domain (Ω^+), the computations still require inclusion of the source and the geological region of interest.

By means of a transformation of variables as part of the Domain Reduction Method (DRM), the total displacement can be expressed as the sum of the free field displacement (u_e^0) due to the background structure and the residual field displacement w_e, that is the relative displacement field with respect to the free field due to the localized geological feature. Thus, the total displacement is expresses as (Bielak et al. 2003a):

$$u_e = u_e^0 + w_e \tag{1.6}$$

Substituting Eq. (1.6) into Eq. (1.3) results in (Bielak et al., 2003a):

$$\begin{bmatrix} M_{ii}^{\Omega} & M_{ib}^{\Omega} & 0 \\ M_{bi}^{\Omega} & M_{bb}^{\Omega} + M_{bb}^{\Omega^+} & M_{be}^{\Omega^+} \\ 0 & M_{eb}^{\Omega^+} & M_{ee}^{\Omega^+} \end{bmatrix} \begin{Bmatrix} \ddot{u}_i \\ \ddot{u}_b \\ \ddot{w}_e \end{Bmatrix} + \begin{bmatrix} C_{ii}^{\Omega} & C_{ib}^{\Omega} & 0 \\ C_{bi}^{\Omega} & C_{bb}^{\Omega} + C_{bb}^{\Omega^+} & C_{be}^{\Omega^+} \\ 0 & C_{eb}^{\Omega^+} & C_{ee}^{\Omega^+} \end{bmatrix} \begin{Bmatrix} \dot{u}_i \\ \dot{u}_b \\ \dot{w}_e \end{Bmatrix} +$$

$$\begin{bmatrix} K_{ii}^{\Omega} & K_{ib}^{\Omega} & 0 \\ K_{bi}^{\Omega} & K_{bb}^{\Omega} + K_{bb}^{\Omega^+} & K_{be}^{\Omega^+} \\ 0 & K_{eb}^{\Omega^+} & K_{ee}^{\Omega^+} \end{bmatrix} \begin{Bmatrix} u_i \\ u_b \\ w_e \end{Bmatrix} = \begin{Bmatrix} 0 \\ -M_{be}^{\Omega^+}\ddot{u}_e^0 - C_{be}^{\Omega^+}\dot{u}_e^0 - K_{be}^{\Omega^+}u_e^0 \\ P_e \; - M_{ee}^{\Omega^+}\ddot{u}_e^0 - C_{ee}^{\Omega^+}\dot{u}_e^0 - K_{ee}^{\Omega^+}u_e^0 \end{Bmatrix} \tag{1.7}$$

By substituting P_e in Eq. (1.5) into Eq. (1.7), the final equation for the DRM is obtained (Bielak et al., 2003a):

$$\begin{bmatrix} M_{ii}^{\Omega} & M_{ib}^{\Omega} & 0 \\ M_{bi}^{\Omega} & M_{bb}^{\Omega} + M_{bb}^{\Omega^+} & M_{be}^{\Omega^+} \\ 0 & M_{eb}^{\Omega^+} & M_{ee}^{\Omega^+} \end{bmatrix} \begin{Bmatrix} \ddot{u}_i \\ \ddot{u}_b \\ \ddot{w}_e \end{Bmatrix} + \begin{bmatrix} C_{ii}^{\Omega} & C_{ib}^{\Omega} & 0 \\ C_{bi}^{\Omega} & C_{bb}^{\Omega} + C_{bb}^{\Omega^+} & C_{be}^{\Omega^+} \\ 0 & C_{eb}^{\Omega^+} & C_{ee}^{\Omega^+} \end{bmatrix} \begin{Bmatrix} \dot{u}_i \\ \dot{u}_b \\ \dot{w}_e \end{Bmatrix} +$$

$$\begin{bmatrix} K_{ii}^{\Omega} & K_{ib}^{\Omega} & 0 \\ K_{bi}^{\Omega} & K_{bb}^{\Omega} + K_{bb}^{\Omega^+} & K_{be}^{\Omega^+} \\ 0 & K_{eb}^{\Omega^+} & K_{ee}^{\Omega^+} \end{bmatrix} \begin{Bmatrix} u_i \\ u_b \\ w_e \end{Bmatrix} = \begin{Bmatrix} 0 \\ -M_{be}^{\Omega^+}\ddot{u}_e^0 - C_{be}^{\Omega^+}\dot{u}_e^0 - K_{be}^{\Omega^+}u_e^0 \\ M_{eb}^{\Omega^+}\ddot{u}_b^0 + C_{eb}^{\Omega^+}\dot{u}_b^0 + K_{eb}^{\Omega^+}u_b^0 \end{Bmatrix} \tag{1.8}$$

The seismic forces P_e in the right hand side of Eq. (1.8) can be replaced by the effective forces P^{eff} which are expressed as (Bielak et al, 2003a):

$$P^{eff} = \begin{Bmatrix} P_i^{eff} \\ P_b^{eff} \\ P_e^{eff} \end{Bmatrix} = \begin{Bmatrix} 0 \\ -M_{be}^{\Omega^+}\ddot{u}_e^0 - C_{be}^{\Omega^+}\dot{u}_e^0 - K_{be}^{\Omega^+}u_e^0 \\ M_{eb}^{\Omega^+}\ddot{u}_b^0 + C_{eb}^{\Omega^+}\dot{u}_b^0 + K_{eb}^{\Omega^+}u_b^0 \end{Bmatrix} \quad (1.9)$$

Since these forces involve only sub-matrices corresponding to the exterior and boundary domain, which vanish everywhere except in a single layer in Ω^+ adjacent to Γ, the forces act within the layer between Γ and its adjacent surface Γ_e as shown in Figure 1.2. As the ground motion near the ROI is considered, the size of the region Ω^+ can be reduced by an exterior region $\widehat{\Omega}^+$and its corresponding outer boundary $\widehat{\Gamma}^+$ (Figure 1.2). By transferring the seismic excitation from the causative fault to the ROI in Step I, the problem within the region is solved in the subsequent step in which the wave field is required at the single layer interface between Γ andΓ_e. Thus, the localized seismic forces P^{eff} provide significant reduction of the computational domain.

1.1.3 Soil-structure interaction for bridge-foundation-ground systems

Significant efforts to further understand the seismic performance of bridges were initiated when the 1971 San Fernando earthquake damaged many bridges including the Northbound Truck Route Undercrossing and the Roxford Street Undercrossing. Among other bridge failures and collapse during the 1994 Northridge earthquake, two connector bridges at the Route 14 and Interstate 5 interchange partially collapsed.

Such observed collapse mechanisms indicated the need for continued studies and assessments. In some cases, SSI was deemed to play a significant role.

In the last decade, seismic analysis of full bridge-foundation-ground systems has been gradually gaining further attention (Jeremic et al. 2004, 2009, Kwon and Elnashai 2008, Zhang et al. 2008, Elgamal et al. 2008). Recent efforts have included more realistic nonlinear materials for the reinforced concrete and soil cyclic loading response, and analysis of liquefaction effects was undertaken (Zhang et al., 2008). Absorbing boundary conditions were addressed in earlier studies to limit fictitious wave reflections (Conte et al., 2002).

Efforts in 3D modeling and analysis of bridges were also reported. Soil vibration induced by high-speed trains on a bridge was studied and isolation effects due to nearby building foundations and piles under the bridge were evaluated (Ju, 2004). Separate models for an elevated highway bridge supported on deep foundations with and without soil-foundation-structure-interaction (SFSI) were considered to evaluate the SFSI beneficial and detrimental effects (Jeremic et al., 2004). Nonlinear-dynamic analysis for a bridge-foundation-ground system was conducted for estimation of settlement and longitudinal/transverse displacements of the abutments and pile foundations due to permanent ground deformation (Elgamal et al., 2008). Using recorded data, responses from a multiplatform simulation of a highway overcrossing bridge were compared for the integrated bridge-ground system as well as for substructures such as the pile foundations and the abutments (Kwon and Elnashai, 2008). Repair concepts such as cost and time loss were addressed using nonlinear time history analysis of a typical highway overpass bridge founded on different soil profiles (Mackie et al., 2012).

High-fidelity models for SFSI were developed to simulate seismic wave propagation (frequency up to 10 Hz) through nonlinear elastic-plastic, soil, piles, and

bridge analyses (Jeremic et al. 2009). Difference in ground motions due to presence of the structure showed that treatment of free-field motions as input for the structural model can be inadequate. Finally, response from simulation models was validated against results of ¼ scale experimental tests as reported by Dryden (2009).

1.2 Objectives and Scope

The 3D nature of a numerical seismic analysis including a causative fault, resulting wave propagation through a large-scale soil domain (depending on a distance from the seismic source), and corresponding ground response imposes significant computational challenges. However, the DRM approach provides a dramatic reduction in overall computational effort. In the end, a relatively efficient model of a large soil domain localized ROI becomes possible. On this basis, the opportunity to conduct SSI studies (within this localized ROI) becomes possible.

As such, the ROI as implemented by Petropoulous (2008) offers a numerical platform to assess seimic loads for overlying super-strucutres such as bridge systems and interchanges. Studies of the full bridge-foundation-ground system (BFGS) configuration, as well as comparisons to results from representative asynchrnous (or unifrom) base ground excitation can be performed.

The overall objective of the research presented in this report is to advance the procedures for conducting large-scale numerical simulations for SSI applications. As a main application, the seismic response of a large highway 3-bridge exchange is modeled and investigated. Salient characteristics dictated by the high stiffness of large embedded

structures are also explored. To achieve this objective, the following specific tasks are addressed:

- Modeling of the highway interchange bridge connectors
- Validation of the bridge modeling procedures using strong motion data recorded for one of these bridge connectors
- Evaluation of the vibration characteristics of the bridge models
- Modeling of the large scale bridge-foundation-ground system (BFGS) using the DRM technique and the ROI
- Evaluation of the effects of soil characteristics (ROI) on the response of the BFGS (linear and nonlinear soil behavior scenarios considered)
- Assessment of fixed-base seismic bridge analyses in light of the BFGS response
- Development and validation of the BFGS model based on the actual local soil conditions and site seismicity characteristics.
- Evaluation of some of the salient response mechanisms associated with the geometry and mass characteristics of large rigid embedded structures (preliminary effort)

1.3 Organization

This report is organised as follows:

This chapter (Chapter 1) presents objectives, scope and layout of the report. A brief review of the relevanr background literature is included.

Chapter 2 presents the details of the FE ROI implementation as reported by Petropoulos (2008). In this effort, earthquake ground motion due to a fault rupture scenario is southern california is employed (the Puente Hills Fault). To this end, some important challenges associated with the FE DRM implementation (for the purposes of this report) are highlighted.

Chapter 3 describes the selected highway interchange and the local topography and site characteristics (3 bridge connectors at the intersection between interstates 10 and 215 in San Bernardino, California). The instrumentation layout and recorded strong motion for one of the conenctors are presented and discussed. Seismic retrofit implemented for these connectors is described. Validation of the modeling techniques is addressed through comparison of the numerical response to recorded strong motion records during a number of past earthquakes.

Chapter 4 is concernd with analysis of the BFGS. Three bridge connectors at the interchange are considered as the structural models. Modeling of the foundations, composed of pile caps and piles, are described. The ROI is adapted as the ground model. Subjected to the seismic input motions discussed earlier in Chapter 2, the corresponding response of the BFGS is addressed.

Chapter 5 evaluates the SSI effects for the BFGS in which one of the bridges, the North-West connector, and the ROI with two types of soil characteristics (stiff and soft soil scenarios) are emloyed. Additional analyses of a fixed-base structure without the soil domain are conducted under multiple support excitation and uniform excitation (using the spatial ground surface motions dictated by the ROI in the absence of the structure).

Chapter 6 presents an analysis of the BFGS with soil nonlinearity in the upper layers. The corresponding responses of the BFGS are discussed. As conducted in Chapter 5, an additional analysis for the fixed-base structure is performed and comparisons are made with the ROI BFGS results.

Chapter 7 describes a developed BFGS model based on the actual local soil conditions at the North-West (NW) connector. Under a potential site specific strong ground motion, response of this system is assessed in terms of displacement and force demands in the bridge columns. An additional bridge model with bilinear moment-curvature behavior for the columns is used to assess the column demands against their idealized capacities.

Chapter 8 studies response of a large rigid structure embedded at a considerable depth within the ROI. Effects of soil characteristics and different embedment levels on the system response are discussed. In order to isolate and study the effects of kinematic interaction, an additional massless structural model scenario is considered and its results are discussed.

Chapter 9 presents a seismic response study of a fully embedded structure in a linear soil domain under uniform excitation. Depending on soil stiffness, a comparison of acceleration response at the top and the base of the structure with the surrounding free-field response is undertaken. Lateral maximum dynamic soil pressure along the height of the structure and the normal maximum base pressure are also discussed.

Finally, Chapter 10 completes this report with concluding remarks. Recommendations are provided for further future research.

Appendix A contains additional plots depicting comparisons of numerical response with the recorded strong motion of the NW bridge connector. Appendix B provides additional ground responses obtained from the linear and nonlinear soil profiles by the employed DRM implementation of Petropoulos (2008). Appendix C provides additional results related to the studies of Chapter 4. Appendix D presents additional plots from the bridge-foundation-ground system caused by the effect of soil nonlinearity (Chapter 6). Appendix E presents additional plots related to the studies of Chapter 7.

1.4 Acknowledgements

Chapter 1 contains material published in the Earthquake Geotechnical Engineering Design (Geotechnical, Geological and Earthquake Engineering, Vol. 28, Springer) titled “Seismic Response of a Large-Scale Highway Interchange System” with authors, Kyung Tae Kim, Ahmed Elgamal, George Petropoulos, Aysegul Askan, Jacobo Bielak, and Gregory L. Fenves (2014). The dissertation author is the first author of this paper.

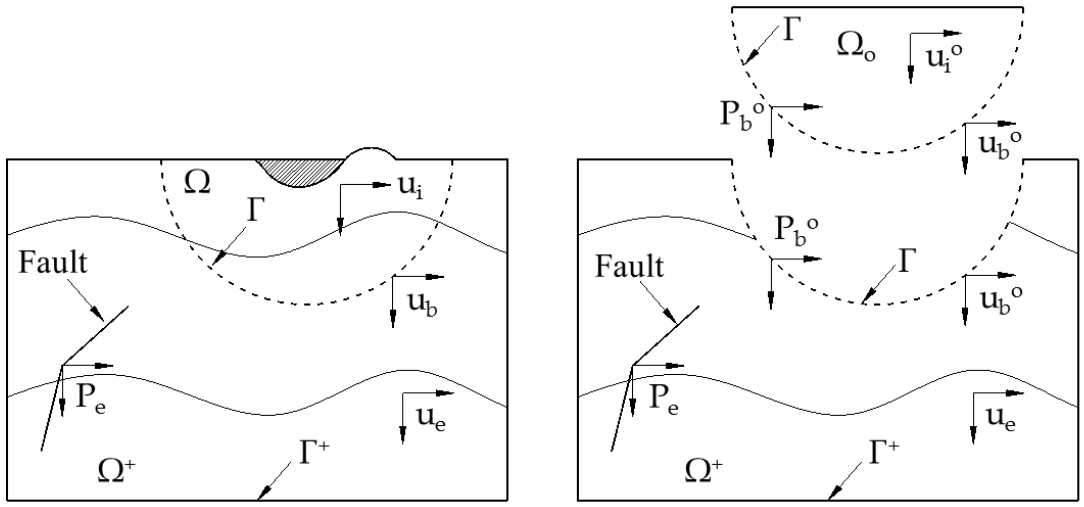

(a) (b)

Figure 1.1: Truncated seismic region. (a) Outer boundary Γ^+ restricting computations to a finite domain into two subdomains: Ω^+ including the seismic source P_e, and Ω containing the localized geological features (b) Regions partitioned explicitly into two substructures across interface Γ (Bielak et al., 2003a)

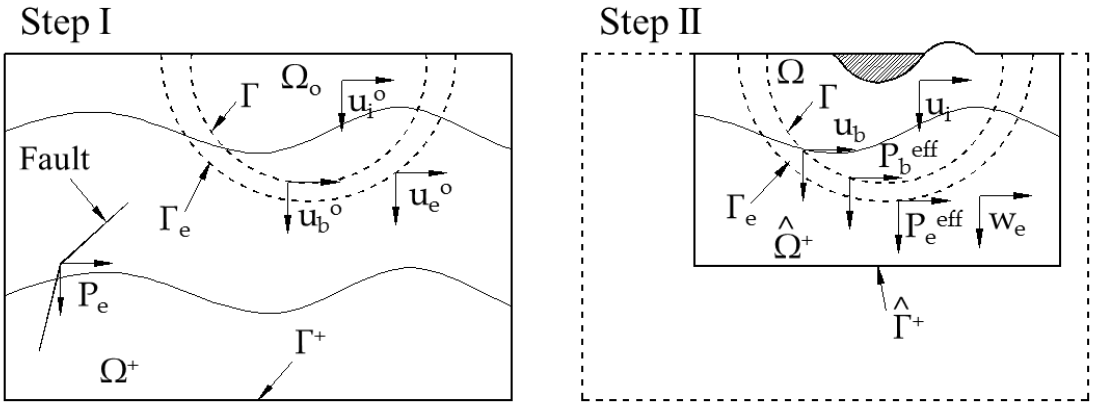

(a) (b)

Figure 1.2: Summary of two-step DRM. (a) Step I: the background geological model to evaluate effective seismic forces P^{eff} (b) Step II: For the reduced region applying the effective seismic forces P^{eff} (within Γ and Γ_e) for the total displacement u_i in Ω and u_b on Γ, and the residual displacements w_e in $\widehat{\Omega}^+$ (Bielak et al. 2003a)

Chapter 2

Ground Response of the Region of Interest

This chapter presents modeling details concerning the Region of Interest (ROI) developed and implemented by Petropolous (2008) on the basis of the Domain Reduction Method (Bielak et al. 2003a). Using low frequency excitation resulting from a realistic fault rupture scenario with superposed broadband inputs, the corresponding ground response is presented and described.

2.1 Region of interest

2.1.1 Domain Reduction Method (DRM) box

As discussed earlier in Section 1.1.2, the Domain Reduction Method (DRM) has been shown to be a robust approach for application of earthquake excitation over a large spatial domain (Bielak et al. 2003a). This approach is employed to create a numerically implemented region of interest (ROI) as described by Petropolous (2008). This ROI is defined as a DRM box with size of 1000 m by 500 m by 100 m as shown in Figure 2.1. In terms of input motion excitation, it was decided to locate this ROI near Los Angeles in California (Figure 2.2) with latitude 34° 5’ 32” N and longitude 118° 19’ 42” W (Petropoulos 2008). Soil material properties as selected by Petropoulos (2008) are shown in Table 2.1 (two layers are specified in the DRM box).

Numerical modeling was developed and performed using OpenSees, an object-oriented, open-source FE analysis framework (McKenna 1997). A special purpose highly efficient 3D brick element was developed (Petropolous 2008) as part of the overall parallel processing implementation framework (Fast Linear Brick (FLB) element). For the stiff soil (Table 2.2) low frequency excitation scenario, uniform 20 m cubical elements for the soil domain were employed with elastic material properties (Petropoulos 2008). This soil domain in this scenario includes 156,156 nodes and 146,250 linear brick elements.

2.1.2 Buffer zone

Petropolous (2008) employed a buffer zone as an absorbing boundary condition to limit fictitious reflections from incident seismic waves back into the ROI (Figure 2.3). As defined for modeling of the DRM box, this 400 m buffer zone has uniform 20 m cubical elements with elastic material properties (Table 2.2). The entire computational domain (Figure 2.3) becomes of the dimensions 1.8 km by 1.3 km by 0.5 km in the X, Y, and Z directions, respectively. The total number of elements in the computational domain becomes 146,250. In addition to this buffer zone, the Lysmer absorbing boundary (Lysmer and Kuhlemeyer, 1969) in the form of dashpots was employed along the outer boundaries of the buffer zone for energy absorption.

2.1.3 Viscous damping

Mass proportional viscous damping was used to represent energy dissipation in the soil based on the recommendations in (Olsen et al., 2003). The damping is defined according to:

$$\zeta = \begin{cases} 25/V_S(m/sec) \; if \; V_S \leq 1500 \, m/sec \\ 5/V_S(m/sec) \quad otherwise \end{cases} \tag{2.1}$$

Petropolous (2008) defined the coefficient for the damping α as:

$$\alpha = 7.2492\zeta \tag{2.2}$$

with the damping matrix defined by:

$$C = \alpha M \tag{2.3}$$

It is noted here that the adopted diagonal mass matrix (and consequently, the diagonal damping matrix) results in major numerical advantages in the employed soil domain explicit integration simulations of Petropoulos (2008). Specifically, this numerical framework greatly reduces the communications needed in conducting the performed multi-processor parallel computations (Petropoulos 2008).

2.1.4 ROI input seismic excitation

The ROI is analyzed (Petropoulos 2008) for low frequency excitation (some cases with added broadband inputs) resulting from a scenario of a magnitude 7.1 (moment magnitude) rupture of the Puente Hills fault (see Figure 2.4 for the location of the ROI with respect to the fault). The Puente Hills fault low frequency motion is the outcome of a large-scale simulation conducted by Professor Jacobo Bielak at Carnegie Mellon University (see Table 2.3 for the rupture characteristics). The input motions were made available by Dr. George Petropolous (for the purposes of this report) in 6 ASCII files in terms of velocities (for each investigated soil property case as shown in Tables 2.1 and 2.2). These velocities (3 entries per time step which are components in X, Y, and Z directions) are defined for 70,080 boundary nodal locations with grid size of 4 m by 4 m by 2 m in 3001 times steps. In the 20 m element length case, these velocities are

interpolated and applied to 14,170 boundary nodal locations of the DRM Box. Input motions for the cases of low frequency, broadband, stiff soil, and soft soil are provided.

2.2 Computational Challenges associated with implementation of the DRM ROI

In the initiation of the research effort reported herein, a numerical formulation that allowed for versatility in modeling stiff structural elements and nonlinear response was envisioned. As such, the soil domain explicit integration implementation (Petropolous 2008) as described briefly in the next section was changed in the following main respects:

1. The current operational version of OpenSees was employed, rather than the Petropoulos (2008) special purpose code. In this version, the standard OpenSees 3D brick element (stdBrick) was used.

2. Instead of the Petropolous (2008) explicit integration formulation, implicit integration was adopted. This overcomes the explicit integration stringent limitations on time step size, but necessitates iterations to achieve convergence. In conducting implicit integration, massive communications take place between the involved processors within the employed parallel computing environment. As such, the solver MUMPS was employed within OpenSeesSP (Single OpenSees Parallel Interpreter, http://opensees.berkeley.edu/OpenSees/parallel/parallel.php).

3. Within this new implicit integration numerical framework, OpenSeesSP requires that the entire FE model resides on one processor first before the FE mesh is

partitioned (Figure 2.5). It was possible to accomplish this task for the 20 m brick soil element with a total number of elements of about 150,000. In this case, the needed processor memory was under 8 GB. Efficient execution of the parallel implicit integration computations was found for this case to occur when 32 processors were employed (larger number of processors results in longer communication computation time between these processors).

4. For the Petropoulos (2008) stiff soil case (Table 2.2), the 20 m brick element permitted 8 nodes to represent a wavelength that corresponds to a maximum frequency of 1 Hz (the narrow band input excitation). For this same soil domain using 10 m brick elements (appropriate for softer soil at a maximum frequency of 1 Hz), the total number of elements is 1.2 million. Such a mesh requires memory space on a single processor (at least 1,000 GB using the employed OpenSeesSP code) well beyond that is available anywhere today (at least as far as the author knows). For that reason, it was not possible to employ a finer soil mesh (within the framework of the adopted implicit integration formulation), for cases of softer soil, or input excitation of higher frequency (the broadband motion).

5. Within the original explicit integration formulation (Petropoulos 2008), it is conceptually possible to extend the analysis scheme towards inclusion of the Bridge super-structure models (supported on the DRM-ROI of the soil mesh). However, the spatially interconnected bridge system necessitates additional substantial work to handle the increased communication between different processors, as dictated by the super-structure connectivity characteristics. In the end, this work requires additional efforts that are well beyond the scope of the current scope, and can be addressed in future studies.

Possibilities include: i) modification and extension of the special purpose C++ codes written by Petropolous (2008) to conduct his studies, or ii) implementation of the newly developed OpenSeesMP platform software to operate on the particular specific parallel computer of interest (http://opensees.berkeley.edu/OpenSees/parallel/parallel.php).

2.2.1 Petropolous (2008) Meshes and Numerical procedures

Based on the DRM (Bielak et al. 2003a), Petropolous (2008) developed appropriate finite element meshes to represent the region of interest (ROI) for stiff and soft soils, as well as for low frequency (up to about 1 Hz) and broadband input excitation (up to 5 Hz). For instance, the soft soil profile with the low frequency input excitation was considered. In this case, the top 30 m layer was a uniform layer with a shear wave velocity (V_s) of 160 m/s. For the underlying ROI 70 m strata, one half V_s of the stiff soil profile was employed (in which a 20 m brick element was used) as discussed in section 2.1. In order to have a mesh with 8 nodal points per wave-length at the target frequency of 1 Hz, a higher resolution in modeling the ROI was necessary. As such, the soft soil was analyzed using a 10 m brick element. With a 400 m buffer zone, the number of elements was 1.17 million.

In an analogous fashion, Petropolous (2008) studied the stiff soil profile with the broadband input excitation as discussed in section 2.1.4. For the target input frequency of 5 Hz, the stiff soil was analyzed using a mesh size of 5 m x 5 m x 2.5 m. With a 400 m buffer zone, the number of elements was 18.7 million.

To implement these large size meshes, a special purpose Fast Linear Brick (FLB) element was developed (Petropoulos 2008), optimized for linear elastic analysis. For

scalability of the employed explicit FE formulation (to use a large numbers of processors of up to 2048 in a parallel computation), a C++ code parallel diagonal solver was also developed (Petropolous 2008).

Petropolous (2008) extended a mixed explicit-implicit time integration scheme such as mE-I time integration (Liu and Belytschko 1982) that allows for modeling nonlinear systems in the implicit partition. Using this mixed time integration approach, a soil-foundation-structure interaction model using simplified 6 degree-of-freedom and lumped mass oscillators was conducted. The soil in the ROI was modeled by uniform 5 m brick elements (18.7 million FLBrick elements analyzed on 1024 processors) for the soft soil profile using the low frequency input.

In the following chapters, the main effort was dedicated to the modeling of extended super-structure models over the ROI (such as bridge systems). For such models, additional substantial work is needed to modify the above-described schemes as implemented by (Petropolous 2008). Highlights of this additional work include:

1. Partition the soil mesh into several processors that are to be integrated explicitly (e.g., using a distributed diagonal solver in mEI_E).

2. Partition the structural model into implicit parts (and possibly use a banded symmetric positive definite solver in mEI_I).

3. Partition the soil-structure interface degrees of freedom into the implicit part (e.g., using mEI_Intfc).

4. Build a communication scheme between the explicit and implicit partitions, to permit parallel computation.

In order for such a mixed time integration scheme to be implemented on the OpenSees platform, a major effort that involves a thorough understanding (and coding capabilities) of OpenSees modeling classes for parallel meshing, partitioning, and solving (written in C++) is required. Such a task is deemed to be well beyond the scope of the current effort.

2.2.2 Limitations in modeling the ROI in this report

Due to the above-described challenges in modeling the ROI with overlying extended structures, the employed soil mesh was limited to the 20 m brick element as coded in the current OpenSees platform (version of 2.4.0). As such, higher frequencies in excess of 1 Hz are captured only with increasingly reduced accuracy. Therefore, the results may not convey an adequately accurate picture of spatial variability, frequency content, and/or peak response due to the frequency components in excess of 1 Hz.

2.3 ROI Seismic Response

2.3.1 Parallel computing approach

The DRM simulations in this report are conducted on the parallel computer *Ranger* at the University of Texas, Austin. Linear and nonlinear analyses are conducted. No gravity loads are applied. For this dynamic analysis, the incremental-iterative procedure used to integrate the equations of motion employed the Newmark-β time-stepping method with the time integration parameters $\gamma = 0.5$ and $\beta = 0.25$. The

simulation (with the employed 20 m length brick element) required about 48 hours clock-time with a time step of 0.02 seconds.

2.3.2 Simulation results using the low frequency input

Figure 2.6 shows acceleration time histories at the ROI surface center node (Stiff soil profile of Table 2.2). The Fourier amplitude spectra of the corresponding accelerations are shown in Figure 2.7. In general, frequency contents are in the range of 0.1 Hz to 1 Hz as dictated by the employed low frequency fault rupture scenario (Petropoulos 2008). This ground response (Figure 2.6) is essentially in the form of near-fault ground motions depicting a predominant velocity pulse (Figure 2.8) and a resulting permanent displacement pulse (see Figure 2.9).

As shown in Figure 2.10 through Figure 2.12, spatial variation of ground motions is displayed. In view of the employed rupture scenario, the variation in the X component is more noticeable than in the Y component along the ROI X center-line and vice versa along the Y direction. Below the surface center node, acceleration time histories are also shown in Figure 2.13. Due to the relatively stiff soil profile (Table 2.2), peak acceleration is nearly the same within the upper 80 m of the 100 m deep ROI.

2.3.3 Simulation results using the broadband input

Seismic response of the ROI for the broadband input is discussed. Figure 2.14 shows acceleration time histories at the ROI surface center node. Fourier amplitude spectra of the accelerations are shown in Figure 2.15. In this figure, frequency contents are not only in the range of 0.1 Hz to 1 Hz but also in the range of 1.5 Hz to 4.5 Hz as a

result of superposition of the low frequency generated deterministically and higher frequency generated stochastically (Petropoulos 2008). Consequently, the broadband input would be expected to induce a larger acceleration response for structures of high frequency resonances (Figure 2.16).

Similar to the result for the low frequency input, ground response is generally in the form of a near-fault ground motion depicting a predominant velocity pulse (Figure 2.17) and a resulting permanent displacement (Figure 2.18). As shown in Figure 2.19 through Figure 2.21, a spatial variation of ground motion is displayed. Below the ROI surface center node, higher variation of peak accelerations is observed compared to the low-frequency input case (Figure 2.22).

2.4 Acknowledgements

Chapter 2 contains material published in the Earthquake Geotechnical Engineering Design (Geotechnical, Geological and Earthquake Engineering, Vol. 28, Springer) titled “Seismic Response of a Large-Scale Highway Interchange System” with authors, Kyung Tae Kim, Ahmed Elgamal, George Petropoulos, Aysegul Askan, Jacobo Bielak, and Gregory L. Fenves (2014). The dissertation author is the first author of this paper.

.

Table 2.1: Material properties for actual and simplified soil profile (Petropolous 2008)

Layer	Density (t/m^3)	V_p (m/s)	V_s (m/s)	Thickness (m)
1	1.5	404.7	164.9	5
2	1.5	1163.5	385.4	10
3	1.5	1337.3	482.2	40
4	1.714	1622.4	584.3	50
5	2.054	2372.9	651.3	50

Table 2.2: Material properties for the stiff soil profile (Petropolous 2008)

Layer	Density (t/m^3)	Vp (m/s)	Vs (m/s)	Thickness (m)	Region
1	1.5	1337.3	482.2	40	Region of Interest
2	1.714	1622.4	584.3	60	Region of Interest
3	1.714	1622.4	584.3	340	Buffer Zone
4	2.054	2372.9	651.3	60	Buffer Zone

Table 2.3: Characteristics of the Puente Hills fault rupture (Petropolous 2008)

Hypocenter global coordinates (X,Y,Z)	(55483.080, 71728.404, 10580.420)
Type of source	Plane
Moment magnitude	7.109162
Extended hypocenter along strike (m)	11500
Extended hypocenter down dip (m)	18900
Extended strike angle (deg)	289
Extended dip angle (deg)	27
Extended average rupture velocity (m/sec)	2800
Source function type	Quadratic
Average rise time (sec)	0.5

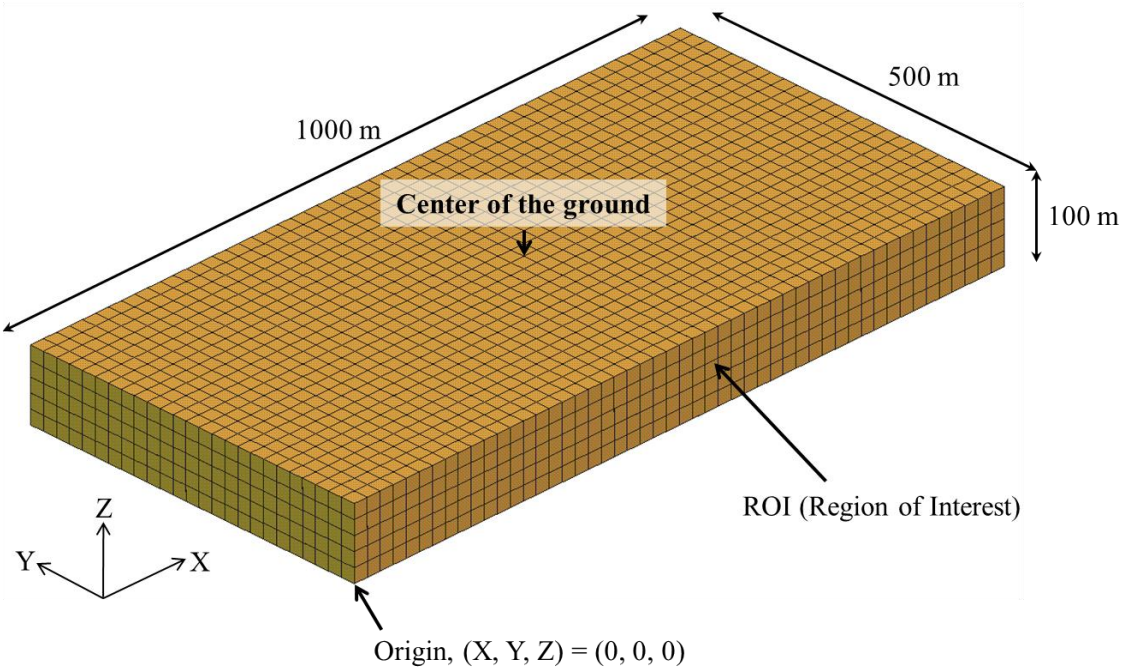

Figure 2.1: DRM box for the region of interest; the origin is 100 m below the surface (Petropoulos, 2008)

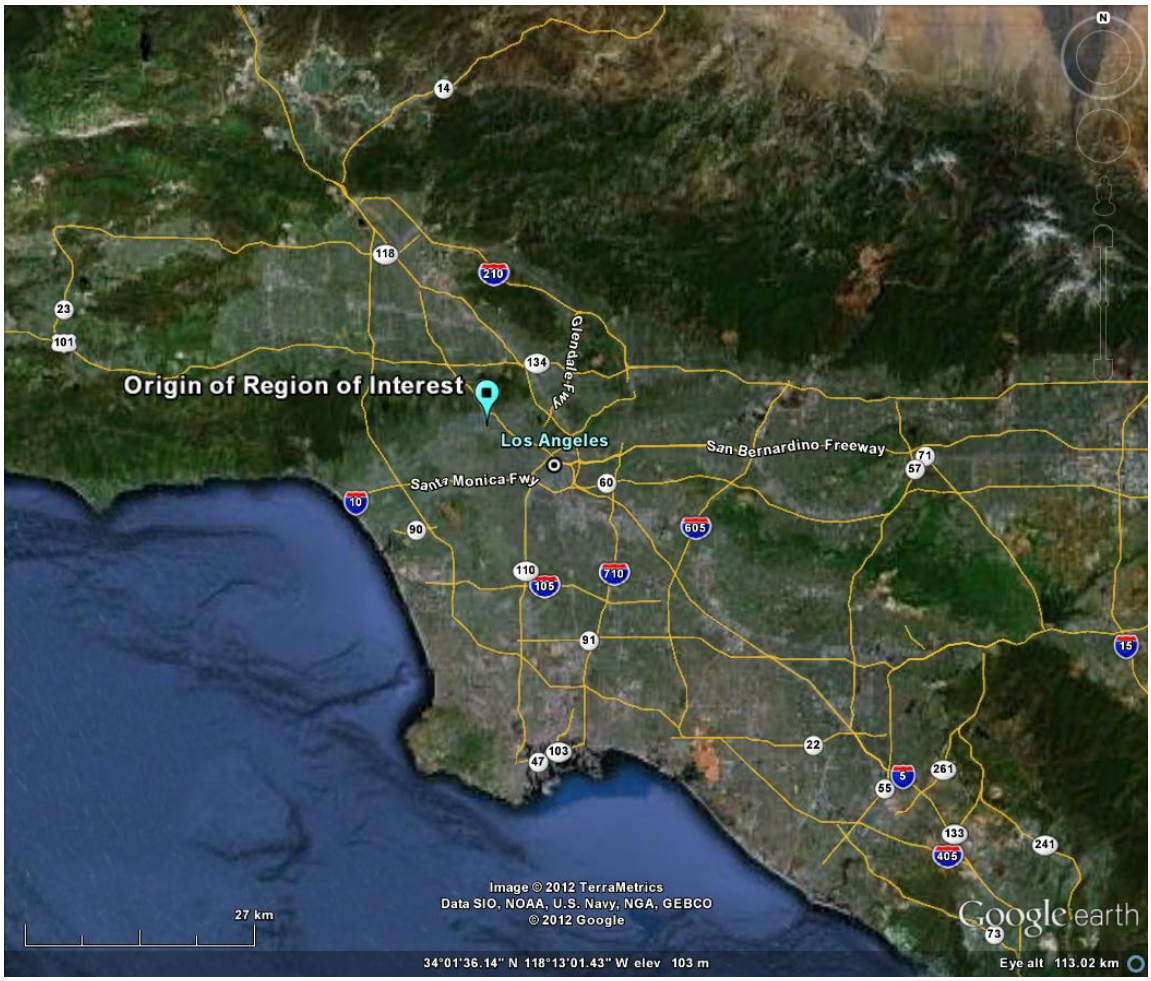

Figure 2.2: Origin of the ROI: latitude 34° 5’ 32” N and longitude 118° 19’ 42” W (©2013 Google - http://maps.google.com)

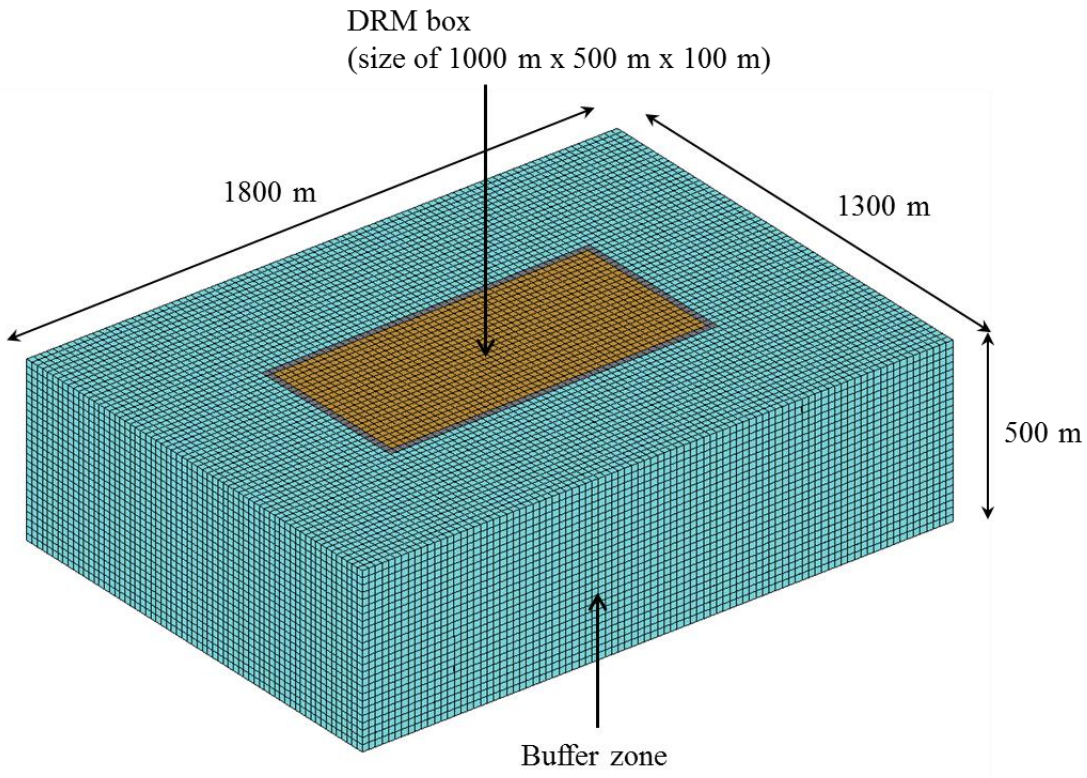

Figure 2.3: The entire DRM FE mesh for the ROI including the buffer zone (Petropoulos, 2008)

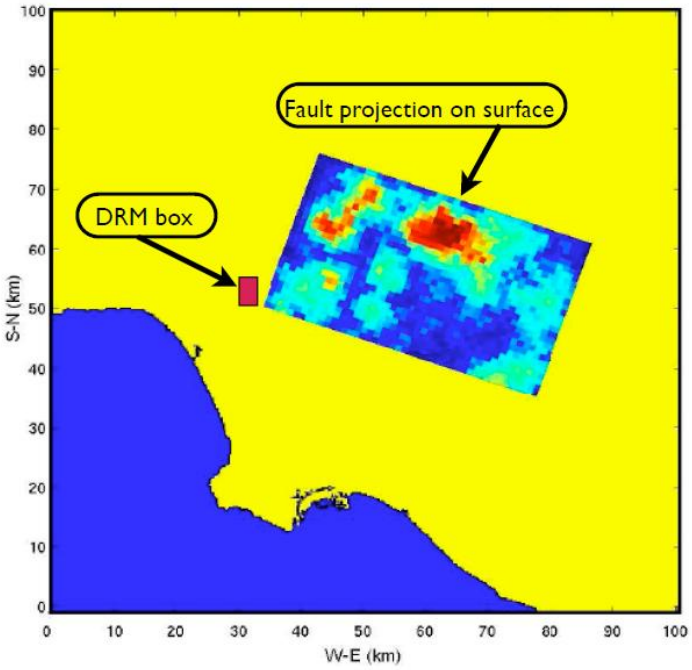

Figure 2.4: The position of the region of interest with respect to the fault projection (Petropolous 2008)

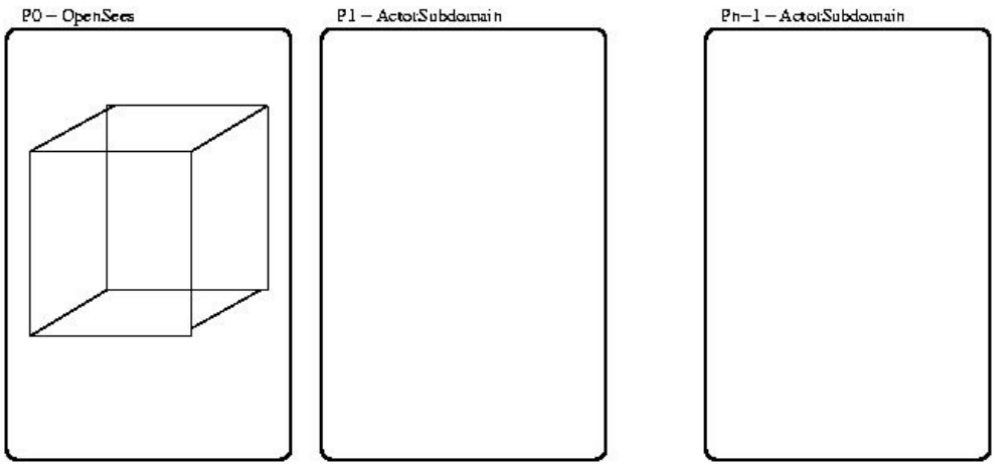

(a) Before an "analyze" command is invoked

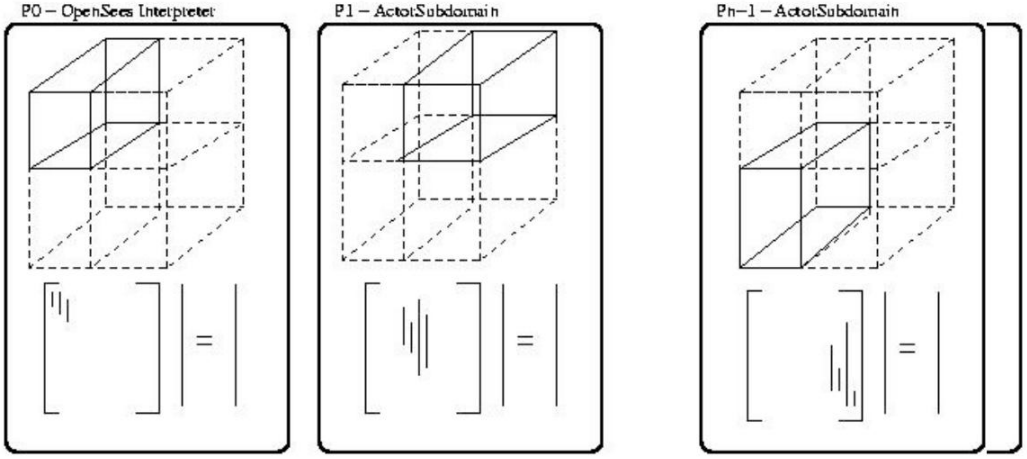

(b) After an analyze command is invoked, the model is partitioned: elements are split and distributed among all n-1 machines

Figure 2.5: Schematic of the partition approach in OpenSeesSP (McKenna and Fenves, 2007)

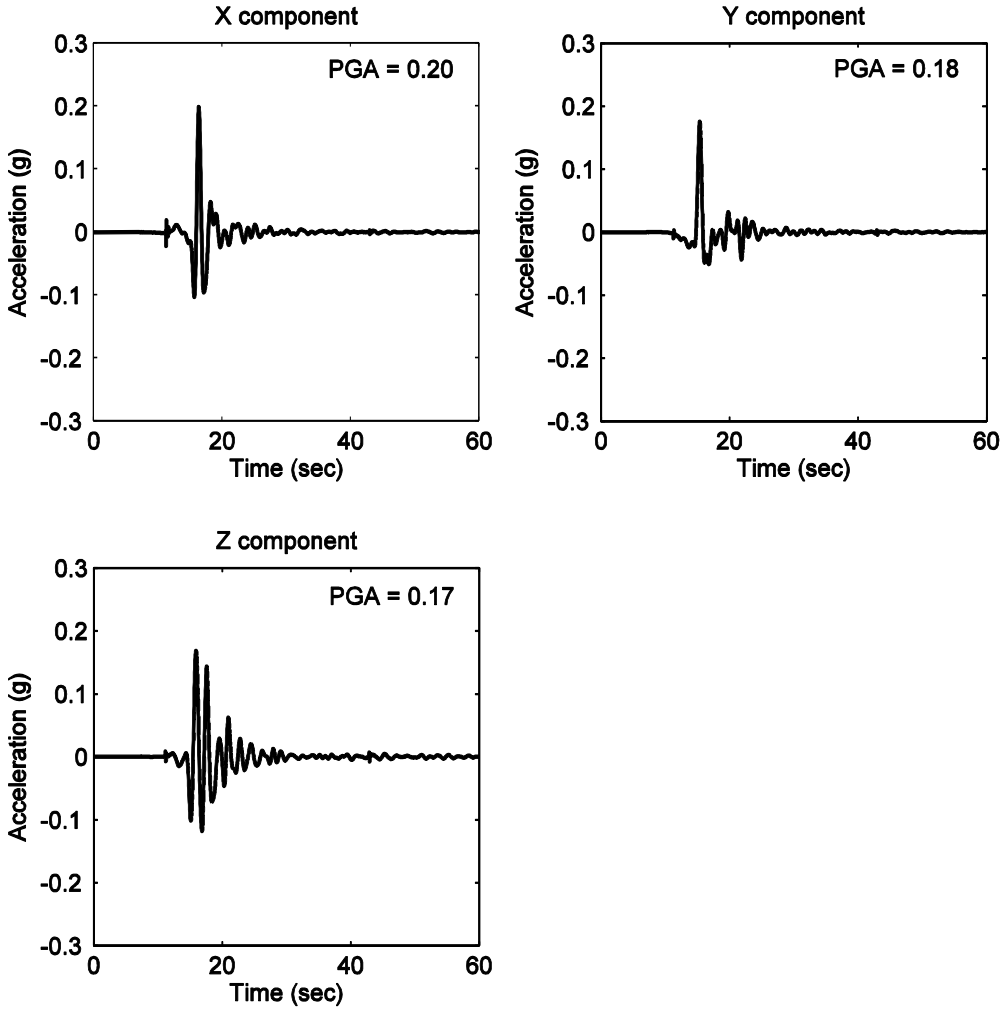

Figure 2.6: Acceleration time histories at the ROI surface center node using the low frequency input (Petropolous 2008)

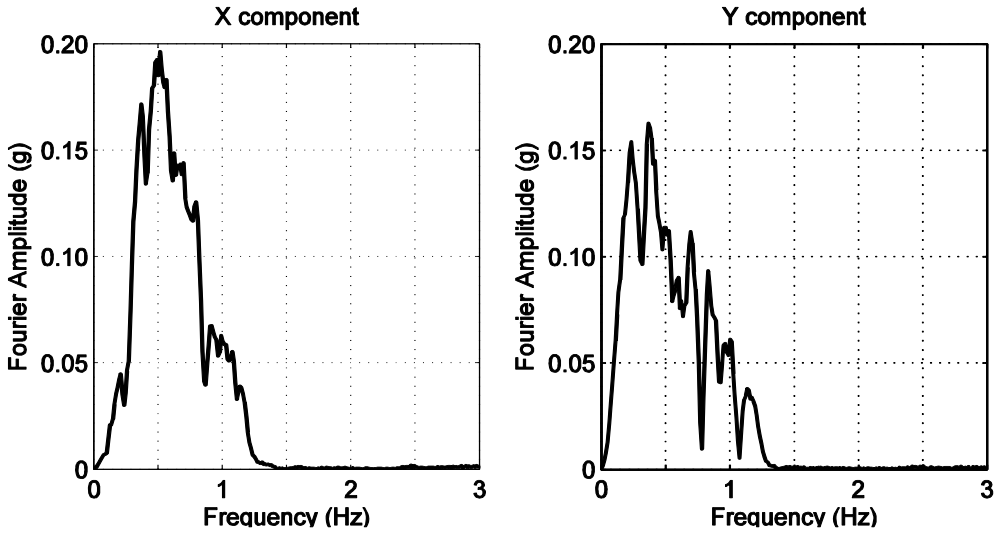

Figure 2.7: Fourier amplitude spectra of ground accelerations at the ROI surface center node using the low frequency input (Petropolous 2008)

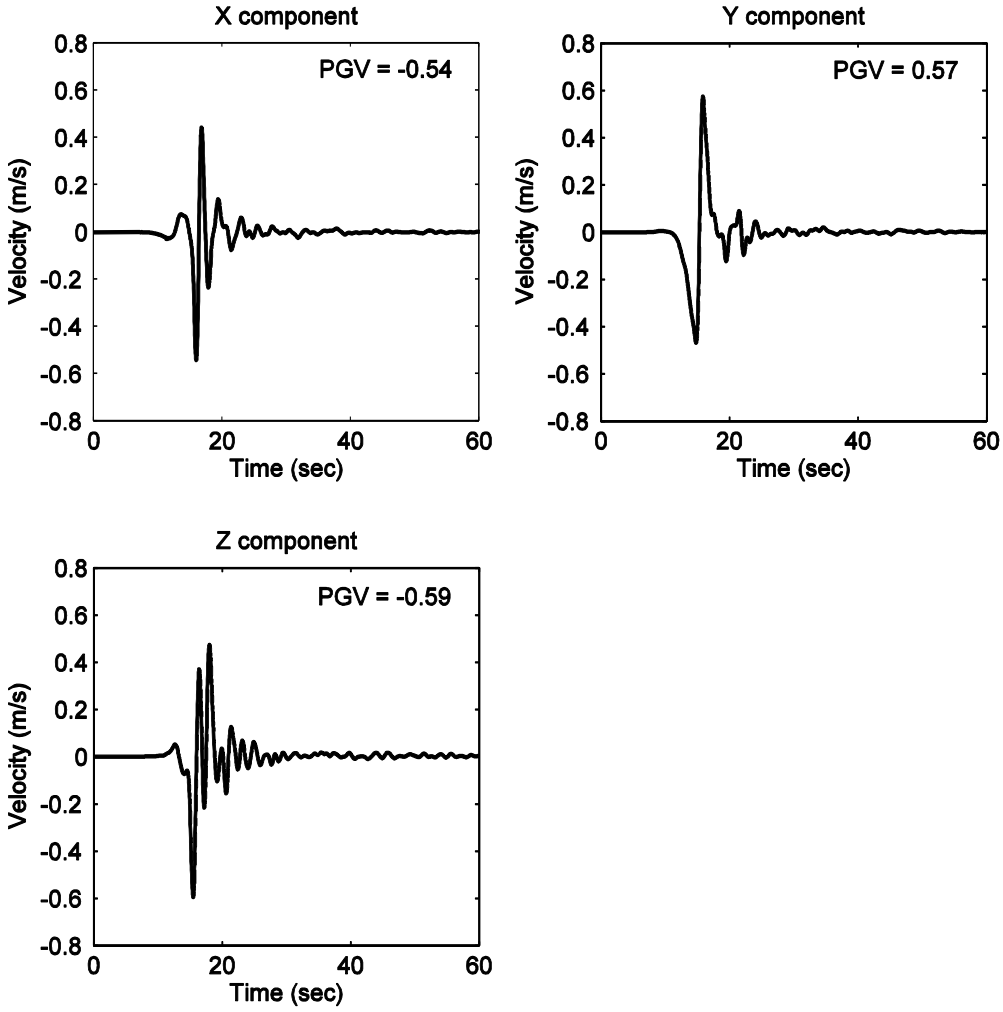

Figure 2.8: Velocity time histories at the ROI surface center node using the low frequency input (Petropolous 2008)

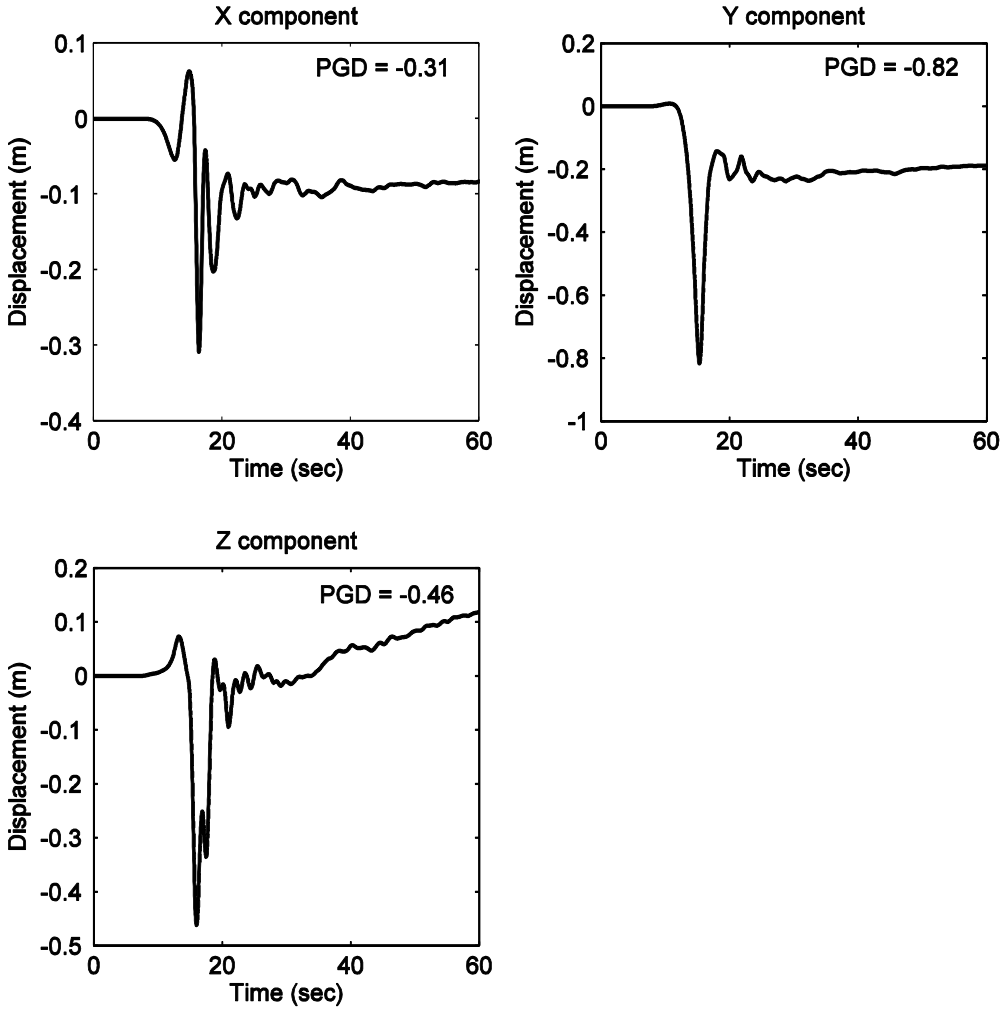

Figure 2.9: Displacement time histories at the ROI surface center node using the low frequency input (Petropolous 2008)

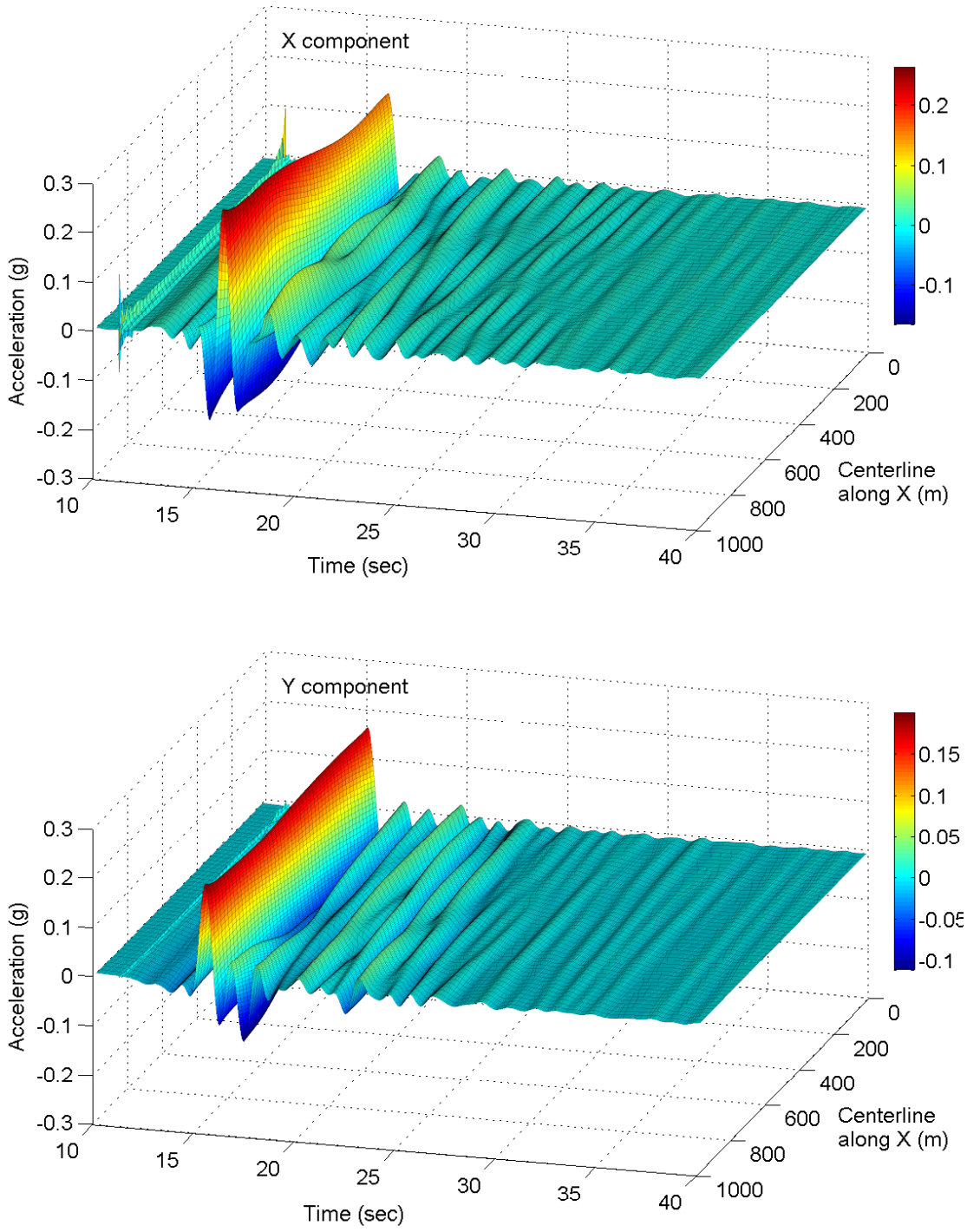

Figure 2.10: ROI X (top) and Y (bottom) components of the ground accelerations along the X center line using the low frequency input (Petropolous 2008)

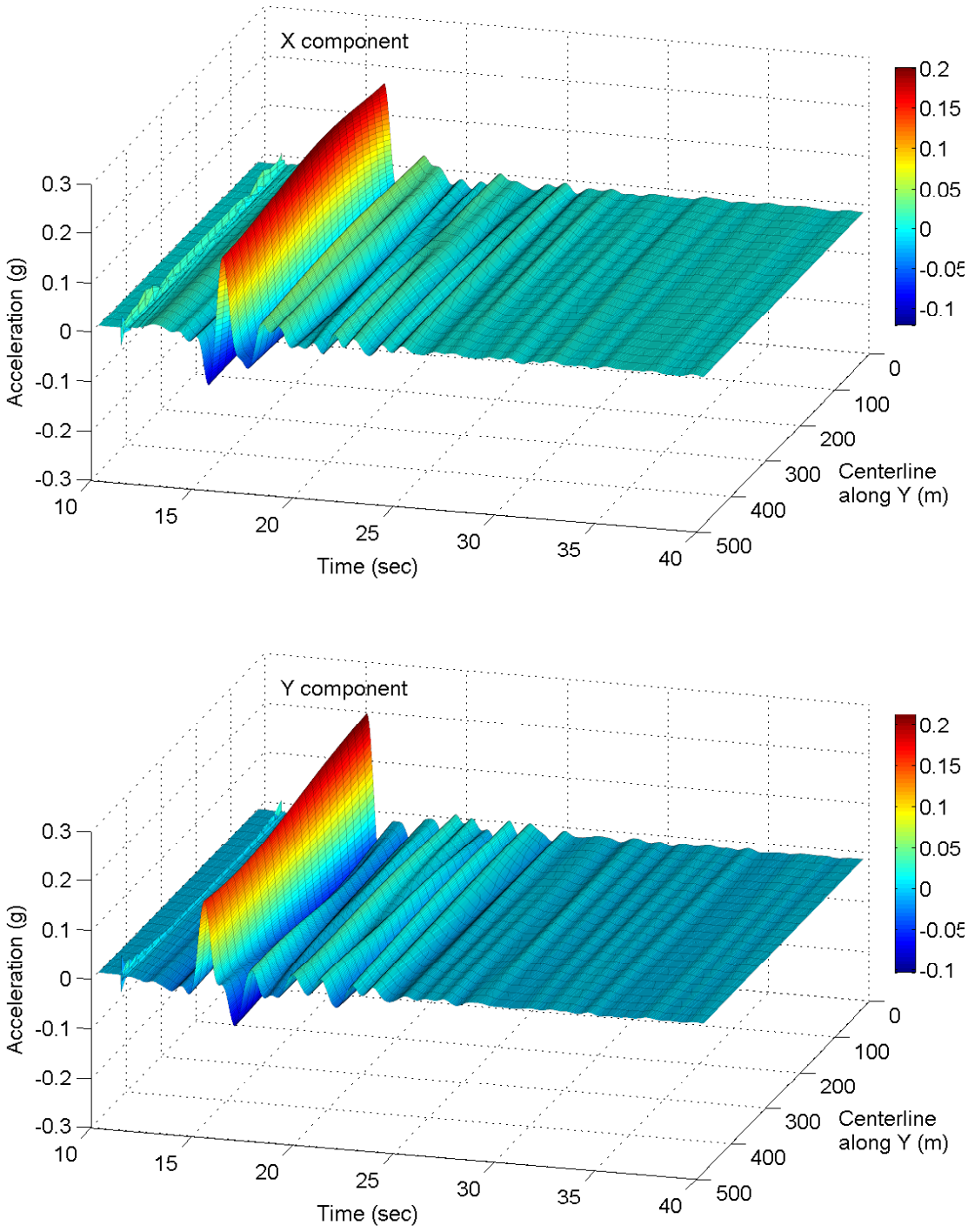

Figure 2.11: ROI X (top) and Y (bottom) components of the ground accelerations along the Y center line using the low frequency input (Petropolous 2008)

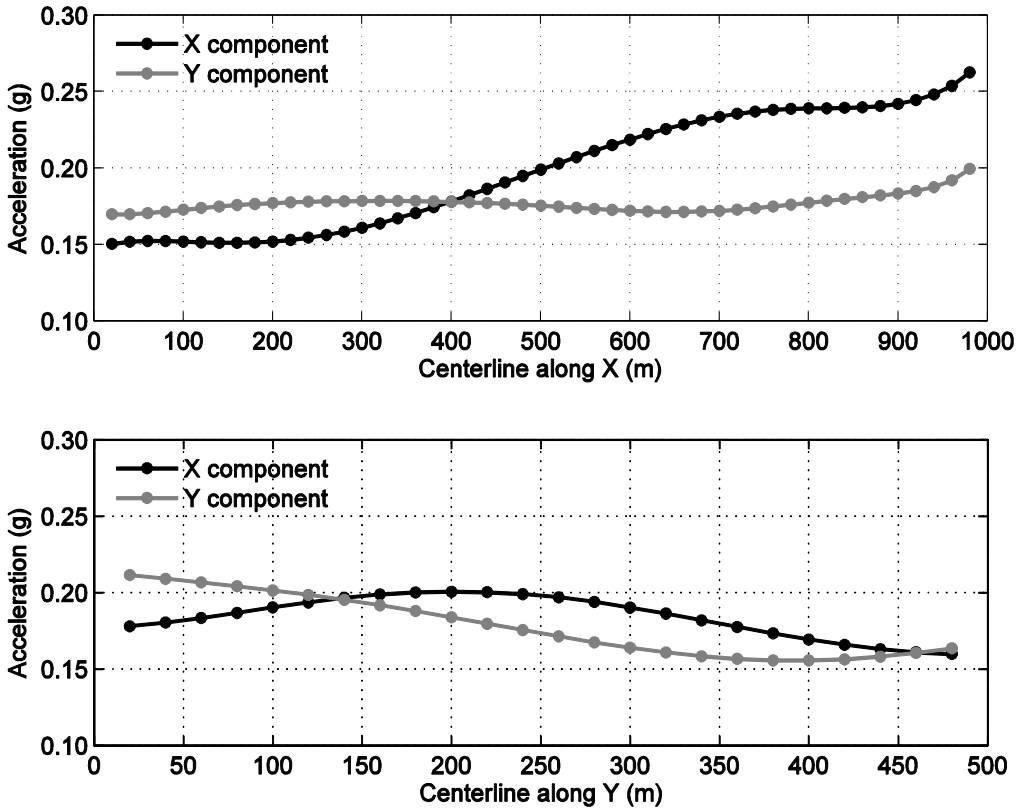

Figure 2.12: Maximum surface acceleration distributions along the ROI X and Y center lines using the low frequency input (Petropolous 2008)

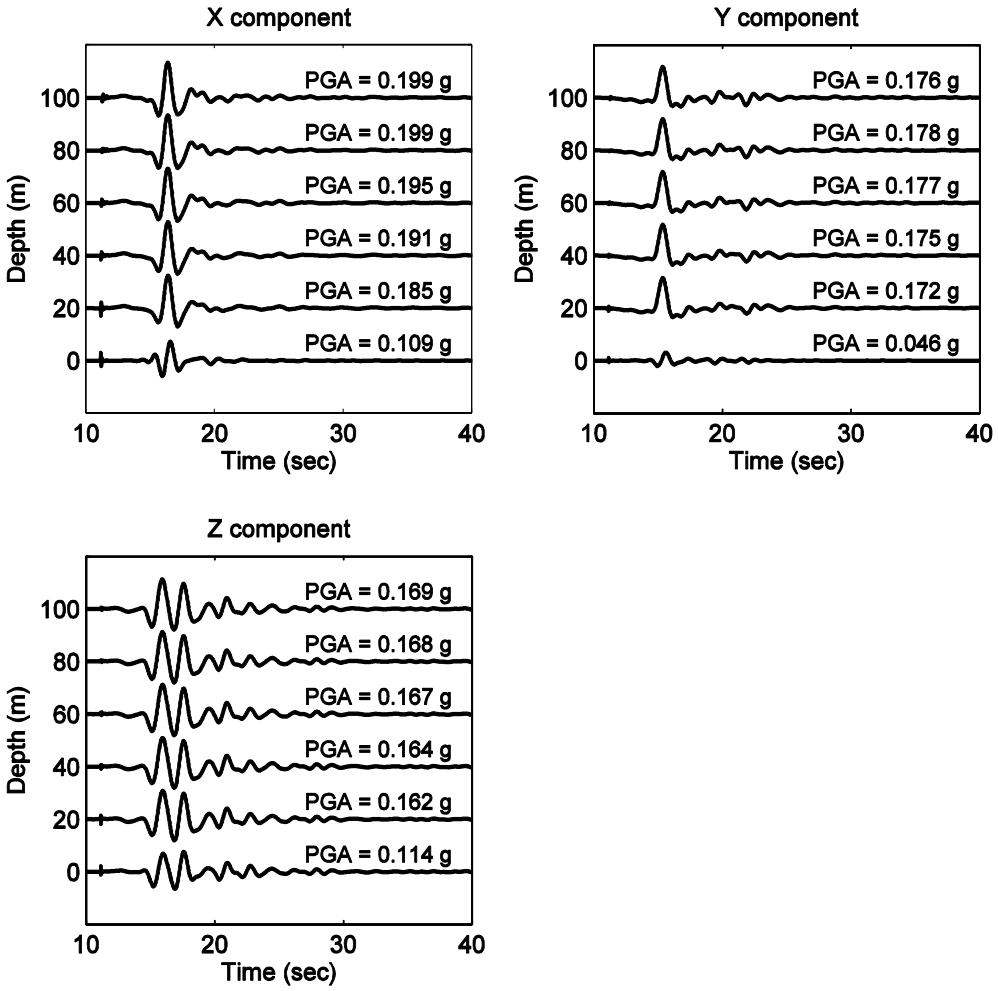

Figure 2.13: Variation of the acceleration at the ROI center nodes with depth using the low frequency input (Petropolous 2008)

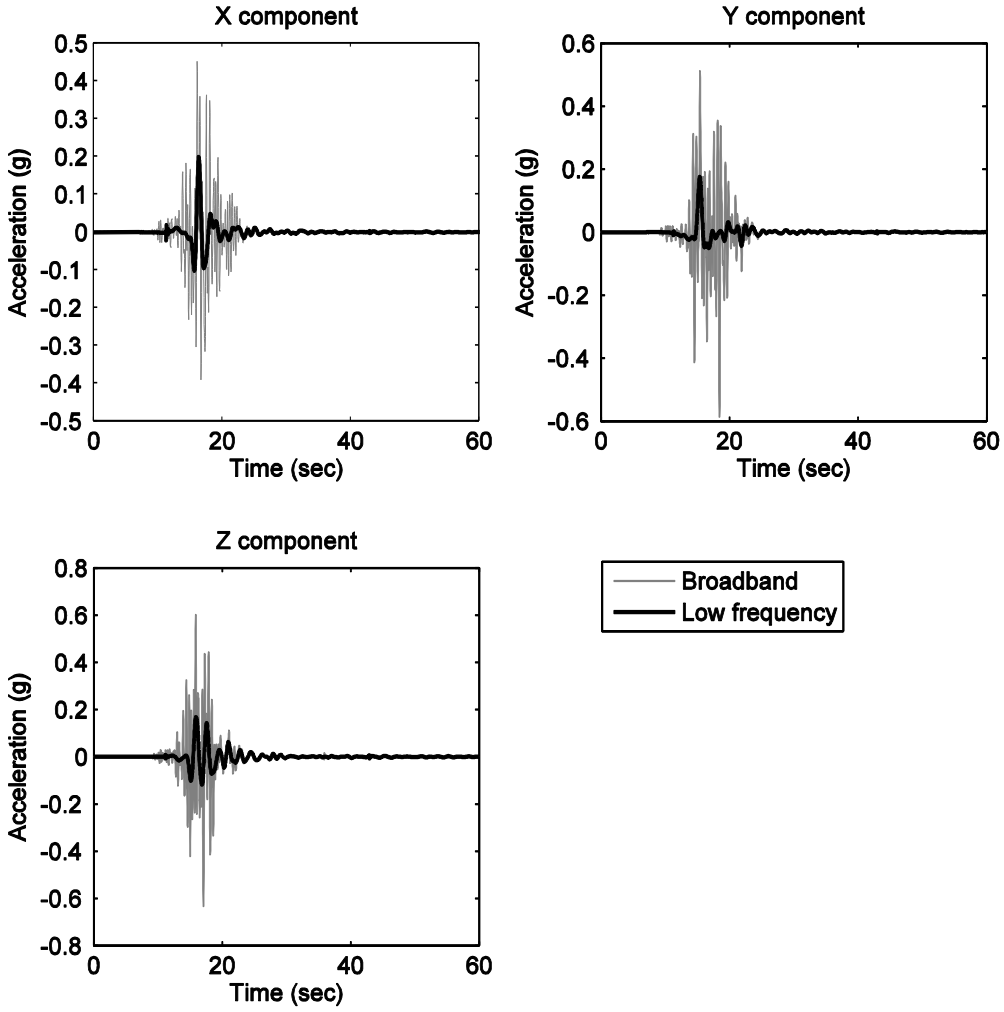

Figure 2.14: Acceleration time histories at the ROI surface center node using the broadband input (Petropolous 2008)

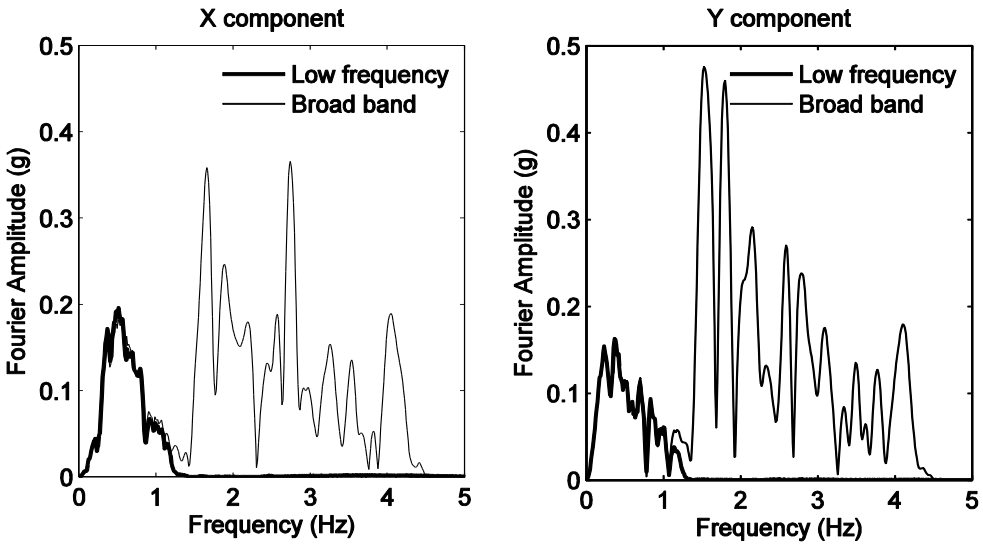

Figure 2.15 Fourier amplitude spectra of ground accelerations at the ROI surface center node using the broadband input (Petropolous 2008)

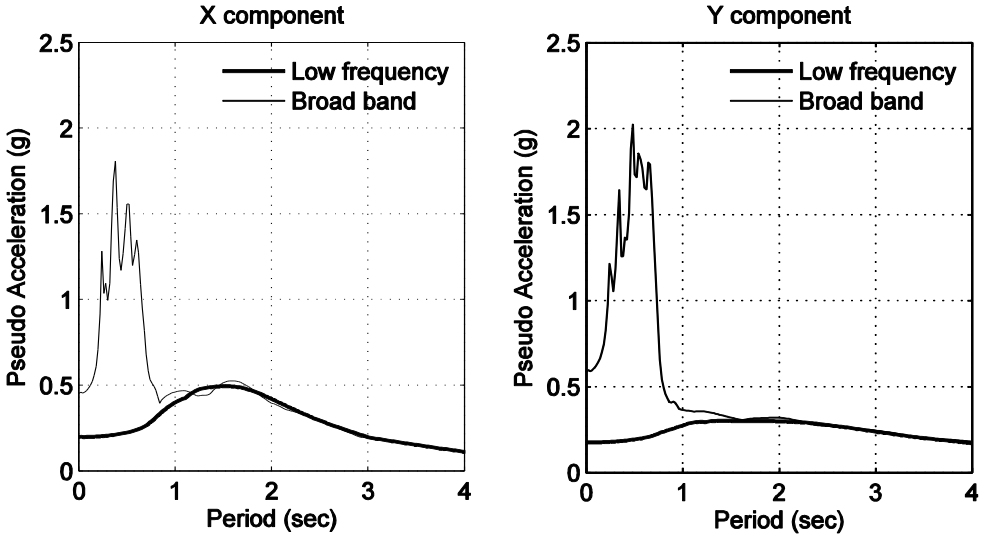

Figure 2.16: Comparison of the X and Y component of 5% damped spectra at the ROI surface center node (Petropolous 2008)

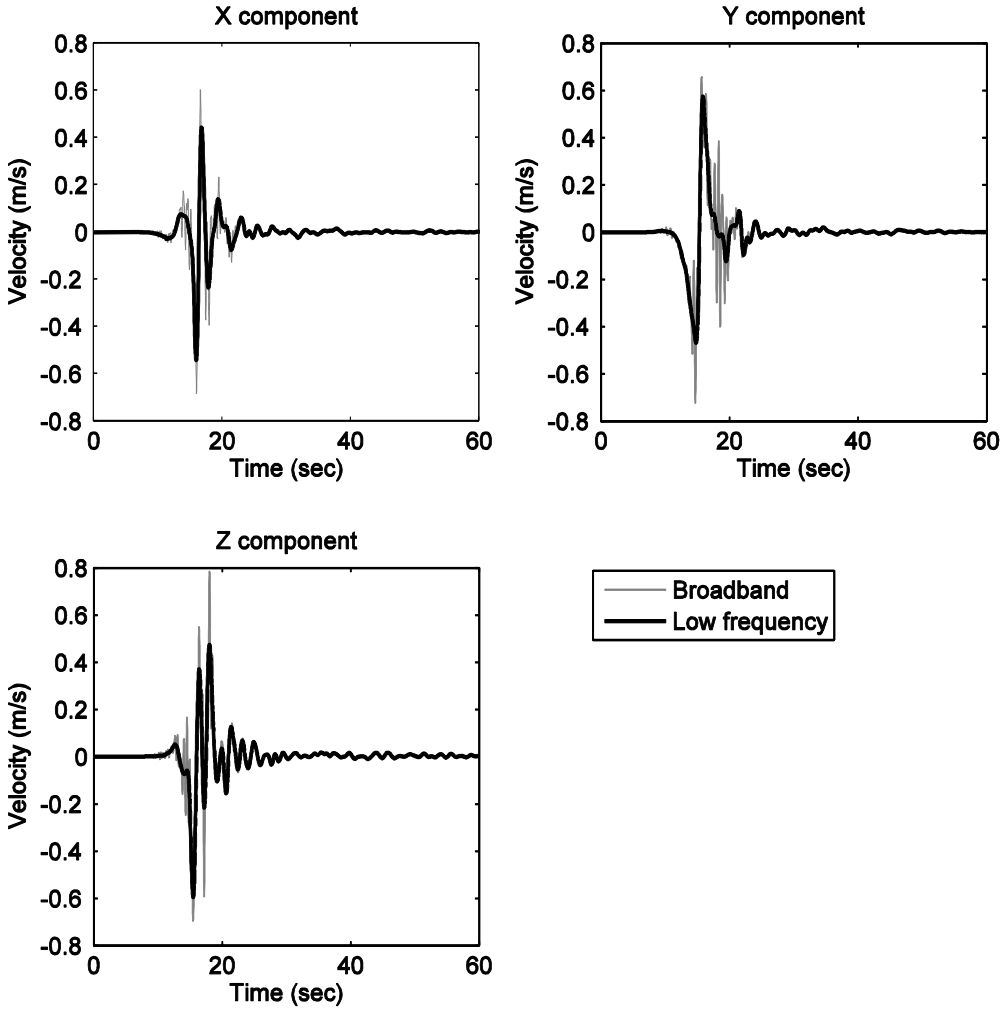

Figure 2.17: Velocity time histories at the ROI surface center node using the broadband input (Petropolous 2008)

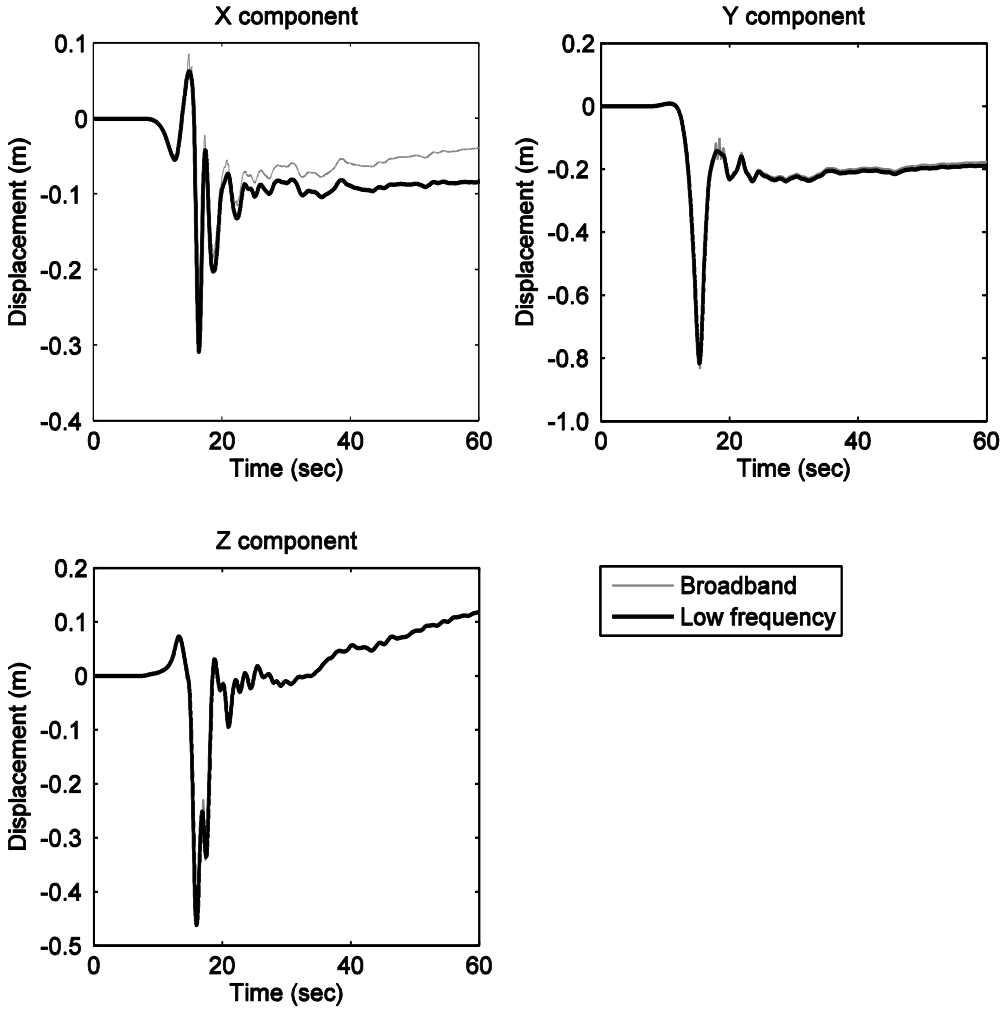

Figure 2.18: Displacement time histories at the ROI surface center node using the broadband input (Petropolous 2008)

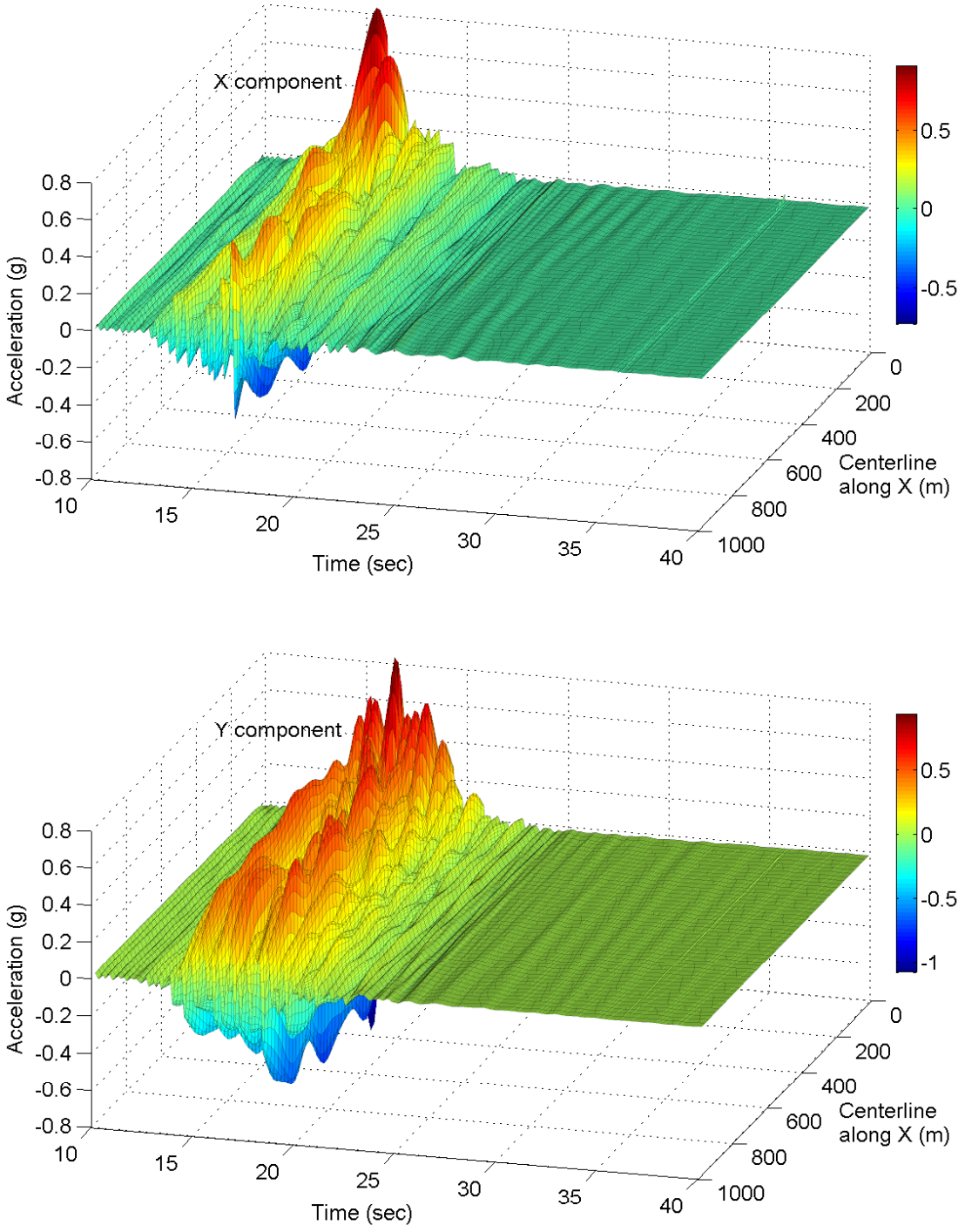

Figure 2.19: X (top) and Y (bottom) components of the ground accelerations along the ROI X center line using the broadband input (Petropolous 2008)

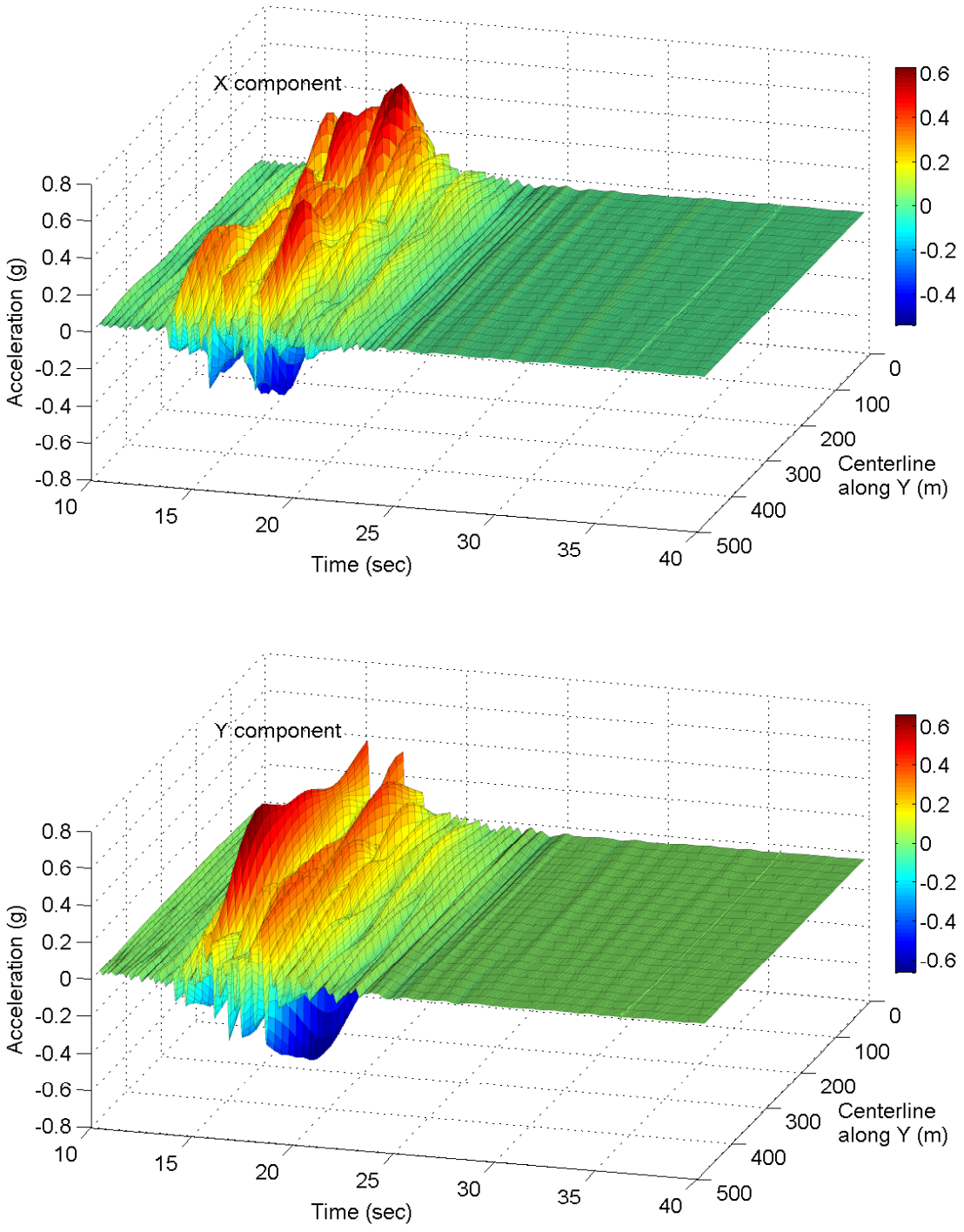

Figure 2.20: X (top) and Y (bottom) components of the ground accelerations along the ROI X center line using the broadband input (Petropolous 2008)

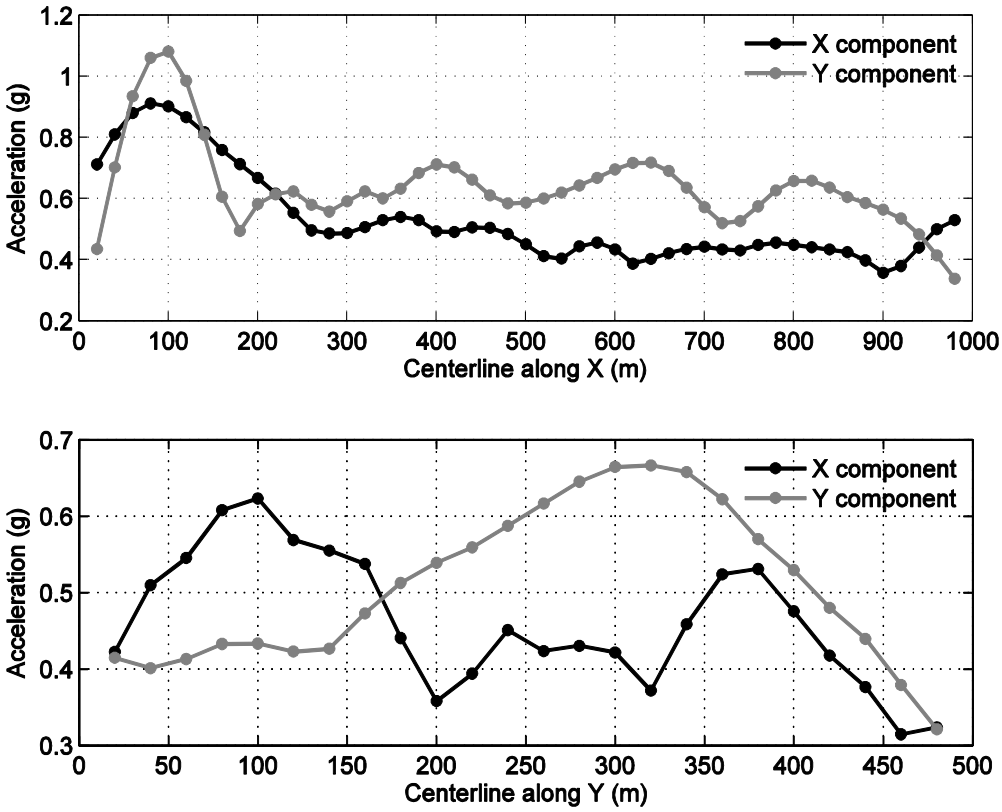

Figure 2.21: Maximum surface acceleration distributions along the ROI X and Y center lines using the broadband input (Petropolous 2008)

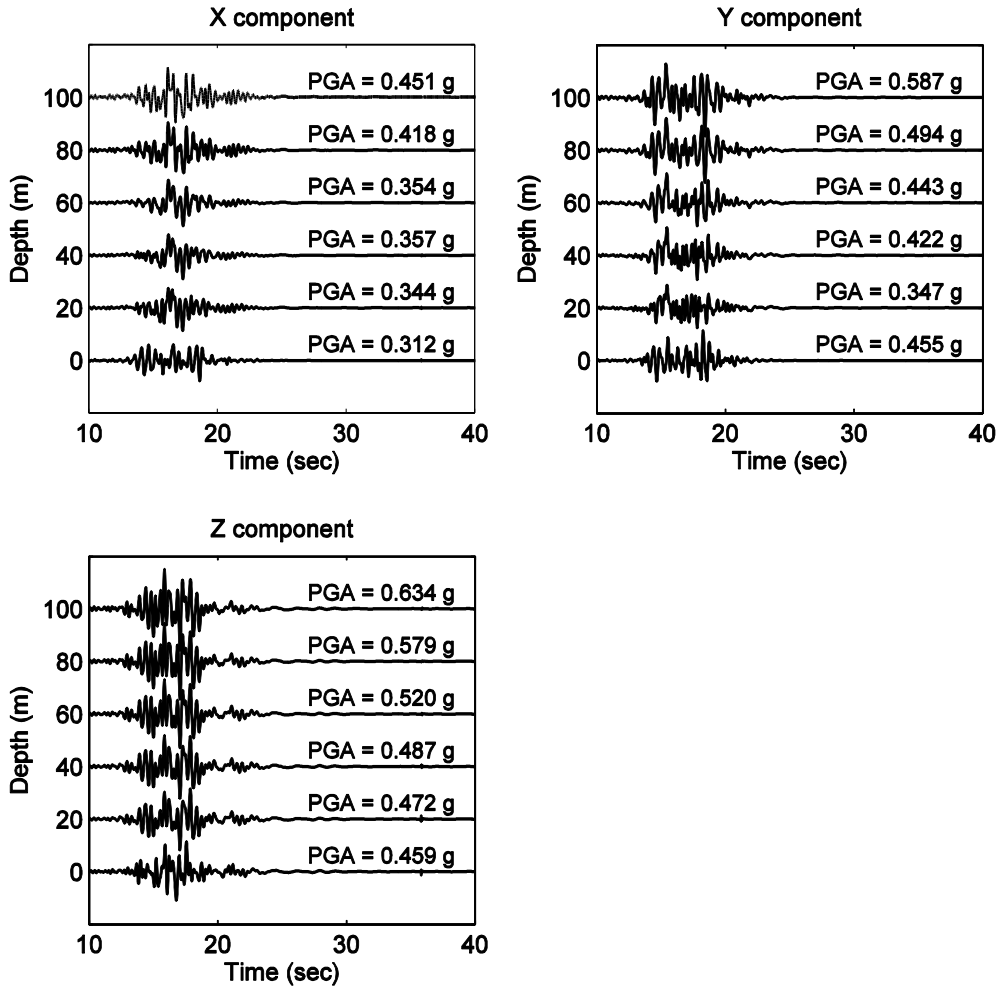

Figure 2.22: Variation of acceleration at the ROI center nodes with depth using the broadband input (Petropolous 2008)

Chapter 3

The Highway Interchange and Structural Modeling

This chapter presents details of a selected highway interchange and its constituent bridges. For the purpose of this report, the spatial geometry and structural characteristics at the California interstate 10 and 215 interchange are defined, in order to provide a representative numerical modeling configuration. At this interchange, three reinforced concrete bridges with different superstructure elevations are investigated. Emphasis is placed on modeling this 3-bridge interchange. Dynamic properties of the bridge models are presented. The developed numerical models are validated through comparison with earlier recorded earthquake response at one of the three represented bridges.

3.1 Description of the I-10/215 interchange

The interstate 10 and 215 interchange (I-10/215) is located in the San Bernardino valley near the Santa Ana River basin (Figure 3.1). In addition to ground roadways, this interchange mainly consists of three curved bridge connectors as shown in Figure 3.2; the North-West connector (NW, Bridge No. 54-823G; see Figure 3.3), the North-East connector (NE, Bridge No. 54-824F; see Figure 3.4), and the South-East connector (SE, Bridge No. 54-822F; see Figure 3.5). Each bridge carries two lanes of traffic from one interstate to another. Although these three connectors were designed in 1969, construction was delayed due to the need for including lessons from the 1971 San Fernando earthquake into new construction. The interchange was completed in 1973.

3.1.1 Geological site condition

Figure 3.6 shows a geological map near the interchange. Jackura (1991) reported that this interchange is located in the San Bernardino valley near the Santa Ana River basin where the valley is mainly composed of alluvial deposits from alluvial fans and river flood plains. In addition, soil profiles were determined from nineteen boreholes drilled in 1968 prior to the original construction, six boreholes drilled in 1989 for the retrofit design, and supplementary borings for liquefaction potential assessments (Jackura, 1991).

Based on as-built Log of Test Boring (LOTB) sheets provided by Caltrans, the defined soil profile is shown in Figure 3.7. The top soil layer mostly contains slightly compact to dense, clean sands and silty sands in the elevation from 283 m (930 ft) to 288

m (945 ft). This layer is also contains silty sands, occasional fines, and coarse gravel at some locations.

During construction of the NW, it was found that its northern one-half crossed a major fault in the San Jacinto fault zone (CDMG, 1977). A drop in water table on the southwest side compared with the northeast side of the fault was observed, with the fault acting as a barrier against ground water flow (Jackura, 1991). Additional information about the fault in the vicinity of the I-10/215 can be found in (Sharp and Survey, 1972; Sieh et al., 1973; Wesnousky et al., 1991; Doser, 1992). Due to presence of sandy soils and high ground water table, a potential for liquefaction was suggested as well.

3.1.2 Strong motion instrumentation at the NW

Due to high seismic vulnerability at the site, the NW has been instrumented with a network of strong motion accelerometers by the Office of Strong Motion Studies, California Division of Mines and Geology (CDMG) in cooperation with the California Transportation Department (Caltrans). The designated California Strong Motion Instrumentation Program (CSMIP) station number is 23631. Figure 3.8 shows the instrumentation plan for a total of 34 accelerometers. Since this instrumentation was completed, strong earthquake motions have been recorded (see Table 3.1 for historic records of earthquakes as well as major events at the NW). Details regarding the recorded accelerations and evaluation of recorded maximum response of the NW during the Landers and Big Bear earthquakes in 1992 were earlier presented in Fenves and DesRoches (1994).

3.2 NW connector

3.2.1 Original design

The NW was designed according to the AASHTO procedures in 1969. This connector consists of four components, which are the superstructure including decks and columns, foundations (pile cap and reinforced concrete piles), intermediate hinges, and abutments. Based on the as-built plans provided by Caltrans, a description of original design for the connectors is presented below.

3.2.1.1 Superstructure

The connector is a 774 m (2540 ft) long sixteen span concrete box girder bridge (Figure 3.9). From Abutment 1 (west-bound direction), the alignment of span has a 301 m length segment on a 366 m radius curve, a 386 m segment on a 396 m radius curve, and a 77 m straight segment at Abutment 17 (north-bound direction). This connector consists of six sections (frames) and these sections are inter-connected by five intermediate hinges (see Figure 3.10 for locations of the hinges). The bridge sections have a cast-in-place box girder superstructure. From Hinge 3 to Hinge 7 and Hinge 9 to Hinge 11, pre-stressed concrete box girders are used. Specified 28 day concrete compressive strength for the girders is approximately 29.6 MPa (4300 psi) for Hinge 3 to Hinge 7 and 24.1 MPa (3500 psi) for Hinge 9 to Hinge 11.

For conventional reinforced frames, translated 28 day compressive strength is approximately 20.7 MPa (3000 psi). Deck slab reinforcement and stirrups are Grade 40 or 50. The typical section is a 2.4 m deep box girder for the conventional reinforced

concrete segments (Figure 3.11). The same overall dimensions apply to the pre-stressed concrete box girder segments with the interior girders being 0.3 m thick instead of 0.25 m.

The intermediate hinges have a seat width of 0.8 m or 0.9 m with a 5 cm expanded polystyrene joint seal. All hinge connections are straight, except for 23 and 13 degree skew for hinges 11 and 13, respectively (Fig. 3.10). Elastomeric bearing pads are used to support the girders at the hinges. At each hinge, relative transverse displacement is prevented by a shear key with 0.6 cm (¼ inch) joint filler in between. Seven cable restrainer units are installed in the longitudinal direction at the hinges.

3.2.1.2 Column

A typical single column bent has an octagonal cross section. Its overall dimensions are 2.4 m by 1.7 m (Figure 3.11). For longitudinal reinforcement, #11, #14, or #18 bars are arranged in one or two rings around the cross-section. For transverse reinforcement, various arrangements of #4 stirrups are spaced at 0.3 m.

The longitudinal reinforcement is extended 1.7 m into the bent cap, except for Bents 4 and 7 which are intended to release moments at the column-bent cap connection. Size of the bent cap is 2.9 m wide and 2.4 m deep. In the bent caps, longitudinal reinforcement varies from 36 to 54 #11 bars. Various arrangements of #6 stirrups are spaced at 0.3 m for the transverse reinforcement (Fenves and DesRoches, 1994)

The column is flared in both directions starting 6.7 m below soffit of the box girder. Measured from top of the pile cap to soffit of the box girder, height of columns varies from 7.3 m for Bent 16 to 23.5 m for Bent 5 (Figure 3.10). Due to soil overburden

at all the bents, the height is measured as 6.1 m (from top of the pile cap to half of the soil) at Bent 23.0 m at Bent 10, 3.7 m at Bent 11, 2.7 m. at Bent 16, and 1.2 to 1.5 m at the other bents. The bents are mostly oriented along the curved longitudinal axis of the bridge, except for Bent 11 (24 degrees) to 15 (13 degrees) on the skew. For the connection between the column and the pile cap, dowels are used.

3.2.1.3 Foundation

Figure 3.11 shows original foundations for the bents comprised of a pile cap and reinforced concrete piles. The largest foundations consist of a 7.3 m by 7.0 m pile cap with 2.1 m thickness and 48 piles (for Bents 4, 5, and 7). The smallest foundations have a 6.4 m by 4.6 m pile cap with 1.5 m thickness and 28 piles (for Bents 12 and 13). The piles using a design load of 70 tons are spaced three to four feet on center, except for Bent 2 with the design load of 100 tons. The pile lengths vary from 6.4 m for Bent 5 to 15.2 m for Bent 8.

3.2.1.4 Abutment

At the diaphragm abutments (Figure 3.12), the box girder is embedded with a 4.0 m high backwall and 5.5 m long tapered wingwalls. A #6 dowel is used at 0.3 m for the connection between the backwall and a 1.5 m wide pile cap. At abutment 1, a total of nine piles are driven (Figure 3.10). The 20 m long piles consist of five vertical and four battered inclined at a slope of 1:3. At Abutment 17, 7 piles with length of 13.1 m are driven, four vertical and three battered.

3.2.2 Seismic retrofit

The NW was strengthened under the Caltrans' Phase II seismic retrofit program (1992) on the basis that the connector crossed the San Jacinto fault. The retrofit was begun in 1991 and was completed in 1992. The retrofit was mainly conducted on the columns, foundations, abutments, and intermediate hinges. Details of the retrofit described herein are referred to Fenves and DesRoches (1994). The techniques and the interpretation from experiments concerning the column retrofit strategies are reported by (Priestley et al. 1996).

3.2.2.1 Column

Figure 3.13 shows the general plan for seismic retrofit. Field-welded steel jackets were used on most bent columns. The jackets were 0.013 m (½ inch) thick steel casting in an elliptical shape around the column. All voids between the shell and the octagonal columns were pressure filled with cement grout. The steel jacket increased confinement, shear strength, and flexural ductility for the column. However, the steel jackets were installed within 0.05 m (2 inches) of the footing in order to limit the increase column flexural strength at this location.

Two types of columns retrofits were used (Figure 3.13). Full-height jackets (Class F jackets) were used to increase column ductility over the full height at 10 of the 15 bents (Bent 3, 4, 5, 6, 7, 9, 10, 11, 13, and 15). Partial-height jackets (Class P jackets) enabled columns to rotate before reaching the full flexural capacity (due to lap splices and dowel connection between the column and the pile cap). The steel jacket was installed over the lower 18 feet of the column (Bents 8, 12, and 14), whereas the jacket extends over the

full height of the column in the Class F. For the Class P, a 0.013 m (½") thick polystyrene filler is placed around the original column to avoid bonding between the cement grout and the jacket (Fenves and DesRoches, 1994). The polystyrene filler allows concrete to expand and the lap slices to slide or pin. Thus the bending moment is not transferred into the footing and the footing does not require retrofit. In addition, a combination of Class F and P jackets were used for the relatively shorter columns of Bents 2 and 16.

3.2.2.2 Foundation

Size of the pile caps was increased along with Class F jacket at 10 bents (out of 15 bents). This was intended in order to transfer the plastic moment through the pile cap and ensure overturning resistance with new additional piles. These new piles were steel pipe piles with 6.3 cm diameter and 0.5 cm thickness along with an upgraded pile cap.

3.2.2.3 Abutment

The abutments were retrofitted by adding a 1.5 m by 0.2 m supplement beam in front of each abutment. This retrofit, addressed concerns related to the early design of the diaphragm abutments and possibilities of large relative displacements from the mapped San Jacinto Fault.

3.2.2.4 Intermediate hinge

The original restrainers had four cable units at each hinge. These were replaced by 0.15 m (5 ¾ inch) diameter twisted strand cables at all five hinges.

3.2.3 Structural modeling of the NW connector

The NW is selected as the reference model in this research effort due to availability of strong motion data recorded during past earthquakes (Table 3.1). Earlier system identification insights concerning the NW (Fenves and DesRoches, 1994; Mosquera et al., 2009), helped in the calibration effort of the bridge model. Since the structural components of the NW did not experience inelastic deformation in the past earthquakes, the main structural components (i.e. columns, spans, and foundations) are modeled herein using elastic material properties. For the intermediate hinges and abutments, nonlinear mechanisms are employed. System modeling is performed using the OpenSees object-oriented open source FE analysis framework (McKenna, 1997).

3.2.3.1 System Identification

Earlier research on the identification of dynamic properties showed some differences of fundamental period associated with the recorded response during past earthquakes (Fenves and DesRoches, 1994; Mosquera et al., 2009). Table 3.2 summarizes the natural periods of the connector from these studies.

Fenves and Desroches (1994) identified fundamental periods for the NW using early recorded data from Landers and Big Bear earthquakes in 1992. They used i) Spectral Analysis and Periodogram Estimate of power spectral density function as a nonparametric evaluation technique, and ii) parametric evaluation using a single input-single output model. The recorded motion at the top face of the foundation at Bent 8 (channel 22 in Figure 3.10) was used as input. This study concluded that the fundamental periods lengthened from 1.56 sec. in the Landers earthquake to 1.75 sec. in the Big Bear

earthquake. The change in the period implied a 25 percent reduction in stiffness of the bridge. They explained that this reduction could be caused by loosened soil and foundations due to compaction or gapping of soil surrounding the piles in the Landers earthquake or changes in the groundwater between the two earthquakes.

Mosquera et al. (2009) defined the natural period using the Eigensystem Realization Algorithm with Observer Kalman Filter Identification (OKID). The fundamental periods varied from 1.09 sec. in Chino Hills earthquake (2008) to 1.14 sec. in Yucaipa earthquake (2005). Identified damping ratios at these periods are 1.18 % in Yucaipa earthquake and 3.24 % in Chino Hills earthquake.

Compared to the earlier earthquakes (i.e. Landers and Big Bear earthquakes in 1992), the recent earthquakes induced a relatively small peak ground acceleration at the NW. Recorded peak accelerations at channel 22 (base at Bent 8) in the NW, are 0.11 g in Yucaipa and 0.07g in Chino Hills compared with 0.18g in Landers and 0.15 g in Big Bear earthquakes. In the pseudo acceleration response spectra with 5% damping, pronounced response in Yucaipa and Chino Hills earthquakes is observed only in the short period range up to 0.5 sec. relatively short period of 1 sec. (i.e., high frequency) compared to the Landers and Big Bear earthquake response (Figure 3.14).

Since the fundamental period varies from 1.09 sec. (0.91 Hz) for the Chino Hills earthquake (2008) to 1.75 sec. (0.57 Hz) for the Big Bear earthquake (1992), these identified natural periods are used to calibrate the bridge model. Change of the period in the structural model will be controlled by the mechanism of hinges opening and closing. To simulate the hinge opening, a nonlinear hinge model will be used to represent a relatively flexible structure of long period. From an additional bridge model without the

hinges, the lower period will be checked. Further details regarding this calibration and the model dynamic properties will be discussed in Section 3.2.4.

3.2.3.2 Strategy of modeling the bridge sub-components

The FE model consists of five components: 1) the superstructure (representing the deck); 2) the columns; 3) the foundations (pile cap and piles; modeling of piles will be used in the numerical simulation of the bridge-foundation-ground system; 4) the intermediate hinges; and 5) the abutments.

The model properties are based on the as-built drawings provided by Caltrans and the earlier developed FE model insights (Fenves and DesRoches, 1994). Linear properties of the superstructure and columns are considered. For the intermediate hinges, longitudinal response is defined to emulate the observed intermittent sharp spikes in earlier recorded accelerations (Huang and Shakal 1995). The simplified abutment model (Aviram et al. 2008) is employed with vertical translation assumed to be identical to translation of soil under the abutment. The foundations are modeled as rigid pile caps and piles, which will be embedded in the soil domain for the bridge-foundation-ground system.

3.2.3.2.1 Superstructure

Elastic Beam-Column Elements are used for the pre-stressed and reinforced concrete box girders (Figure 3.10). Longitudinal elements along the span and additional transverse elements at the top of the bents and at the hinges are used. For these elements, geometric properties are determined by the cross sectional shape (Figure 3.11). The 28-

day compressive strength specified in the as-built plan increases by 20 % to account for over-strength. Based on the ACI code for the secant modulus for normal-weight concrete (unit weight of 150 lb/ft^3 in this study), the modulus of elasticity is defined (Table 3.3).

In order to account for smaller effective width near the bent cap, two section properties are used for each span in the longitudinal direction (Table 3.4). Within one quarter span near the bent cap, partial effective width (7.3 m; three times larger than the transverse width of the column) is taken into consideration. Consequently, moments of inertia are reduced by 35% for transverse bending by 45 % for torsion. No reduction is assumed for the middle one-half of the span (DesRoches and Fenves, 1997). For the conventionally reinforced concrete box girder, moment of inertia of the cross-section is reduced by 25 % to account for cracking. No reduction is considered for the pre-stressed concrete spans.

In the transverse direction, rigid and massless elements are used. These elements are to provide diaphragms at the hinges and to visualize twist of the structure in the deformed shape configurations. Mass is determined by self-weight of the superstructure. To account for rotational mass moment of inertia about the longitudinal axis of the superstructure, 40 % of vertical mass in half of each span is lumped at the ends of the transverse elements and remainder is lumped at the top of columns. (Fenves and DesRoches, 1994).

3.2.3.2.2 Columns

The length of each column is measured from the centroid of the deck to the pile cap, except for bents with deep overburden soils (2, 10, 11, and 16). For those bents, base

nodes are located halfway between the pile cap and the overburden soil surface. The number of elements for columns is determined by ratio of height to width (longer axis) of the cross section. Distributed mass of columns is computed by self-weight. Two local directions on the cross section are defined. The longitudinal direction is associated with the weak axis against bending (tangential to the longitudinal direction). For the transverse direction, the strong axis against bending is assigned.

Since the steel jackets increase stiffness of the columns, moments of inertia increase 15 % for the Class F jacket and 10 % for the Class P jacket based on experiments for steel jacketed columns (Priestley et al., 1992), The torsional moment of inertia is reduced by a factor of 0.25 and 0.12 to account for cracking by the Class F jacket and the Class P jacket, respectively. In accordance with those class types, the employed moments of inertia for the columns are provided in Table 3.5.

In general, the linear modulus of elasticity (E) for each column is determined based not only on gross moment of inertia but also on arrangement of longitudinal reinforcement. However, in this study, one single E value is used for all columns to have the identified vibration properties, specified in the later section of 3.2.3. The employed E is 32.0 GPa (4640 ksi). In order to validate the structural model controlled by this parameter, a comparison of computed response with strong motion data recorded at the bridge from historic earthquakes will be conducted later in Section of 3.2.5

3.2.3.2.3 Intermediate hinges

One of the intermediate hinges near Bent 3 in the NW is shown in Figure 3.12. The hinge represents opening-closing mechanisms with an initial gap, tension-only

restrainers with initial slack, and elastomeric bearing pads in the longitudinal direction (tangential to alignment). In the transverse direction (radial to alignment), shear key constrains the relative displacement at the hinge.

In the transverse direction, rigid elastic beam-column elements representing width of the box girder (12.5 m) are employed. For Hinges 11 and 13, the beam elements are oriented with skewed angles of 23 and 13 degrees, respectively. Along the beam elements, three nodes are specified at both ends and center of the diaphragm (Figure 3.15).

In the longitudinal direction, zero-length elements (in OpenSees) are employed representing two nodes at the same location (Figure 3.15). Compression-only elements (closing) are located at both ends of the transverse diaphragm. Tension-only elements (opening) are located at the center of the diaphragm. The center two nodes (at the same location) are constrained to be zero for relative vertical displacement, transverse displacement, and twisting (θ_x) dictated by the shear key. Meanwhile, nodes at both ends of the diaphragm are free to move in all translations and rotations.

The tension-only element consists of two material properties which represent the elastomeric bearing pad (Figure 3.16) and restrainer cables (Figure 3.17) with initial slack of 0.013 m (0.5 inches). An initial gap of 0.051 m (2 inches) is included (filled with expanded polystyrene joint seal) at the hinge In order to avoid sudden pounding from gap closing, a gradual increase in stiffness scheme is implemented via an exponential function (Figure 3.18). As the gap closes, the compressive concrete stiffness is reached.

3.2.3.2.4 Abutments

A simplified abutment model developed by Aviram et al. (2008) is employed. However, vertical translation is constrained to be identical to the response of the underlying ground below the diaphragm abutment. This modified model consists of rigid elements and zero-length elements (Figure 3.19). The rigid element represents width of the abutment in the transverse direction, connected to the centerline of the superstructure.

For the zero-length elements, in the longitudinal direction, an elastic-perfectly-plastic backbone curve with abutment stiffness (K_{abut}) and ultimate strength (P_{dia}) is employed, obtained from section 7.8.1 of the Caltrans Seismic Design Criteria document (Caltrans, 2010). Since there is no information on the embankment fill material, it is assumed that initial stiffness for the embankment fill material meets the Caltrans Standard Specification requirements. As specified in the requirements, the initial stiffness shall be adjusted proportional to backwall and diaphragm height. In the full scale abutment test of Maroney (1995), the passive pressure at the abutment can increase linearly with displacement up to an ultimate static force. As such, the employed abutment stiffness (K_{abut}) is defined as 207.524 kN/mm and the ultimate strength (P_{dia}) is chosen as 13,790 kN (using this defined stiffness, two elements are aligned in the longitudinal direction as shown in Figure 3.20).

In the transverse direction, the longitudinal stiffness is modified using factors corresponding to wall effectiveness of 2/3 and participation coefficients (CW) of 4/3 (Maroney and Chai, 1994). The wing wall length is assumed to be 1/3 of the backwall length. Corresponding abutment stiffness (K_{abut}) is 61.564 kN/mm and the ultimate

strength (P_{dia}) is 4,086 kN (using this defined stiffness, two elements are aligned in the longitudinal direction as shown in Figure 3.21).

3.2.3.2.5 Foundations

An original or retrofitted foundation consists of a pile cap and piles. For the pile cap, rigid elements are used on the basis of its dimensions (Figure 3.22). Four or eight line elements aligned on the bottom face are connected to a center node at the same level. An additional rigid vertical element representing thickness of the pile cap is connected from the bottom center node to an additional center node on the top face of the pile cap.

Rigid solid elements are employed to represent the pile groups (Figure 3.23). Horizontal dimensions of these elements are measured from the center to center of the outer piles (retrofitted piles or original piles aligned along the exterior perimeter). The vertical direction is determined by height of the original piles.

3.2.3.2.6 Damping

Rayleigh damping is included at a value of 5 %. Based on the first and sixth natural frequencies, mass-proportional and stiffness-proportional damping constants, α and β respectively, are specified (Table 3.6). The corresponding damping matrix is thus defined for the columns and the superstructure in the structural model.

3.2.4 Vibration properties

In order to evaluate vibration properties of the structural model, an eigenvalue analysis is conducted. In this analysis, the foundation including pile caps and piles is not

considered and column bases are fixed in translation and rotation (Figure 3.23). The corresponding FE model includes 236 nodes and 228 elements. From the analysis, transverse properties are mainly discussed, associated with the strong axis of the cross section of columns. Figure 3.24 shows lower vibration modes resulting from the model with the hinges, specified in the transverse direction. The periods for first second, third, and fourth modes are 1.5 sec (0.67 Hz), 1.07 sec. (0.94 Hz), 1.03 sec. (0.97 Hz), and 0.85 sec. (1.17 Hz), respectively.

As discussed earlier in Section 3.2.3.1, the identified fundamental period varied from 1.09 sec. (0.92 Hz) to 1.56 sec. (0.64 Hz). To investigate the short period of 1.09 sec., an additional model is employed with no hinge opening allowed. Figure 3.27 shows lower vibration modes resulting from this additional model. As no hinge opening is observed in this model, stiffness of the connector increases. Thus, the natural period of 1.2 sec. can be compared to the relatively short period (1.09 sec.) defined in the system identification.

Although it can be expected that overall stiffness of the model changes with the corresponding hinge model openings/closings, vibration properties are similar, except for the first mode (where the hinge open/close behavior appears to possibly play a bigger role). In the first mode, about 20% reduction in stiffness of the model is observed due to the hinge opening (1.5 sec. versus 1.2 sec.).

In addition to the eigenvalue analysis, early recorded data at the NW connector during the Landers earthquake (1992) are used to evaluate the natural period (note: this event occurred after the modeled retrofit was done). Figure 3.25 shows acceleration time histories recorded at the base of Bent 8 (as input; channels of 22, 23, and 24 in Figure

3.8). The bases of all columns (without foundations) are fixed and the connector is excited uniformly using this recorded motion at the base of Bent 8. Figure 3.26 shows variation (time history) of the natural period during this Landers earthquake simulation. The computed fundamental period varies from 1.25 sec. to 1.49 sec as defined in the earlier system identification study (Fenves and DesRoches, 1994; Mosquera et al., 2009).

3.2.5 Numerical simulation of the fixed-base bridge

Since the NW was heavily instrumented, a large amount of data obtained from the past earthquake events are available to allow for validating the FE model. As conducted earlier in the 3.2.4, the fixed-base model without the corresponding foundation is considered (Figure 3.23). Three components of accelerations at the base of Bent 8 are used as input under uniform excitation conditions. The channels (ch) 22, 23, and 24 shown in Figure 3.8 are associated with two horizontal and one vertical direction, respectively. Load cases considered in the response evaluation are dead load and the earthquake ground motion. No effect of spatially varying ground motions at the supports is considered (obviously, recorded earthquake response is affected to some degree by such variability). This variability can be assessed by the fact that responses recorded at different location at the ground surface (ch 1, 2, and 3 at Abutment 1, ch 4 and 6 at Bent 3, and ch 34, 35, and 36 at Abutment 17) display differences compare to the response at Bent 8.

As such, the earlier recorded data during the Landers earthquake (1992) are used to perform the numerical simulation. At the base of Bent 8 (ch 22, 23, and 24), peak ground accelerations (PGA) are 0.16g, 0.18g, and 0.07g in the longitudinal, transverse,

and vertical directions, respectively. The corresponding acceleration time histories are shown in Figure 3.25 Figure 3.28 shows the velocity time histories and Figure 3.29 shows the displacement time histories (note that the response spectrum with 5% damping for the acceleration at the ch 22 (transverse) was shown earlier in Figure 3.14). Among a total of 34 channels, total displacement time histories at 20 channels will be compared below with the corresponding computed responses (vertical responses near the top of Bent 8 are also not investigated due to lack of a corresponding node in the model).

Figure 3.30 presents a comparison of total displacements. The transverse response is generally captured well by the model. For ch 19 and 20, near Bent 7 and Hinge 7, some of the recorded transverse peaks are underestimated by the model. Among other reasons, preclusion or relative transverse motion at the hinges (as modeled herein) might have led to an overall somewhat stiffer lateral bridge response (in the actual NW, relative transverse translation is allowed by a small gap at the hinge shear keys as discussed earlier).

Generally, computed phase response is very good in the transverse and longitudinal directions (Figure 3.30). However, the phase is slightly off in the vertical direction (might indicate that rotation of the box girder is slightly underestimated by the model).

Due to presence of available data at the base of Bent 3 and Bent 8, relative top displacements at those columns with respect to the base are investigated. Figure 3.31 shows a comparison of the relative displacement time histories in the transverse and longitudinal directions. The model generally captures the relative displacement well in the longitudinal direction, except for some overestimation at Hinge 3. Peaks for the

transverse motion are underestimated by the model (Figure 3.31) as already mentioned above.

Figure 3.32 shows a comparison of total accelerations near hinges in the time window 15 to 35 sec. The computed acceleration shows good agreement with the corresponding records. It can be seen that pounding due to the hinge opening and closing mechanisms is captured very well in the longitudinal direction, while the model produces higher peaks (partially, due to lack of energy dissipation in the developed hinge model).

Additional simulations of the structural model for the Big Bear earthquake in 1992 and the Northridge earthquake in 1994 are conducted. The corresponding comparison results are provided in Appendix A. In very general terms, the Landers input simulation, appears to have resulted in closer matches to the corresponding recorded response. While discrepancies are larger, many locations still show a close matches, within specific time windows during these two shaking events.

3.3 NE connector

3.3.1 Original design

The NE was designed according to the AASHTO procedures in 1969. This connector consists of four components, which are the superstructure including decks and columns, foundations (pile cap and reinforced concrete piles), intermediate hinges, and abutments. Based on as-built plans provided by Caltrans, a brief description of the original design for the connector is presented below.

3.3.1.1 Superstructure

The connector is a 474 m long nine span concrete box girder bridge (Figure 3.9). From Abutment 1 (east-bound direction), the bridge has a 43 m straight segment and a 431 m curved segment (at a 259 m radius curve) reaching Abutment 10 (north-bound direction). This structural system consists of three frames (sections) inter-connected by two intermediate hinges (Figure 3.33).

As a cast-in-place box girder structure (Figure 3.33), the bridge deck from Hinge 6 to Abutment 10 (one frame) is post-tensioned in the longitudinal direction. For the other two frames, conventional reinforced concrete construction is used. For the post-tensioned reinforced frame, translated 28 day compressive strength is approximately 26.2 MPa (3800 psi). For the conventionally constructed reinforced frames, translated 28 day compressive strength is approximately 20.7 MPa (3000 psi). Reinforcement steel is Grade 60, except for deck slab and stirrups where Grade 40 or 50 are used. The typical section is a 2.4 m deep box girder for the conventional reinforced concrete segments. The same overall dimensions apply to the pre-stressed concrete box girder segment with the interior girders being 0.3 m thickness instead of 0.25 m.

The two intermediate hinges have a seat width of 0.8 m with a 5 cm expanded polystyrene joint seal. All hinges are aligned to be normal to the corresponding girders. Elastomeric bearing pads are used to support the girders at the hinges. At each hinge, relative transverse displacement is prevented by a shear key with 0.6 cm (¼ in.) joint filler in between. In the longitudinal direction, seven cable restrainer units are installed.

3.3.1.2 Column

As constructed in the NW, a typical single column has an octagonal cross section with overall dimensions of 2.4 m by 1.7 m. The reinforcement steel layout (configuration) is similar to that in the NW. Details of the reinforcement steel configuration can be found earlier in Section 3.2.1.2. Height of the columns varies from 9.1 m at Bent 2 to 16.8 m at Bent 9 (measured from top of the pile cap to soffit of box girder). Soil overburden exists at all the bents (above the pile cap), except for Bent 6 (Figure 3.33). The bents are mostly oriented along the curved longitudinal axis of the bridge.

3.3.1.3 Foundation

Original foundations for the bents are comprised of a pile cap and reinforced concrete piles. The largest foundation consists of a 6.4 m by 6.4 m pile cap with 2.1 m thickness and 49 piles at Bent 7. The smallest foundation has a 5.5 m by 4.6 m pile cap with 1.5 m thickness and 30 piles at Bent 3. The piles are spaced from 0.9 m to 1.1 m on center with the design load of 70 tons for all bents. The pile lengths vary from 5.4 m (Bent 9) to 12.7 m (Bent 6).

3.3.1.4 Abutment

At the diaphragm abutments (Figure 3.33), the box girder is embedded with a 4.0 m high backwall and 5.5 m long tapered wingwalls. At Abutment 1, a total of nine piles are driven. The 12.5 m long piles consist of five vertical and four battered inclined at a slope of 1:3. At Abutment 10, eleven piles with length of 19.5 m are driven, six vertical and five battered inclined at a slope of 1:3.

3.3.2 Seismic retrofit

As discussed earlier in the NW (Section 3.2.2), the NE was also strengthened under Caltrans' Phase II seismic retrofit program (1992). For the columns, Class F jackets were used at Bents 2, 3, 4, 6, 7, and 9 (i.e., 6 out of 9). Class P jackets were employed at Bents 5 and 8. Dimensions of the pile caps increased along with the Class F jackets. Steel piles with 0.4 m diameter were added along the perimeter of the strengthened pile cap. At Abutment 10, a supplement beam with size of 1.5 m by 0.2 m was added in its front. Original restrainers with four cable units were replaced by 0.15 m (5 ¾ inch) diameter twisted strand cables at the two hinges.

3.3.3 Structural modeling of the NE connector

Due to lack of recorded response of the NE during past earthquake excitations, the connector is modeled as discussed earlier in Section 3.2.3 for the NW, except for the superstructure and the columns (linear material properties based on its as-built drawing provided by Caltrans). As modeled in the NW, elastic beam-column elements are used for the superstructure (spans). Table 3.8 provides the employed modulus of elasticity for the conventional reinforced and pre-stressed concrete box girders. For the columns, Table 3.9 summarizes gross section properties associated with the steel jackets. As discussed earlier in Section 3.2.3.2.2, moments of inertia in the column cross sections increase 15 % for the Class F jacket and 10 % for the Class P jacket (based on experiments for steel jacketed columns, Priestly et al., 1992). The linear modulus of elasticity (E) of 32 GPa (4640 ksi) is employed for all the bents as modeled in the NW.

Rayleigh damping is included at a value of 5 %. Based on the first and sixth natural frequencies, Table 3.10 provides mass-proportional and stiffness-proportional damping constants, α and β respectively. The corresponding damping matrix is specified for the columns and the superstructure.

3.3.4 Vibration properties

Figure 3.34 shows the FE model of the NE including 120 nodes and 113 elements (excluding the foundations). Figure 3.35 shows lower vibration modes in the transverse response, for which three individual frames are inter-connected by the hinge model with both compression-only and tension-only zero-length elements. As discussed earlier in Section 3.2.4, additional vibration modes resulting from the compression-only hinge model are shown in Figure 3.36. The first period is 0.81 Hz (1.23 sec.) and the second mode period is 0.73 Hz (1.38 sec.). Table 3.11 summarizes the lower six vibration frequencies (periods) from the two hinge models. Particularly, response at the abutments is noteworthy in the higher modes, 3to 6.

3.4 SE connector

3.4.1 Original design

The SE was designed according to the AASHTO procedures in 1969. This connector consists four components, which are the superstructure including decks and columns, foundations (pile cap and reinforced concrete piles), intermediate hinges, and

abutments. Based on as-built plans provided by Caltrans, a brief description of original design for the connectors is presented below.

3.4.1.1 Superstructure

The connector is a 800 m long seventeen span concrete box girder bridge (Figure 3.37). From Abutment 1 (south-bound direction), the bridge has a 129 m straight segment, a 502 m length segment on a 427 m radius curve, and a 169 m segment on a 305 m radius curve reaching Abutment 18 (east-bound direction). This structural system consists of five frames (sections) inter-connected by four intermediate hinges (Figure 3.37).

As a cast-in-place box girder structure, the bridge deck from Hinge 11 to Hinge 14 is post-tensioned with translated 28 day compressive strength of 29.0 MPa (4200 psi) approximately. For the conventional reinforced concrete construction, translated 28 day compressive strength is approximately 20.7 MPa (3000 psi). Reinforcement steel is Grade 60, except for deck slab and stirrups where Grade 40 or 50 are used. The typical section is a 2.4 m deep box girder for the conventional reinforced concrete segments. The same overall dimensions apply to the pre-stressed concrete box girder segment with the interior girders being 0.3 m thickness instead of 0.25 m.

The intermediate hinges have a seat width of 0.8 m with 5 cm expanded polystyrene joint seal. All hinges are aligned to be normal to the curved span, except for a 10 degree skew for Hinge 11. Elastomeric bearing pads are used to support the girders at the hinges. At each hinge, relative transverse displacement is prevented by a shear key with 0.6 cm (¼ in.) joint filler in between. In the longitudinal direction, seven cable restrainer units are installed.

3.4.1.2 Columns

As constructed in the NW and the NE, the typical single column has an octagonal cross section with overall dimensions of 2.4 m by 1.7 m, except for size of 7.3 m by 0.9 m for Bents 2 to 5. The typical column is flared in both directions near the top. However, Bents 2 to 5 are flared in the short dimension direction. For the typical columns, the reinforcement steel layout is similar to that in the NW and the NE (see Section 3.2.1.2. for the details). For the Bents 2 to 5, one hundred #10 bars are placed in one ring. The transverse reinforcement consists of various arrangements of #4 stirrups spaced at 0.3 m. Except for Bents 4 and 7, the longitudinal reinforcement is extended 1.7 m into the bent cap.

The bent cap (2.4 m thickness) is 2.9 m wide for the typical columns and 0.9 m wide for Bents 2 to 5. Top longitudinal reinforcement varies from 36 to 54 #11 bars, except for eight #11 bars for Bents 2 to 5. Transverse reinforcement consists of various arrangements of #6 stirrups spaced at 0.3 m for the typical columns and 6 or 9 #6 stirrups in Bents 2 to 5. Dowels are used for connection between the column and the pile cap by lap sliced forty bar diameters with longitudinal reinforcement for the typical columns and minimum forty bar diameters on approximately 50% of column reinforced steel bars for the Bents 2 to 5.

The column height from top of pile cap to soffit of box girder varies from 10.1 m for Bent 2 to 25.9 m for Bent 14 (Figure 3.37). Soil overburden (above the pile cap) exists at all the bents (its height varies from 2.6 m at Bent 2 to 4.0 m at Bent 13). The

bents are mostly oriented along the curved longitudinal axis of the bridge, except for the Bents 2 to 5 with 10 degree skew (clockwise).

3.4.1.3 Foundation

Original foundations for the bents are comprised of a pile cap and reinforced concrete piles. For the typical octagonal columns, the largest foundation consists of a 7.3 m by 6.4 m pile cap with 2.1 m thickness and 56 piles for Bent 4. The smallest foundation has a 6.4 m by 5.5 m pile cap with 1.7 m thickness and 42 piles for Bents 8, 9, 10, 16, and 17. For the foundations in Bents 2 to 5, the largest size is a 10.1 m by 2.7 m pile cap with 1.4 m thickness and 33 piles (used for Bents 4 and 5). The smallest size is a 8.2 m by 2.7 m pile cap with 1.4 m thickness and 27 piles for Bent 3. The piles are spaced from 0.9 m to 1.4 m on center with the design load of 70 tons except for 45 tons at the abutments. The pile lengths vary from 8.2 m (Bent 6) to 18.6 m (Bent 9).

3.4.1.4 Abutment

At the diaphragm abutments (Figure 3.37), the box girder is embedded with a 4.0 m high backwall and 5.5 m long tapered wingwalls. At Abutment 1, a total of seven piles are driven. The 21.9 m long piles consist of four vertical and three battered inclined at a slope of 1:3. At Abutment 18, eleven piles with length of 24.1 m are driven, six vertical and five battered at 1:3.

3.4.2 Seismic retrofit

As discussed earlier in the NW (Section 3.2.2), the SE was also strengthened under Caltrans' Phase II seismic retrofit program (1992). For the columns, Class F jackets were used at 6 of the 9 bents (Bents 2, 3, 4, 6, 7, and 9). Class P jackets were employed at Bents 5 and 8. Dimensions of the pile caps increased along with the Class F jackets. Steel piles were added with 0.4 m diameter along the perimeter of the strengthened pile cap. Both abutments were retrofitted by adding 1.5 m by 0.2 m supplement beams in their front. Original restrainers with four cable units at each hinge were replaced by 0.15 m (5 ¾ inch) diameter twisted strand cables at the four hinges.

3.4.3 Structural modeling of the SE connector

Due to lack of recorded response of the SE during past earthquake excitations, the connector is modeled as discussed earlier in Section 3.2.3 for the NW, except for the superstructure and the columns (linear material properties based on its as-built drawing provided by Caltrans). As modeled in the NW and the NE, elastic beam-column elements are used for the superstructure (see Figure 3.11). Table 3.12 the employed modulus of elasticity for the conventional reinforced and pre-stressed concrete box girders. For the columns, Table 3.13 summarizes gross section properties associated with the steel jackets (Class F and P). As discussed earlier in Section 3.2.3.2.2, moments of inertia in the column cross sections increase 15 % for the Class F jacket and 10 % for the Class P jacket (based on experiments for steel jacketed columns, Priestley et al., 1992). The linear modulus of elasticity (E) of 32 GPa (4640 ksi) is employed for all the bents as modeled in the NW and the NE.

Rayleigh damping is included at a value of 5 %. Based on the first and sixth natural frequencies, Table 3.14 provides mass-proportional and stiffness-proportional damping constants, α and β respectively. The corresponding damping matrix is specified for the columns and the spans.

3.4.4 Vibration properties

Figure 3.38 shows the FE model of the SE including 255 nodes and 244 elements (excluding the foundations). Figure 3.39 shows lower vibration modes in the transverse response. As conducted for the NW and the NE, additional vibration modes resulting from the compression-only hinge model are shown in Figure 3.40. The first period is 1.66 Hz (0.60 sec.) and the second mode period is 1.21 Hz (0.83 sec.). Table 3.15 summarizes lower six vibration frequencies (periods) from the two hinge models.

3.5 Summary

Structural modeling of the existing bridge connectors (the NW, the NE, and the SE) at the I-10/215 was presented. Linear material properties for the superstructure, the columns, and the foundations were employed based on the corresponding geometric configurations. For the intermediate hinges, longitudinal properties were employed to simulate presence of intermittent sharp spikes shown in the recorded accelerations at the NW during past earthquake excitations. A simplified abutment model was employed, with vertical translation assumed to be identical to translation of soil under the abutment.

Vibration properties of the three connectors were investigated. Eigenvalue analysis of these models with nonlinear hinge mechanism resulted in the first transverse mode at the fundamental period of 1.5 sec. for the NW. For the NE and the SE, the fundamental periods were 0.8 and 1.7 sec., respectively. For the comparison with hinge openings/closings mechanism, the vibration modes of the closed hinge models (no hinge opening allowed) in which the hinges resist only compression were investigated.

Validation of the numerical model was conducted in comparison of the recorded strong motions at the NW (CSMIP station No. 23631). In general, the phase of the model longitudinal/transverse response (reflecting period of vibration) compared well to that of the records. In comparison of the response at the intermediate hinges, pounding due to hinge open/close behavior was captured in the longitudinal direction.

3.6 Acknowledgements

Chapter 3 contains material published in the Earthquake Geotechnical Engineering Design (Geotechnical, Geological and Earthquake Engineering, Vol. 28, Springer) titled “Seismic Response of a Large-Scale Highway Interchange System” with authors, Kyung Tae Kim, Ahmed Elgamal, George Petropoulos, Aysegul Askan, Jacobo Bielak, and Gregory L. Fenves (2014). The dissertation author is the first author of this paper.

Table 3.1: Historic events occurred at the North-West connector

Date	Event
1969	Design completed
1972	San Jacinto fault zone mapped near the Connector
1973	Construction completed
1987	Expansion joint seals replaced
1990	Seismic retrofit design completed
1991	Seismic retrofit construction completed
Jan. 1992	Strong motion instrumentation installation completed
April 22, 1992	Joshua Tree earthquake
June 28, 1992	Landers and Big Bear earthquakes
Jan. 17, 1994	Northridge earthquake
Feb. 22, 2003	Big Bear City earthquake
June 16, 2005	Yucaipa earthquake
July 29, 2008	Chino Hills earthquake
Jan. 8, 2009	San Bernardino earthquake
April 4, 2010	Calexico earthquake
July 7, 2010	Borrego Springs earthquake

Table 3.2: Identified transverse vibration periods and damping ratios (Fenves and DesRoches, 1994; Mosquera et al., 2009)

Mode	Landers (1992)		Big Bear (1992)		Yucaipa (2005)		Chino Hills (2008)	
	Period (sec)	Damping Ratio (%)	Period (sec)	Damping Ratio (%)	Period (sec)	Damping Ratio (%)	Period (sec)	Damping Ratio (%)
1	1.56	3.1	1.75	8.2	1.14	1.18	1.09	3.24
2	1.30	11.0	1.29	2.1	1.11	7.32	0.96	10.5
3	0.98	5.0	1.09	15.0	0.97	1.49	-	-
4	0.83	7.0	0.96	7.0	0.81	0.39	0.75	7.17

Table 3.3: Concrete properties for superstructure in the North-West connector

Frame	Section	Type	Modulus of Elasticity (GPa)
1	Abutment 1 –Hinge 3	Reinforced	24.6 (3420ksi)
2	Hinge 3-Hinge 7	Prestressed	28.2 (4090ksi)
3	Hinge 7-Hinge 9	Reinforced	24.6 (3420ksi)
4	Hinge 9-Hinge 11	Prestressed	25.4 (3690ksi)
5	Hinge 11-Abutment 17	Reinforced	24.6 (3420ksi)

Table 3.4: Section properties for two types of superstructure in the North-West connector in the local coordinate system (weak axis, y, and strong axis, z, against bending)

Type	Effective width	Moment of Inertia		
		I_z (m^4)	I_y (m^4)	J (m^4)
Prestressed	Full	5.895	68.444	19.972
Prestressed	Partial	3.858	68.444	10.806
Reinforced	Full	4.238	47.039	14.837
Reinforced	Partial	2.788	47.039	8.018

Table 3.5: Gross section properties for columns in North-West connector in the local coordinate system (weak axis, y, and strong axis, z, against bending)

Bent	Retrofit	Moments of Inertia		
	Class type	I_z (m^4)	I_y (m^4)	J (m^4)
2	P/F	0.831	1.700	2.304
3 - 7	F	0.872	1.778	2.304
8	P	0.831	1.700	2.304
9 -11	F	0.872	1.778	2.304
12	P	0.831	1.700	2.304
13	F	0.872	1.778	2.304
14	P	0.831	1.700	2.304
15	F	0.872	1.778	2.304
16	P/F	0.858	1.751	2.304

Table 3.6: Properties of Rayleigh damping for the NW connector

Connectors	α (Mass-proportional)	β (Stiffness-proportional)
North-West	2.388×10^{-1}	9.778×10^{-3}

Table 3.7: Vibration properties of North-West connector with nonlinear hinges and closed hinges mechanism

Mode	Type	Nonlinear hinge mechanism		Closed hinge
		Transverse	Longitudinal	Transverse
1	Symmetric	1.497		
			1.208	
				1.193
2	Anti-symmetric	1.069		1.075
3	Anti-symmetric	1.027		
4	Anti-symmetric	0.852		0.911
			0.814	
5	Symmetric	0.753		0.744
			0.704	
6	Anti-symmetric	0.677		0.690

Table 3.8: Concrete properties for superstructure in the NE connector

Frame	Section	Type	Modulus of Elasticity (GPa)
1	Abutment 1 –Hinge 3	Reinforced	24.6 (3420 ksi)
2	Hinge 3-Hinge 6	Prestressed	26.5 (3850 ksi)
3	Hinge 6- Abutment 10	Reinforced	24.6 (3420 ksi)

Table 3.9: Gross section properties for columns in NE connector in the local coordinate system (weak axis, y, and strong axis, z, against bending)

Bent	Retrofit	Moments of Inertia		
	Class type	I_z (m^4)	I_y (m^4)	J (m^4)
2– 4	F	0.872	1.778	2.304
5	P	0.831	1.700	2.304
6 – 7	F	0.872	1.778	2.304
8	P	0.831	1.700	2.304
9	F	0.872	1.778	2.304

Table 3.10: Properties of Rayleigh damping for the NE connector

Connectors	α (Mass-proportional)	β (Stiffness-proportional)
North-East	2.703×10^{-1}	8.541×10^{-3}

Table 3.11: Vibration properties of North-East connector with nonlinear hinges and closed hinges mechanism

Mode	Type	Nonlinear hinge mechanism		Closed hinge
		Transverse	Longitudinal	Transverse
1	Symmetric	0.812		
2	Anti-symmetric	0.727		0.721
3	Symmetric	0.657		0.696
				0.608
			0.574	
4	Anti-symmetric	0.557		0.557
			0.487	
5	Symmetric	0.455		0.461
				0.450
6	Anti-symmetric	0.393		

Table 3.12: Concrete properties for superstructure in the SE connector

Frame	Section	Type	Modulus of Elasticity (GPa)
1	Abutment 1 – Hinge 4	Reinforced	24.6 (3420 ksi)
2	Hinge 4- Hinge 11	Reinforced	24.6 (3420 ksi)
3	Hinge 11- Hinge 14	Prestressed	27.9 (4047 ksi)
4	Hinge 14- Abutment 18	Reinforced	24.6 (3420 ksi)

Table 3.13: Gross section properties for columns in SE connector in the local coordinate system (weak axis, y, and strong axis, z, against bending)

Bent	Retrofit	Moments of Inertia		
	Class type	I_z (m^4)	I_y (m^4)	J (m^4)
2	P/F	0.413	29.413	27.114
3 - 4	P (outrigger)	2.446	456.001	458.745
5	P	0.413	29.413	27.114
6 – 7	F	0.872	1.778	2.304
8	P	0.831	1.700	2.304
9 - 10	P/F	0.831	1.700	2.304
11 – 17	F	0.872	1.778	2.304

Table 3.14: Properties of Rayleigh damping for the SE connector

Connectors	α (Mass-proportional)	β (Stiffness-proportional)
South-East	4.392×10^{-1}	5.075×10^{-3}

Table 3.15: Vibration properties of South-East connector with nonlinear hinges and closed hinges mechanism

Mode	Type	Nonlinear hinge mechanism		Closed hinge
		Transverse	Longitudinal	Transverse
1	Anti-symmetric	1.661		
			1.327	
				1.310
2	Anti-symmetric	1.210		1.225
3	Anti-symmetric	1.097		
4	Anti-symmetric	1.080		
5	Anti-symmetric	0.952		1.00
				0.886
			0.779	
6	Anti-symmetric	0.763		0.761

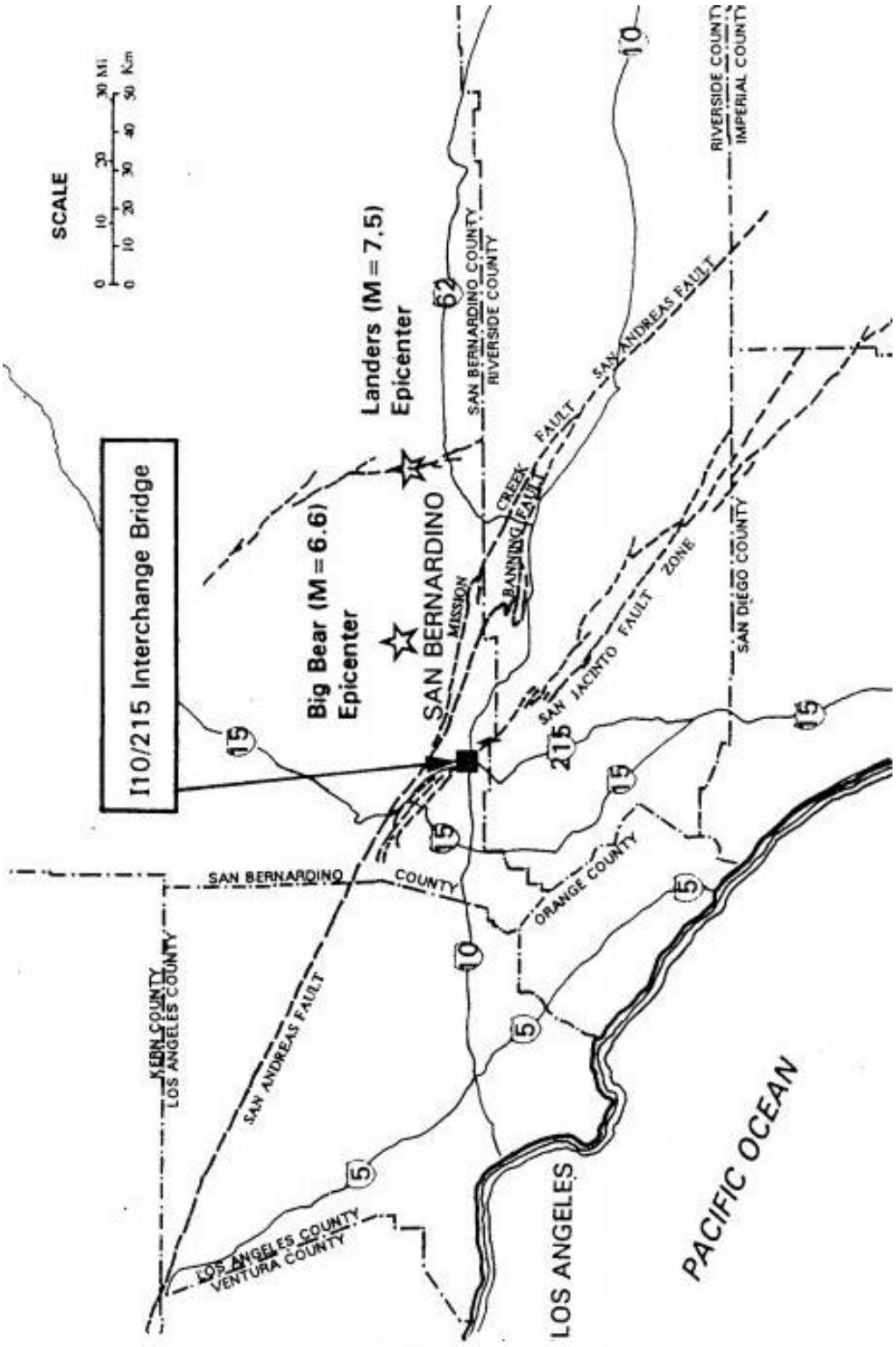

Figure 3.1: Location of the I-10/215 interchange (Huang et al. 1995)

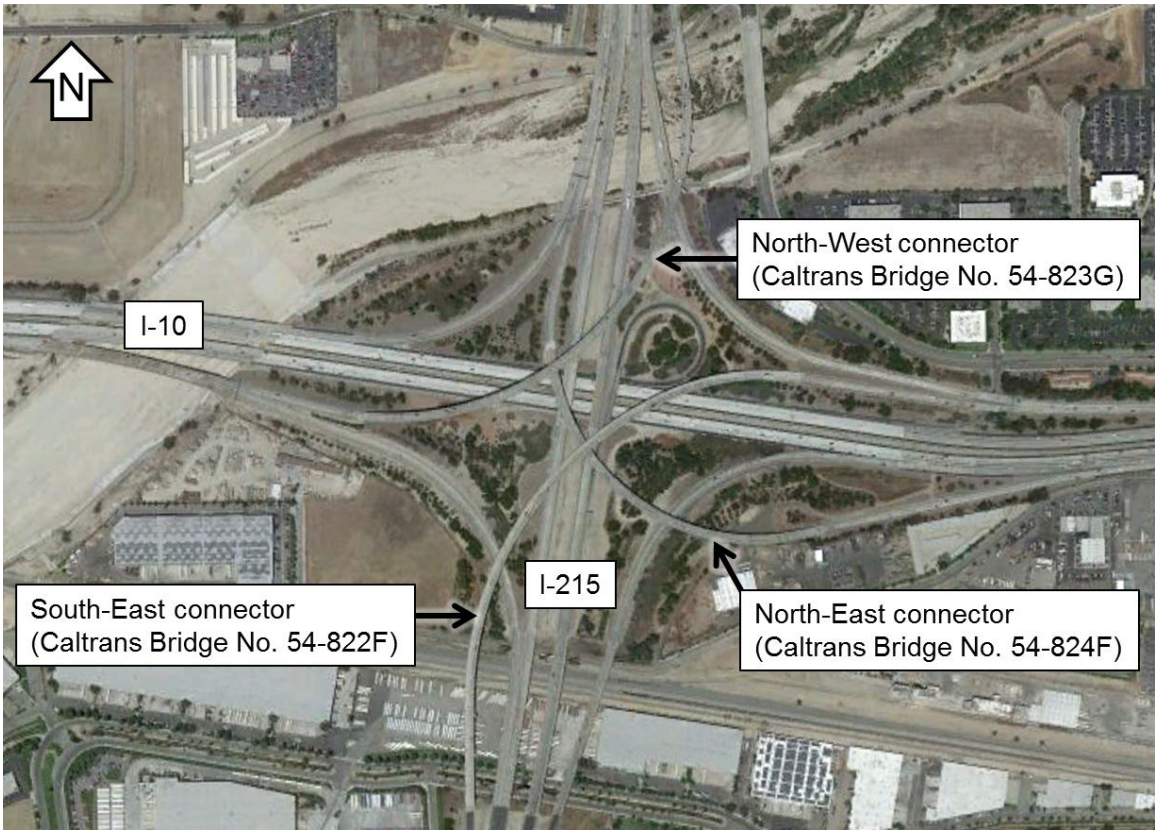

Figure 3.2: Aerial photograph of the I-10/215 interchange (©2013 Google - http://maps.google.com

Figure 3.3: Aerial photograph of the NW connector at the I-10/215 interchange (©2013 Google - http://maps.google.com)

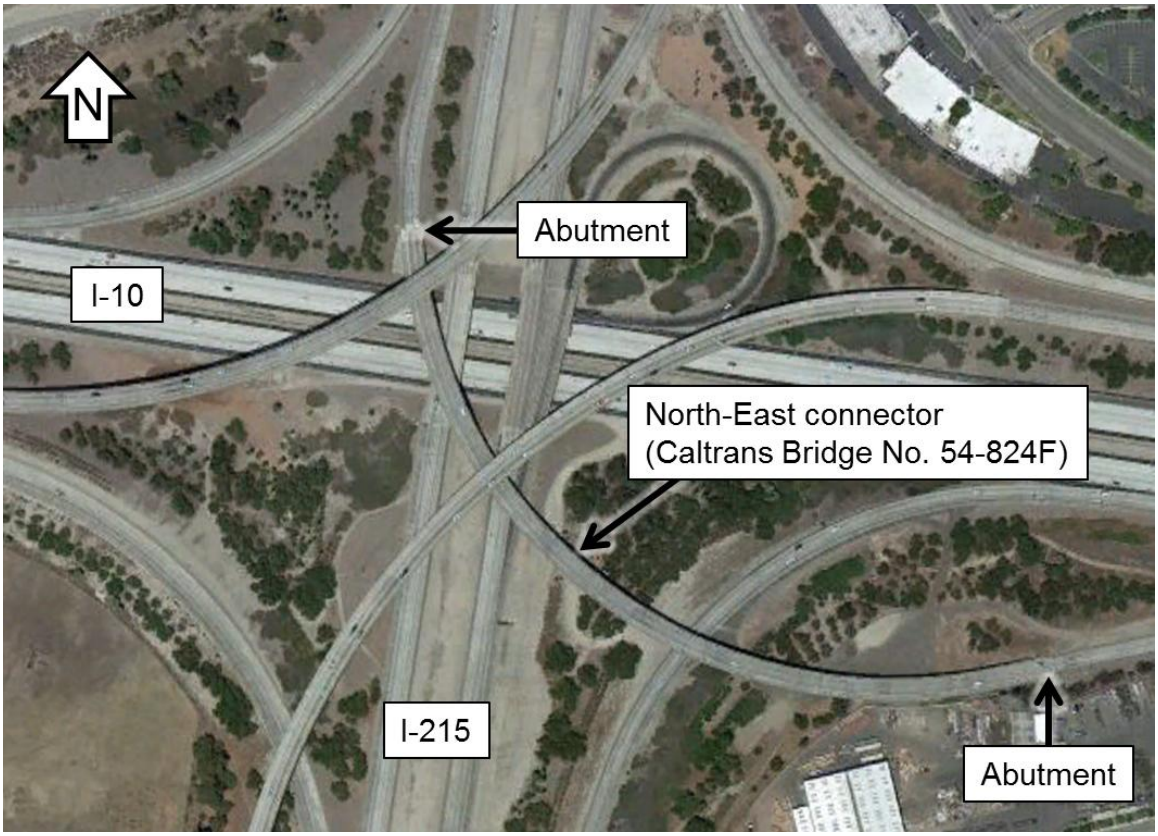

Figure 3.4: Aerial photograph of the NE connector at the I-10/215 interchange (©2013 Google - http://maps.google.com)

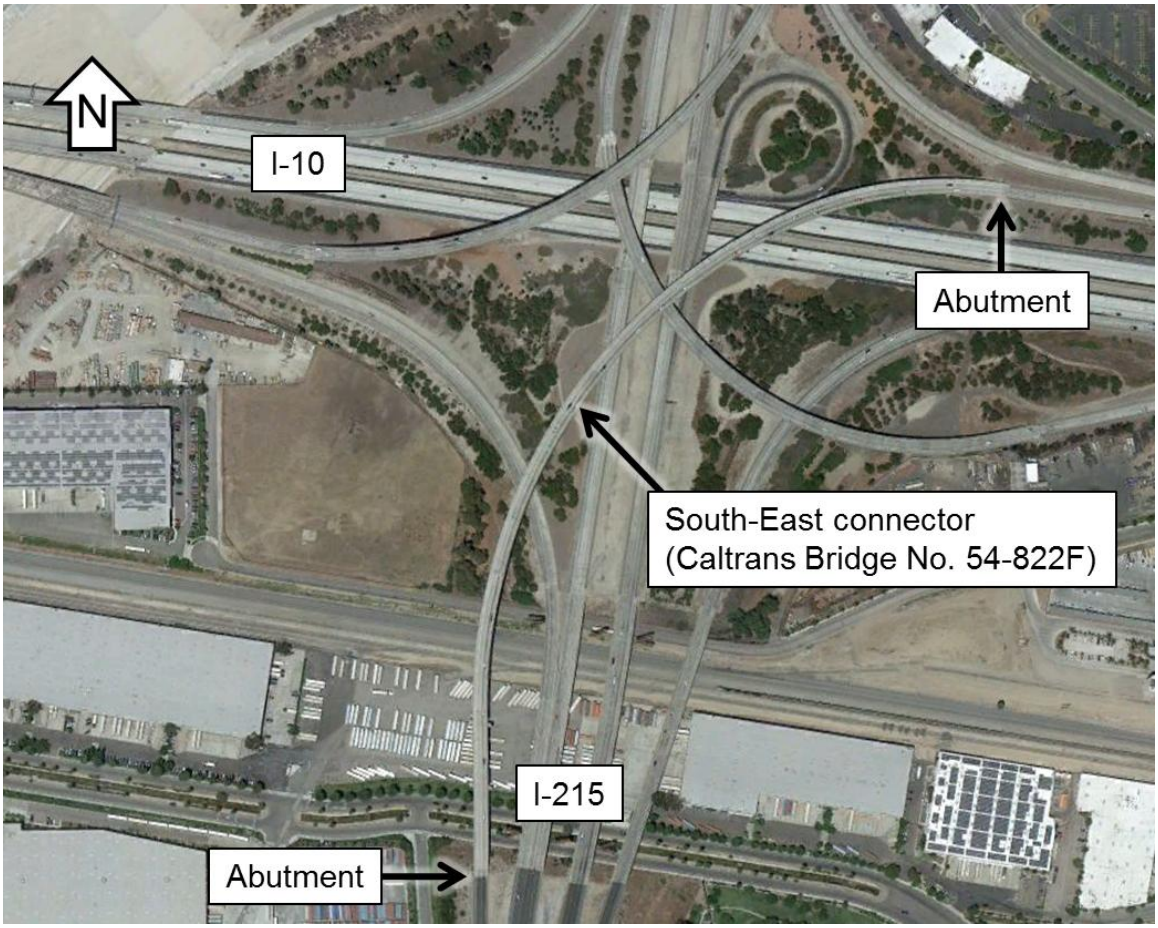

Figure 3.5: Aerial photograph of the SE connector at the I-10/215 interchange (©2013 Google - http://maps.google.com)

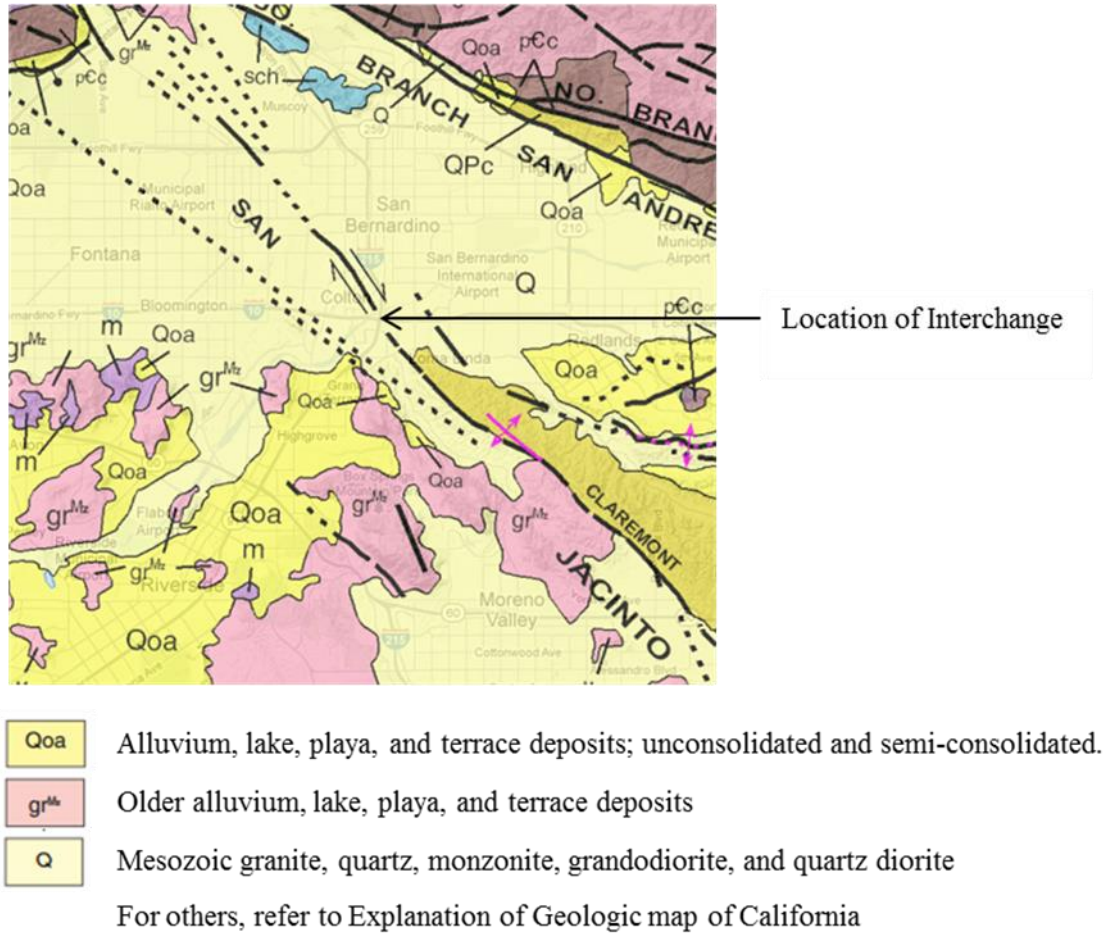

Figure 3.6: Geological map near the I-10/215 interchange (2010 State Geological Map of California)

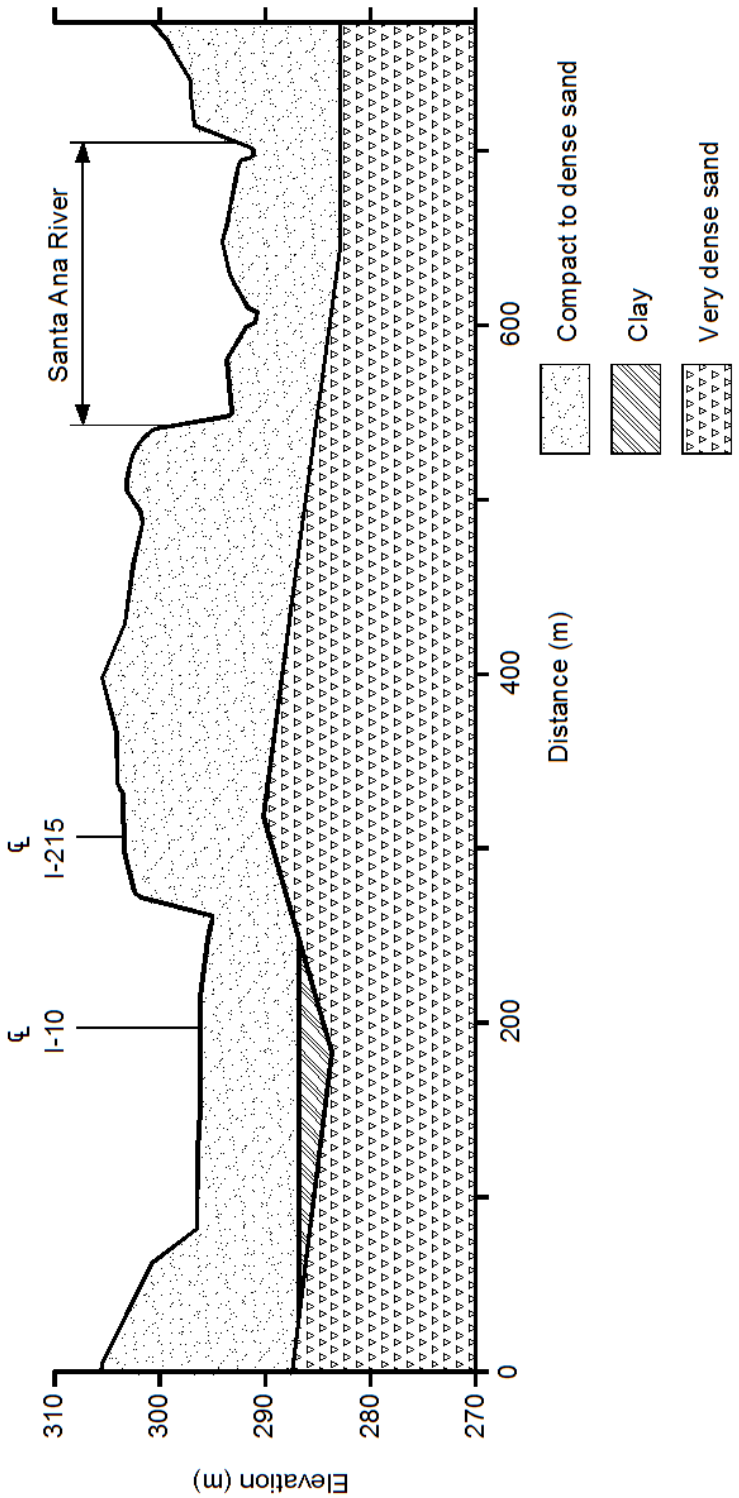

Figure 3.7: Soil profile at the I-10/215 interchange

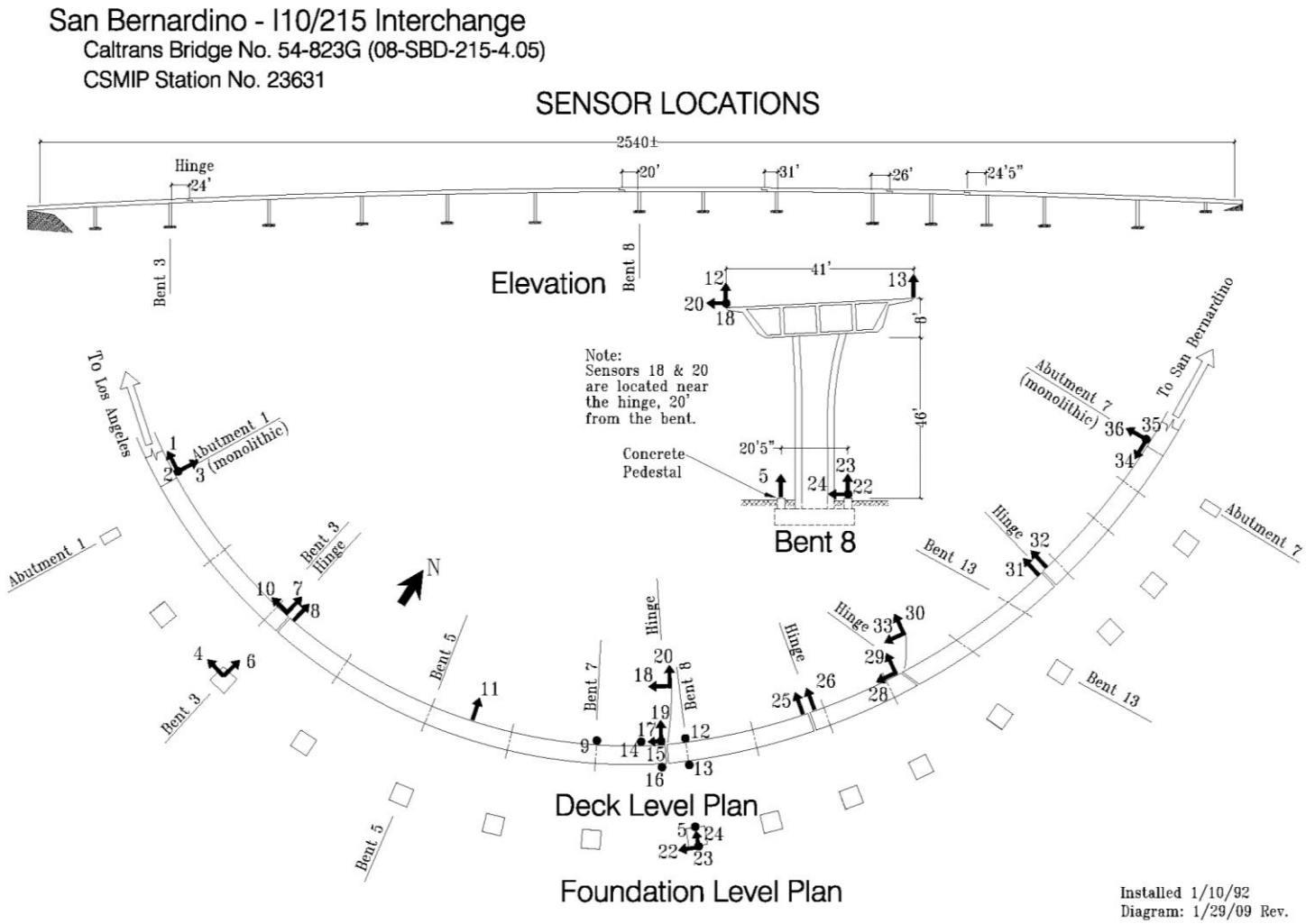

Figure 3.8: Seismic instrumentation for the North-West connector

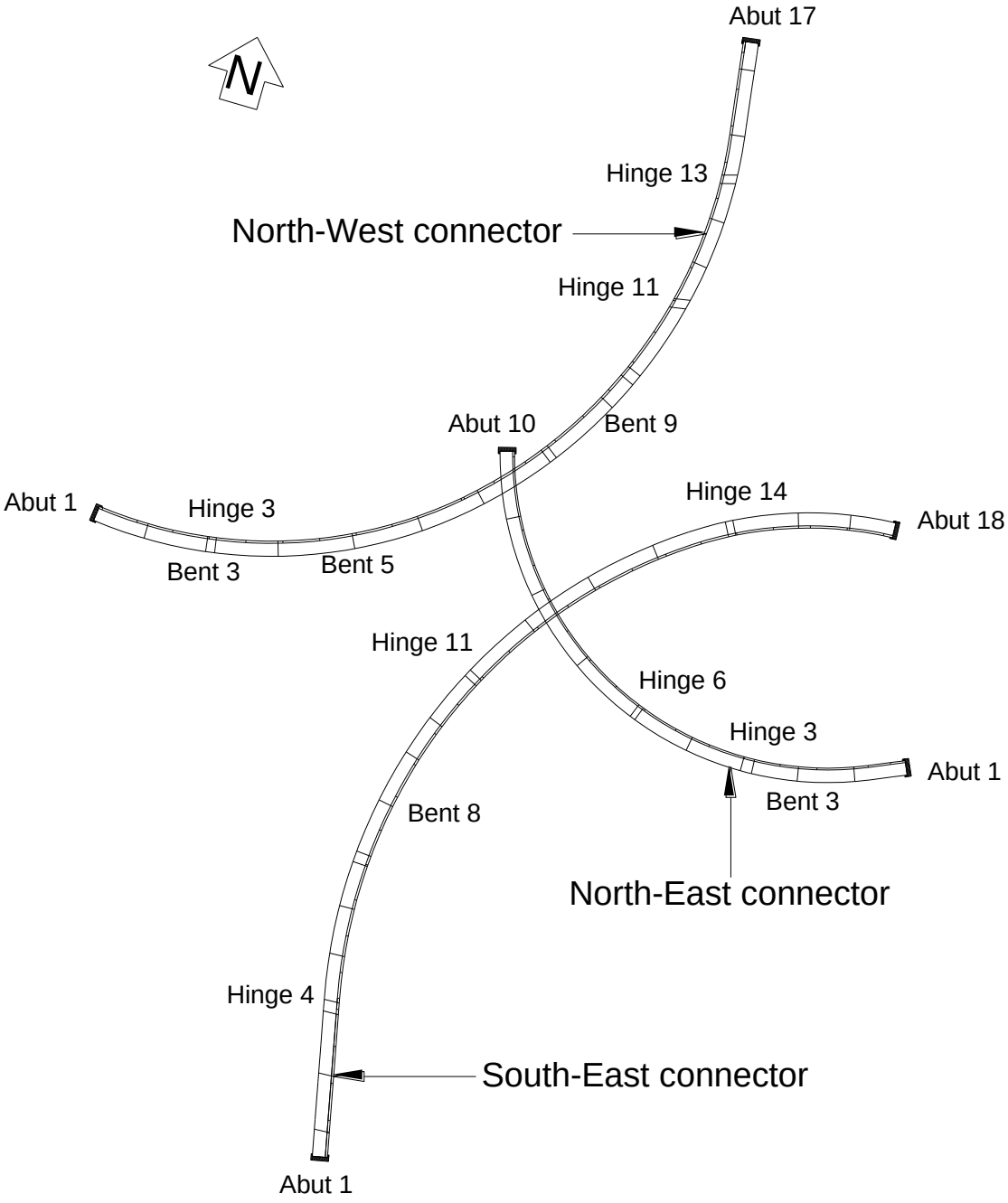

Figure 3.9: General plan view of NW, NE, and SE connectors

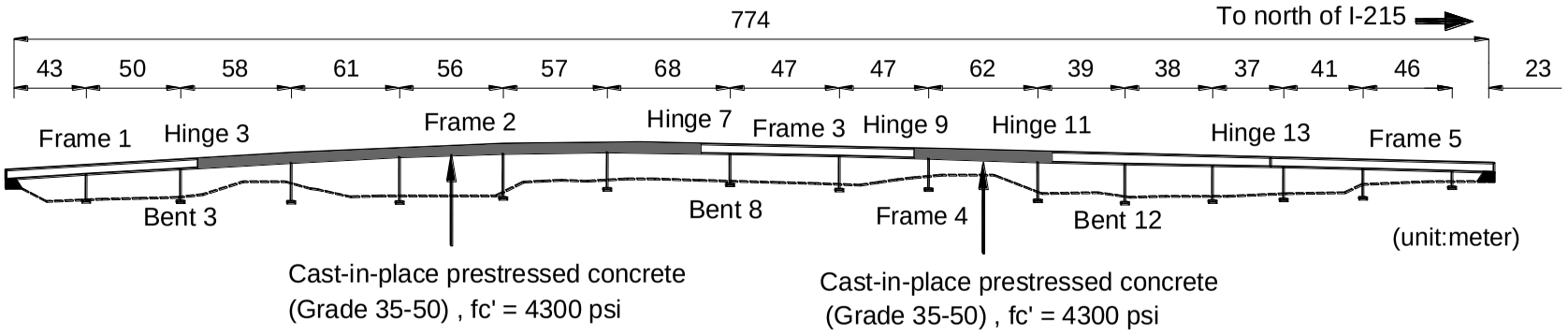

Figure 3.10: Elevation view of the NW connector

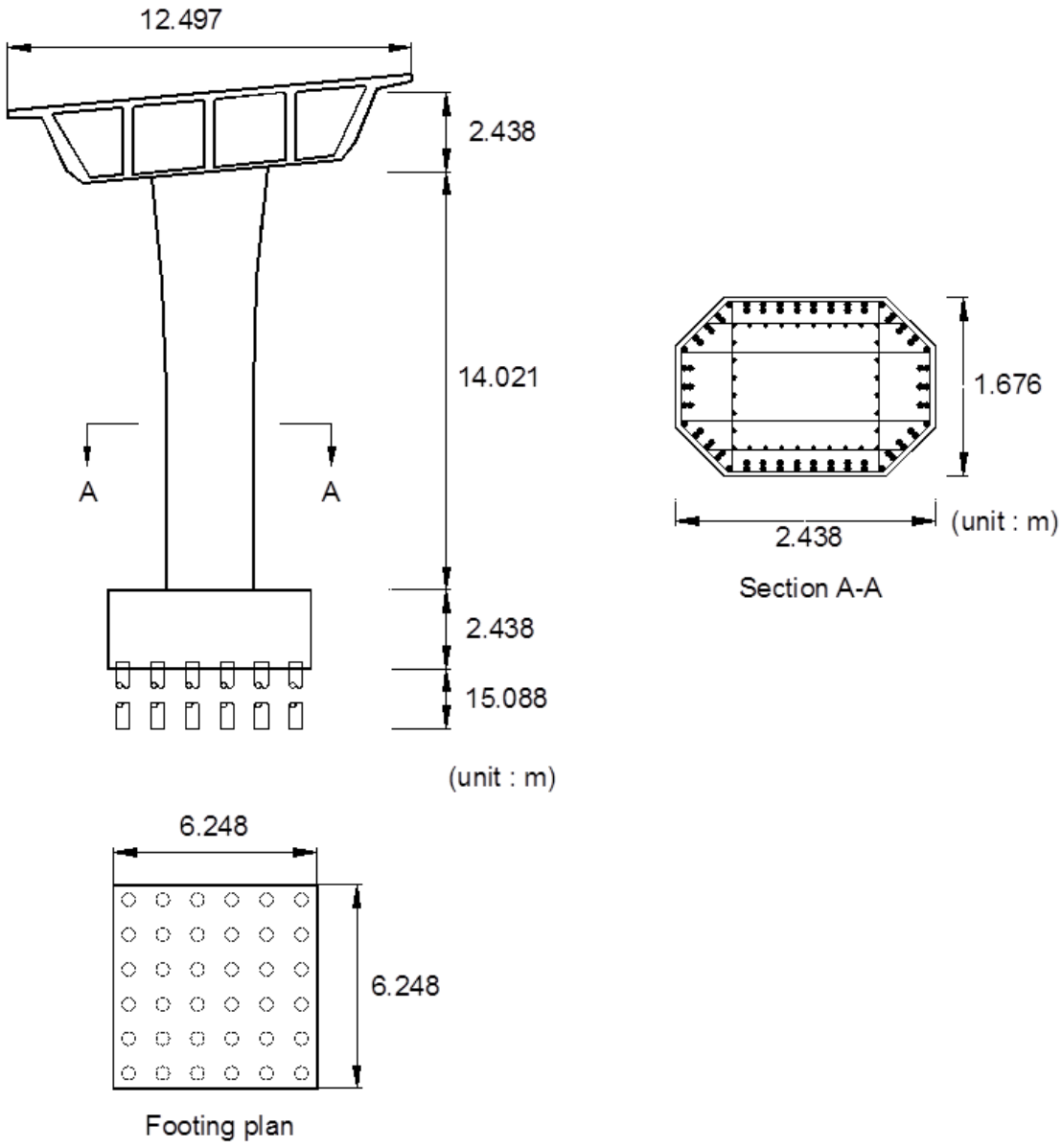

Figure 3.11: Elevation view of the single column bent and footing plan (Bent 8 of the North-West connector)

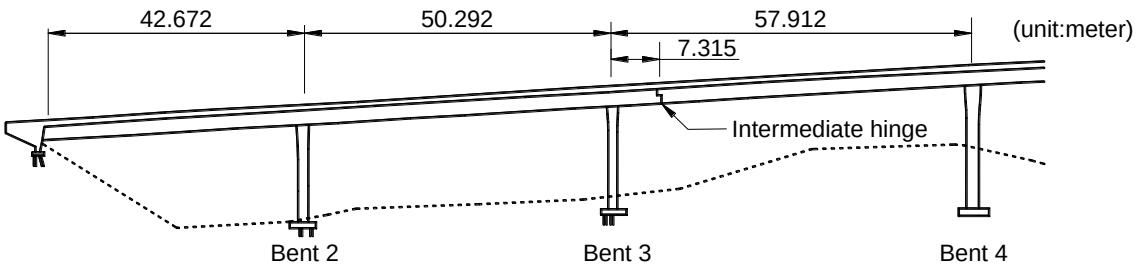

Figure 3.12: Elevation view from the Abutment to Bent 4 in the North-West connector

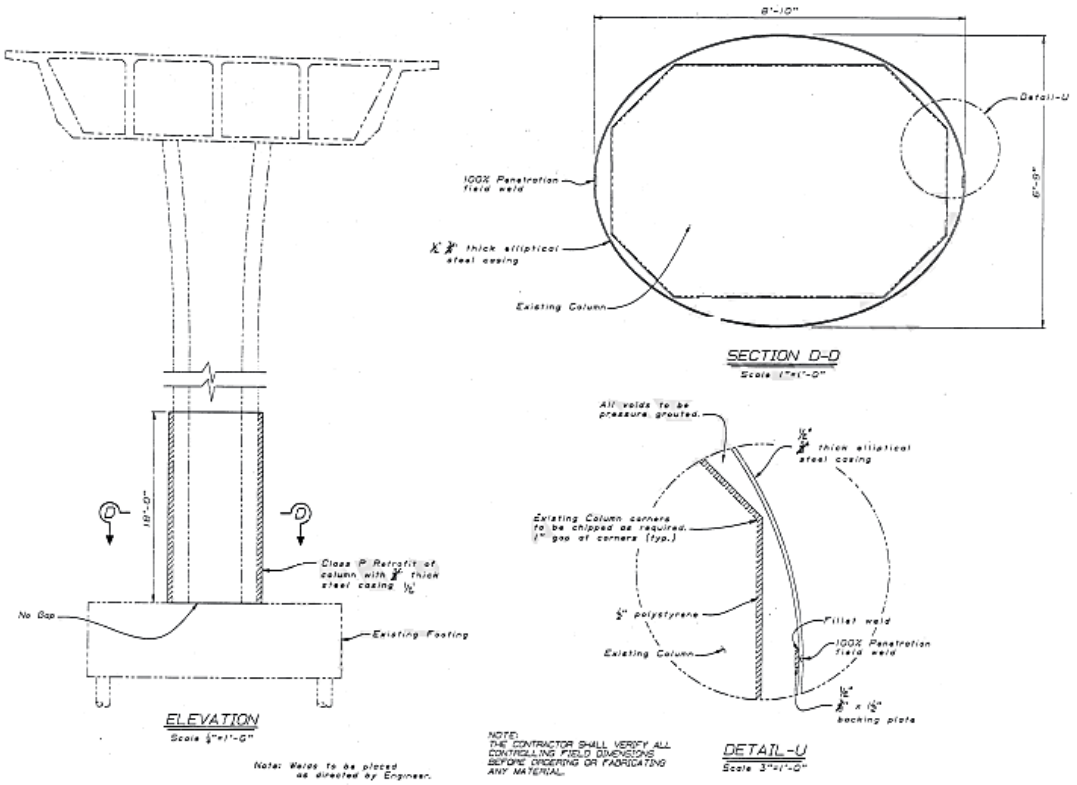

(a) Class P column

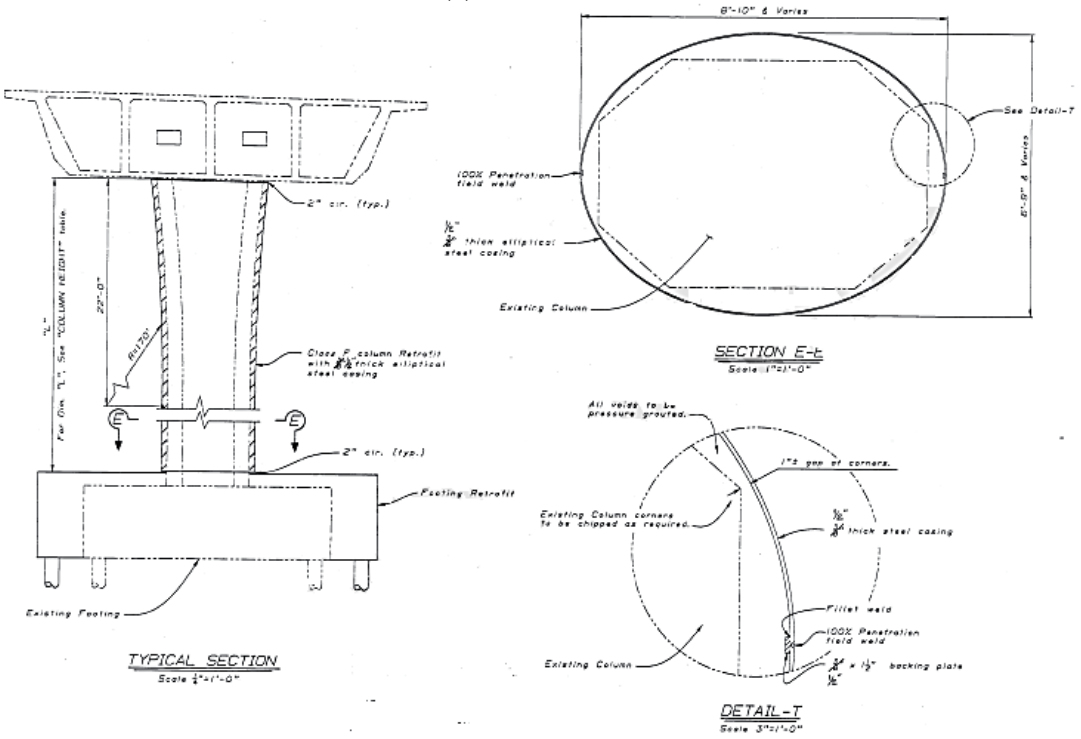

(b) Class F column

Figure 3.13: As-built plan for the column retrofit (Caltrans)

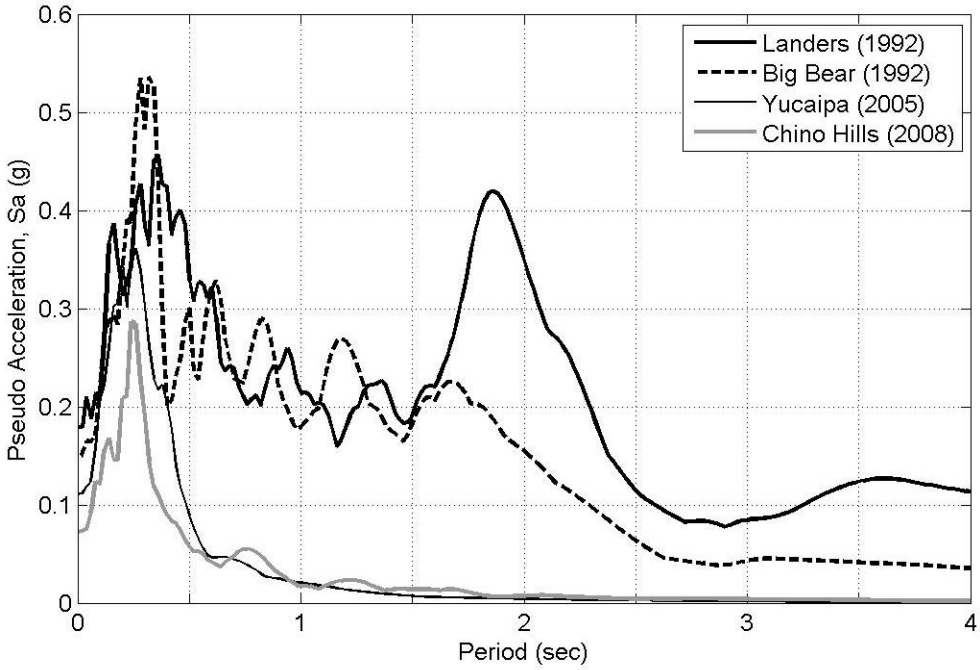

Figure 3.14: Elastic response spectra with 5% damping for records at the foundation of Bent 8 (channel 22) in the transverse direction

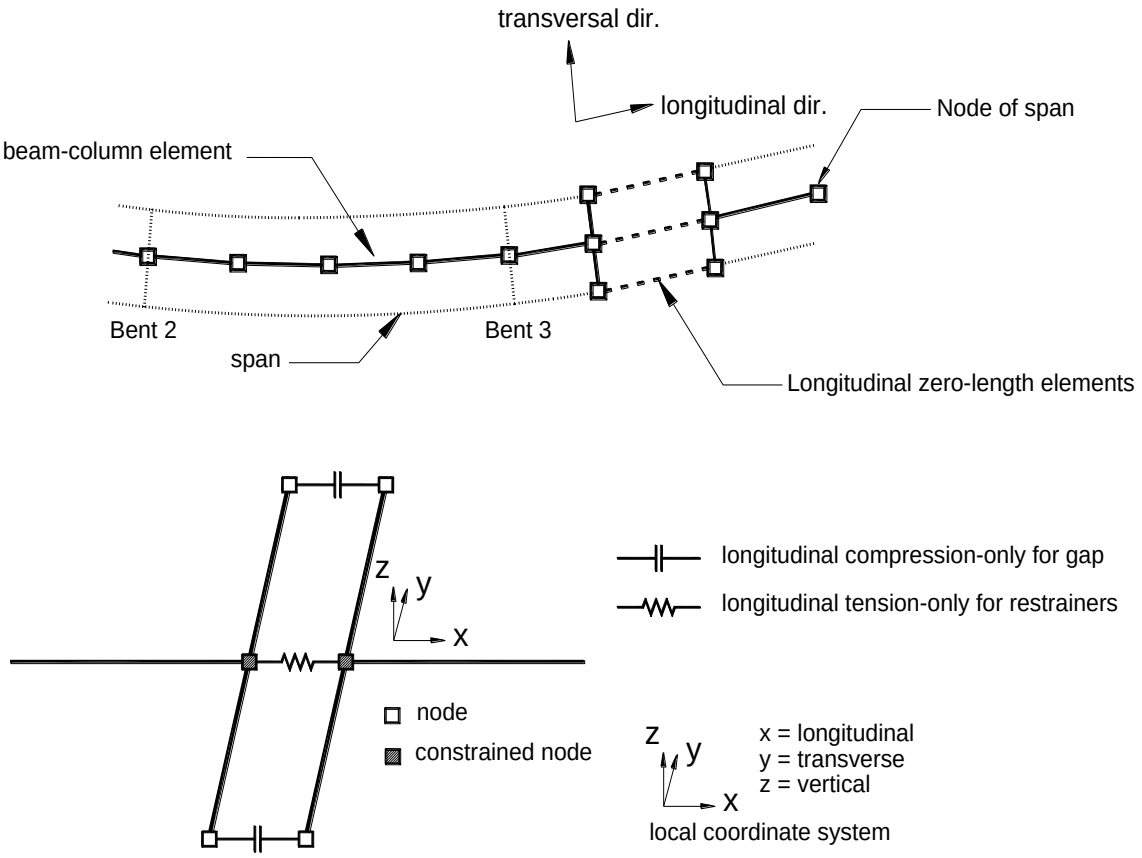

Figure 3.15: Schematic plan view of the hinge model

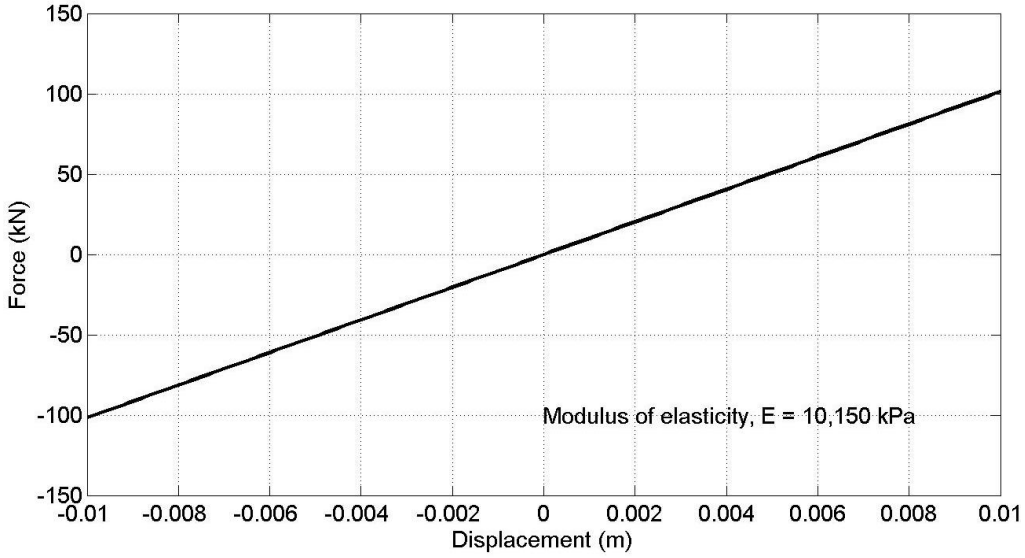

Figure 3.16: Relation of force and displacement for the bearing material

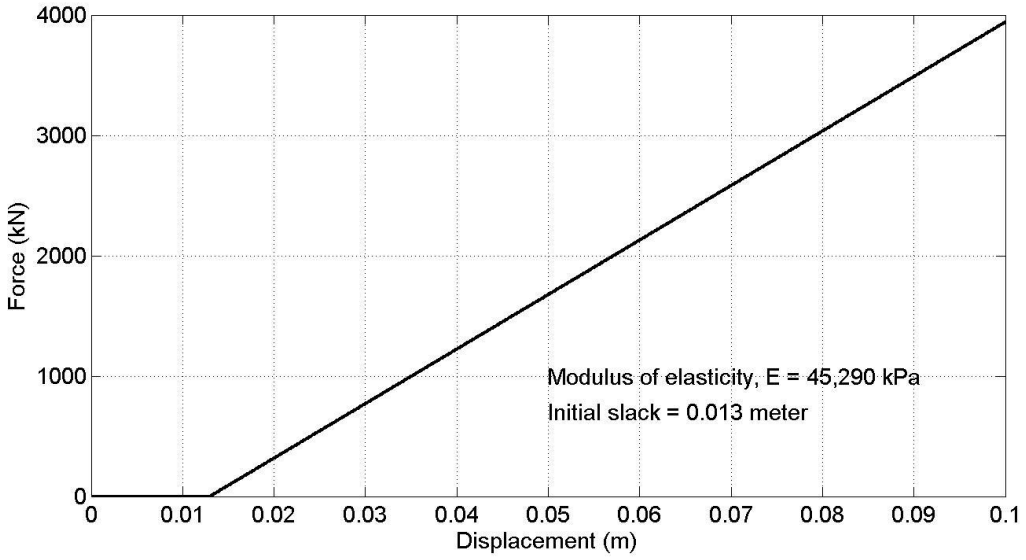

Figure 3.17: Relation of force and displacement for the restrainer cable

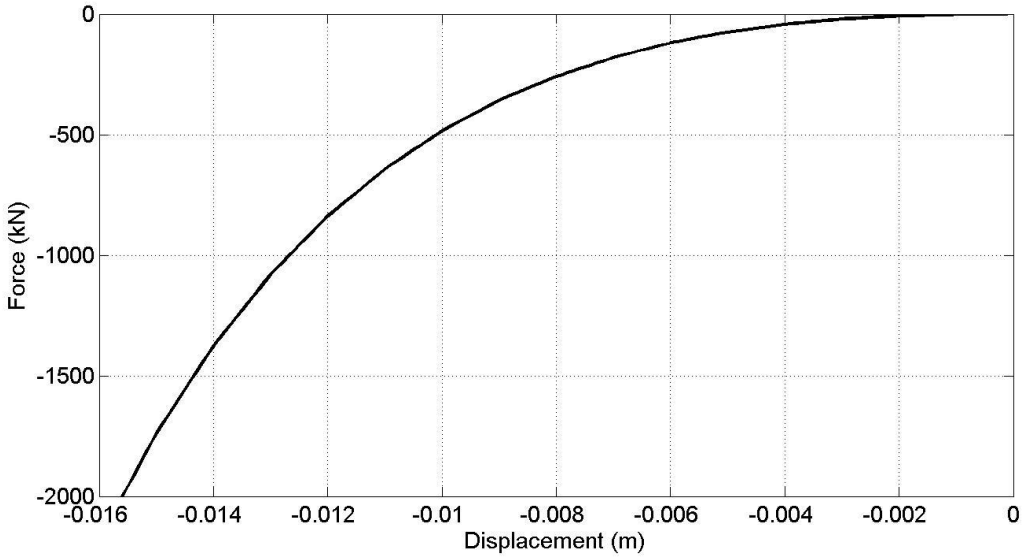

Figure 3.18: Force-displacement relation in longitudinal compression-only for gap

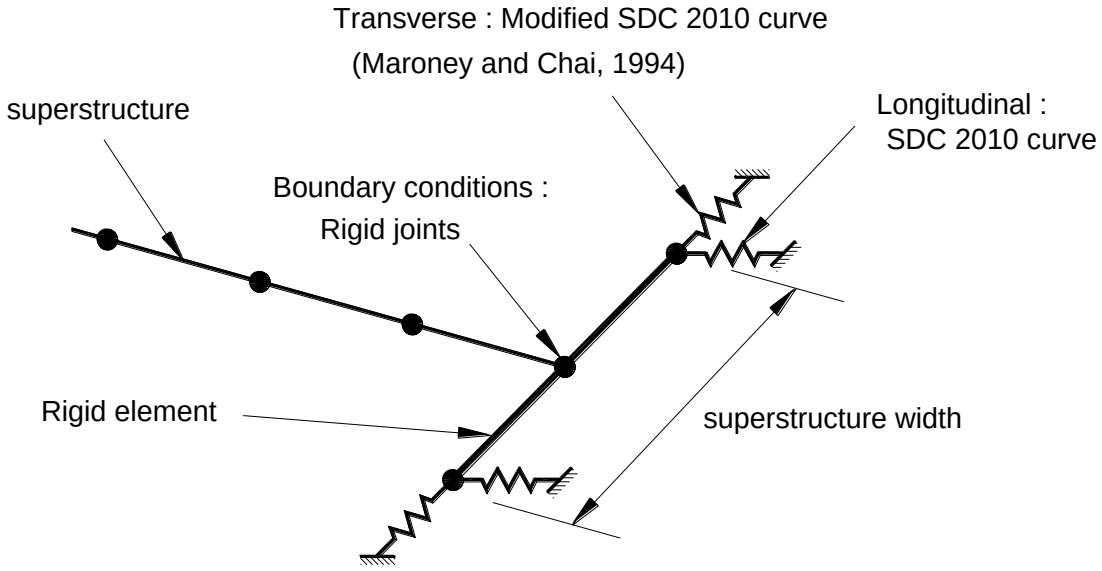

Figure 3.19: Schematic view of the abutment model

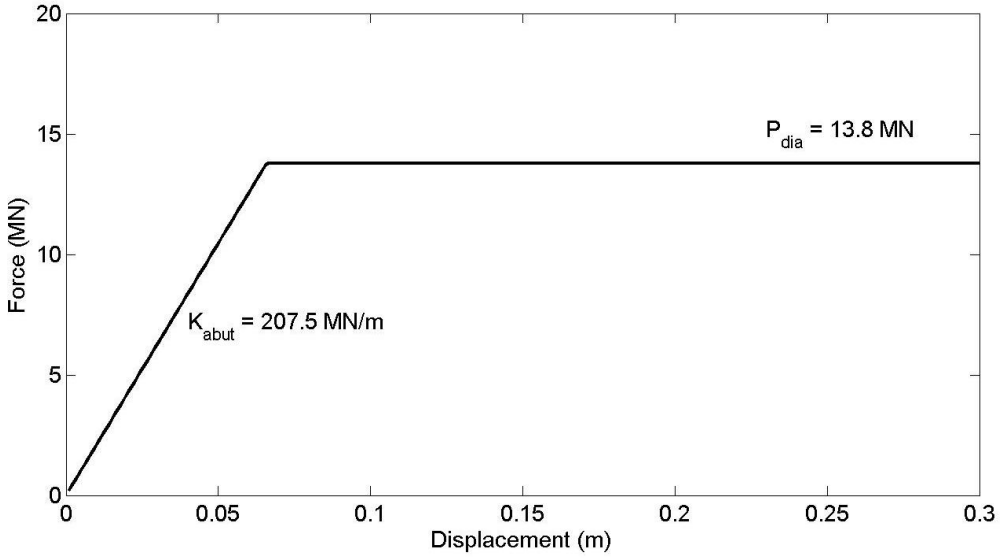

Figure 3.20: Force-displacement relation for the longitudinal spring model

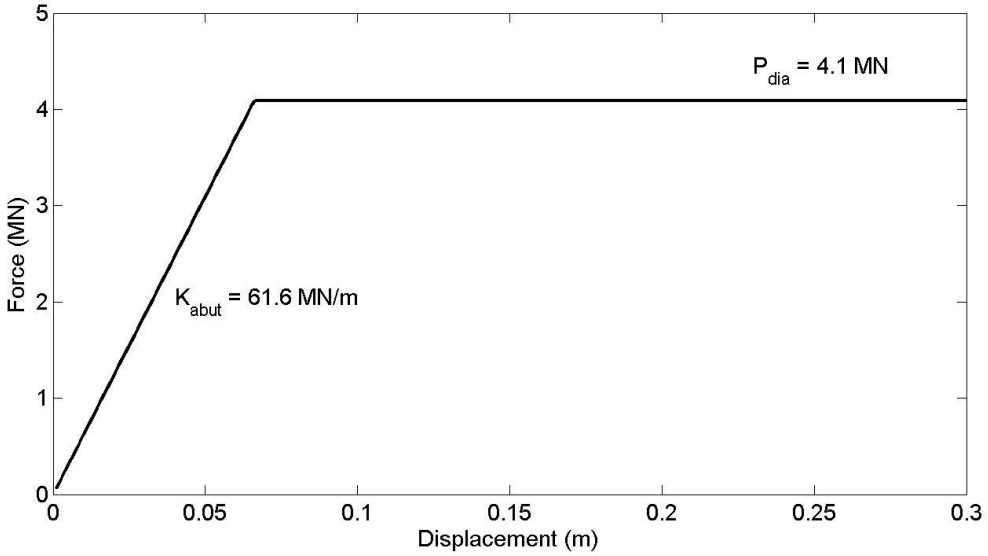

Figure 3.21: Force-displacement relation for the transverse spring model

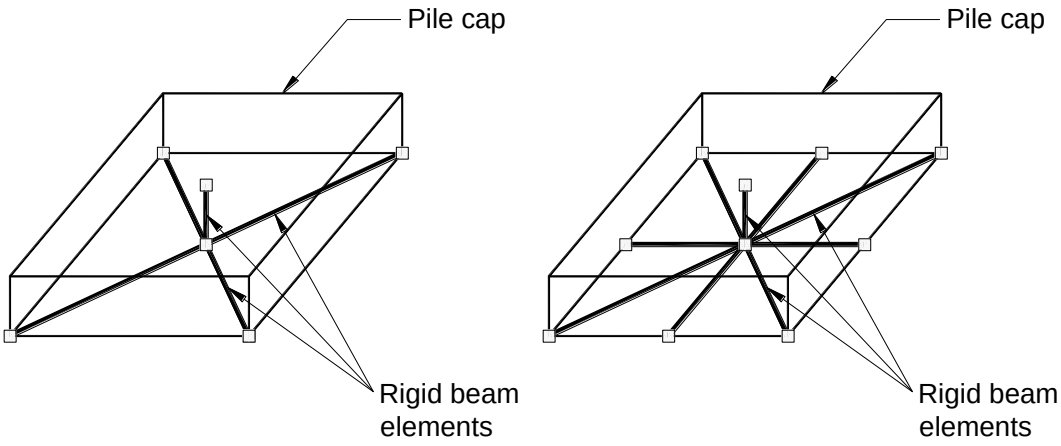

(a) For Bents 2, 6, 10, 11, 12, 14, and 16 (b) For Bents 3, 4, 5, 7, 8, 9, 13, and 15

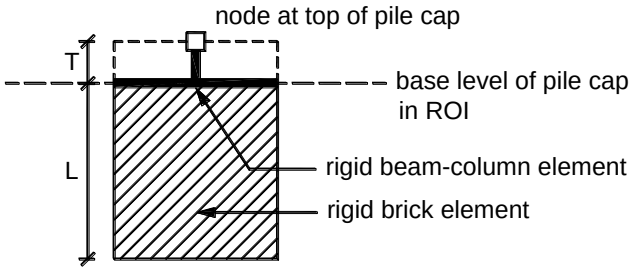

(c) Rigid elements for the pile group foundation

Figure 3.22: Schematic view of the pile cap model

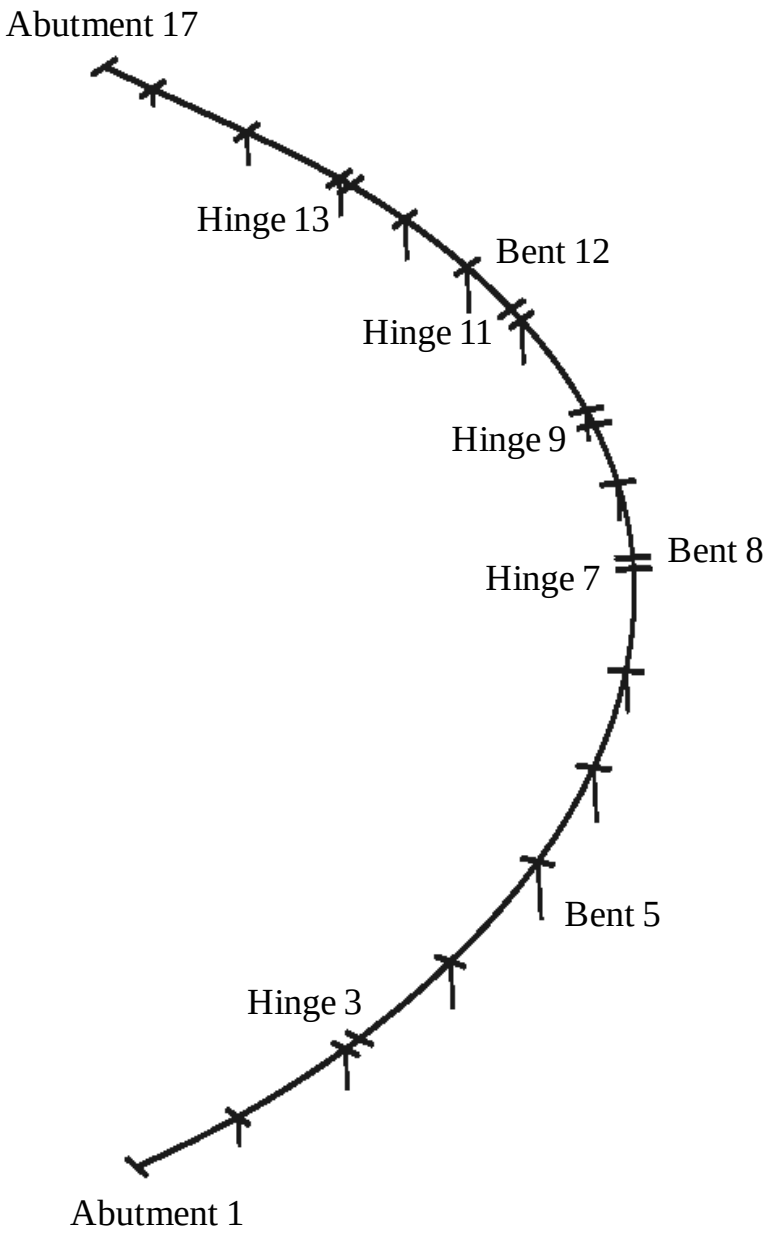

Figure 3.23: 3D view of the North-West connector (foundations are not shown)

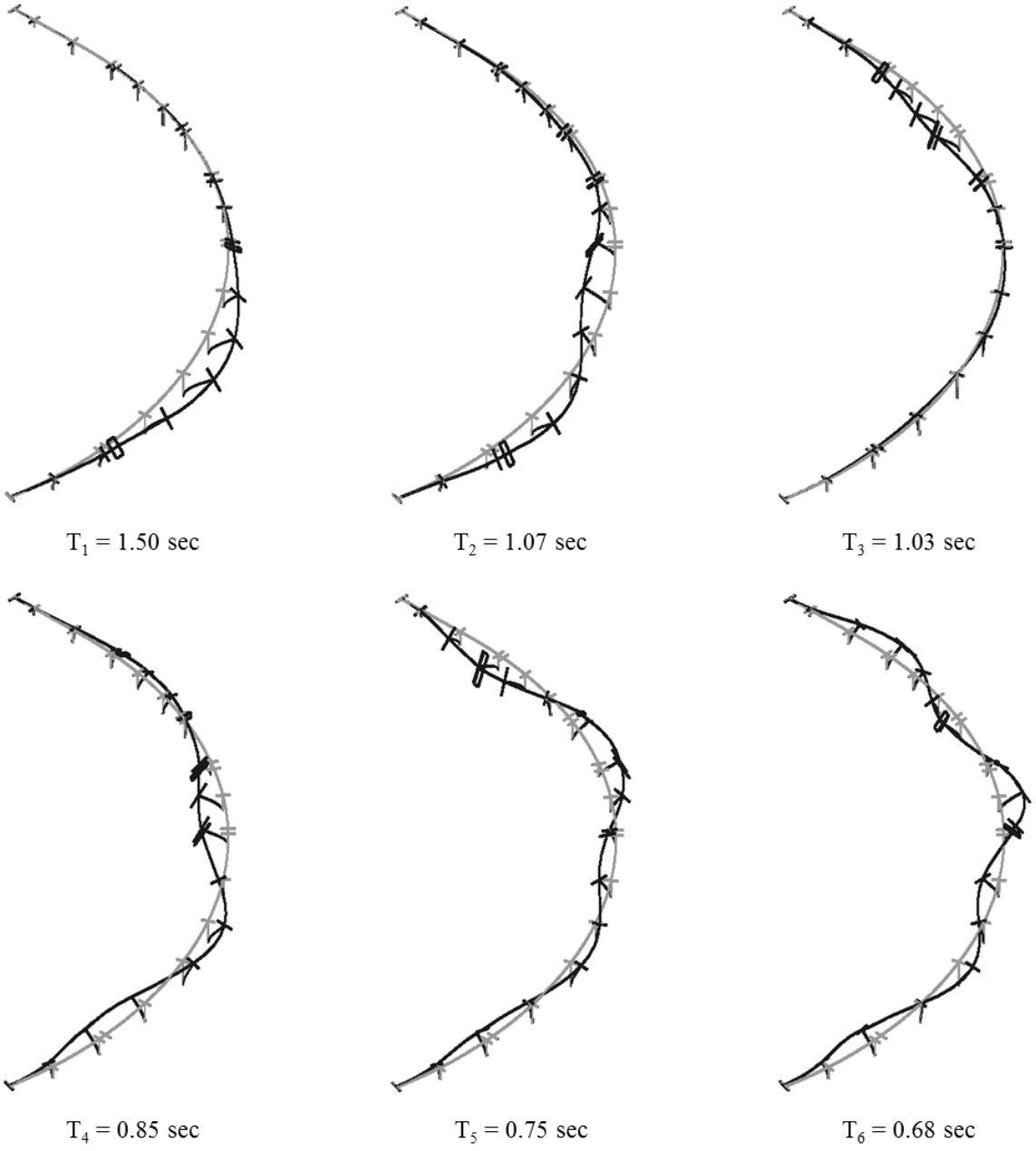

Figure 3.24: Lower frequency modes of the North-West connector with the nonlinear hinge mechanism

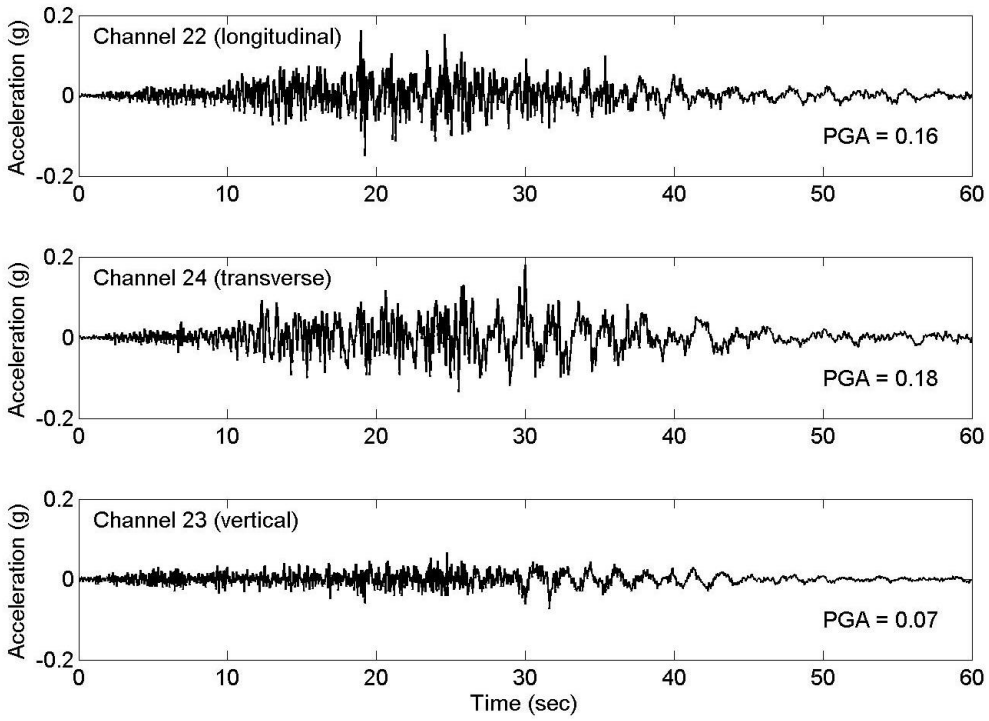

Figure 3.25: Acceleration time histories recorded at the base of Bent 8 during Landers earthquake in 1992

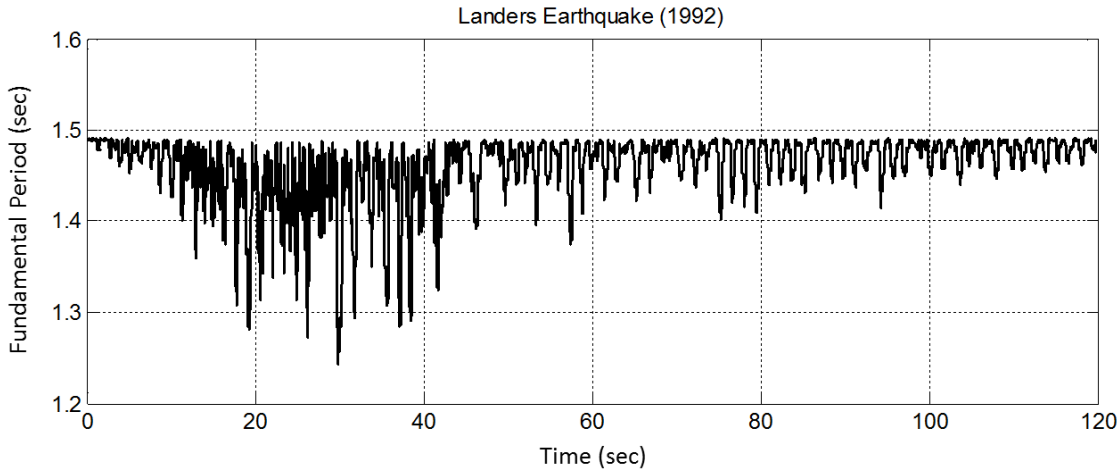

Figure 3.26: Variation of the fundamental period of the North-West connector during the Landers Earthquake

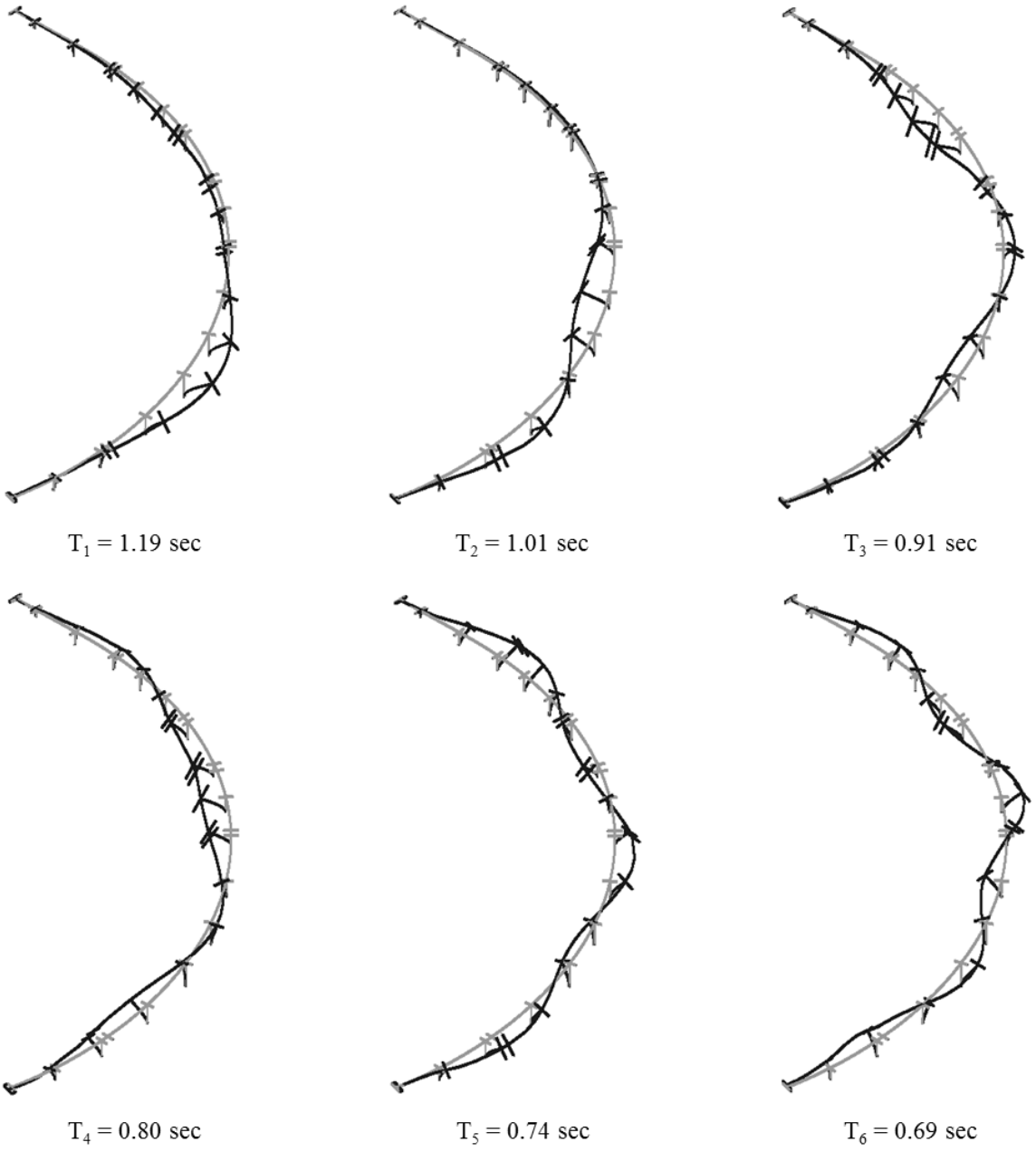

Figure 3.27: Lower frequency modes of the North-West connector with only compression hinge mechanism

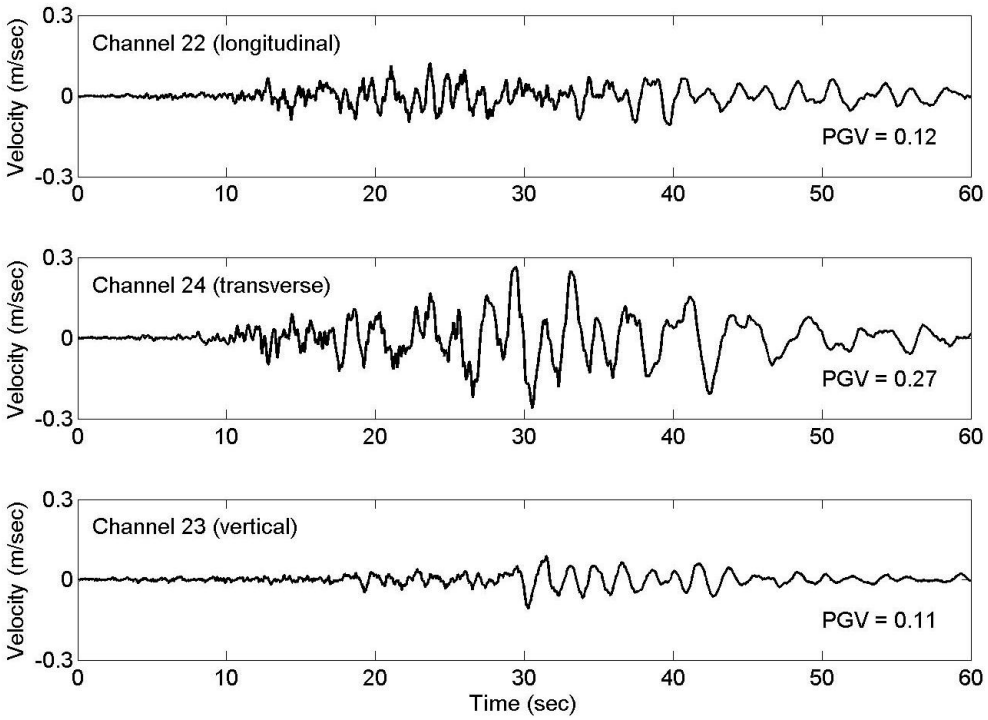

Figure 3.28: Velocity time histories recorded at the base of Bent 8 during Landers earthquake in 1992

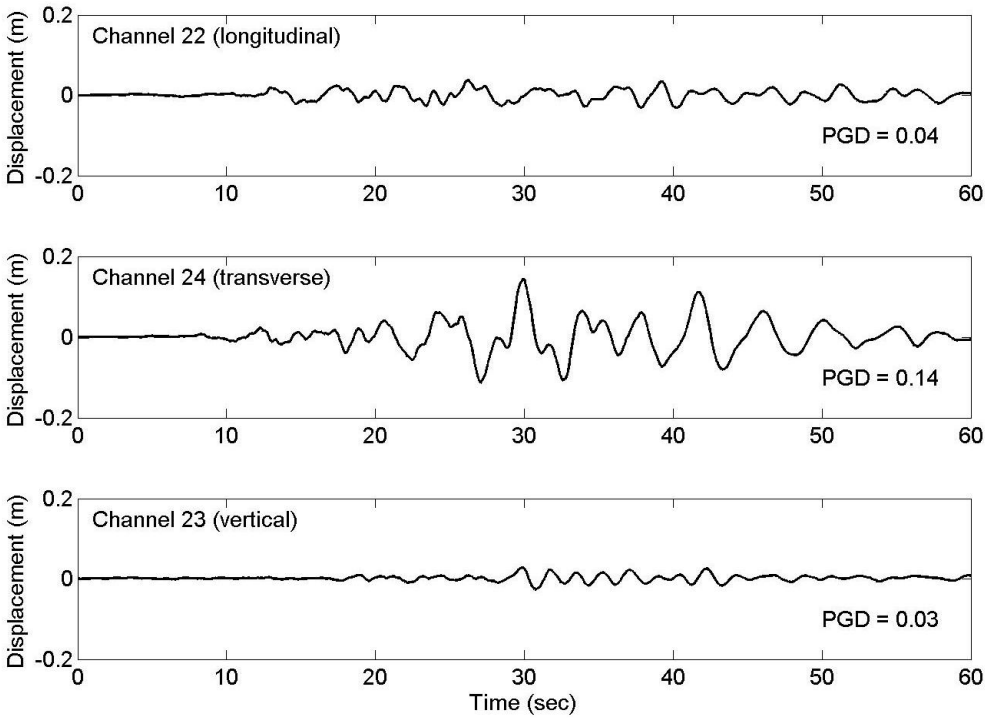

Figure 3.29: Displacement time histories recorded at the base of Bent 8 during Landers earthquake in 1992

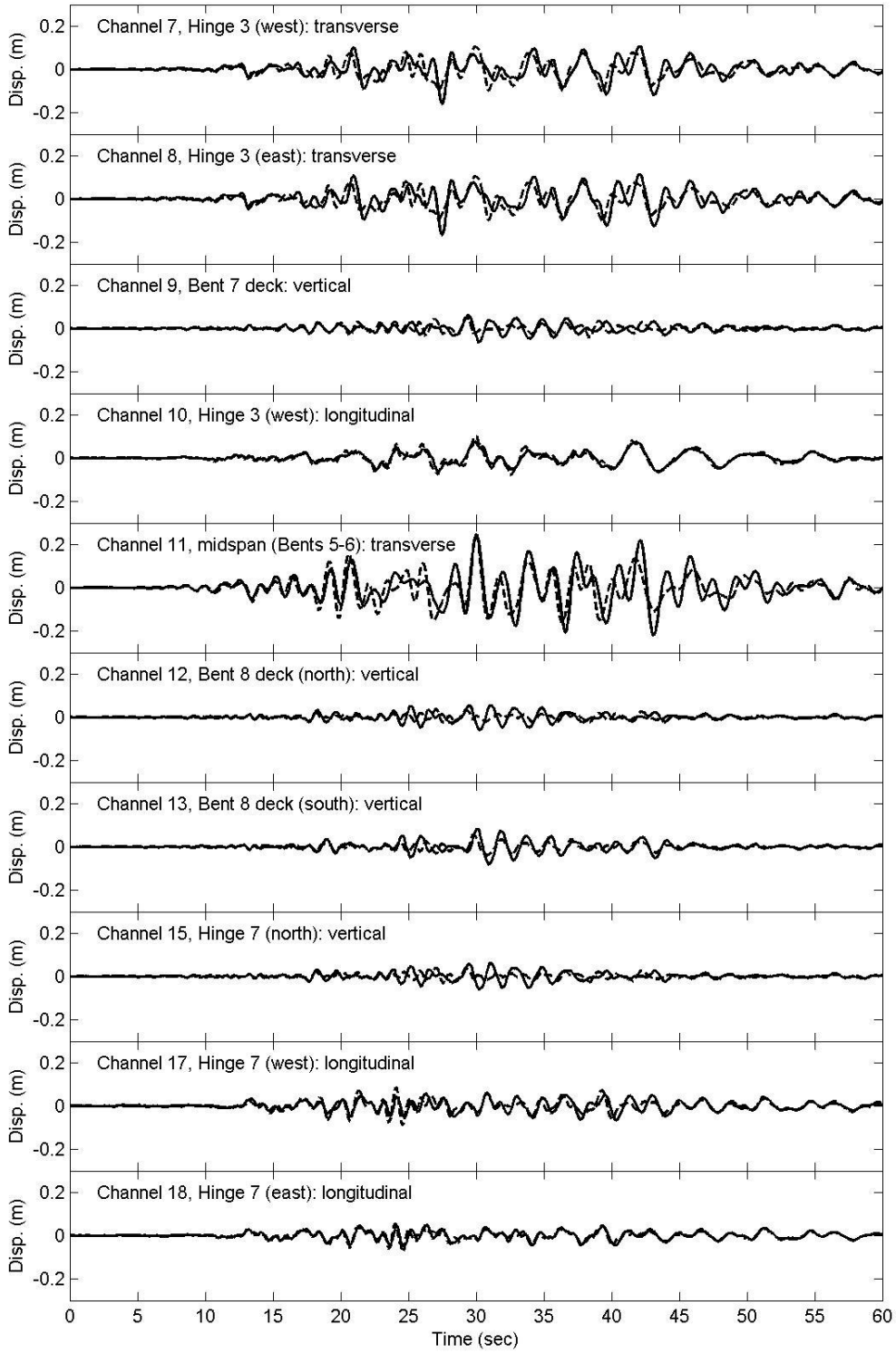

Figure 3.30: Comparison of recorded total displacement (solid line) with computed total displacement (dashed line) for Landers earthquake

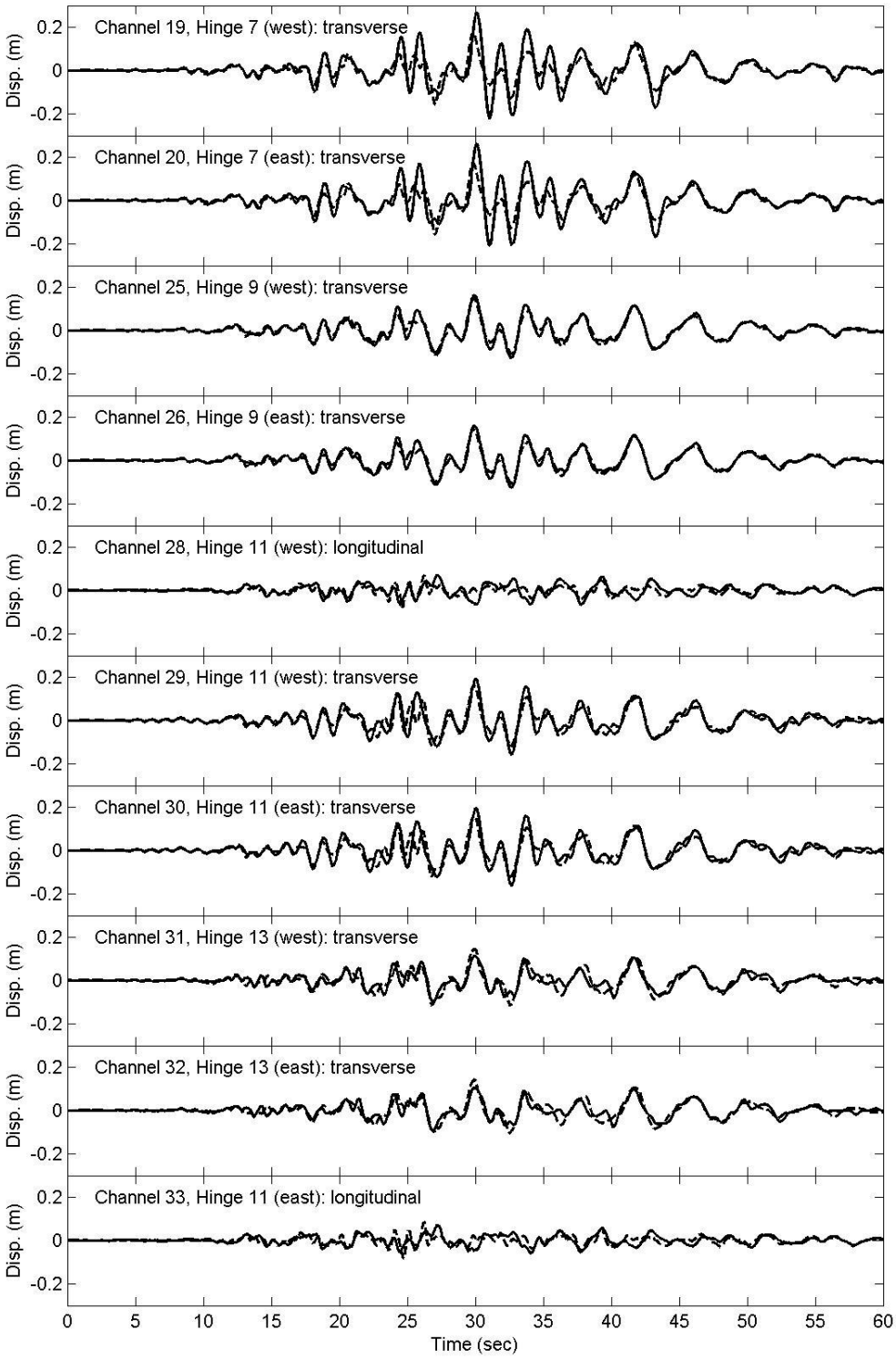

Figure 3.30 (continued): Comparison of recorded total displacement (solid line) with computed total displacement (dashed line) for Landers earthquake (continued from previous page)

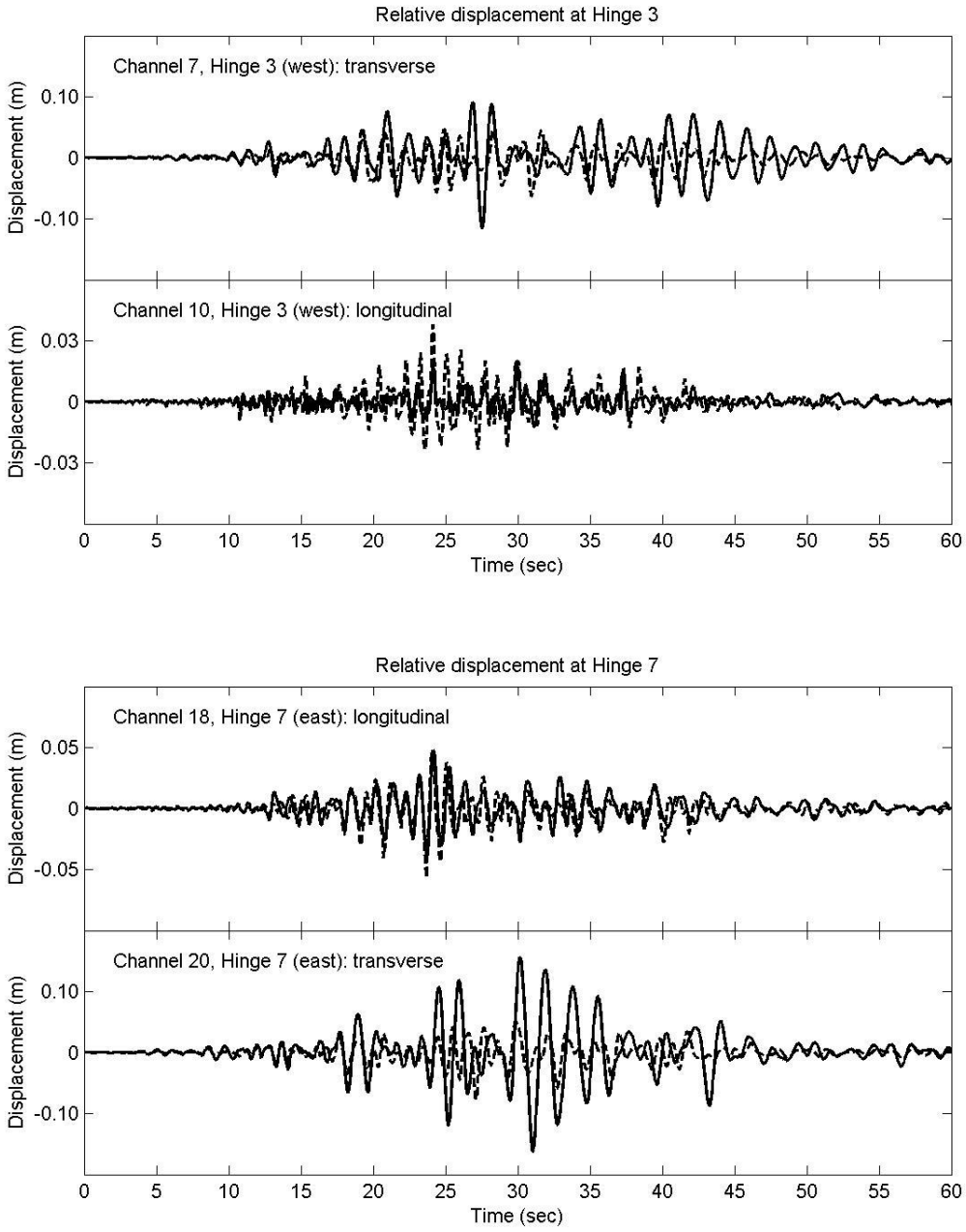

Figure 3.31: Comparison of relative displacement of deck relative to pile cap in Landers earthquake (solid for recorded, dashed for model)

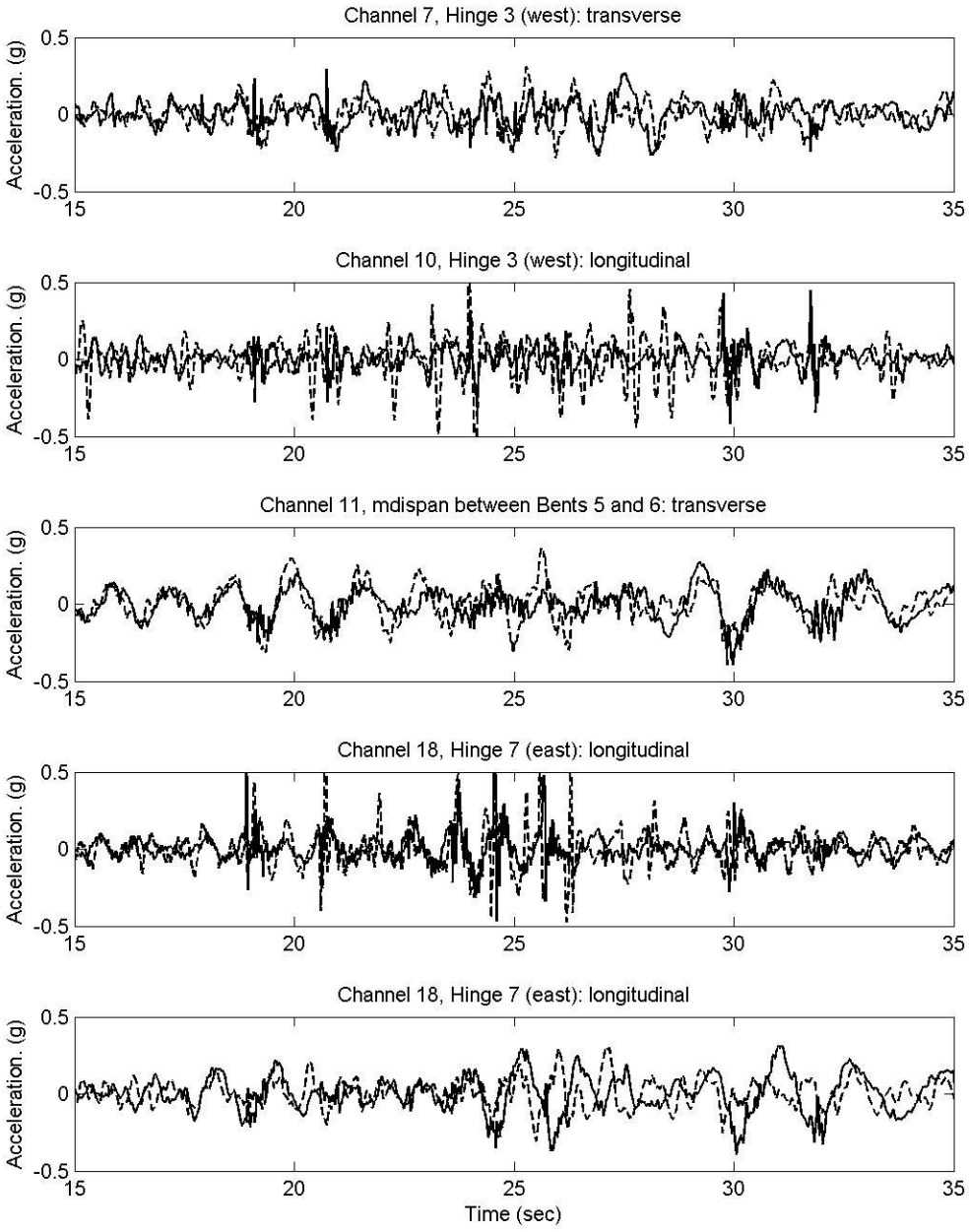

Figure 3.32: Comparison of recorded acceleration (solid line) with computed acceleration (dashed line) for Lander earthquake

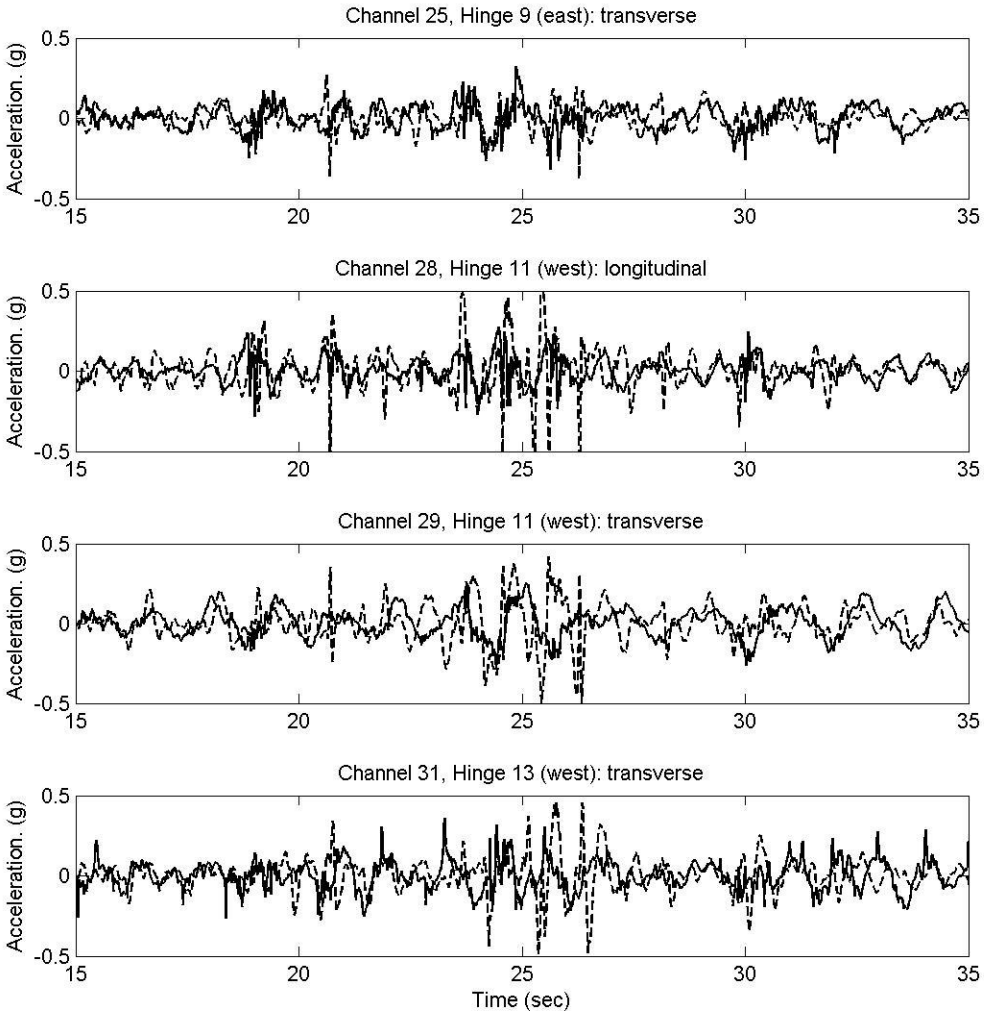

Figure 3.32 (continued): Comparison of recorded acceleration (solid line) with computed acceleration (dashed line) for Lander earthquake (continued from previous page)

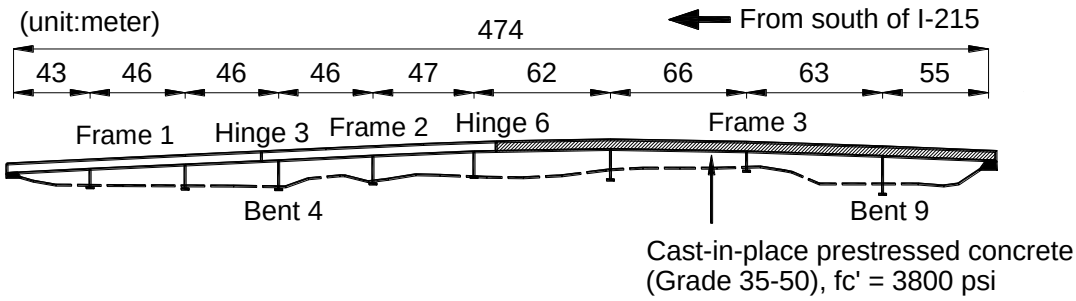

Figure 3.33: Elevation view of the NE connector

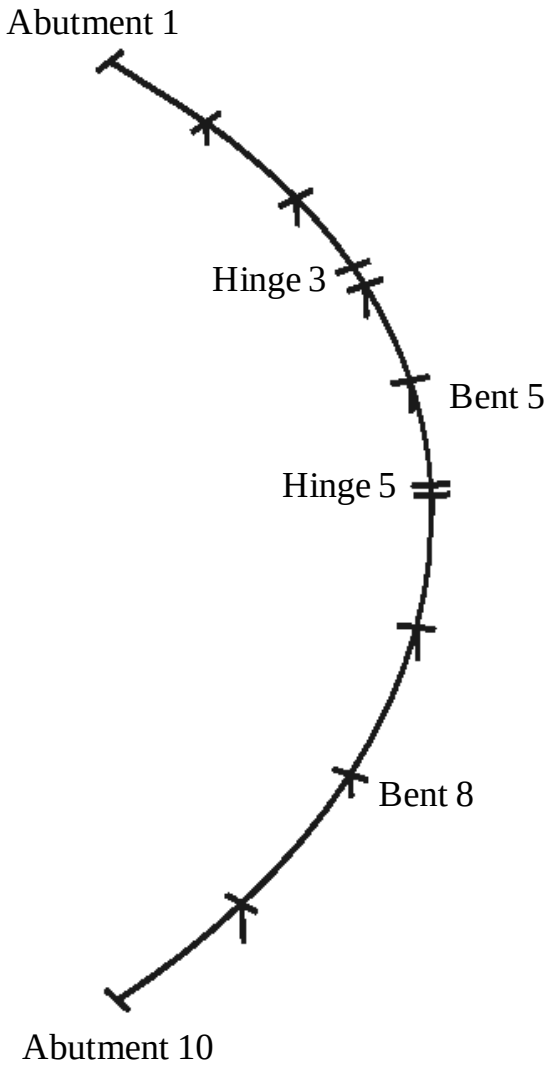

Figure 3.34: 3D view of the North-East connector (foundations are not shown)

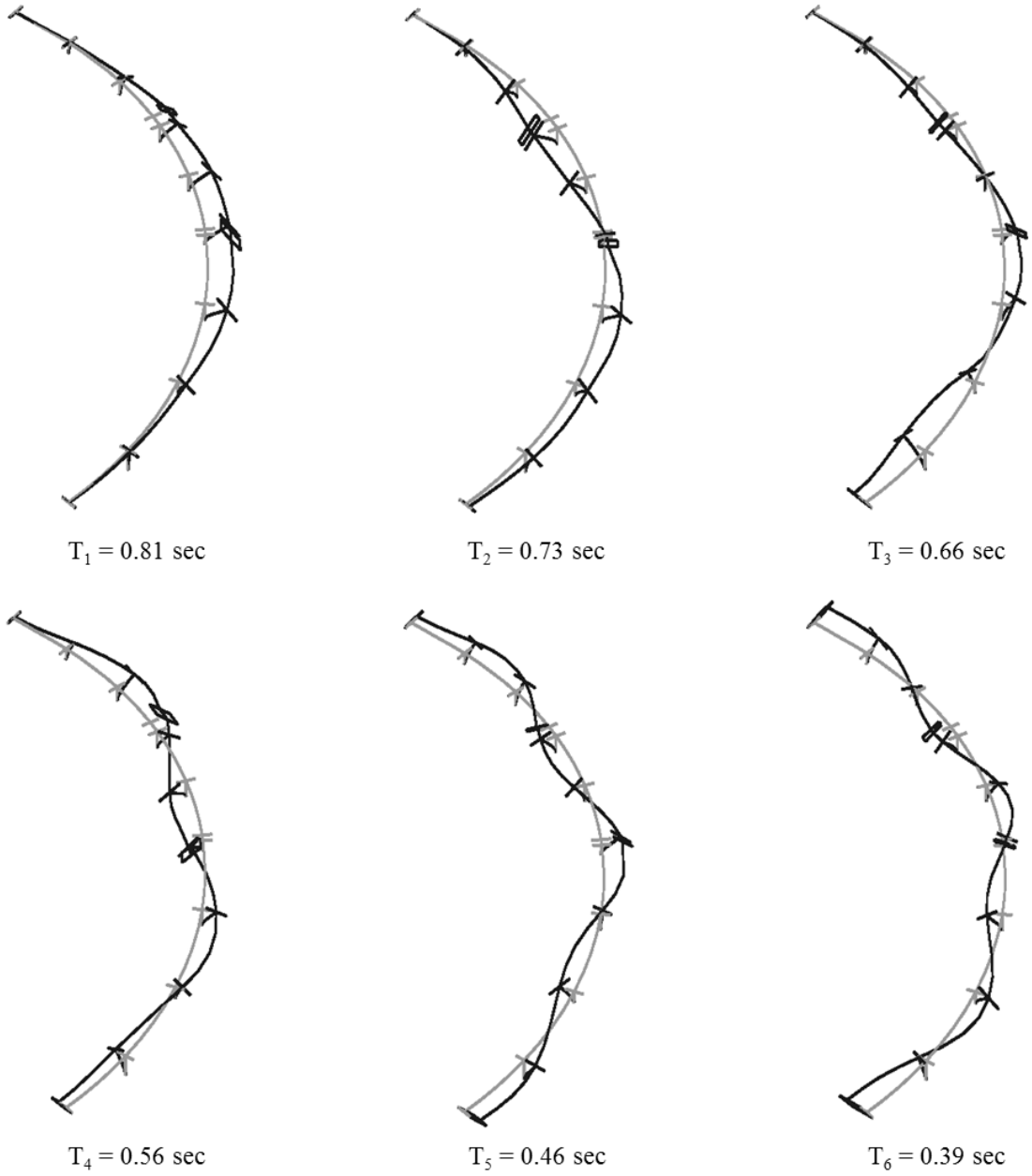

Figure 3.35: Lower frequency modes of the North-East connector with the nonlinear hinge mechanism

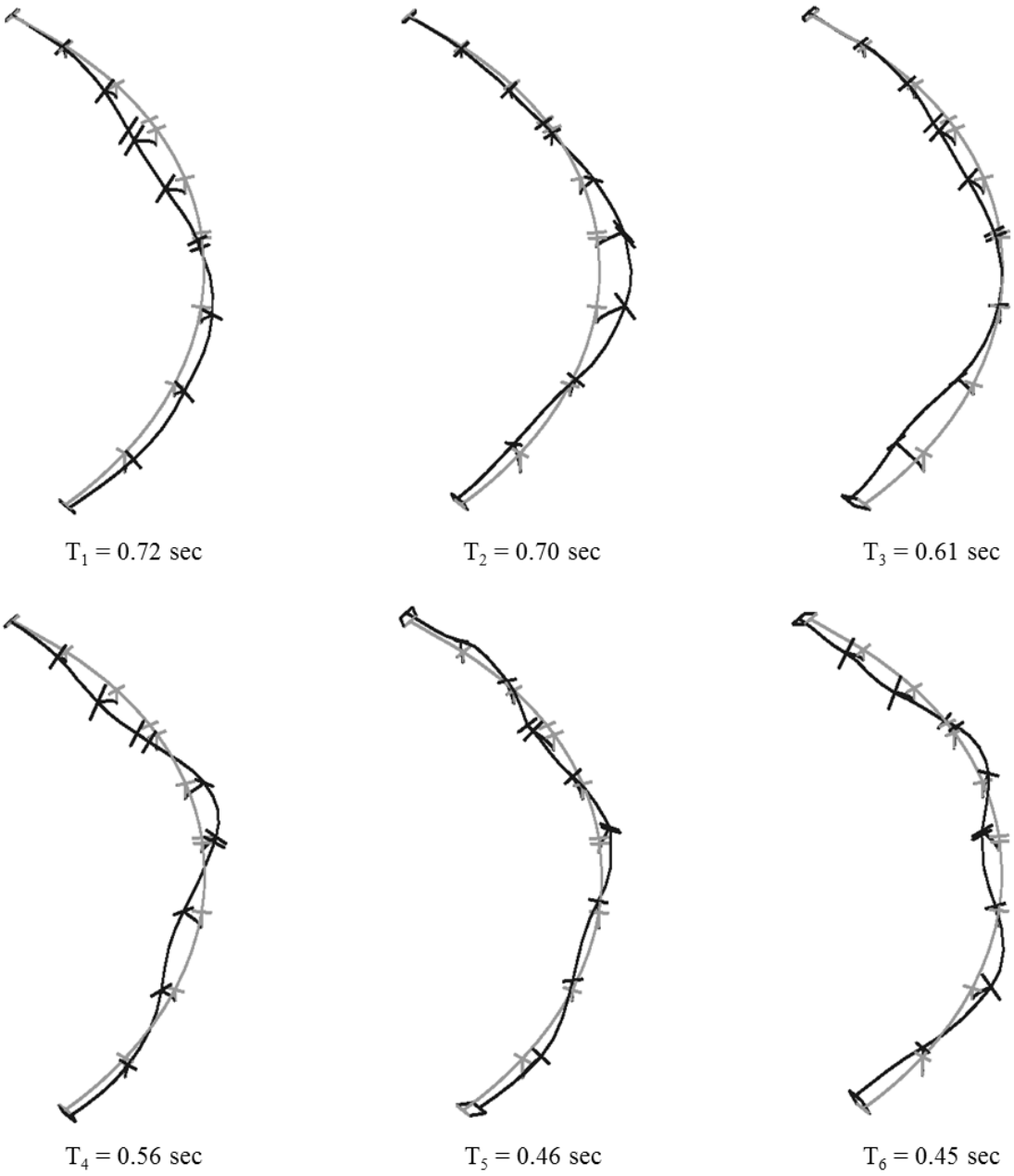

Figure 3.36: Lower frequency modes of the North-East connector with only compression hinge mechanism

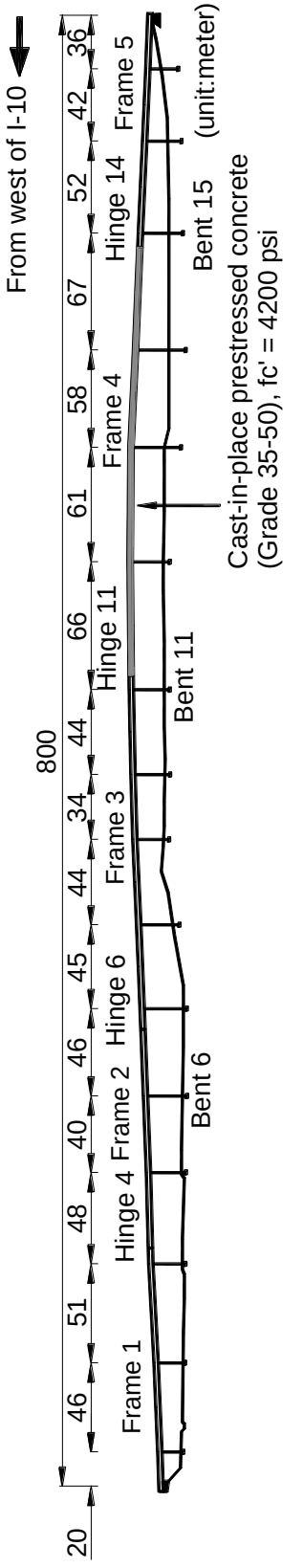

Figure 3.37: Elevation view of the SE connector

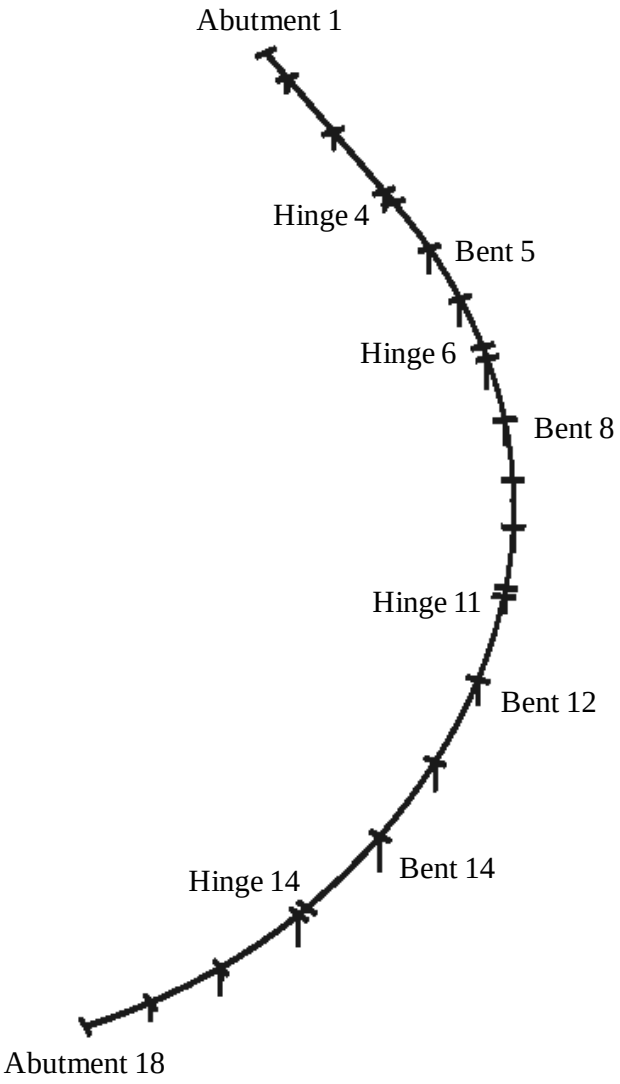

Figure 3.38: 3D view of the South-East connector (foundations are not shown)

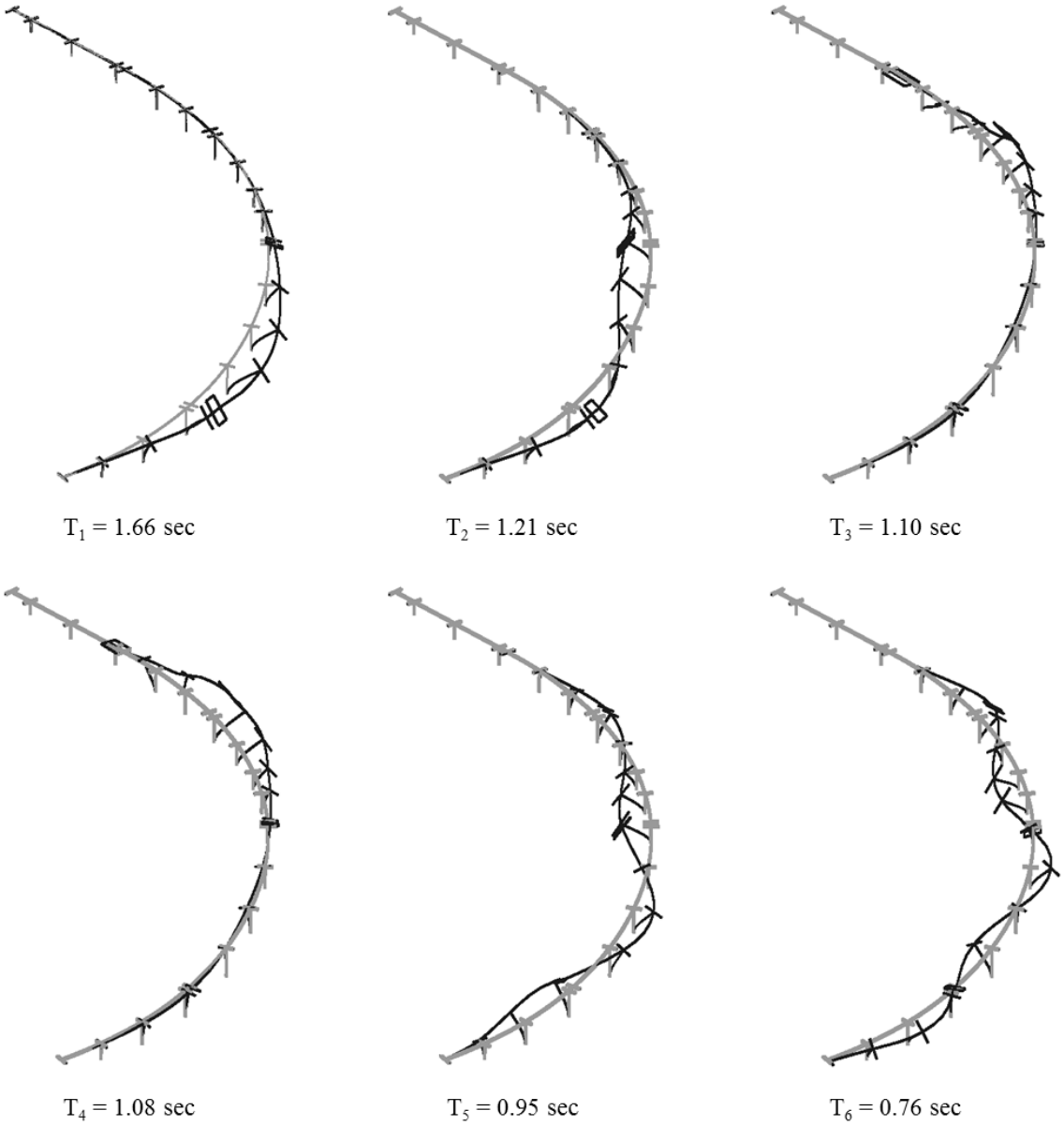

Figure 3.39: Lower frequency modes of South-East connector with the nonlinear hinge mechanism

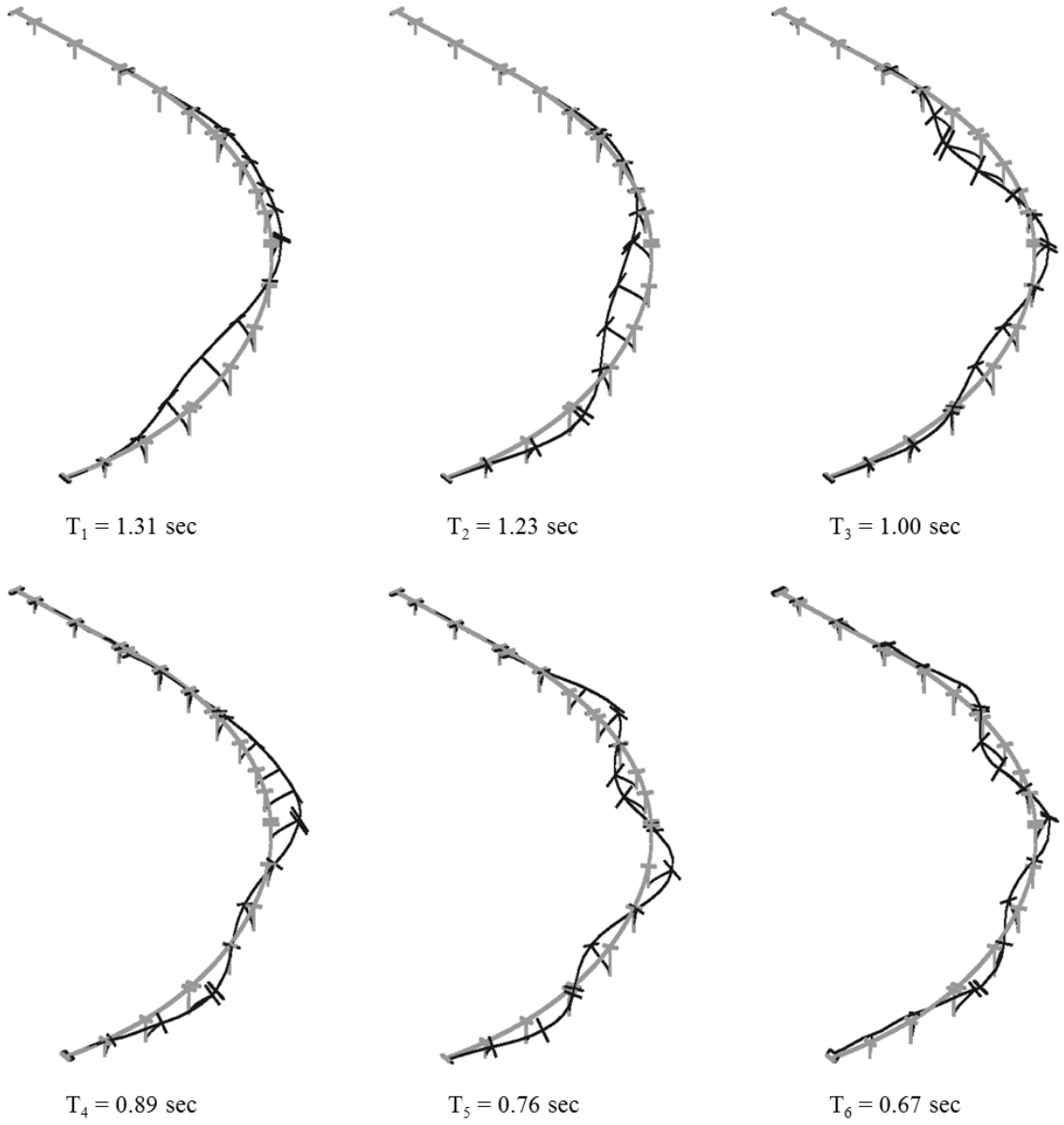

Figure 3.40: Lower frequency modes of the South-East connector with only compression hinge mechanism

Chapter 4

Seismic Response of a Large Scale Highway Bridge System

This chapter presents the employed modeling scheme for the bridge-foundation-ground system. Three connectors at the intersection of interstates 10 and 215 are represented. The region of interest (ROI) developed by Petropolous (2008) is adapted as the ground domain. The strategy for accommodation of the foundations into the ground ROI is also presented. Subjected to incident seismic waves propagated from a realistic fault rupture scenario based on the Domain Reduction Method (Bielak et al., 2003a), the corresponding seismic response is analyzed and discussed.

4.1 Description of the bridge-foundation-ground system

In the developed bridge-foundation-ground system (BFGS), the region of interest (ROI, Petropolous 20008; see Section 2.1) is used as the ground model. Three bridge connectors supported on pile groups at the intersection of interstates 10 and 215 (I-10/215; Section 3.1) are represented. A modified relative-position geometric configuration of the connectors to be placed on the ROI is described. In addition, a strategy for representing the pile group foundation within the ground is discussed.

4.1.1 Ground model

Modeling details concerning the ROI (Petropolous, 2008) were presented earlier in Section 2.1. Soil material properties were shown in Table 2.2. Resulting from two different input motions (low-frequency and broadband input motions), the corresponding ground response can be seen in the earlier Section 2.3.

4.1.2 Bridge interchange

Three highway bridges, the North-West connector (NW), the North-East connector (NE), and the South-East connector (SE), are considered as the structural models in the BFGS. Calibration of these structural models was described earlier in Section 3.2.3. Dynamic properties can be found in Section 3.2.4 for the NW, Section 3.3.4 for the NE, and Section 3.4.4 for the SE.

4.1.2.1 Re-orientation of the bridge locations

Due to the limited lateral spatial extent of the ROI, actual relative locations of the bridges with respect to each other had to be somewhat modified (Figure 4.1). In the global coordinate system, chords of the curved span of the NW and the SE are oriented parallel to the global X direction, while chord of the NE is slightly rotated from the global Y direction (17º counterclockwise).

4.1.2.2 Strategy of modeling the foundation

In the employed BFGS, the ROI ground surface is perfectly in the horizontal plane. Since actual surface topography at the I-10/215 interchange is irregular, a procedure is devised to couple the structural and ground models in order to create a model of the complete soil–structure system. Figure 4.2 shows the adopted procedure to connect the bridge columns and their foundations (pile cap and piles) to the underlying ground. The shaded volume, which is physically occupied by any pile group, is replaced by a relatively rigid brick element embedded in the soil domain (Figure 4.2).

Rigid beam–column elements representing the pile cap are then connected to the solid (pile-group) elements. The connectivity is done only for the translational degrees-of-freedom (DOFs; three for each node), while the three beam-column rotational DOFs remain free. For the connection between the column base and the pile cap, translations and rotations of the two nodes at the top of the pile cap and at the base of the column are constrained to be identical (Figure 4.2).

To accommodate the pile group rigid brick element, geometry, the soil mesh configuration near ground surface is modified below the location of each bridge column (Figure 4.3). As such, the mesh of the top 20 m thick layer in the ROI was refined to crudely include the pile group geometry/stiffness effects below the bridge columns. Since a typical size of the original pile group foundation is 7.47 m by 7.47 m (in the X-Y plane), the uniform FE grid (20 m cubical elements) is modified in one single brick element or 4 brick elements (Figure 4.3) depending on a location of the particular bridge column (with respect to the soil mesh nodal coordinates). Except for the pile group locations, the rest of mesh remained at the 20 m by 20 m 20 m original configuration. Finally, the entire computational BFGS model is shown in Figure 4.4.

4.2 Seismic response of the bridge-foundation-ground system

The BFGS is analyzed for the low frequency input generated from the Puente Hill fault rupture scenario as discussed earlier in Section 2.1.4. Responses of the three bridges are discussed in terms of variation in column base motions, acceleration and displacement at top and base of columns, shear forces/bending moments in columns, and response at the intermediate hinges and abutments.

4.2.1 Column base accelerations

Maximum accelerations at column base for the three bridges are shown in Figure 4.5 for the NW, Figure 4.6 for the NE, and Figure 4.7 for the SE. In this simulation

approach, the non-uniform base accelerations are associated with spatial variation of ground motions in the ROI (section 2.3.2).

4.2.2 Relative support motions

The non-uniform ground motions induce relative translations of the foundations as shown in Figure 4.8. This Figure shows the maximum relative displacements between any two adjacent supports of the NW in the global coordinate system (X and Y). The positive value indicates that the two supports are moving away from each other and vice versa. Relatively larger displacements are observed near the middle bents and in the Y direction (perpendicular to the chord in the curved geometry). Similar observations are also shown for the NE and the SE (Figures 4.9 and 4.10). Generally, these relative motions depend on the particular column location and orientation of the structure. Although the NW and SE are placed both along the X direction, more variation of the relative motions is observed near both ends of the SE (see Figure 4.10). In the NE, placed aligned along the Y direction, the variation is more noticeable in the X direction (see Figure 4.9).

4.2.3 Accelerations at the top of columns

Total acceleration at the top of the columns are investigated in the longitudinal (weak axis of the column against bending) and transversal (strong axis) directions. Intermittent spikes are observed in these time histories (Figure 4.11). The spikes are primarily observed in the longitudinal direction, while a certain amount of transverse response is also generated (“head-on impact” mechanism as mentioned in Malhotra et al.,

1995). Two adjacent bridge decks impact one another at a slight angle due to the curved geometry. Upon impact, a pair of transverse forces is simultaneously generated as depicted by the transverse spikes.

Although peak accelerations of about 0.2 g are observed at the level of the foundations, it can be seen that peak column top accelerations (Figure 4.12) are greater than 1g (SE). The spikes are not quite as noticeable in the NE (see Figure 4.13). Responses at other locations are included in Appendix B.

4.2.4 Relative displacement and drift ratio at the top of columns

In the present model, the bridge deck is modeled with elastic material properties and is relatively stiff in the axial direction (longitudinal direction along the deck; positive direction from Abutment 1 to Bent 2). However, the curved structural geometry induces large displacements in both longitudinal and transverse directions (positive in the convex direction). As expected generally (Figures 4.14-4.16), larger transverse displacements at the top of columns relative to the base are observed in the relatively flexible frames (with longer columns), in spite of the higher moment of inertia in this direction (strong axis against bending).

Figure 4.14 shows total displacement time histories at top and base of representative bents and corresponding relative displacements at the top relative to the base in the NW. Bent 5 has a 24.3 m high column (the longest column) and is located at the middle of frame 2. Bent 16 has the shortest column with a length of 7.2 m. Bent 10 is located at the middle of the superstructure near Hinge 9. It can be seen that the displacements under frames 1-3 (from Abutment 1 to Bent 9) and frames 4-6 (from Bent

10 to abutment 17), are out-of phase in the longitudinal direction. Meanwhile, in the transverse direction, displacements display in-phase behavior. In general, transverse displacements are large due to the pronounced response of the structures in this direction. The longitudinal displacements are mainly dictated by the ground pulse predominant velocity pulse. This behavior is also observed in the SE (Figure 4.15). However, in the NE, displacements in both directions are mostly induced by the pulse (Figure 4.16).

Drift ratio in terms of deformation is computed for the columns. The deformation is evaluated from the relative displacement at the top to the base of the column (reduced by the amount due to rocking of the foundation). In general, transversal drift ratios are greater than those in the longitudinal direction in the NW (Figure 4.17). A larger drift ratio is observed in the positive direction.

Larger drift ratios are observed in the negative transverse direction in the NE (Figure 4.18). The increased relative support motions induce the deformation shown in Figure 4.19. In the SE, large drift ratios are observed in both directions (Figure 4.20). Large deformations are observed in the relatively flexible frame near Abutment 18. In addition, relatively large longitudinal deformation is seen near Abutment 1.

Rocking of the foundations is found to be generally small because the employed soil is relatively stiff. Although the difference is relatively small between the relative displacement and the part causing deformation, beneficial or detrimental effects of rocking are noted depending on the particular column location in the NW and SE. Nevertheless, rocking induces larger deformation demands in the NE. The deformation compared with the relative displacement is summarized in Table 4.1 for the NW, Table 4.2 for the NE, and Table 4.3 for the SE.

4.2.5 Column forces

Displacements at the top relative to the base induce large bending moments both longitudinally and transversely. The columns are fixed to the pile caps at the base and connected to the bridge deck frames which are interconnected by the intermediate hinges. Consequently, the maximum bending moments occur at the base of the columns. The maximum forces are summarized in Table 4.4 for the NW, Table 4.5 for the NE, and Table 4.6 for the SE.

As expected, larger bending moments are observed in the relatively flexible frame (with the longer columns). As shown by the relative displacement at the top of columns, the bridge response induces large force demands in the transverse direction. Depending on the particular column, large demands may be also observed in the longitudinal direction.

It is also noted that a sudden spike in the longitudinal shear force is observed near Abutment 17 in the NW (Figure 4.21). This spike is induced by pounding at the nearby hinge in the longitudinal direction. Such behavior is not quite as noticeable in the NE and the SE (see Appendix B for the time histories).

4.2.6 Intermediate hinges

Longitudinal relative displacements between any two adjacent deck segments are induced by the opening of the intermediate hinges (Figure 4.19). Table 4.7 provides maximum opening displacements at the hinges in the longitudinal direction and corresponding axial stresses in the restrainer cables. The employed linear-tension model

for the restrainer cables shows stresses that exceed the tensile capacity (due to the excessive relative displacements). In comparison to the yield stress of 1.213 GPa, computed cable stresses are 1.74 GPa (41% higher) at Hinge 3 in the NW and 2.74 GPa (225% higher) at Hinge 14 in the SE. However, at other locations, displacements and stresses are much less.

4.2.7 Abutments

Table 4.8 provides backwall abutment forces per unit width (1 m) of the wall (12.5 m). Longitudinal response toward Abutment 1 induces larger forces than that at the other end for the NW and the SE. This behavior is essentially dictated by overall longitudinal response of the bridges due to the different base support motions.

In the transversal direction toward the wingwalls, maximum forces are 1,118 kN (about 15% of the longitudinal force) at Abutment 1 and 99 kN (about 3%) at Abutment 17 in the NW. Similarly, maximum forces are 1001 kN (about 13%) at Abutment 1 and 484 kN (about 28%) at abutment 18 in the SE, while maximum forces are 288 kN (about 13%) at Abutment 1 and 1,043 kN (about 30%) at Abutment 10 in the NE.

4.3 Effect of the broadband input

With the significant limitations mentioned earlier in mind (dictated by the 20 m element length) the BFGS is analyzed for the broadband input motion (see Section 2.3.3 for ground responses). Due to the frequency content of up to 5Hz, more prominent response of the bridges is observed. In addition, the higher amplitudes of ground

accelerations induce larger force/displacement demands than those in the analysis for the low frequency input motions.

4.3.1 Force demand

Figure 4.22 through Figure 4.24 show a comparison of the normalized total bridge column base shear (total base shear divided by self-weight of each bridge). Compared to the low frequency input case, the base shear increases up to 43% and 21% in the NW and SE, respectively. In the NE (relatively stiff bridge), the base shear increases as much three times (response is affected to a greater degree by the high frequency input components). Due to this increased base shear, larger column shear forces and bending moments are developed. Compared to the low frequency input, differences of the maximum forces at the base of the columns are summarized in Table 4.9 for the NW, Table 4.10 for the NE, and Table 4.11 for the SE (in these Tables, LF and BB indicate the low frequency and broadband input, respectively).

4.3.2 Displacement demand

Although the extent of rocking at the foundation is very similar to that for the low frequency input, larger column deformations (i.e. top displacement relative to its base excluding the amount induced by rocking of the foundation) are observed in the broadband input case. The deformation time histories are shown in Figure 4.25 at Bent 12 in the NW, Figure 4.26 at Bent 4 in the NE, and Figure 4.27 at Bent 8 in the SE. In addition, maximum drift ratios in terms of deformation are compared through Figure 4.28

and Figure 4.30. The drift increases by up to 300% in the NW and NE, depending on the particular column location.

4.4 Effect of adjacent structures

In order to study effects of adjacent structures (the NE and the SE) on the other structure (the NW), an additional analysis is employed. In this analysis, the NW is only used as the structural model (Figure 4.31) subjected to the low frequency and broadband inputs. Responses at the top and the base of the columns are discussed.

4.4.1 Column base motions

Compared to the results from the three bridges case (Figure 4.4), column base displacements and accelerations are very similar. Change in the support motions is also negligible (Figure 4.32). This is attributed to the relatively stiff soil properties.

4.4.2 Responses at the top of column

Although change in the base response of the columns is found to be small, slight changes in response are observed at the top of the columns. Such change can be observed in column top displacements relative to the base (Figure 4.33) and column top accelerations (Figure 4.34) during the strong shaking phase. It can be also seen that frequency of the oscillation is slightly altered with less amplification, compared to the three bridges case. In addition, spikes induced by pounding at the hinges are more noticeable in the acceleration time histories (Figure 4.34).

Figure 4.35 shows peak displacements at the top of the columns relative to the base. In the relatively flexible columns (Bents 5, 6, and 7), larger peaks are observed in the additional NW case (without the other bridges). Particularly at Bent 5, the displacement in the global X direction increases as much 41% (for the low frequency input scenario), compared to the three bridges case.

In this current study, accurate identification of the period changes in the overall bridge system based on the number of involved structures is beyond the scope. However, when the three connectors are simultaneously represented, it appears that presence of the NE and the SE near the NW has resulted in some impacts as far as overall dynamic response is concerned. Further studies of this bridge-to-bridge interaction mechanism (with a finer mesh) are certainly in order.

4.5 Summary and conclusions

The simulation of the BFGS including the three bridge connectors, the foundations, and the soil domain was presented. Subjected to the incident seismic waves (in the low-frequency range of up to 1 Hz) resulting from a realistic fault rupture scenario, the response of the BFGS was discussed in terms of the foundation response, the accelerations/relative displacements at the top of columns, the hinge opening, and the force demands in the columns, hinges, and abutments. The effect of including adjacent bridge structures on the overall response was also discussed. Additional analyses were conducted using a broadband input motion (frequency content up to 5 Hz) and the

corresponding results were compared to those of the low-frequency input. From the results of the present study, the main observations are:

- For the low-frequency input (up to 1 Hz):

1. Longitudinal structural response was generally influenced by the ground motions (non-uniform support excitation), while the transverse response was more influenced by the bridge flexibility in this direction (particularly for the relatively flexible NW and the SE). The spatial variation of ground motion may have a contribution to the pounding effects of the deck at the intermediate hinges. Although the peak ground acceleration attained about 0.2g, the structural peak acceleration reached greater than 1g (because of the spikes caused by pounding).
2. In the columns, larger shear forces were generally observed in the longitudinal direction, particularly near both abutments. Maximum bending moments mostly occurred at the base of the columns. In the relatively tall frames of the NW and the SE, larger transverse bending moments were observed due to their more pronounced flexible response in this direction.
3. Beneficial or detrimental effects of soil-structure interaction were observed due to the displacement components induced by foundation rocking. In view of the relatively stiff soil properties in this study, the additional column top displacement dictated by rocking was generally small. However, this displacement very slightly increased or decreased the column deformation and the internal forces (i.e. shear forces and bending moments) depending on the particular column location.

4. Large relative displacement in the longitudinal direction was associated with large gaps opening at the hinges between adjacent frames. The observed corresponding axial stresses at one of the hinges exceeded the actual yield stress of the restrainer cables in the NW and the SE.
5. Presence of the NE and SE along with the NW appeared to stiffen the overall investigated system response to some degree. Larger accelerations and displacements of the NW were computed when these two additional bridges were included in the model.

- For the broadband input (up to 5 Hz):

Compared to results for the low-frequency input, the broadband input induced much higher spatial variation of ground motion over the ground surface, and more pronounced response of the employed structural models. Consequently, the base shear increased and larger force/displacement demands in the columns are observed in all three bridges.

4.6 Acknowledgements

Chapter 4 contains material published in the Earthquake Geotechnical Engineering Design (Geotechnical, Geological and Earthquake Engineering, Vol. 28, Springer) titled “Seismic Response of a Large-Scale Highway Interchange System” with authors, Kyung Tae Kim, Ahmed Elgamal, George Petropoulos, Aysegul Askan, Jacobo Bielak, and Gregory L. Fenves (2014). The dissertation author is the first author of this paper.

Table 4.1: Maximum relative displacements and drift ratios (%) at the top of bents in the North-West connector

			Longitudinal direction			Transversal direction		
Frame	Bent	Height (m)	Top relative to base (m)	Deformation (m)	Drift (%)	Top relative to base (m)	Deformation (m)	Drift (%)
1	2	11.88	0.055	0.055	0.46	0.033	0.032	0.27
	3	16.59	0.058	0.057	0.34	0.068	0.066	0.40
2	4	19.41	0.140	0.140	0.72	0.139	0.137	0.71
	5	24.26	0.116	0.117	0.48	0.211	0.208	0.86
	6	22.50	0.091	0.092	0.41	0.225	0.223	0.99
	7	17.32	0.076	0.075	0.44	0.164	0.163	0.94
3	8	15.24	0.058	0.057	0.37	0.061	0.062	0.41
	9	15.77	0.063	0.062	0.39	0.048	0.052	0.33
4	10	12.88	0.047	0.046	0.36	0.051	0.054	0.42
	11	18.26	0.039	0.039	0.21	0.088	0.090	0.49
5	12	18.80	0.035	0.032	0.17	0.095	0.096	0.51
	13	16.94	0.032	0.031	0.18	0.079	0.080	0.47
6	14	15.62	0.019	0.017	0.11	0.056	0.057	0.37
	15	13.69	0.019	0.017	0.12	0.028	0.029	0.21
	16	7.23	0.018	0.016	0.22	0.005	0.005	0.06

Table 4.2: Maximum relative displacements and drift ratios (%) at the top of bents in the North-East connector

			Longitudinal direction			Transversal direction		
Frame	Bent	Height (m)	Top relative to base (m)	Deformation (m)	Drift (%)	Top relative to base (m)	Deformation (m)	Drift (%)
1	2	9.75	0.015	0.016	0.16	0.005	0.007	0.07
	3	12.38	0.014	0.015	0.12	0.013	0.012	0.10
2	4	14.75	0.025	0.027	0.18	0.024	0.025	0.17
	5	14.30	0.015	0.018	0.13	0.034	0.035	0.24
	6	13.41	0.016	0.016	0.12	0.044	0.045	0.34
3	7	14.60	0.032	0.035	0.24	0.049	0.050	0.35
	8	10.36	0.021	0.023	0.22	0.030	0.031	0.29
	9	17.59	0.018	0.016	0.09	0.030	0.031	0.17

Table 4.3: Maximum relative displacements and drift ratios (%) at the top of bents in the South-East connector

			Longitudinal direction			Transversal direction		
Frame	Bent	Height (m)	Top relative to base (m)	Deformation (m)	Drift (%)	Top relative to base (m)	Deformation (m)	Drift (%)
1	2	11.35	0.044	0.044	0.38	0.003	0.001	0.01
	3	13.34	0.040	0.038	0.28	0.003	0.000	0.00
	4	15.32	0.040	0.038	0.25	0.004	0.000	0.00
2	5	18.80	0.054	0.050	0.27	0.012	0.010	0.05
	6	19.61	0.057	0.054	0.27	0.057	0.057	0.29
3	7	21.97	0.047	0.045	0.21	0.097	0.100	0.45
	8	18.29	0.048	0.046	0.25	0.084	0.086	0.47
	9	15.44	0.052	0.051	0.33	0.064	0.066	0.43
	10	18.03	0.056	0.055	0.31	0.066	0.069	0.38
	11	18.44	0.065	0.065	0.35	0.083	0.087	0.47
4	12	18.57	0.099	0.101	0.54	0.123	0.123	0.66
	13	21.51	0.119	0.121	0.56	0.170	0.169	0.79
	14	25.44	0.136	0.140	0.55	0.169	0.170	0.67
5	15	22.91	0.132	0.134	0.59	0.163	0.164	0.72
	16	20.07	0.126	0.127	0.63	0.067	0.068	0.34
	17	13.69	0.121	0.121	0.88	0.027	0.029	0.21

Table 4.4: Maximum shear forces and bending moments in the local directions in the North-West connector

			Longitudinal direction		Transversal direction	
Frame	Bent	Height (m)	Shear force (MN)	Bending moment (MN-m)	Shear force (MN)	Bending moment (MN-m)
1	2	11.88	7.345	49.004	3.748	38.265
	3	16.59	2.959	27.015	3.097	43.065
2	4	19.41	5.333	53.968	3.568	63.199
	5	24.26	2.731	31.747	2.917	62.288
	6	22.50	2.607	28.534	3.700	76.161
	7	17.32	3.911	35.584	5.747	93.174
3	8	15.24	3.663	30.826	2.721	41.488
	9	15.77	4.136	34.981	1.806	32.112
4	10	12.88	4.684	34.947	4.142	53.221
	11	18.26	1.787	16.861	2.920	46.935
5	12	18.80	1.408	12.872	2.485	43.756
	13	16.94	1.942	15.425	2.876	46.697
6	14	15.62	1.207	9.216	2.434	37.291
	15	13.69	1.914	13.355	1.795	24.898
	16	7.23	9.098	37.580	1.729	13.306

Table 4.5: Maximum shear forces and bending moments in the local directions in the North-East connector

			Longitudinal direction		Transversal direction	
Frame	Bent	Height (m)	Shear force (MN)	Bending moment (MN-m)	Shear force (MN)	Bending moment (MN-m)
1	2	9.75	3.291	18.427	1.309	11.785
	3	12.78	1.626	11.447	1.078	13.077
2	4	14.75	1.864	15.883	1.332	19.489
	5	14.30	1.792	13.218	1.978	28.142
	6	13.41	1.134	9.130	3.469	43.779
3	7	14.6	2.963	23.147	3.094	41.411
	8	10.36	4.684	26.827	4.881	47.328
	9	17.59	0.966	8.314	1.281	18.359

Table 4.6: Maximum shear forces and bending moments in the local directions in the South-East connector

			Longitudinal direction		Transversal direction	
Frame	Bent	Height (m)	Shear force (MN)	Bending moment (MN-m)	Shear force (MN)	Bending moment (MN-m)
1	2	11.35	4.521	26.008	3.168	35.339
	3	13.34	8.573	68.864	3.728	46.392
	4	15.32	5.616	52.467	3.905	54.138
2	5	18.80	1.676	12.928	4.241	81.017
	6	19.61	2.189	21.327	1.491	25.248
3	7	21.97	1.257	13.739	1.927	35.985
	8	18.29	2.106	19.662	2.428	41.420
	9	15.44	3.531	28.906	2.913	44.169
	10	18.03	2.688	24.617	1.653	31.882
	11	18.44	2.372	24.526	2.334	42.098
4	12	18.57	4.436	42.758	3.480	60.616
	13	21.51	3.765	40.507	3.363	64.124
	14	25.44	2.767	34.080	2.042	45.861
5	15	22.91	2.911	34.438	2.795	55.438
	16	20.07	4.643	47.513	1.402	27.233
	17	13.69	11.524	87.045	2.273	27.117

Table 4.7: Maximum opening displacement and axial stresses in the restrainer cables in the longitudinal direction

Bridge	**Hinge location**	**Maximum opening displacement (cm)**	**Axial stress in the restrainer cables (GPa)**
NW	Hinge 3	10.1	1.74
	Hinge 7	7.0	1.16
	Hinge 9	2.5	0.28
	Hinge 10	2.0	0.19
	Hinge 13	4.0	0.57
NE	Hinge 3	4.7	0.70
	Hinge 6	4.4	0.65
SE	Hinge 4	3.6	0.50
	Hinge 6	2.8	0.34
	Hinge 11	5.6	0.87
	Hinge 14	15.2	2.74

Table 4.8: Backwall abutment forces per unit meter of the 12.5 m width wall at the abutments

Bridge	Abutment location	Backwall abutment force (kN/m)
NW	Abut. 1	591.6
	Abut. 17	295.0
NE	Abut. 1	181.6
	Abut. 10	276.5
SE	Abut. 1	617.5
	Abut. 18	141.7

Table 4.9: Comparison of column force in the North-West connector using the low frequency (LF) and the broadband (BB) inputs

	Longitudinal direction (weak axis against bending)						**Transverse direction (strong axis against bending)**					
	Shear force (MN)			**Bending moment (MN-m)**			**Shear force (MN)**			**Bending moment (MN-m)**		
Bent	**LF**	**BB**	**Increase (%)**	**LF**	**BB**	**Increase (%)**	**LF**	**BB**	**Increase (%)**	**LF**	**BB**	**Increase (%)**
2	7.3	11.9	62.5	49.0	79.9	63.1	3.7	7.9	109.8	38.3	86.5	126.2
3	3.0	4.2	42.9	27.0	38.3	41.8	3.1	4.6	50.0	43.1	56.4	30.9
4	5.3	4.5	-14.8	54.0	46.1	-14.5	3.6	5.5	54.6	63.2	77.7	22.9
5	2.7	2.5	-8.1	31.7	26.7	-15.8	2.9	3.4	15.5	62.3	64.8	4.1
6	2.6	2.8	8.5	28.5	29.1	2.1	3.7	4.5	22.8	76.2	84.4	10.8
7	3.9	4.4	13.6	35.6	40.5	13.7	5.7	6.7	16.2	93.2	93.4	0.3
8	3.7	4.6	25.1	30.8	40.0	29.8	2.7	7.9	190.3	41.5	103.5	149.4
9	4.1	5.6	35.1	35.0	47.2	34.8	1.8	4.6	153.0	32.1	74.2	130.9
10	4.7	8.3	78.1	34.9	62.0	77.3	4.1	6.5	56.8	53.2	78.6	47.8
11	1.8	4.1	131.2	16.9	44.8	165.7	2.9	4.7	60.0	46.9	66.8	42.3
12	1.4	4.3	203.6	12.9	43.3	236.4	2.5	3.8	52.1	43.8	69.2	58.2
13	1.9	5.9	205.0	15.4	55.3	258.7	2.9	4.2	46.9	46.7	78.2	67.5
14	1.2	3.6	195.1	9.2	29.8	223.4	2.4	4.8	95.6	37.3	72.2	93.6
15	1.9	5.4	184.5	13.4	38.2	186.3	1.8	4.6	157.1	24.9	63.3	154.2
16	9.1	25.0	174.8	37.6	103.6	175.7	1.7	4.5	159.0	13.3	33.0	148.3

Table 4.10: Comparison of column force in the North-East connector using the low frequency (LF) and the broadband (BB) inputs

	Longitudinal direction (weak axis against bending)						Transverse direction (strong axis against bending)					
	Shear force (MN)			Bending moment (MN-m)			Shear force (MN)			Bending moment (MN-m)		
Bent	**LF**	**BB**	**Increase (%)**	**LF**	**BB**	**Increase (%)**	**LF**	**BB**	**Increase (%)**	**LF**	**BB**	**Increase (%)**
2	3.3	12.4	276.4	18.4	69.7	278.1	1.3	5.6	324.8	11.8	51.9	340.7
3	1.6	7.2	339.8	11.4	47.0	311.0	1.1	6.7	520.7	13.1	82.7	532.3
4	1.9	5.8	213.7	15.9	50.3	216.6	1.3	7.4	452.9	19.5	112.5	477.0
5	1.8	8.0	347.9	13.2	60.8	360.0	2.0	6.5	226.5	28.1	97.5	246.4
6	1.1	7.3	545.6	9.1	58.4	540.2	3.5	5.8	66.6	43.8	68.1	55.6
7	3.0	11.2	279.1	23.1	88.5	282.5	3.1	6.6	113.4	41.4	80.9	95.4
8	4.7	24.0	411.9	26.8	139.7	420.8	4.9	10.9	124.1	47.3	128.7	172.0
9	1.0	6.4	566.0	8.3	59.4	613.9	1.3	4.6	258.3	18.4	57.4	212.8

Table 4.11: Comparison of column force in the South-East connector using the low frequency (LF) and the broadband (BB) inputs

	Longitudinal direction (weak axis against bending)						Transverse direction (strong axis against bending)					
	Shear force (MN)			Bending moment (MN-m)			Shear force (MN)			Bending moment (MN-m)		
Bent	**LF**	**BB**	**Increase (%)**	**LF**	**BB**	**Increase (%)**	**LF**	**BB**	**Increase (%)**	**LF**	**BB**	**Increase (%)**
2	4.5	7.0	54.2	26.0	41.1	58.0	3.2	5.4	71.4	35.3	56.0	58.6
3	8.6	14.4	68.1	68.9	118.5	72.1	3.7	10.7	187.4	46.4	132.7	186.0
4	5.6	9.1	61.7	52.5	82.9	58.0	3.9	10.6	172.1	54.1	146.0	169.7
5	1.7	3.1	84.3	12.9	22.4	73.4	4.2	9.3	119.6	81.0	186.4	130.1
6	2.2	3.5	60.1	21.3	34.5	61.8	1.5	3.4	125.9	25.2	53.1	110.2
7	1.3	3.0	137.6	13.7	31.8	131.7	1.9	3.9	102.4	36.0	62.0	72.3
8	2.1	4.0	91.6	19.7	36.4	85.0	2.4	5.7	132.8	41.4	87.0	110.1
9	3.5	5.6	57.8	28.9	46.1	59.4	2.9	5.7	94.1	44.2	76.0	72.0
10	2.7	4.2	58.0	24.6	39.4	60.2	1.7	2.4	42.6	31.9	45.7	43.2
11	2.4	3.4	45.0	24.5	35.9	46.3	2.3	3.8	61.7	42.1	63.9	51.7
12	4.4	5.0	13.6	42.8	48.7	14.0	3.5	5.6	60.5	60.6	79.1	30.5
13	3.8	4.0	6.6	40.5	42.9	6.0	3.4	4.8	41.5	64.1	77.1	20.3
14	2.8	3.0	8.8	34.1	35.8	5.2	2.0	4.0	97.3	45.9	53.1	15.7
15	2.9	3.0	3.5	34.4	36.1	4.7	2.8	3.1	11.9	55.4	45.6	-17.7
16	4.6	4.7	0.9	47.5	47.9	0.8	1.4	3.5	146.4	27.2	55.5	103.7
17	11.5	11.2	-2.5	87.0	85.1	-2.2	2.3	5.0	121.7	27.1	59.8	120.5

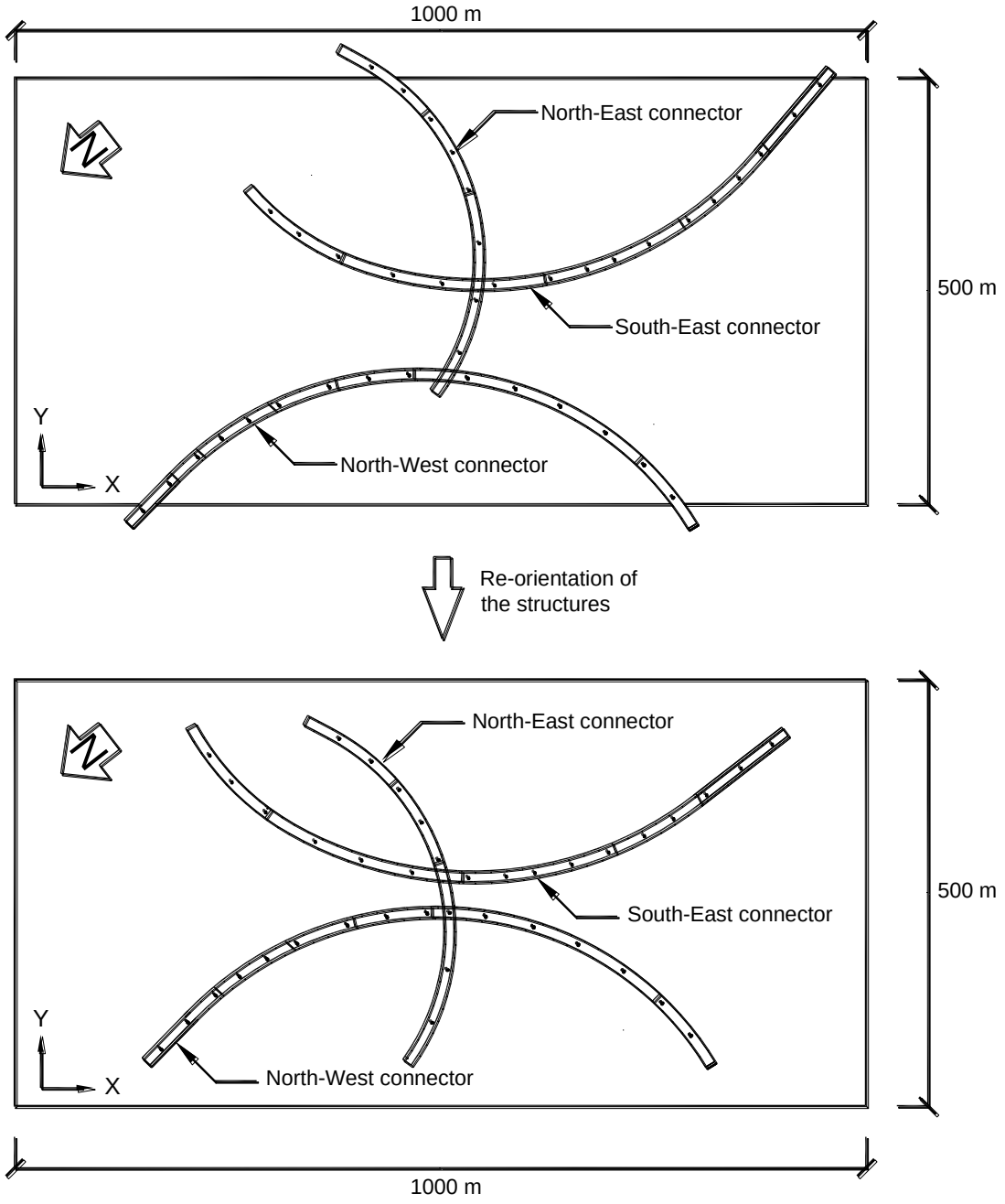

Figure 4.1: Re-orientation of the the structures on the ground surface

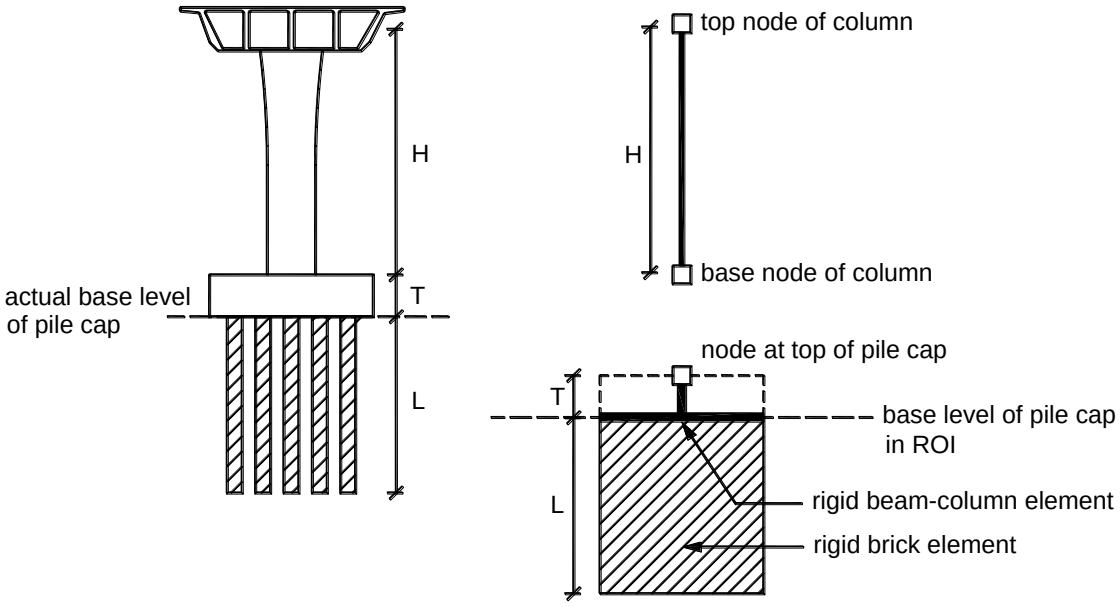

Figure 4.2: Schematic view of connection between column and soil including pile groups

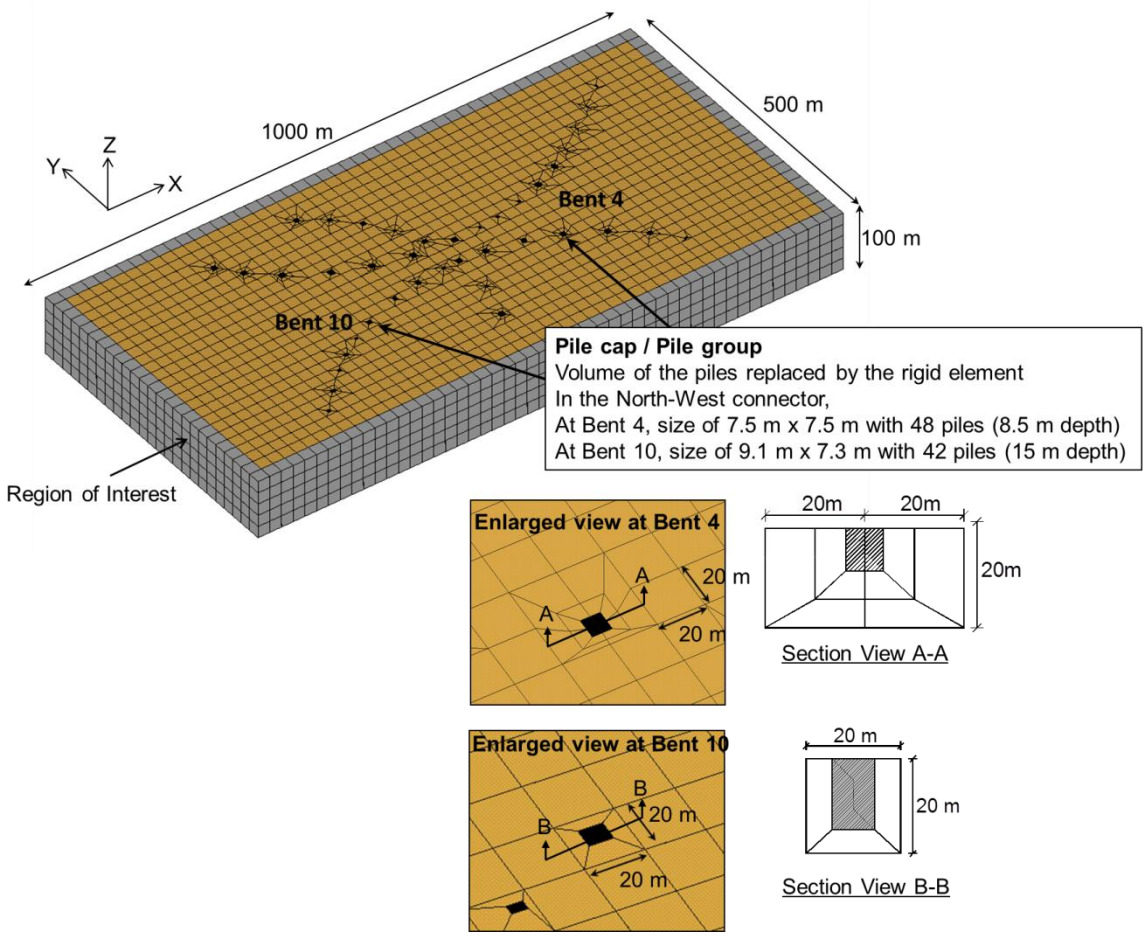

Figure 4.3: Modified soil mesh configuration near the foundation of the bridge connectors

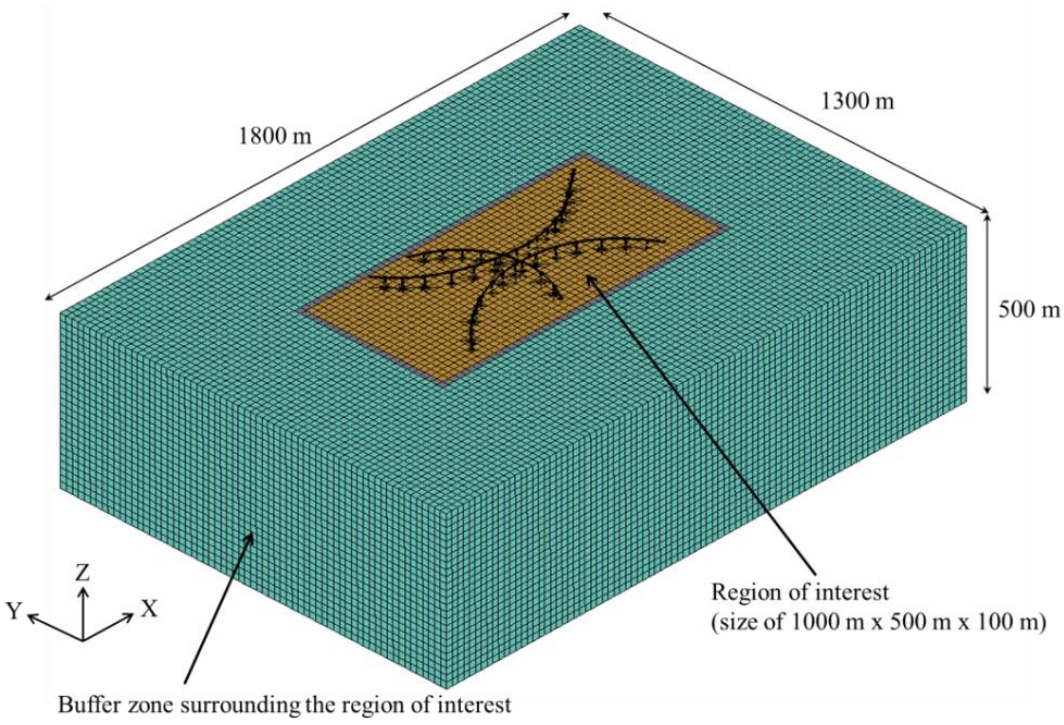

(a) Entire FE mesh including the structural model in the ROI and buffer zone

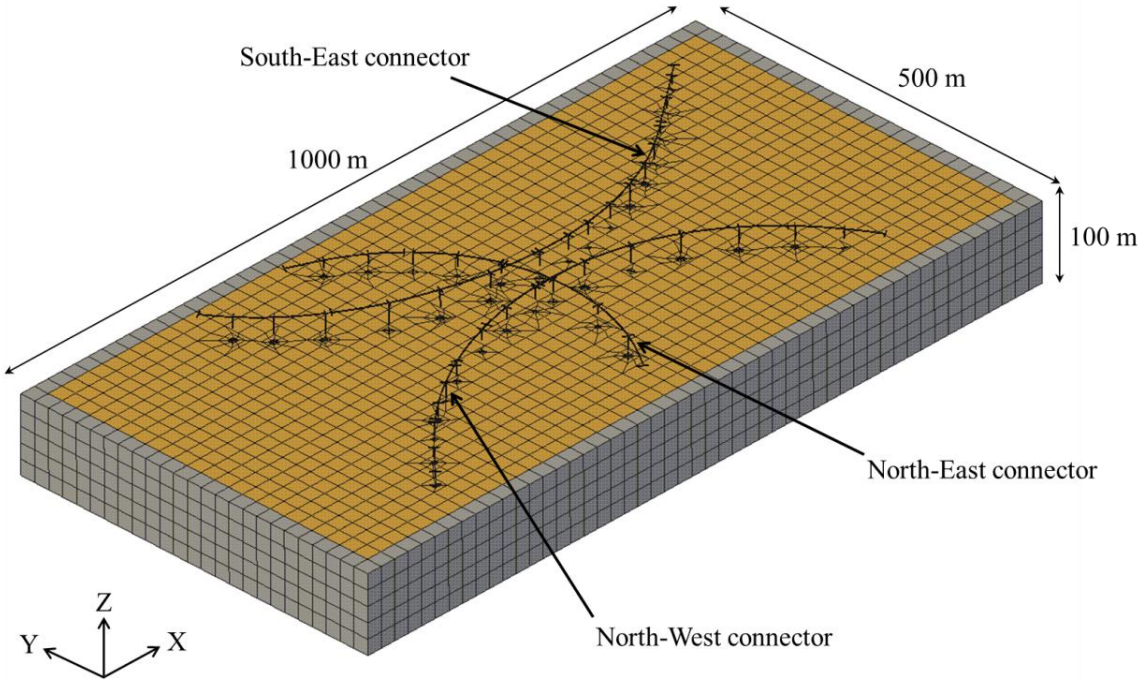

(b) ROI only shown

Figure 4.4: 3D view of the BFGS model

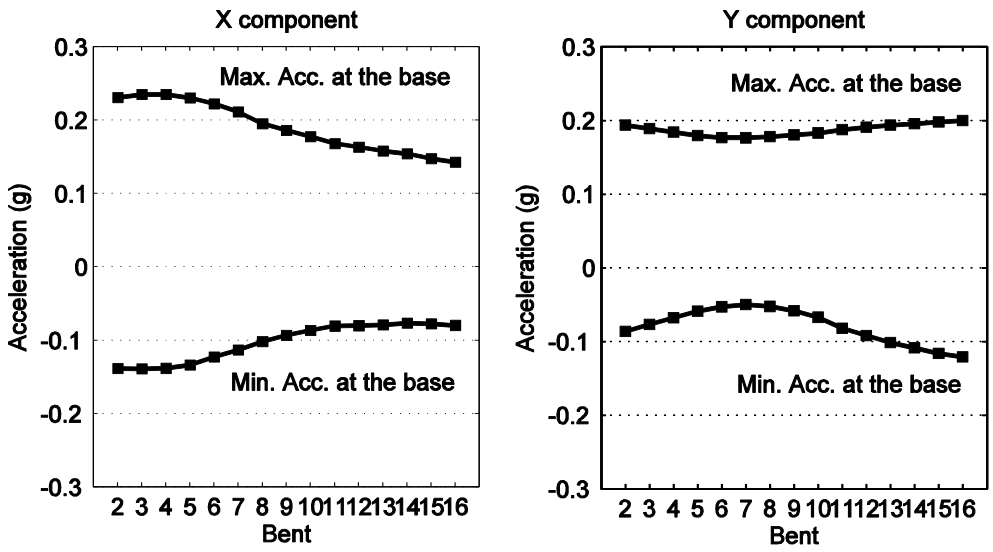

Figure 4.5: The maximum accelerations at the base of columns in the NW

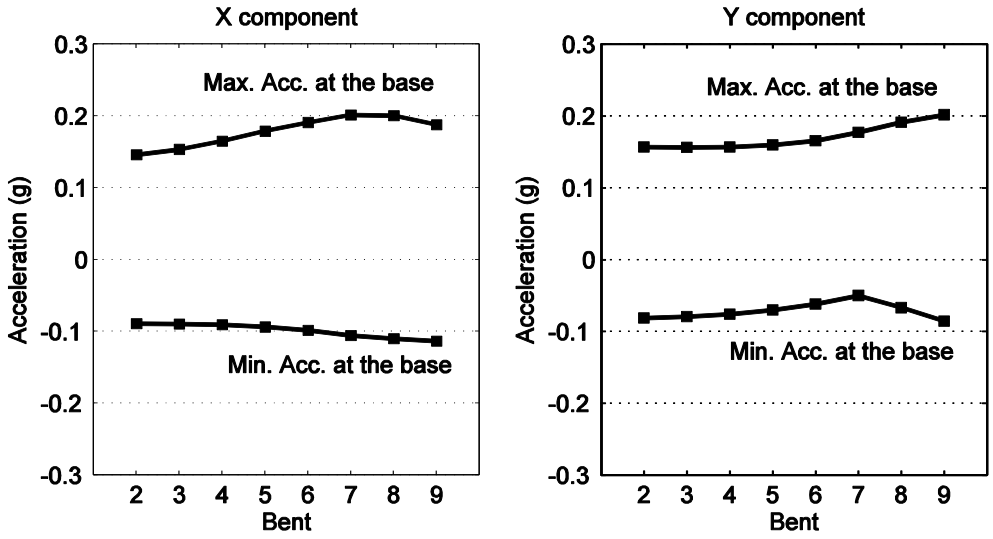

Figure 4.6: The maximum accelerations at the base of columns in the NE

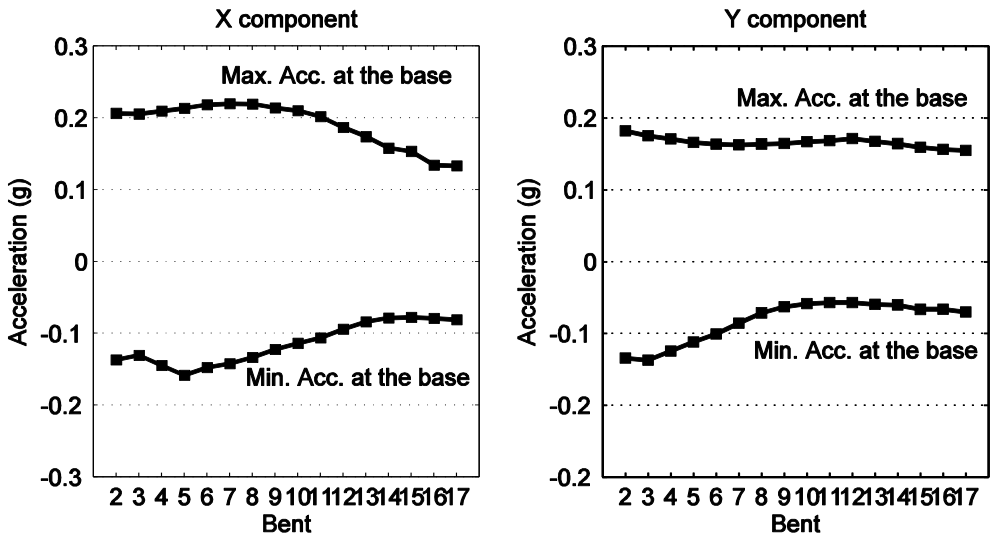

Figure 4.7: The maximum accelerations at the base of columns in the SE

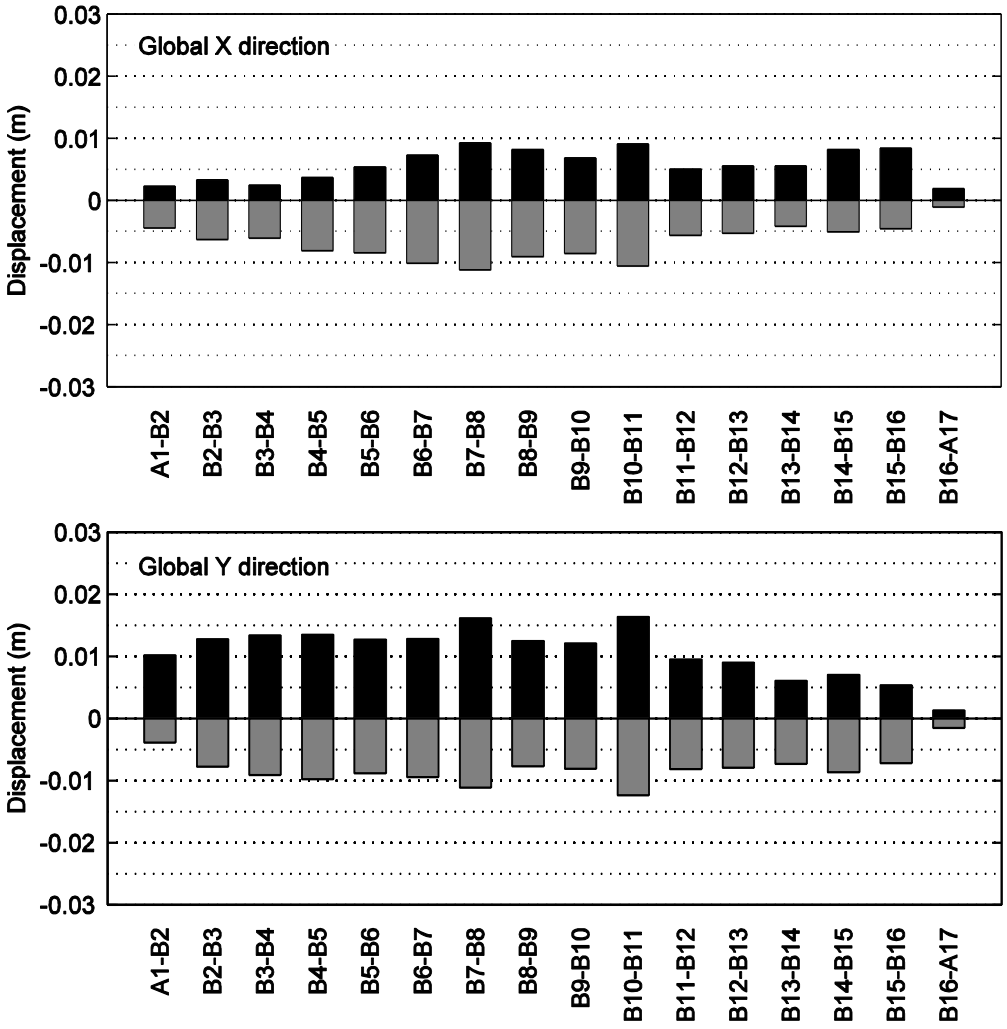

Figure 4.8: Relative support motions between two adjacent bents in the NW

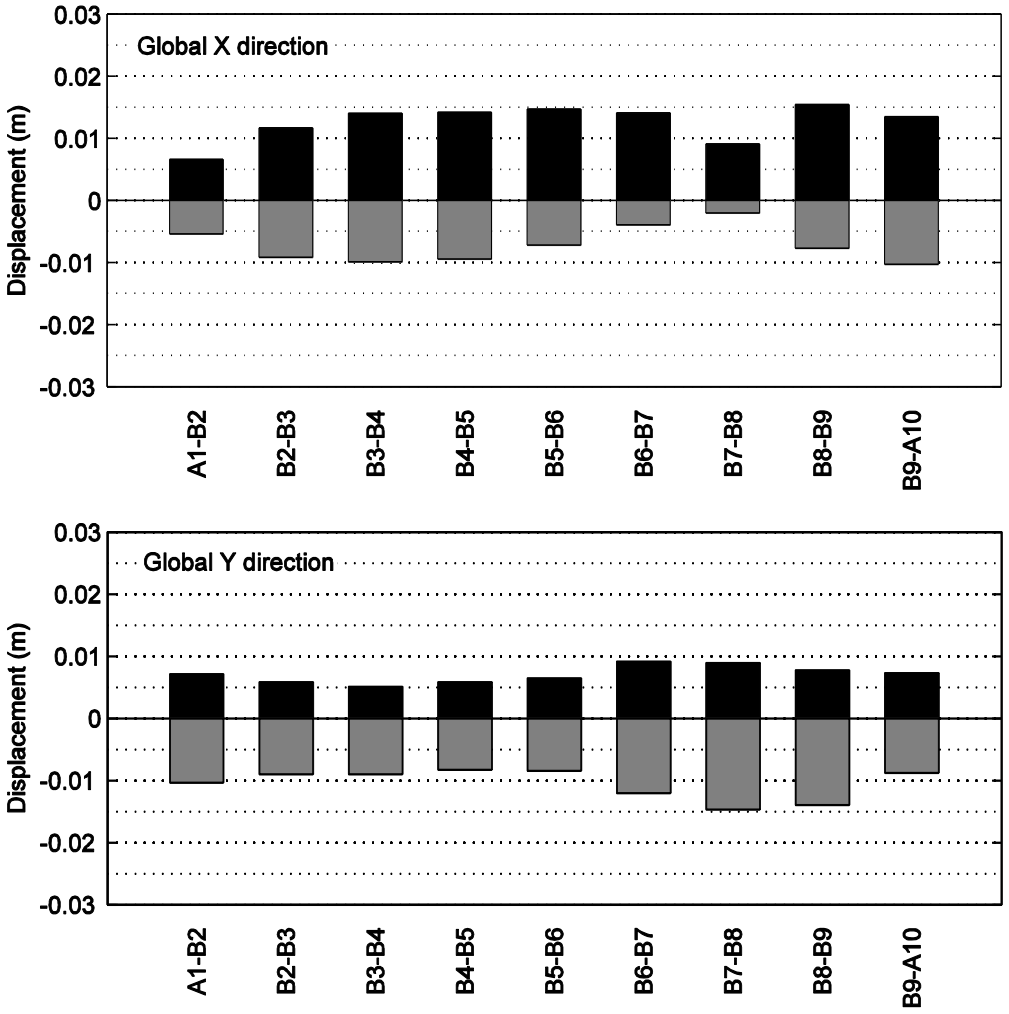

Figure 4.9: Relative support motions between two adjacent bents in the NE

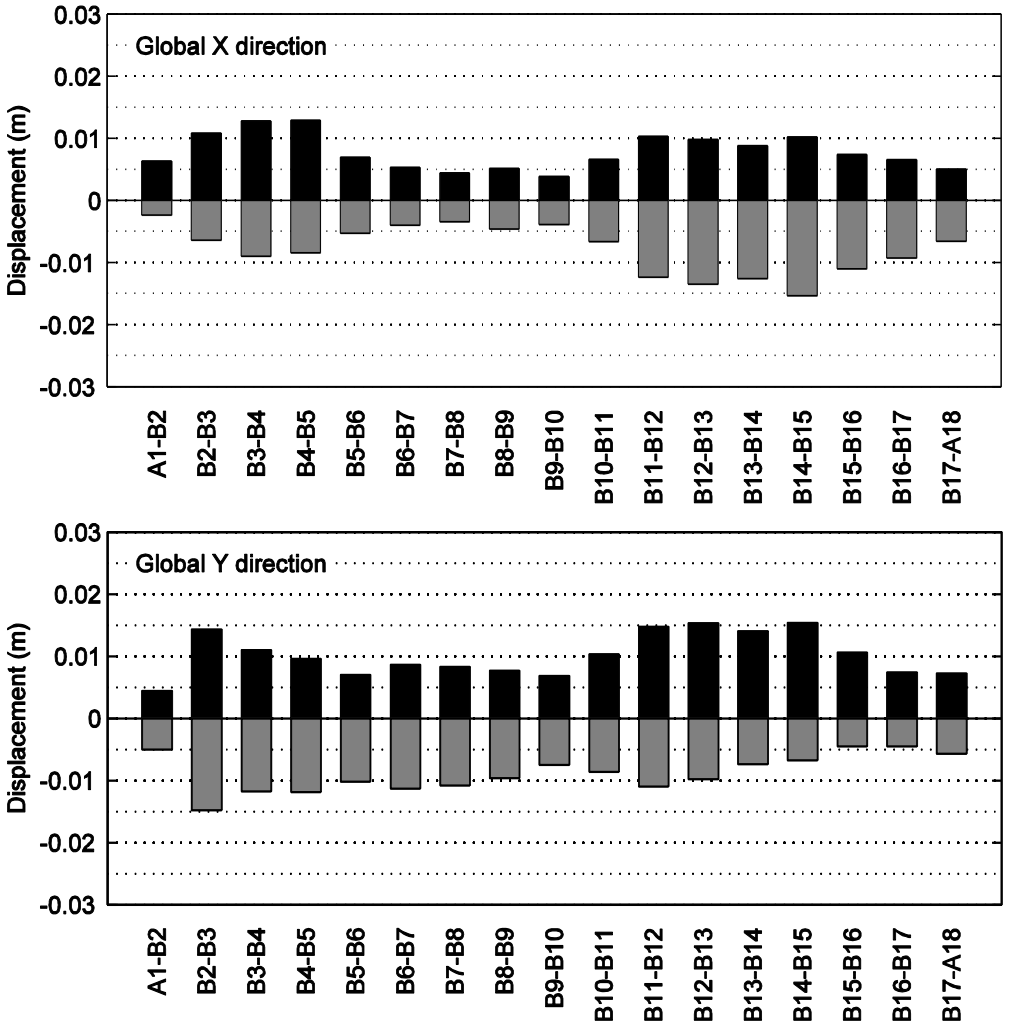

Figure 4.10: Relative support motions between two adjacent bents in the SE

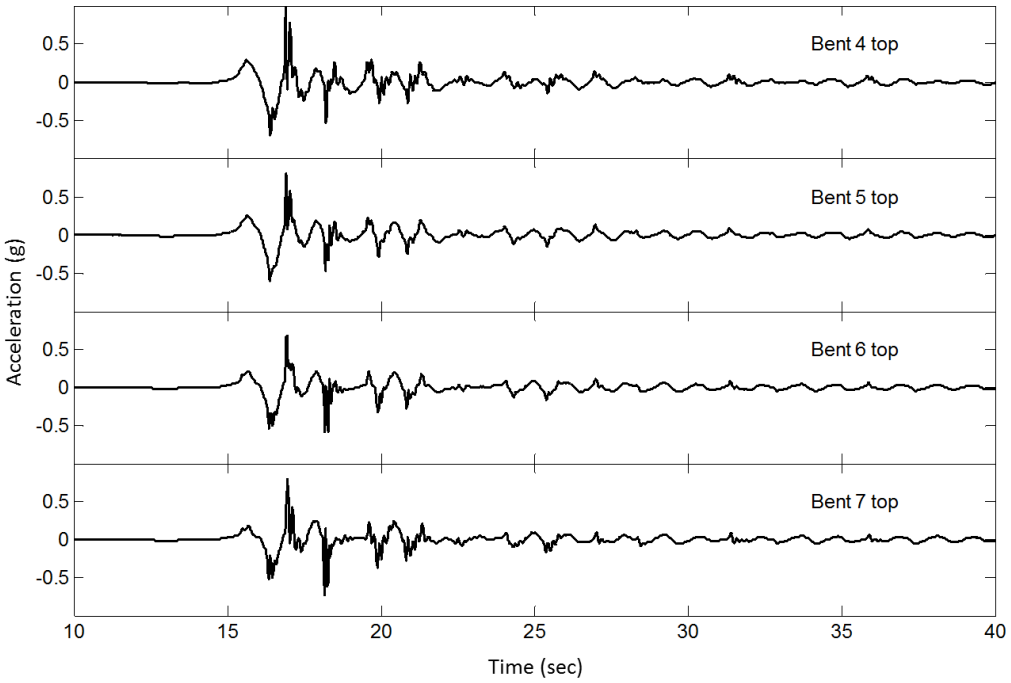

(a) Longitudinal direction

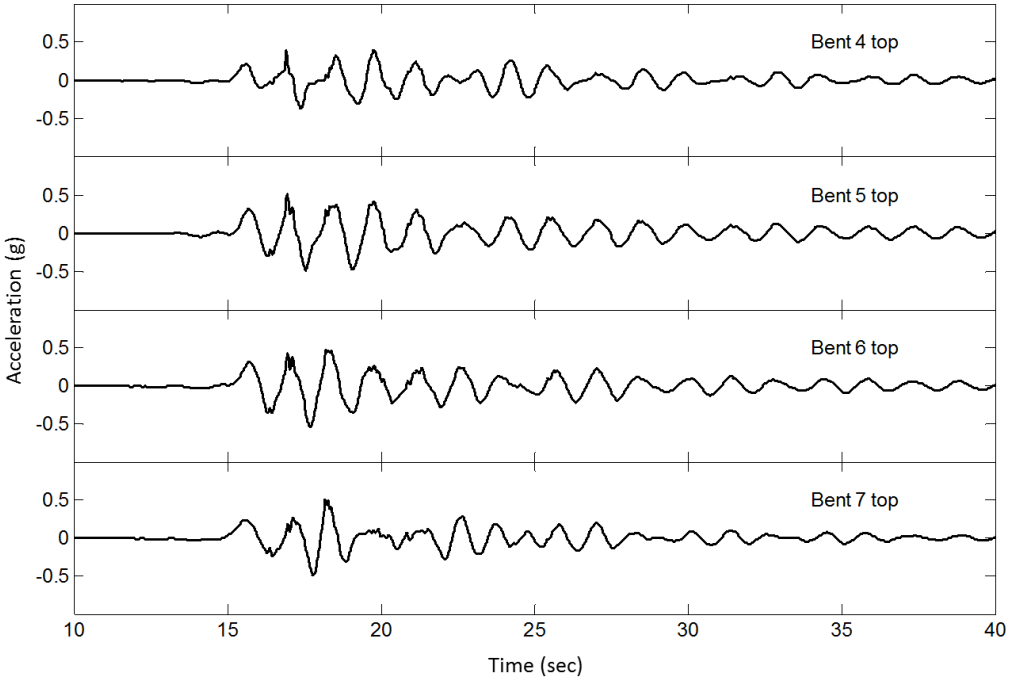

(b) Transversal direction

Figure 4.11: Acceleration time histories at deck locations in the frame 2 of the North-West connector

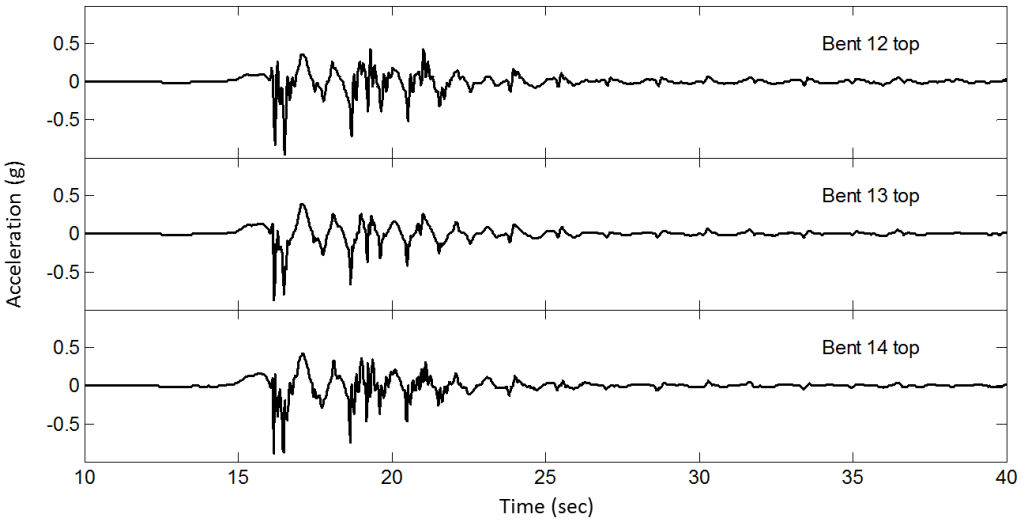

(a) Longitudinal direction

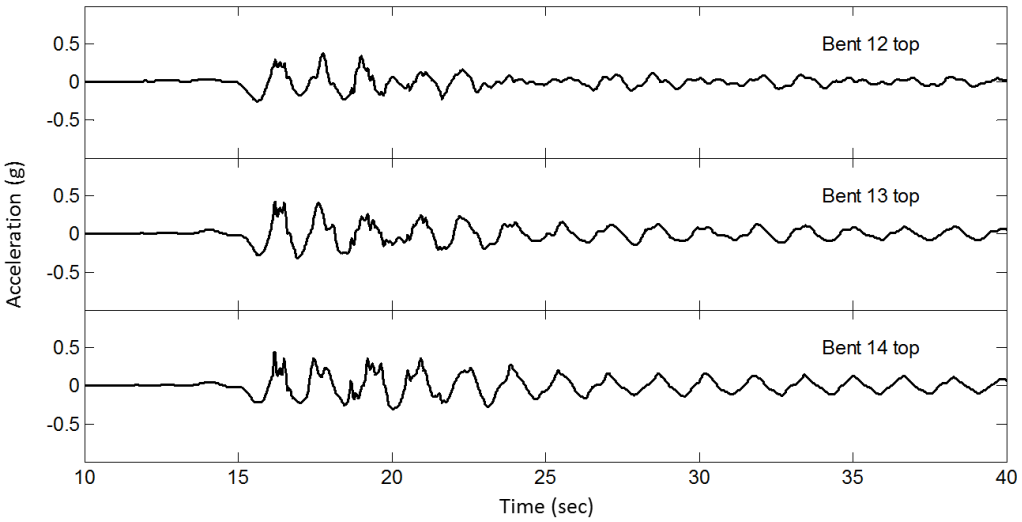

(b) Transversal direction

Figure 4.12: Acceleration time histories at deck locations in the frame 4 of the South-East connector

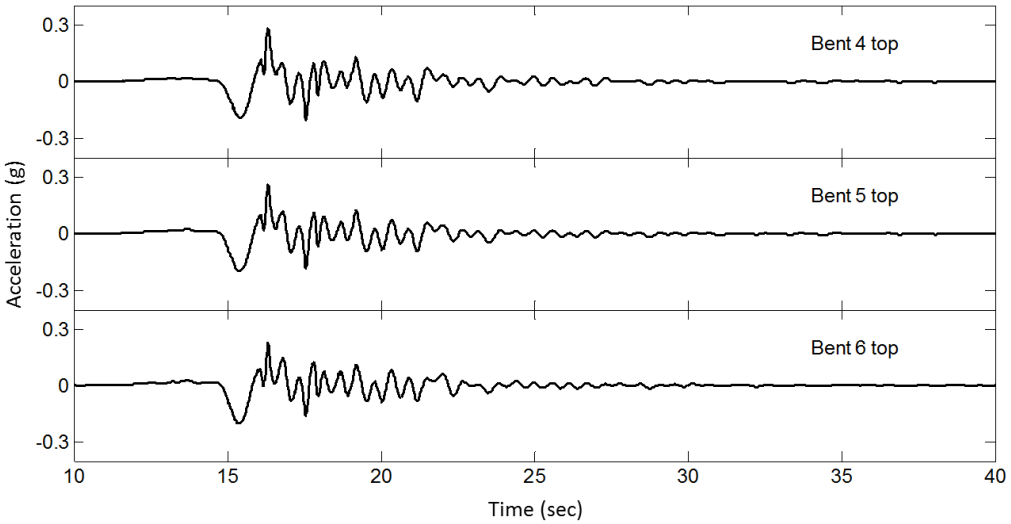

(a) Longitudinal direction

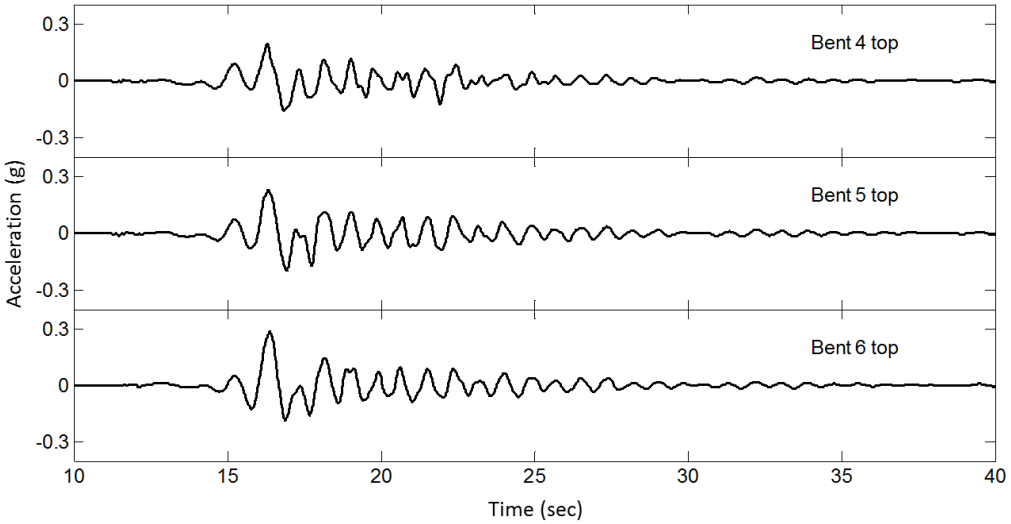

(b) Transversal direction

Figure 4.13: Acceleration time histories at deck locations in the frame 2 of the North-East connector

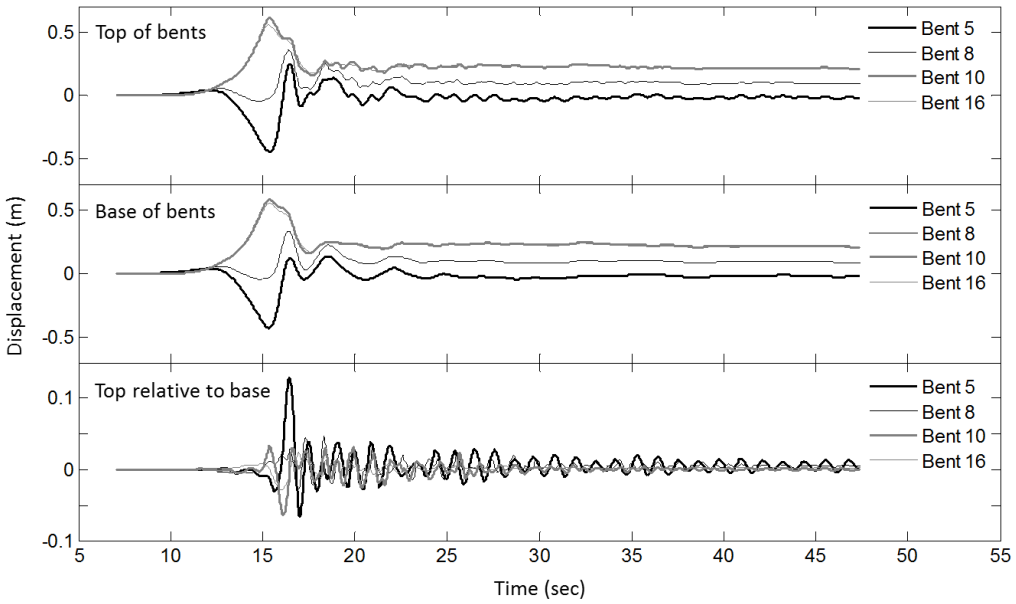

(a) Longitudinal direction

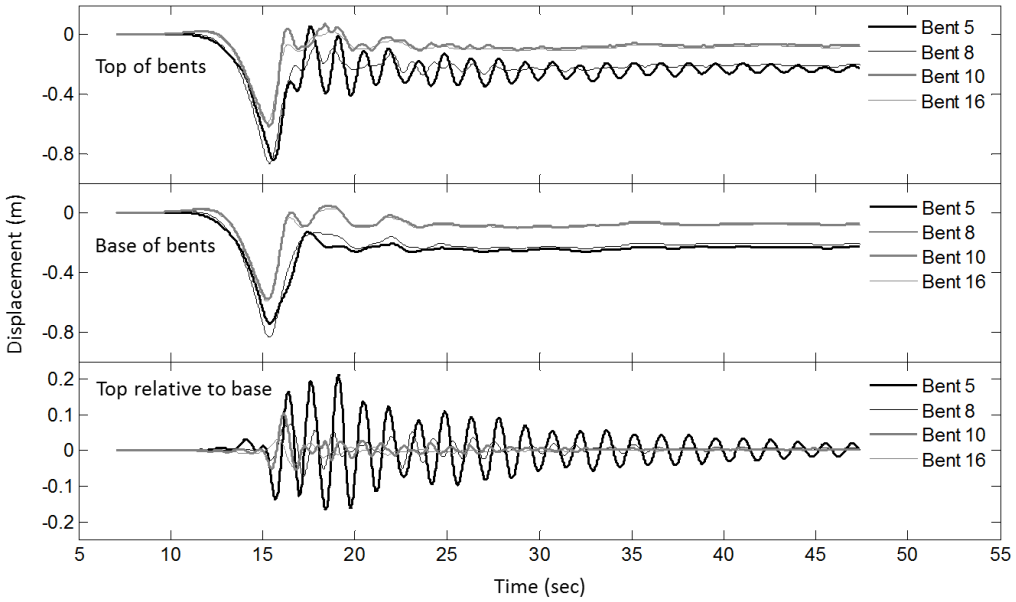

(b) Transversal direction

Figure 4.14: Displacement time histories at top and base of Bents 5, 8, 10, and 16 in the North-West connector

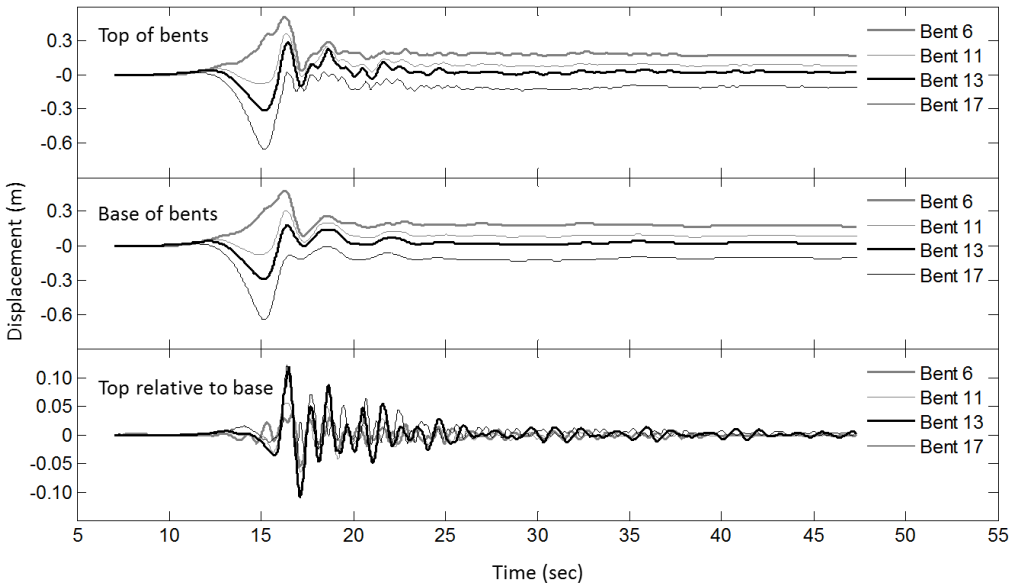

(a) Longitudinal direction

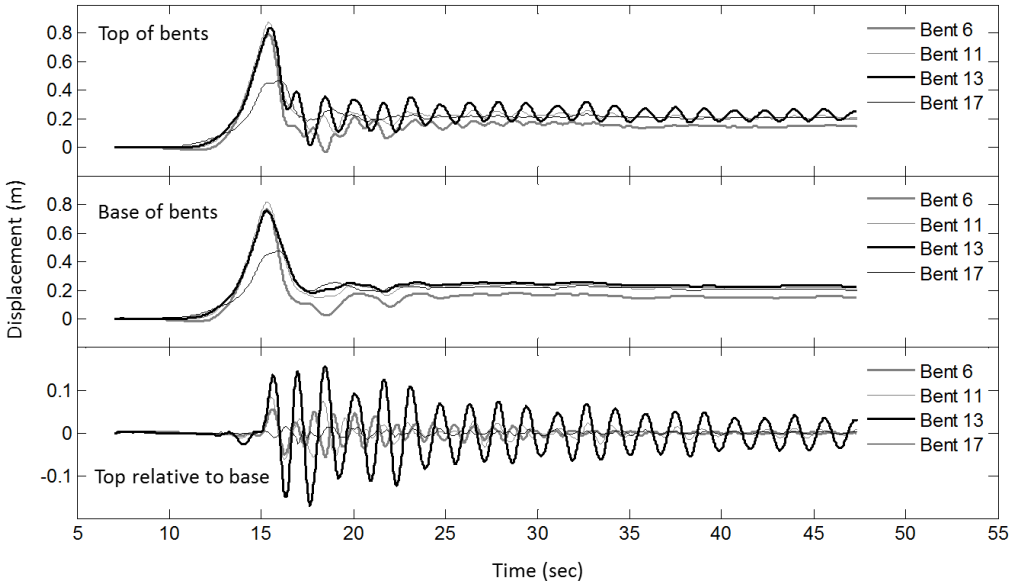

(b) Transversal direction

Figure 4.15: Displacement time histories at top and base of bents 6, 11, 13, and 17 in the South-East connector

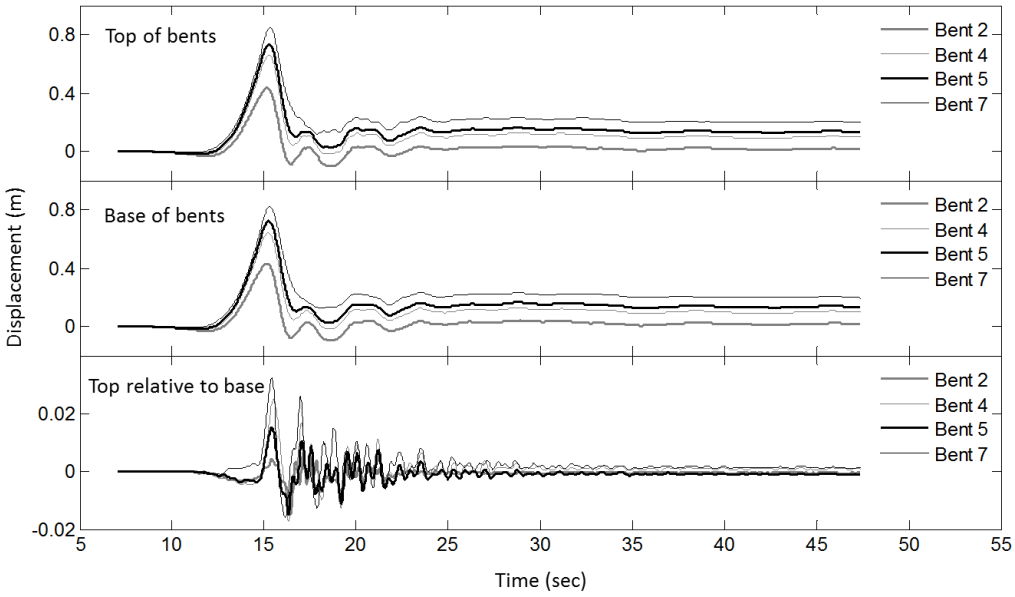

(a) Longitudinal direction

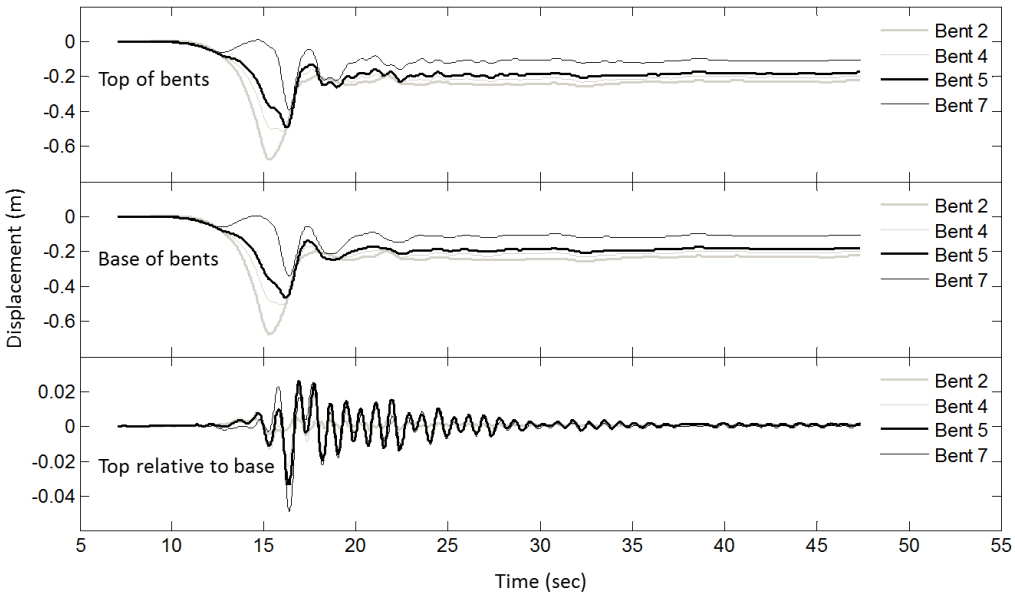

(b) Transversal direction

Figure 4.16: Displacement time histories at top and base of bents 2, 4, 5, and 7 in the North-East connector

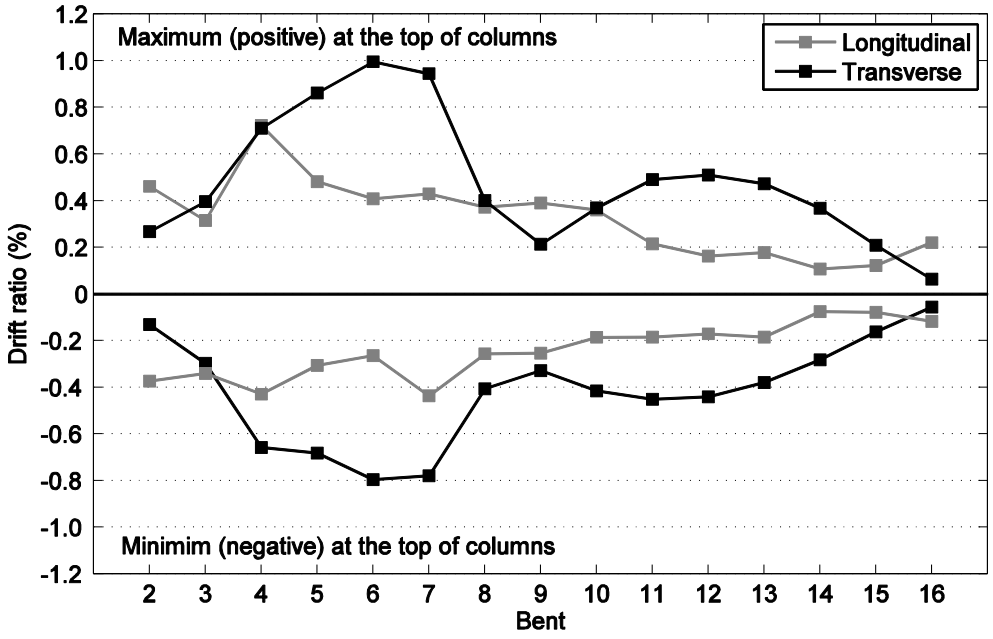

Figure 4.17: Maximum drift ratios at the top of columns in the NW

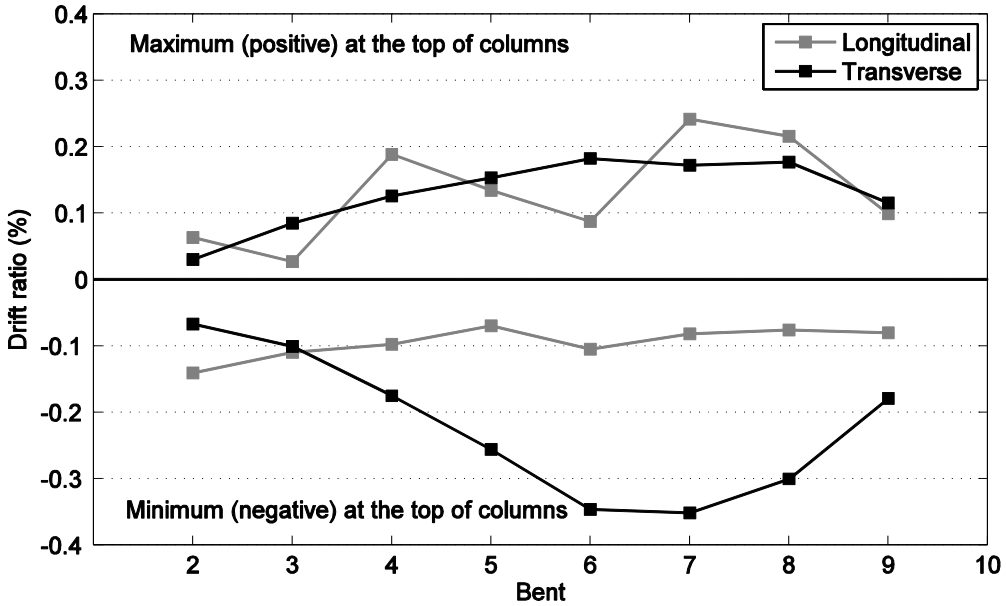

Figure 4.18: Maximum drift ratios at the top of columns in the NE

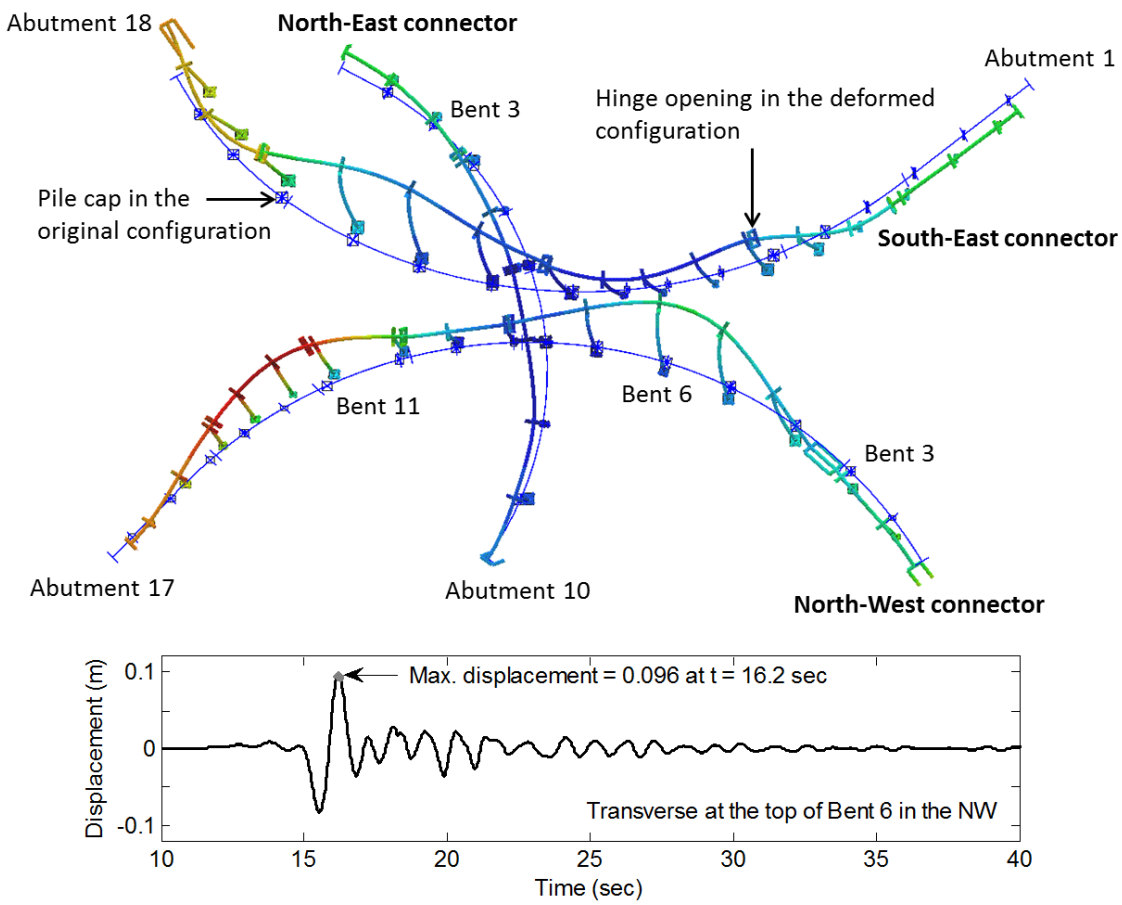

Figure 4.19: Relative deformed configuration of the structural model relative to the center surface in the ROI at T = 16.2 sec. (scale factor of 350)

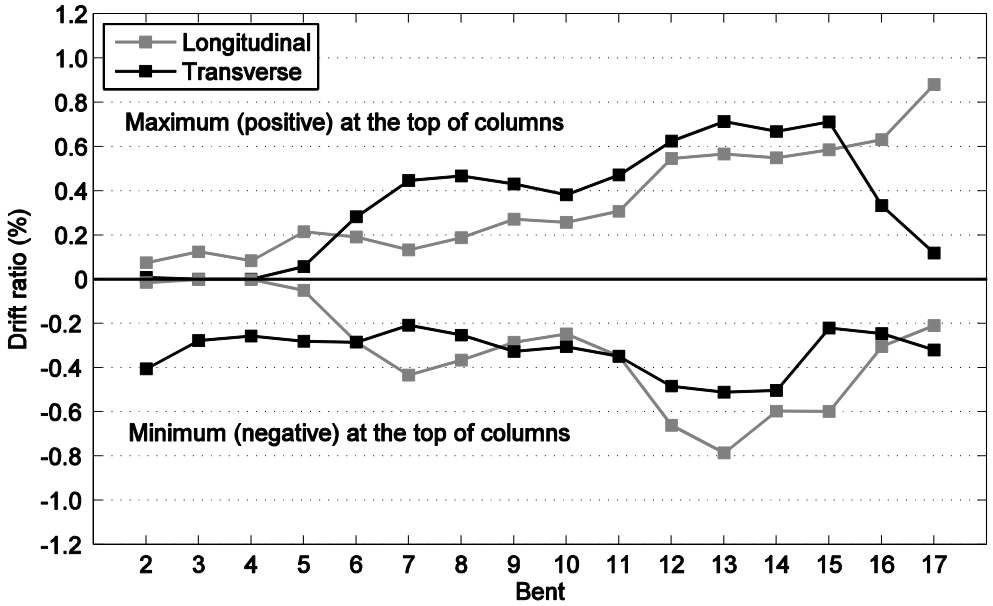

Figure 4.20: Maximum drift ratios at the top of columns in the SE

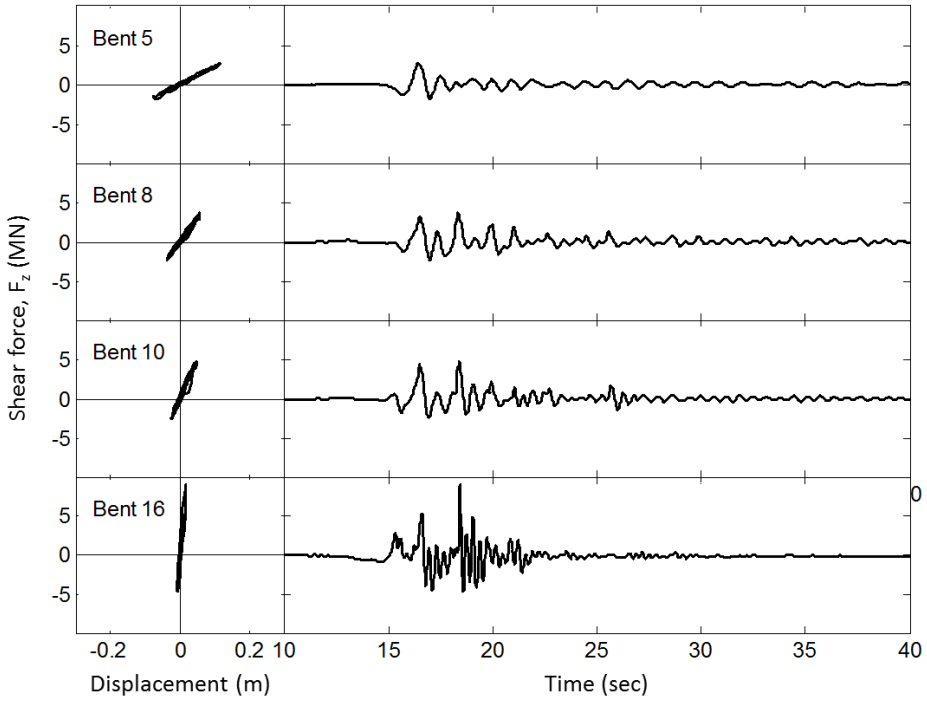

(a) Longitudinal direction

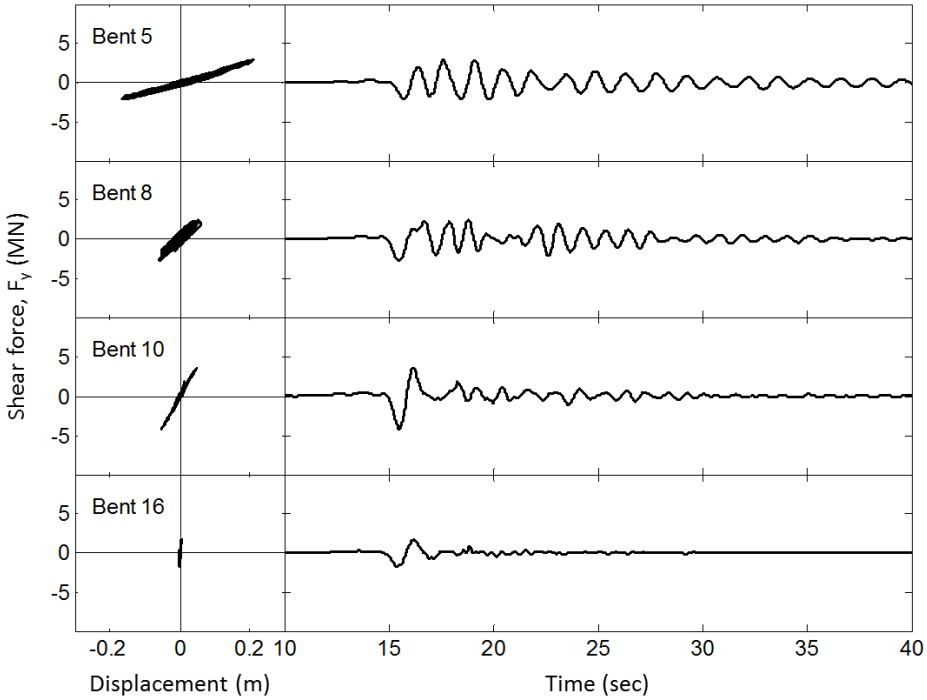

(b) Transversal direction

Figure 4.21: Relation of shear forces and relative displacements at the top to the base along with shear force time histories in the North-West connector

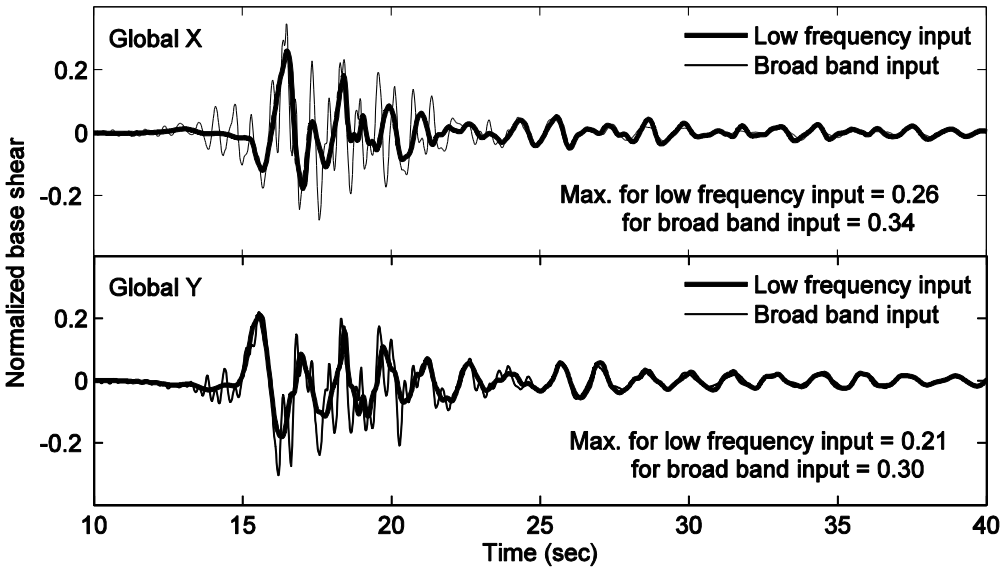

Figure 4.22: Comparison of the normalized base shear in the North-West connector

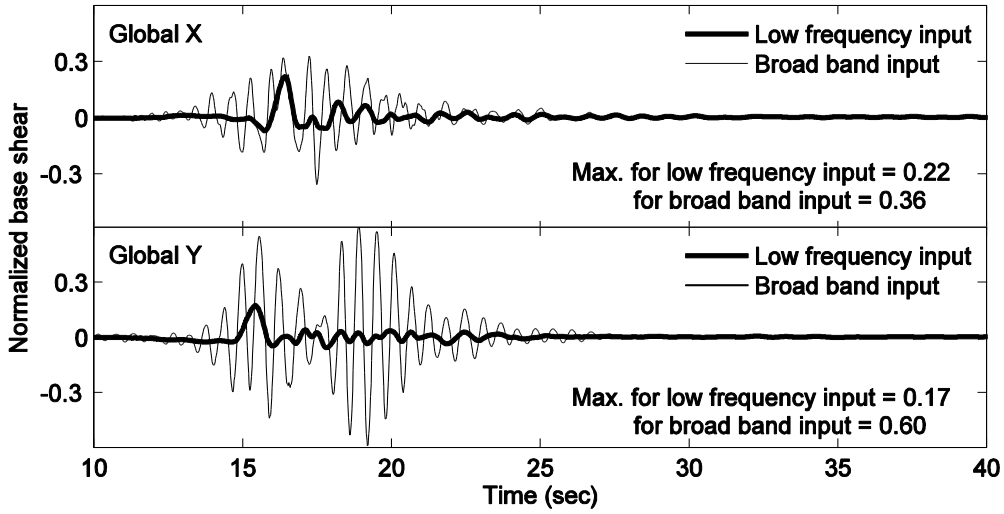

Figure 4.23: Comparison of the normalized base shear in the North-East connector

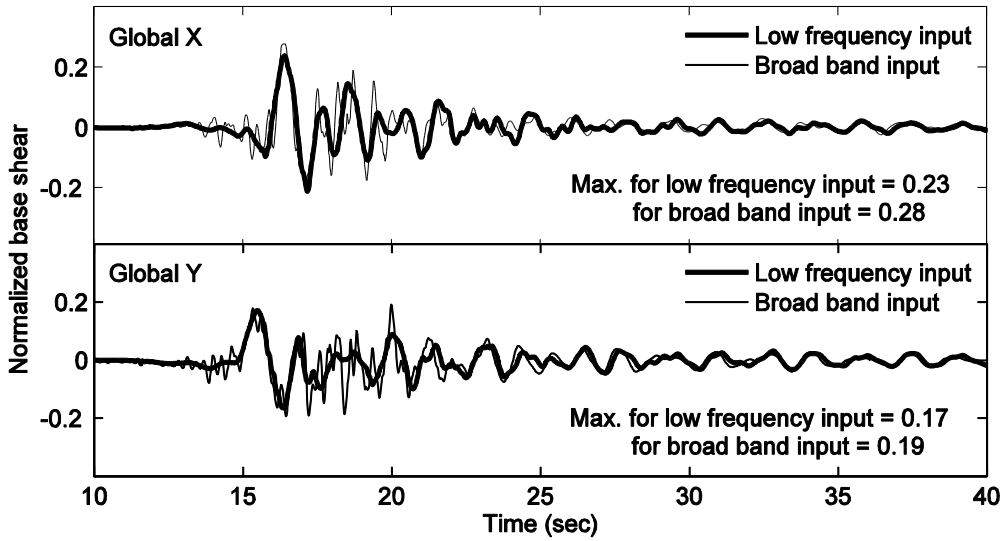

Figure 4.24: Comparison of the normalized base shear in the South-East connector

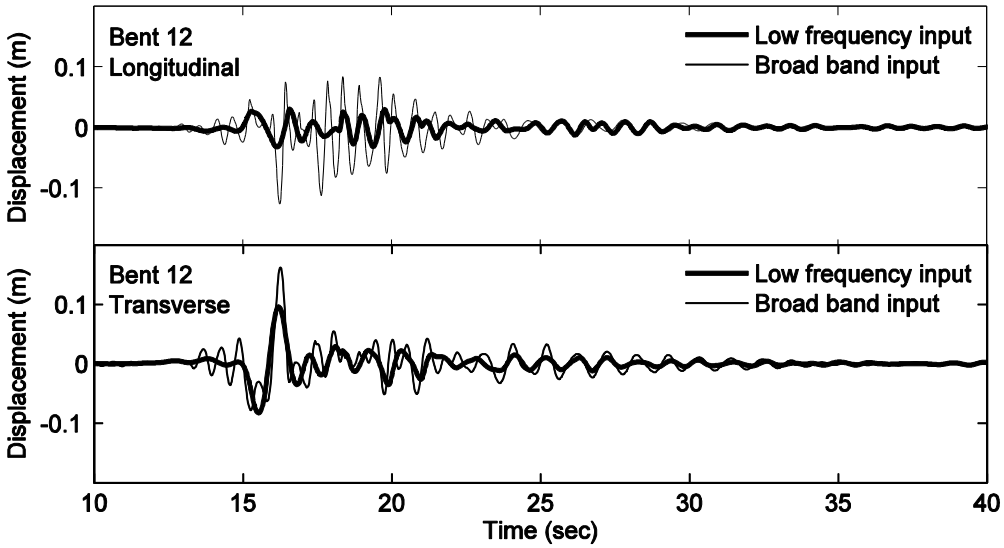

Figure 4.25: Comparison of the top displacement excluding the displacement induced by the base rocking in the North-West connector

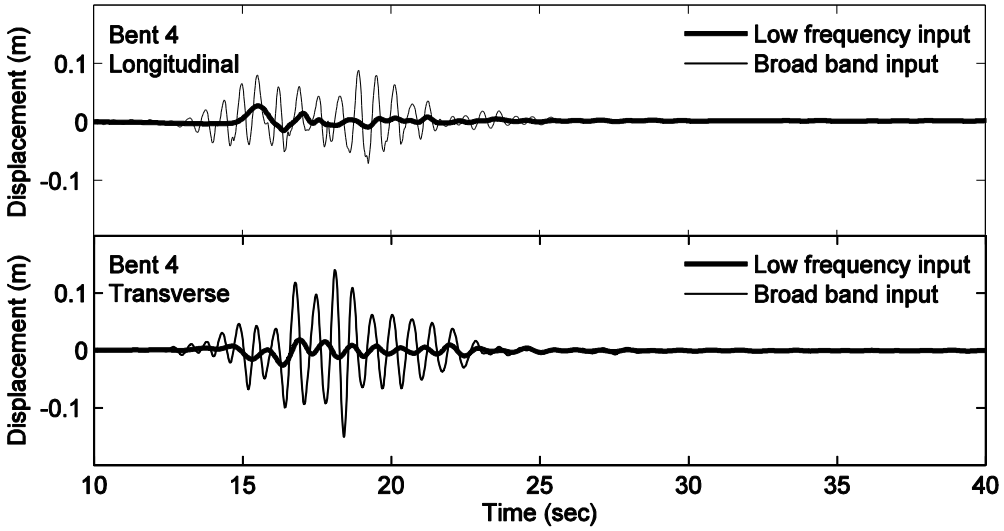

Figure 4.26: Comparison of the top displacement excluding the displacement induced by the base rocking in the North-East connector

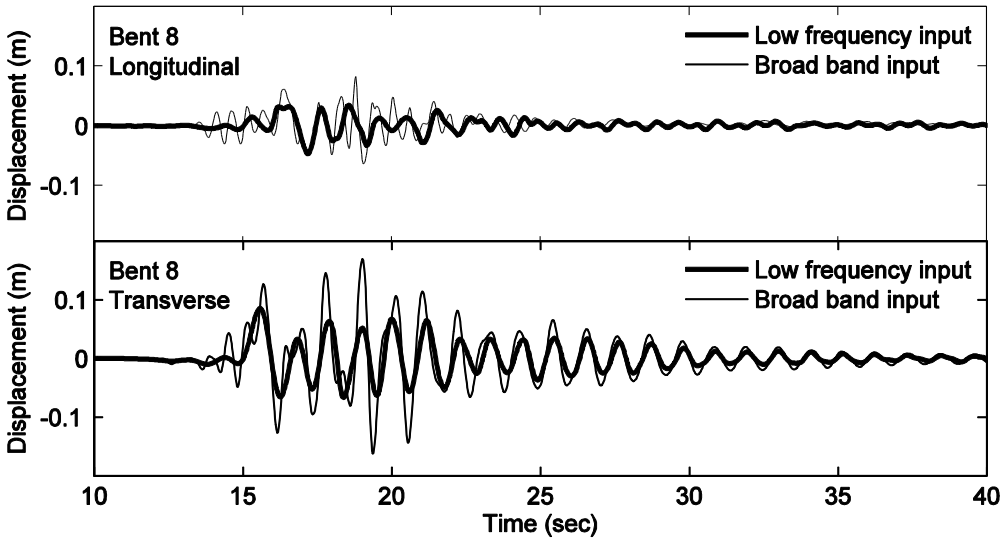

Figure 4.27: Comparison of the top displacement excluding the displacement induced by the base rocking in the South-East connector

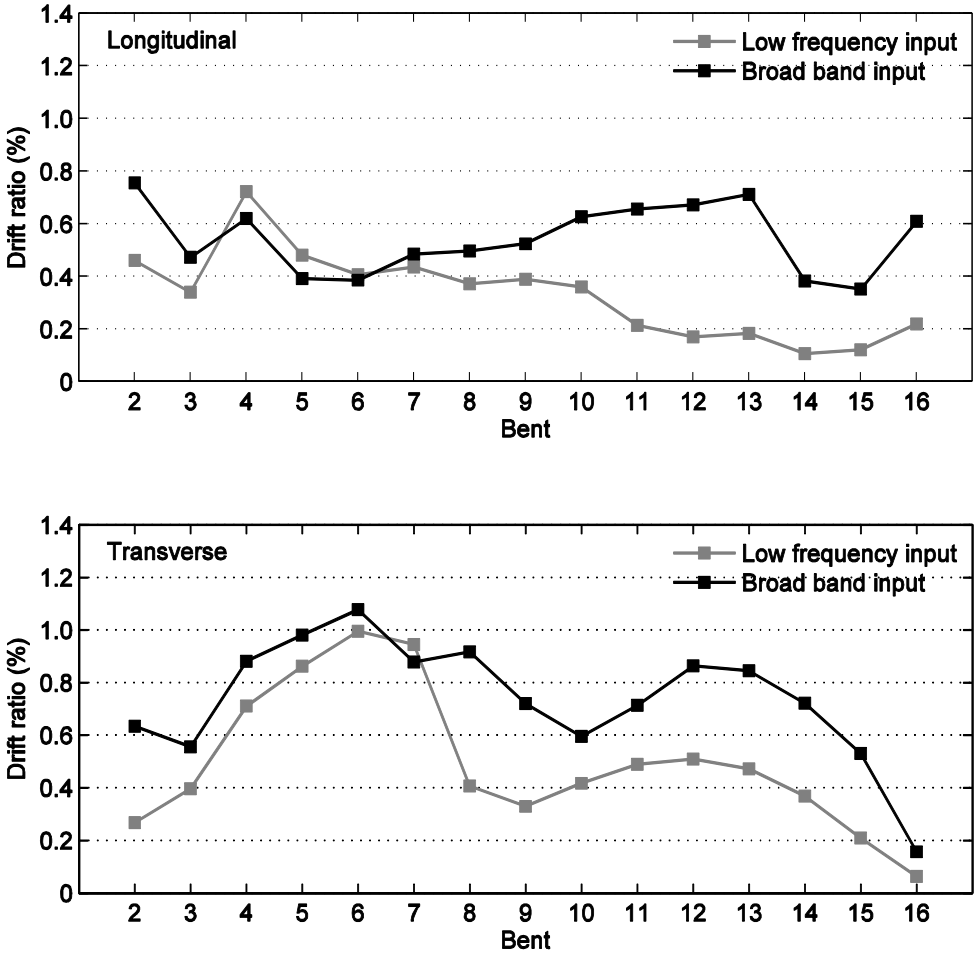

Figure 4.28: Comparison of the maximum drift ratios in the North-West connector

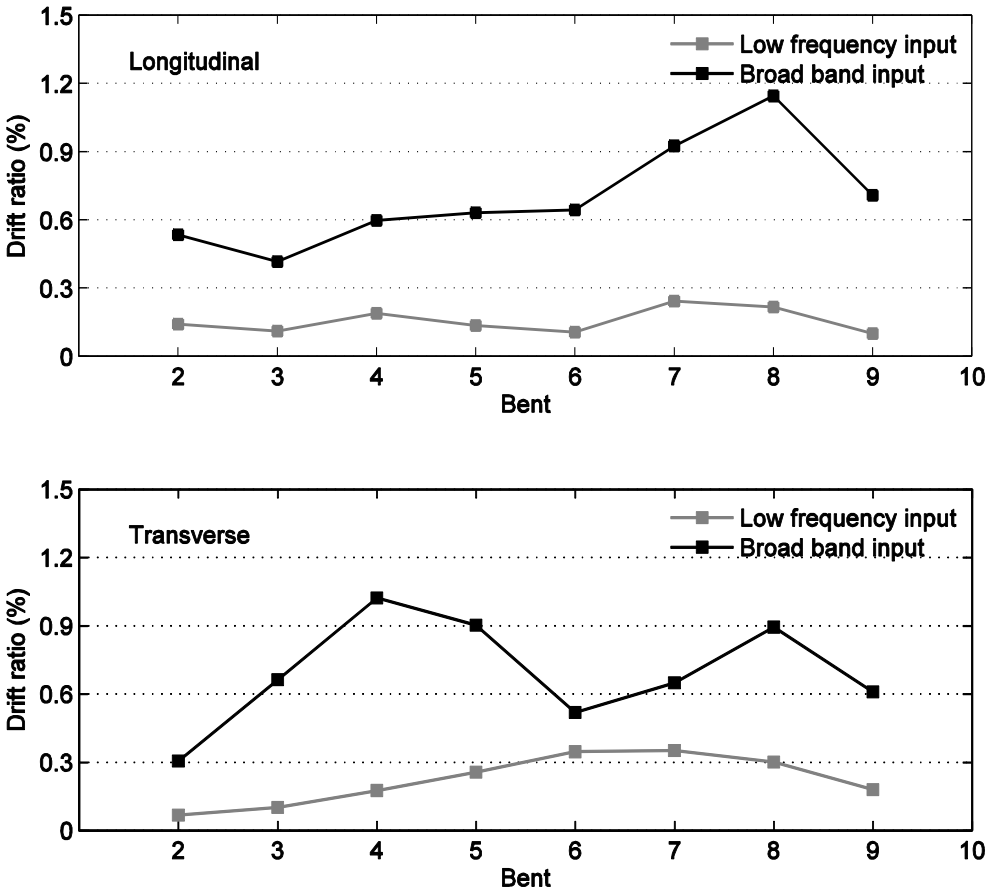

Figure 4.29: Comparison of the maximum drift ratios in the North-East connector

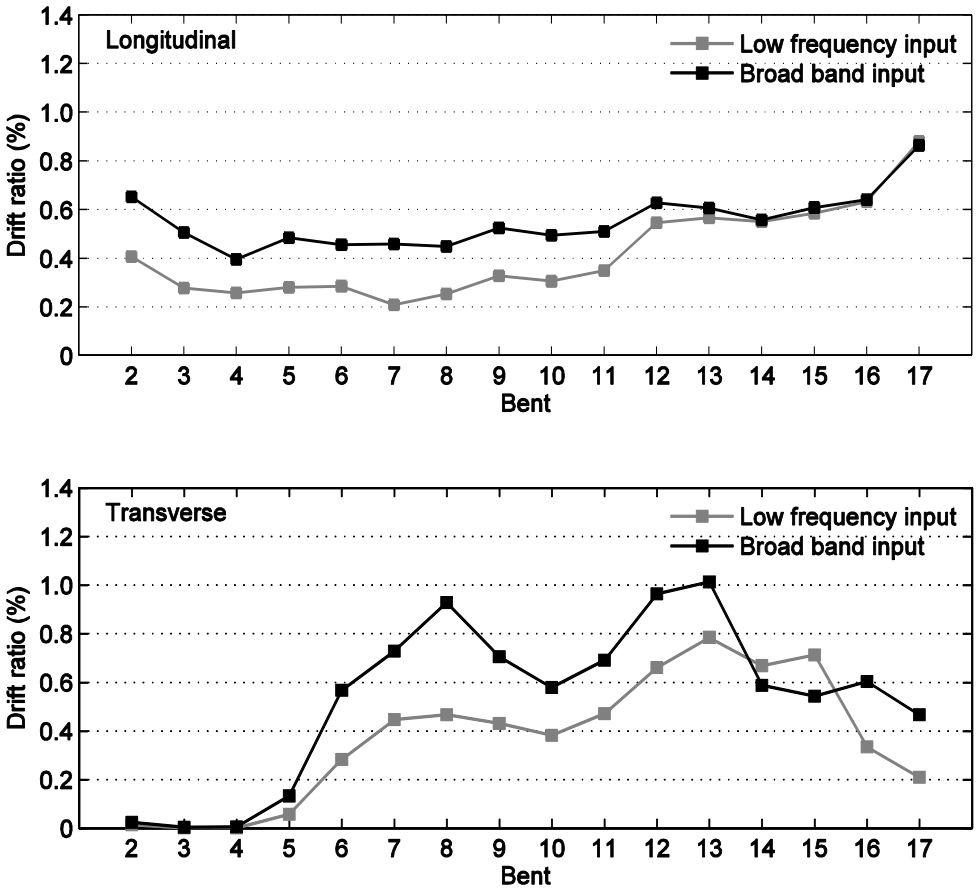

Figure 4.30: Comparison of the maximum drift ratios in the South-East connector

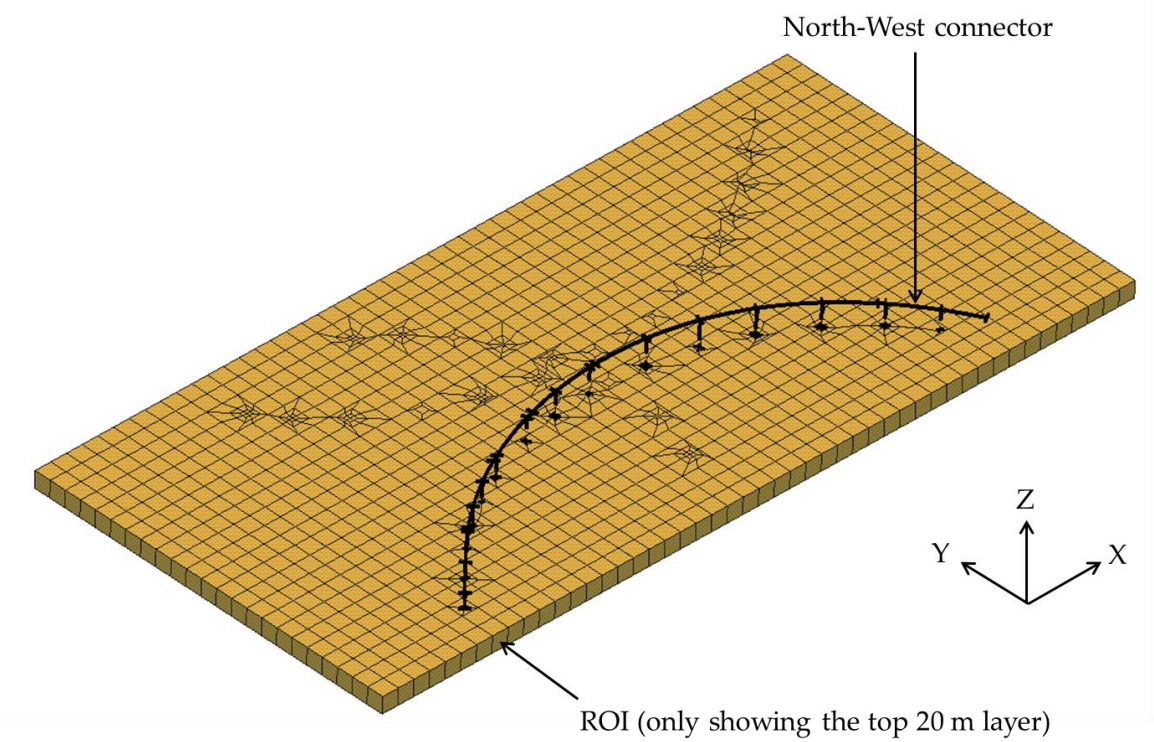

Figure 4.31: FE model for the analysis of NW only in the ROI

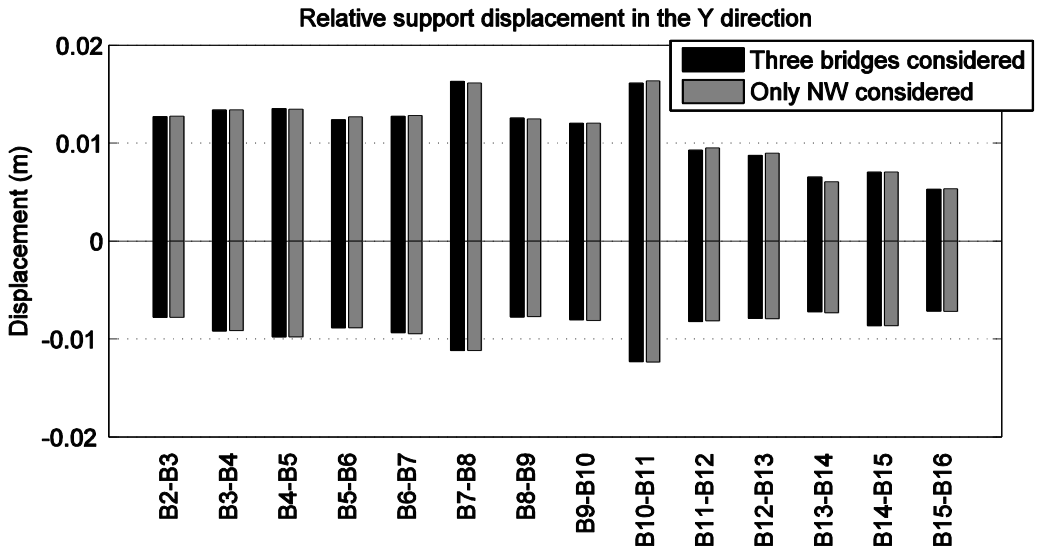

(a) Low frequency input used

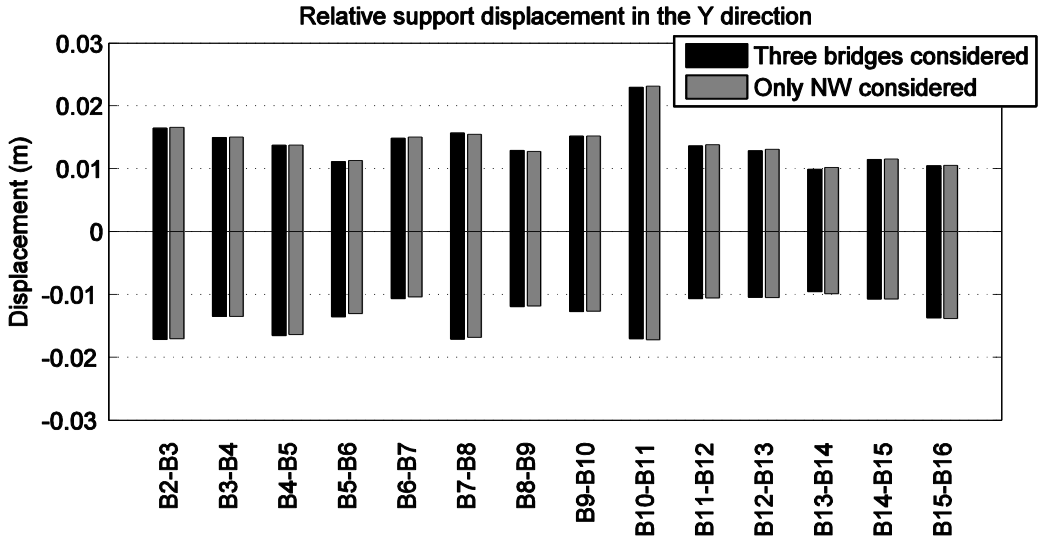

(b) Broadband input used

Figure 4.32: Comparison of the relative support motions obtained from three connectors and only NW considered.

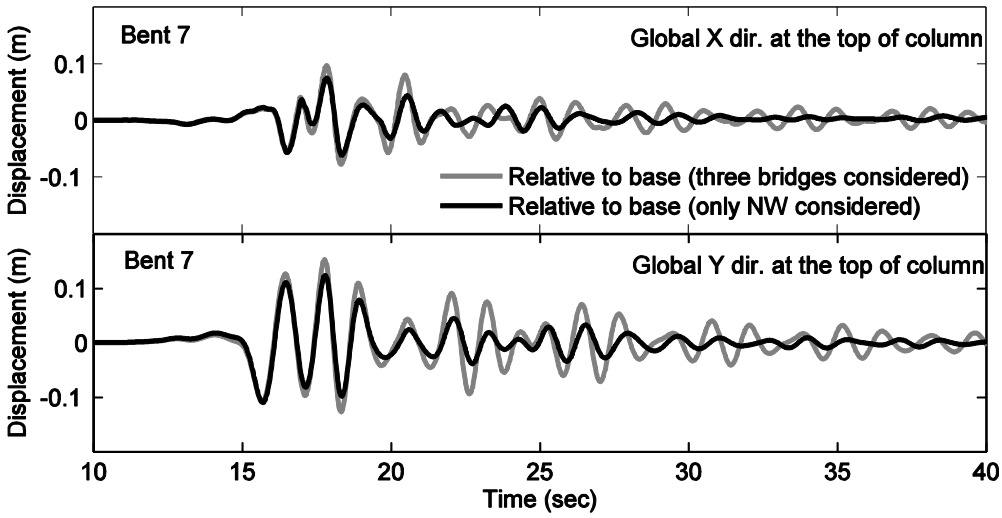

(a) Low frequency input used

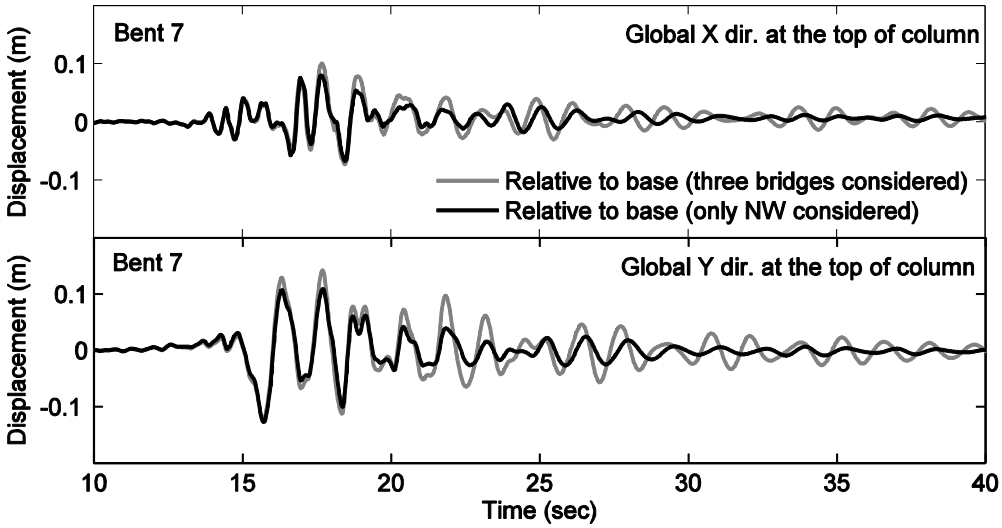

(b) Broadband input used

Figure 4.33: Relative displacements at the top to the base of Bent 7 obtained from three bridges and only NW considered

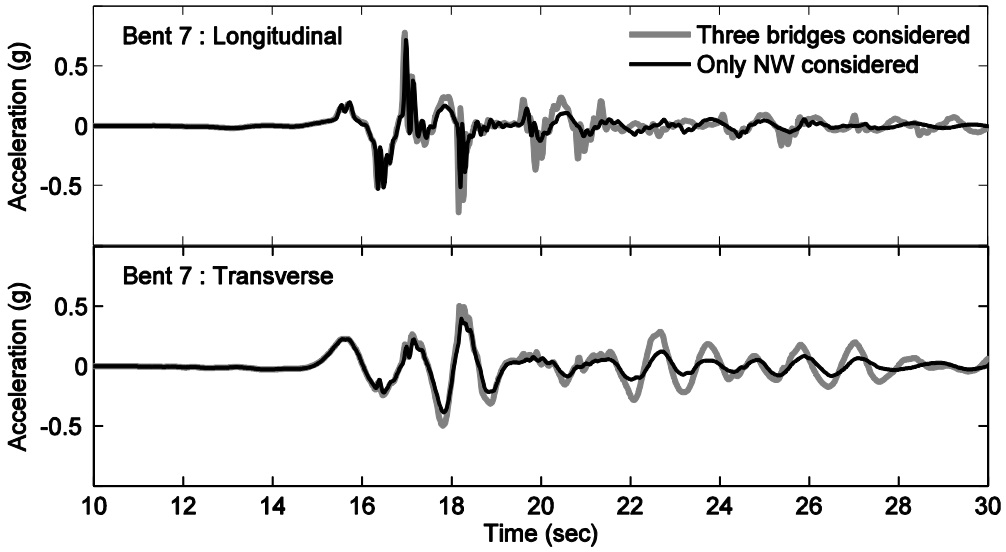

(a) Low frequency input used

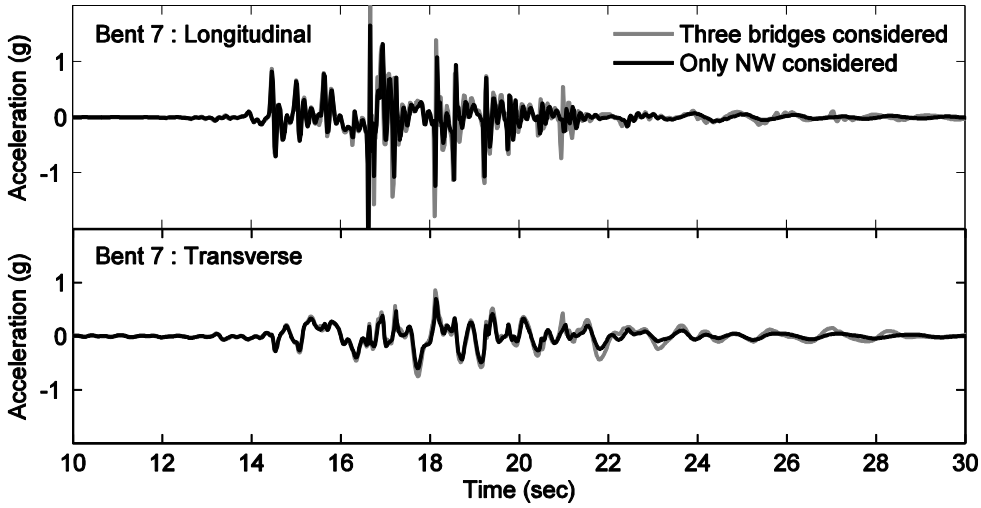

(b) Broadband input used

Figure 4.34: Total acceleration at the top of Bent 7 obtained from three bridges and only NW considered

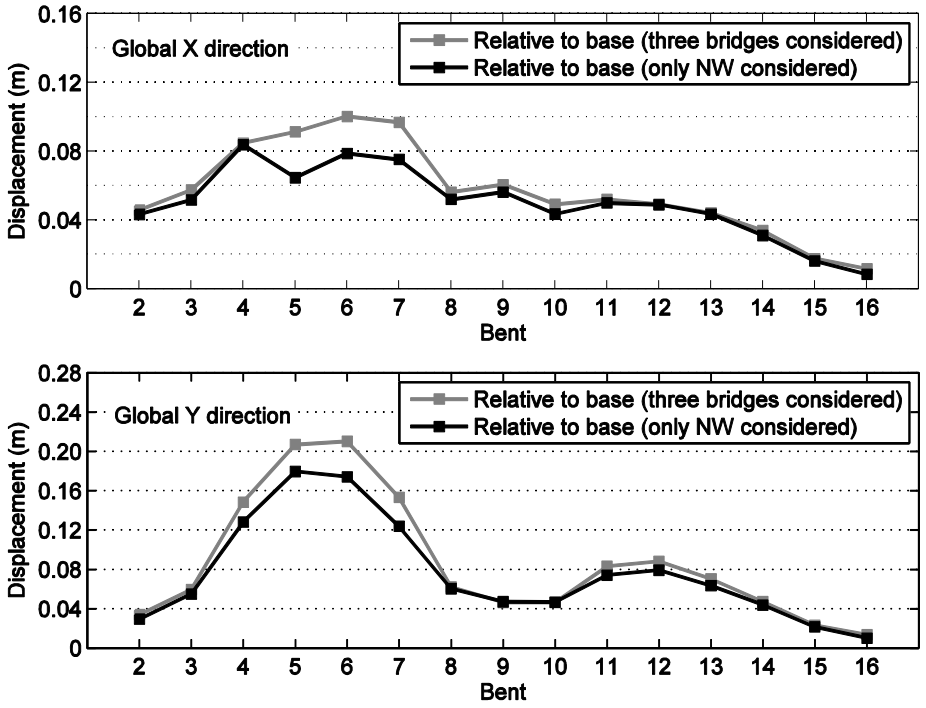

(a) Low frequency input used

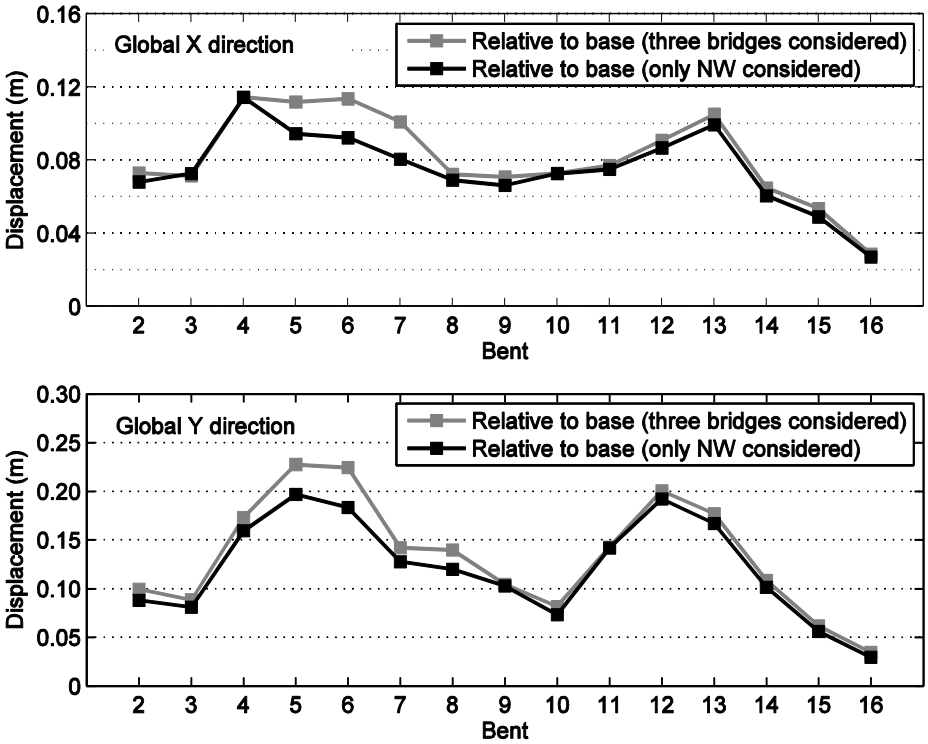

(b) Broadband input used

Figure 4.35: Maximum relative displacements at the top of columns obtained from three bridges and only NW considered

Chapter 5

Evaluation of the NW Soil-Structure-Interaction Effects

This chapter presents an evaluation of soil-structure interaction (SSI) on the seismic response of the NW model. The pile foundations are embedded in the ROI to form the bridge-foundation ground system (BFGS). Influence of ground flexibility on the bridge response is emphasized. Efforts include an investigation of the response under non-uniform support motions resulting from the BFGS simulation. Results of the BFGS are compared to those obtained from those of the fixed-base structural shaking scenario without the soil domain.

5.1 Introduction

In Chapter 4, seismic response of the three bridges as a BFGS was discussed. Although these bridge structures are located in the vicinity of each other at the actual highway interchange, effects of adjacent structures were negligible because of the relatively stiff ground soil. The bridge structures were exposed to non-uniform ground motion over the large ROI area. This spatial variation of the ground motion is dependent on the material properties of the soil profile. Soft soils generally result in amplification and more pronounced spatial variability of the ground motions. Consequently, soil-structure interaction (SSI) may play a more significant role when evaluating the structure's seismic response.

In order to assess SSI effects, two different types of the ground model are considered (stiff and soft soil cases). The North-West connector (NW) at the interstate 10 and 215 interchange (I-10/215; see Section 3.1 for details) is used as a structural model. Linear material properties for two types of soil profiles are considered. Depending on the different soil scenarios, the corresponding structural response in terms of base shears at the level of the foundation, and relative displacements/internal forces in the columns are discussed. Furthermore, results from an additional analysis of a fixed-base structure are compared with those of the BFGS. The study is focused mainly on the low frequency input generated by the Puente Hill fault rupture scenario (see Section 2.1.4). In the end of this chapter, effects of the broadband input are also discussed.

5.2 Description of the BFGS

5.2.1 Ground model

In the BFGS (Figure 5.1 shows the computational FE model), the region of interest (ROI) of Petropoulos (2008) is adopted as the ground model. The modeling scheme is presented earlier in Section 2.1. Two types of soil material properties representing the stiff and soft soil profile scenarios are discussed in the following section.

5.2.1.1 Stiff soil profile

As conducted earlier in Chapter 4, the ROI is employed with the stiff soil profile (shear wave velocity of 482 m/s in the top 40 m layer). The employed linear material properties can be found in Table 5.1. Ground response was presented earlier in Section 2.3.

5.2.1.2 Soft soil profile

In this scenario, half the shear wave velocity for the top stiff soil 40 m layer is specified. Proportionately, material properties for the underlying layers in the stiff soil profile are reduced as well (Table 5.2). Compared to the response in the stiff soil scenario, horizontal peak ground acceleration (PGA) in the soft soil is amplified by as much as 60%. Meanwhile, the vertical component is significantly reduced. The PGA profile along the depth is shown in Figure 5.2. Figure 5.3 shows total acceleration at the center surface node (Spectra are shown in Figures 5.4-5.6). In addition, ground velocity and displacement at the center are shown in Figure 5.7 and Figure 5.8, respectively.

In Figure 5.4 through Figure 5.6, Fourier amplitude spectra of total accelerations at the surface center node and along the centerline in the X direction over the surface are shown. It can be seen that amplitudes at the frequencies of interest (≤ 2 Hz, corresponding the primary resonances of the bridge) are much amplified in the soft soil. As expected, more noticeable variation of ground motion over the soil surface is observed in the soft soil profile (Figure 5.5 and Figure 5.6).

5.2.2 Bridge model

The NW is considered as the structural model in this BFGS simulation. Modeling details can be found in the earlier Section 3.2.3. Dynamic properties of the bridge were presented in Section 3.2.4. As discussed earlier in Section 4.1.2.2, the soil mesh configuration near the ground surface was modified (below the location of each bridge column) in order to accommodate the structural model pile-group foundation geometry as shown in Figure 5.1 (b).

5.3 Seismic response of the BFGS

5.4 Assessment of soil-structure interaction effects

The domain reduction method, DRM (Bielak et al. 2003a), provides the advantage of capturing free-field motions at desired locations on the ground surface in the ROI. This method also enables one to analyze a fixed-base structure using the resulting multiple base excitations at the location of each column foundation. More crudely, ground motion

at a specific location near the structure may be used as representative base uniform excitation. In modeling such a fixed-base structure scenario, potential relative motion between the pile groups are not accounted for under this uniform excitation assumption.

On this basis, results for analysis of the BFGS may be compared with those from uniform base excitation and multi-support excitation without the soil domain. Various seismic response quantities, such as support accelerations, base-shears, acceleration / displacements at the top of columns, and column drift ratios/forces are considered to further examine the role of SSI.

5.4.1 Numerical simulation of fixed-base structures

The NW is analyzed in the form of the fixed-base structure without considering the pile foundations. As input, free-field motions obtained from the soil domain without any structure are applied to the fixed-base model.

5.4.1.1 Multiple-support excitation

Spatially variable ground motions in terms of displacements are applied at the corresponding location of each column. Via the DRM approach, the ground motions are obtained for the two types of employed soil (stiff and soft) at the actual location of the bridge foundations in the absence of the structure (i.e., free-field motions). As such, seismic excitation is dictated by the free-field motions at the base of the columns.

5.4.1.2 Uniform excitation

Computed from the ROI without the structure, the free-field motion of the surface center node is taken as the representative structural uniform base excitation. This ground motion in terms of base acceleration, computed for the two soil profiles (stiff and soft) is used to excite the structure uniformly in the horizontal and vertical directions. The ground acceleration in the three translational directions is applied at the base of each column and no rotation is allowed at the supports.

5.4.2 Comparison of responses

Structural response obtained from the analysis of the fixed-base bridge is compared with those from the BFGS. Depending on the employed soil types (stiff and soft), the ground motion as input may increase or decrease the bridge response as discussed herein.

5.4.2.1 Ground acceleration at the base of columns

Maximum accelerations at the base under the three types of loading conditions are shown in Figure 5.17 (for the stiff soil profile) and Figure 5.18 (for the soft soil profile) in the global X (parallel to the chord of the curved geometry) and Y direction (perpendicular to the chord; associated with overall transverse bridge response). Levels of base acceleration within the soil domain (i.e., in the BFGS and the multiple support excitation scenario) vary significantly along the longitudinal direction. Comparing the

results of the BFGS the multiple support excitation scenario, maximum accelerations are very similar (in both the stiff and the soft soil scenarios).

5.4.2.2 Seismic base shears

The normalized total column base shear forces divided by self-weight of the bridge (about 160 MN) are compared with and without the soil domain. Table 5.5 provides the maximum base shears in the global coordinate system in which the Y axis corresponds to the more flexible direction of the bridge's overall response (see Figure 5.1).

Under the multiple support excitation condition, the base shear is similar to that of the BFGS case, except for the Y component in the soft soil case (10% reduction). In the X direction, the base shear decreases 2% for the stiff soil and 0.3 % for the soft soil. In the Y direction, the base shear increases 3% for the stiff soil and decrease 10% for the soft soil profile.

On the other hand, there is much variation of the base shear under uniform excitation in the soft soil scenario. For the stiff soil, the base shear increase 4 % in the X direction and decrease 5% in the Y direction, while the base shear in the X direction for the soft soil increases significantly by as much as 40%.

5.4.2.3 Acceleration at the top of the columns

Acceleration response of the NW is examined with and without the soil domain. Figure 5.19 and Figure 5.20 show acceleration time histories at the top of Bent 6 (height of 22.5 m). These results are obtained from the stiff soil (Figure 5.21) and the soft soil

(Figure 5.22) simulations. The results generally indicate that there is not much variation in accelerations for the stiff soil scenario (note that the level of intermittent spikes in the longitudinal direction is reduced for the uniform excitation case). For the soft soil scenario, differences in response are more visible, in terms of amplitude as well as in the spikes due to pounding (resulting from relative motion at the intermediate hinges between the bridge frames). In addition, compared to the fixed-base analyses, the BFGS caused a longer visible phase of vibration response (up to 40 seconds in duration).

5.4.2.4 Relative displacement at the top of the columns

Relative horizontal displacements between the top and the base of the columns are discussed. For comparison, the relative BFGS displacement will be shown excluding the amount induced by rocking (the fixed-base analysis scenarios do not give rise to rocking).

From the three different loading scenarios, relative displacement time histories at Bent 6 are shown in Figure 5.23 for the stiff soil and Figure 5.24 for the soft soil. In the stiff soil, the maximum transverse displacement in the BFGS is generally larger than that in the fixed-base structure. The uniform base excitation increases longitudinal displacements with the higher base acceleration, compared to that in the other two loading cases. Although resonance response of the bridge is not much affected by the stiff soil domain, it can be seen that the soft soil slightly induces a period lengthening of the structure (Figure 5.24).

In addition, the drift ratio of columns is compared in the three cases. Maximum drift ratios at all the columns are shown in Figure 5.25 and Figure 5.26 (the character H indicates locations of intermediate hinges along the span). In general, the transverse drifts

in the relatively flexible frame (Bents 3 through 8) are larger for the coupled soil-structure case and smaller for the fixed-base structure under uniform excitation. However, this trend is not consistent in the longitudinal direction. Comparison between BFGS with soil domain and the multiple supports excitation case shows that the drift ratios increase due to SSI, with the SSI effects being beneficial or detrimental depending on the location of each particular column.

5.4.2.5 Column forces

The computed column relative displacements induce significant shears and bending moments in the longitudinal (weak axis against the bending moment) and transverse (strong axis) directions of the columns. From Table 5.6 to Table 5.13, comparisons of the maximum column forces are summarized as computed under the BFGS, the multiple support excitation, and the uniform excitation scenarios.

In the stiff soil, SSI induces larger shear forces and bending moments. When the non-uniform ground motions are considered (multiple support excitation) without the effect of SSI, the computed moments are generally close to the ones with SSI, while the uniform excitation results in much deviation from the SSI scenario. Depending on the particular column location, the internal column forces are underestimated or overestimated. In the longitudinal direction, the shear forces and bending moments without the soil domain decrease up to 24.5% and 22.4% at Bent 16 under the multiple support excitation and 39.5% and 45.6% at Bent 14 under the uniform excitation scenario, respectively.

In the soft soil, much higher variation of the column forces is observed. Compared with the stiff soil, the columns forces under the multiple support excitation scenario are generally reduced. The maximum reduction in shear is 33.2% in the transverse direction at Bent 8. In bending moments, the longitudinal moment decreases by as much 34.7% at Bent 13. In particular, larger bending moments are generated under uniform excitation without SSI, providing an upper bound for the estimated moments in this case, except for the transverse forces in the relatively flexible frames (long columns).

Thus, in analyzing the fixed-base structure for the cases studied herein, non-uniform free-field motion obtained from the soft soil may not provide an accurate estimation of the column forces. On this basis, it is necessary to consider the soil domain in order to obtain a more reliable prediction of structural response that takes into consideration the effects of SSI.

5.4.3 Effect of the broadband input

In this subsection, the BFGS is analyzed for the broadband input (see Section 2.3.3 for ground response in the stiff soil case). Due to the frequency content of up to 4.5 Hz, more pronounced response of the bridge is observed. In addition, high amplitudes of ground acceleration induce larger force/displacement demands than those from the low frequency input.

5.4.3.1 Free-field response

Figure 5.27 shows horizontal acceleration time histories at the surface center node in the stiff and the soft soil profiles. As discussed earlier in Section 2.3.3, the frequency

content is in the range of 0.1 Hz to 4.5 Hz (Figure 5.28). In comparison to the response in the stiff soil case, higher peak ground accelerations are observed in the soft soil case.

5.4.3.2 Base acceleration

Maximum acceleration at the base under the three types of loading conditions is shown in Figure 5.29 for the stiff soil and Figure 5.30 for the soft soil cases. As shown earlier for the low frequency input (Section 5.4.2), the level of column base accelerations varies significantly in the BFGS and the fixed-base analysis with multiple support excitation (without the soil domain). On the other hand, the representative input motion for the uniform excitation considerably deviates from the base motion dictated by spatially variable ground motion, depending on the soil material property.

5.4.3.3 Comparison of drift ratios

Maximum drift ratios in term of the column deformation under the three types of loading conditions are shown in Figure 5.31 for the stiff and Figure 5.32 for the soft soil cases. As shown in Section 5.4.2 for the low frequency input, larger displacement demand is observed in the soft soil case. It is also observed that the fixed-base structure analysis with multiple support excitation generally underestimates the bridge response in the relatively flexible frame (long columns). The results under the uniform excitation condition overestimate or underestimate the bridge response, depending on the particular column location.

5.4.4 Modification of ground motion due to presence of the structure

Due to the relatively small size foundations (pile cap and pile groups), deviation of foundation motions from the corresponding free-field response (i.e. without the NW) is small in both the stiff and soft soil scenarios. In terms of maximum velocity at the foundations, almost identical ground motions (about 0.5% difference) are observed (Figure 5.9). For the soft soil, the effect is still low, about 2% at Bent 16 in the X direction and at Abutment 1 in the Y direction (Figure 5.10).

5.4.5 Relative support motions

Figure 5.11 and Figure 5.12 show maximum relative displacements between two adjacent supports in the stiff and soft soil profiles, respectively. Positive displacements indicate that the supports move closer to each other, and vice versa. It can be seen that significant variation of relative support motions are observed in the soft soil case in both the X and Y directions. Due to the curved geometry of the NW, this aspect of the system behavior can affect the superstructure response characteristics such as deformation/forces in the columns, restrainer cable demands induced by hinge opening, depending on the particular column location.

5.4.6 Seismic base shear

Due to the higher amplification of ground motion (soft versus stiff soil), seismic base shears at the bottom of the columns significantly change. The normalized total bridge column base shear (in which the total peak base shear is divided by self-weight of

the NW connector 160 MN) is shown in Figure 5.13. The normalized base shear increases 48 % for the X component and 78 % for the Y component for the soft soil scenario.

5.4.7 Relative displacement and drift ratio at the top of the columns

Figure 5.14 shows the BFGS simulation deformed shape of the NW relative to the base of Bent 8 (15.24 m height) at the time instant of 17.1 sec for the soft soil case. At this time, the top displacement relative to the base reaches 0.13 m at Bent 7 in the global Y direction (soft soil case). Due to the flexible soil layers, more pronounced rocking of the foundation is observed as well (Figure 5.14).

Figure 5.15 and Figure 5.16 show transverse displacement time histories at the top of Bent 8 in the stiff and soft soil cases, respectively. Lateral displacement induced by rocking at the foundations and deformation (the relative displacement reduced by the amount resulting from rocking) are also shown in these figures. Due to in-phase response of the rocking component in the stiff soil, the deformation increases compared to the relative displacement (Table 5.3). Meanwhile, deformation (induced by rocking) increases or decreases in the soft soil case (Table 5.4), depending on the particular column location (mostly decreases).

In addition, drift ratio is calculated in terms of deformation (Table 5.3 and Table 5.4). In the stiff soil, transverse drift ratios are mostly greater than those in the longitudinal direction, except for Bents 2 and 16 (relatively short columns located near the abutments). This exception is due to relative large displacements between the abutments and the bridge deck. In the transverse direction, the largest ratio is 1% with the

maximum relative displacement of 0.21 m at Bent 6 (height of 22.5 m). The smallest observed drift ratio of 0.1 % occurred at Bent 16 (height of 7.2 m). In the soft soil, the maximum drift ratio of 2.3% is observed in the transverse direction at Bent 5 and 0.9% in the longitudinal direction at Bent 4.

5.5 Summary and conclusions

The influence of SSI on the bridge response with two types of the ground model (based on the DRM) is investigated. For comparison with the full SSI simulation (i.e. the BFGS), the fixed-base structure analysis under multiple support excitation and uniform excitation was considered using free-field motions obtained from the soil domain in the absence of the structure. From the results of the present study, the main observations are:

- In the BFGS subjected to low-frequency and broadband input motions

1. The soft soil scenario induces amplification of the ground response and larger relative support motions than the stiff soil. Consequently, larger force/displacement demands (in terms of peak column shear forces and bending moments and column drift ratios) are developed in the soft soil case.
2. In the stiff soil case, although the displacement induced by rocking of the foundations was generally small, beneficial or detrimental SSI effects, as evaluated by the column deformation, depended on the particular column location. The soft soil increased the rocking response noticeably. As a consequence, a beneficial effect was mostly observed (for the case studied).

- Assessment of SSI effects with and without the soil domain

1. Compared to the BFGS (with the soil domain), the total column base shear decreased under the multiple support excitation scenario. However, it significantly increased for the uniform excitation case due to the relatively large input acceleration, compared to the multi-support support motions in the other two analyses.
2. For the soft soil scenario, the analysis of the fixed-base bridge (and to some extent the multiple support scenario) resulted in outcomes that were noticeably different as compared to the full BFGS simulation (e.g., drift ratios at the column bents, shear forces / bending moments in the columns). In this case, the free-field ground motions at the footprints of the supports in the absence of the bridge displayed some marked differences from the actual BFGS motions at these locations.
3. The Intermittent spikes induced by pounding between the adjacent bridge decks were much affected for the fixed-base bridge scenarios, compared the BFGS case (both stiff and soft soil scenarios).
4. Compared to the results for the low-frequency excitation, the broadband input scenario induced more prominent response of the bridge. For all cases, larger force and displacement demands were observed than those for the low frequency input. In addition, much deviation of the base input motions for the fixed-base structure cases were noted compared to the BFGS scenario. This deviation resulted in markedly different response of the fixed-base bridge (drift ratios in the columns) in both the stiff and the soft soil cases.

Thus, in order to obtain satisfactory predictions of the bridge response supported on soft soil, a detailed analysis that considers the full coupling between the structure and the surrounding soil may become necessary.

5.6 Acknowledgements

Chapter 5 contains material published in the Earthquake Geotechnical Engineering Design (Geotechnical, Geological and Earthquake Engineering, Vol. 28, Springer) titled “Seismic Response of a Large-Scale Highway Interchange System” with authors, Kyung Tae Kim, Ahmed Elgamal, George Petropoulos, Aysegul Askan, Jacobo Bielak, and Gregory L. Fenves (2014). The dissertation author is the first author of this paper.

Table 5.1: Linear material properties for the stiff soil scenario (Petropolous 2008)

Layer	**Density (t/m^3)**	**Vp (m/s)**	**Vs (m/s)**	**Thickness (m)**	**Region**
1	1.5	1337.3	482.2	40	Region of Interest
2	1.714	1622.4	584.3	60	Region of Interest
3	1.714	1622.4	584.3	340	Buffer Zone
4	2.054	2372.9	651.3	60	Buffer Zone

Table 5.2: Linear material properties for the soft soil scenario

Layer	Density (t/m^3)	V_p (m/s)	V_s (m/s)	Thickness (m)	Region
1	1.5	668.7	241.1	40	Region of Interest
2	1.714	811.2	292.2	60	Region of Interest
3	1.714	811.2	292.2	340	Buffer Zone
4	2.054	1186.5	325.7	60	Buffer Zone

Table 5.3: Stiff soil profile: maximum relative displacements and drift ratios at the top of columns in the North-West connector

			Longitudinal direction			Transversal direction		
Frame	Bent	Height (m)	Top relative to base (m)	Deformation (m)	Drift (%)	Top relative to base (m)	Deformation (m)	Drift (%)
1	2	11.88	0.049	0.050	0.42	0.032	0.030	0.26
	3	16.59	0.048	0.049	0.29	0.081	0.080	0.48
2	4	19.41	0.118	0.119	0.61	0.145	0.147	0.76
	5	24.26	0.102	0.101	0.42	0.205	0.209	0.86
	6	22.50	0.084	0.083	0.37	0.192	0.194	0.86
	7	17.32	0.071	0.071	0.41	0.131	0.129	0.75
3	8	15.24	0.051	0.053	0.34	0.064	0.061	0.40
	9	15.77	0.054	0.056	0.35	0.041	0.045	0.28
4	10	12.88	0.042	0.044	0.34	0.044	0.047	0.36
	11	18.26	0.034	0.035	0.19	0.071	0.073	0.40
5	12	18.80	0.036	0.034	0.18	0.075	0.078	0.41
	13	16.94	0.035	0.034	0.20	0.064	0.066	0.39
6	14	15.62	0.018	0.016	0.10	0.045	0.047	0.30
	15	13.69	0.017	0.015	0.11	0.023	0.025	0.18
	16	7.23	0.015	0.013	0.19	0.004	0.004	0.06

Table 5.4: Soft soil profile: maximum relative displacements and drift ratios at the top of columns in the North-West connector

			Longitudinal direction			Transversal direction		
Frame	Bent	Height (m)	Top relative to base (m)	Deformation (m)	Drift (%)	Top relative to base (m)	Deformation (m)	Drift (%)
1	2	11.88	0.091	0.087	0.73	0.060	0.057	0.48
	3	16.59	0.091	0.087	0.53	0.147	0.143	0.86
2	4	19.41	0.176	0.171	0.88	0.380	0.374	1.93
	5	24.26	0.146	0.141	0.58	0.568	0.560	2.31
	6	22.50	0.113	0.107	0.48	0.473	0.468	2.08
	7	17.32	0.142	0.141	0.81	0.271	0.268	1.55
3	8	15.24	0.109	0.108	0.71	0.103	0.100	0.66
	9	15.77	0.107	0.106	0.67	0.100	0.099	0.62
4	10	12.88	0.079	0.078	0.60	0.087	0.085	0.66
	11	18.26	0.052	0.051	0.28	0.155	0.152	0.83
5	12	18.80	0.050	0.048	0.26	0.165	0.160	0.85
	13	16.94	0.049	0.047	0.28	0.137	0.134	0.79
6	14	15.62	0.025	0.024	0.15	0.098	0.094	0.60
	15	13.69	0.024	0.022	0.16	0.047	0.046	0.34
	16	7.23	0.020	0.018	0.25	0.007	0.007	0.09

Table 5.5: Seismically-induced total base shear with and without the soil domain

		With SSI	Without SSI			
Soil profile	Base shear	BFGS	Multiple-support excitation	Difference (%)	Uniform excitation	Difference (%)
Stiff	V_x/W	0.253	0.249	-1.6	0.263	4.0
	V_y/W	0.182	0.188	3.3	0.173	-4.9
Soft	V_x/W	0.372	0.371	-0.3	0.523	40.6
	V_y/W	0.324	0.291	-10.2	0.350	8.0

Table 5.6: Stiff soil profile; comparison of the maximum shear forces (MN) in the longitudinal direction

Bent	Longitudinal shear forces (MN) induced by the stiff soil profile				
	BFGS	Multiple-support excitation	Difference (%)	Uniform excitation	Difference (%)
2	6.73	6.35	-5.5	5.36	-20.3
3	2.63	2.42	-7.7	2.27	-13.7
4	4.55	4.17	-8.5	4.48	-1.6
5	2.36	2.19	-6.9	2.58	9.5
6	2.42	2.30	-4.9	2.75	13.9
7	3.75	3.69	-1.5	4.45	18.9
8	3.28	3.12	-4.8	3.59	9.5
9	3.84	3.82	-0.4	3.85	0.3
10	4.47	4.41	-1.4	3.92	-12.4
11	1.83	1.79	-1.9	1.43	-21.7
12	1.45	1.43	-1.6	1.66	14.2
13	1.82	1.78	-2.3	2.18	19.7
14	1.09	0.91	-16.4	0.66	-39.5
15	1.70	1.32	-22.2	1.02	-39.6
16	7.52	5.68	-24.5	4.39	-41.6

Table 5.7: Stiff soil profile; comparison of the maximum shear forces (MN) in the transverse direction

Bent	Transverse shear forces (MN) induced by the stiff soil profile				
	BFGS	Multiple-support excitation	Difference (%)	Uniform excitation	Difference (%)
2	3.38	3.09	-8.8	3.14	-7.2
3	3.42	3.09	-9.8	2.48	-27.5
4	3.93	3.68	-6.5	3.01	-23.6
5	2.90	2.56	-11.8	2.31	-20.2
6	3.25	2.76	-15.3	2.43	-25.2
7	4.54	3.67	-19.1	3.17	-30.2
8	2.54	2.54	0.0	2.60	2.6
9	1.58	1.62	2.7	1.69	7.3
10	3.64	3.81	4.6	3.76	3.4
11	2.51	2.46	-2.3	2.42	-3.8
12	2.10	2.09	-0.3	2.32	10.7
13	2.46	2.36	-3.9	2.62	6.5
14	2.01	1.95	-3.1	2.13	5.9
15	1.58	1.49	-6.1	1.69	7.0
16	1.77	1.65	-6.7	1.65	-6.7

Table 5.8: Stiff soil profile; comparison of the maximum bending moments (MN-m) in the longitudinal direction

Bent	Longitudinal bending moments (MN-m) induced by the stiff soil profile				
	BFGS	Multiple-support excitation	Difference (%)	Uniform excitation	Difference (%)
2	44.82	42.24	-5.8	35.78	-20.2
3	23.70	21.77	-8.1	20.85	-12.0
4	45.92	42.09	-8.4	45.59	-0.7
5	27.26	25.50	-6.5	30.32	11.2
6	26.15	25.04	-4.3	30.49	16.6
7	34.02	33.59	-1.3	40.98	20.4
8	27.41	27.21	-0.7	31.40	14.5
9	32.07	31.78	-0.9	32.23	0.5
10	33.15	32.67	-1.4	29.05	-12.4
11	16.44	16.11	-2.0	12.52	-23.8
12	13.25	13.01	-1.8	15.65	18.1
13	16.23	15.28	-5.8	19.16	18.1
14	8.87	7.72	-13.0	4.83	-45.6
15	11.86	9.55	-19.5	6.86	-42.2
16	31.30	24.31	-22.4	18.25	-41.7

Table 5.9: Stiff soil profile; comparison of the maximum bending moments (MN-m)) in the transverse direction

Bent	Transverse bending moments (MN-m) induced by the stiff soil profile				
	BFGS	Multiple-support excitation	Difference (%)	Uniform excitation	Difference (%)
2	35.85	32.90	-8.2	33.18	-7.5
3	50.61	46.33	-8.5	37.10	-26.7
4	68.14	63.56	-6.7	51.40	-24.6
5	62.31	55.36	-11.2	49.03	-21.3
6	66.41	56.33	-15.2	49.23	-25.9
7	73.53	59.52	-19.1	51.89	-29.4
8	39.94	38.38	-3.9	39.19	-1.9
9	27.75	28.90	4.2	29.71	7.1
10	46.63	48.68	4.4	47.95	2.8
11	39.11	39.58	1.2	36.71	-6.1
12	35.94	35.94	0.0	37.09	3.2
13	38.89	37.02	-4.8	39.37	1.2
14	30.50	29.28	-4.0	30.90	1.3
15	21.51	20.17	-6.2	21.79	1.3
16	13.14	12.11	-7.8	12.17	-7.4

Table 5.10: Soft soil profile; comparison of the maximum shear forces (MN) in the longitudinal direction

Bent	Longitudinal shear forces (MN) induced by the stiff soil profile				
	BFGS	Multiple-support excitation	Difference (%)	Uniform excitation	Difference (%)
2	11.92	11.38	-4.5	8.50	-28.7
3	4.99	4.10	-17.8	3.69	-26.0
4	6.59	6.00	-8.9	6.15	-6.6
5	3.37	3.09	-8.4	3.20	-5.0
6	3.21	3.05	-5.0	4.13	28.8
7	6.98	4.81	-31.1	9.73	39.4
8	6.44	5.00	-22.4	8.64	34.1
9	7.11	5.71	-19.6	9.08	27.8
10	7.61	6.46	-15.1	9.48	24.5
11	2.47	2.36	-4.5	3.41	38.0
12	2.07	1.52	-26.4	4.18	102.0
13	2.69	1.81	-32.5	5.54	106.3
14	1.50	1.05	-30.0	1.55	3.3
15	2.54	1.75	-31.0	2.36	-6.9
16	10.73	9.65	-10.1	10.32	-3.9

Table 5.11: Soft soil profile; comparison of the maximum shear forces (MN) in the transverse direction

Bent	Transverse shear forces (MN) induced by the stiff soil profile				
	BFGS	Multiple-support excitation	Difference (%)	Uniform excitation	Difference (%)
2	7.10	6.63	-6.6	6.99	-1.6
3	6.00	5.81	-3.2	5.38	-10.3
4	9.31	7.78	-16.5	8.24	-11.5
5	7.35	6.20	-15.6	6.62	-9.9
6	7.98	6.33	-20.7	6.93	-13.1
7	9.29	6.21	-33.2	7.20	-22.5
8	6.23	5.66	-9.2	4.75	-23.8
9	5.02	4.28	-14.7	4.42	-11.9
10	6.36	5.76	-9.4	10.45	64.3
11	4.96	4.58	-7.7	6.42	29.2
12	4.21	3.95	-6.1	4.72	12.3
13	4.93	4.60	-6.7	4.96	0.6
14	4.08	3.88	-4.9	3.51	-14.0
15	2.97	2.81	-5.6	2.09	-29.7
16	2.67	2.53	-5.2	2.50	-6.3

Table 5.12: Soft soil profile; comparison of the maximum bending moments (MN-m) in the longitudinal direction

Bent	Longitudinal bending moments (MN-m) induced by the stiff soil profile				
	BFGS	Multiple-support excitation	Difference (%)	Uniform excitation	Difference (%)
2	78.79	75.98	-3.6	56.83	-27.9
3	43.56	36.39	-16.5	33.51	-23.1
4	66.23	60.36	-8.9	62.84	-5.1
5	38.79	35.67	-8.1	37.86	-2.4
6	34.29	32.94	-3.9	46.81	36.5
7	65.46	44.12	-32.6	91.11	39.2
8	56.12	43.79	-22.0	75.82	35.1
9	59.99	47.61	-20.6	76.28	27.2
10	57.83	48.74	-15.7	73.06	26.3
11	21.71	20.54	-5.4	36.06	66.1
12	19.19	13.08	-31.9	41.83	117.9
13	23.86	15.58	-34.7	50.20	110.4
14	12.69	8.83	-30.4	13.41	5.7
15	17.81	12.40	-30.3	16.83	-5.5
16	43.87	40.42	-7.9	42.95	-2.1

Table 5.13: Soft soil profile; comparison of the maximum bending moments (MN-m)) in the transverse direction

Bent	Transverse bending moments (MN-m) induced by the stiff soil profile				
	BFGS	Multiple-support excitation	Difference (%)	Uniform excitation	Difference (%)
2	69.71	65.78	-5.6	70.37	0.9
3	80.69	80.58	-0.1	74.19	-8.1
4	169.24	134.77	-20.4	147.42	-12.9
5	163.68	132.55	-19.0	146.20	-10.7
6	161.19	128.52	-20.3	141.58	-12.2
7	151.79	104.99	-30.8	120.67	-20.5
8	75.97	65.64	-13.6	65.77	-13.4
9	69.69	60.47	-13.2	75.62	8.5
10	83.81	75.90	-9.4	134.68	60.7
11	79.71	73.23	-8.1	103.03	29.3
12	73.41	68.43	-6.8	84.03	14.5
13	78.74	73.12	-7.1	81.52	3.5
14	61.67	58.24	-5.6	56.48	-8.4
15	40.56	38.03	-6.2	29.75	-26.6
16	19.77	18.80	-4.9	17.26	-12.7

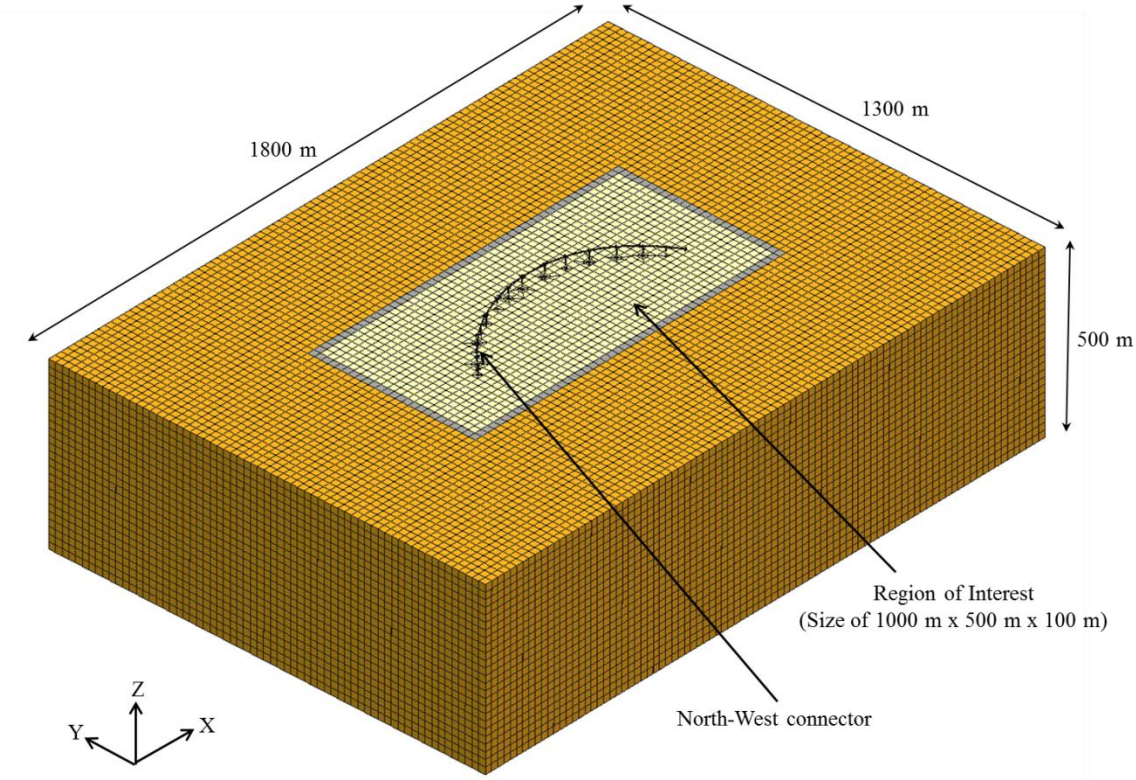

(a) 3D view of the entire FE model

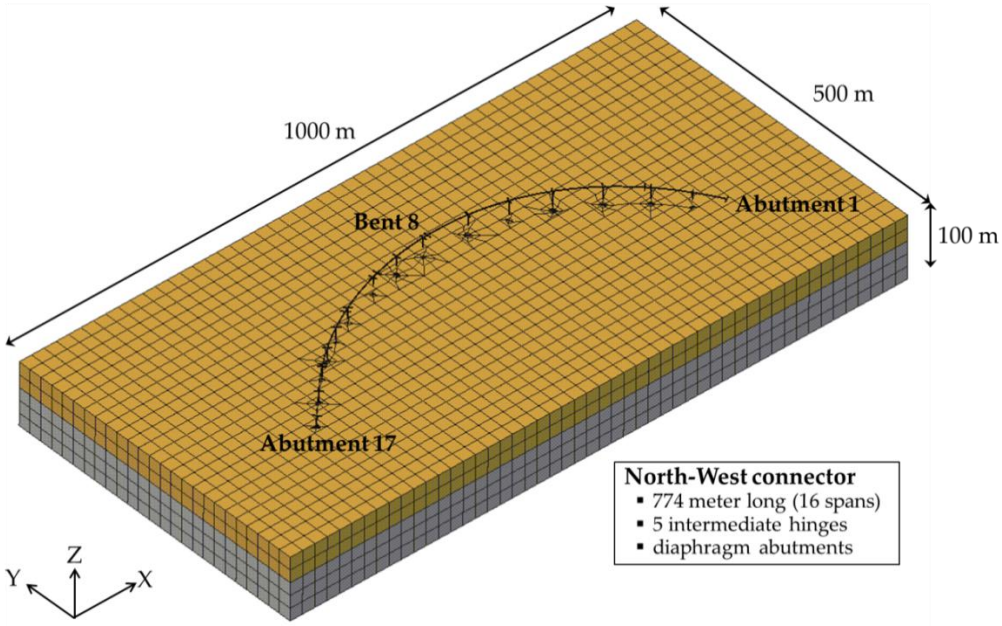

(b) Enlarged 3D view of NW connector built on the region of interest

Figure 5.1: 3D view of FEM mesh for bridge-ground system in Region of Interest surrounded by buffer zone

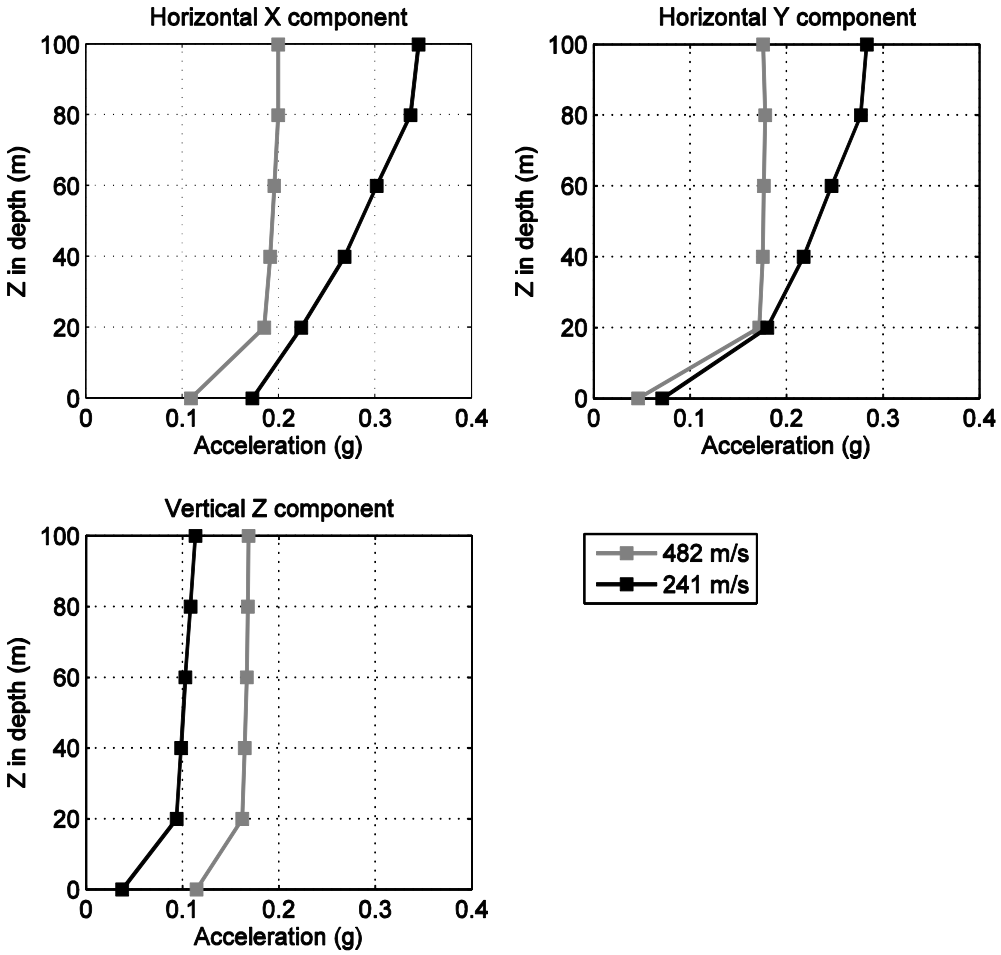

Figure 5.2: Peak ground acceleration profile along depth in the soil domain

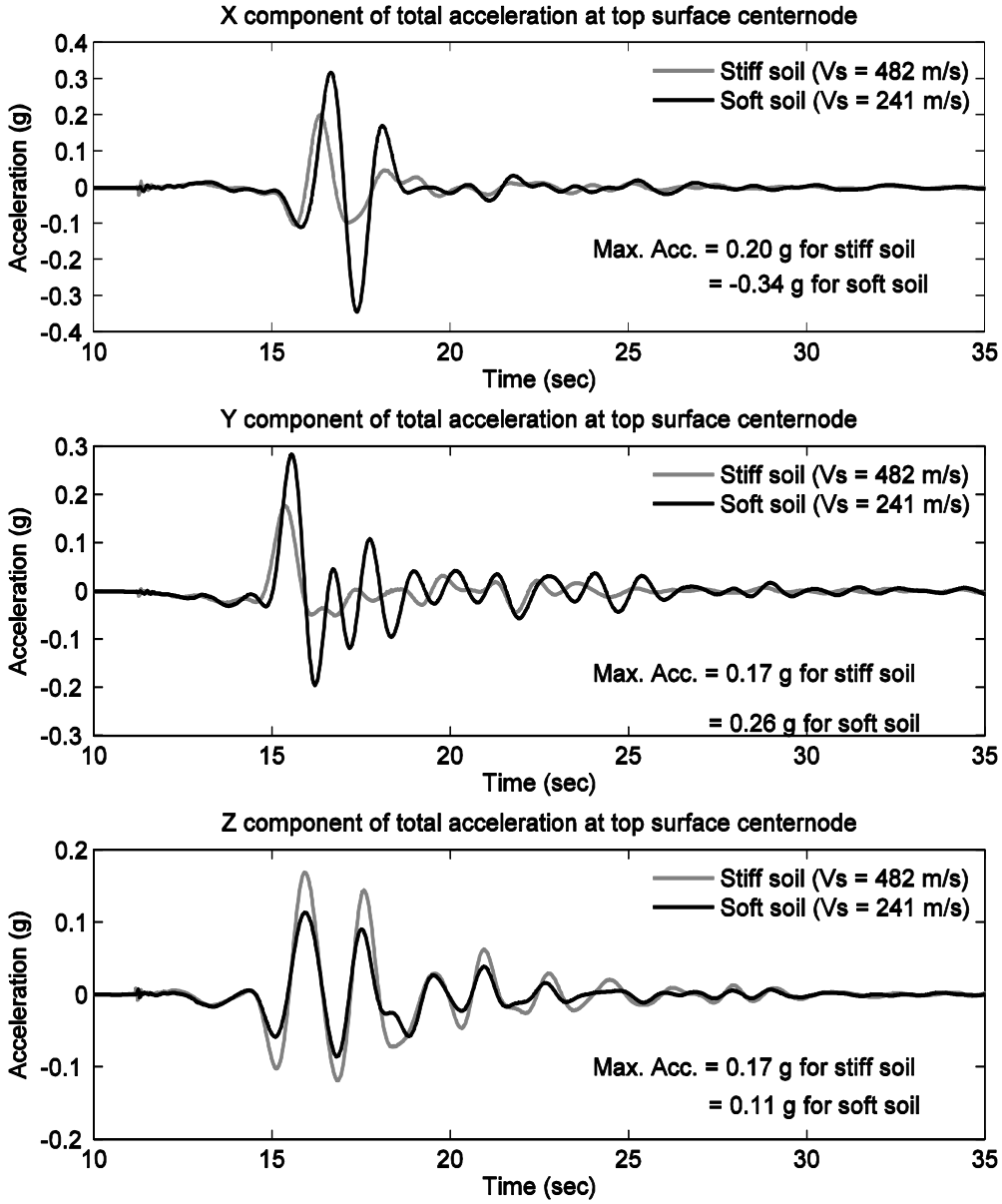

Figure 5.3: Total acceleration time histories at the surface center node in the stiff and soft soil profiles

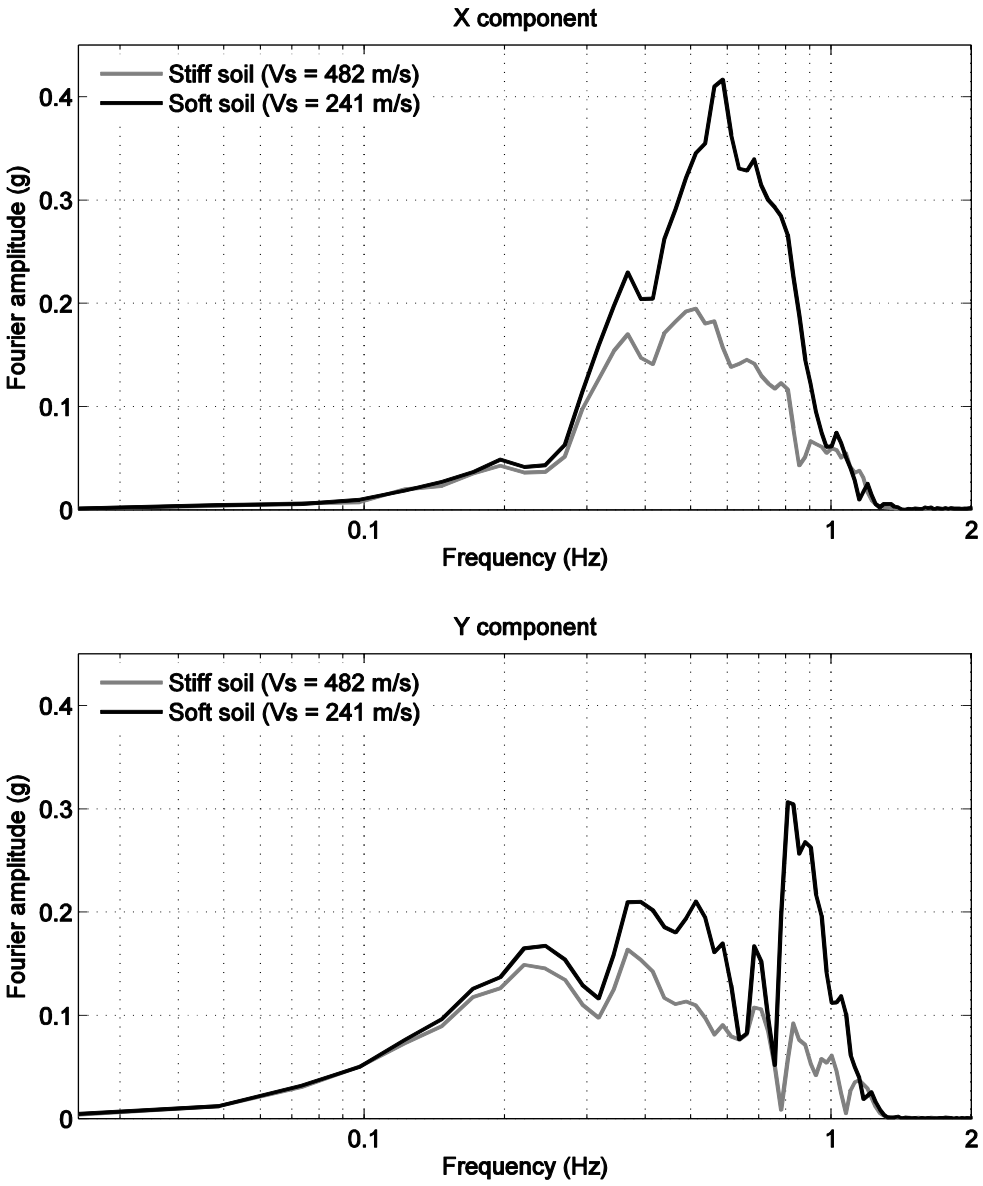

Figure 5.4: Fourier amplitude spectra of horizontal total accelerations at the surface center node in the stiff and soft soil

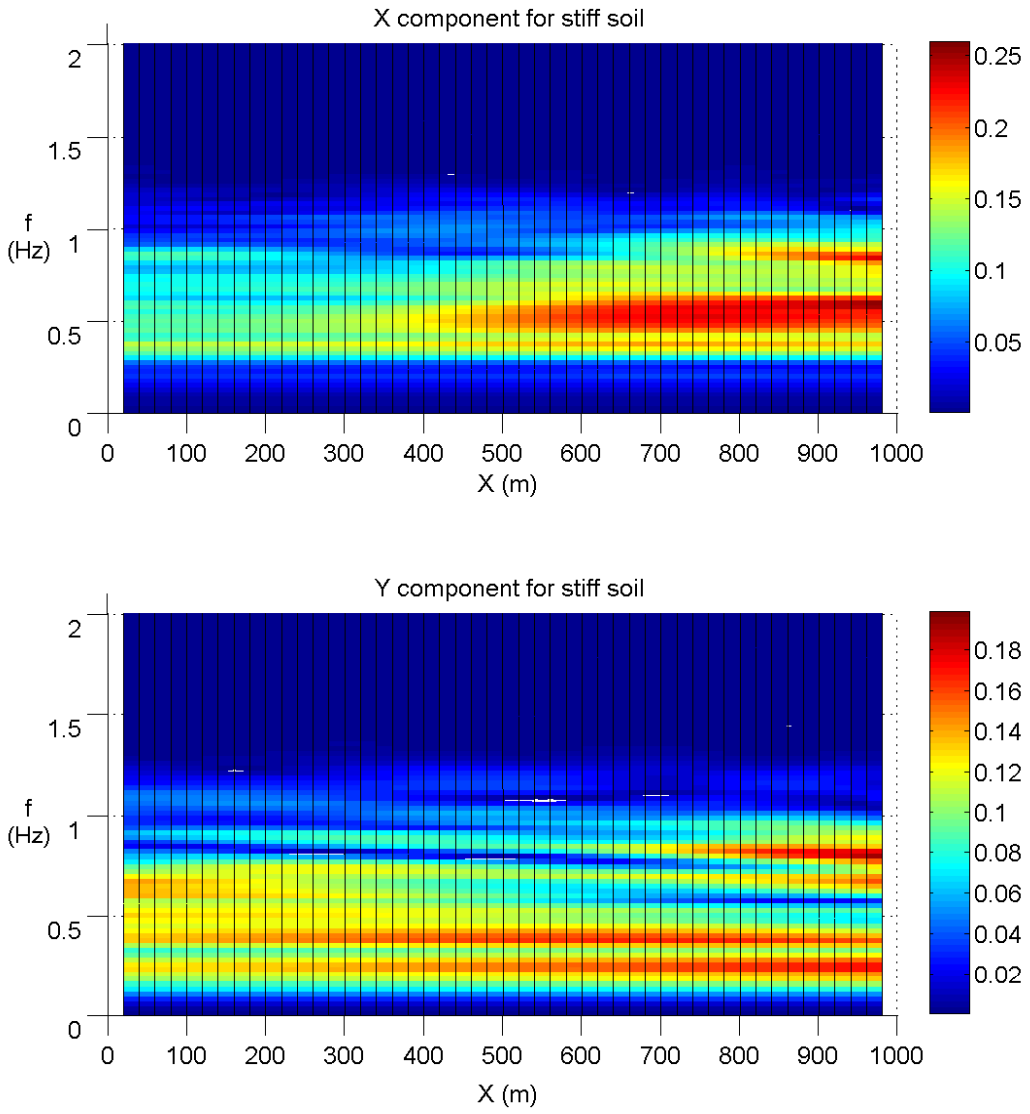

Figure 5.5: Fourier amplitude spectra along the centerline in X direction obtained from the stiff soil

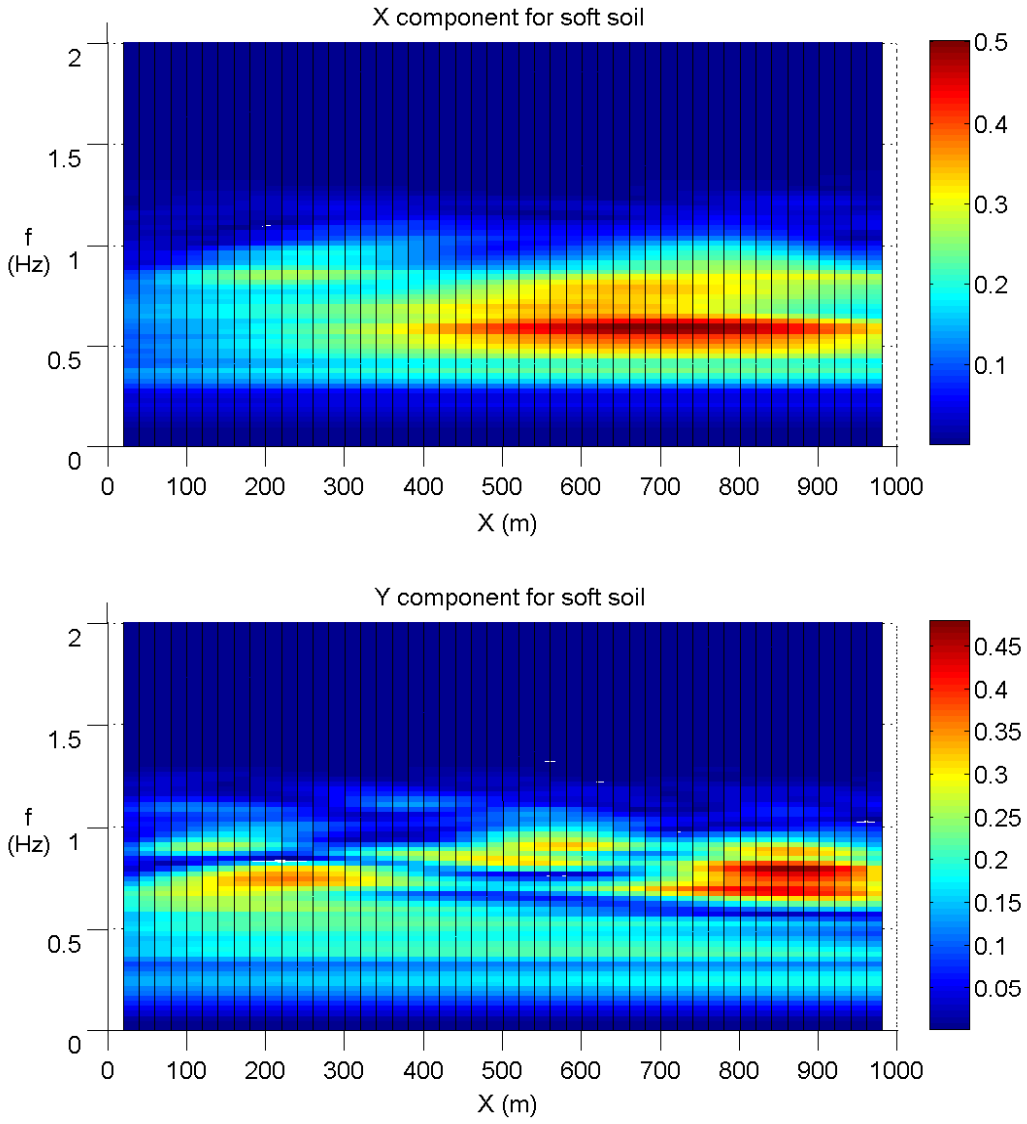

Figure 5.6: Fourier amplitude spectra along the centerline in X direction obtained from the soft soil

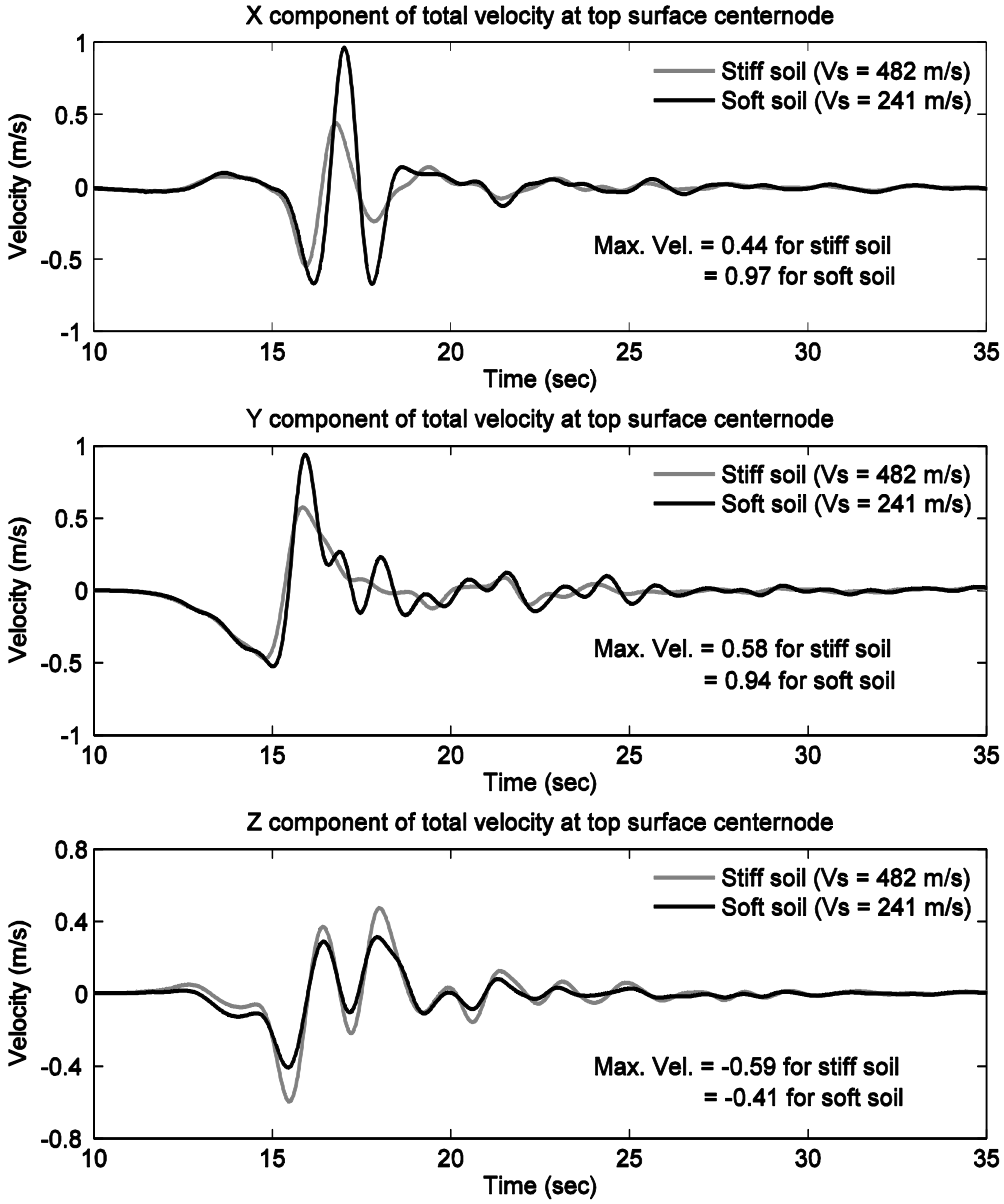

Figure 5.7: Total velocity time histories at the surface center node in the stiff and soft soil profiles

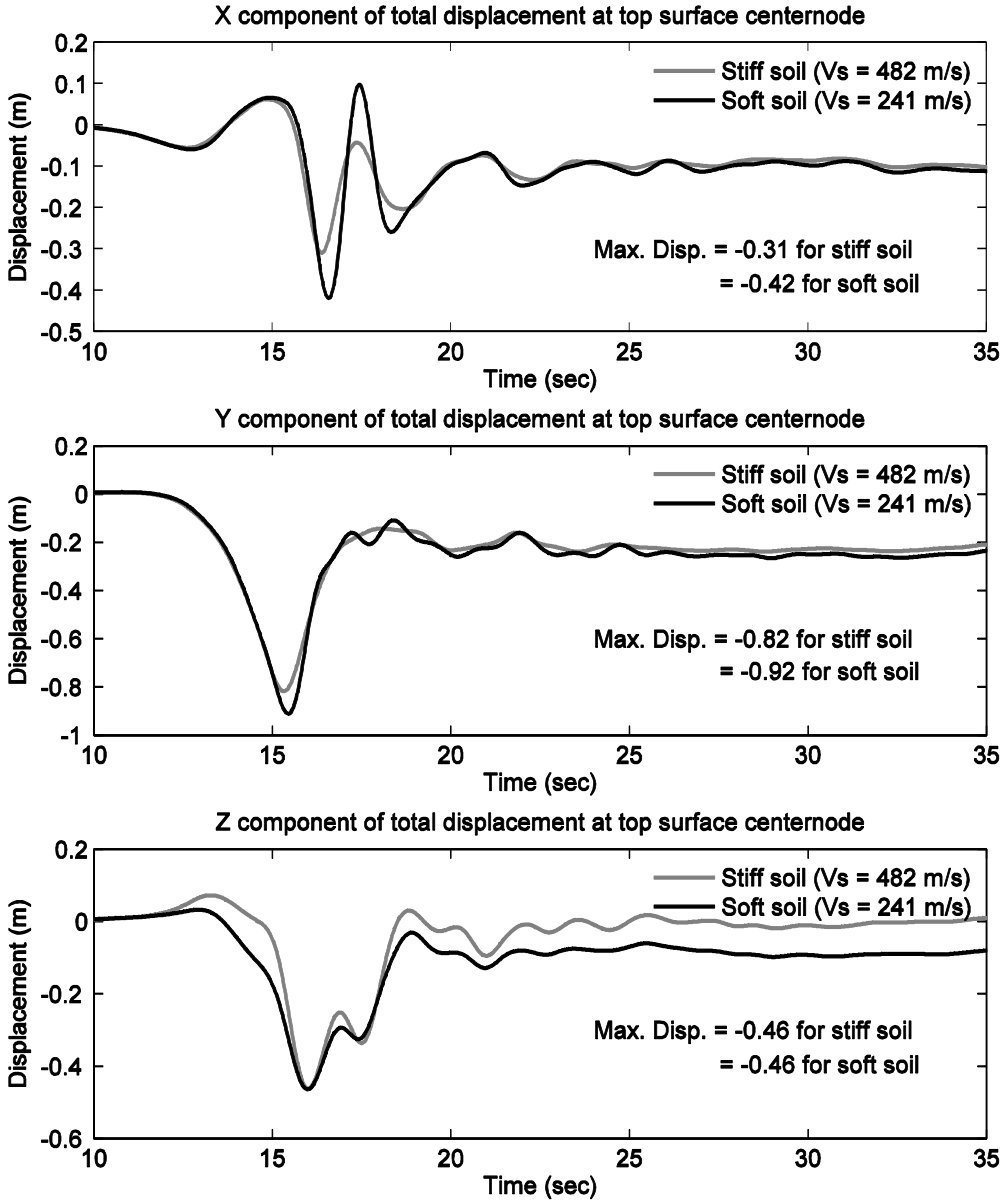

Figure 5.8: Total displacement time histories at the surface center node in the stiff and soft soil

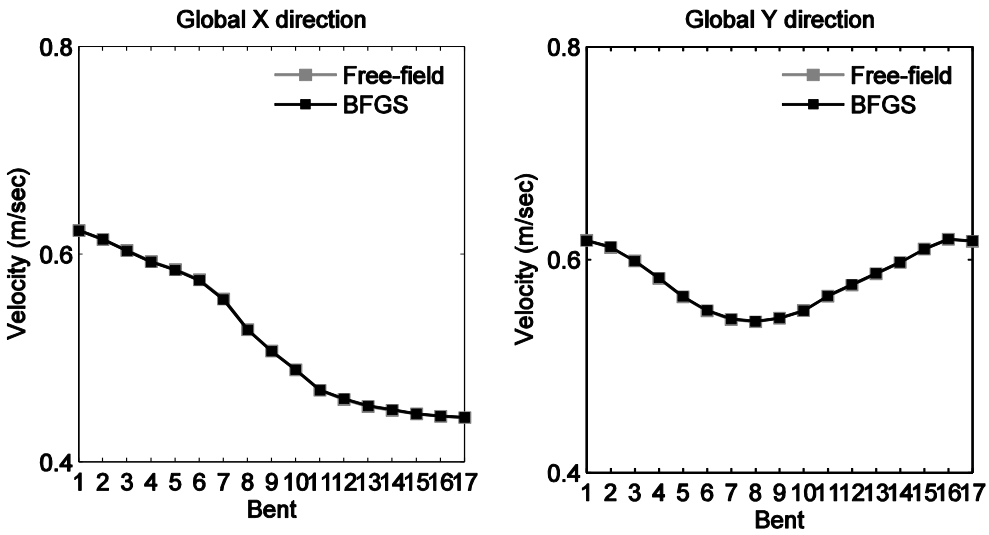

Figure 5.9: Stiff soil profile: comparison of peak ground velocity with and without the NW connector

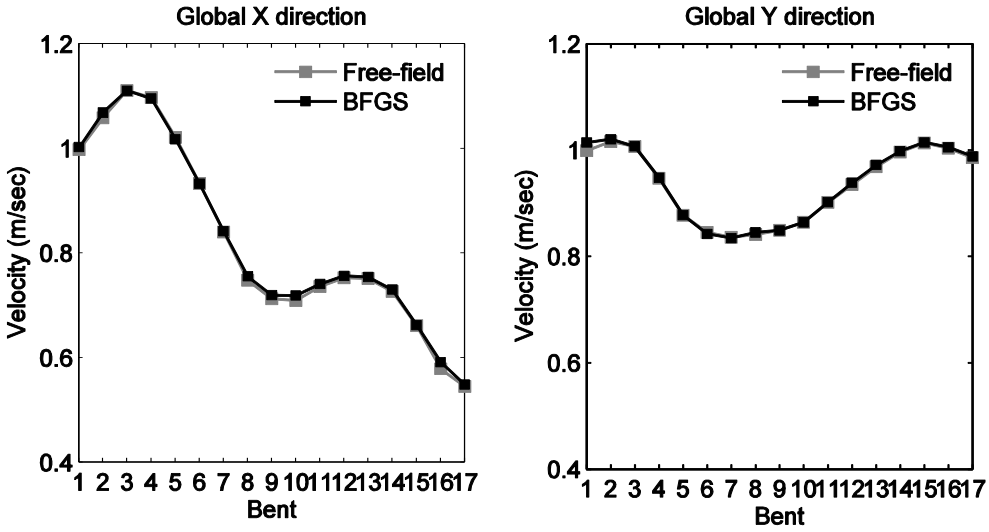

Figure 5.10: Soft soil profile: comparison of peak ground velocity with and without the NW connector

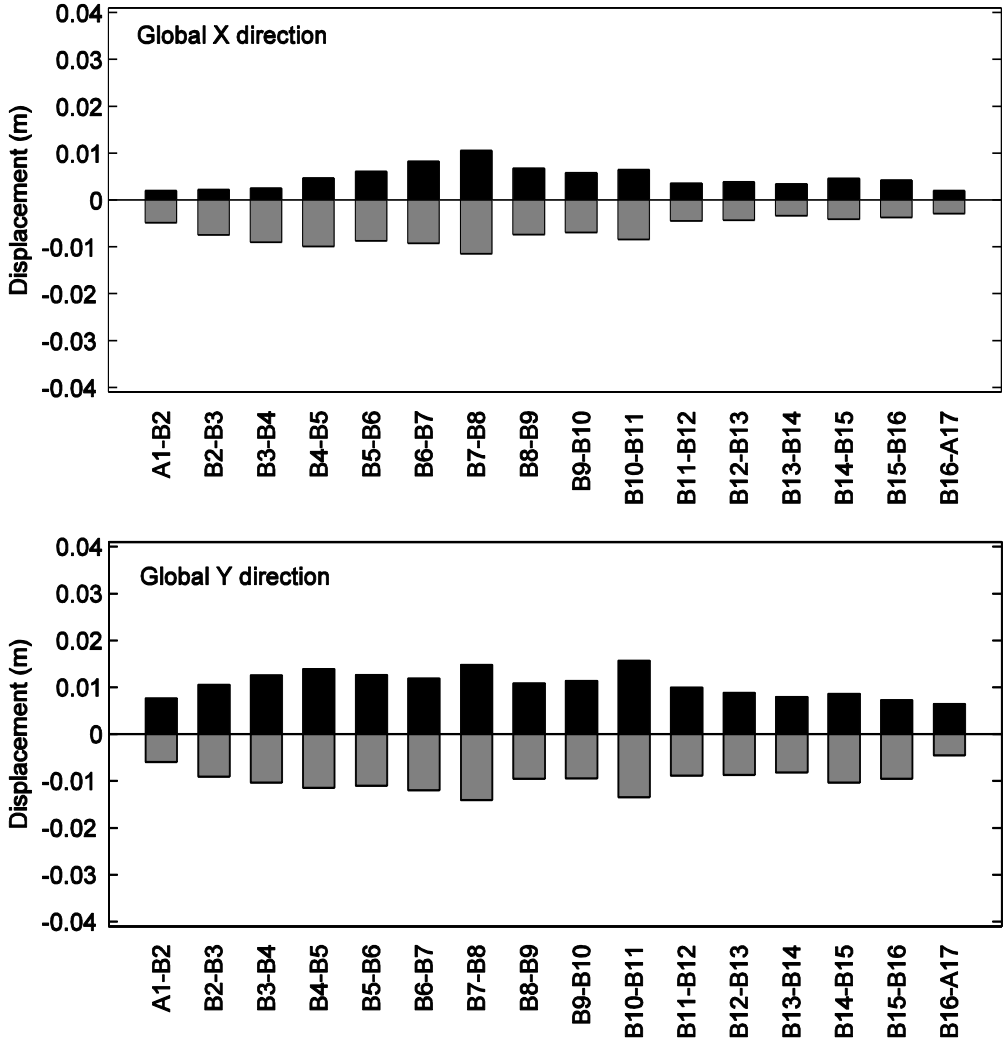

Figure 5.11: Relative support motions at the base of bents for the stiff soil profile

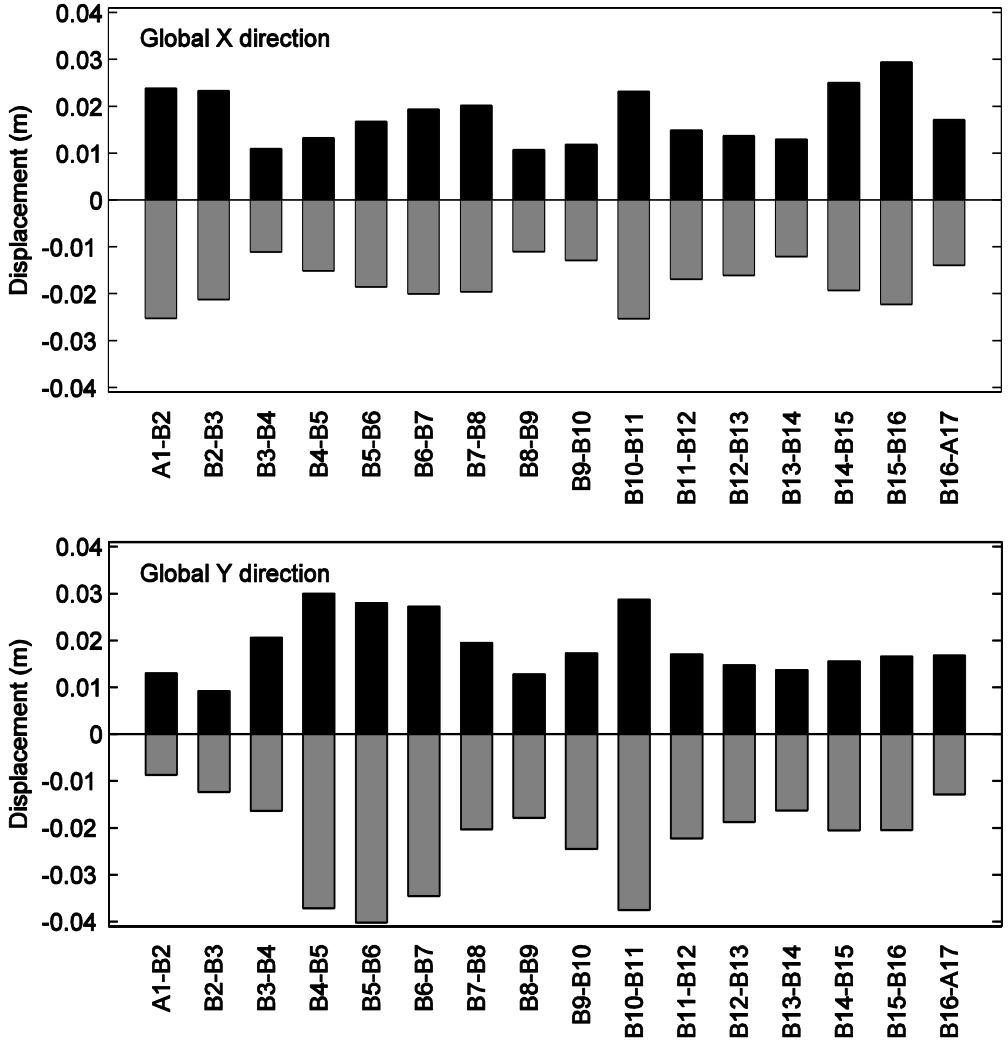

Figure 5.12: Relative support motions at the base of bents for the soft soil profile

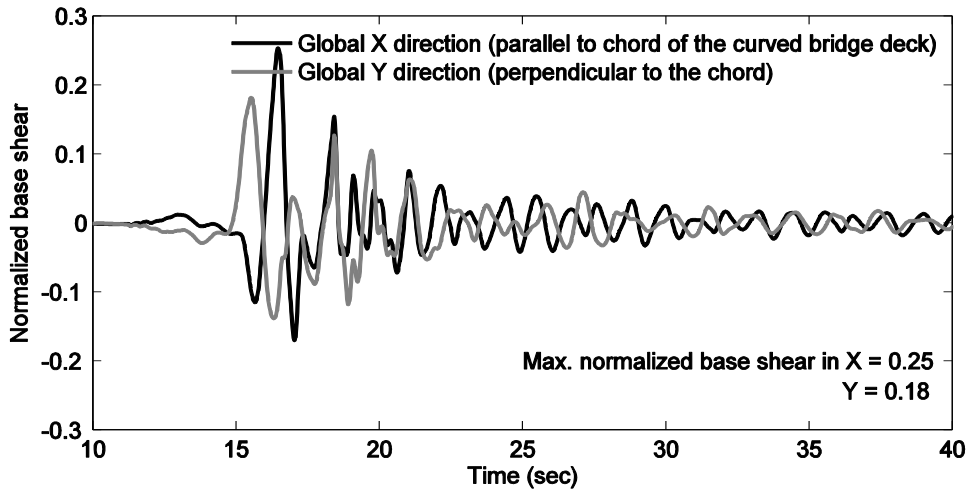

(a) Stiff soil

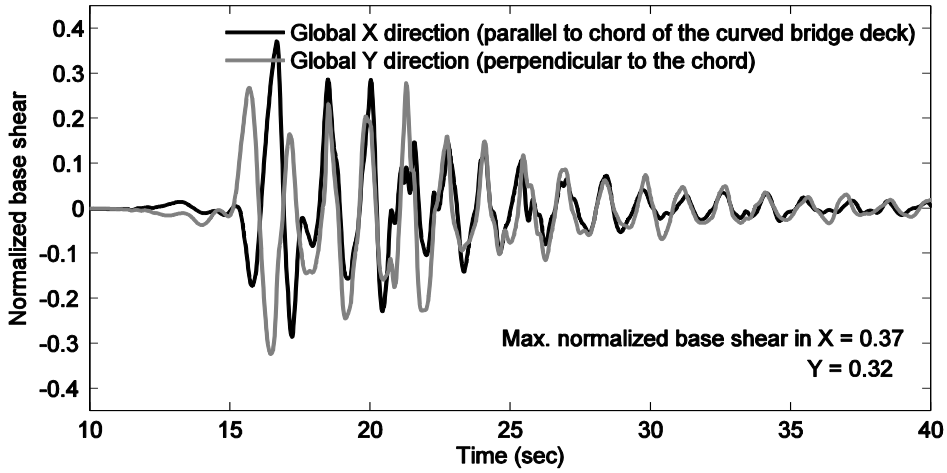

(b) Soft soil

Figure 5.13: Normalized base shear time histories in the global directions

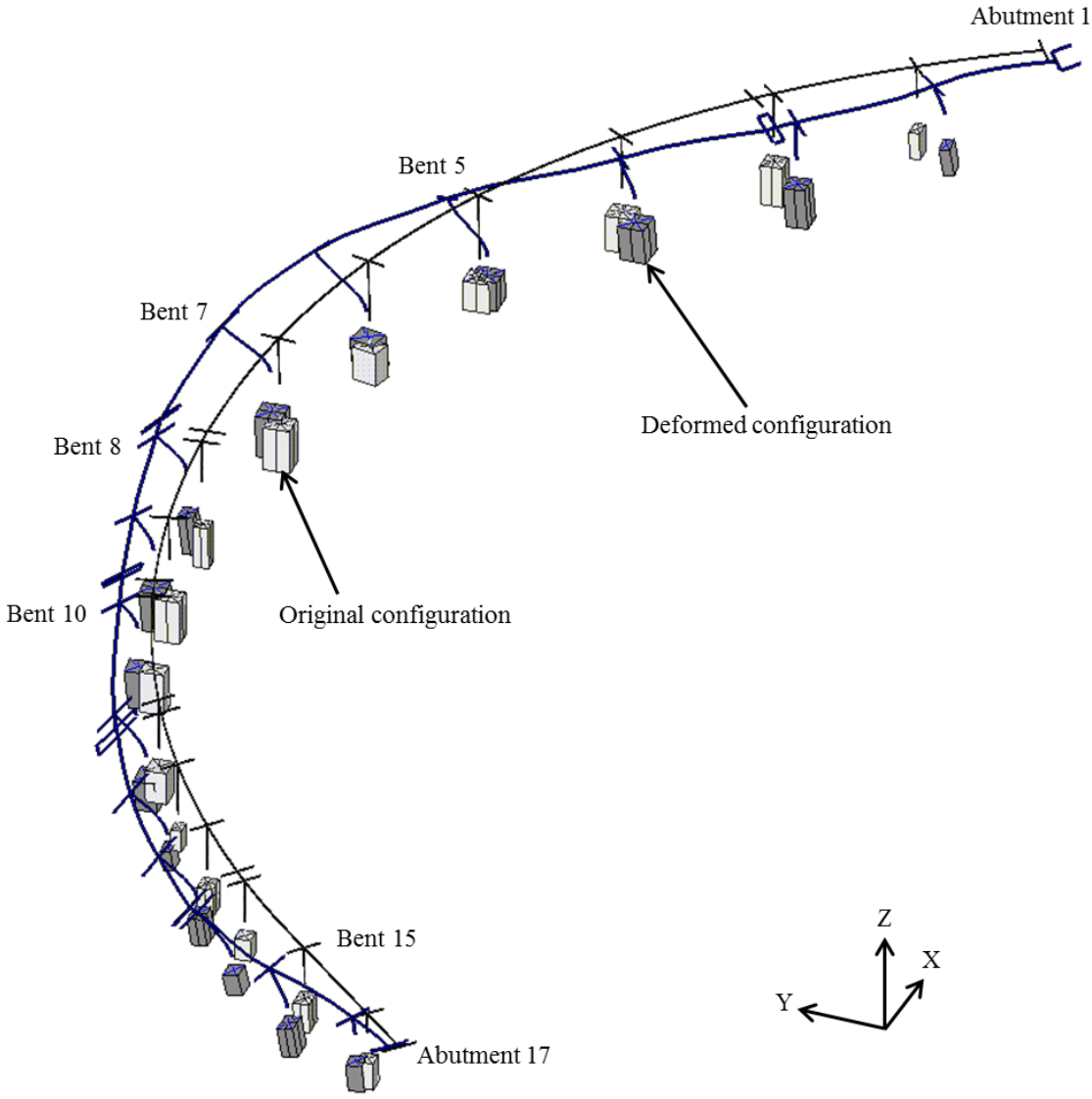

Figure 5.14: Deformed shape of North-West connector with pile groups at the time instant of 17.1 seconds (soft soil case)

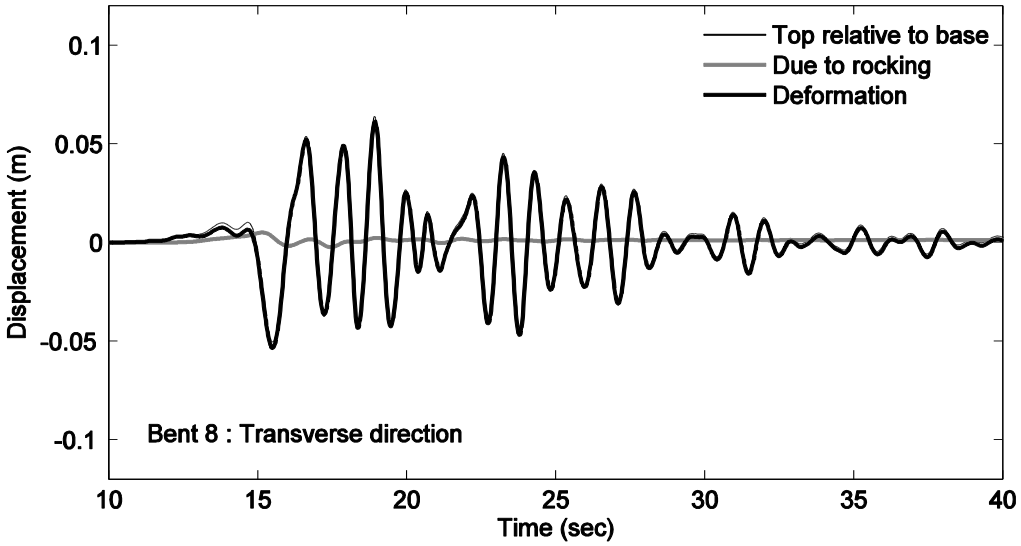

Figure 5.15: Stiff soil: displacement time histories at the top of Bent 8 in NW connector

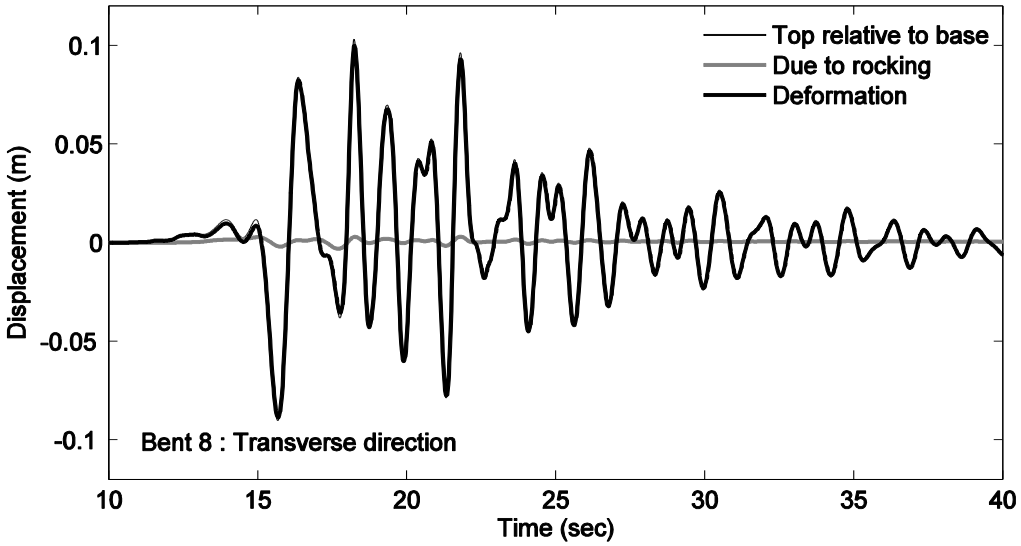

Figure 5.16: Soft soil: displacement time histories at the top of Bent 8 in NW connector

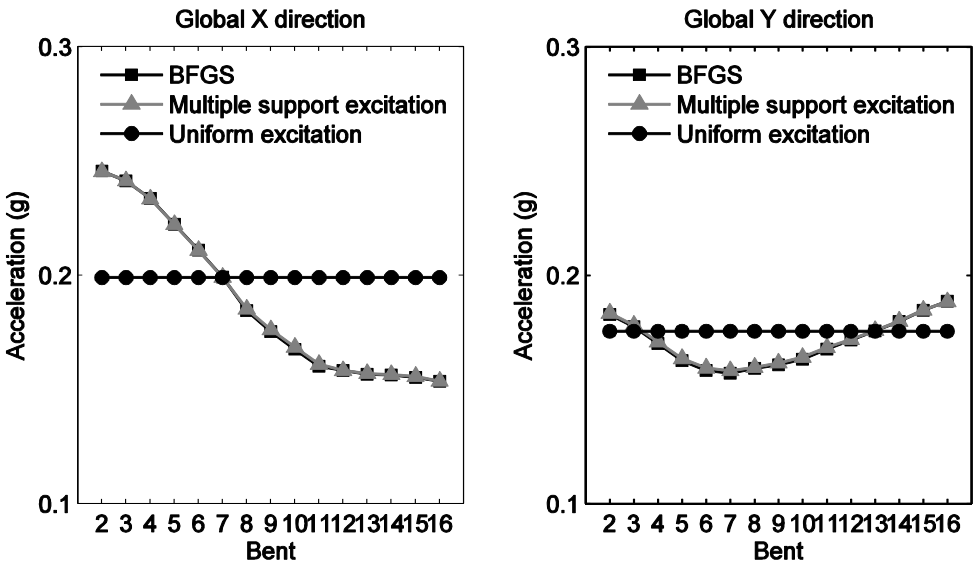

Figure 5.17: Peak acceleration at the base of bents induced by the stiff soil

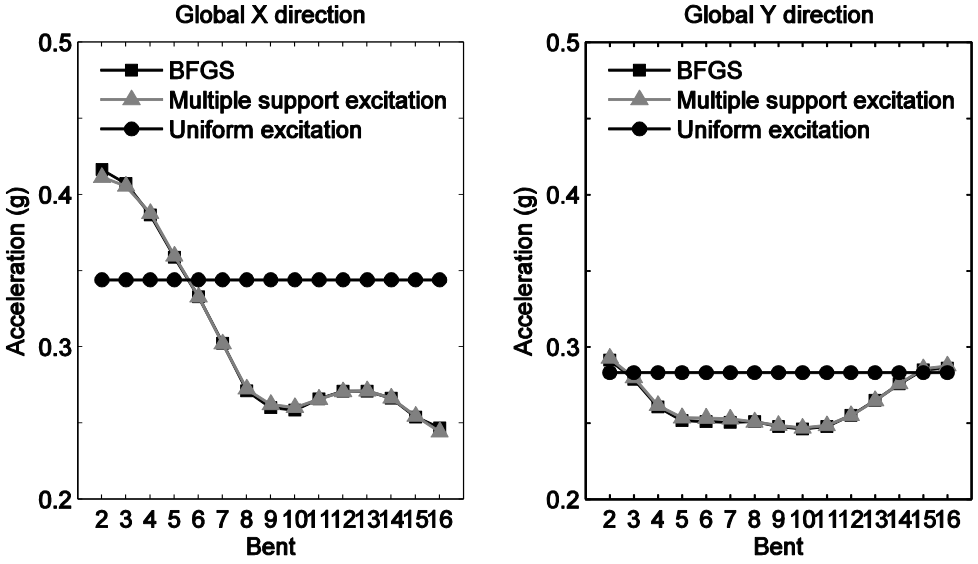

Figure 5.18: Peak acceleration at the base of bents induced by the soft soil

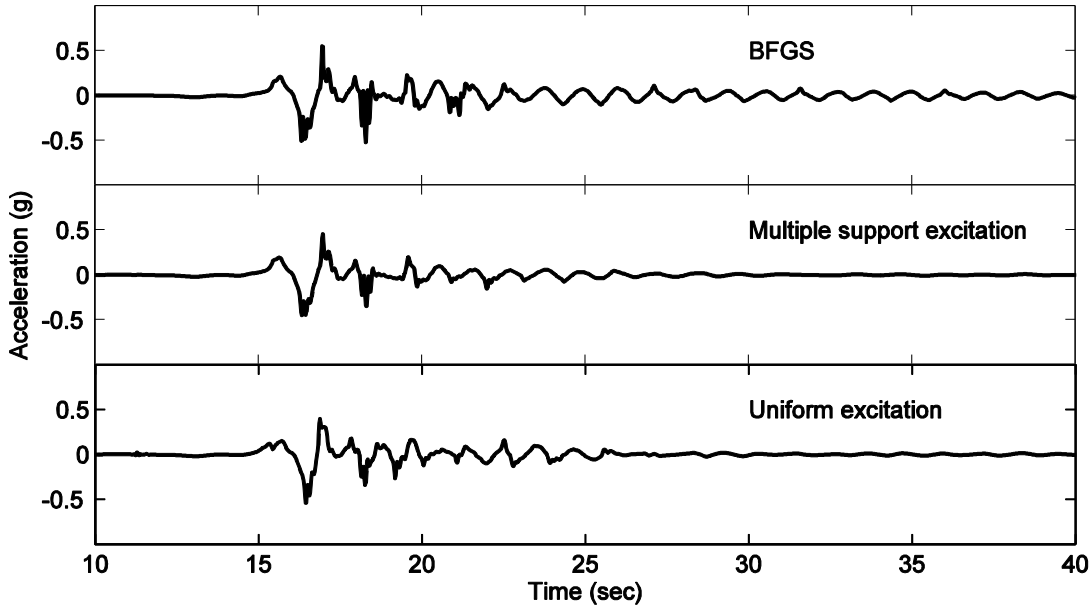

Figure 5.19: Stiff soil profile: longitudinal acceleration time histories at the top of Bent 6 in the North-West connector

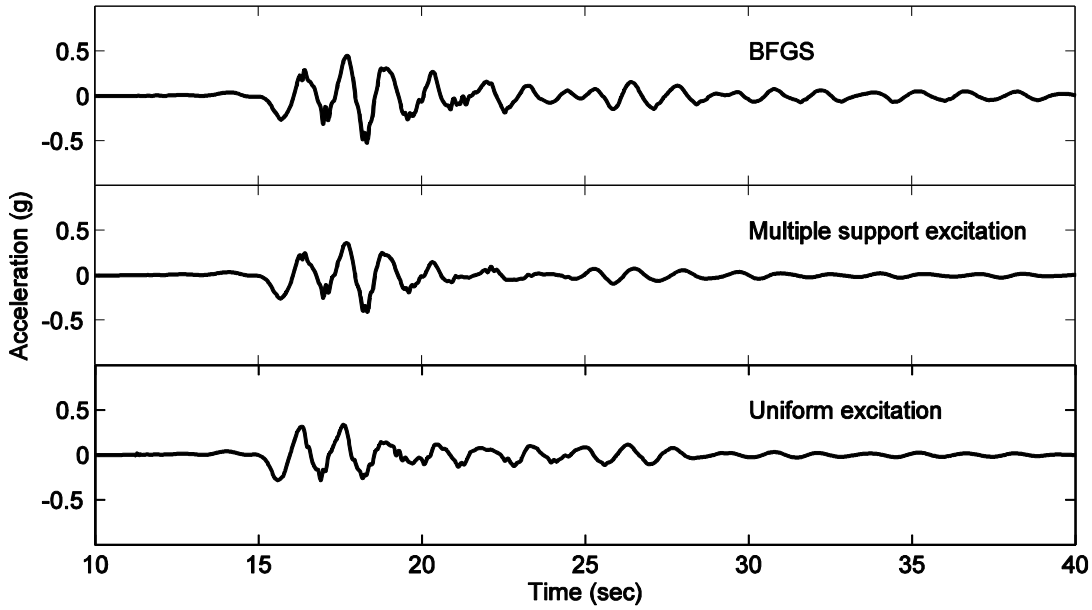

Figure 5.20: Stiff soil profile: transverse acceleration time histories at the top of Bent 6 in the North-West connector

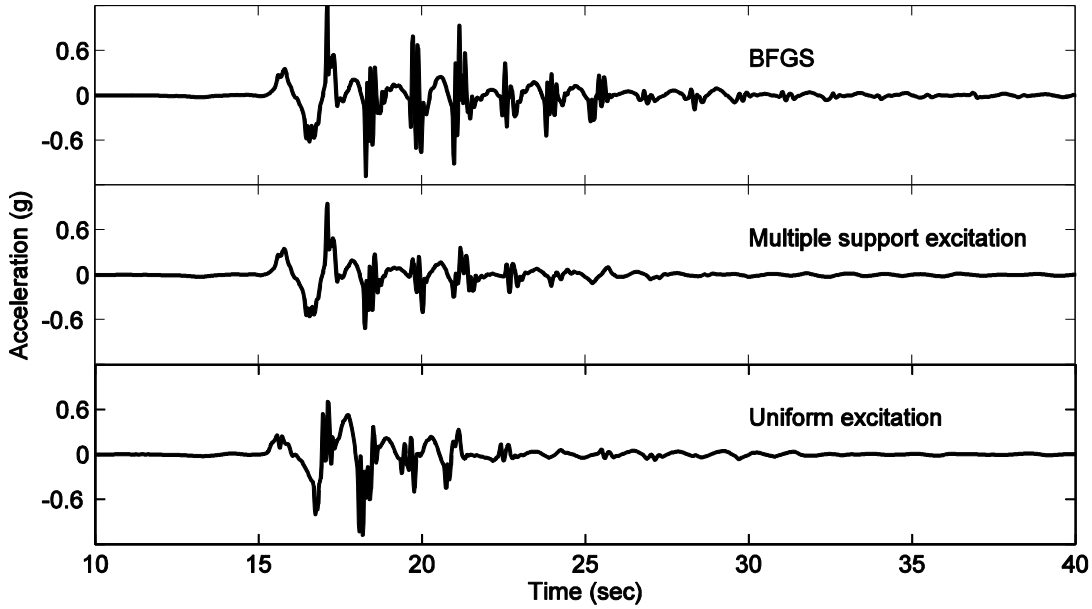

Figure 5.21: Soft soil profile: longitudinal acceleration time histories at the top of Bent 6 in the North-West connector

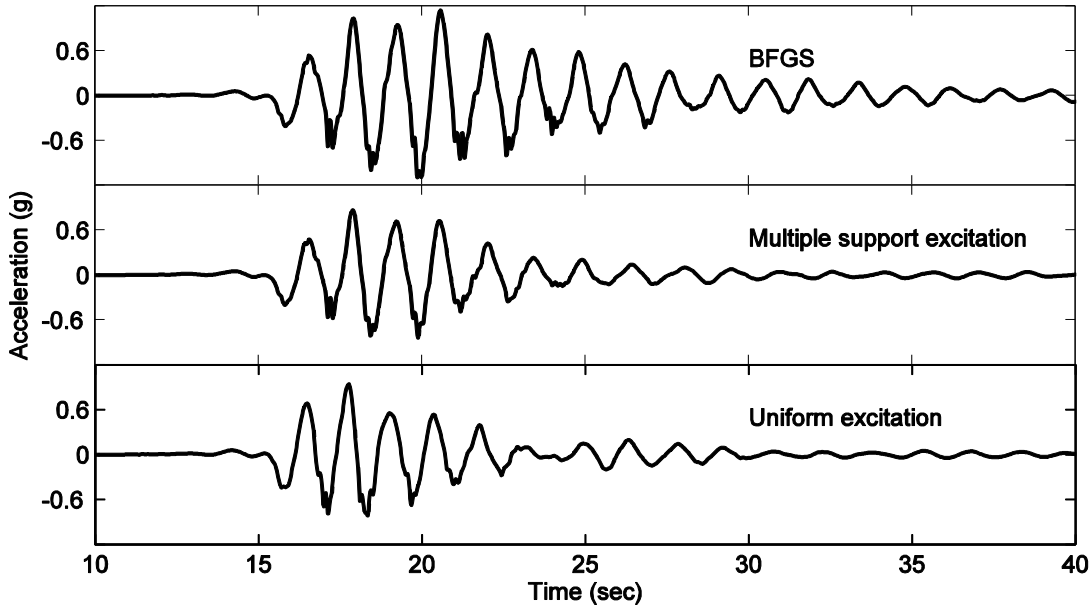

Figure 5.22: Soft soil profile: transverse acceleration time histories at the top of Bent 6 in the North-West connector

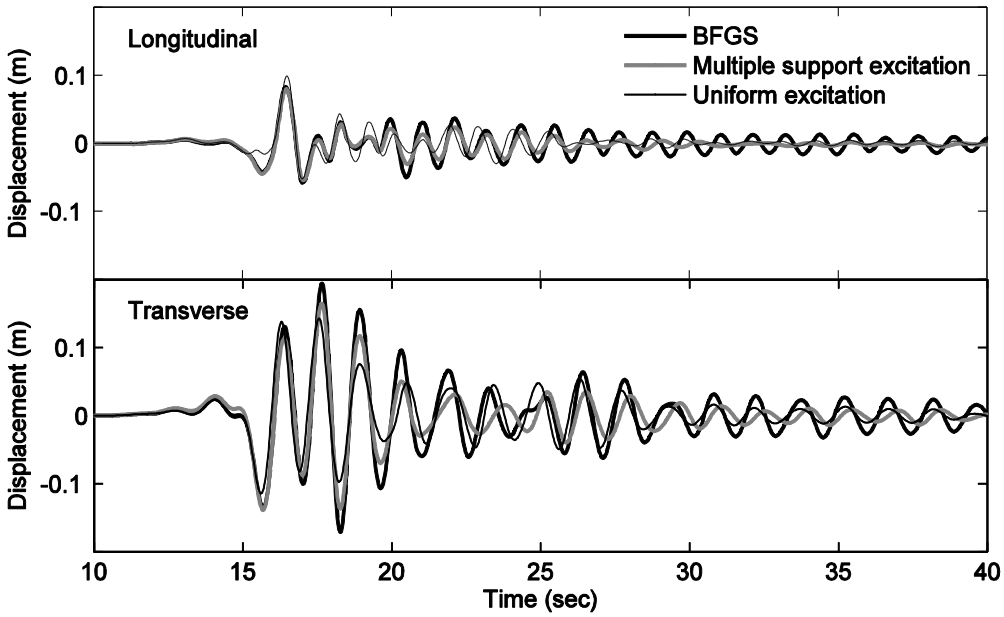

Figure 5.23: Stiff soil profile: relative displacement time histories at the top of Bent 6 in the North-West connector

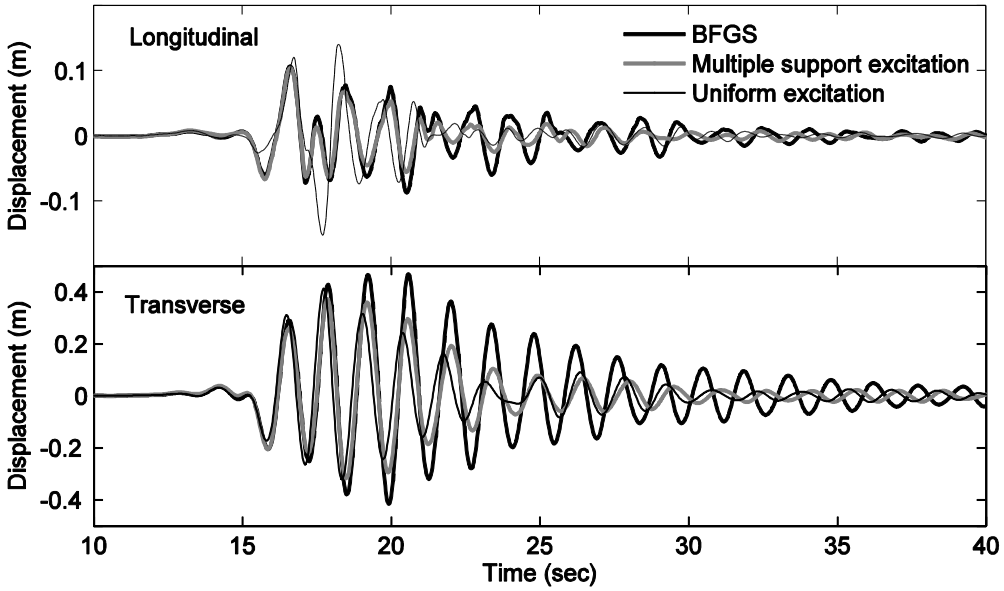

Figure 5.24: Soft soil profile: relative displacement time histories at the top of Bent 6 in the North-West connector

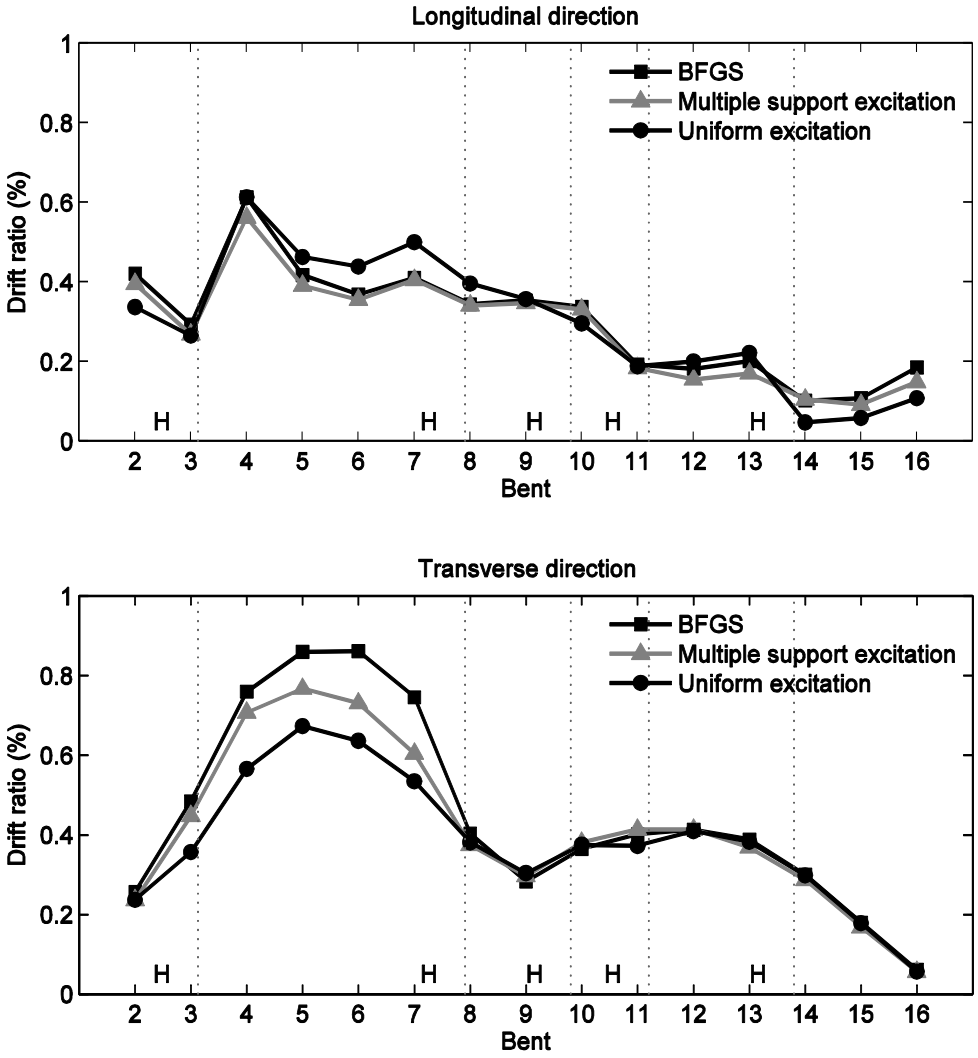

Figure 5.25: Stiff soil; maximum drift ratios for all columns in NW connector

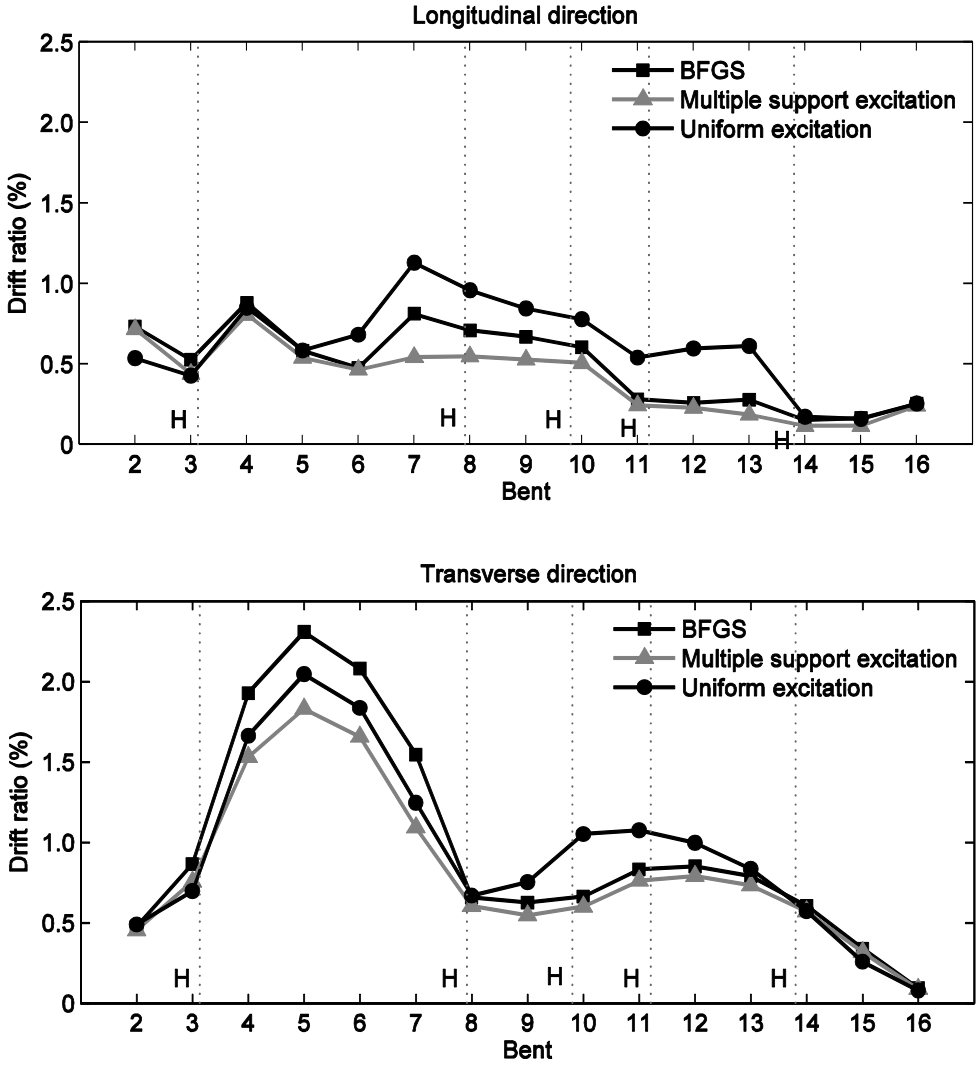

Figure 5.26: Soft soil profile; maximum drift ratios for all columns in NW connector

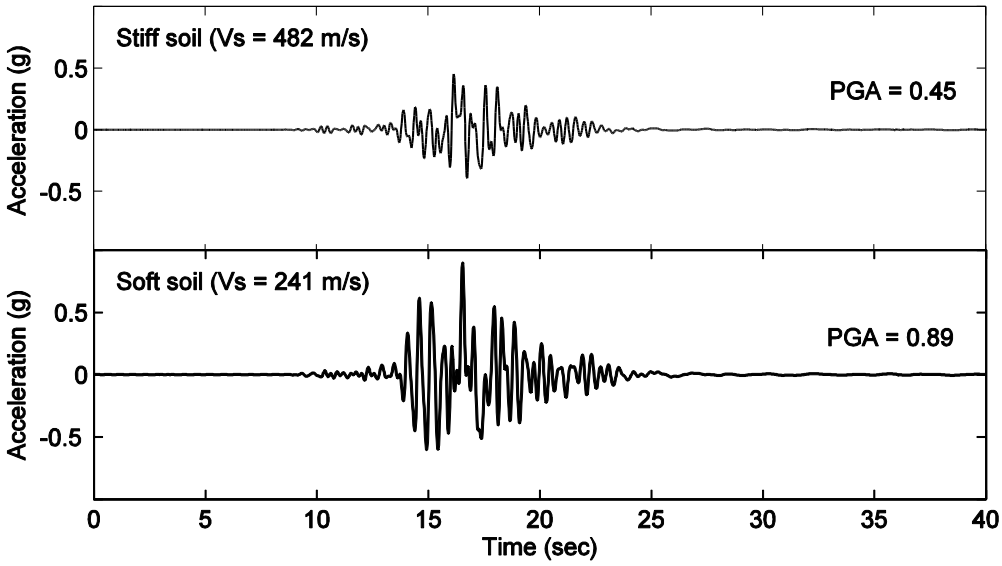

(a) X component

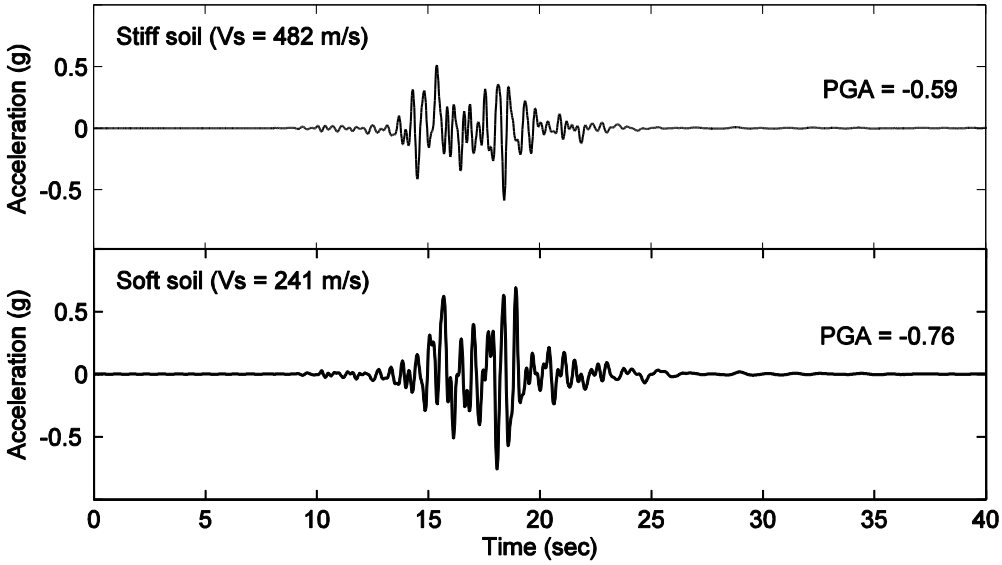

(b) Y component

Figure 5.27: Acceleration at the surface center node in the stiff and soft soil for the broadband input; (a) X component and (b) Y component

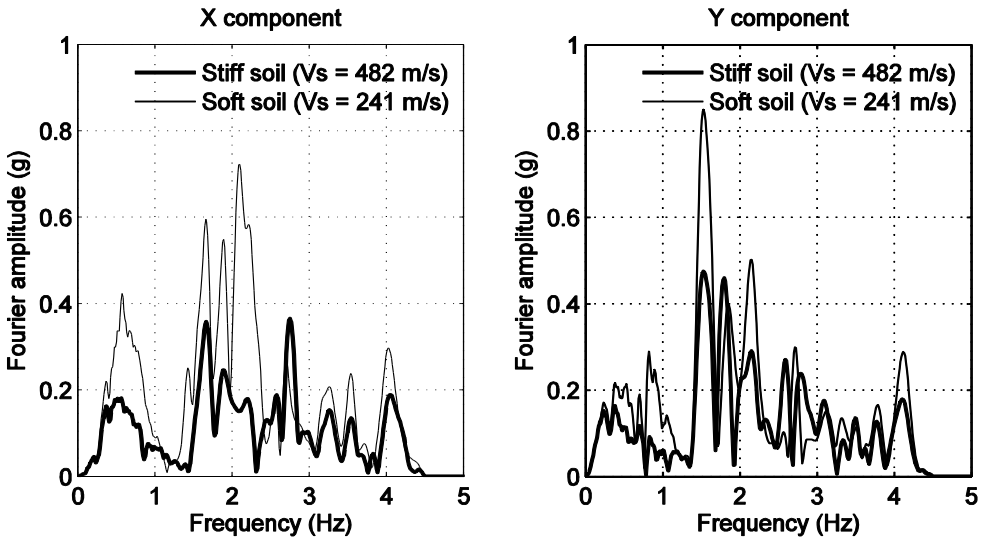

Figure 5.28: Fourier amplitude spectra of the acceleration at the surface center node in the stiff and soft soil for the broadband input

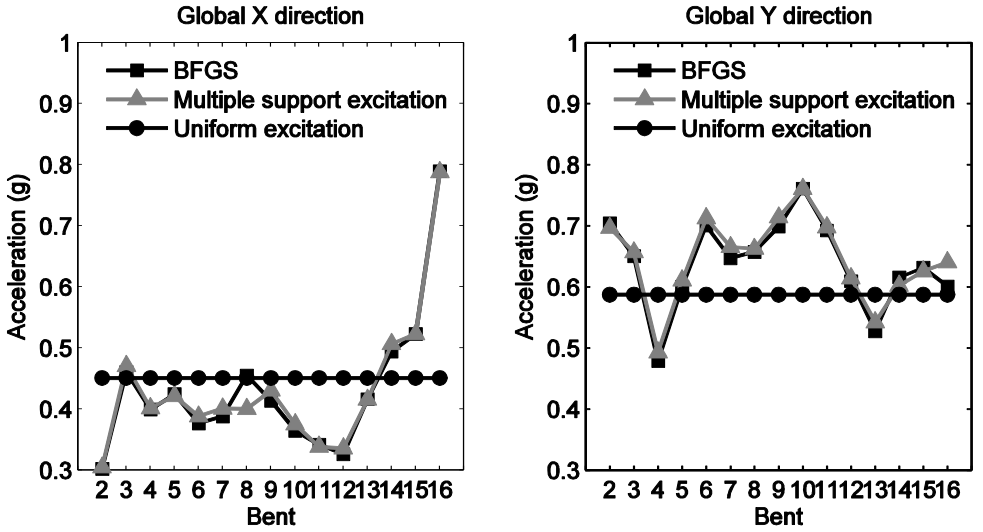

Figure 5.29: Peak base acceleration in the stiff soil for the broadband input

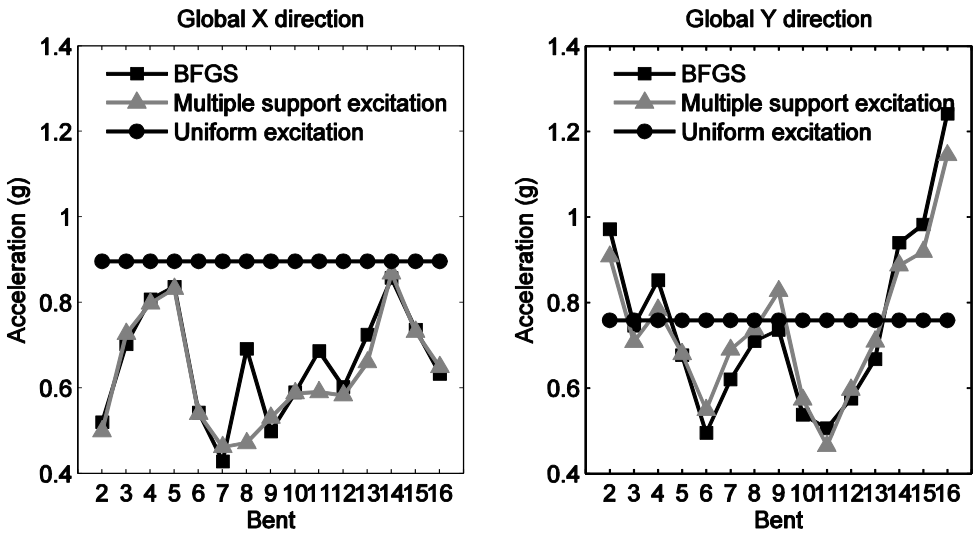

Figure 5.30: Peak base acceleration in the soft soil for the broadband input

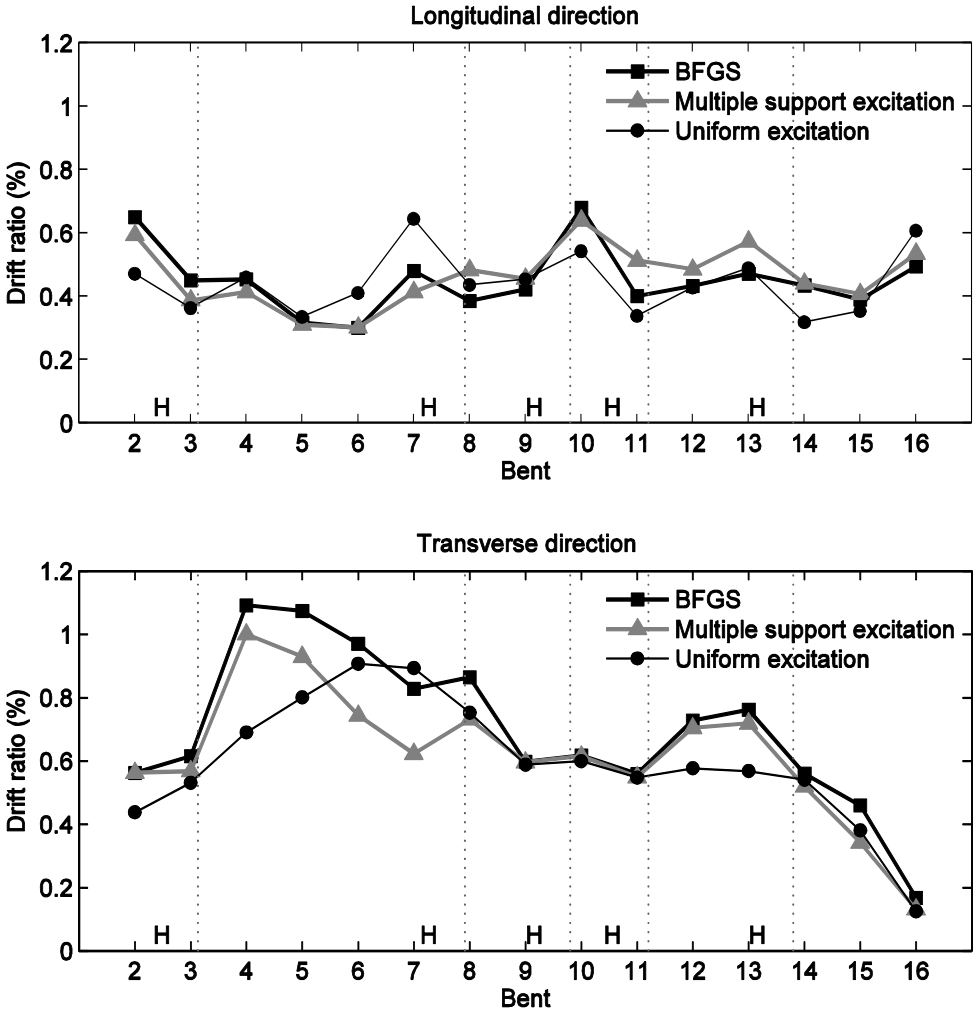

Figure 5.31: Comparison of the maximum drift ratio in the stiff soil for the broadband input

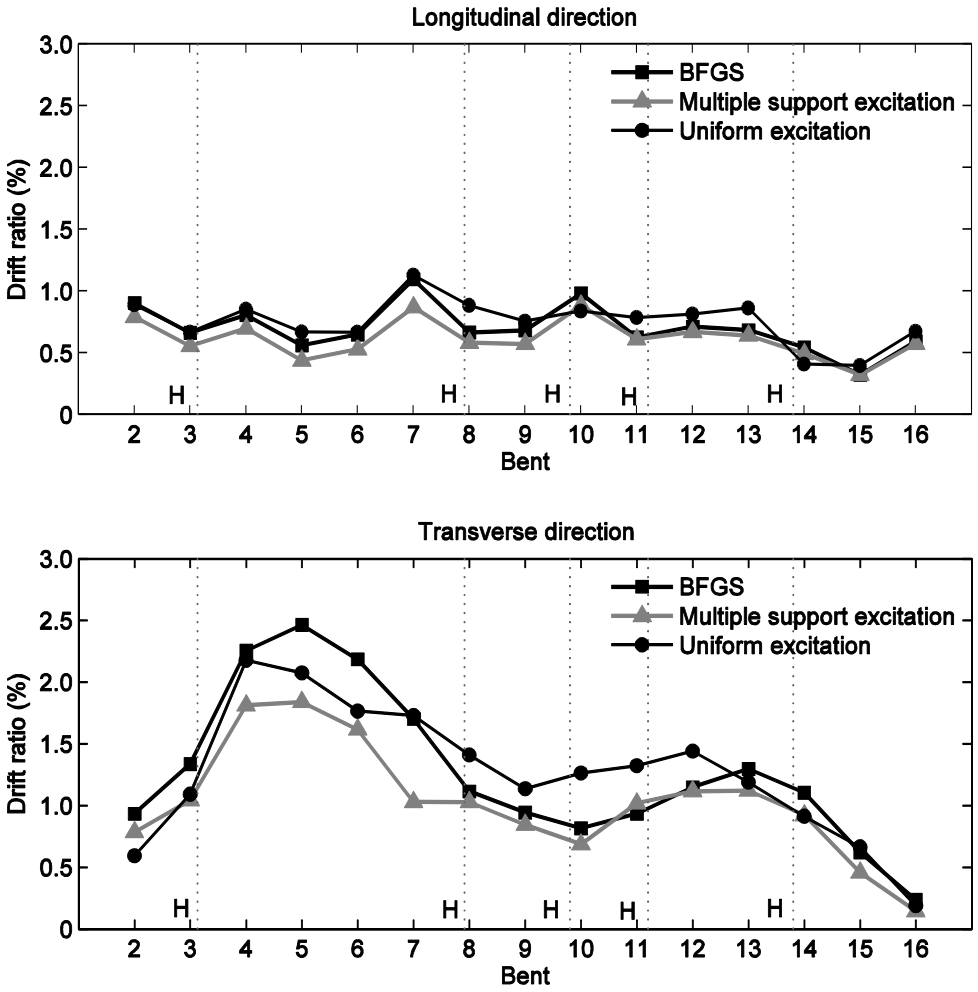

Figure 5.32: Comparison of the maximum drift ratio in the soft soil for the broadband input

Chapter 6

Influence of Soil Nonlinearity on the NW Connector Seismic Response

This chapter presents an evaluation of soil-structure interaction (SSI) on the NW bridge connector subjected to seismic waves based on the Domain Reduction Method. Emphasis is placed on modeling of the bridge-foundation-ground system (BFGS) with soil nonlinearity. Efforts include investigation of the nonlinear soil behavior on seismic response of the BFGS, with comparisons to results from additional fixed-base structure analysis under multiple support excitation and under uniform excitation.

6.1 Introduction

A numerical simulation of the bridge-foundation-ground system (BFGS) was conducted earlier in Chapter 5. Depending on the extent of ground stiffness (stiff and soft soil profiles with linear material properties were studied), the effect of SSI on the bridge was investigated.

In order to further explore potential SSI effects, possible contribution of nonlinearity emanating from presence of a weak soil stratum near the ground surface is investigated in this chapter. The North-West connector (NW) at the interstate 10 and 215 interchange (I-10/215; see Section 3.1) is used as the structural model. As conducted in Chapter 5, an emphasis is placed on the comparison of the structural response between the BFGS and the fixed-base structure without the ground under multiple support excitation and uniform excitation for the low frequency input (see Section 2.3.2). In addition, similar comparisons are made for the broadband input scenario (Section 2.3.3).

6.2 Description of the BFGS

6.2.1 Ground model

For the BFGS (Figure 6.1), the region of interest, ROI, (Petropolous 2008) with linear properties (see Section 2.1) is modified to include soil nonlinearity. The top 40 m layer of the ROI is represented by a low shear strength un-drained clay material model. Below this layer, the soil remains the same as that described earlier (Table 6.1). For the

un-drained clay material model, a relatively low peak shear strength of about 5 kPa is prescribed (to crudely simulate strength upon occurrence of a hypothetical site liquefaction scenario).

6.2.1.1 Nonlinear soil material

The top 40 m thick layer is modeled as a nonlinear hysteretic material (Prevost, 1978; Parra, 1996) with a Von Mises multi-surface (Iwan, 1967; Mroz, 1967) kinematic plasticity model (Pressure IndependMultiYield model in OpenSees). This material is to reproduce the soil hysteretic elastoplastic shear response and to account for permanent deformation. A nonlinear shear stress-strain backbone curve is represented by the hyperbolic relation (Kondner, 1963) defined by two material constants which are low strain shear modulus and ultimate shear strength.

6.2.1.2 Ground response

Peak amplitudes of ground motion (acceleration, velocity, and displacement) at the surface center node are examined in Figure 6.2 through Figure 6.4. Regarding the acceleration, the result shows a notable reduction in peak amplitudes for this nonlinear soil domain scenario (lateral directions). Compared to the horizontal peak ground acceleration of about 0.2 g for the earlier linear soil scenario, the accelerations decrease to about 25 %. This is attributed to the particularly low prescribed soil shear strength (crudely mimicking a post-liquefaction type response in terms of shear strength).

Figure 6.5 shows the Fourier amplitude spectra of acceleration at the surface center node. Although magnitudes of the amplitude are significantly lower (less than 0.1

g for horizontal response), a range of frequency content from 0.1 Hz to about 3 Hz is observed.

Figure 6.6 shows the variation of accelerations along depths from the surface (0 m) to the base of the ROI (100 m) below the center node. The 40 m upper soil responding nonlinearly is seen to reduce the amplitudes in a very clear fashion (Trifunac and Todorovska, 1998).

Soil shear stress-strain response at different depths below the center node is shown in Figure 6.7 and Figure 6.8. Near the base of the nonlinear soil layer (40 m depth), yielding is observed at about 5 kPa in the Y-Z plane corresponding to the global Y direction, providing a base isolation mechanism at this soil layer. Consequently, low levels of shear stress are transmitted to the upper 20 m layer. These low levels of shear stress in the top 20 m layer induce lower ground surface acceleration peaks at the ground surface.

Figure 6.9 and Figure 6.10 show displacement time histories along the global X and Y center lines over the soil surface, respectively. In these figures, variation of ground motion throughout the soil domain can be more clearly visualized.

6.2.2 Bridge model

The NW is considered as the structural model in this BFGS simulation (Figure 6.11). Details of this structural model were described earlier in Section 3.2.3. The dynamic properties of the bridge were also presented in Section 3.2.4. As discussed earlier in Section 4.1.2.2, the soil mesh configuration near the ground surface was

modified (below the location of each bridge column) in order to accommodate the structural model pile-group foundation geometry as shown in Figure 6.1 (b).

6.3 Seismic response of the bridge-foundation-ground system

While a low level of horizontal peak ground accelerations was developed at the ground surface, the weak nonlinear layer induced permanent deformations over the surface. Resulting from these changes in the soil domain behavior, response of the BFGS is discussed below.

6.3.1 Effect of the presence of the structure

Figure 6.12 shows horizontal peak ground velocities at the location of bridge foundations in the BFGS and at the corresponding location of the ground without the bridge (i.e. free-field response). It can be seen that, due to presence of the bridge, differences of the peaks are about 17% at Bent 7 in the global X direction and 6% at Bent 3 in the global Y direction. In addition, Figure 6.13 shows deviation of horizontal base displacements from the free-field response (without the bridge). As might be expected, due to the limited amplification of ground motions at the soil surface, a low level of the difference is observed.

6.3.2 Shear stress and strain of the ground near the pile foundation

Figure 6.14 shows a contour of the maximum soil shear stress (X-Z plane) near foundations of the bridge within the top 20 m layer. As mentioned earlier (Figure 6.7 and

Figure 6.8), the low level of shear stress were shown in this layer due to the underlying base isolation mechanism. Although lower levels of shear stresses are generally induced in the left side of the surface (i.e. a range of 0 m – 500 m in the X direction), some yielding is observed in the vicinity of the foundations.

Figure 6.15 shows shear stress-strain response in the soil surrounding the foundation at Bent 12 (see the location in Figure 6.14). It may be recalled that a rigid solid element occupying the volume of the pile group is enclosed within four solid elements representing the un-drained clay stratum. In the absence of the bridge (i.e. free-field response), shear stress-strain response near the foundation at Bent 12 is compared to the corresponding BFGS result. Presence of the bridge (foundations) induces a higher level of shear stress (X-Z plane), except for element 1 which decreases 57%. Element 2 experiences 38% higher shear stress with large inelastic deformation. The shear stress (Y-Z plane) increases 51% with large deformation, while lower levels of shear stress in elements 2 and 4 are observed.

6.3.3 Bridge response

Figure 6.16 shows the deformed shape of the bridge without showing the soil domain (relative to the surface center node; see Figure 6.11 for the center node) scaled by a factor of 200. It is captured at the time instant of 20.84 sec. when peak drift ratio reaches 0.22% at the top of Bent 5 (24.3 m height) in terms of column deformation (i.e. excluding the amount induced by rocking).

6.3.3.1 Relative support motions

Figure 6.17 shows maximum relative displacement between adjacent supports. Positive displacements indicate that one support moves close to the other and vice versa. The maximum displacements of about 0.02 m and 0.03 m are observed between bents 4-5 and bents 7-8 in the global X and Y directions.

6.3.3.2 Seismic base shear

Figure 6.18 shows normalized total column base shear time histories for which column base shears are divided by self-weight of the NW (160 MN). The low level of the ground acceleration results in significantly lower base shears (about 7% of the self-weight) in the horizontal directions.

6.3.3.3 Acceleration at the bridge deck level

Acceleration time histories at the level of the bridge deck are investigated in the longitudinal and transversal directions. The longitudinal direction is consistent with tangent to the curved geometry (weak axis of column against bending) and transversal direction corresponds to the radial direction (strong axis of column against bending), except for Bent 11 (24 degrees off radial counterclockwise) to 15 (13 degrees off radial counterclockwise). In the bridge, a total of six frames are connected by five intermediate hinges.

Figure 6.19 shows acceleration time histories in the relatively flexible frame 2 (from Bent 4 to Bent 7; see Appendix B for other locations). Peak accelerations show

noticeably amplification (compared to the ground response). Spikes are seen as well particularly in the longitudinal direction due to opening and closing of the intermediate hinges.

6.3.3.4 Relative displacements and drift ratios at the top of columns

In the present model, the bridge deck is modeled with elastic material properties and is relatively stiff in the axial direction (longitudinal direction along the deck; positive direction defined from Abutment 1 to Bent 2). However, the curved structural geometry induces large displacements in both the longitudinal and transverse directions (positive direction in the convex orientation). As expected, larger displacements at the top of columns relative to the base are observed in the relatively flexible frame 2 (i.e. with longer columns) in the transverse direction (see Table 6.2), in spite of the higher moment of inertia in this direction (strong axis against bending).

Due to the employed weak soil upper layer, it can be seen that some of the displacement at the top of columns is induced by rocking of the foundations. Rocking generally induces a beneficial effect in regards to column deformation (excluding the displacement resulting from rocking). In particular, at Bent 12, in-phase response between the top relative displacement and the amount from rocking dramatically reduces the deformation in the transverse direction (Figure 6.20). The reduction due to rocking varies from 3.8% at Bent 14 to 62 % at Bent 16 in the longitudinal direction (Table 6.2). In the transverse direction, the variation is from 16 % at Bent 4 to 87 % at Bent 16.

A drift ratio in terms of the deformation may be calculated (Table 6.2). As expected, transverse drift ratios are mainly larger than those in the longitudinal direction.

The largest drift ratios are 0.16% at Bent 7 (17.3 m height) in the longitudinal direction and 0.22% at Bent 5 (the highest column of 24.3 m) in the transversal direction (Table 6.2).

6.3.3.5 Intermediate hinges

Figure 6.21 shows relative displacements time histories between two adjacent deck segments at the intermediate hinges. It can be seen that a maximum opening of 4 cm is developed at Hinge 7. From the employed linear tension model for the restrainer cables (four sets of 5-3/4" cables), the cable stress is 0.548 GPa (45% of the actual yield stress) at this hinge. The second maximum opening displacement is 3 cm and the corresponding stress is 0.453 GPa (37% of the yield stress) at Hinge 3. At other hinges, the computed displacements and stresses are much less.

6.3.3.6 Abutments

Figure 6.22 shows time histories of backwall (12.5 m) abutment forces per unit width (1 m). At abutment 1, a force of 67.7 kN/m is developed. At abutment 17, a larger force of 163.1 kN/m (2.4 times larger) is induced. Maximum longitudinal displacements to pull the abutments away from the approach ramp are 1 cm and 3 cm at Abutment 1 and 17, respectively.

In the transversal direction, maximum forces are 292.7 kN (about 35% of the longitudinal force) at Abutment 1 and 343.7 kN (about 17% of the longitudinal force) at abutment 17. The corresponding displacements are 0.5 cm and 0.6 cm, respectively.

6.4 Evaluation of soil-structure interaction

As discussed earlier in Section 5.4, an additional fixed-base structure analysis is employed using free-field ground motions at the column base locations over the soil surface in the ROI (without the bridge). The structure is analyzed under the multiple support excitation (see Section 5.4.1.1) and under the scenario of uniform excitation (see Section 5.4.1.2). In this section, structural response under the three types of loading conditions (BFGS, multiple support excitation, and uniform excitation) is compared.

6.4.1 Base acceleration

Figure 6.23 shows maximum accelerations at the base of columns for the three types of loading conditions. Notable is the differences between the BFGS and the multiple-support excitation scenarios.

6.4.2 Seismic base shear

Table 6.3 shows the normalized base shears under the three loading conditions. The level of the base shear is very low due to the low ground surface acceleration. Under the multiple support excitation conditions, the base shear decreases about 10% and 8% in X and Y directions, respectively.

Under the uniform excitation condition, as larger acceleration is generally developed at the column base in the X direction (Figure 6.23), the base shear increases about 9%. In the Y direction, the base shear decreases about 9% consistent with the corresponding low level of base accelerations.

6.4.3 Acceleration at the top of the columns

Acceleration response of the NW is examined with and without the soil domain. Figure 6.24 shows acceleration time histories at the top of Bent 6 (22.5 m height) obtained from the three types of loading conditions. The results indicate that larger accelerations are generally developed in the BFGS and to some extent in the multiple support motions without the soil domain (under the multiple support excitation). As indicated in Section 6.3.1, the deviation between the base response and the free-field motion (without the bridge) results in different support motions.

In the longitudinal direction, a high level spike is observed at about 17.5 sec. in the positive direction (toward Abutment 17) for the BFGS and the multiple supports excitation scenario. Another large spike in the negative direction is observed at about 19 sec. under the multiple supports excitation but a magnitude of the spike in the BFGS case is rather low. Accelerations under the uniform excitation scenario are seen to be noticeably different.

6.4.4 Relative displacement and drift ratios at the top of columns

Figure 6.25 shows relative displacement time histories at the top with respect to the base at Bent 6. Drift ratio in terms of the deformation for the BFGS and the relative displacement at the top to the base for the cases without the soil domain are compared next. Figure 6.26 shows maximum drift ratios in the three cases. Again, it is noteworthy to highlight the difference in response for the BFGS case and the multi-support case.

6.4.5 Column forces

Compared to the result in the BFGS, the column forces without the soil domain significantly decrease or increase, depending on the particular column location. Under the multiple support excitation condition, longitudinal shear force/bending moments generally increased. In the transverse direction, shear forces (bending moments) increase up to 151% (180%) at Bent 16 and decrease as much 31% (37%) at Bent 11. Under the uniform excitation, longitudinal shear forces (bending moments) increase 176% (303%) at Bent 16 and decrease 42% (43%) at Bent 3. Meanwhile, transverse forces increase in most of the columns, except for Bent 11, 13, 14, and 15. The maximum column forces in terms of shear forces and bending moments are summarized in Table 6.4 through Table 6.7.

6.4.6 Effect of the broadband input

In this subsection, the BFGS is analyzed for the broadband input with the frequency content up to 5Hz (see Section 2.3.3 for ground response in the ROI). Results in the BFGS are compared to those in the fixed-base structure analysis under multiple support/uniform excitation.

6.4.6.1 Free-field response

Free-field response at the surface center node is shown in Figure 6.27 for the acceleration, Figure 6.28 for the velocity, and Figure 6.29 for the displacement. Compared to the response for the low frequency input, high frequency is clearly observed

as shown in Figure 6.30. As discussed earlier, the base isolation mechanism emanating from the weak un-drained clay layer in the top 40 m is also observed in Figure 6.31.

6.4.6.2 Bridge responses

Figure 6.32 shows the difference in ground displacements without the bridge (i.e. free-field) and base displacements in the BFGS. Compared to the result for the low-frequency input (see Figure 6.13), much deviation is observed, particularly at Bents 2 and 12. This deviation results in a different behavior pattern for the columns in terms of displacement at the top relative to the base under the multiple support excitation scenario as shown in Figure 6.33.

In the comparison of the maximum drift ratio at the top of the columns (Figure 6.34), the multiple support excitation scenario generally overestimates displacement demands for the broadband input. However, as discussed in Section 6.4.4 for the low-frequency input, the displacement demands under the uniform excitation is overestimated or underestimated depending on the column location.

6.5 Summary and conclusions

The influence of an upper weak soil layer on the bridge response was investigated using the low frequency input resulting from the realistic fault rupture scenario (DRM). The free-field response (without the bridge) and near the foundation of the bridge were investigated. The bridge responses in terms of the base shear, the acceleration/ relative displacement (deformation) at the top of columns, and the column forces were discussed.

For comparison with the full SSI simulation (i.e. BFGS), the fixed-base structure analysis under multiple support excitation and uniform excitation was considered using free-field motions obtained from the soil domain in the absence of the structure. The comparison in the result using the broadband input was also discussed. From the results of the present study, the main observations are:

1. Relative support motions induced by permanent ground deformation due to the presence of the weak upper stratum played a role in the longitudinal responses of the bridge (drift ratios in this direction, hinge opening/yield stresses of restrainer cables, abutment forces against bridge approach ramp).
2. Although the base isolation mechanism emanating from the weak upper layer limited amplification of the ground acceleration at the ground surface, yielding of the soil in the vicinity of the structure foundation was observed. Consequently, the level of deformation in the columns was further reduced by rocking of the foundation embedded within the weak upper soil stratum.
3. In spite of the low level of the ground acceleration, impacts at the intermediate hinges between adjacent frames were observed.
4. Analyzing the fixed-base bridge under multiple support excitation did not lead to accurate prediction of structural response (e.g. drift ratios at the top of columns, internal columns forces, and opening gap at the intermediate hinges in this study). Free-field ground motions (in the absence of the bridge) at the footprint of the supports significantly differed from the actual base motions in the presence of the bridge. In general, the analyses under multiple support excitation and uniform excitation provided overestimation of the structural response.

5. For the broadband input scenario, much deviation of the free-field motion from the actual motion at the supports (in the BFGS) was observed, compared to that for the low-frequency input. This deviation resulted in overestimation of structural response under the multiple support excitation condition. However, under uniform excitation, overestimation or underestimation was observed, depending on the particular column location (in the studied case).

Thus, in order to obtain more representative predictions of response of the bridge structure (the employed weak layer scenario), a detailed analysis that considers the permanent ground deformation and the full coupling between the structure and the surrounding soil may become necessary.

Table 6.1: Material properties for the soil domain

(a) Nonlinear soil layer for the top 40 m thickness in the region of interest

Depth (m)	Density (t/m^3)	Shear Modulus (kPa)	Bulk Modulus (kPa)	Octahedral Shear Strength (kPa)	Octahedral Shear strain at maximum shear strength (%)
0 - 40	1.3	13,000	65,000	4.714	10

(b) Linear soil layers for the region of interest and buffer zone

Depth (m)	Density (t/m^3)	V_p (m/s)	V_s (m/s)	Region
40 – 100	1.714	1622.4	584.3	Region of Interest
100 - 440	1.714	1622.4	584.3	Buffer Zone
440 - 500	2.054	2372.9	651.3	Buffer Zone

Table 6.2: Maximum relative displacements and drift ratios (%) at the top of bents in the North-West connector

			Longitudinal direction			Transversal direction		
Frame	Bent	Height (m)	Top relative to base (m)	Deformation (m)	Drift (%)	Top relative to base (m)	Deformation (m)	Drift (%)
1	2	11.88	0.017	0.008	0.07	0.011	0.004	0.04
	3	16.59	0.023	0.020	0.12	0.027	0.020	0.12
2	4	19.41	0.047	0.030	0.15	0.048	0.040	0.21
	5	24.26	0.045	0.031	0.13	0.068	0.054	0.22
	6	22.50	0.040	0.032	0.14	0.066	0.050	0.22
	7	17.32	0.035	0.028	0.16	0.051	0.037	0.21
3	8	15.24	0.023	0.012	0.08	0.035	0.013	0.09
	9	15.77	0.022	0.013	0.08	0.034	0.016	0.10
4	10	12.88	0.015	0.008	0.06	0.034	0.013	0.10
	11	18.26	0.025	0.020	0.11	0.055	0.028	0.15
5	12	18.80	0.015	0.012	0.06	0.061	0.022	0.12
	13	16.94	0.015	0.010	0.06	0.052	0.022	0.13
6	14	15.62	0.009	0.009	0.06	0.045	0.016	0.10
	15	13.69	0.006	0.002	0.02	0.023	0.008	0.06
	16	7.23	0.005	0.002	0.03	0.009	0.001	0.02

Table 6.3: Peak base shear in the North-West connector with and without the soil domain induced by the nonlinear soil layer

Base shear	With SSI	Without SSI			
	BFGS	Multiple support excitation	Difference (%)	Uniform excitation	Difference (%)
V_x/W	0.067	0.060	-10.1	0.073	8.6
V_y/W	0.056	0.052	-7.5	0.051	-8.9

Table 6.4: Comparison of maximum shear forces (MN) in the longitudinal direction

Bent	Longitudinal shear forces (MN)				
	BFGS	Multiple-support excitation	Difference (%)	Uniform excitation	Difference (%)
2	1.47	1.58	7.43	1.37	-6.90
3	1.07	0.66	-38.39	0.62	-42.04
4	1.38	1.59	15.07	1.28	-7.16
5	0.85	0.74	-12.33	0.63	-25.32
6	0.96	0.85	-12.26	0.72	-24.84
7	1.63	1.67	2.37	1.30	-19.97
8	0.98	1.31	32.97	0.95	-3.63
9	1.08	1.63	51.90	1.11	3.09
10	0.98	1.71	73.83	1.28	30.25
11	0.52	0.73	41.22	0.56	8.19
12	0.35	0.68	94.76	0.93	168.77
13	0.53	0.66	23.86	1.24	133.30
14	0.29	1.22	316.46	0.38	30.47
15	0.25	1.08	329.57	0.60	138.89
16	0.96	1.69	76.36	2.65	175.65

Table 6.5: Comparison of the maximum shear forces (MN) in the transverse direction

Bent	Transverse shear forces (MN)				
	BFGS	Multiple-support excitation	Difference (%)	Uniform excitation	Difference (%)
2	0.45	0.73	61.21	0.90	97.70
3	0.69	0.98	41.66	0.98	41.81
4	1.05	1.41	33.89	1.25	18.79
5	0.78	0.93	19.10	0.96	22.62
6	0.86	0.94	9.36	1.14	31.48
7	1.37	1.11	-18.99	1.32	-3.35
8	0.62	0.87	40.99	1.27	105.11
9	0.68	0.53	-21.72	0.84	23.77
10	0.97	0.99	2.00	1.27	30.15
11	0.92	0.64	-30.71	0.70	-24.07
12	0.58	0.52	-11.28	0.63	7.85
13	0.90	0.66	-26.46	0.65	-27.45
14	0.72	0.63	-11.91	0.59	-17.60
15	0.61	0.45	-26.53	0.46	-25.04
16	0.45	1.13	151.41	0.46	2.16

Table 6.6: Comparison of the maximum bending moments (MN-m) in the longitudinal direction

Bent	Longitudinal bending moments (MN-m)				
	BFGS	Multiple-support excitation	Difference (%)	Uniform excitation	Difference (%)
2	8.53	10.85	27.21	9.07	6.31
3	9.75	6.59	-32.48	5.51	-43.47
4	13.12	16.35	24.55	13.32	1.50
5	9.64	8.92	-7.50	7.84	-18.73
6	10.03	9.71	-3.13	8.23	-17.87
7	14.39	15.48	7.57	12.18	-15.37
8	7.61	11.29	48.31	8.24	8.17
9	7.86	13.88	76.54	9.28	18.09
10	6.88	12.98	88.49	9.60	39.38
11	6.35	7.58	19.42	5.25	-17.36
12	3.45	6.99	102.92	9.10	164.08
13	4.77	6.08	27.52	11.06	131.95
14	3.15	11.31	259.28	3.09	-1.91
15	1.74	8.29	377.36	4.22	143.11
16	2.73	7.43	172.06	11.03	303.53

Table 6.7: Comparison of the maximum bending moments (MN-m)) in the transverse direction

Bent	Transverse bending moments (MN-m)				
	BFGS	Multiple-support excitation	Difference (%)	Uniform excitation	Difference (%)
2	4.91	7.98	62.37	9.27	88.67
3	11.67	17.08	46.38	16.87	44.64
4	18.57	25.33	36.41	22.39	20.54
5	16.41	20.28	23.55	20.65	25.84
6	17.10	18.87	10.34	22.42	31.07
7	21.18	18.15	-14.31	22.25	5.06
8	9.19	11.80	28.34	19.50	112.05
9	10.36	8.63	-16.69	14.98	44.57
10	12.82	11.84	-7.64	17.01	32.67
11	14.73	9.30	-36.87	11.35	-22.92
12	9.98	8.62	-13.70	11.25	12.68
13	13.13	10.62	-19.17	10.50	-20.03
14	10.54	8.96	-14.99	8.64	-18.00
15	7.62	6.26	-17.92	6.10	-19.99
16	2.44	6.81	179.52	3.21	31.81

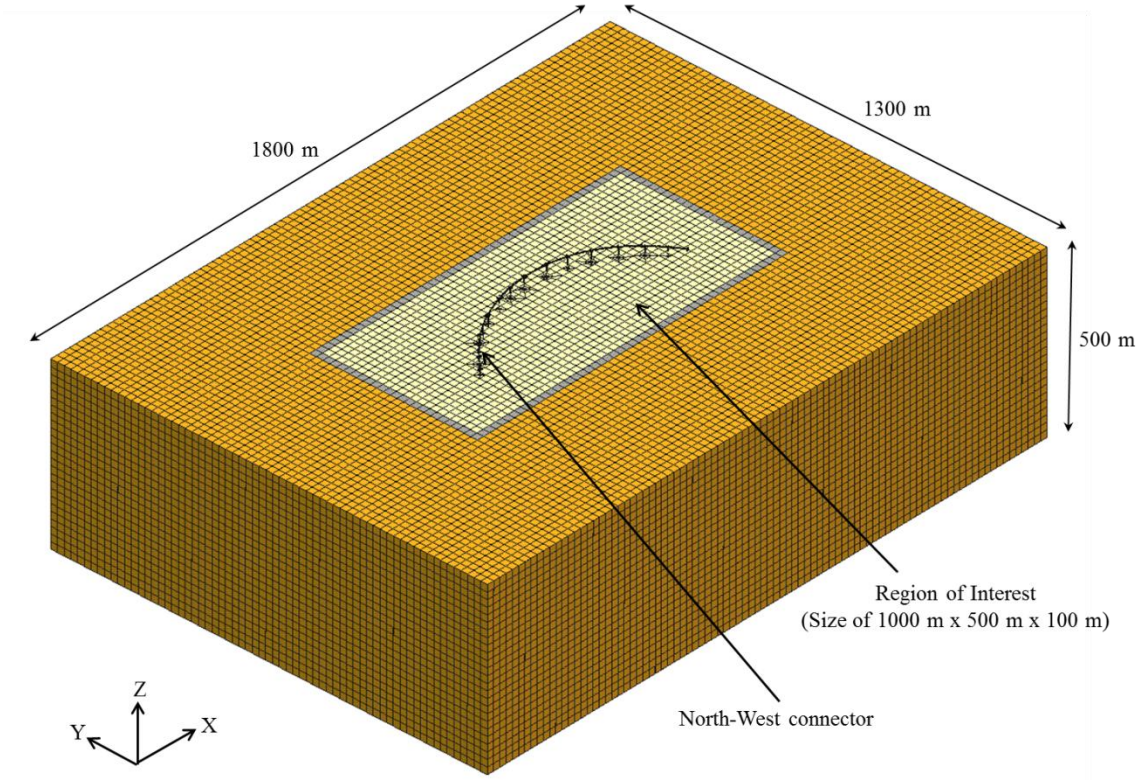

(a) 3D view of the entire FE model

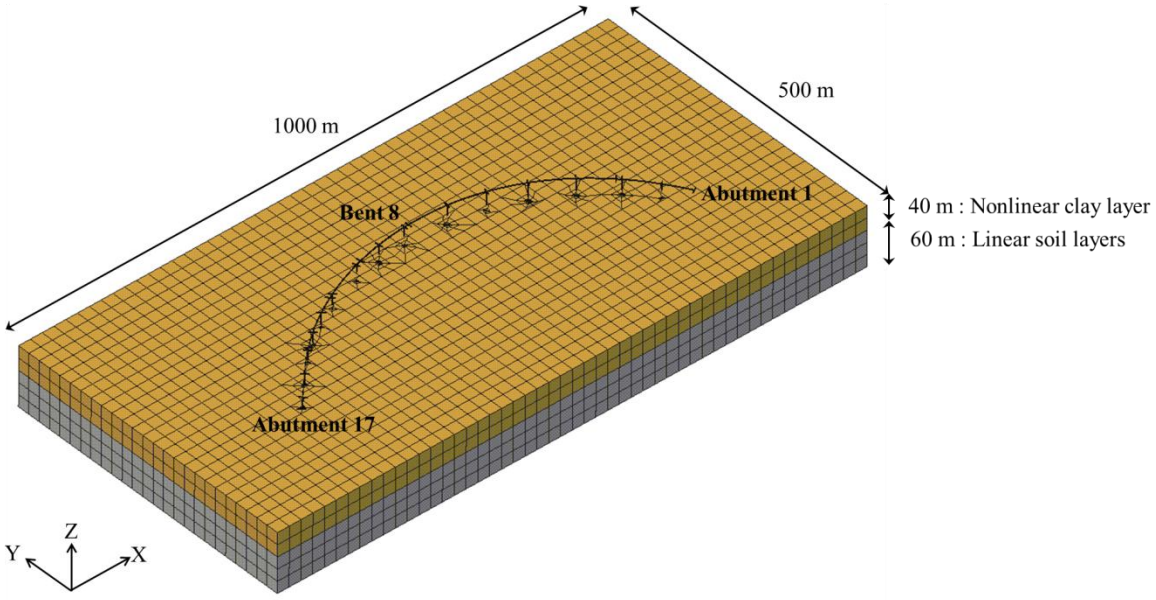

(b) Enlarged 3D view of three connectors built on the region of interest

Figure 6.1: 3D view of FEM mesh for bridge-ground system in Region of Interest surrounded by buffer zone

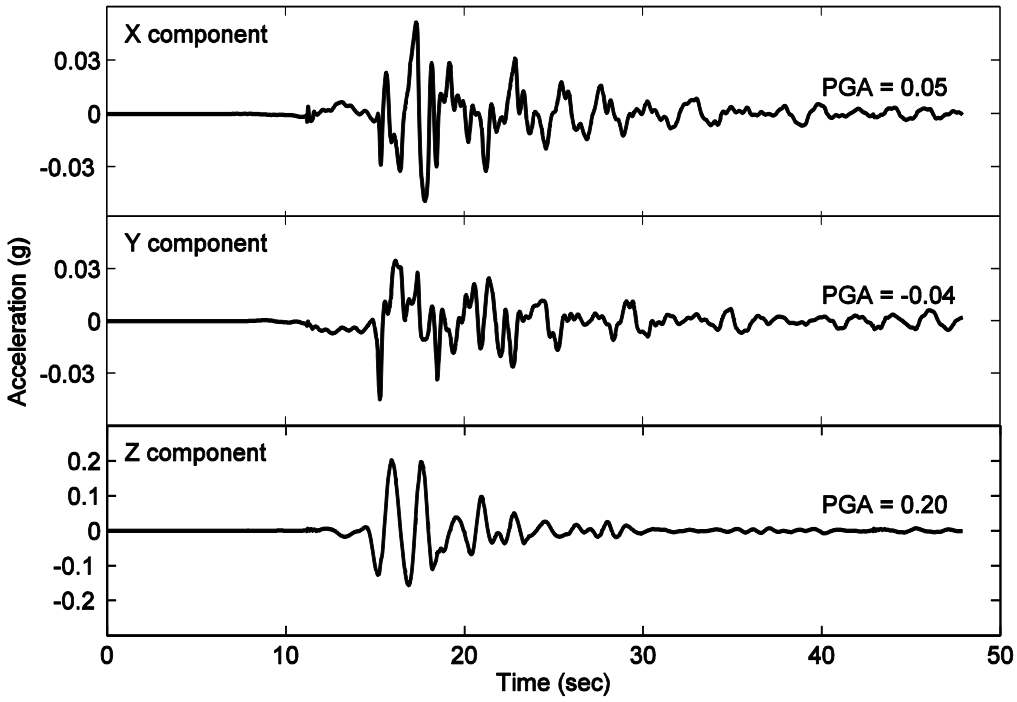

Figure 6.2: Acceleration time histories at the ground surface center node

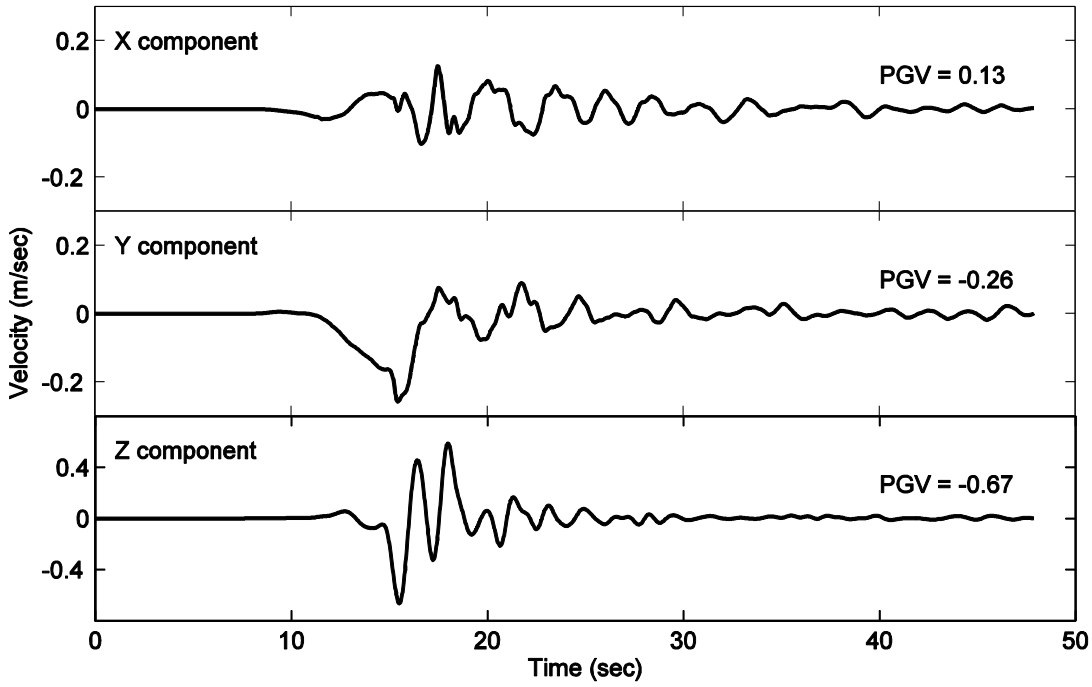

Figure 6.3: Velocity time histories at the ground surface center node

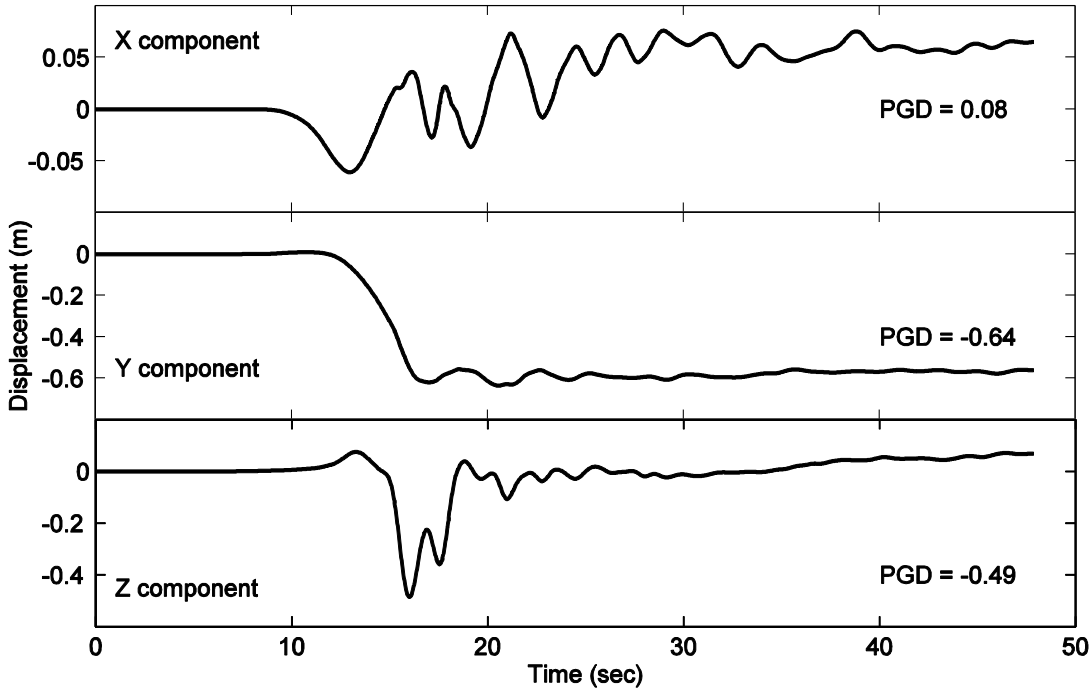

Figure 6.4: Displacement time histories at the ground surface center node

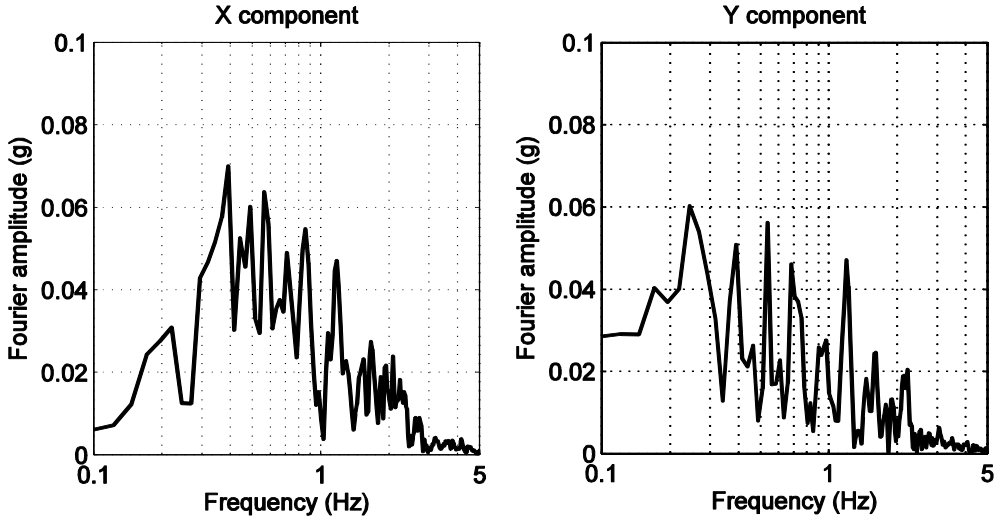

Figure 6.5: Fourier amplitude spectra of ground accelerations at the ground surface center node

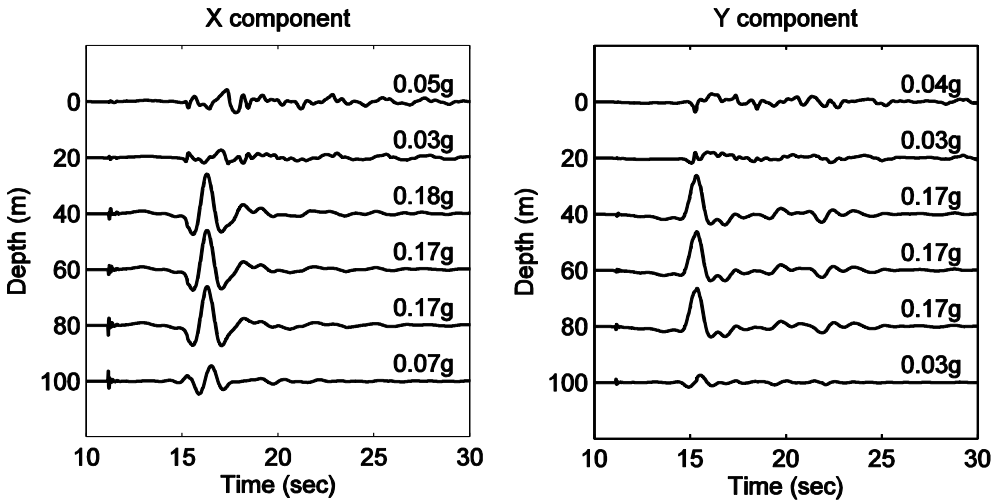

Figure 6.6: Variation of ground accelerations in X direction (left) and Y direction (right) with depth below the ground surface center node

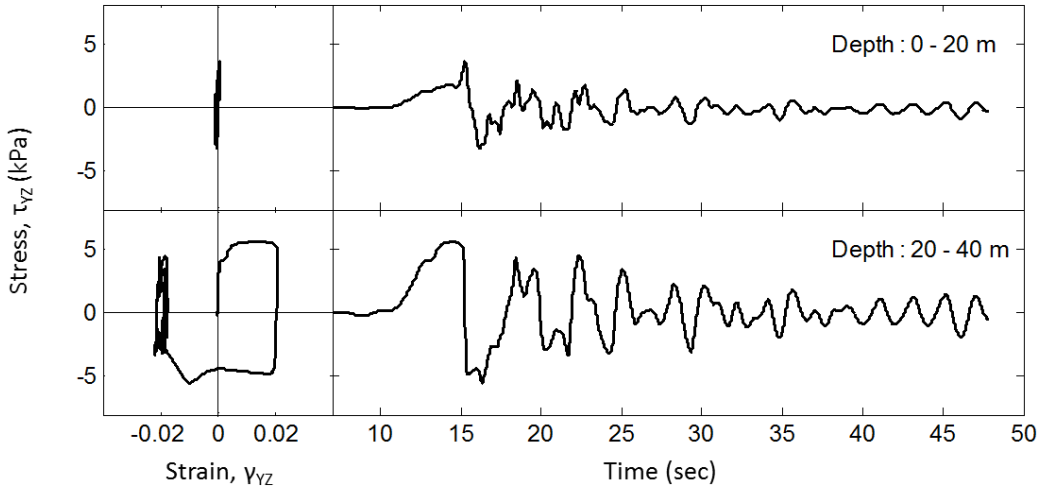

(a) In the top 40 m layer composed of nonlinear un-drained clay

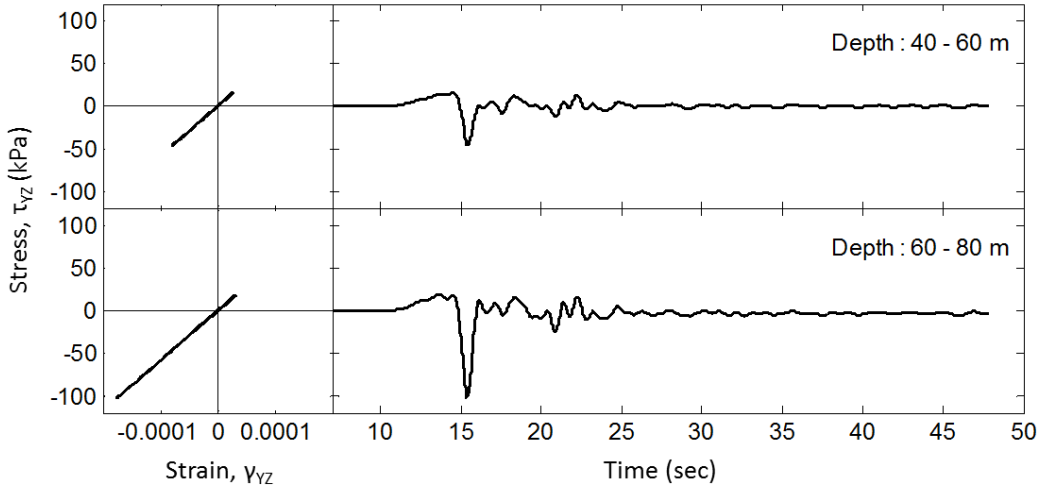

(b) In the elastic-linear 40 m layer below the un-drained clay

Figure 6.7: Shear stress-strain response (yz) at different depths below the ground surface center node

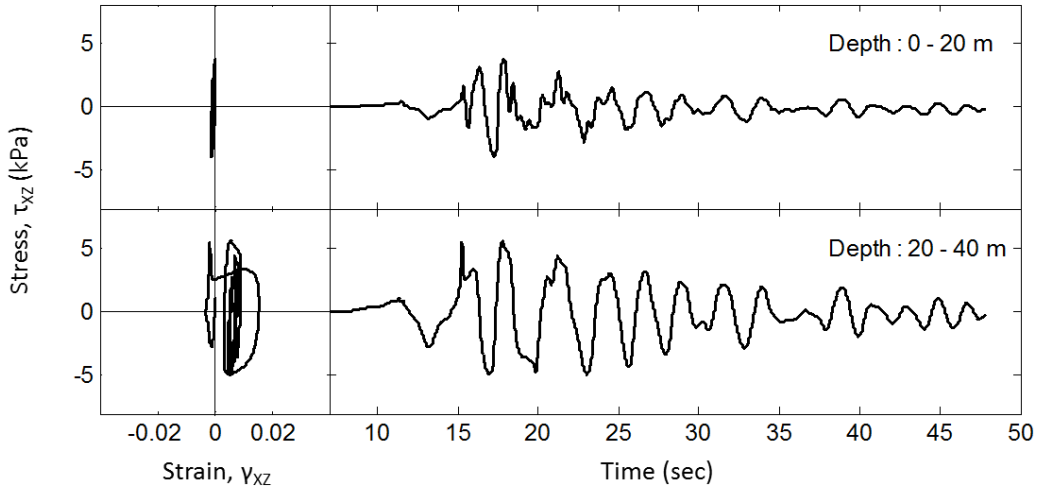

(a) In the top 40 m layer composed of nonlinear un-drained clay

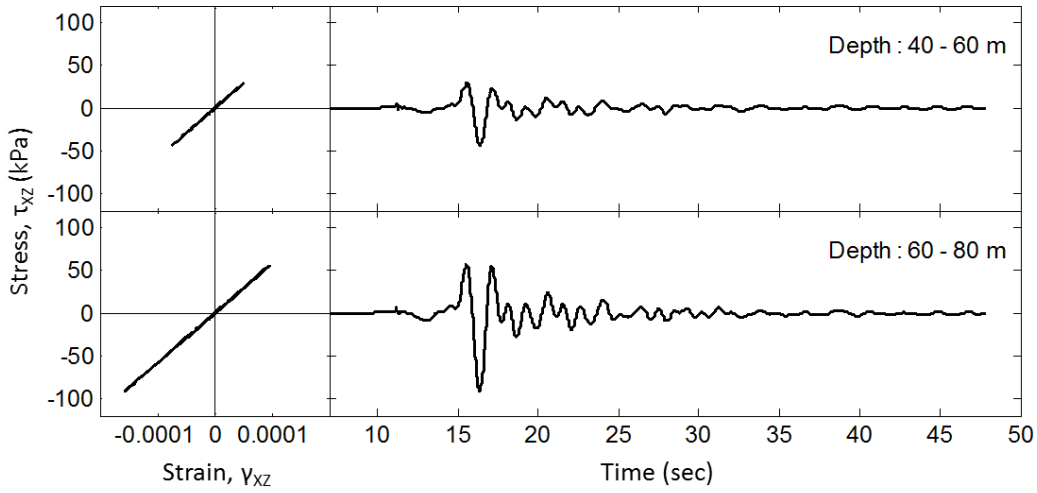

(b) In the elastic-linear 40 m layer below the un-drained clay

Figure 6.8: Shear stress-strain response (xz) at different depths below the ground surface center node

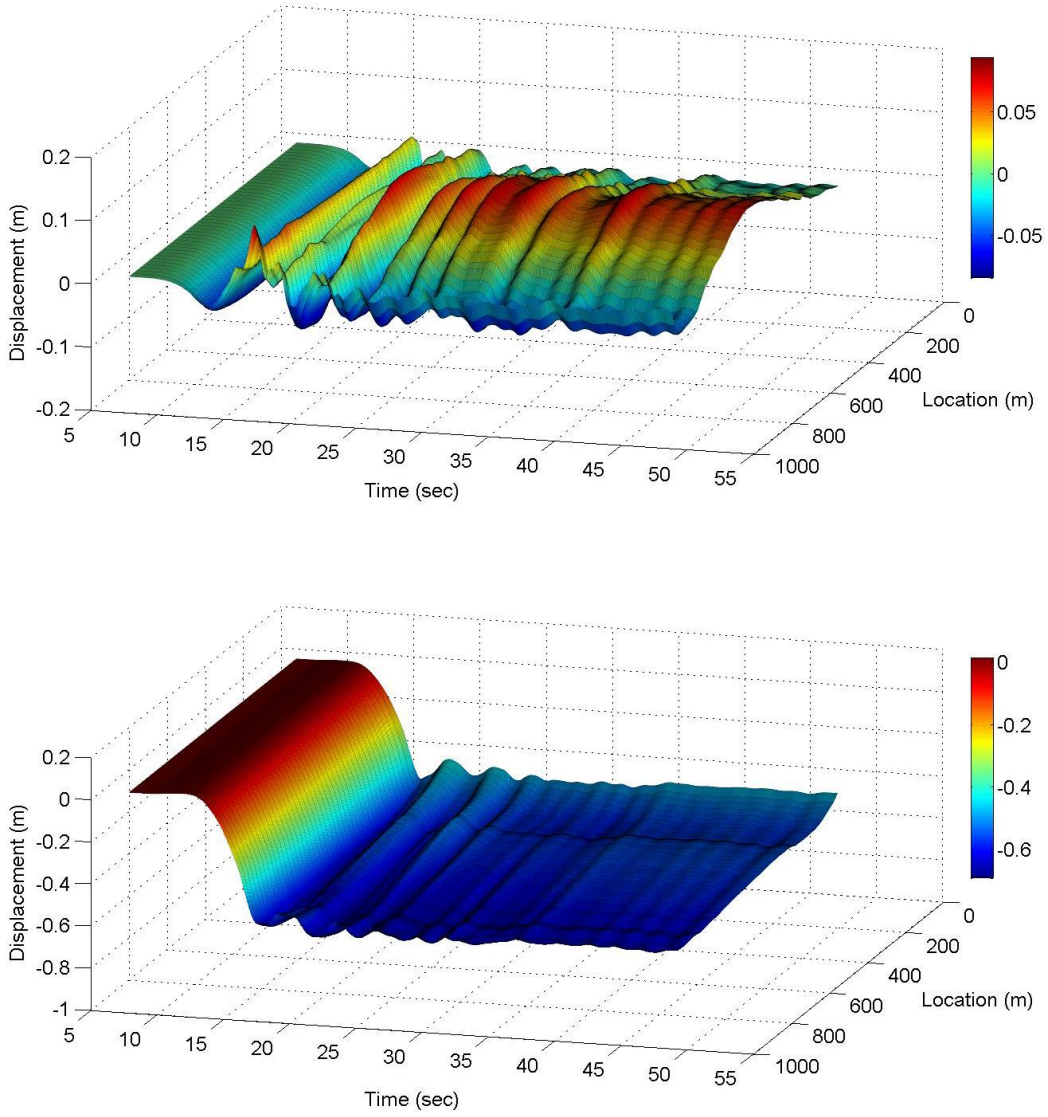

Figure 6.9: X (top) and Y (bottom) component of ground displacement along X centerline of surface of region of interest with the nonlinear un-drained clay soil profile

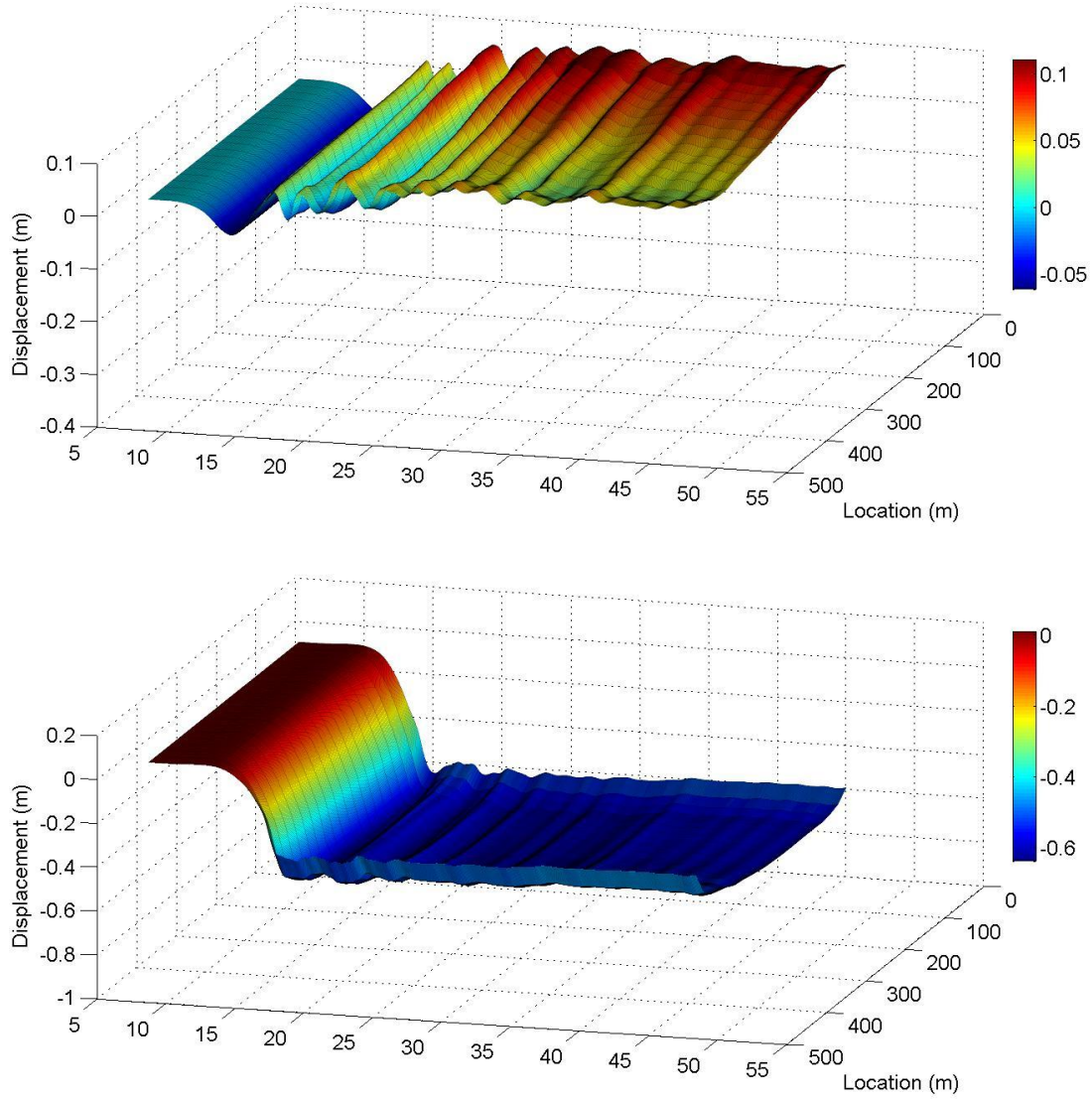

Figure 6.10: X (top) and Y (bottom) component of ground displacements along Y centerline of surface of region of interest with the nonlinear un-drained clay soil profile

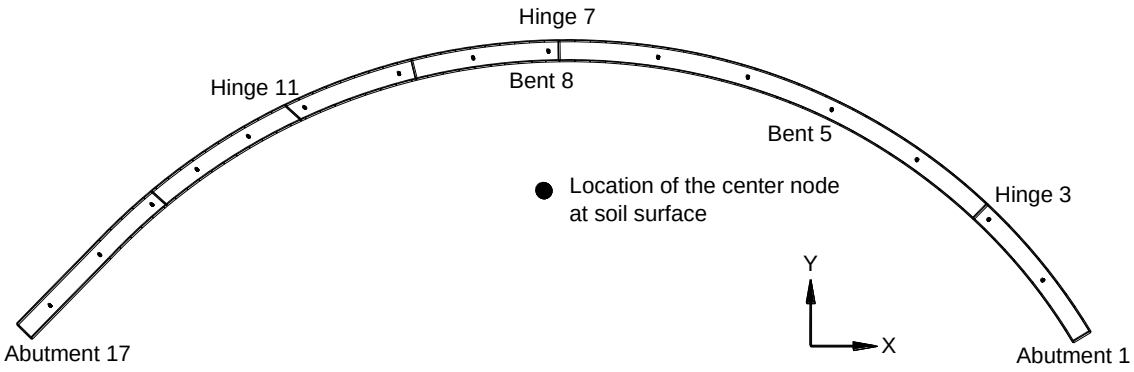

Figure 6.11: Plan view of North-West connector for the nonlinear soil profile

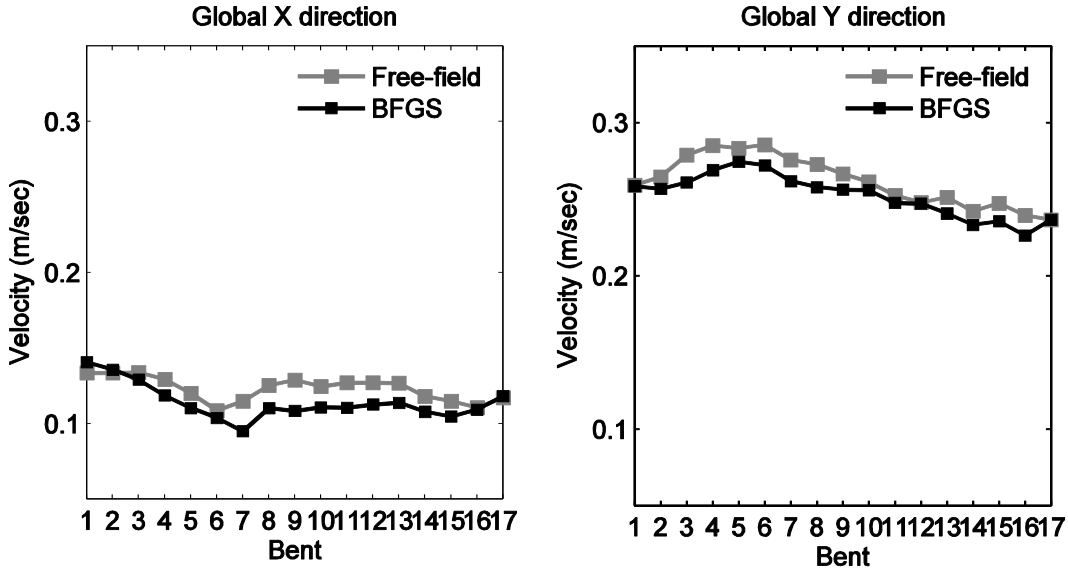

Figure 6.12: Comparison of peak ground velocities with and without the North-West connector

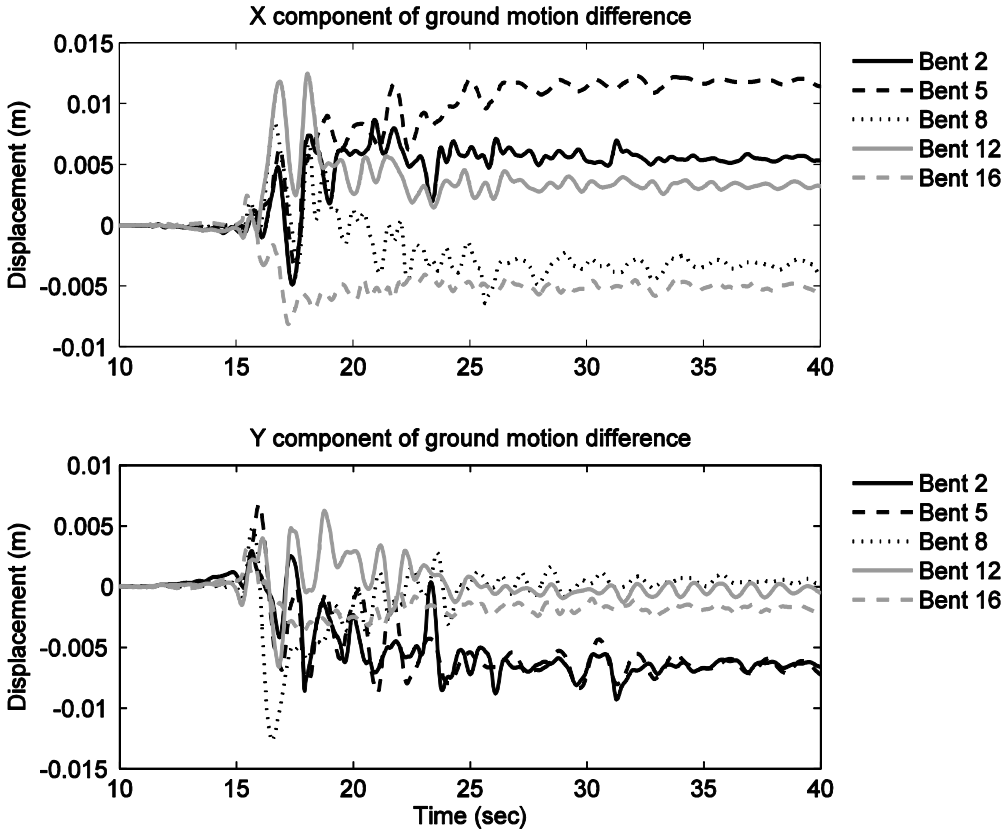

Figure 6.13: Ground displacement difference in the presence of the structure compared to the free-field under the base of bents 2, 5, 8, 12, and 16

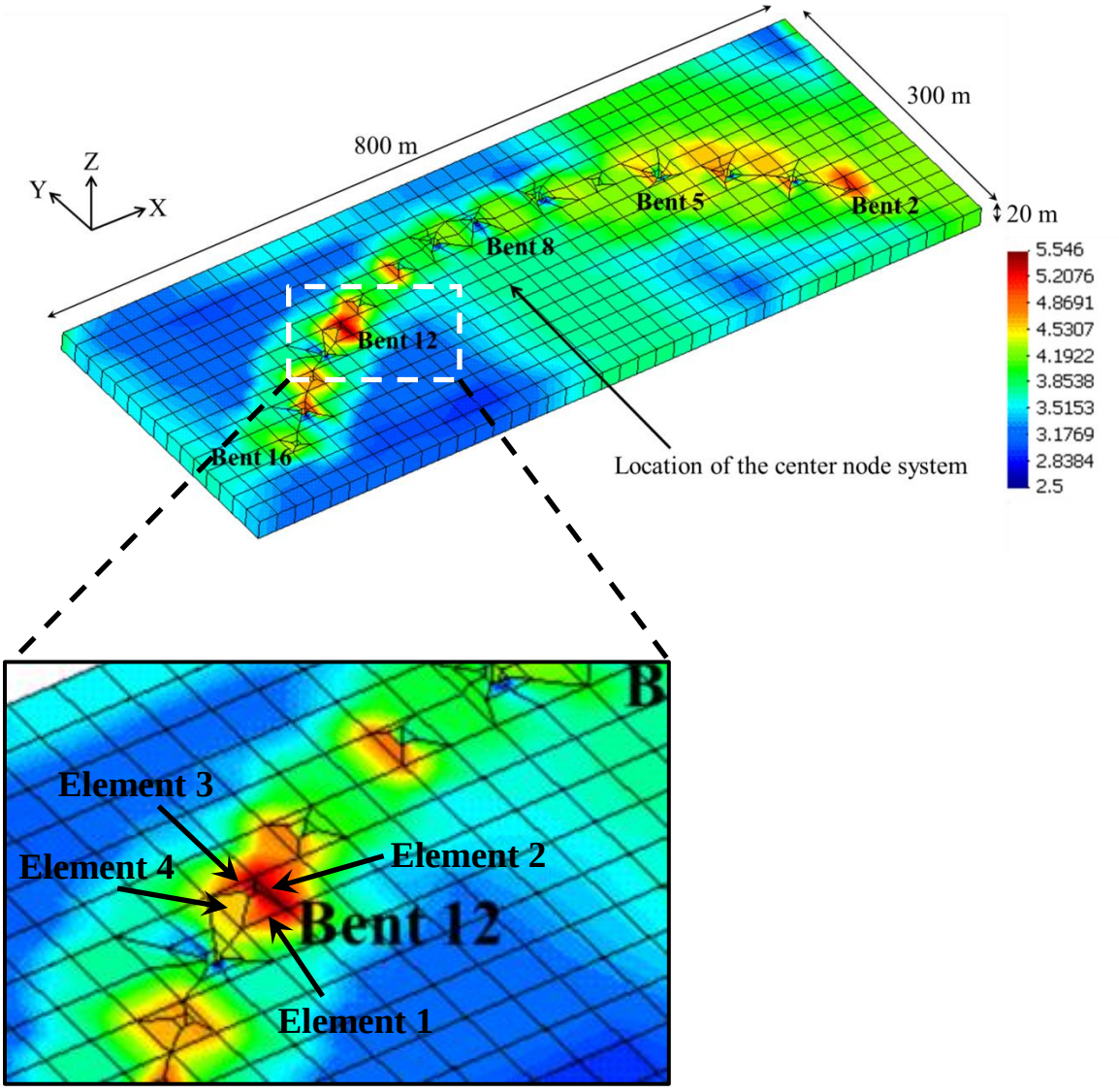

Figure 6.14: Contour of the maximum shear stress (xz) near the foundation of the North-West connector in the top 20 m layer (units in kPa)

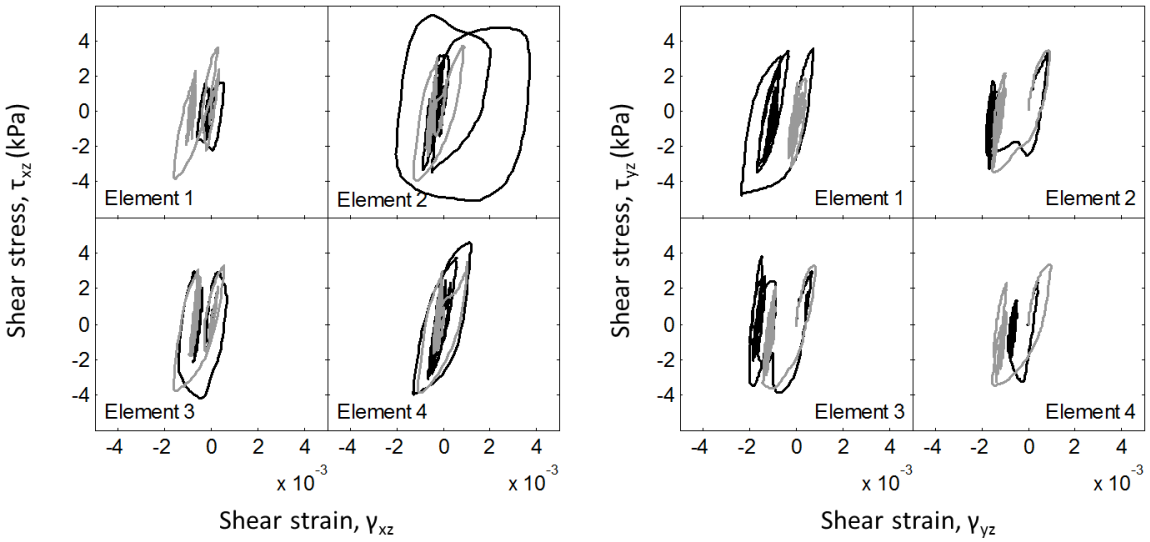

Figure 6.15: Comparison of shear stress-strain response in the soil surrounding the foundation at Bent 12 in the presence of (black line) and absence of the connector (gray line)

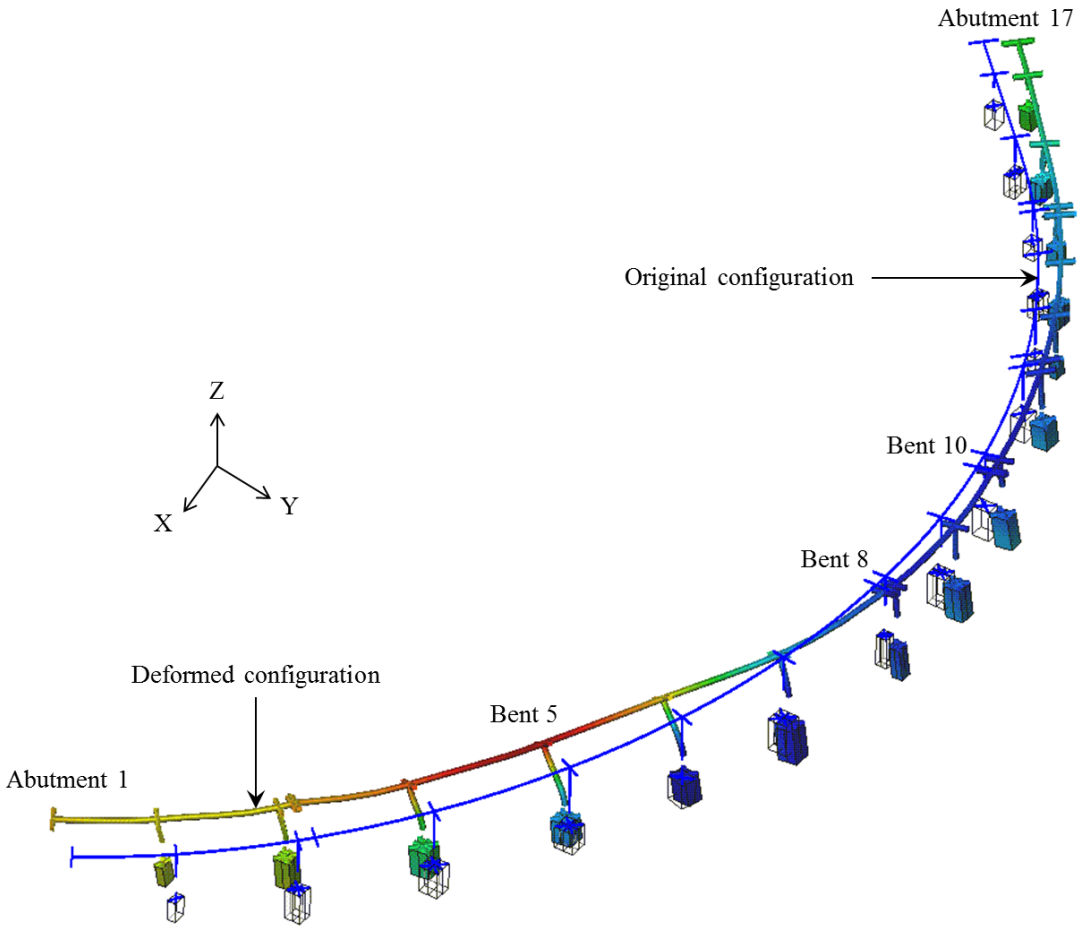

Figure 6.16: Deformed shape of North-West connector with piles at 20.84 sec. when the maximum drift ratio occurs at the top of Bent 6

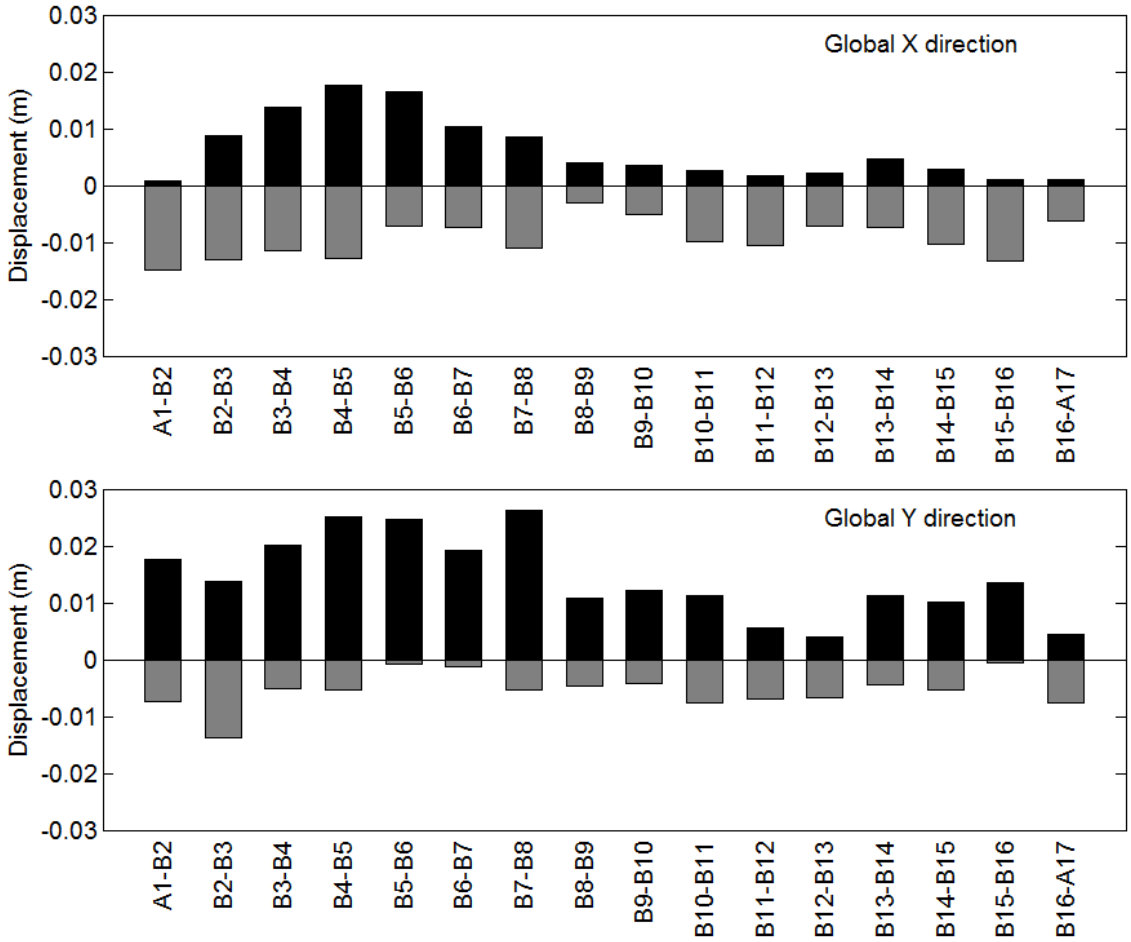

Figure 6.17: Relative support motions induced by the non-uniform ground motion

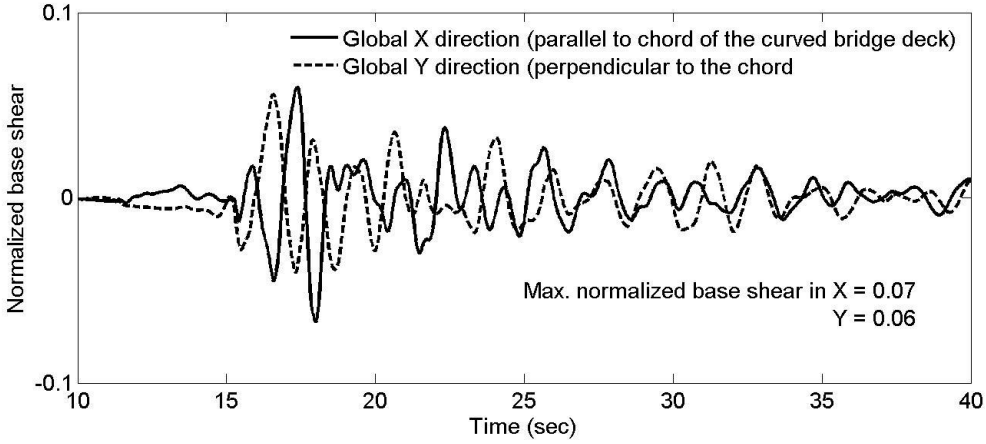

Figure 6.18: Normalized base shear time histories in the global directions

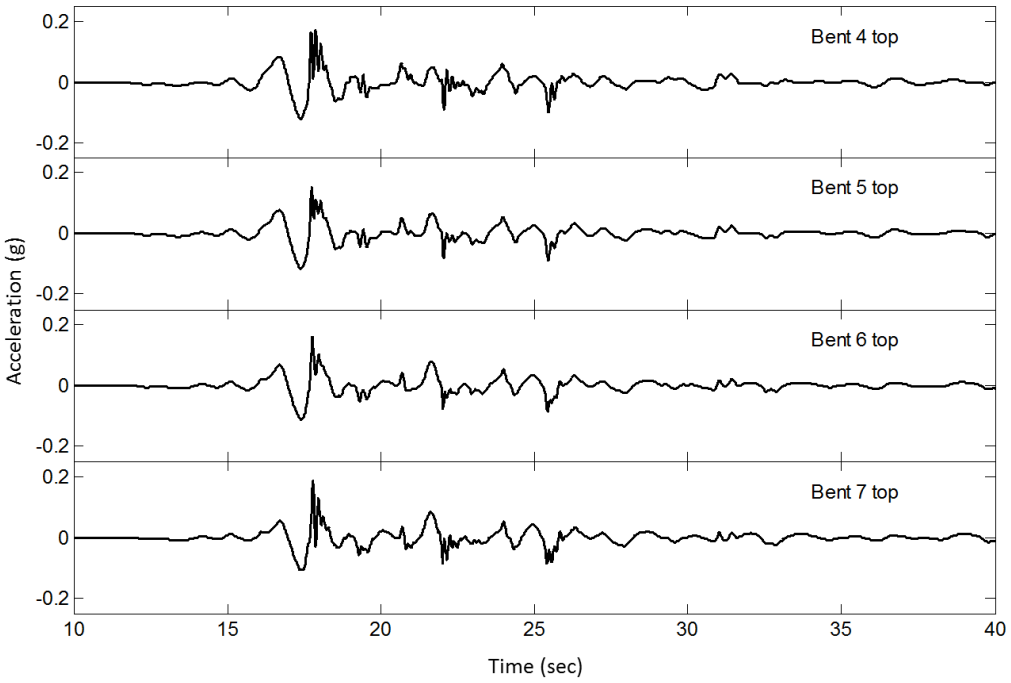

(a) Longitudinal direction

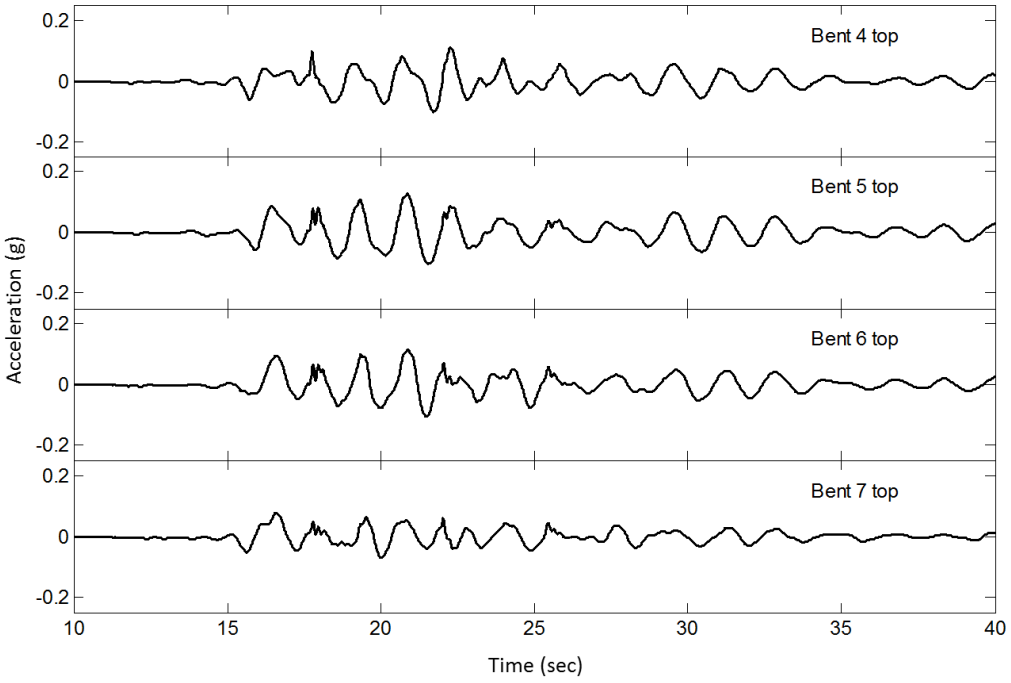

(b) Transversal direction

Figure 6.19: Acceleration time histories at deck locations of frame 2

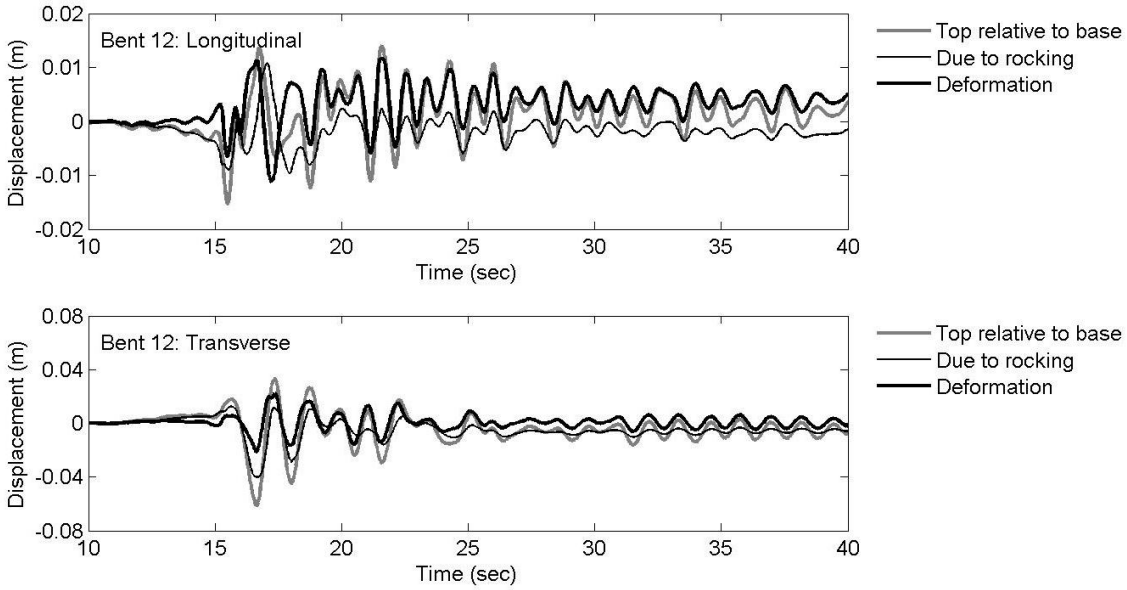

Figure 6.20: Displacement time histories at the top of Bent 12

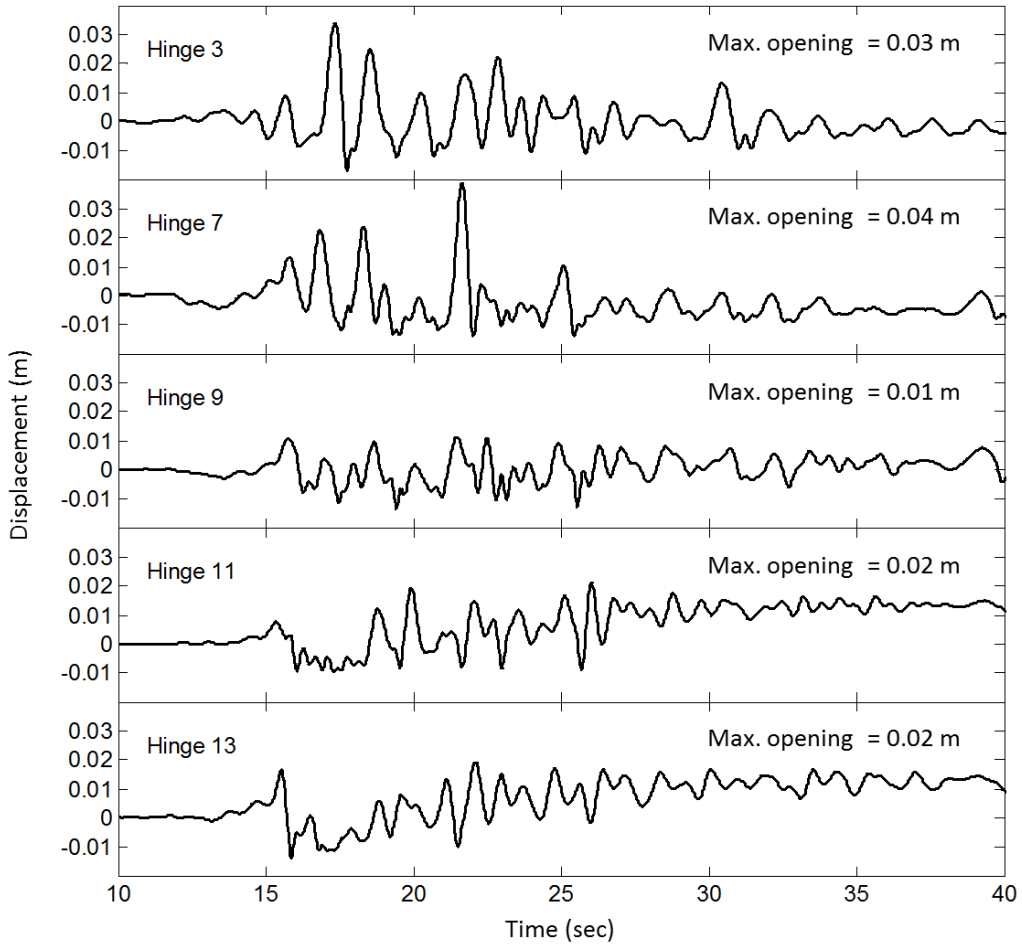

Figure 6.21: Longitudinal hinge displacements

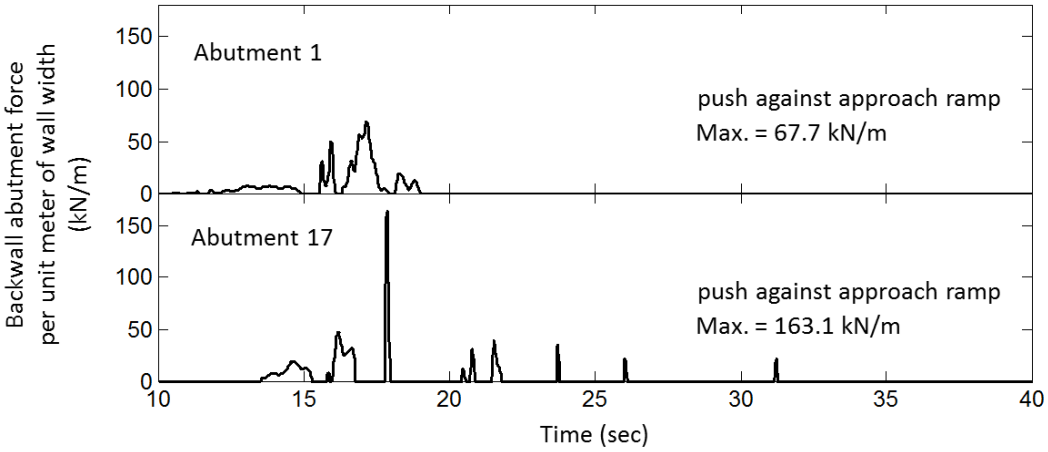

Figure 6.22: Time histories of backwall abutment force per unit meter of wall width (12.5 m)

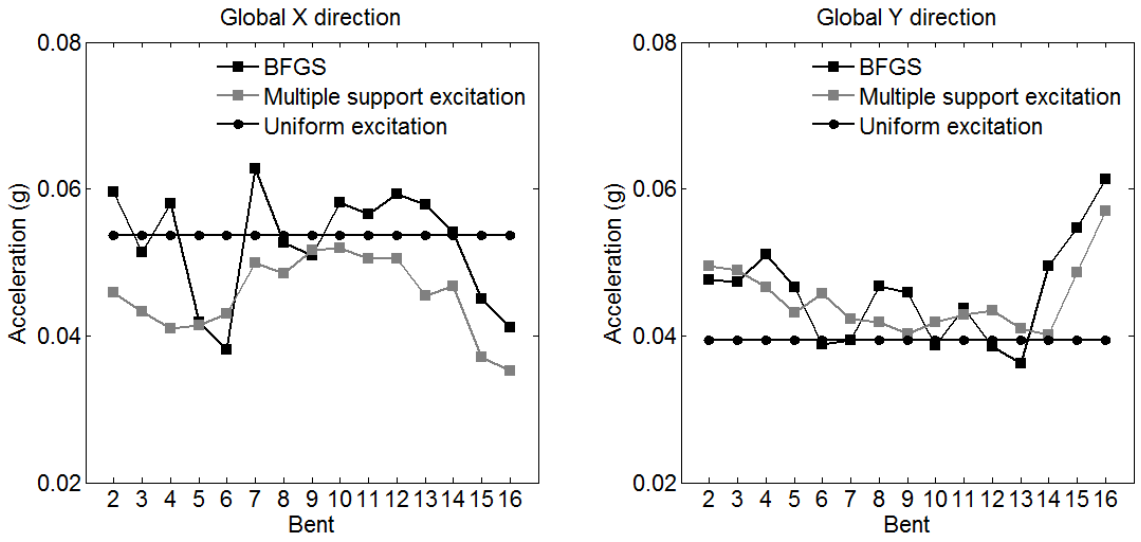

Figure 6.23: Nonlinear soil profile: maximum acceleration at the base of bents for the scenarios of bridge-foundation-ground system, multiple support excitation, and uniform excitation

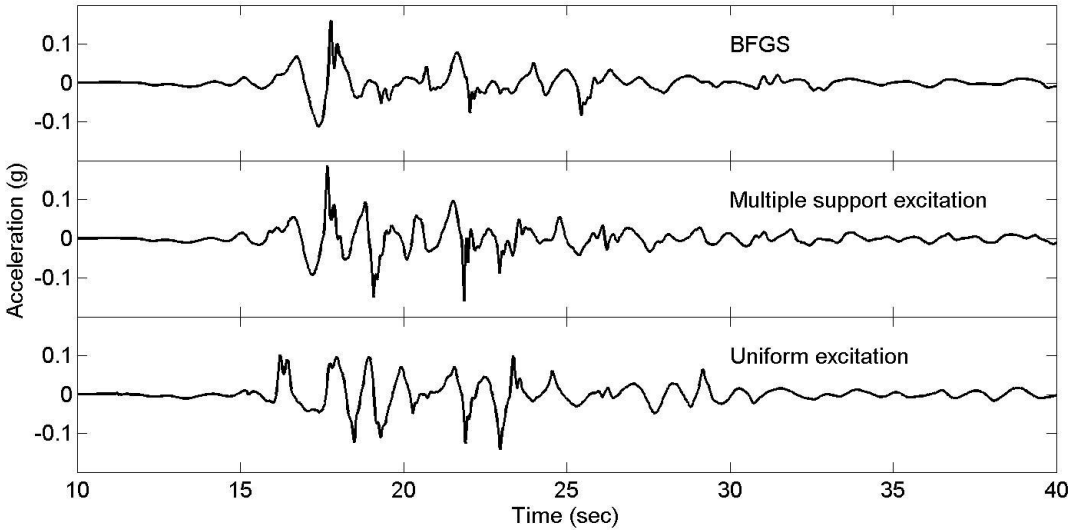

(a) Longitudinal direction

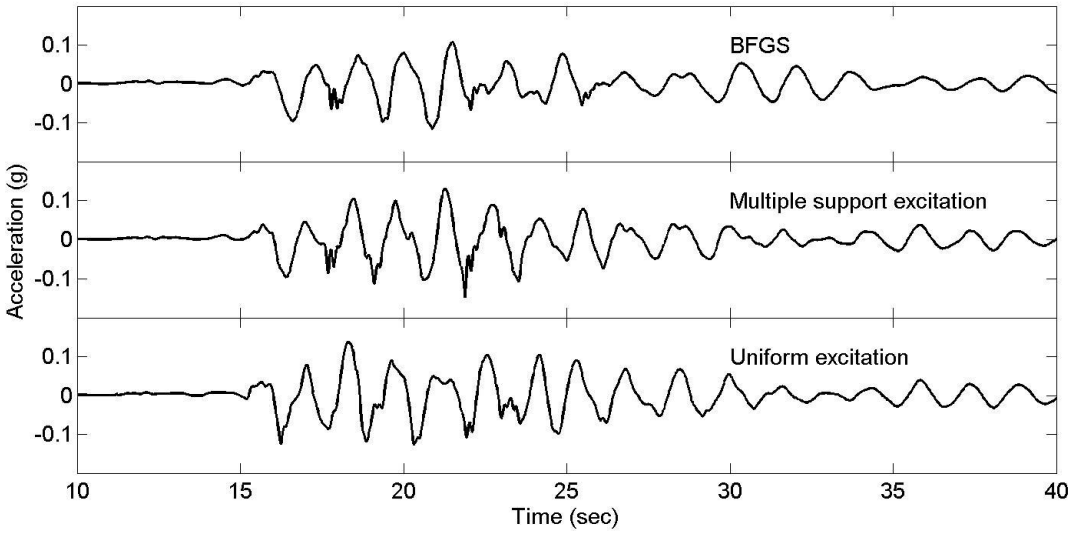

(b) Transversal direction

Figure 6.24: Nonlinear soil profile: acceleration time histories at the top of Bent 6 in the North-West connector

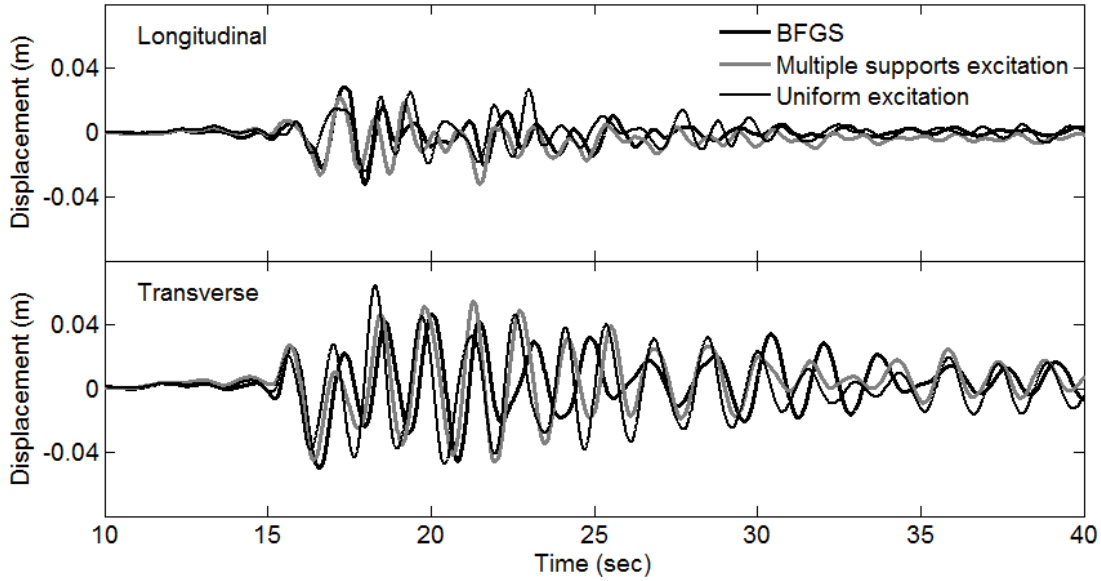

Figure 6.25: Displacement (excluding rocking-induced displacement for the BFGS) time histories at the top relative to the base of Bent 6 in North-West connector

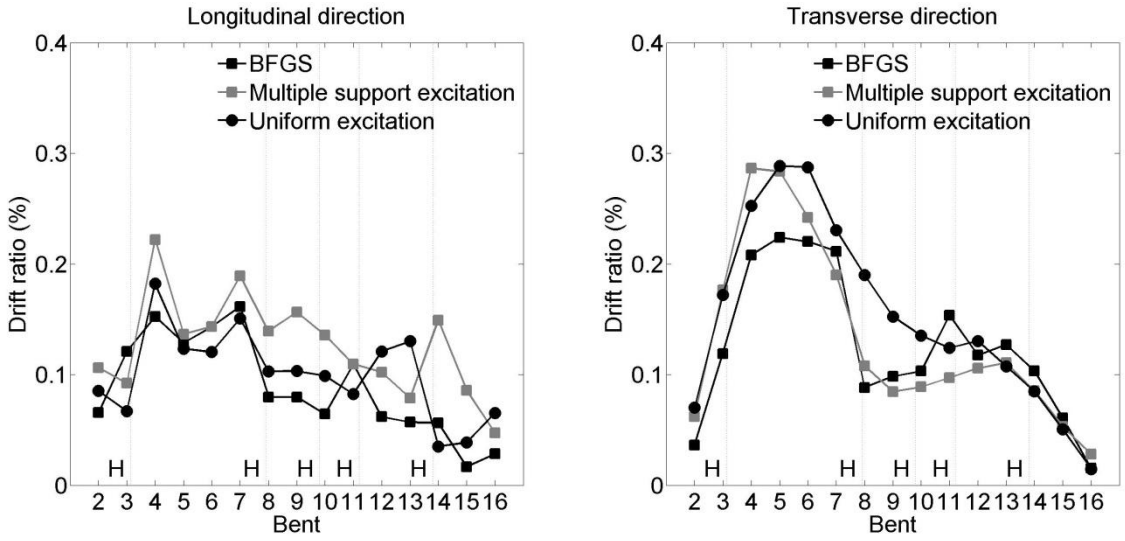

Figure 6.26: Maximum drift ratios at the top of the North-West connector bents

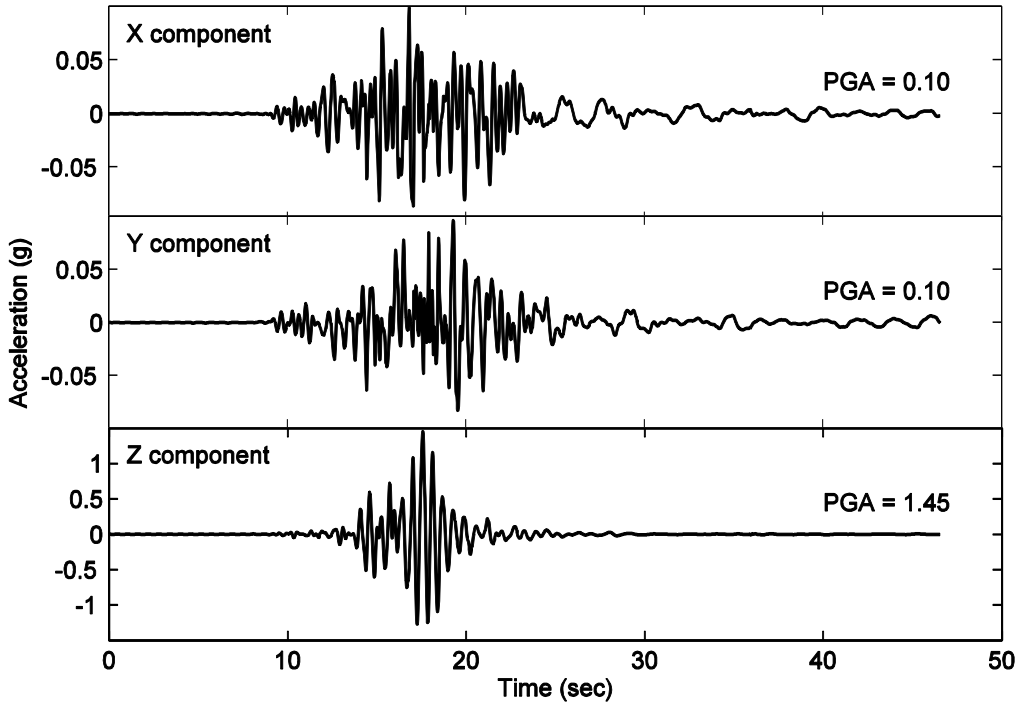

Figure 6.27: Acceleration time histories at the ground surface center node for the broadband input

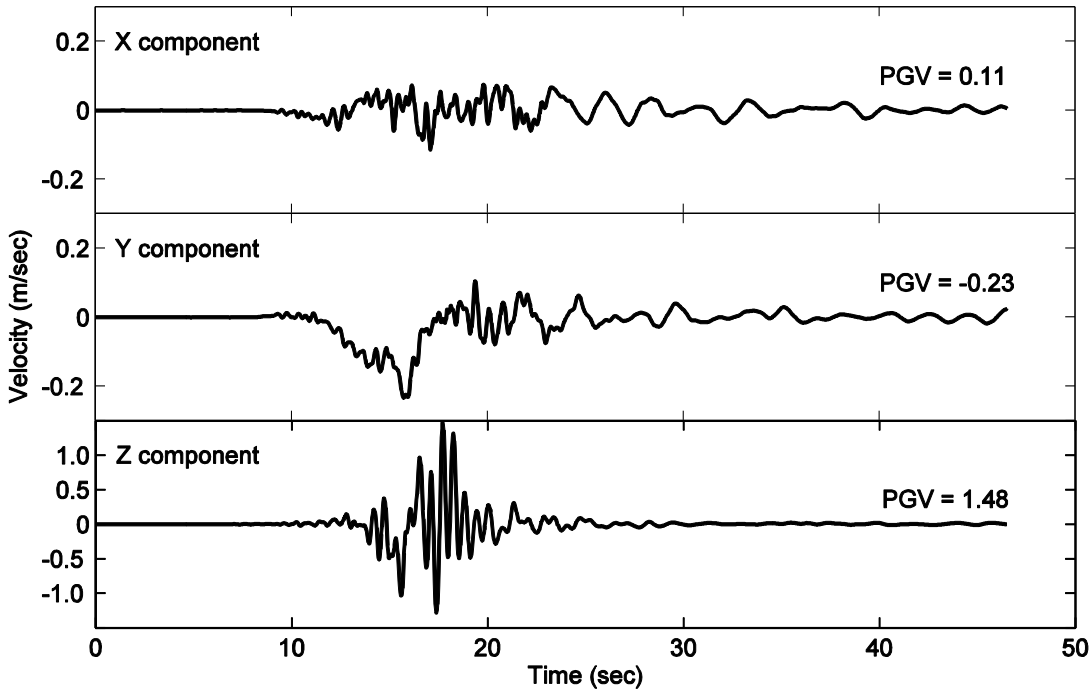

Figure 6.28: Velocity time histories at the ground surface center node for the broadband input

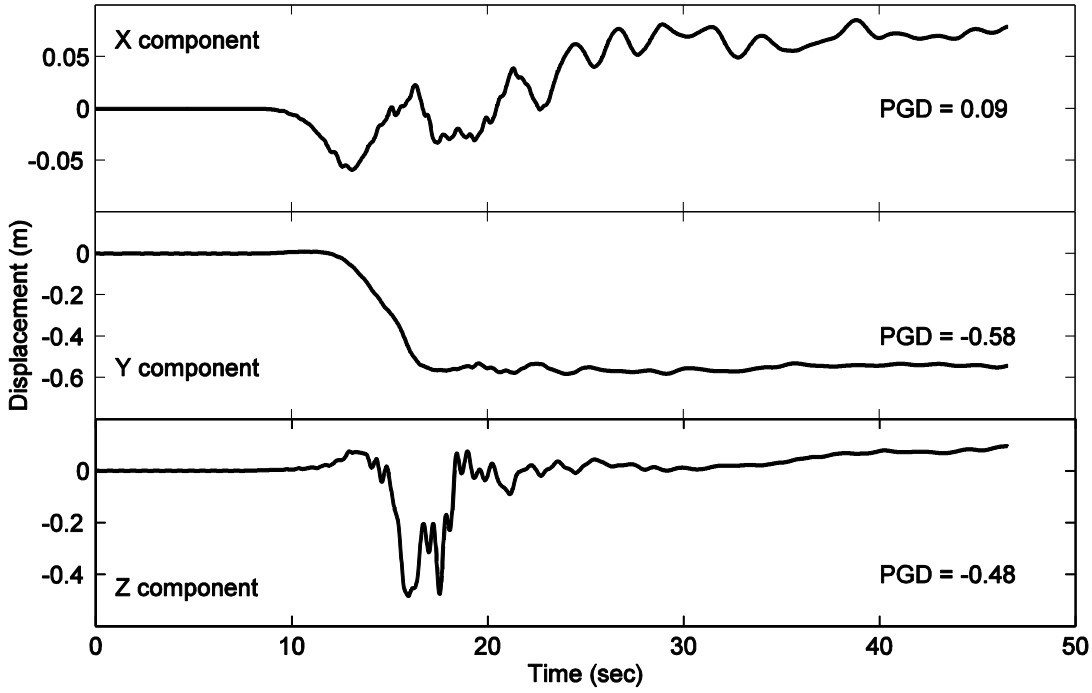

Figure 6.29: Displacement time histories at the ground surface center node for the broadband input

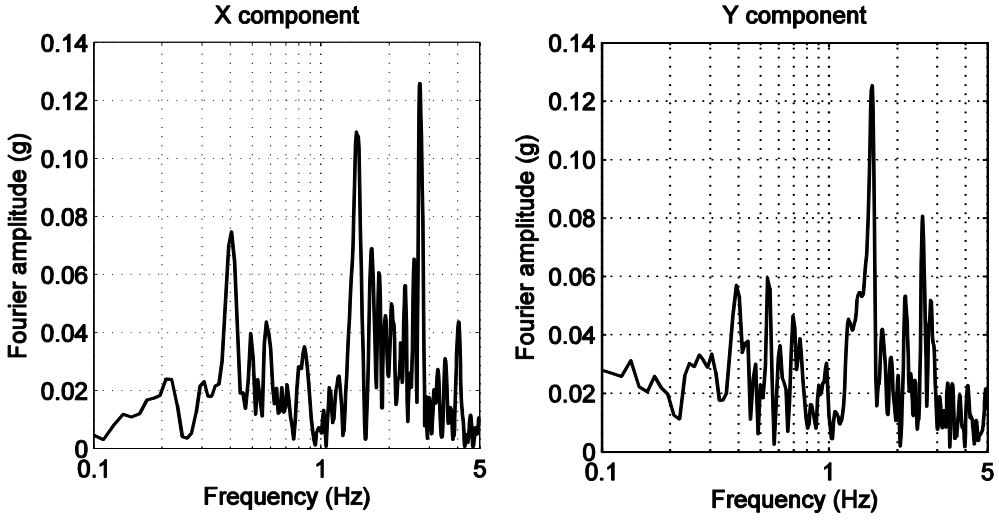

Figure 6.30: Fourier amplitude spectra of ground accelerations at the ground surface center node for the broadband input

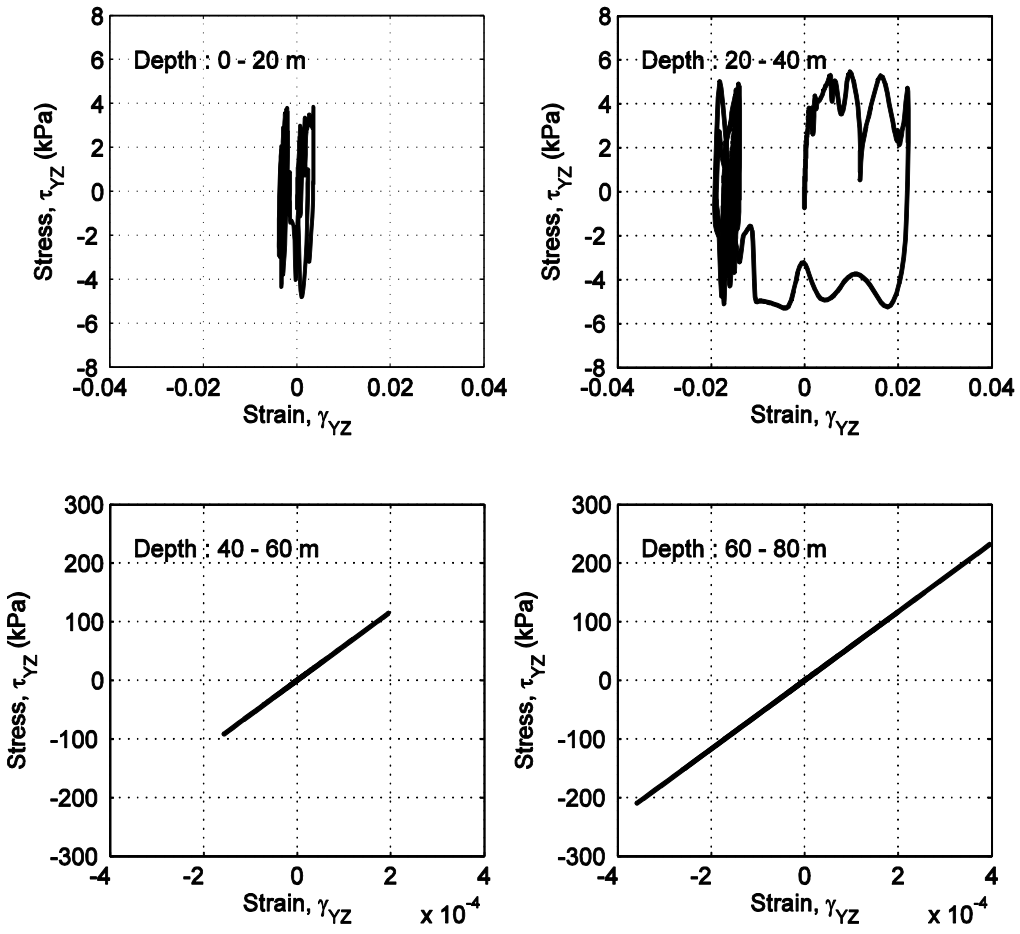

Figure 6.31: Shear stress-strain response (yz) at different depths below the ground surface center node for the broadband input

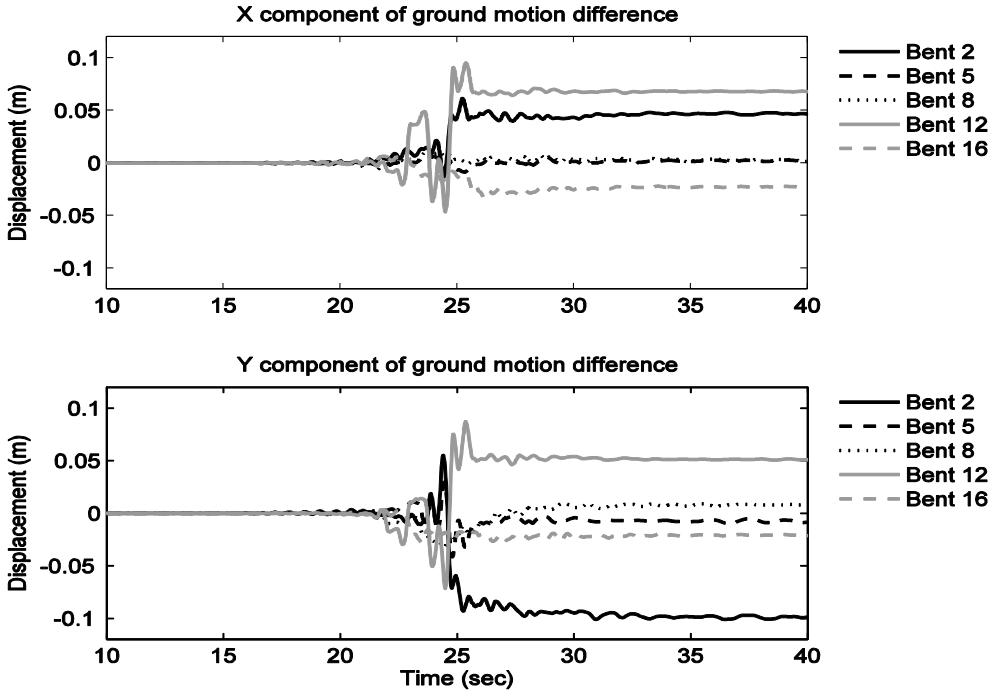

Figure 6.32: Difference in ground displacements in the presence of the structure and free-field under the base of bents 2, 5, 8, 12, and 16 for the broadband input

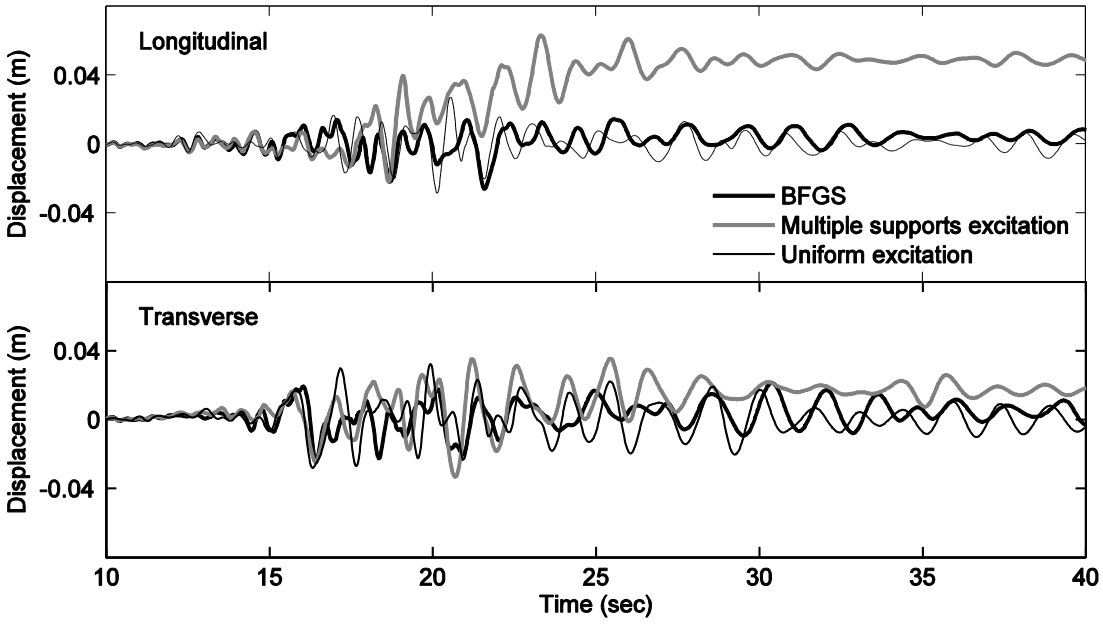

Figure 6.33: Displacement (excluding rocking-induced displacement for the BFGS) time histories at the top relative to the base of Bent 6 in the North-West connector for the broadband input

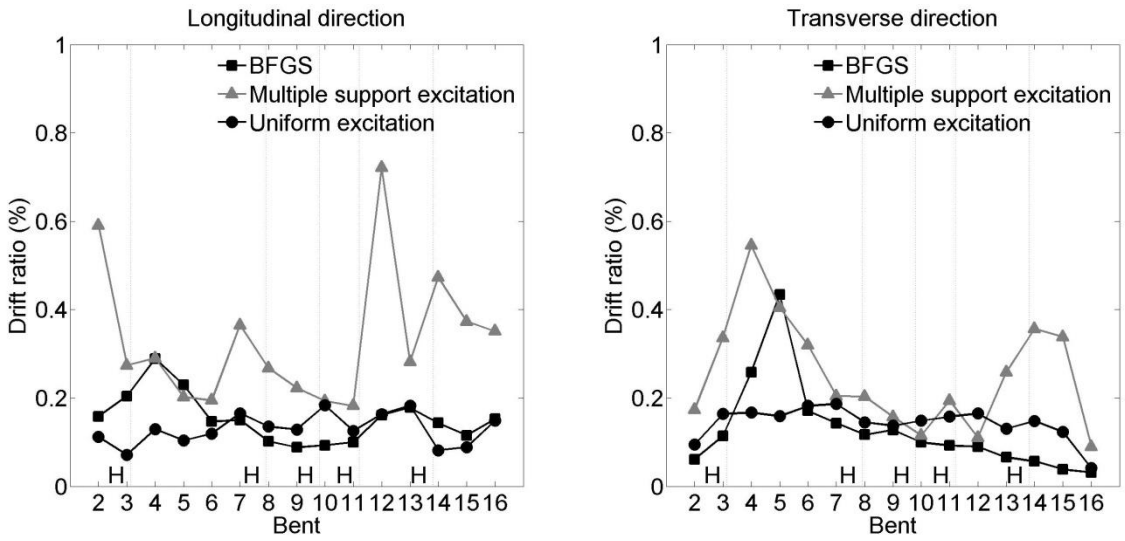

Figure 6.34: Maximum drift ratios at the top of the NW connector bents for the broadband input

Chapter 7

Three-Dimensional Seismic Response of the NW Connector Bridge-Foundation-Ground System

This chapter presents seismic response simulations of the North-West connector at the interstate 10 and 215 interchange. A three dimensional (3D) bridge-foundation-ground system is modeled with nonlinear properties of the ground based on the actual local site conditions. Efforts include implementation and validation of a transmitting boundary at the base of the soil domain. Using this formulation, the bridge-foundation-ground system response is compared and validated against earthquake records at the bridge and local site. Under a potential site specific strong ground motion at this

geographic location, an emphasis is placed on studying the response of this system in terms of displacement and force demands

7.1 Introduction

An effort is made to study the North-West connector bridge-foundation-ground system (BFGS) using a strong site specific earthquake motion. This BFGS is developed on the basis of the structural configuration and local soil condition of the North-West connector (NW) at the interstate 10 and 215 interchange (I-10/215).

The first part of this chapter describes the implementation and validation of a base shaking transmitting boundary for the employed soil domain. Using this transmitting boundary (TB), results from the BFGS based on linear behavior (as conducted earlier in Chapter 4) are compared and validated against the DRM response (presented earlier in Chapter 4). Development of the site-specific ground domain properties is then presented based on the available information at this location. Using the bridge and foundation models developed earlier in Chapter 4, the BFGS response is compared with available recorded earthquake motions at the site. The effort to develop the employed site specific base excitation is then presented. Simulation results for the BFGS are shown during this site specific strong earthquake event. Finally, the BFGS response (linear columns used in the bridge structure) is compared with those obtained from a nonlinear column bridge model representation for this BFGS.

7.2 Implementation and validation of transmitting boundary conditions

7.2.1 The Lysmer-Kuhlemeyer transmitting boundary

In modeling the ground, it is appropriate to limit the depth of the soil domain for computational efficiency. For the BFGS considered in this study, the computational soil base is located at a depth of 60 m. During seismic excitation, soil strata below this depth can be replaced by a TB. For that purpose, the Lysmer-Kuhlemeyer (1969) boundary is employed along the base of the ground domain to avoid spurious wave reflections as a simple and effective numerical approach. At each base node, three dashpots are activated, two in the horizontal (shear) directions, and one in the vertical (normal) direction. As such, an incident seismic wave is defined by three dynamic equivalent nodal forces. The description of a one dimensional shear wave equation framework to obtain the nodal force is presented in Zhang et al. (2003). Implementation of the TB for a two dimensional (2D) BFGS model can be found in Zhang et al. (2008) and for a 3D BFGS model in Elgamal et al. (2008).

7.2.2 One dimensional wave propagation application

To validate the TB, a 2D plane strain rectangular soil domain with size of 25 m in width by 60 m in height (uniform element size of 1 m) is employed. The natural frequency of this soil domain is 0.44 Hz for the fixed base case. System modeling and response computations are performed using the OpenSees framework (McKenna, 1997). The soil domain is homogeneous, elastic, and undamped (shear wave velocity of 548 m/s;

mass density of 2000 kg/m^3; Poisson's ratio of 0.4). The Newmark-β time-stepping method is employed to integrate the equation of motion with the integration parameters γ = 0.5 and β = 0.25. Horizontal dashpots are defined at each node along the ground base. For the lateral boundaries, a shear beam condition is used to enforce identical translations in the horizontal and vertical directions. The coefficient of the dashpots tangential to the base boundary is defined as ρV_s, where ρ and V_s are the density and shear wave velocity of the soil base material. For the purpose of comparison, a fixed-boundary condition (FB) is employed along the base of the soil domain to check spurious wave reflections within the soil domain.

A single Ricker wavelet with a peak acceleration of 0.05g at a frequency of 3.9 Hz is used as an incident wave at the soil mesh base. Figure 7.1 shows the total acceleration time histories along the depth. For the FB (Figure 7.1a), it is clearly shown that the propagated wave is reflected back into the soil domain, while the boundary absorbs the wave for the TB case (Figure 7.1b).

In addition, Cyclic1D, a PC-based graphical user interface for execution of site response simulations (Elgamal et al., 2006), is used to check these responses. The resulting acceleration time history at ground surface is shown in Figure 7.2a. The absolute peak acceleration profile is shown in Figure 7.2b.

7.2.3 3D simulation application

To further explore the performance of the TB, a part of the ground model (region of interest, ROI) considered earlier in Chapter 4 is employed. The 60 m top layer of the ROI (Figure 7.3) is analyzed with and without the bridge structure (NW). To maintain

simplicity, linear soil is considered (see Table 2.2 for the soil properties). Horizontal and vertical dashpots are prescribed at the soil domain base for the tangential and normal components. Along the soil domain depth, lateral boundaries are constrained to be identical in the horizontal and vertical response directions (i.e. shear beam condition).

For an input motion, soil response at the depth of 60 m in the ROI is considered (results from the study of Chapter 4). Figure 7.4 (a-c) shows the total acceleration time histories along depth below the center node in the X, Y, and Z directions, respectively. The acceleration at the 60 m depth is then integrated into a velocity for the equivalent nodal force dictated by the dashpots, representing the underlying layer below this depth.

Responses resulting from the soil domain without the structure (i.e. free-field) and with the structure (considered as the BFGS) are presented below. These responses are compared with those shown earlier in Chapter 4.

7.2.3.1 Comparison of the ground response

Figure 7.5 shows the ground displacement time histories along the center line in the global X direction at the ground surface relative to the center node. These displacements are compared to the DRM response (discussed earlier in Chapter 4). Under the TB condition, essentially zero displacements are observed over the surface in view of the imported uniform base excitation. Conversely, the non-uniform DRM excitation displays variation along the surface reaching peaks of 0.06 m and 0.11 m (X and Y components).

Figure 7.6 shows a comparison of the acceleration time histories at the center node. Close agreement can be seen between the TB and the DRM results. In the

corresponding Fourier amplitude spectra (Figure 7.7), a relatively small difference reaching about 10% is observed. In terms of velocities at ground surface, the peak difference is only 6.5 % for the X component (Figure 7.8). In the displacement response, much less differences (about 3%) are observed (Figure 7.9).

7.2.3.2 Comparison of the BFGS response

Figure 7.10 shows the normalized total bridge column base shear in the X and Y directions. For this normalized force, the sum of the column base shear forces is divided by the self-weight (160.0 MN) of the NW. The base shear slightly decreases under the TB condition (i.e. uniform base excitation). The base shear decreases 3.9% for the X component (corresponding to longitudinal direction near Bent 8) and 14.3% for the Y component (corresponding to transverse direction near Bent 8).

In addition, deformation in the columns is compared. To calculate this deformation, top column displacement relative to the base is reduced by the amount resulting from rocking at the foundation. As such, the maximum drift ratio due to deformation only is shown in Figure 7.11. Using the TB, the transverse drift ratios are generally somewhat underestimated, compared to those from the DRM excitation. At Bents 3 and 7, the ratios decrease by about 24%. The drift ratios from Bent 10 to Bent 15 agree well with those under the DRM excitation (less than 6%). It is noted that local areas under Bent 2 through Bent 8 were subjected to higher ground accelerations under the DRM excitation (i.e. non-uniform base excitation). On the other hand, the longitudinal drift ratios decrease about 19% at Bent 2 and increase about 16% at Bent 7. Meanwhile,

the ratios at Bents 11 through 16 are different by less than 0.2%, compared to the DRM response.

7.3 Definition of the bridge-foundation-ground system

Development of the soil domain properties are based on the actual soil characteristics at the site of the I-10/215. In the BFGS using this soil domain, the NW is employed as the bridge structure as conducted earlier in Chapter 4. Using one of the past earthquake events (Landers Earthquake 1992), the BFGS response is compared with the actual recorded motion (on the bridge and at the ground surface).

7.3.1 Bridge structure

The NW is considered as the structural model in this BFGS simulation. Calibration of this structural model was described earlier in Section 3.2.3. The dynamic properties for the NW were also discussed in Section 3.2.4. Modeling of the pile-group foundation can be found in Section 4.1.2.2.

7.3.2 Soil domain

7.3.2.1 Evaluation of the shear wave velocity

As discussed earlier in Section 3.1.1, the I-10/215 local site generally consists of stratified layers of loose to very dense sand, silty sand, and gravelly sand (see Figure 3.7 for the soil profile). The shear wave velocity profile is idealized using measured data at

the nearby geotechnical array (I10/215 W Geotech Array; CSMIP station No. 23793; see Figure 7.12). Adapted from this station, the idealized profile is shown in Figure 7.13.

7.3.2.2 Ground model

As defined earlier, the dimensions of the ground domain are 1000 m by 500 m by 60 m (Figure 7.3). Based on the discretization of the soil profile for the shear wave velocity, the ground model consists of 10 layers. Soil material properties in each layer (Table 7.2) are based on the field data measured by borehole 1 (B-1) in the log of the test boring (LOTB) sheet provided by Caltrans (Personal Communications). The layers 1 through 4 are refined down to a 2.5 m thickness for numerical accuracy to be one-fifth of the shortest wavelength considered in the analysis. Below layer 4, the thickness varies from 5 m for Layer 5 and 6 to 10 m for the remaining layers. Through these defined layers, Figure 7.14 shows the bridge-foundation layout.

The 60 m thick layer is modeled as a nonlinear hysteretic material (Prevost, 1978; Parra, 1996) with a Von Mises multi-surface (Iwan, 1967; Mroz, 1967) kinematic plasticity model (Pressure IndependMultiYield model in OpenSees). This material is to reproduce the soil hysteretic elastoplastic shear response with permanent deformation. The nonlinear shear stress-strain backbone curve is represented by the hyperbolic relation (Kondner, 1963) defined by two material constants in terms of low strain shear modulus and ultimate shear strength.

The TB is defined at each node along the ground base. The coefficient of dashpots in the normal and tangent directions is based on the material properties of the underlying layer below the base. Along the soil domain depth, lateral boundaries are constrained to

be identical in the horizontal and vertical directions (i.e. shear beam condition). The entire FE model for the BFGS in this subsection is shown in Figure 7.15.

7.3.3 Input excitation

7.3.3.1 Earthquake motion

The BFGS model is implemented and validated using an earthquake ground motion recorded at the local site. The Landers Earthquake (magnitude of 7.3) in 1992 is considered. During this earthquake, the geotechnical array (I10/215 W Geotech Array; CSMIP station No. 23793) did not capture this particular event. Consequently, free-field motions recorded at a nearby strong motion station (San Bernardino – E & Hospitality, CSMIP Station No. 23542) are used. This station exists approximately 280 m east of Bent 8 in the NW (see Figure 7.16 for the location). Figure 7.17 shows the acceleration time histories recorded at this station. These motions are reoriented into the global coordinate system of the BFGS.

7.3.3.2 Deconvolution

In order to derive an incident earthquake motion at the ground base (60 m depth), the computer program Shake 91 (Idriss and Sun 1993) is used for deconvolution (Kramer 1996). Peak accelerations of the computed incident motion at this depth are 0.032g, 0.034, and 0.033g in the X, Y, and Z directions, respectively, compared to 0.085g, 0.089g, and 0.051g at the ground surface (Figure 7.18).

7.3.3.3 Synchronization of free-field and bridge motion records

The strong motion station (CSMIP Station 23631) includes the instrumentation of the NW (as shown earlier in Figure 3.8). The motions recorded at this station are not time synchronized with the free-field motion (as mentioned above) during the same earthquake event. To estimate time lag between the free-field and the structure records, a cross-correlation analysis is performed Figure 7.20. To reduce soil-structure interaction (SSI) influences, vertical displacements at the free-field and base of bent 8 in the NW are used. Figure 7.20 shows the vertical displacement time histories for the free-field and base of Bent 8 with the time lag removed.

7.3.4 Response comparison

Results obtained from the BFGS model are compared to the recorded response (Landers 1992). Figure 7.21 shows a comparison of the free-field motions (recorded at the CSMIP Station No. 23542) to the computed motions at the ground surface. A good agreement is observed. The Fourier amplitude spectra of these accelerations are compared as shown in Figure 7.22. Although amplitudes at higher frequencies are slightly overestimated by the model, the computed response matches well with the recorded motion.

Figure 7.23 shows a comparison of total displacement in the NW (CSMIP Station 23631; see **Error! Reference source not found.** for the locations). Although the ongitudinal (ch.17 at Hinge 7 and ch.10 at Hinge 3) and the transverse (ch.7 at Hinge 3) responses are slightly overestimated by the model, the computed response generally

agrees with the records. Frequency content appears to be also close. The lower frequency vibration periods in this comparison are in good agreement as well.

Figure 7.24 shows a comparison of total acceleration in the NW (in the time window 10 to 50 sec). In the longitudinal responses at certain locations (ch.17 at Hinge 17 and Ch.10 at Hinge 3), the BFGS model produces higher peaks and frequency content due to the lack of energy dissipation in the hinge model. Nevertheless, it appears that transverse computed motions are comparable to the recorded response in terms of the magnitude of acceleration and phase of the lower frequency components.

7.4 Seismic response of BFGS for a site-specific ground motion

The developed BFGS representing the NW at the I-10/215 local site is analyzed for a site specific strong earthquake scenario. A recorded earthquake motion from Northridge 1994 is considered as the input, as detailed below. Seismic response of the BFGS is presented and discussed.

7.4.1 Seismic vulnerability of the interchange site

The I-10/215 site is located in a highly seismic region. Based on the California Geologic Survey (Jennings and Bryant, 2010) and Caltrans ARS Online tool (http://dap3.dot.ca.gov/ARS_Online/), the San Bernardino section of the San Jacinto fault zone is present approximately 300 m northeast of the site. In addition, the San Bernardino Valley section of the fault zone exists approximately 485 m southwest of the bridge. Both of these faults are right lateral strike slip with 90 degrees dipping. On the basis of the

distance from the fault to the site, the San Bernardino section of the San Jacinto fault is a predominant source for a potential strong earthquake event with moment magnitude (M_w) of 7.7. The governing characteristics of the fault are summarized in Table 7.1. Based on this potential magnitude, the probability map is shown in Figure 7.25.

7.4.2 Design response spectrum

The design response spectrum is adapted from the Caltrans ARS Online tool as shown in Figure 7.26. Based on the deterministic response spectrum and probabilistic response spectrum specified in Appendix B of the Caltrans SDC (2010), the upper envelope (probabilistic response spectrum; USGS 5% in 50 years hazard) determines the design response spectrum.

7.4.3 Selection of the strong ground motion

Based on the characteristics of the site and fault, a January 17, 1994 Northridge (Moment Magnitude of 6.7) earthquake ground motion is selected as the potential strong ground scenario. Figure 7.27 shows the free-field ground motion recorded at CSMIP Station 24279 (Newhall, Fire station). This station is located approximately 20 km north of the epicenter. To determine principal directions for the horizontal ground acceleration components, a covariance matrix (Kubo and Penzien 1997) is used. Figure 7.28 shows the ground acceleration in the principal directions (only 20 sec shown out of 60 sec). The computed principal axes are 58º and 302º for the major and minor directions, respectively, referred to the direction of Channel 1 (east).

Figure 7.29 shows the pseudo acceleration spectra for the horizontal ground accelerations, with five percent damping, along with the design response spectrum. Although the pseudo acceleration from the major principal acceleration is higher than the target spectrum (i.e. design response spectrum) in the range of 0.5 Hz to 0.8 Hz, the frequency content generally agrees within the main frequency range of interest (less than 1.5 Hz based on the dynamic property of the bridge).

As discussed in Section 7.3.3.2, the incident motion along the base of the ground model is needed. Using the horizontal accelerations in the principal directions and the vertical acceleration (Channel 2), Shake 91 (Idriss and Sun 1993) is used for deconvolution. Figure 7.30 shows the results from the deconvolution as the outcrop motion at 60 m depth (the Shake 91 outcrop motion is twice the incident motion at any depth). As an input to the BFGS model, half of each outcrop motion is used as an incident motion at the base of the ground model (Kramer 1996). For the simulation in this subsection, the principal major direction corresponds to the global Y direction (transverse direction at the Bent 8). As such, the principal minor direction is associated with the global X direction.

7.4.4 Seismic response

7.4.4.1 Free-field response

Figure 7.31 shows the acceleration time history at the ground surface center node, compared to the Northridge earthquake motion recorded at the CSMIP Station 24279 (Newhall, Fire station). Although lower peak ground accelerations are computed in the FE model, the overall response matches well with the records. Fourier amplitude of the

horizontal acceleration is shown in Figure 7.32. In the range of 0.5 Hz to 1.5 Hz (associated with the dynamic property of the bridge), much higher energy is observed for the Y component. This component is perpendicular to the chord of the curved structure geometry (Figure 7.15). Peak ground acceleration along the depth is shown in Figure 7.34.

The soil shear stress-strain response at different depths below the surface center is shown in Figure 7.34 and Figure 7.35 in the global X and Y, respectively. Compared to the response during the Landers earthquake (discussed in Section 7.3.4; see Figure 7.36 for the stress-strain response), some yielding is observed at relatively low strain levels (less than 1%) in the Y direction (at depths from 5m to 30m). Relatively large inelastic deformation at the depth of 10m imposes a limit on the acceleration transferred to the upper layer. Consequently, a lower ground surface acceleration (Y component) is observed as shown in Figure 7.33.

7.4.4.2 Bridge response

Figure 7.37 (a) shows the deformed shape of the BFGS relative to the base of the ground, scaled by a factor of 100. It is shown at the time instant of 5.92 sec when the maximum achieved deformation drift ratio of 1.0 % occurs (i.e. excluding the rocking effect) at the top of Bent 8 (15.2 m height). It is shown that piles are translated with rotation in the transverse direction (Figure 7.37 b). However, it the degree of this deviation is rather small due to the relatively stiff soil properties surrounding the piles. Translation at the pile cap relative to the tip of the pile group is generally less than 0.5% of the pile group length.

7.4.4.2.1 Base shear

Figure 7.38 shows a normalized total NW column base shear in the horizontal directions, for which this base shear is divided by the self-weight (160 MN). In both directions, the base shear demand is observed to be about 70% of the weight.

7.4.4.2.2 Response at top of the columns

Figure 7.39 shows total acceleration time histories in the relatively flexible frame (Bent 4 through Bent 7). Spike response is primarily observed in the longitudinal direction due to the pounding by hinge opening and closing known as a "head-on impact" (Malhotra et al., 1995). A small level of this spike response is also generated in the transverse direction. Compared to the peak ground acceleration of 0.6g in the global Y direction (associated with the transverse direction at Bent 8), the peak acceleration reaches about 2g in the transverse direction at Bent 6. Acceleration responses at other locations can be found in Appendix F.

The site-specific strong ground motion induces large displacement demands in the columns. Table 7.3 summarizes the maximum top column displacement relative to the base as well as deformation (excluding the rocking effect). It appears that rocking at the foundation slightly reduces the displacement demand (Figure 7.40). In addition, the maximum drift ratio (due to deformation only) is computed (Table 7.3). Corresponding to the prominent flexible direction in the bridge, the transverse drift ratio is generally larger than the longitudinal response (Table 7.3). Larger transverse drift ratios are observed in the relatively flexible frames (i.e. with longer columns).

7.4.4.2.3 Column forces

The displacement demands induce significant shear forces and bending moments in the columns. The columns are modeled by fixed-fixed boundary conditions at the pile cap and bridge deck locations. Considering the free rotation of the deck in the transverse direction, maximum bending moments are developed mostly at the base of the columns. During the imparted earthquake excitation, longitudinal response causes the bridge deck in frames 1 and 6 to move towards both abutments, resulting in significant levels of shear force and bending moment in the adjacent columns (i.e. Bents 2 and 16). In the transverse direction, the relatively flexible columns experience larger shear force and bending moment (see Table 7.4 for the maximum forces in all the columns).

For each column, in order to compare the load demands with the capacity, a pushover analysis is conducted. For this analysis, fiber section nonlinear beam-column elements are used. In the fiber section, the uniaxial Kent-Scott-Park model with degraded linear unloading/reloading stiffness (i.e. Concrete02 in OpenSees; see Table 7.5 for constitutive model parameters) is used for the concrete material. The reinforcing steel is presented by a uniaxial Gluffre-Menegotoo-Pinto model with isotropic strain hardening (i.e. Steel02 in OpenSees). Effects of the steel jacket are not considered in this study. A static axial force based on self-weight of the pertinent deck segments is imposed. The base of the column is fixed in translations and rotations. At the top of the column, the rotation is constrained to be zero and a lateral force is applied.

In general, the load demand is greater than the idealized capacity in most of the columns. In the longitudinal direction at Bent 7, the shear force and bending moment

exceed 32% and 35% of the peak strength reaching 9 MN and 80 MN-m, respectively (Figure 7.41b). In the transverse direction, the shear force exceeds 12% of the peak strength (12MN). The bending moment demand is about twice as high as the strength of 103 MN-m (Figure 7.41c). Details for the other columns will be discussed in the following section.

7.4.5 BFGS response with the nonlinear bridge columns

In order to further compare the seismic demand, the bridge is modeled with nonlinear columns in the BFGS. As discussed in the previous section, in the BFGS, a simple bridge model is developed for analyzing performance of the columns with bilinear moment-curvature behavior. This behavior is essentially based on the pushover analysis as described in the previous section.

7.4.5.1 Definition of the nonlinear column

In the NW, the bridge columns are modeled with bilinear behavior (in the moment-curvature relationship) whose properties are: (1) initial stiffness (identical to the elastic stiffness in the linear bridge columns); (2) post-yield stiffness with a hardening ratio of 0.01; (3) idealized moment capacity based on the previous pushover analysis.

For simplicity, the steel jacketing is not considered in computing the capacity. However, as discussed earlier in Chapter 3 (see Section 3.2.3.2.2), the 15% (full jacket) and 10% (partial jacket) stiffness enhancement by the jacketing takes into account the initial stiffness. For axial and torsional behavior, the column remains elastic as modeled

in the linear case. The moment capacities defined in the longitudinal and transverse directions are summarized in Table 7.6.

7.4.5.1.1 Variation of dynamic properties in the fixed-base bridge model

A fixed-base bridge model (without the foundation and the ground) is analyzed to evaluate the difference in dynamic properties with the linear columns (LC) and the bilinear columns (BC). During the Northridge earthquake (recorded at CSMIP Station 24279; Newhall, Fire station as discussed in Section 7.4.3), the variation of the eigenvalues (i.e. natural periods) in the first mode (transverse) and the second mode (longitudinal) is shown in Figure 7.42. As the ground acceleration input reaches the peak at about 5.4 sec, the period is lengthened up to 3 sec in the first mode (Figure 7.42 a). At this period, the pseudo acceleration (see Figure 7.29) is 0.2 g about four times as low as that at 1.5 sec. (the fundamental period in the linear column bridge model; as defined earlier in Chapter 3). In the second mode (Figure 7.42 b), the period lengthening (about 50%) is also observed in the BC bridge model. This lengthening induces a lower acceleration amplitude about 60%, compared to the LC model.

7.4.5.2 Comparison of the BFGS response

Figure 7.43 shows a comparison of the normalized total bridge column base shear with the LC and the BC. In the BC case, a large reduction is observed about 52% and 64% in the global X and Y directions, respectively.

Figure 7.44 shows acceleration time histories at Bents 2, 6, 8 and 11 in the longitudinal and transverse directions. In both directions, a significant reduction of the

peak acceleration amplitudes is observed in the BC bridge. The spike response generated by pounding at the hinges is primarily reduced in the longitudinal direction. The high frequency content is also filtered out by the BC (partially due to larger energy dissipation in the nonlinear moment-curvature relation).

Figure 7.45 shows relative top-to-base displacements time histories (excluding the amount resulting from the foundation rocking) at representative locations (for the acceleration). As might be expected, peak displacements are reduced by the BC. In the transverse direction (Figure 7.45 b), permanent deformation is induced by the bending moment exceeding the moment capacity in the BC model (will be discussed later).

In addition, the maximum drift ratio (due to deformation only) is compared in both models (Figure 7.46). In the BC model, the maximum drift ratio is significantly reduced in most of the columns except for Bent 16 (about 6% increase). The maximum reduction of about 51% is observed at Bent 8 in the longitudinal direction. In the transverse direction, the drift ratio is decreased about 32% at Bent 14 (see Table 7.7 for difference in all columns).

Figure 7.47 shows the moment-curvature response and bending moment time histories in the BC base cross-sections. In the longitudinal direction (Figure 7.47 a), the demand at Bent 2 exceeds the capacity of 38 MN-m. Meanwhile, the bending moment at Bent 6, 8, and 11 are observed to be in the elastic range. However, in the transverse direction (Figure 7.47 b), the bending moments reach the defined moment capacity in all the shown representative columns.

As discussed earlier in Section 7.4.4.2.3, the difference of the shear forces and the bending moments induced by the LC and the BC are presented (see Table 7.8 for the

differences in all columns). Particularly, the bending moment response (BC model) in the transverse direction is about three times as low as in the LC model at Bent 12. Shear in the transverse direction is reduced by about 66% at Bent 8. Meanwhile, the longitudinal response is reduced about 55% at Bent 9 for the shear and bending moments.

7.5 Summary and conclusions

Based on the actual local site at the I-10/215, the BFGS model is implemented using the TB. The computed response from this model is validated with the earthquake motions recorded during the Landers earthquake in 1992. During the potential site specific strong earthquake, the ground response and the structural response (displacement/force demands in the linear column) are discussed. These demands are compared with the results of the nonlinear columns with bilinear behavior (the moment-curvature relation). From the results of the present study, the main observations are:

1. The developed BFGS model provides a reasonable agreement with the Landers earthquake 1992recorded seismic response (in terms of free-field and structural acceleration/displacement response).
2. For the site specific strong ground motion, larger displacement/column force demands are computed. In terms of the shear and bending moment in the base of the column, the force demand exceeds the idealized strength in most of the columns (compared to the response resulting from the bilinear column model) for the case studied. However, as the bilinear column model is employed, a large reduction in the seismic response is observed due to the greater energy dissipation in the moment-

curvature response and the variation in dynamic properties (i.e. the period lengthening).

3. During this potential site specific strong earthquake, a limitation in peak acceleration transferred to the ground surface is observed due to the relatively large inelastic deformation emanating from the soil behavior nonlinearity at depths from 7.5 m to 20 m in the ground.
4. The beneficial effect of soil-structure interaction is discussed in terms of the column deformation. Due to the relatively stiff soil properties surrounding the pile foundation, the effect is generally small. However, it appears that the amount from the rocking of the pile-group foundation reduces the deformation in most of the columns.
5. Compared to the case study scenario with spatial variation of ground motion (as discussed earlier in Chapter 4), the seismic response resulting from the uniform base excitation employed by the TB is slightly underestimated in the transverse direction compared to the DRM excitation. On the other hand, the longitudinal deformation is higher/lower depending on the particular column location (for the case studied).

Table 7.1: Governing deterministic fault parameters (adapted from Caltrans ARS online)

Fault Name	San Jacinto (San Bernardino Valley section)
Maximum Magnitude (M_{Max})	7.7
Fault Type	Strike Slip
Fault Dip	90 Degrees
Dip Direction	Vertical
Bottom of Rupture Plane	15 km
Top of Rupture Plane (Z_{tor})	0 km
R_{rup}	0.2 km
R_{jb}	0.2 km
R_x	0.2 km
F_{norm}	0
F_{rev}	0

Table 7.2: Soil layer properties for the ground model at the I-10/215 interchange site

Layer	Depth (m)	Density (ton/m^3)	Poisson's ratio	Shear wave velocity (m/s)	Shear modulus (kPa)	Vertical stress (kPa)	Horizontal stress (kPa)	Friction angle (°)	Shear strength (kPa)
1	0 – 2.5	1.9	0.4	221.15	92,924	46.60	31.08	32	20.58
2	2.5 – 5	1.9	0.4	221.15	92,924	93.20	62.16	35	44.55
3	5 – 7.5	1.9	0.4	197.79	74,330	139.79	93.24	39	73.33
4	7.5 – 10	1.9	0.4	197.79	74,330	186.39	124.32	39	97.77
5	10 – 15	2.1	0.4	244.20	125,231	309.02	206.11	45	182.13
6	15 – 20	2.1	0.4	269.81	152,875	412.02	274.82	45	242.83
7	20 – 30	2.1	0.4	400.22	336,370	618.03	412.23	45	364.25
8	30 – 40	2.1	0.4	607.92	776,090	824.04	549.63	45	485.67
9	40 – 50	2.1	0.4	664.44	927,109	1,030.05	687.04	45	607.08
10	50 - 60	2.1	0.4	613.24	789,733	1,236.06	824.45	45	728.50

Table 7.3: Maximum relative displacements and drift ratios (%) at the top of bents in the North-West connector

			Longitudinal direction			Transversal direction		
Frame	Bent	Height (m)	Top relative to base (m)	Deformation (m)	Drift (%)	Top relative to base (m)	Deformation (m)	Drift (%)
1	2	11.88	0.14	0.12	1.02	0.08	0.08	0.66
	3	16.59	0.18	0.17	1.01	0.27	0.27	1.61
2	4	19.41	0.23	0.22	1.15	0.54	0.53	2.72
	5	24.26	0.22	0.21	0.87	0.65	0.64	2.64
	6	22.50	0.23	0.22	0.99	0.64	0.64	2.83
	7	17.32	0.24	0.23	1.32	0.44	0.44	2.53
3	8	15.24	0.16	0.16	1.02	0.31	0.28	1.87
	9	15.77	0.17	0.16	1.01	0.24	0.24	1.50
4	10	12.88	0.13	0.13	0.97	0.27	0.25	1.98
	11	18.26	0.25	0.26	1.41	0.44	0.43	2.34
5	12	18.80	0.19	0.19	1.00	0.45	0.41	2.16
	13	16.94	0.15	0.14	0.84	0.33	0.31	1.80
6	14	15.62	0.10	0.08	0.48	0.22	0.20	1.26
	15	13.69	0.09	0.06	0.45	0.10	0.09	0.65
	16	7.23	0.06	0.03	0.45	0.03	0.01	0.19

Table 7.4: Maximum shear forces and bending moments in the local directions in the North-West connector

			Longitudinal direction		Transversal direction	
Frame	Bent	Height (m)	Shear force (MN)	Bending moment (MN-m)	Shear force (MN)	Bending moment (MN-m)
1	2	11.88	17.5	113.6	8.9	86.4
	3	16.59	8.3	78.8	10.9	168.2
2	4	19.41	8.1	54.2	14.0	244.2
	5	24.26	4.9	57.5	8.8	190.3
	6	22.50	6.2	69.9	12.9	233.4
	7	17.32	11.6	107.7	13.4	231.1
3	8	15.24	9.5	82.3	14.9	194.1
	9	15.77	11.2	92.7	8.8	150.7
4	10	12.88	12.9	95.8	20.0	254.3
	11	18.26	4.6	70.2	14.3	221.6
5	12	18.80	4.2	50.3	11.0	186.9
	13	16.94	5.8	56.1	10.4	175.4
6	14	15.62	4.5	37.8	7.6	122.2
	15	13.69	7.3	50.1	5.4	70.9
	16	7.23	24.4	91.1	6.6	41.9

Table 7.5: Model parameters for the Concrete02 material (http://cyclic.ucsd.edu/opensees)

Parameters	Description	Value
(a) Confined concrete		
f_{pc}	concrete compressive strength at 28 days	45 MPa
ε_{c0}	concrete strain at maximum strength	0.003
f_{pcu}	concrete crushing strength	9 MPa
ε_u	concrete strain at crushing strength	0.015
λ	ratio between unloading slope at ε_u and initial slope	0.1
f_t	tensile strength	14.65 MPa
E_{ts}	tension softening stiffness '	6.3 MPa
(b) Unconfined concrete		
f_{pc}	concrete compressive strength at 28 days	34 MPa
ε_{c0}	concrete strain at maximum strength	0.002
f_{pcu}	concrete crushing strength	6.9 MPa
ε_u	concrete strain at crushing strength	0.003
λ	ratio between unloading slope at ε_u and initial slope	0.1
f_t	tensile strength	4.8 psi
E_{ts}	tension softening stiffness '	3.2 MPa

Table 7.6: Bending moment capacities and curvatures (no effect of the steel jacketing)

	Longitudinal		Transverse	
Bent	**Moment (MN-m)**	**Curvature**	**Moment (MN-m)**	**Curvature**
2	35.1	0.00136	47.4	0.00090
3	38.0	0.00140	51.2	0.00090
4	84.5	0.00310	108.0	0.00196
5	82.5	0.00310	105.5	0.00191
6	83.4	0.00310	106.6	0.00193
7	79.7	0.00300	103.2	0.00188
8	42.4	0.00165	57.2	0.00109
9	38.1	0.00142	51.2	0.00094
10	55.0	0.00200	73.6	0.00134
11	52.5	0.00195	70.1	0.00126
12	28.0	0.00110	37.7	0.00070
13	29.7	0.00110	39.6	0.00072
14	42.4	0.00165	57.2	0.00110
15	39.1	0.00146	53.0	0.00096
16	49.7	0.00190	66.5	0.00126

Table 7.7: Maximum drift ratio in the bilinear column bridge and reduction of the drift ratio compared to the linear column bridge

			Longitudinal		Transverse	
Frame	**Bent**	**Height (m)**	**Drift ratio (%)**	**Reduction referenced to linear columns (%)**	**Drift ratio (%)**	**Reduction referenced to linear columns (%)**
1	2	11.88	0.85	-16.0	0.58	-11.6
	3	16.59	0.63	-37.5	1.14	-28.9
2	4	19.41	1.01	-12.3	2.10	-22.7
	5	24.26	0.64	-26.3	2.40	-8.8
	6	22.5	0.65	-34.7	2.53	-10.6
	7	17.32	0.93	-29.3	2.41	-4.6
3	8	15.24	0.50	-50.8	1.57	-15.7
	9	15.77	0.56	-45.0	1.10	-26.3
4	10	12.88	0.62	-36.0	1.41	-28.4
	11	18.26	0.93	-34.2	1.66	-29.3
5	12	18.8	0.74	-25.6	1.77	-18.0
	13	16.94	0.79	-5.2	1.46	-19.1
6	14	15.62	0.35	-28.2	0.86	-31.9
	15	13.69	0.38	-15.5	0.47	-27.6
	16	7.23	0.48	6.0	0.17	-13.8

Table 7.8: Maximum shear forces and bending moments in the bilinear column bridge and reduction relative to the linear column bridge scenario

		Longitudinal				Transverse			
Bent	**Height (m)**	**Shear (MN)**	**Reduction referenced to linear columns (%)**	**Moment (MN·m)**	**Reduction referenced to linear columns (%)**	**Shear (MN)**	**Reduction referenced to linear columns (%)**	**Moment (MN·m)**	**Reduction referenced to linear columns (%)**
2	11.88	7.2	-59.2	41.9	-63.1	5.7	-35.9	51.8	-66.8
3	16.59	4.6	-45.3	41.6	-47.2	4.8	-56.6	55.1	-205.2
4	19.41	7.1	-13.1	73.8	-12.3	7.0	-50.0	115.1	-112.2
5	24.26	3.3	-33.5	40.3	-29.9	5.3	-40.6	111.1	-71.3
6	22.5	4.3	-30.8	47.0	-32.8	6.4	-50.4	112.9	-106.7
7	17.32	8.4	-28.0	76.6	-28.9	8.6	-35.9	139.3	-65.9
8	15.24	5.5	-42.5	41.2	-50.0	5.1	-65.7	62.1	-212.6
9	15.77	5.0	-55.0	41.9	-54.8	4.3	-51.6	54.6	-175.8
10	12.88	7.4	-42.8	57.5	-40.0	7.1	-64.4	79.7	-219.1
11	18.26	4.4	-6.6	52.9	-24.6	5.0	-65.0	75.1	-195.0
12	18.8	3.3	-21.5	31.0	-38.3	3.2	-71.0	42.1	-343.9
13	16.94	4.1	-28.9	33.5	-40.3	3.4	-67.6	44.8	-291.8
14	15.62	3.7	-18.6	30.3	-19.8	4.3	-44.1	61.0	-100.2
15	13.69	6.1	-16.6	41.9	-16.5	4.5	-17.6	55.4	-28.0
16	7.23	16.5	-32.6	60.7	-33.4	6.4	-2.7	37.3	-12.2

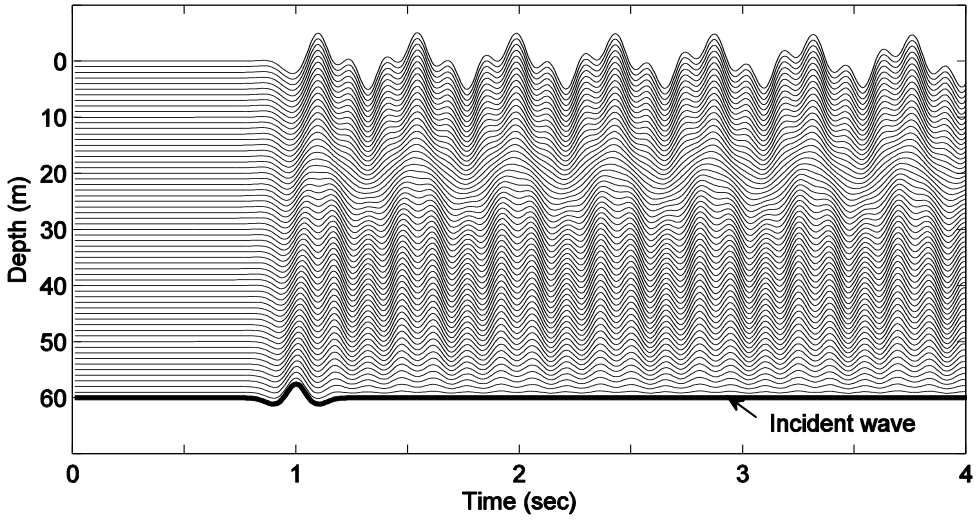

(a) Fixed-base condition

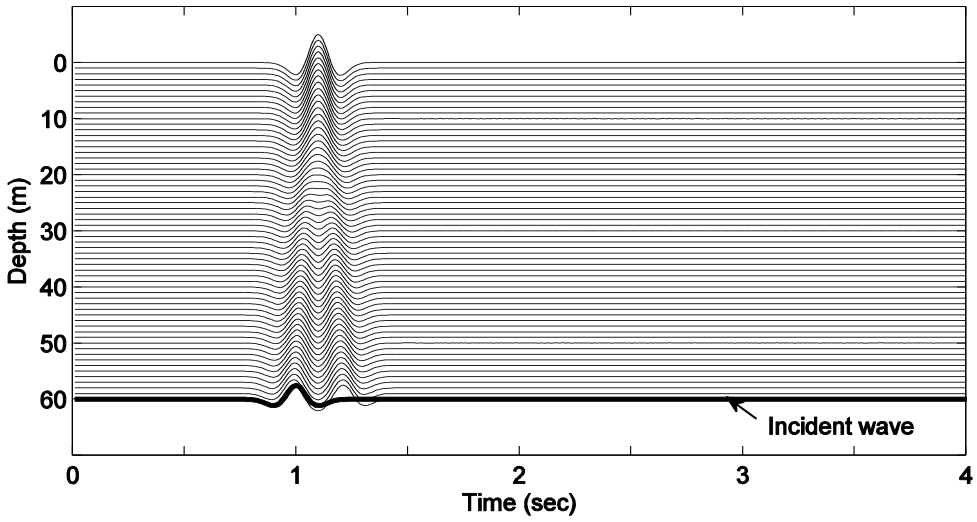

(b) Transmitting boundary condition

Figure 7.1: Wave propagation through the 60 m depth resulting from a single Ricker wavelet as an incident wave

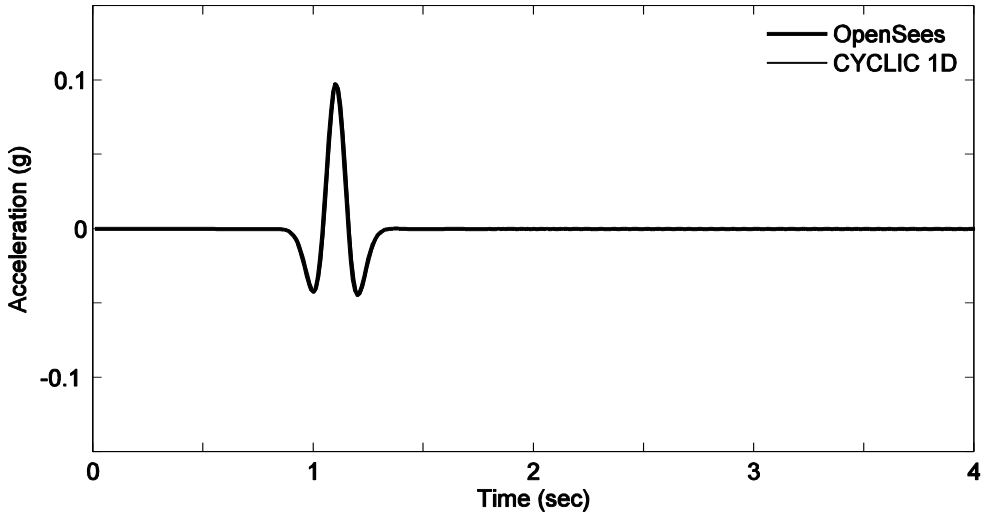

(a) Total acceleration time history at the ground surface

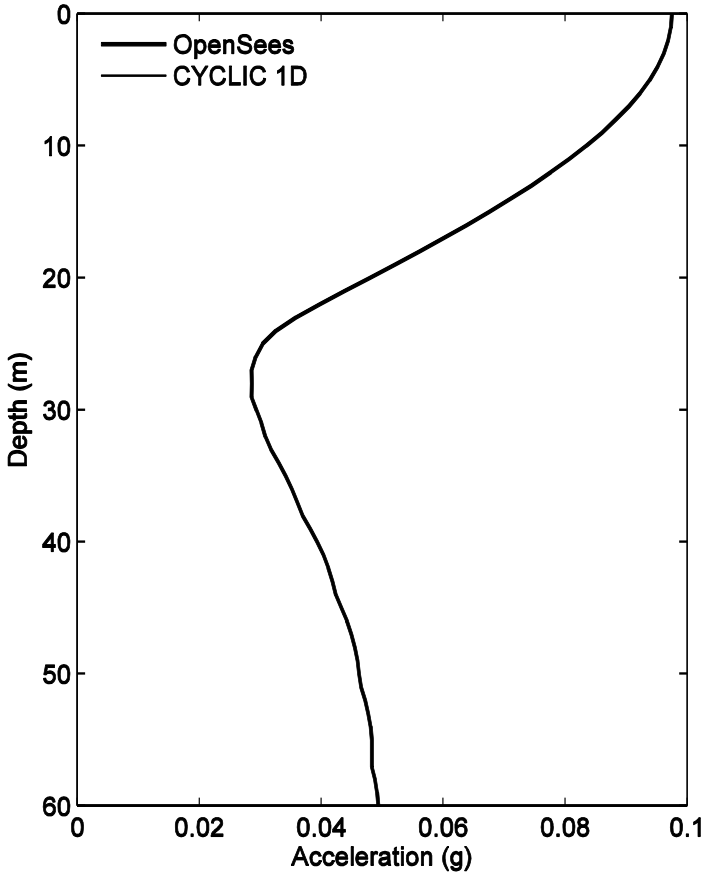

(b) Peak total acceleration profile along the depth

Figure 7.2: Comparison of acceleration response with CYCLIC1D

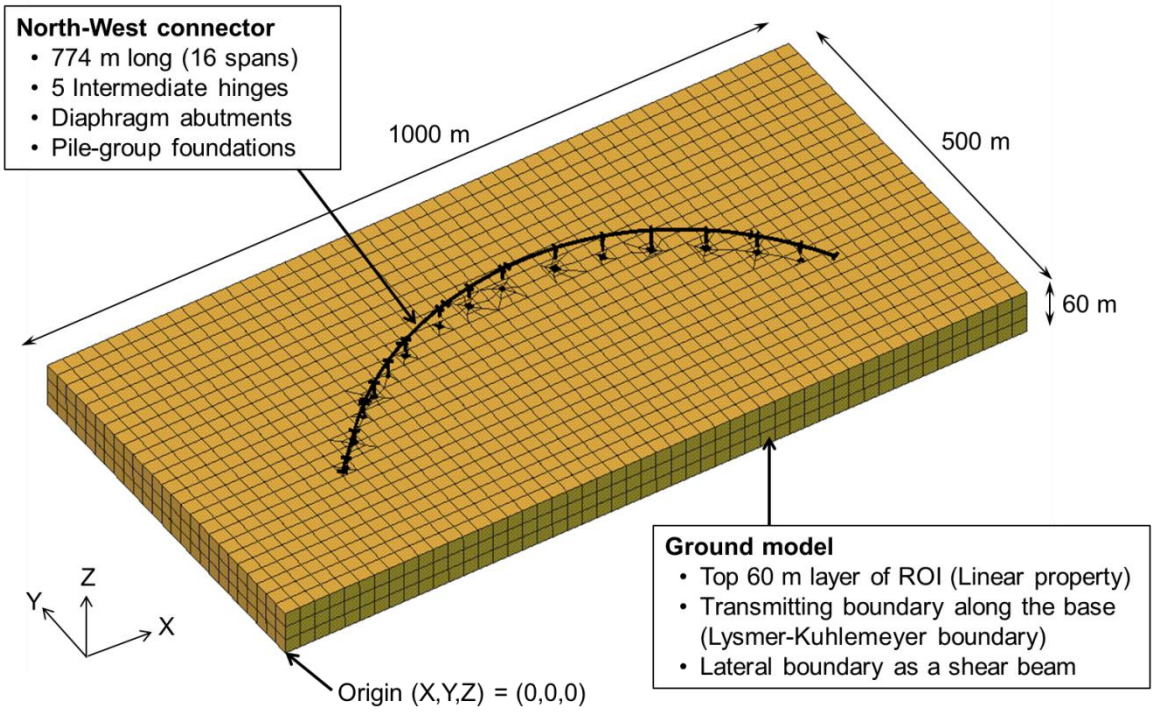

Figure 7.3: 3D model of the BFGS using the transmitting boundary condition

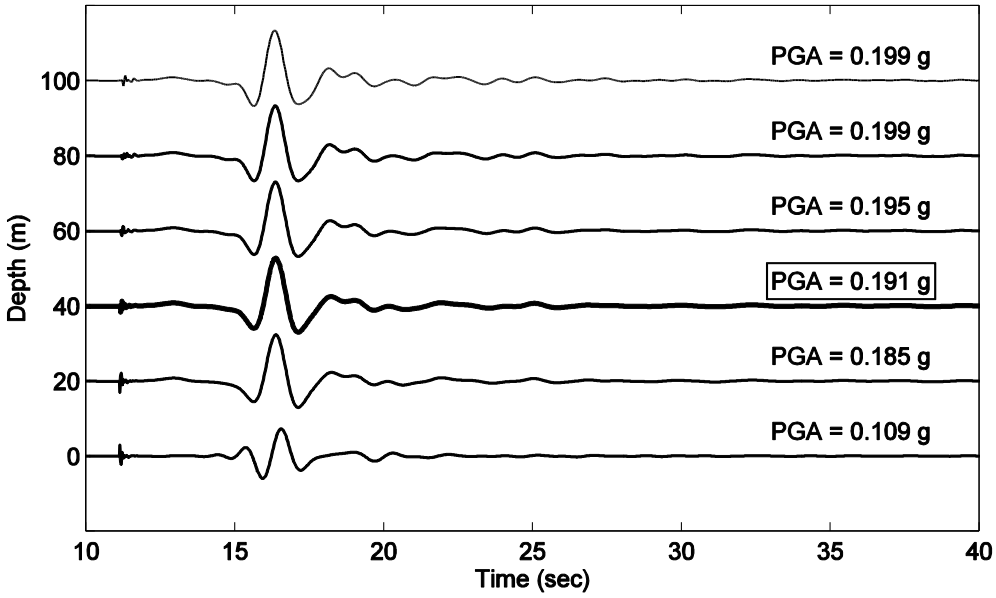

(a) X component

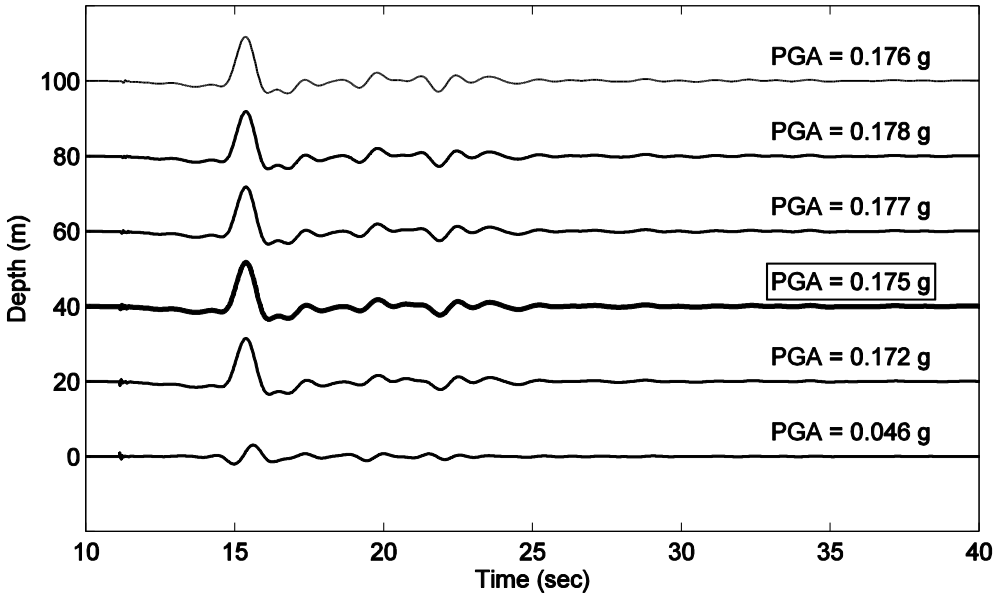

(b) Y component

Figure 7.4: Total ground accelerations along the depth below the center node in ROI

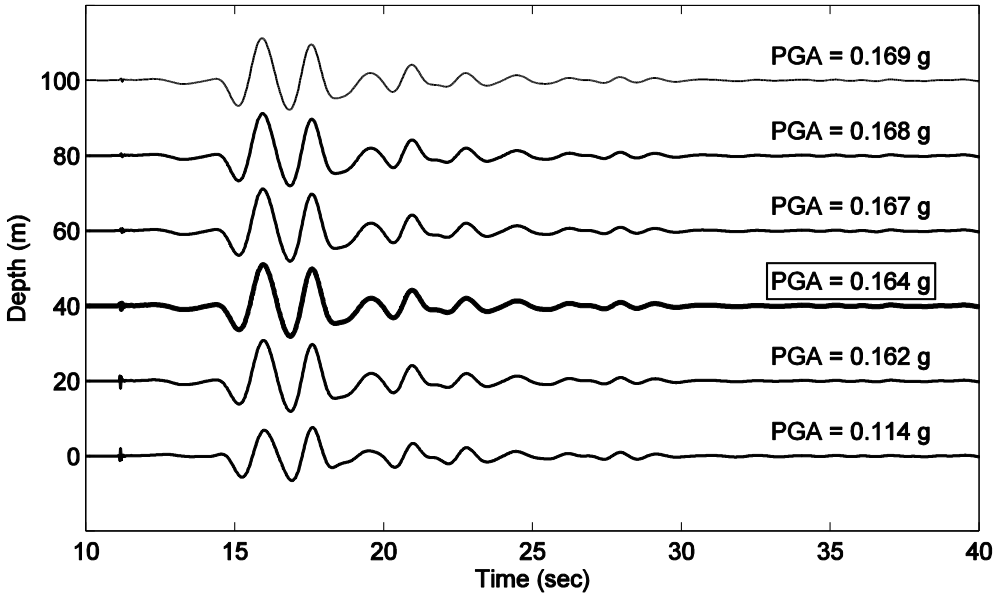

(c) Z component

Figure 7.4: (continued) Total ground accelerations along the depth below the center node in ROI

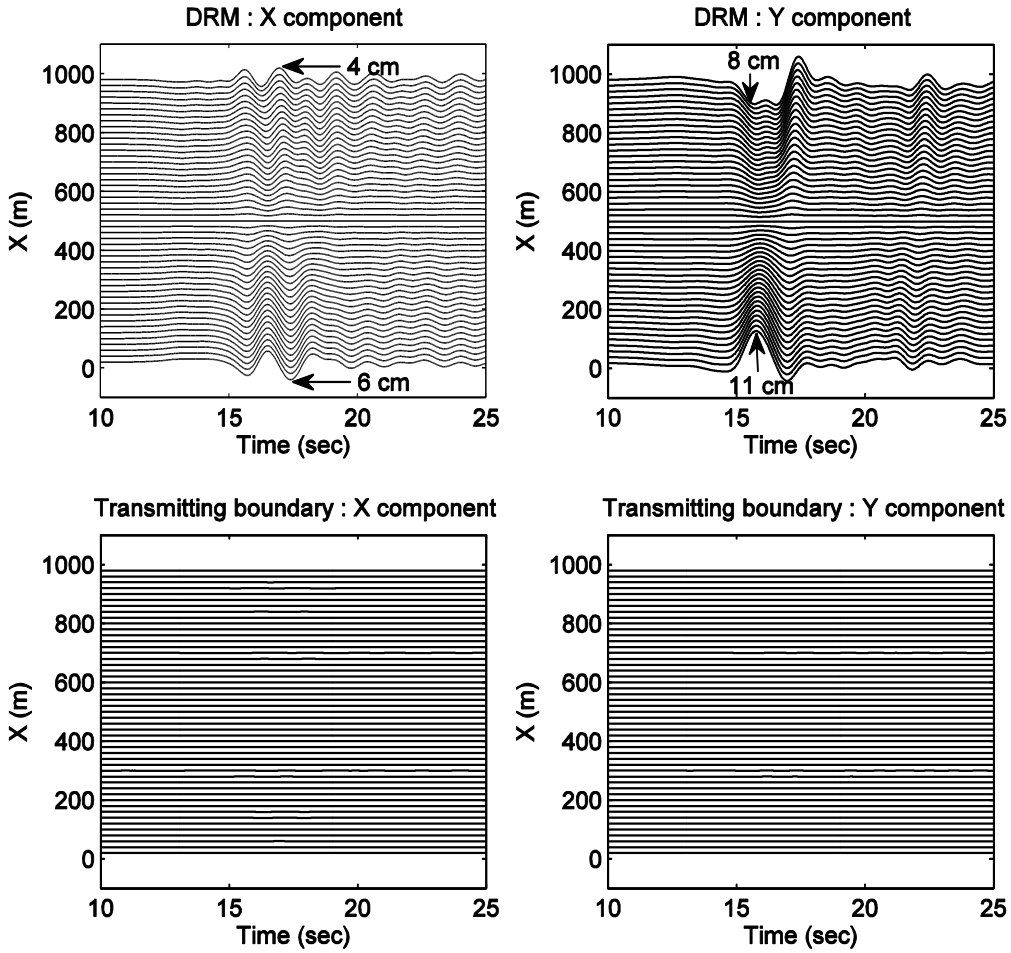

Figure 7.5: Ground surface displacements along the X-center line relative to the center node

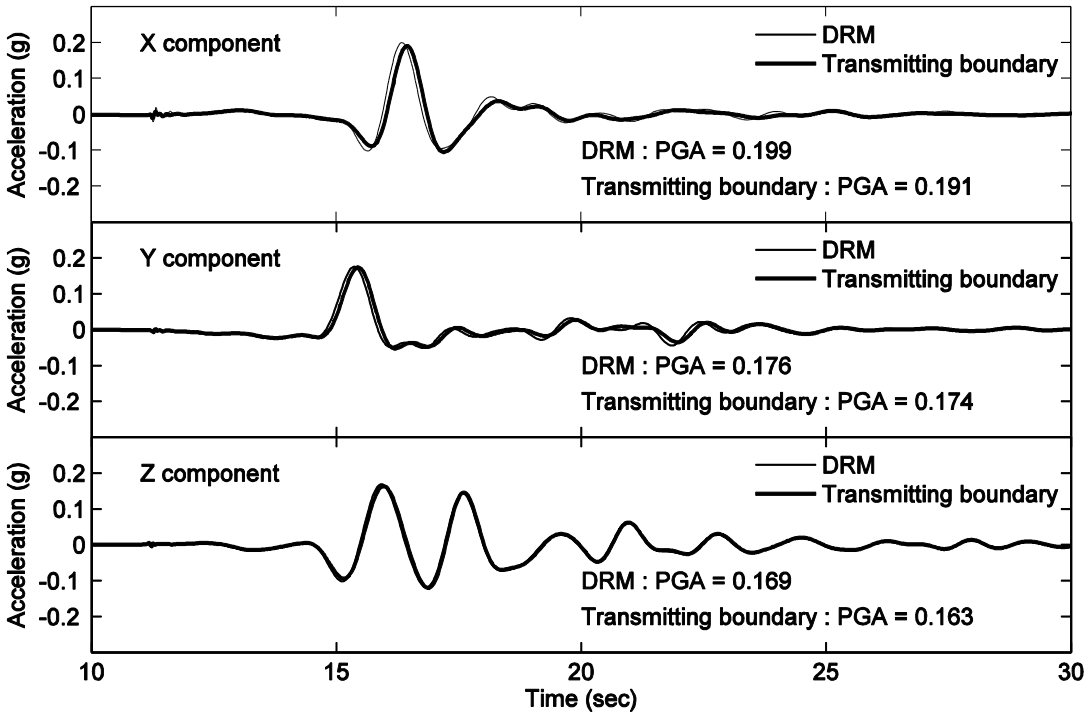

Figure 7.6: Comparison of ground surface accelerations at the center node

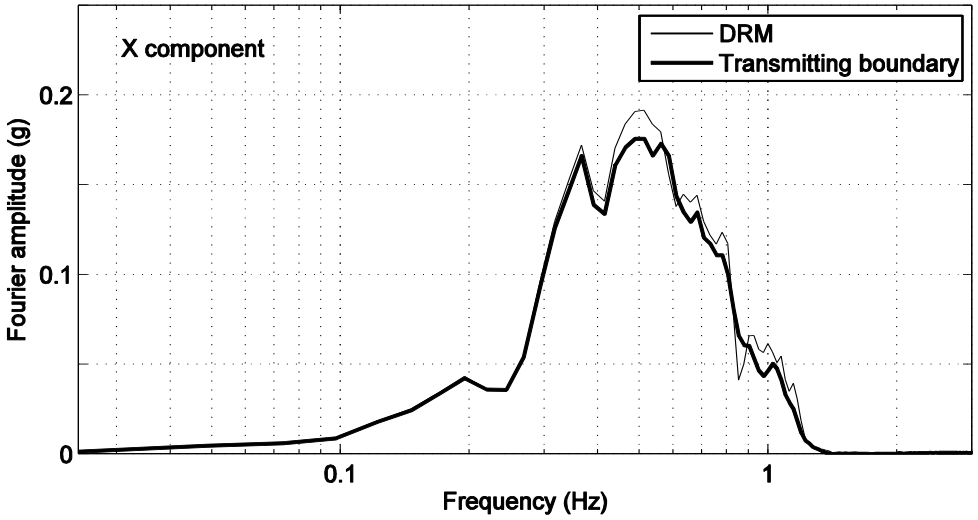

(a) X component

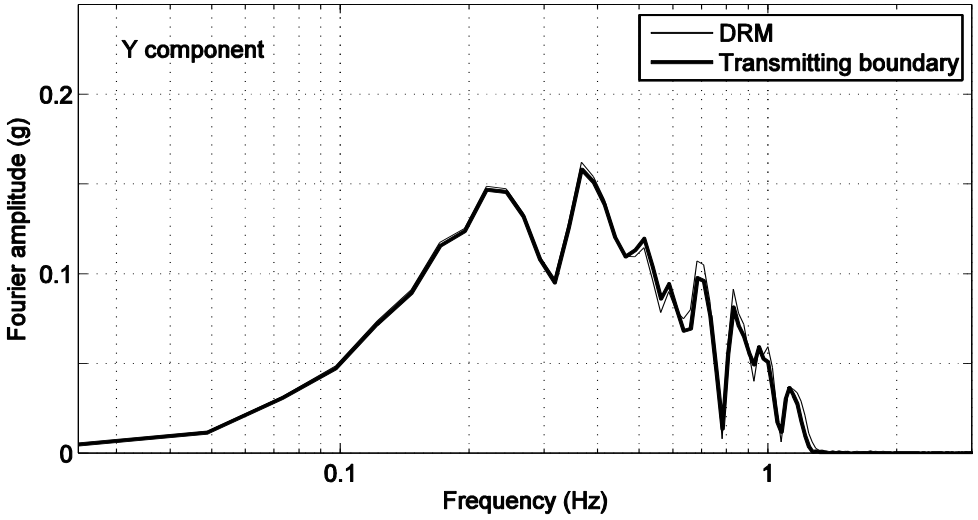

(b) Y component

Figure 7.7: Fourier Amplitude spectra for the surface acceleration at the center node

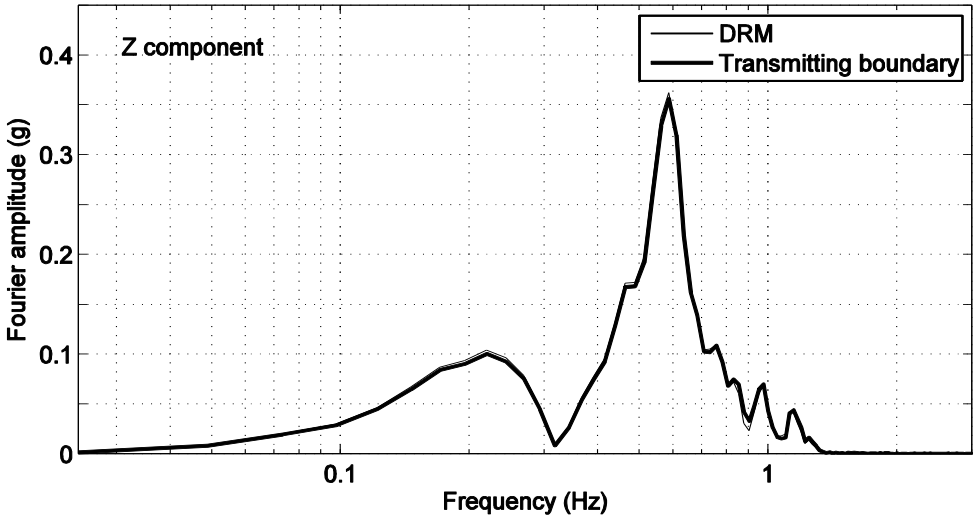

(c) Z component

Figure 7.7: (continued) Fourier Amplitude spectra for the surface acceleration at the center node

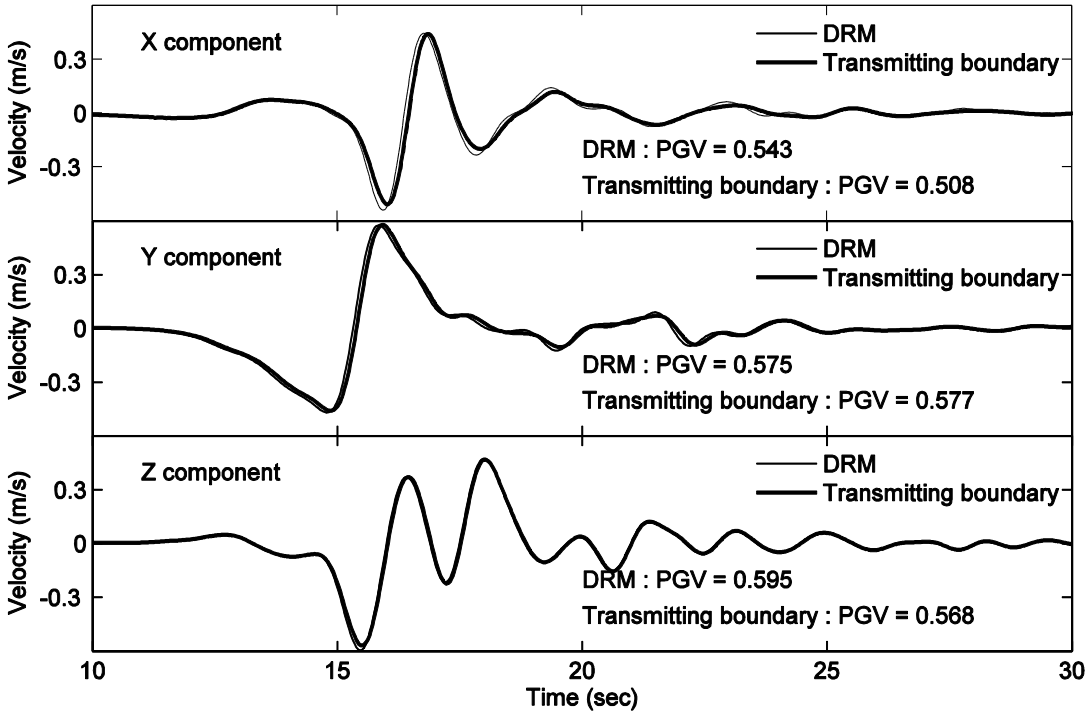

Figure 7.8: Comparison of ground surface velocities at the center node

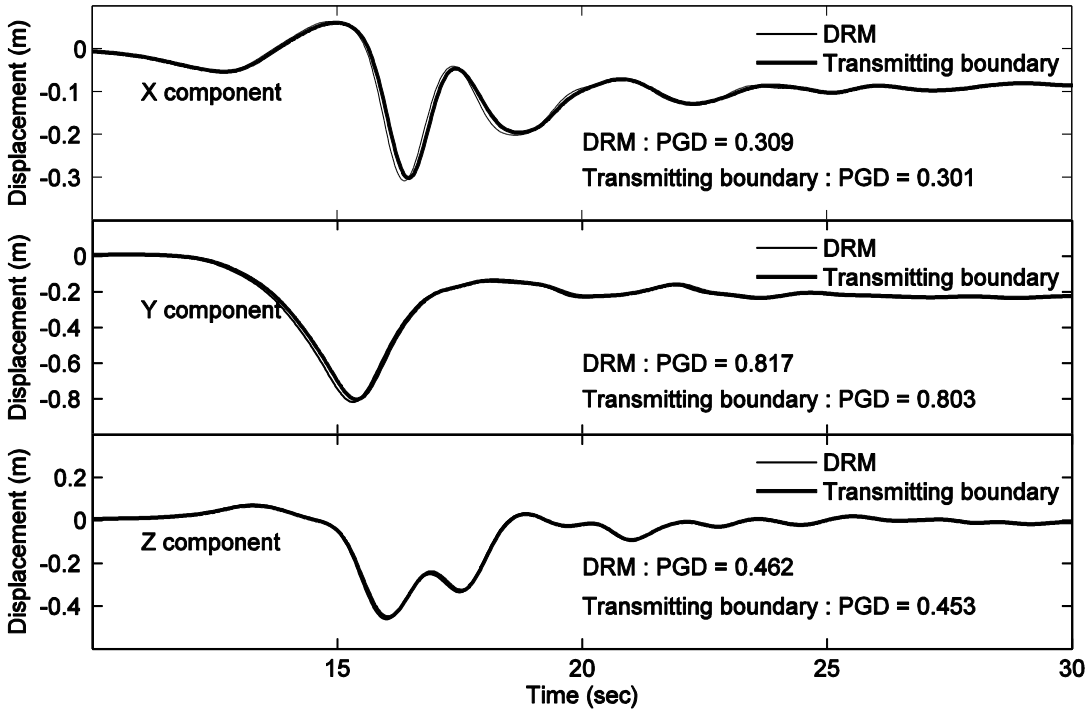

Figure 7.9: Comparison of ground surface displacements at the center node

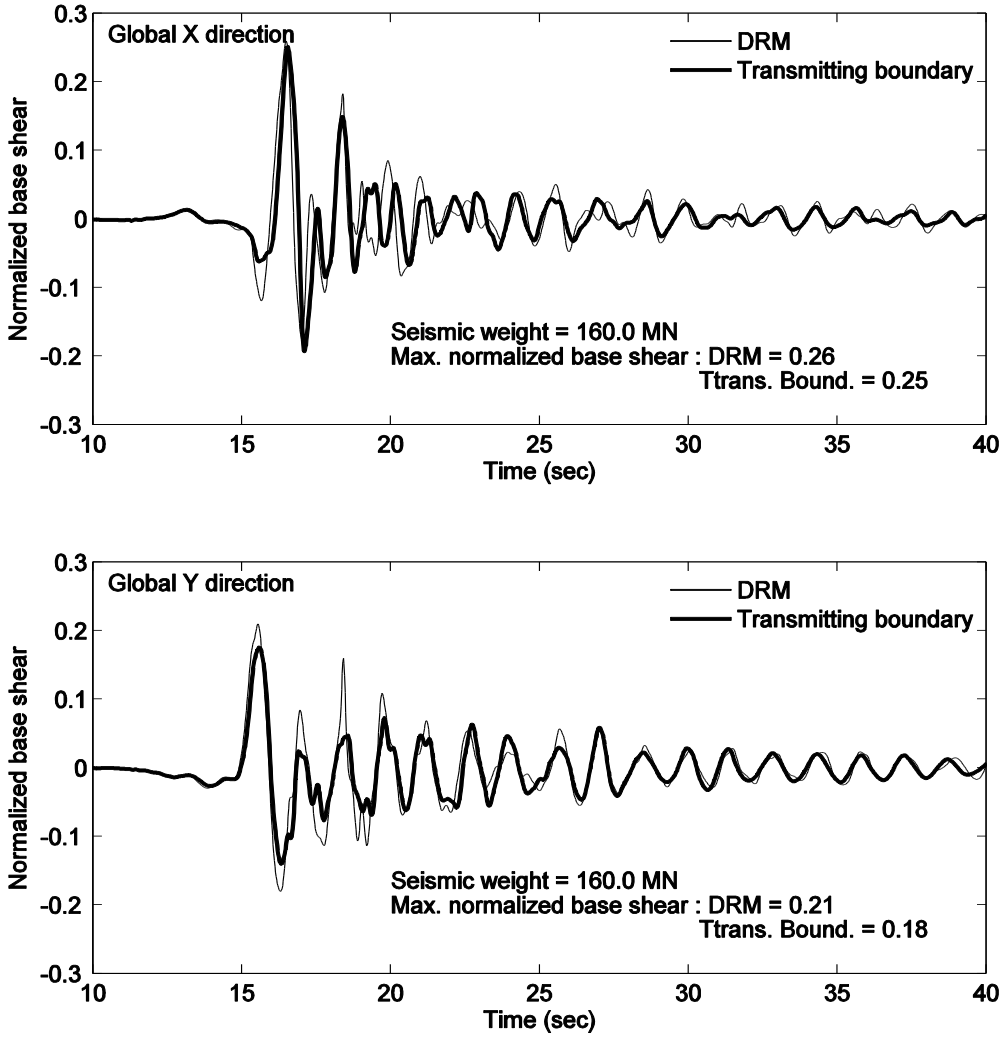

Figure 7.10: Normalized base shear time histories in the global X and Y directions

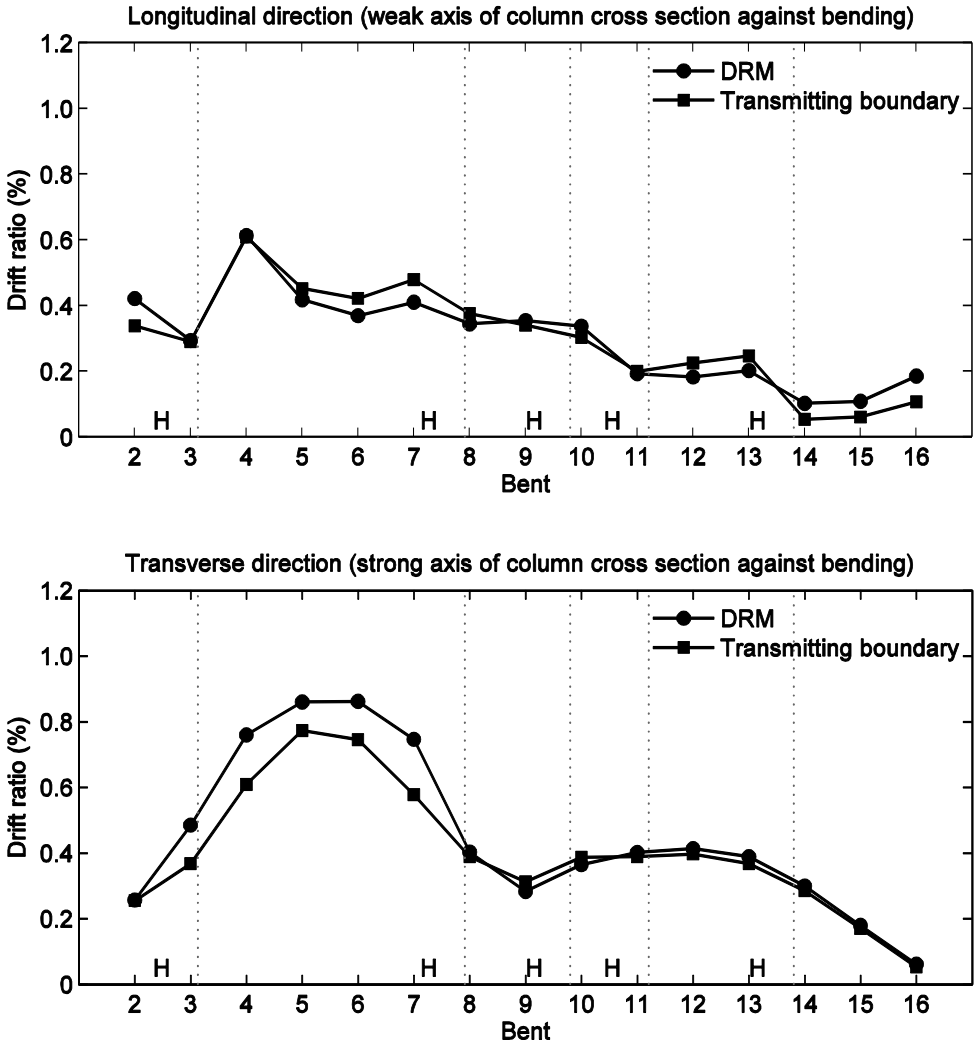

Figure 7.11: Comparison of the maximum drift ratios at all columns in the NW connector

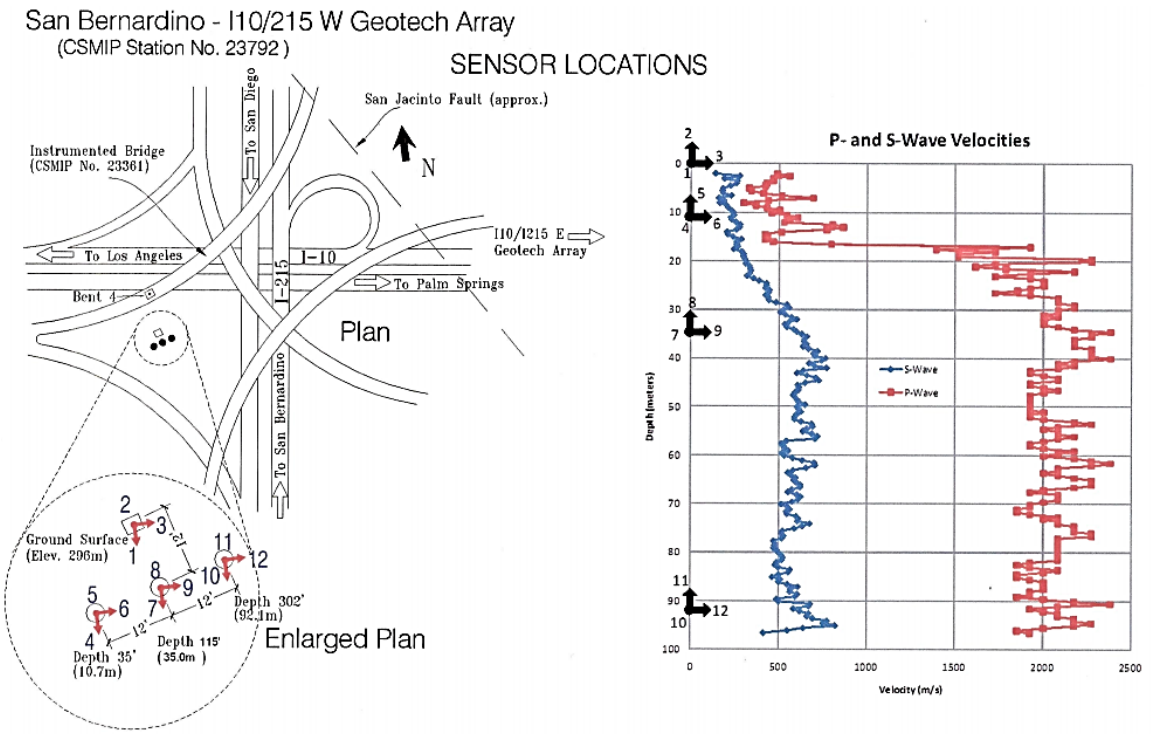

Figure 7.12: Seismic instrumentation (I10/215 W Geotech Array, CSMIP Station No. 23793)

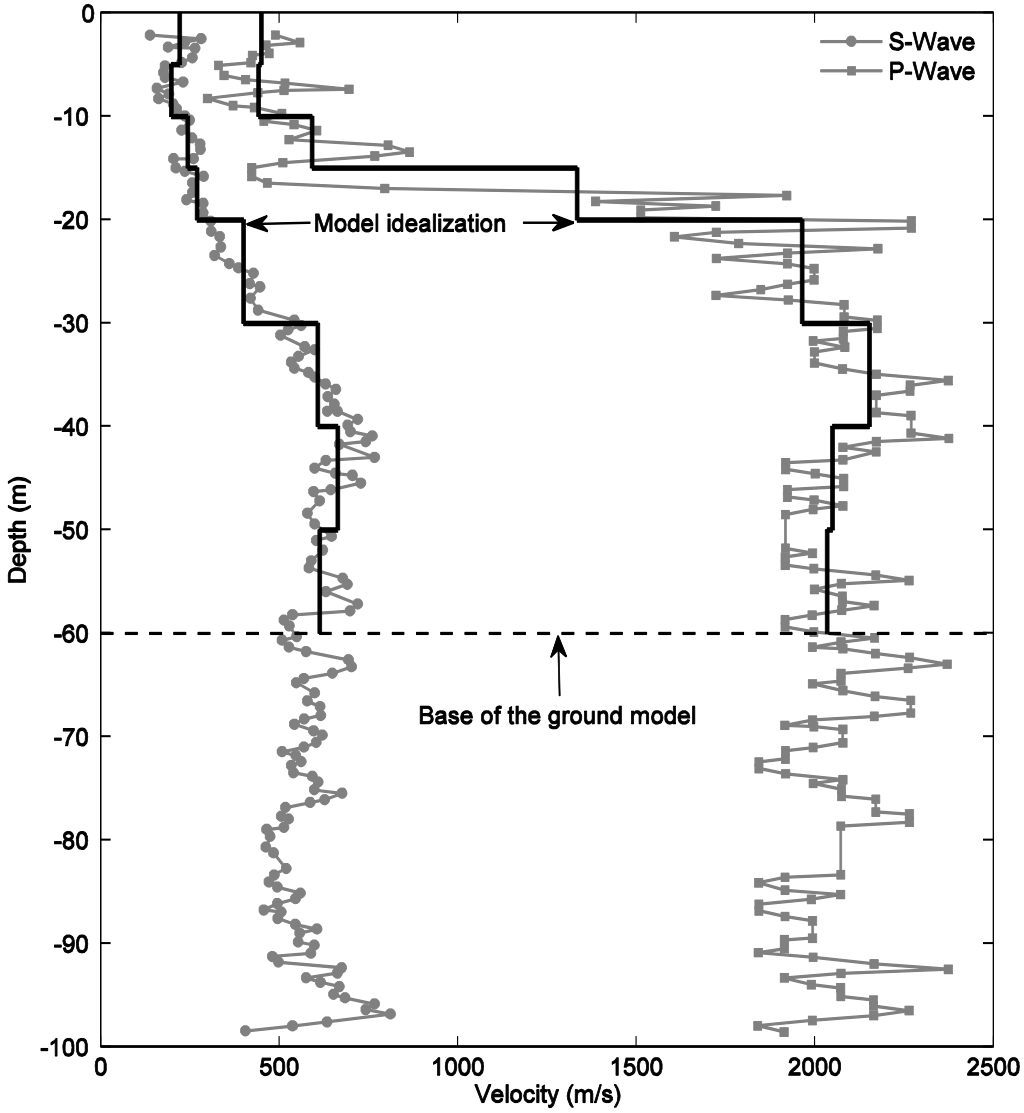

Figure 7.13: Idealized and measured soil wave velocity profile adapted from I10/215 W Geotech Array (CSMIP Station No. 23793)

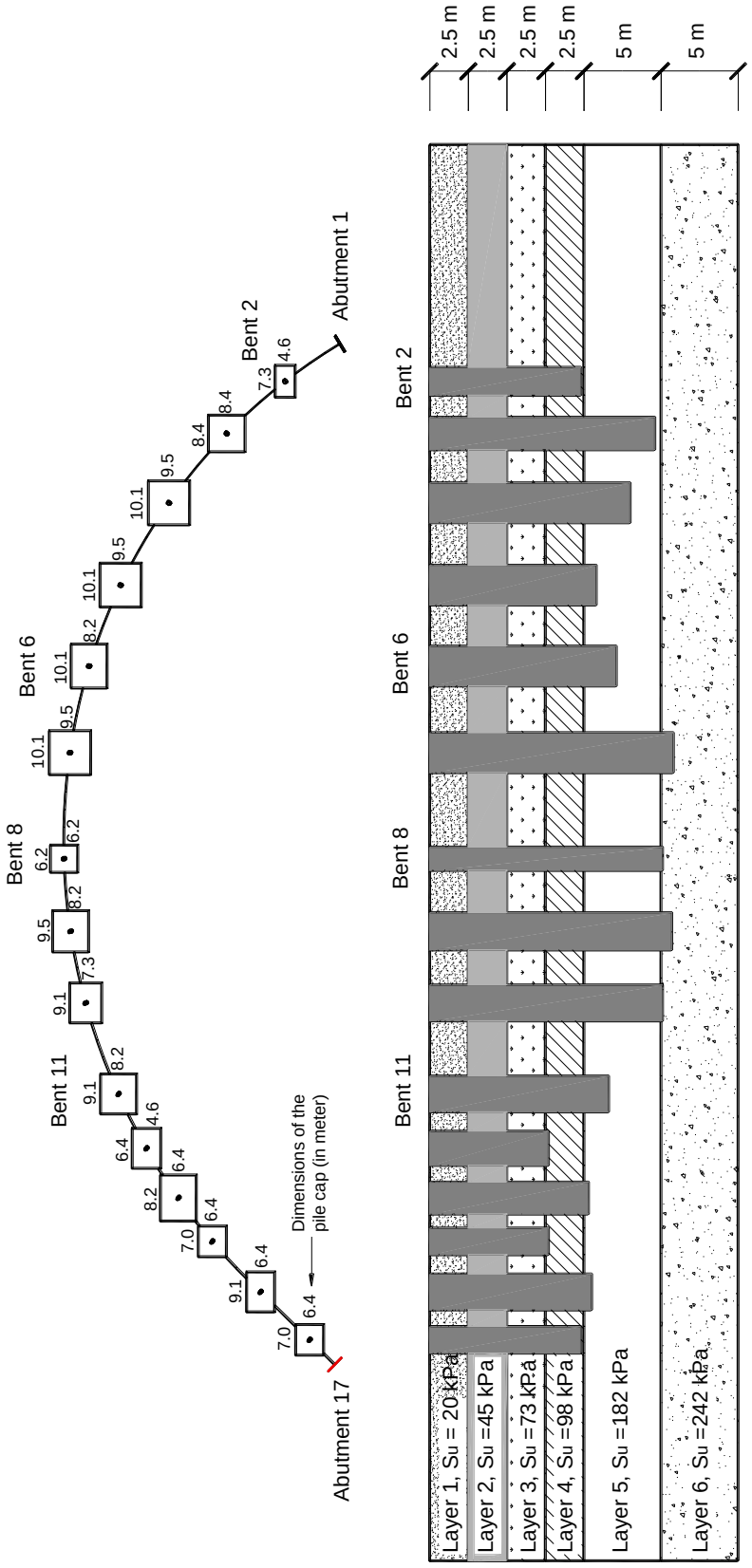

Figure 7.14: Schematic view of the foundation layout

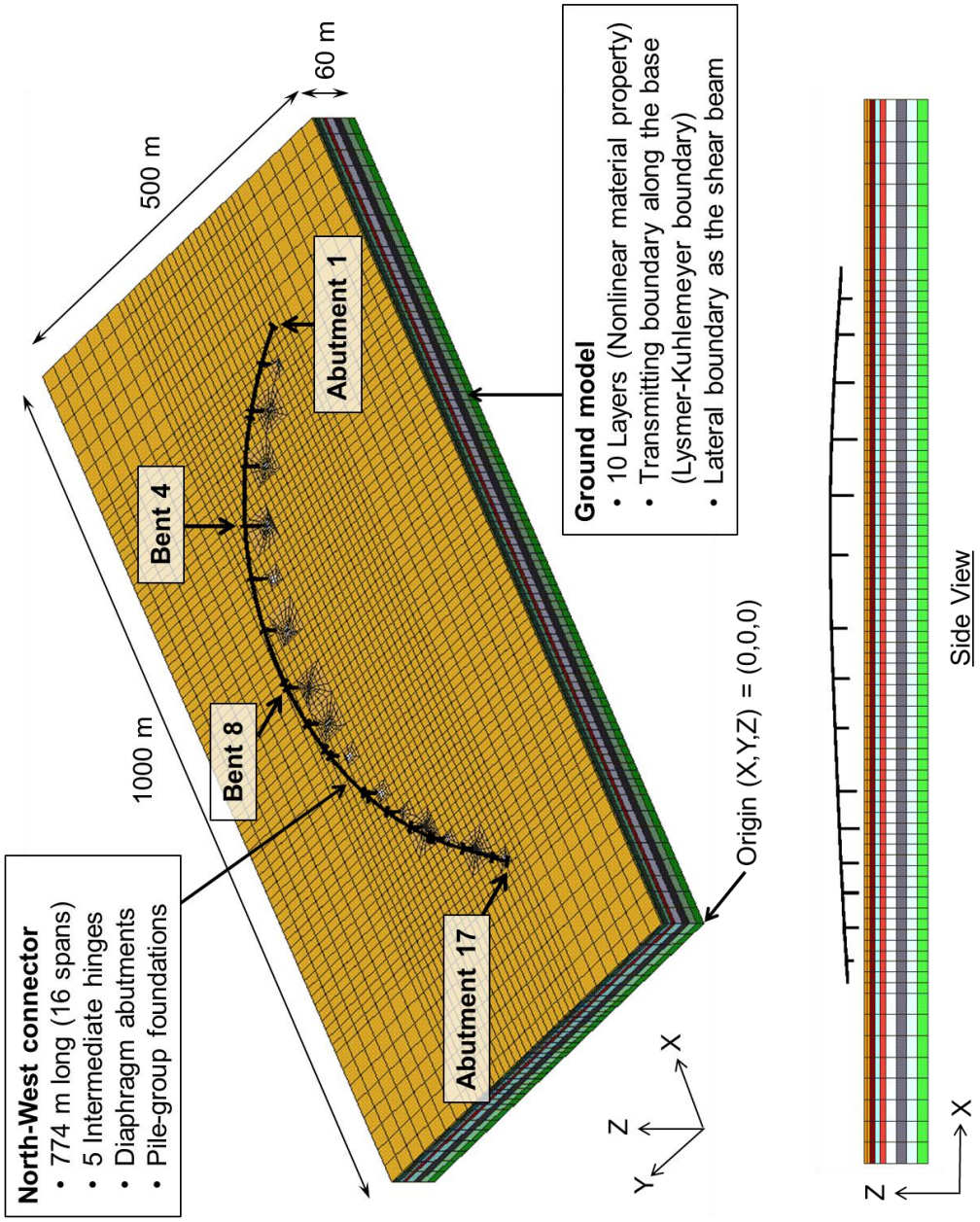

Figure 7.15: 3D view of the BFGS

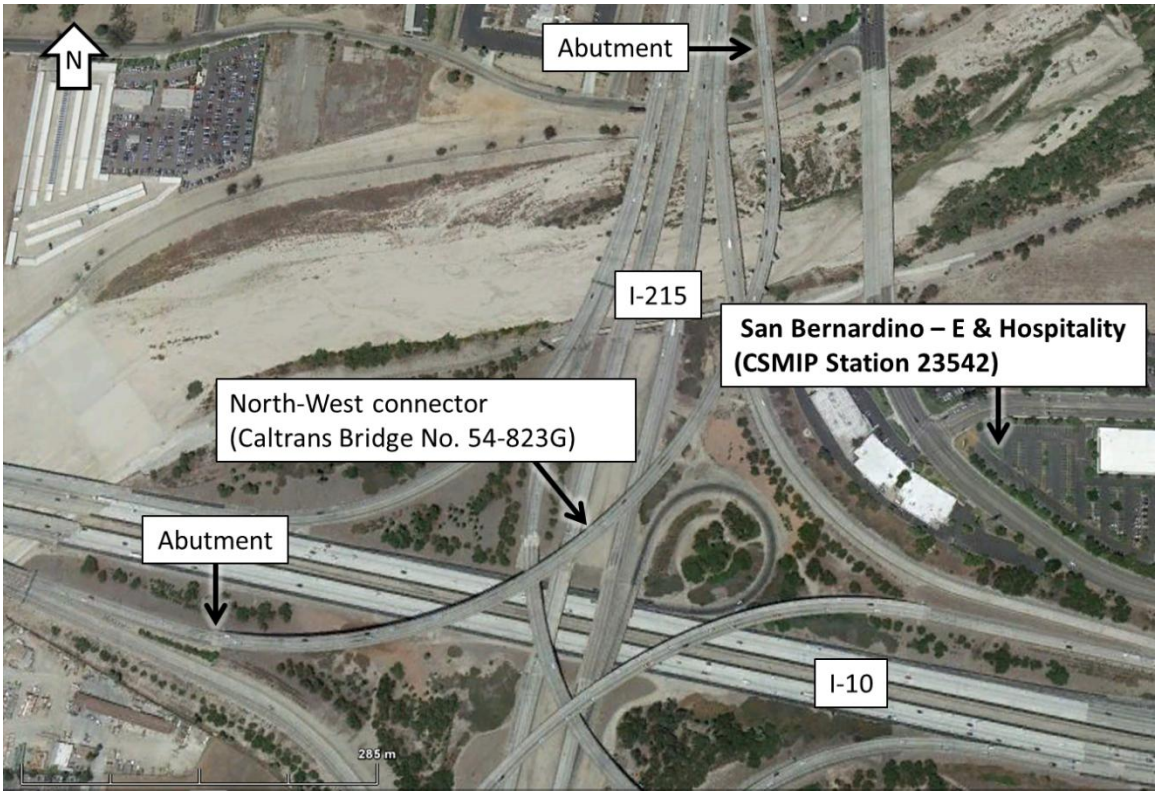

Figure 7.16: Location of San Bernardino – E & Hospitality Station (CSMIP Station No. 23542) near the I-10/215 interchange (©2013 Google - http://maps.google.com)

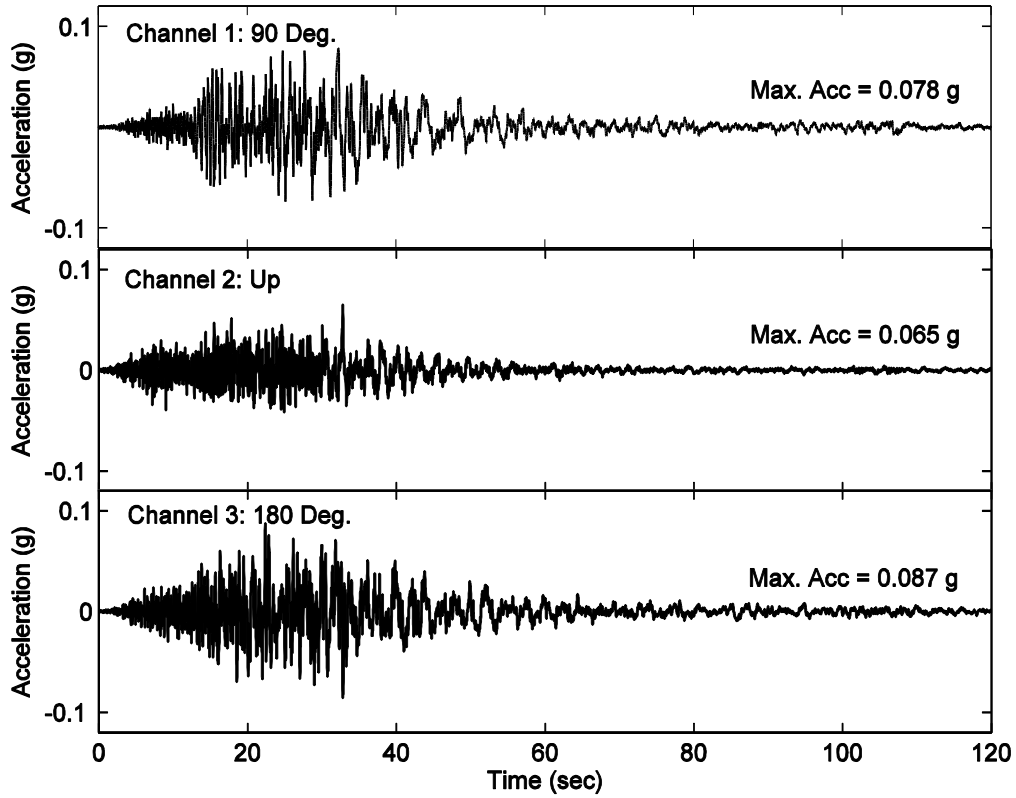

Figure 7.17: Recorded data during Landers Earthquake in 1992 at San Bernardino – E & Hospitality Station (CSMIP Station No. 23542)

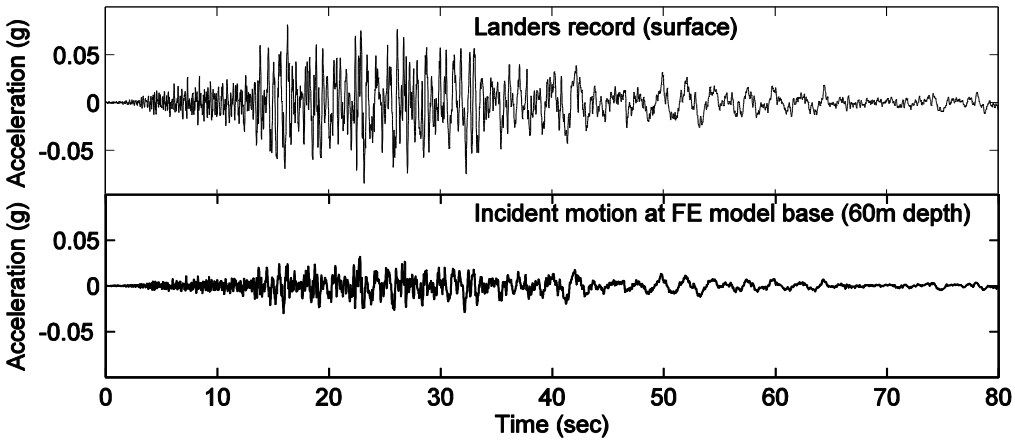

(a) X component

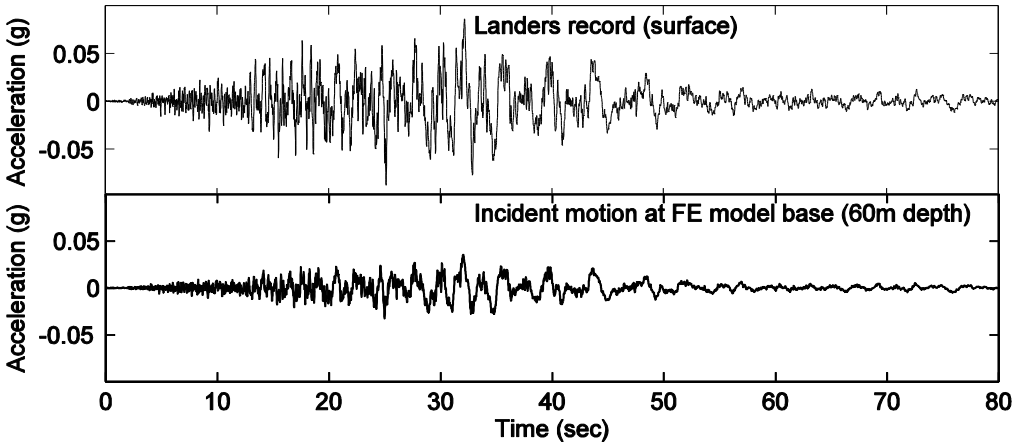

(b) Y component

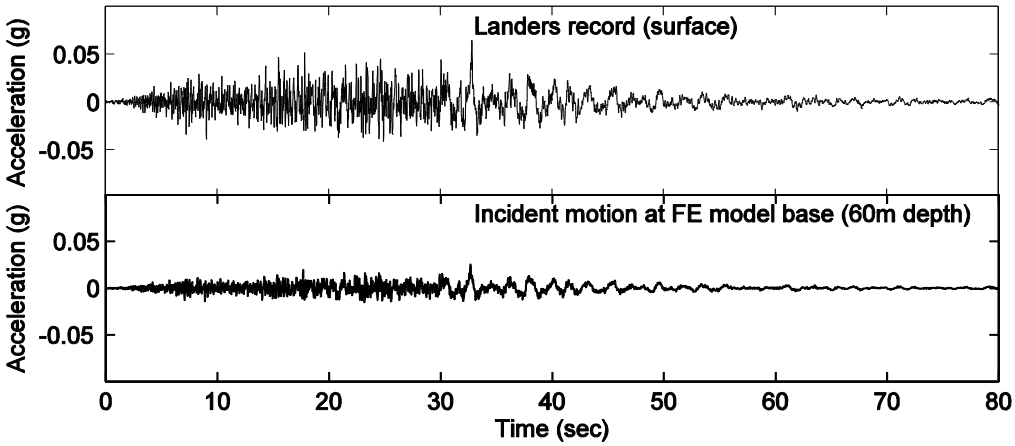

(c) Z component

Figure 7.18: Results of deconvolution: acceleration time histories of the surface motion and incident motion at the base of the ground model; (a) X component (horizontal), (b) Y component (horizontal), and (c) Z component (vertical)

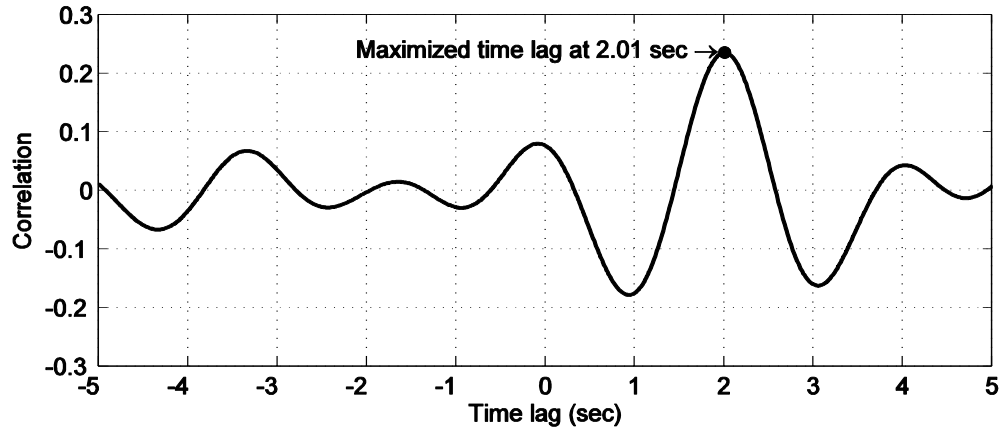

Figure 7.19: Cross-Correlation between vertical displacements at the base of Bent 8 and the free-field

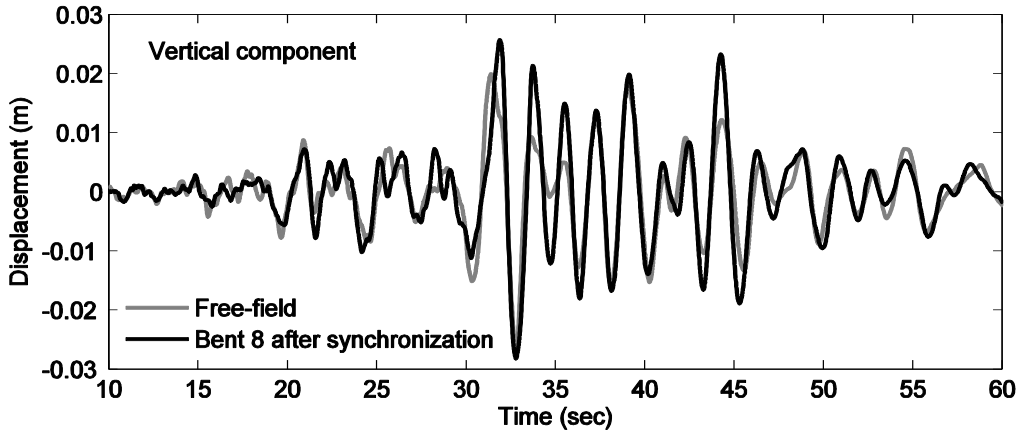

Figure 7.20: Free-field vertical displacement and Bent 8 base vertical displacement with the time lag removed

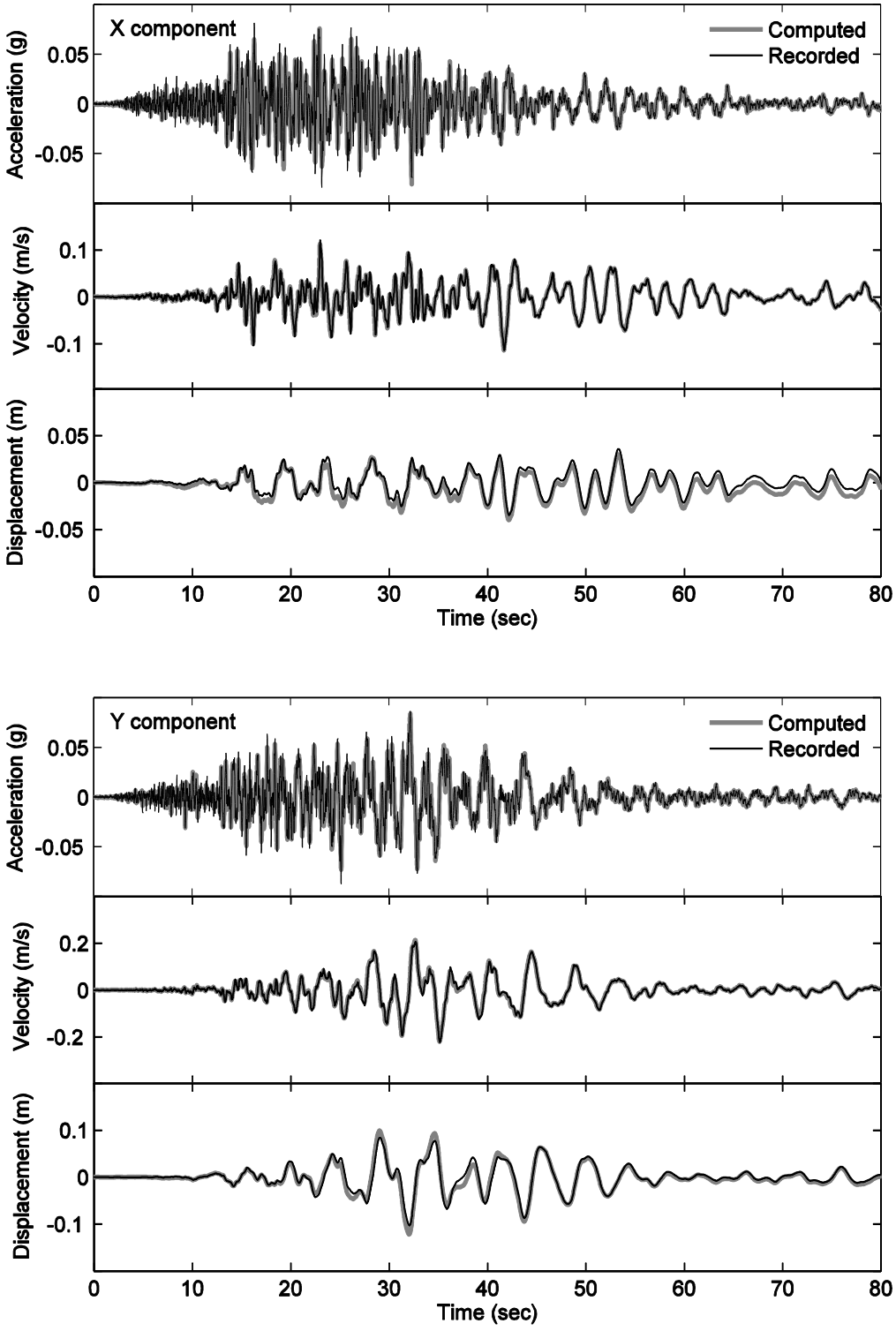

Figure 7.21: Comparison of recorded free-field motions (black line) with computed free-field motions (gray line) for Landers earthquake 1992

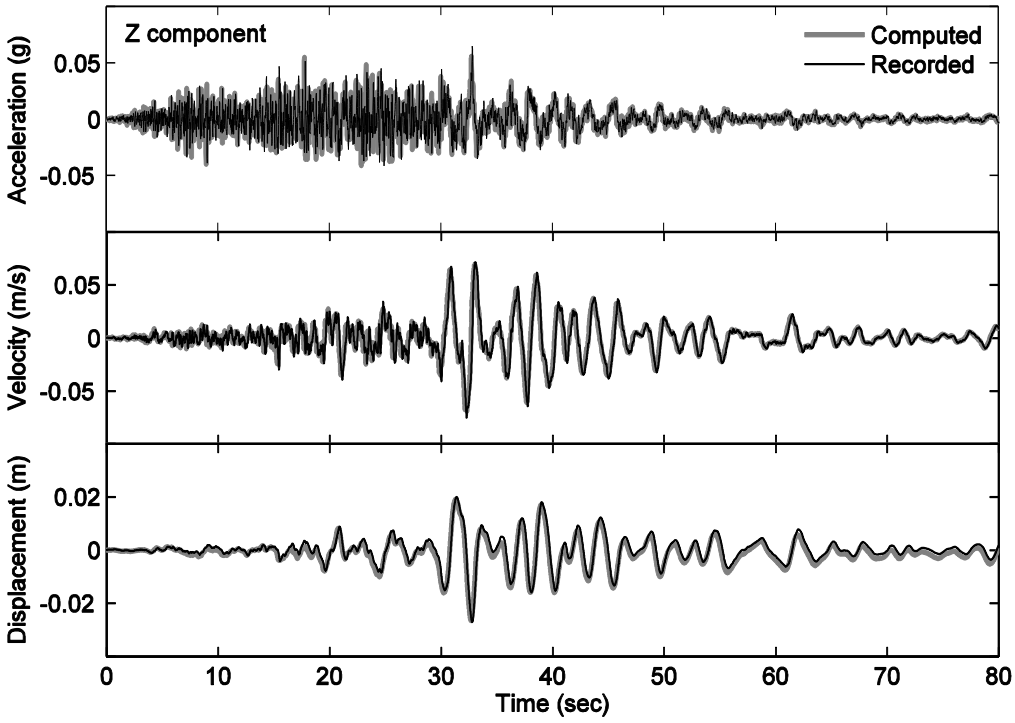

Figure 7.21: (continued) Comparison of recorded free-field motions (black line) with computed free-field motions (gray line) for Landers earthquake 1992

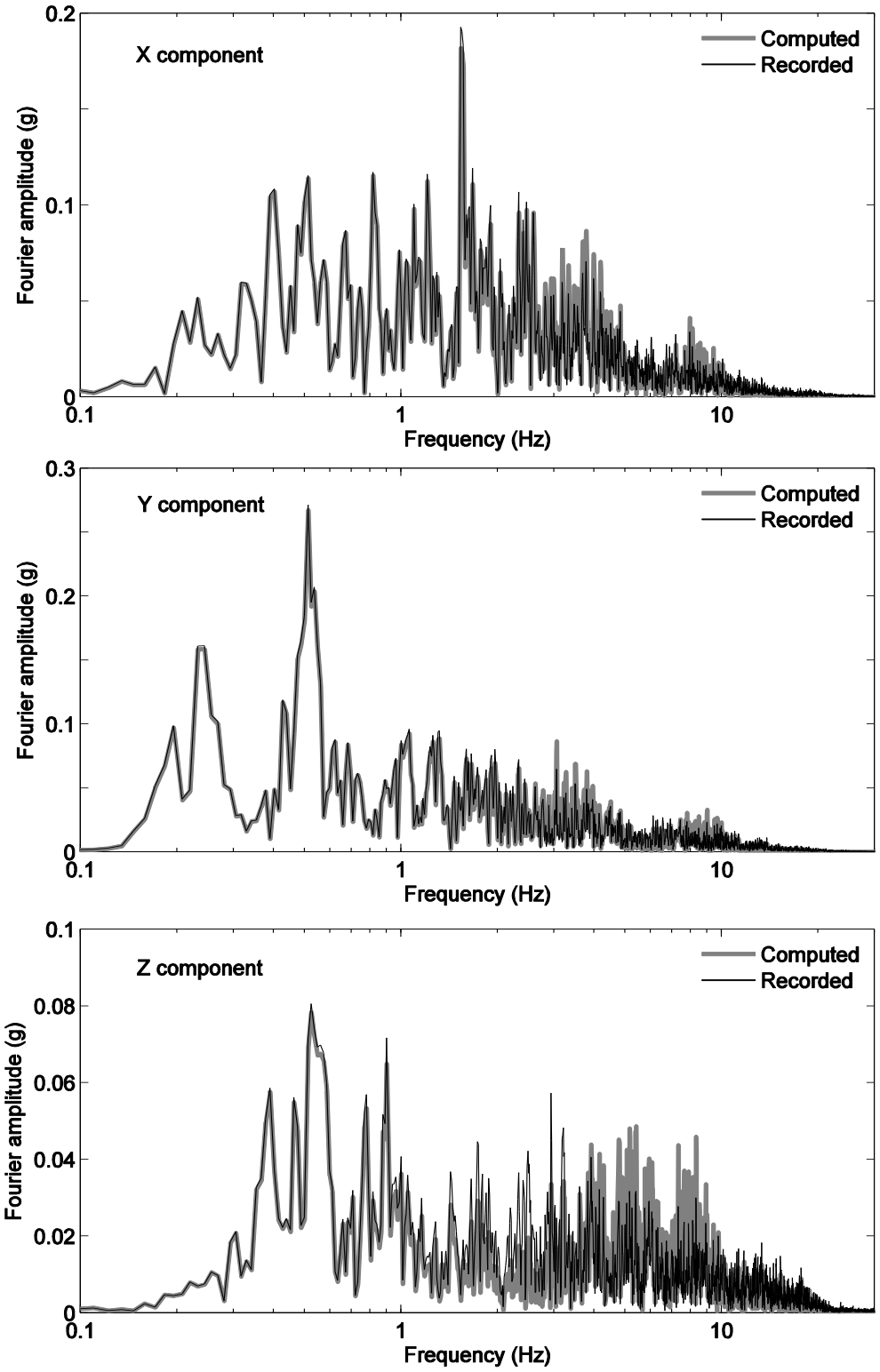

Figure 7.22: Comparison of Fourier amplitude of recorded free-field motions (black line) with computed free-field motions (gray line) for Landers earthquake 1992

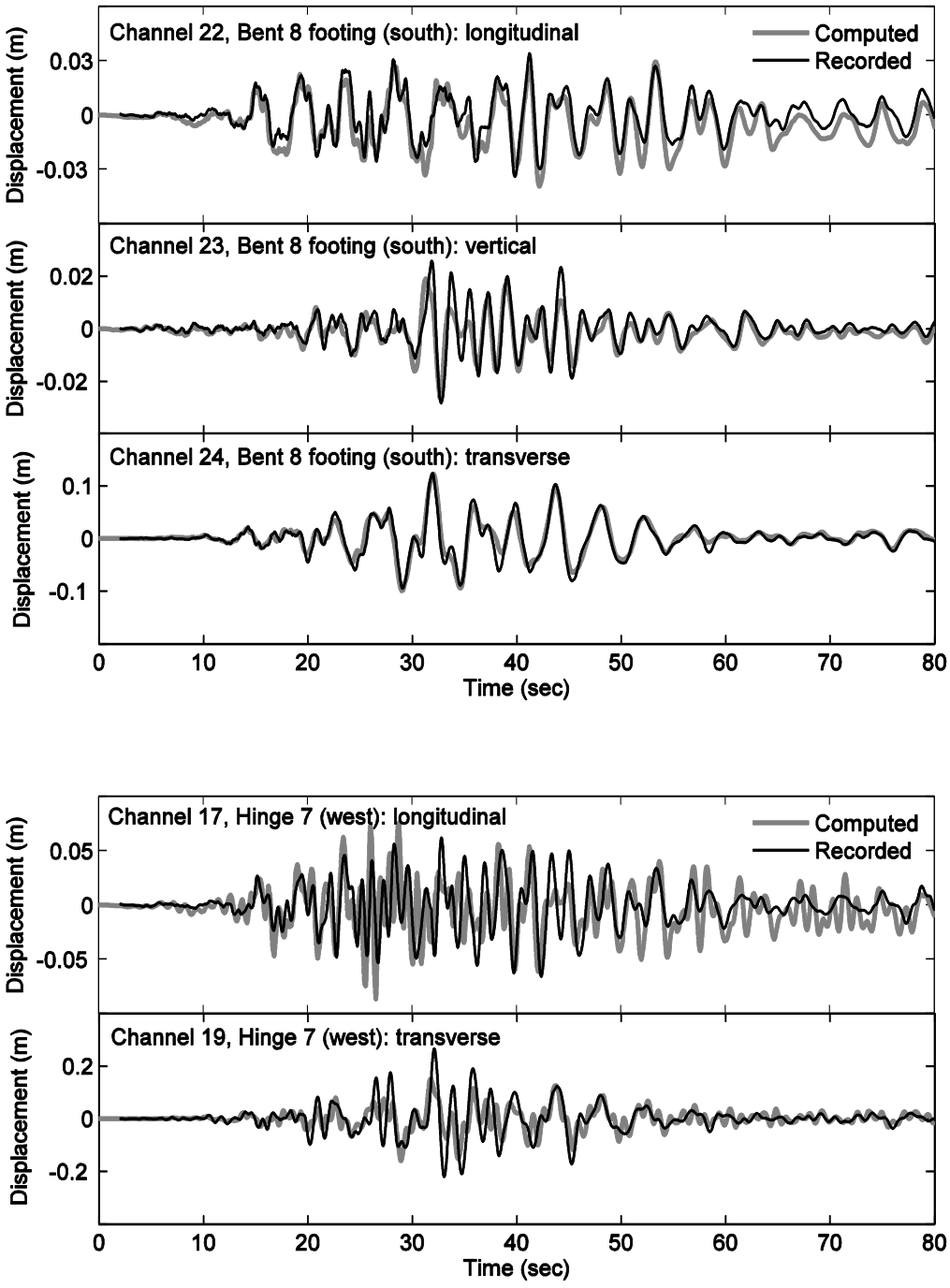

Figure 7.23: NW Comparison of recorded total displacement (black line) with computed displacement (gray line)

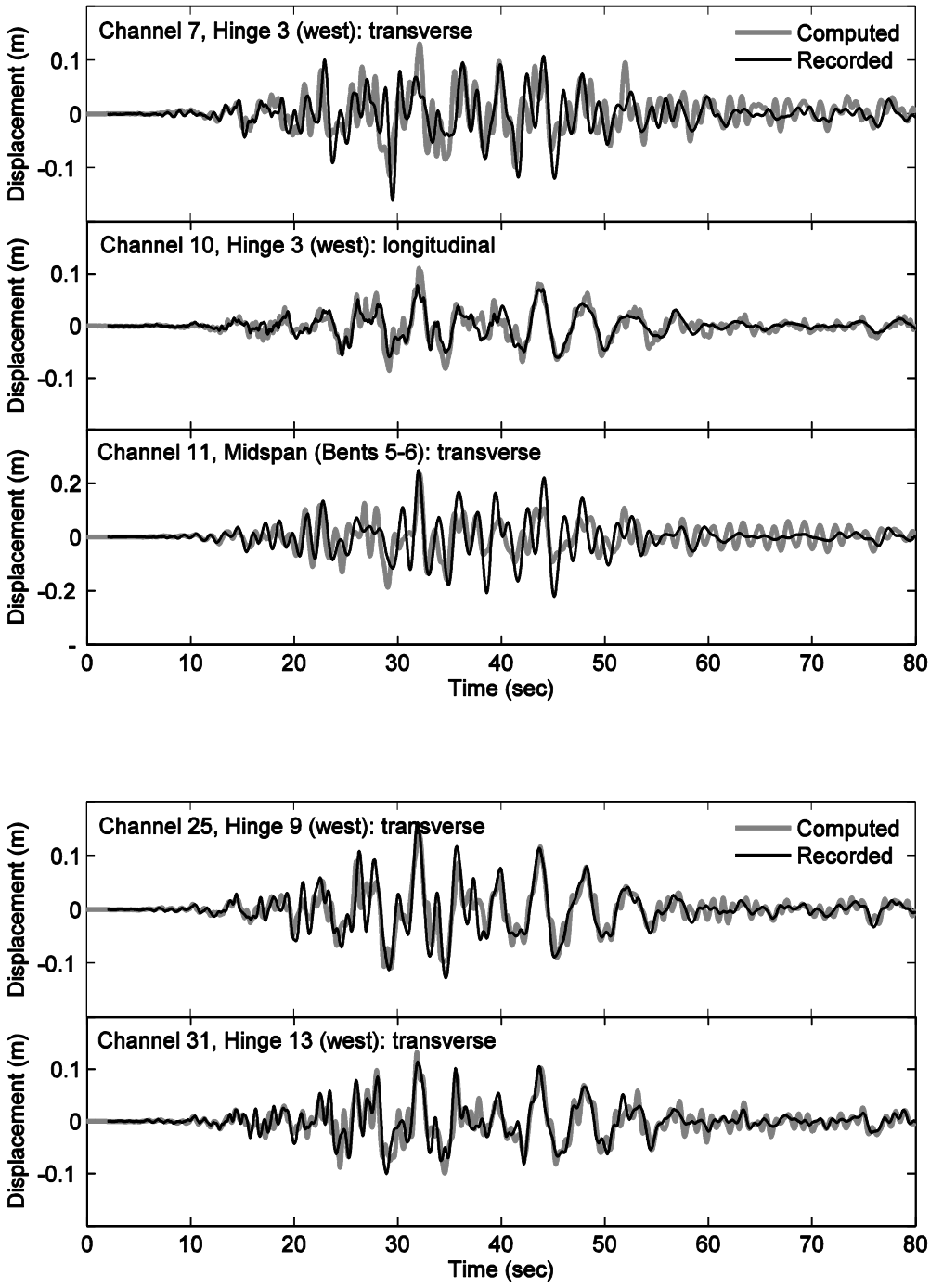

Figure 7.23: (continued) NW Comparison of recorded total displacement (black line) with computed displacement (gray line)

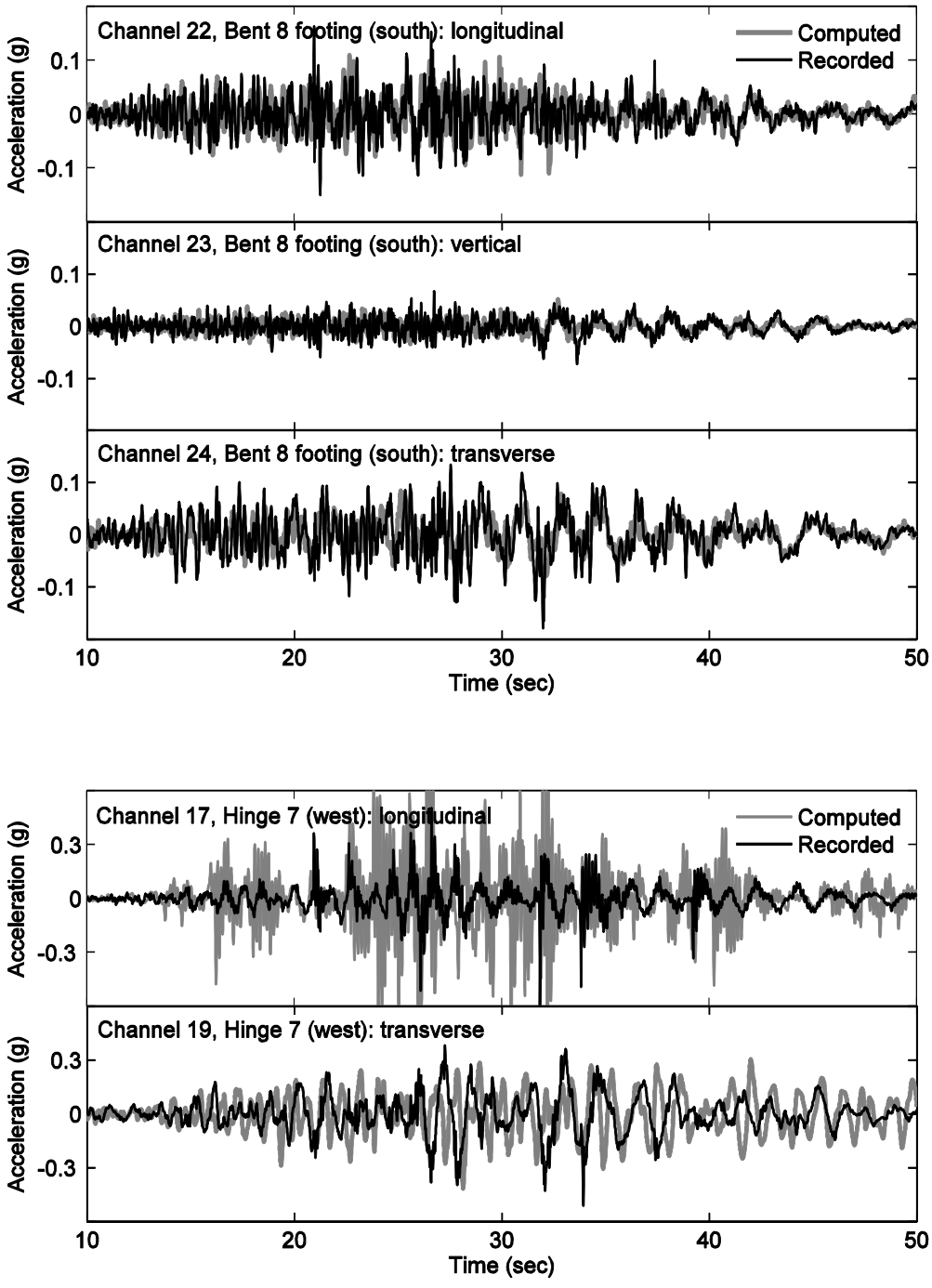

Figure 7.24: Comparison of recorded total acceleration (black line) with computed displacement (gray line) on the NW

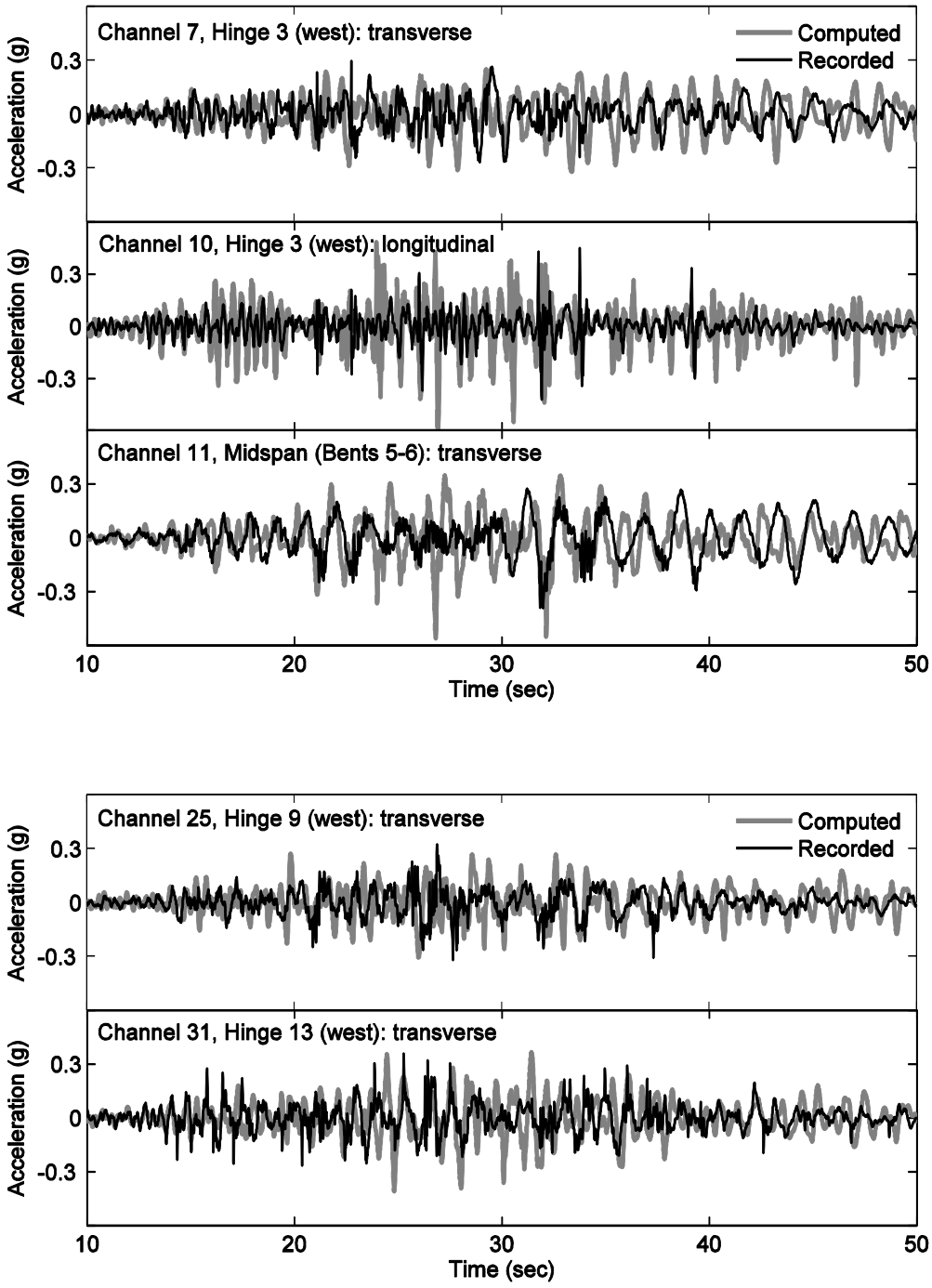

Figure 7.24: (continued) Comparison of recorded total acceleration (black line) with computed displacement (gray line) on the NW

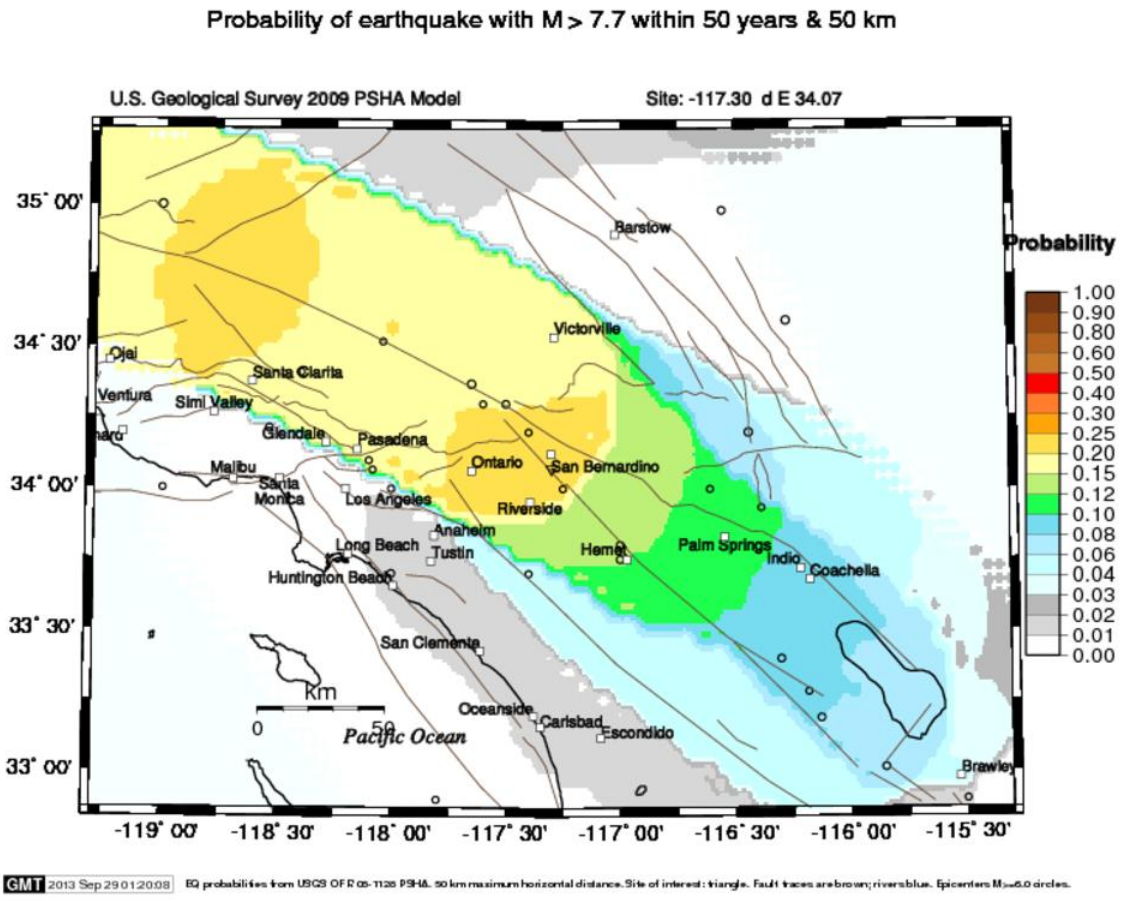

Figure 7.25: Earthquake probability map on the I-10/215 interchange (The 20% probability of exceedance in 50 years, https://geohazards.usgs.gov/eqprob/2009/index.php)

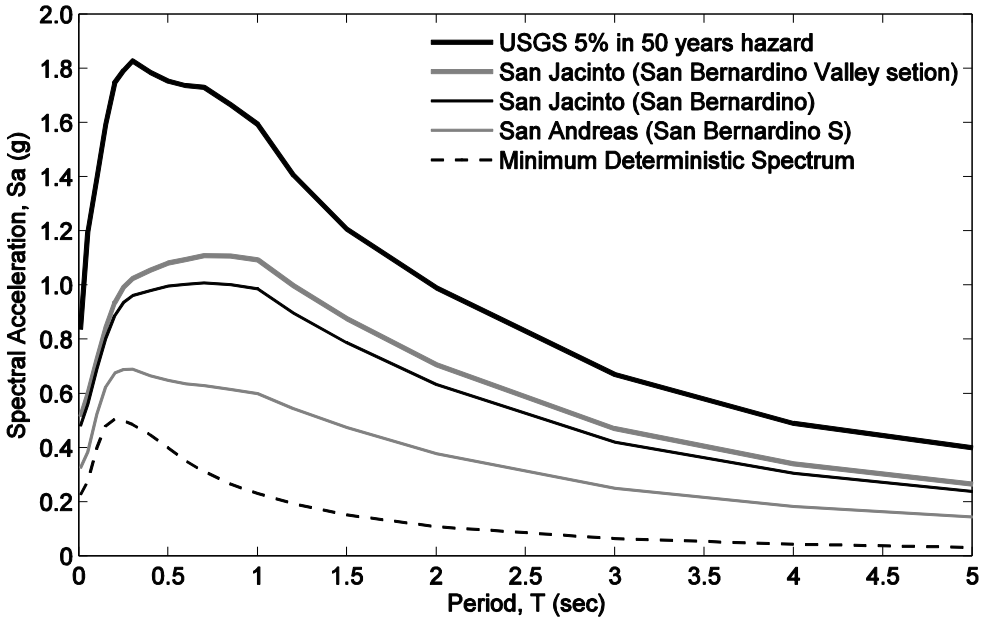

Figure 7.26: Design response spectrum at the I-10/215 interchange (Caltrans ARS Online)

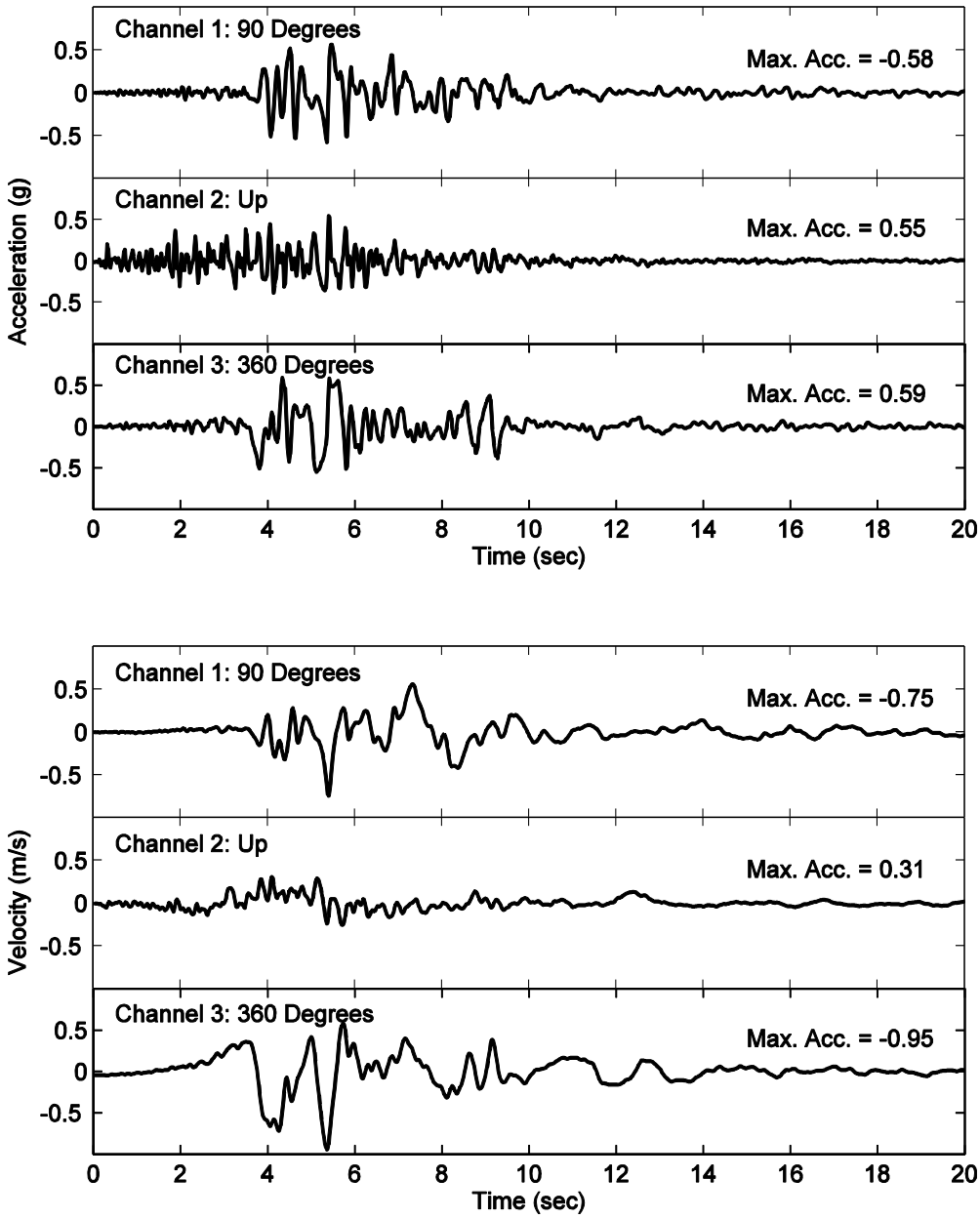

Figure 7.27: Ground responses recorded at Newhall – County Fire Station (CSMIP Station No. 24279) for Northridge earthquake 1994

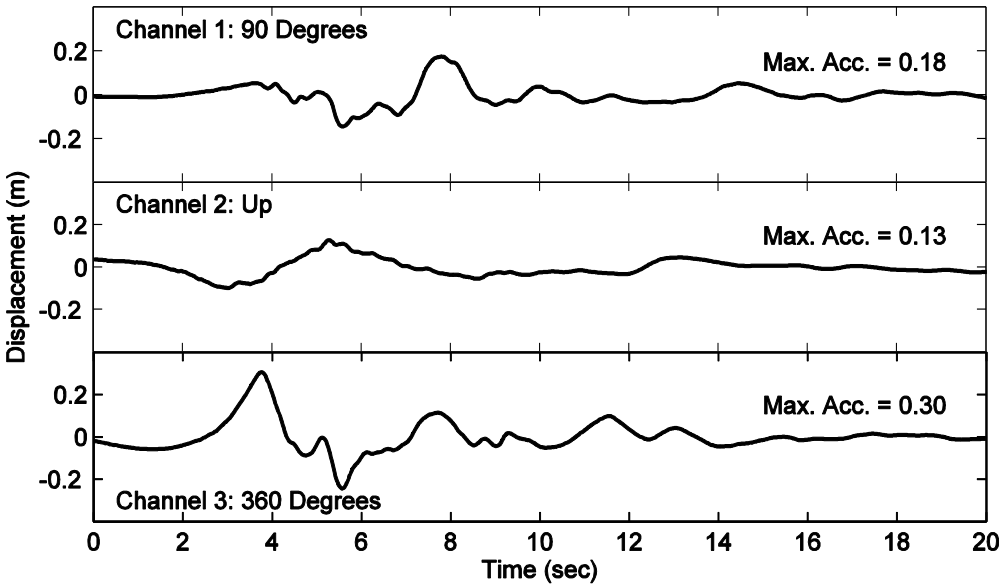

Figure 7.27: (continued) Ground responses recorded at Newhall – County Fire Station (CSMIP Station No. 24279) for Northridge earthquake 1994

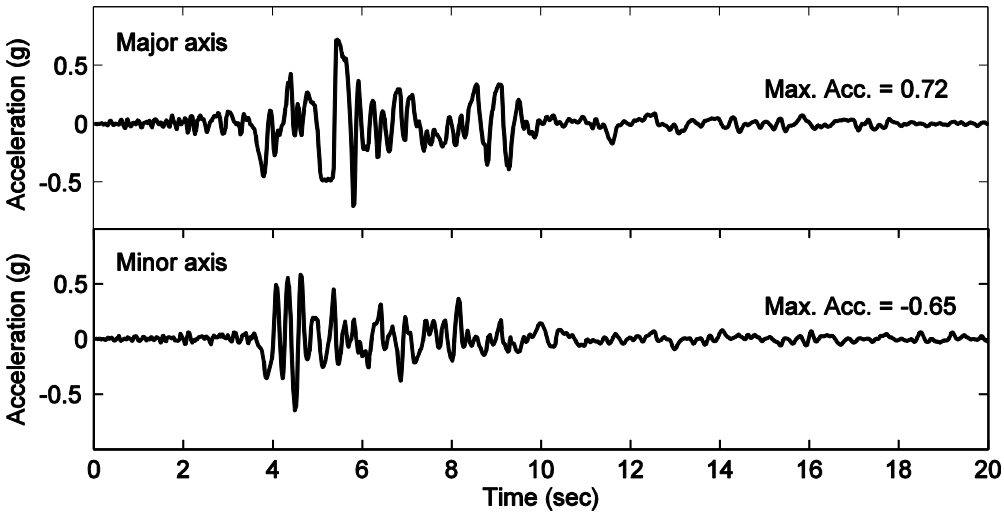

Figure 7.28: Northridge ground acceleration in the principal major axis (58º) and minor axis (302º)

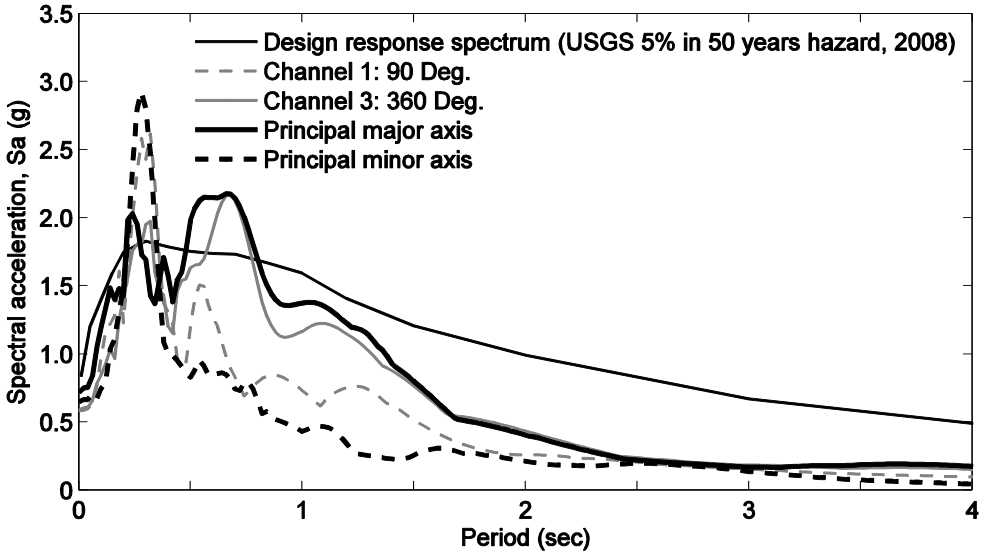

Figure 7.29: Response spectra for Northridge free-field ground motion

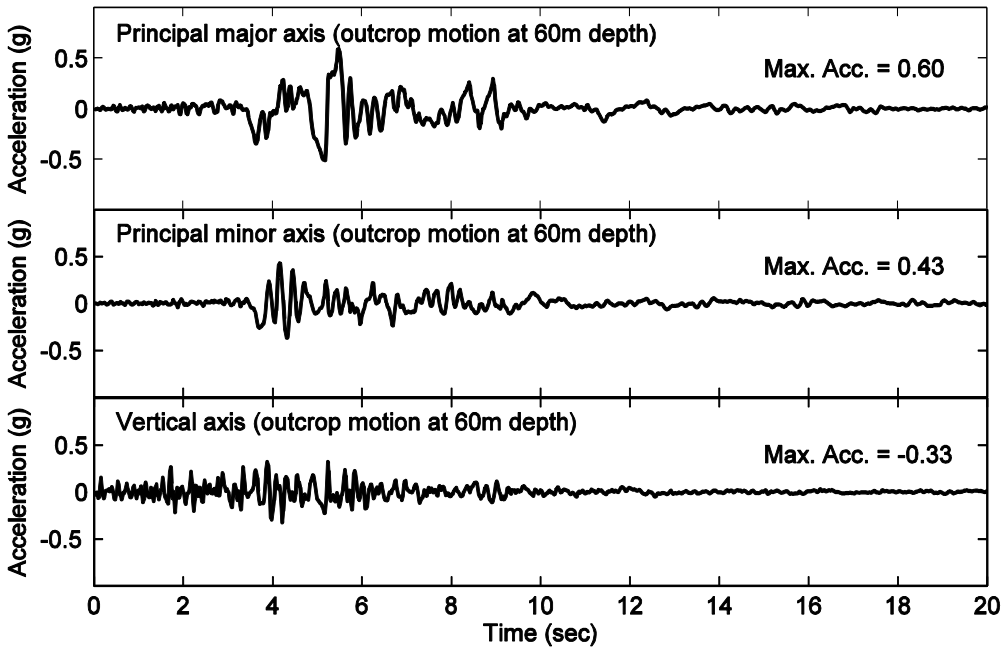

Figure 7.30: Results of deconvolution at the 60 m depth (at the base of the ground model)

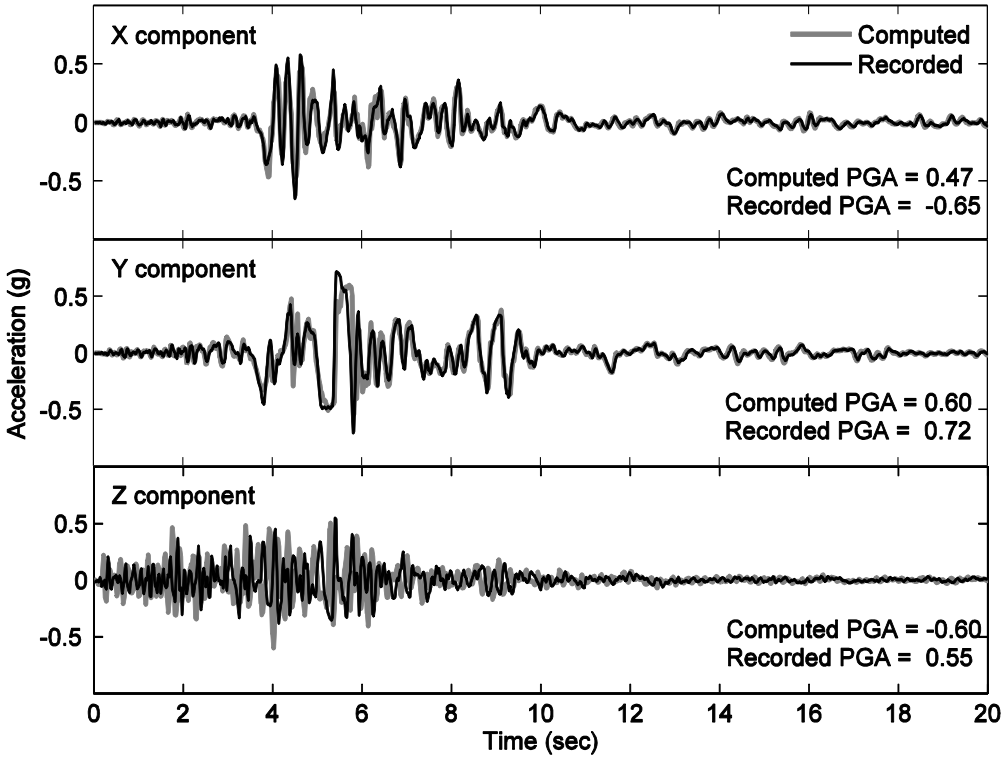

Figure 7.31: Total acceleration at the ground surface center node

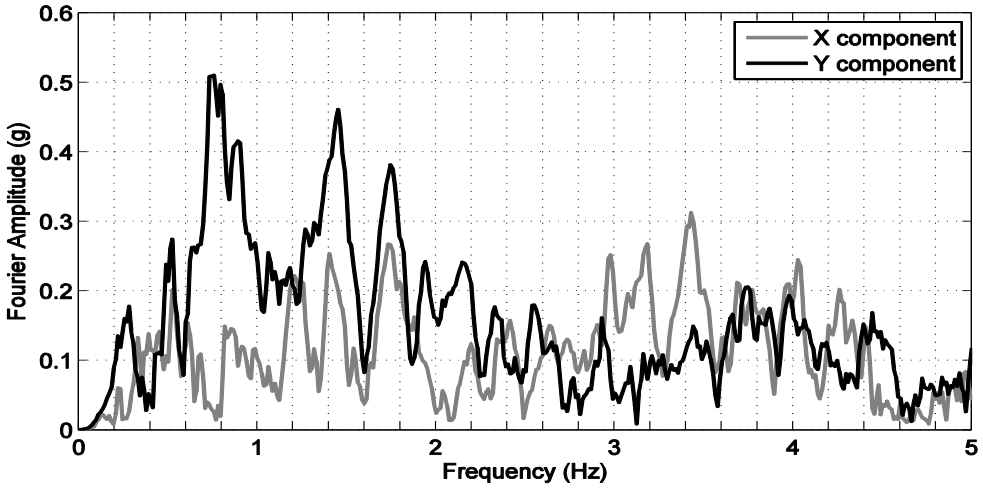

Figure 7.32: Fourier amplitude of the horizontal acceleration at the ground surface center node

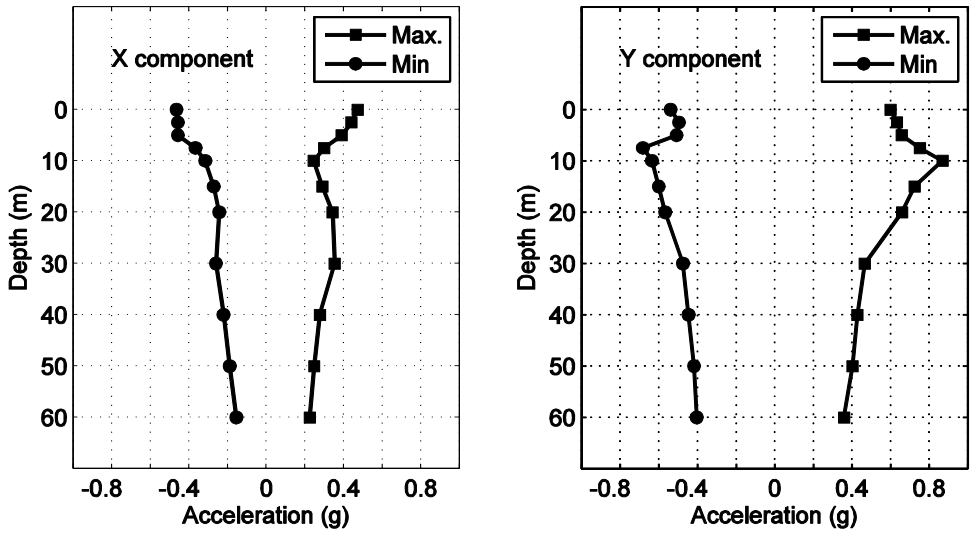

Figure 7.33: Peak ground acceleration profile along the depth below the center node

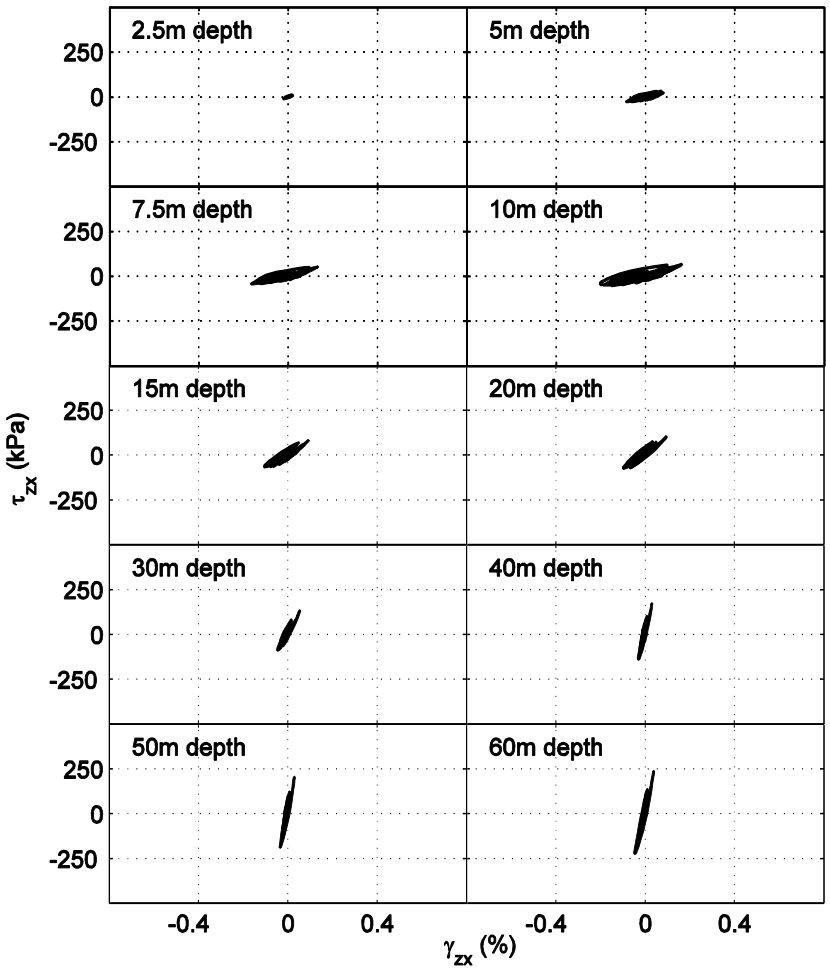

Figure 7.34: In the global X direction (zx), shear stress-strain response at different depths below the surface center for the Northridge earthquake in 1994

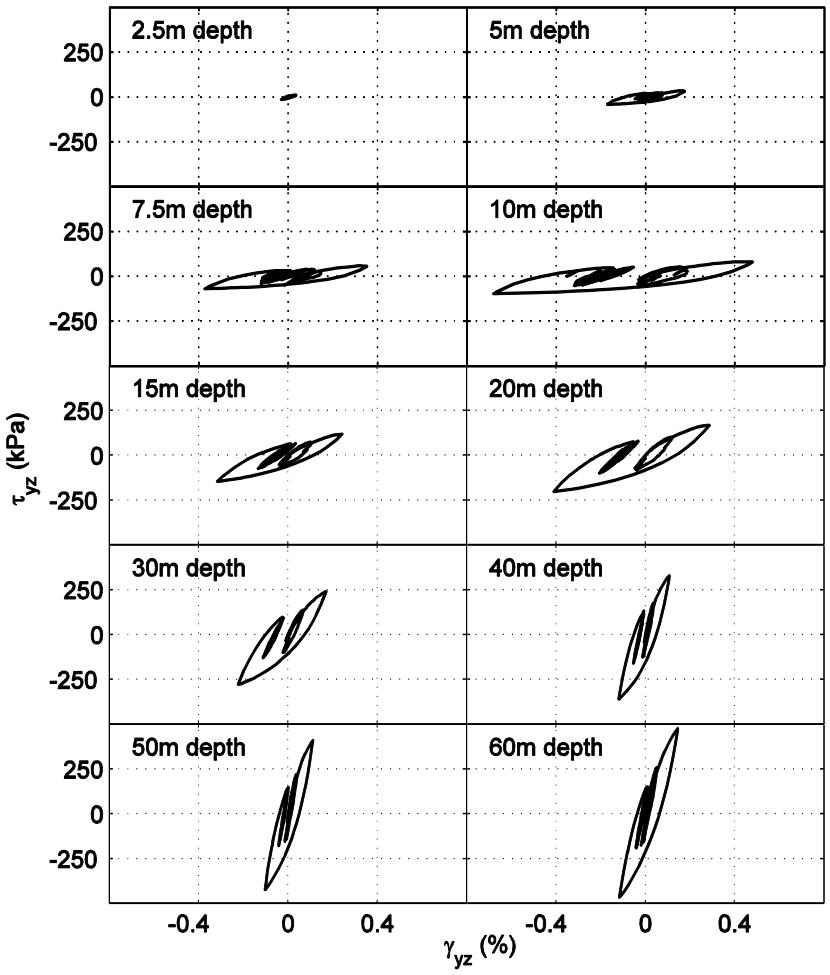

Figure 7.35: In the global Y direction (yz), shear stress-strain response at different depths below the surface center for the Northridge earthquake in 1994

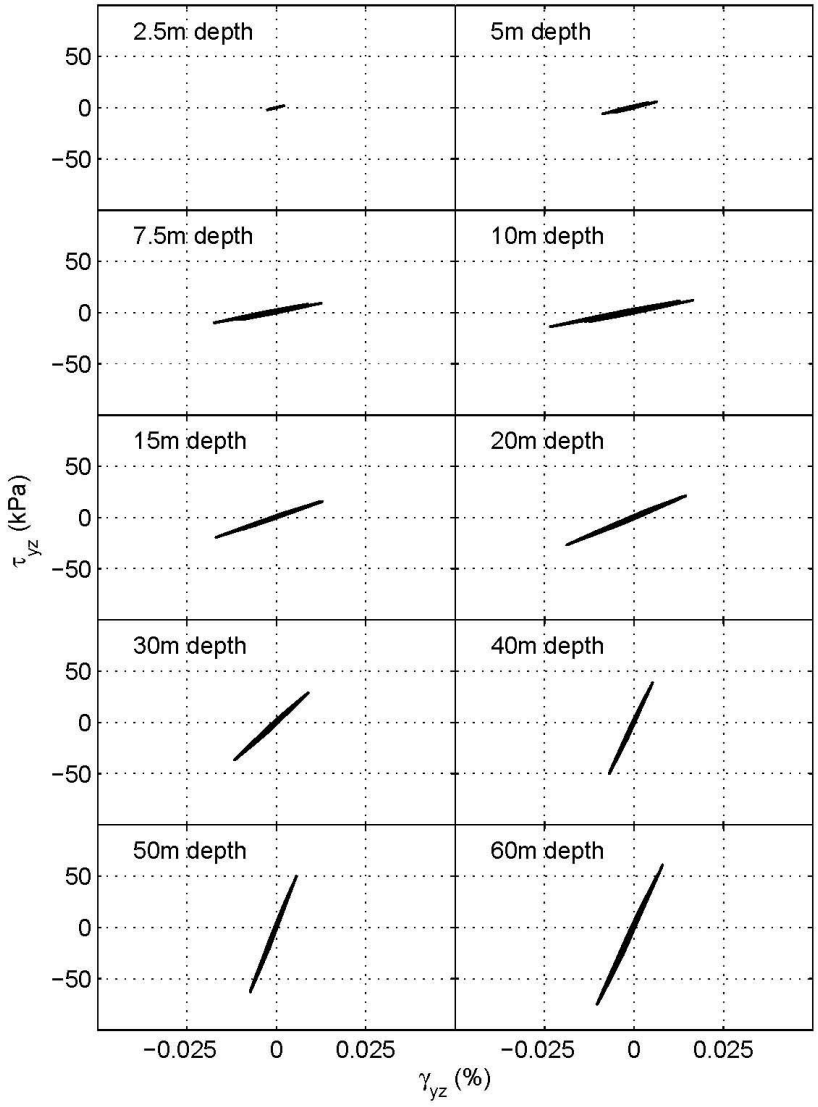

Figure 7.36: Shear stress-strain response at different depths below the surface center for Landers earthquake in 1992; global X direction (yz)

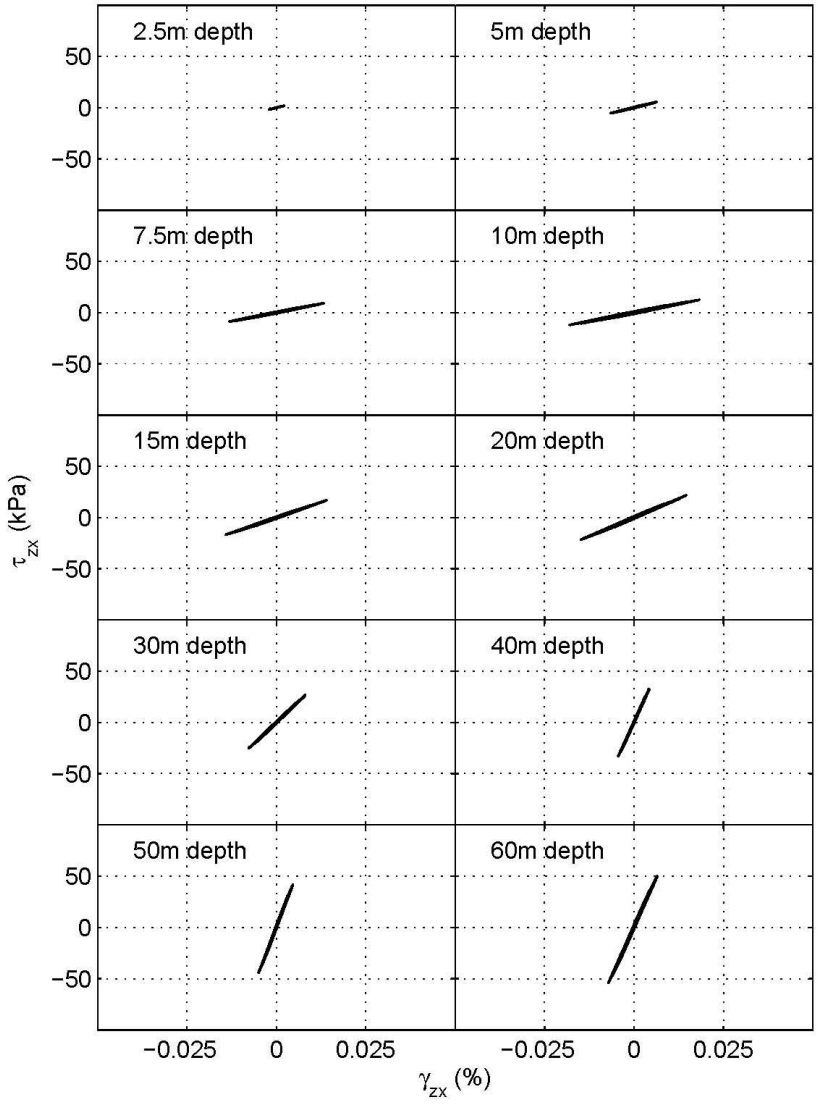

Figure 7.36: (Continued) Shear stress-strain response at different depths below the surface center for Landers earthquake in 1992; global Y direction (zx)

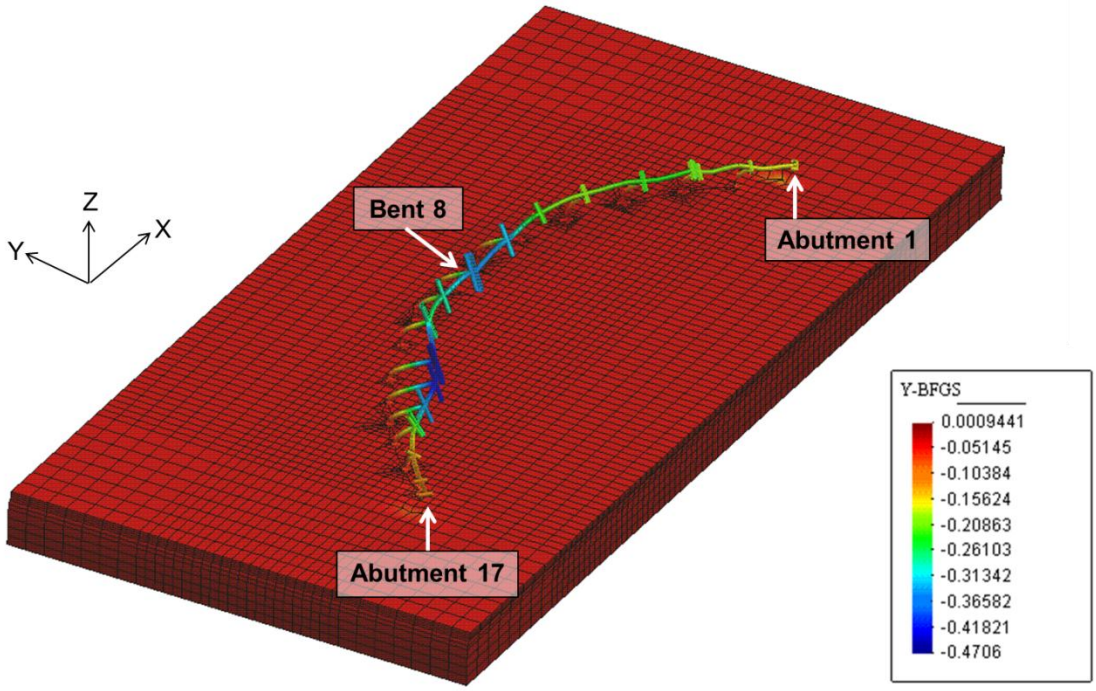

(a) Deformed shape (factor of 100) of the BFGS

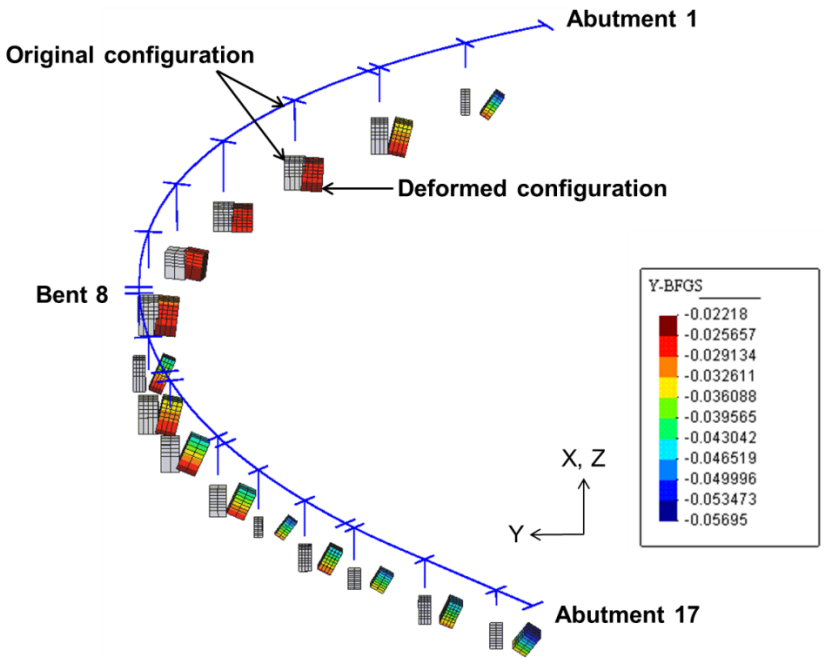

(b) Deformed shape (factor of 300) of the pile foundation

Figure 7.37: Deformed shape of the BFGS at 5.92 sec. when the maximum drift ratio occurs at the top of Bent 8

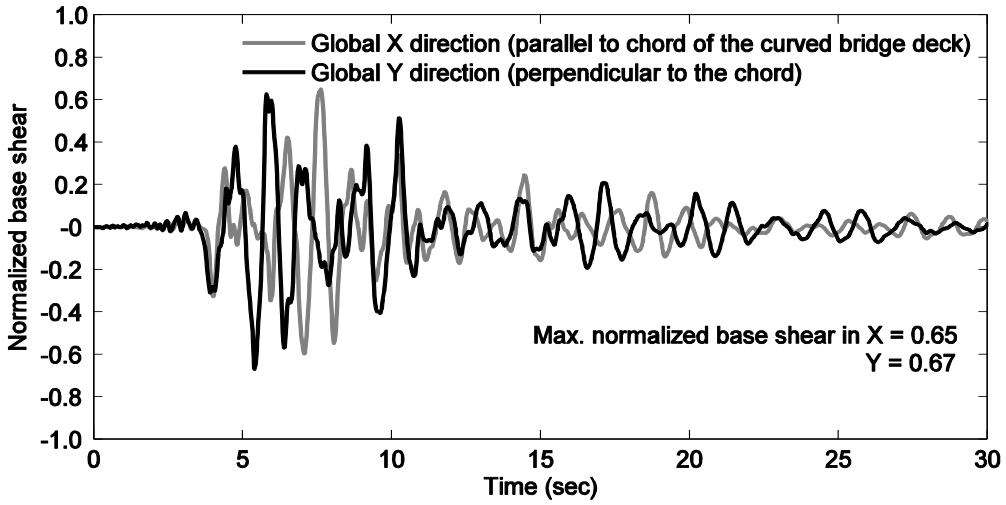

Figure 7.38: Normalized base shear time history in the global direction

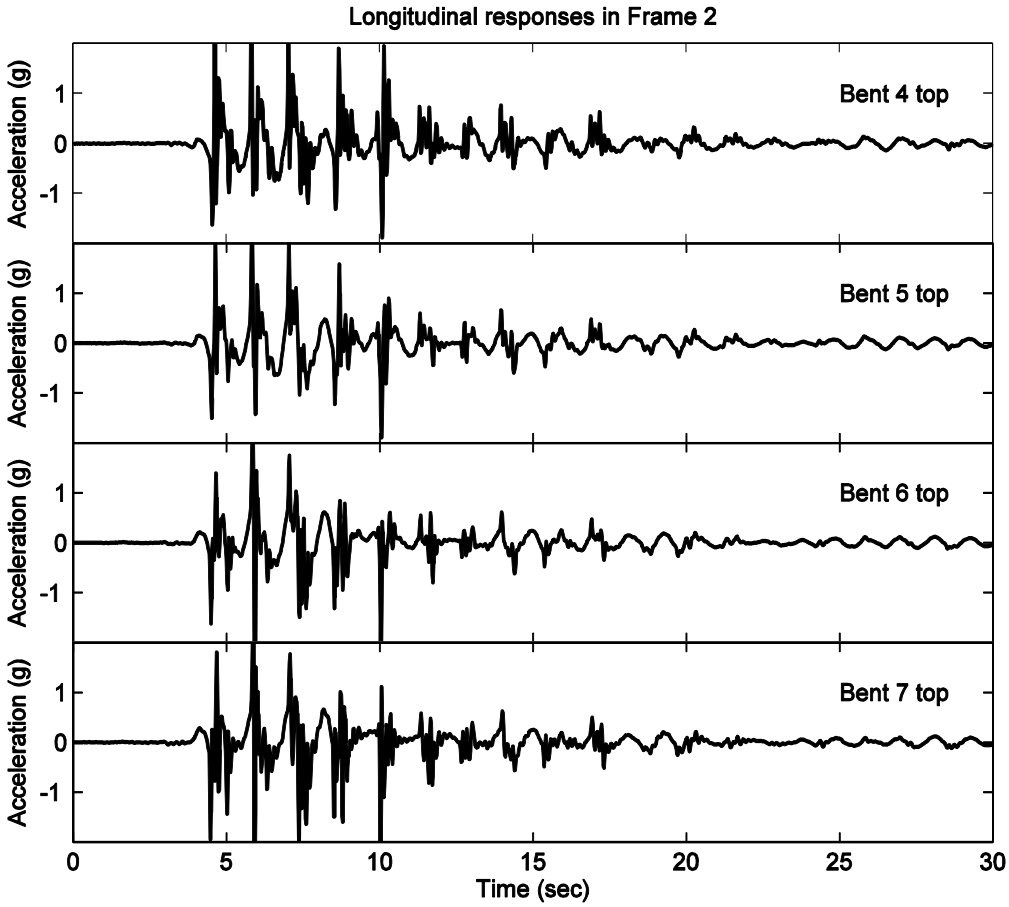

(a) Longitudinal direction

Figure 7.39: Total acceleration time history in the relatively flexible Frame 2 (Bent 4 through Bent 7)

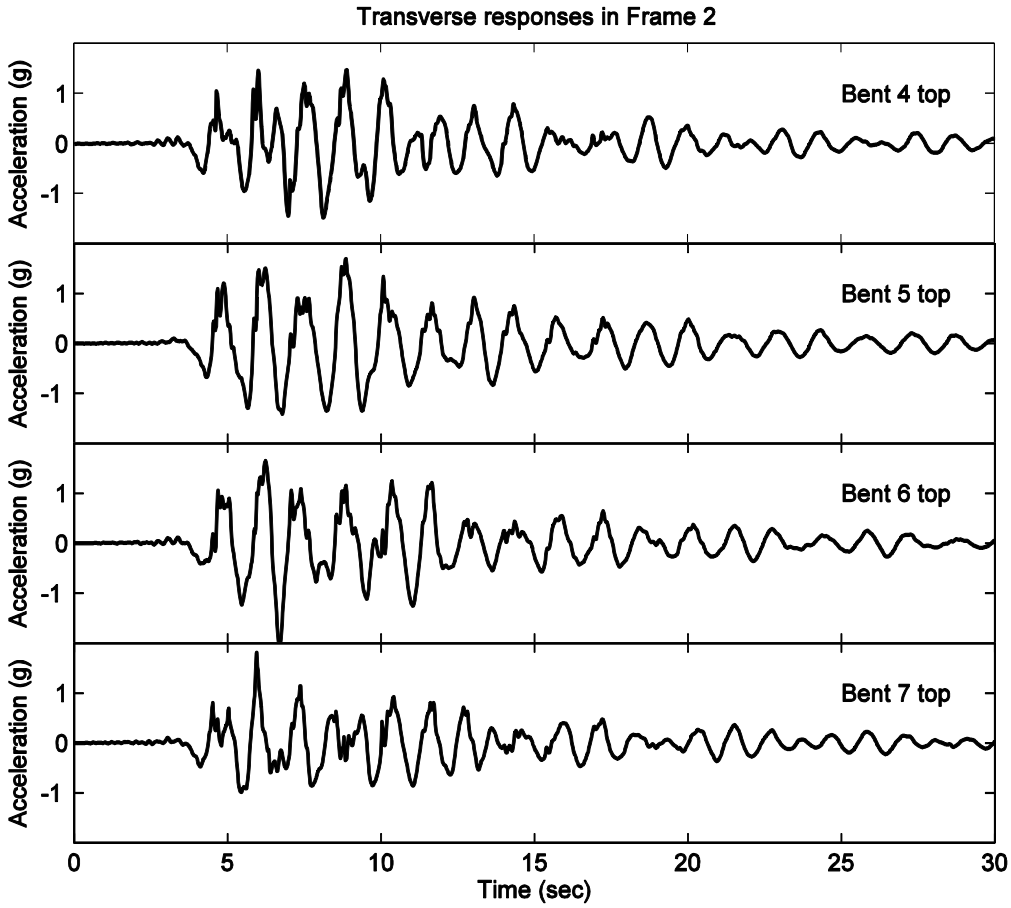

(b) Transverse direction

Figure 7.39: (continued) Total acceleration time history in the relatively flexible Frame 2 (Bent 4 through Bent 7)

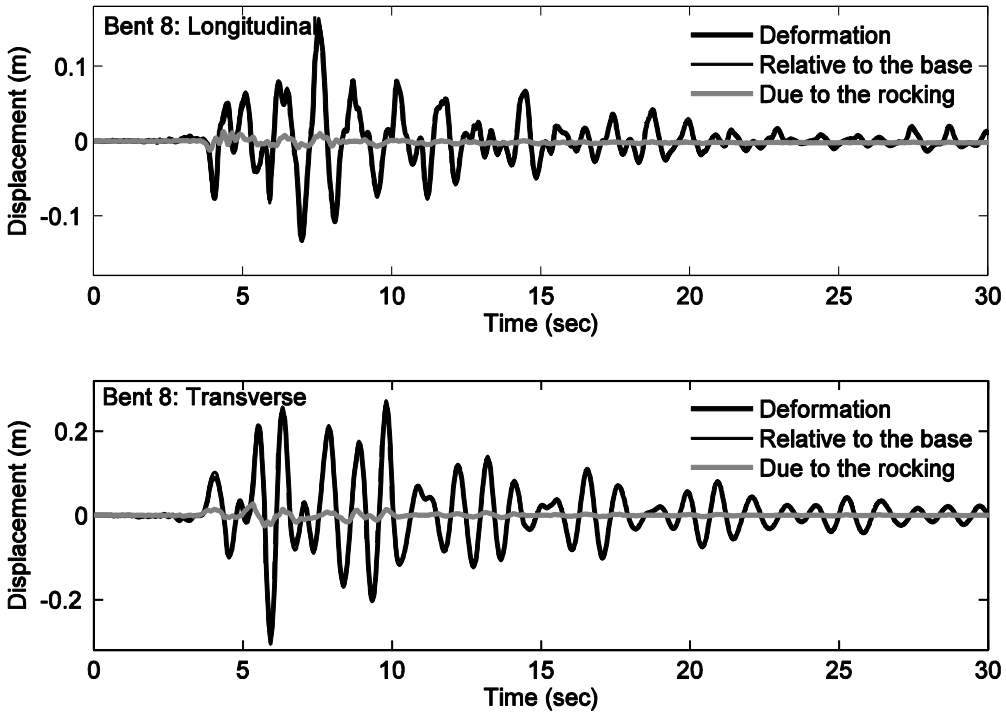

Figure 7.40: Displacement time history at the top of Bent 8

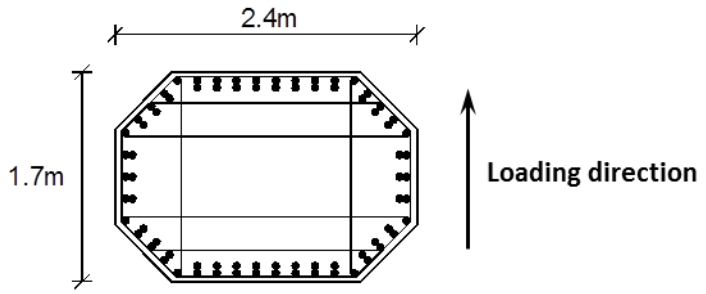

(a) Cross-section for Bent 7

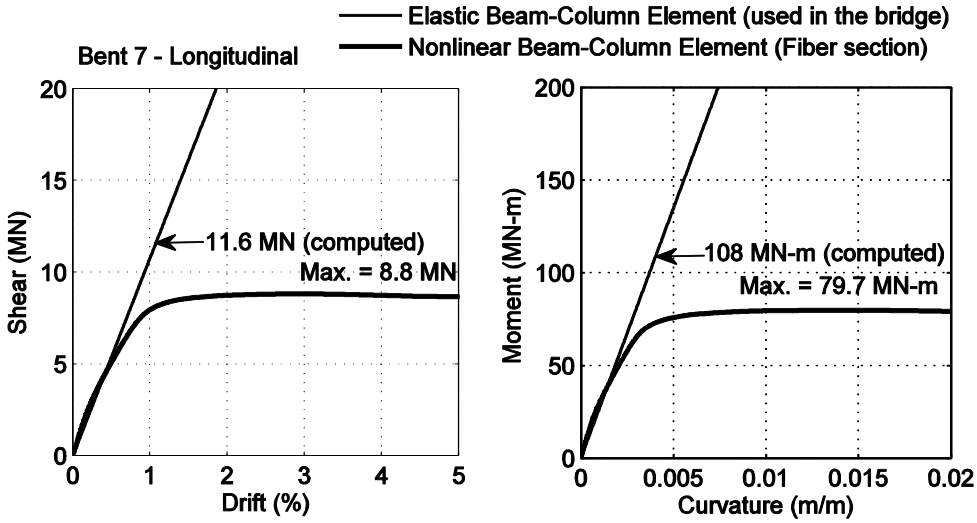

(b) Longitudinal direction

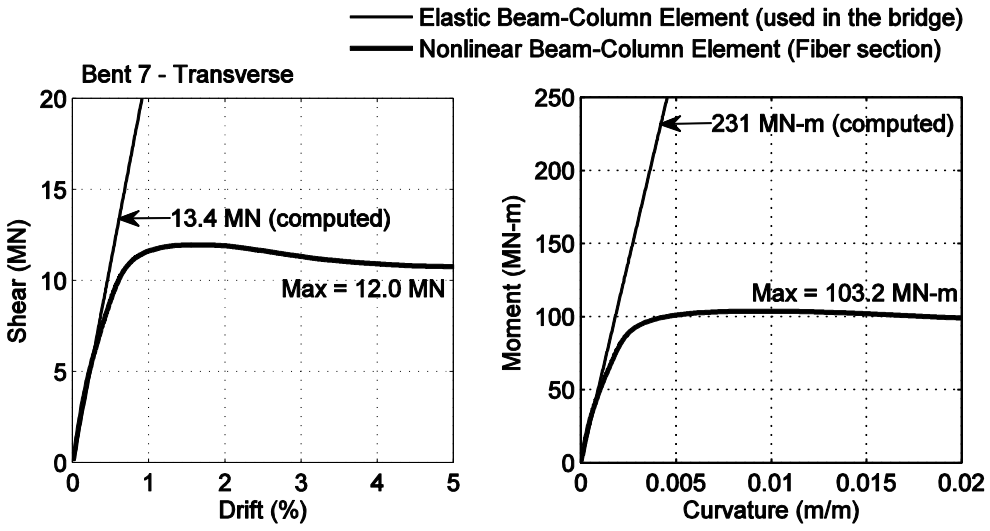

(c) Transverse direction

Figure 7.41: Comparison of the force demand obtained from the analysis with the idealized peak strength of the column in the longitudinal direction at Bent 7

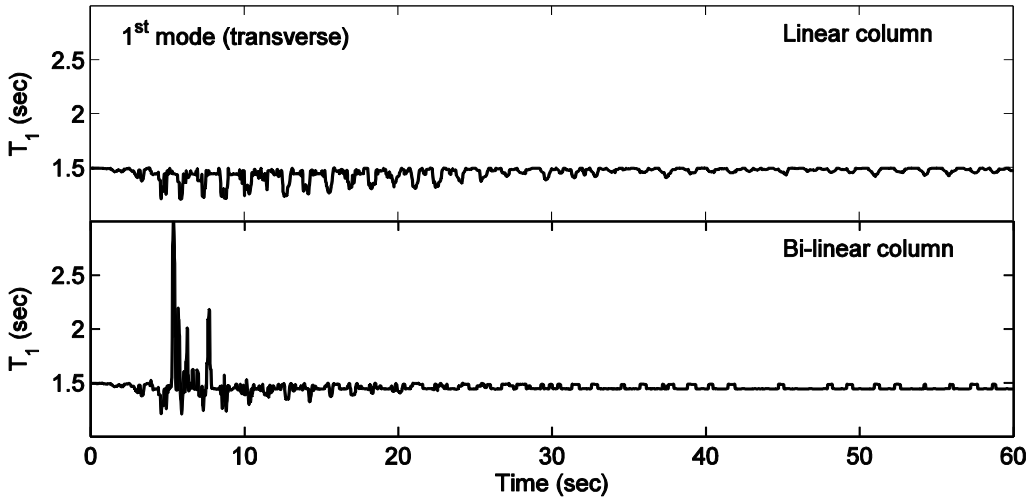

(a) In the 1st mode associated with the transverse response

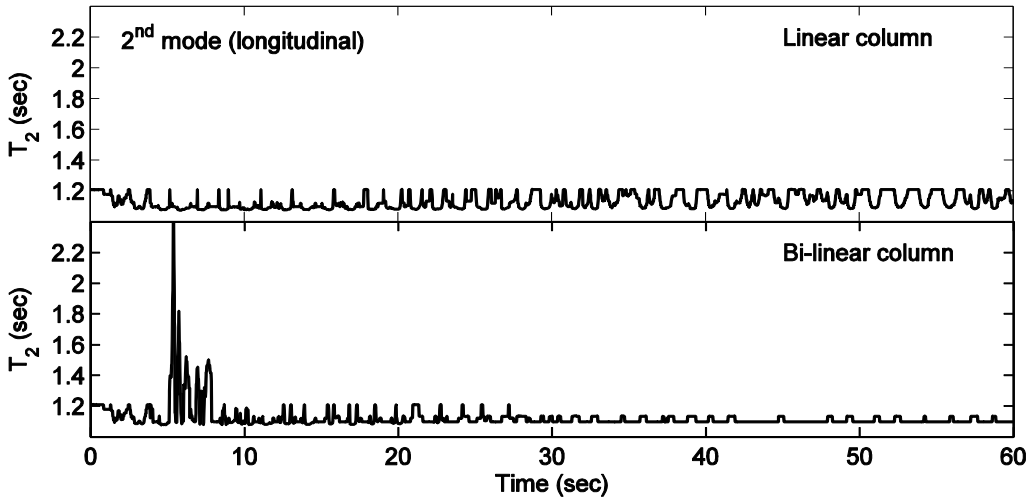

(b) In the 2nd model associated with the longitudinal response

Figure 7.42: Comparison of the dynamic period variation in the analysis of the fixed-base bridge with the linear columns and bilinear columns during the 1994 Newhall Fire station Northridge earthquake

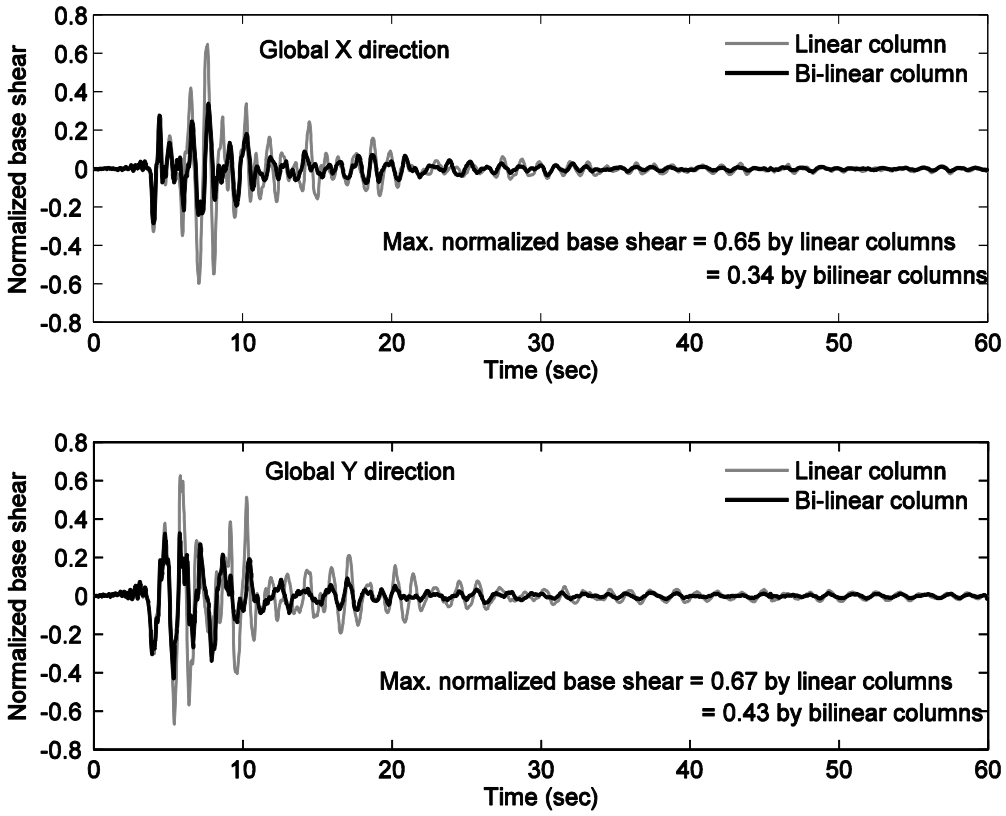

Figure 7.43: Comparison of the normalized base shear with linear columns and bilinear columns

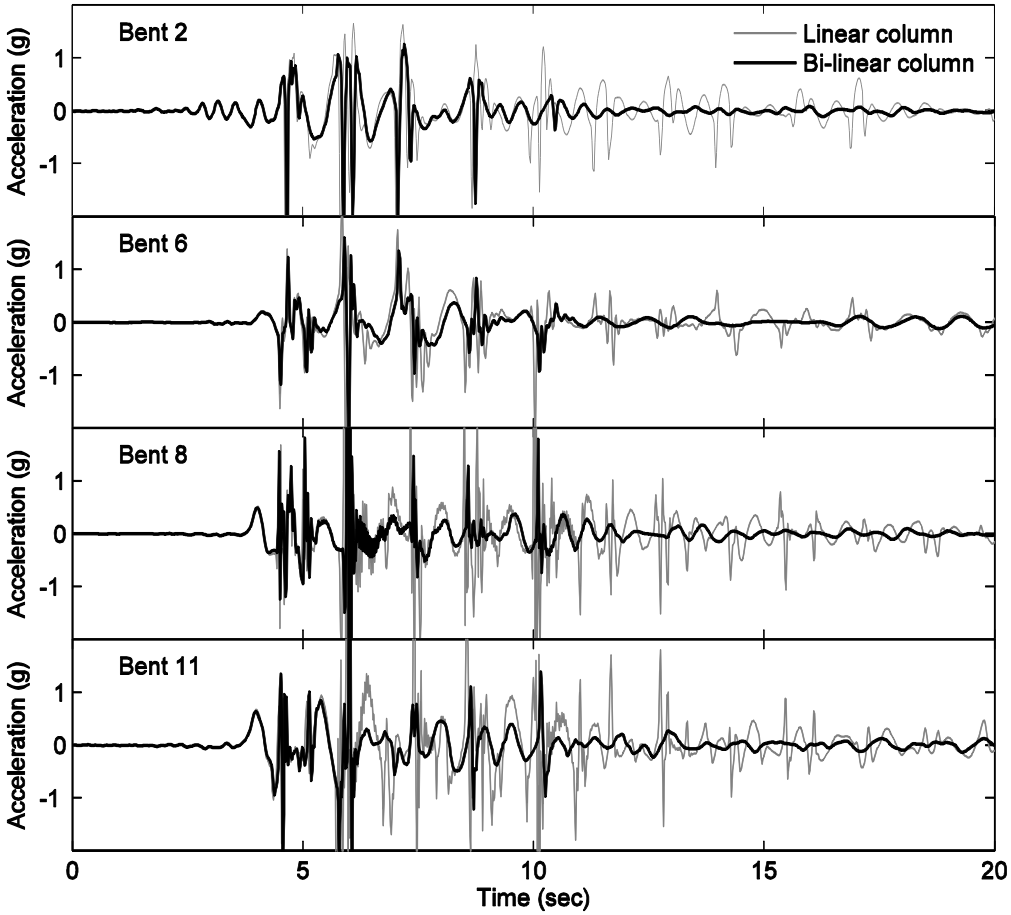

(a) Longitudinal direction

Figure 7.44: Acceleration time histories at the top of Bents 2, 6, 8, and 11 with linear columns and bilinear columns

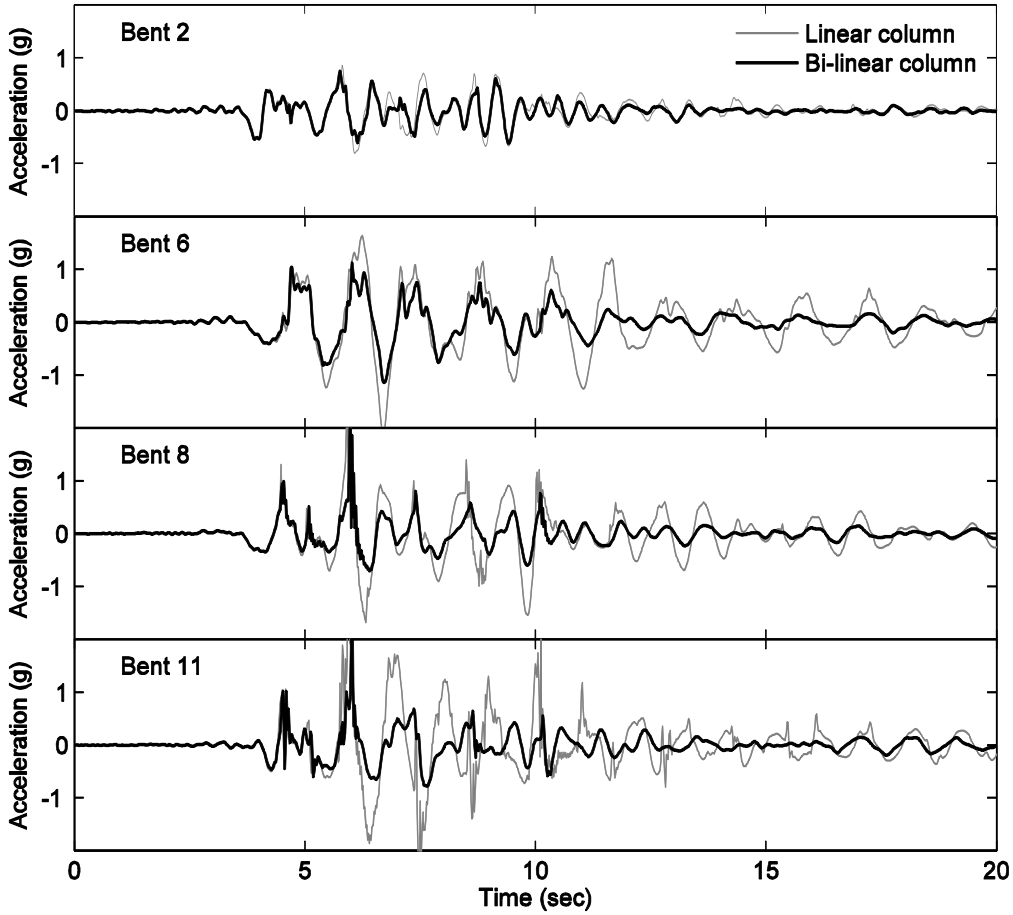

(b) Transverse direction

Figure 7.44: (continued) Acceleration time histories at the top of Bents 2, 6, 8, and 11 with linear columns and bilinear columns

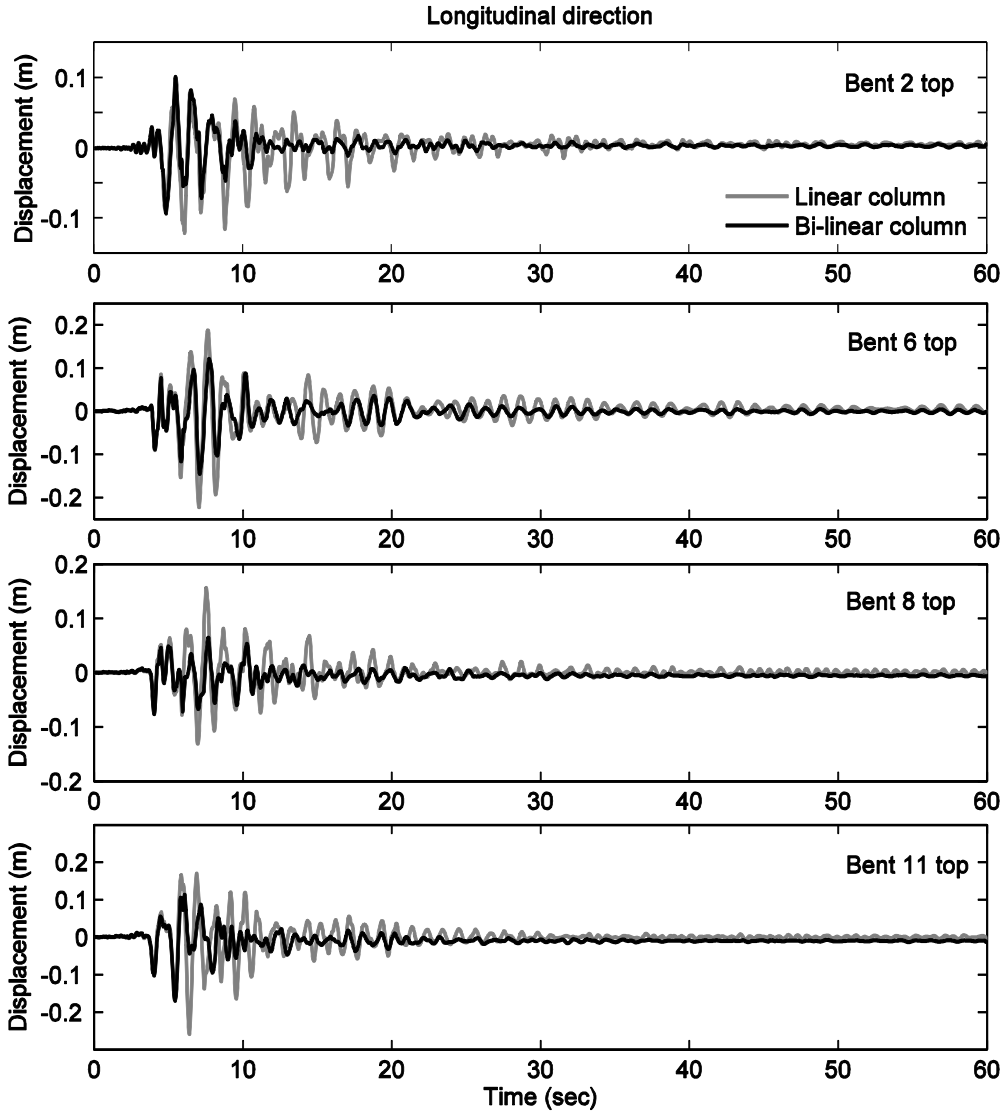

(a) Longitudinal direction

Figure 7.45: Displacement time histories at the top of Bents 2, 6, 8, and 11 with linear columns and bilinear columns

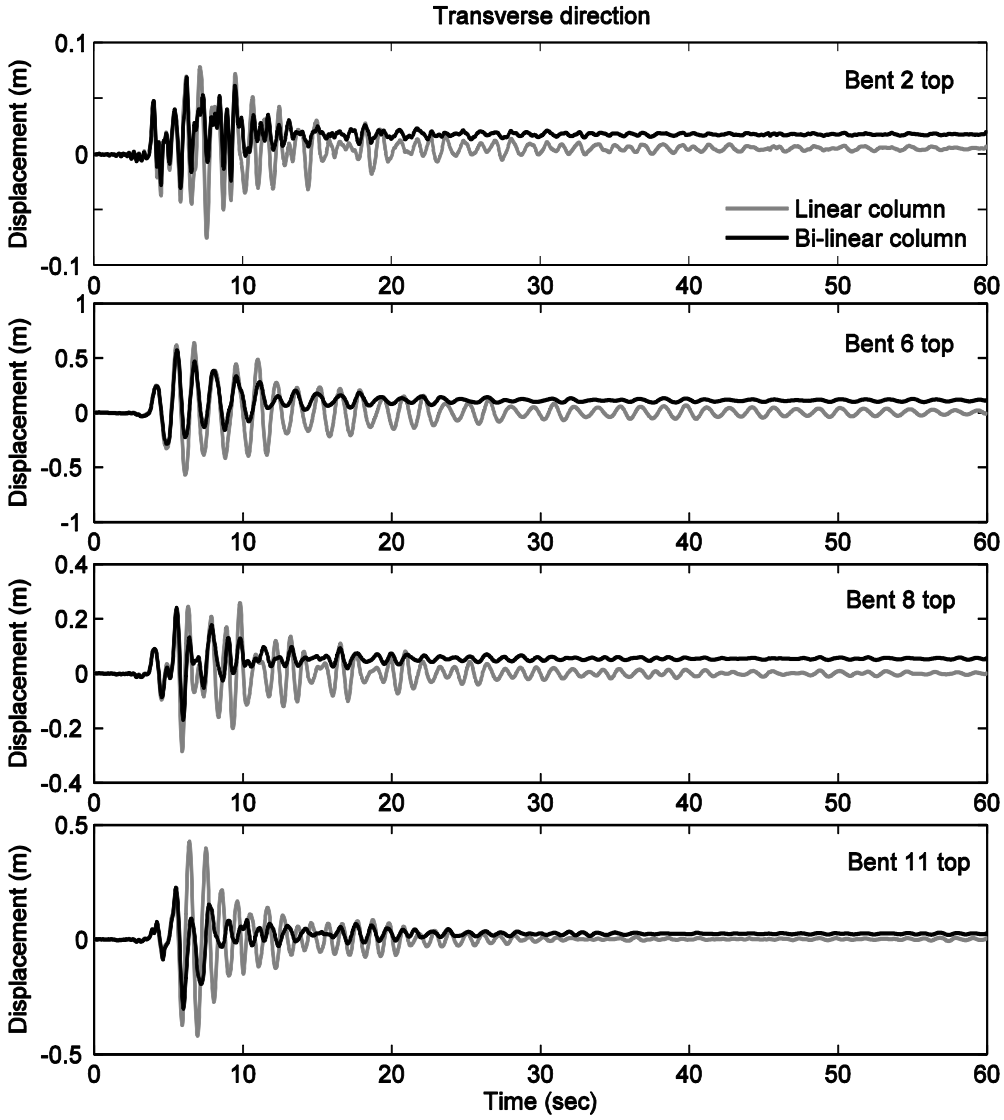

(b) Transverse direction

Figure 7.45: (continued) Displacement time histories at the top of Bents 2, 6, 8, and 11 with linear columns and bilinear columns

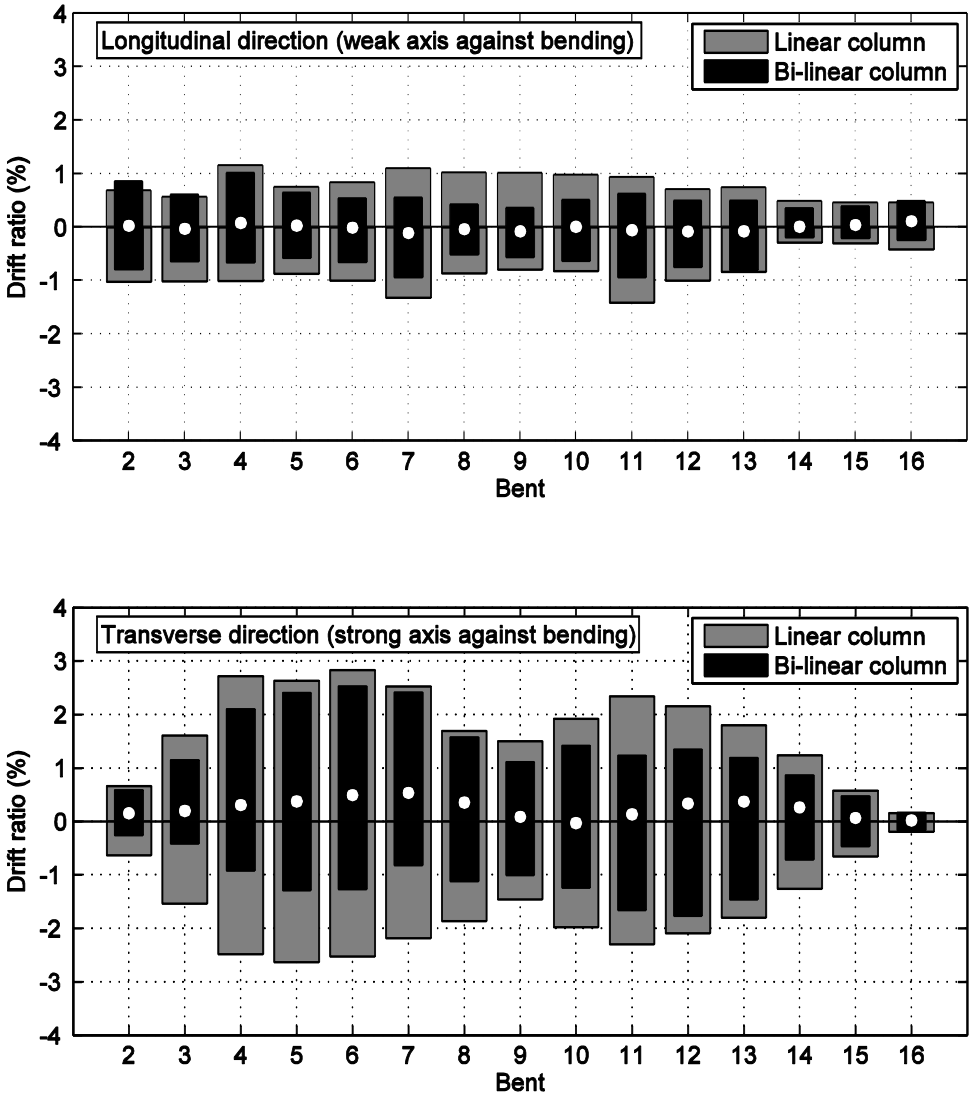

Figure 7.46: Comparison of the maximum drift ratio with linear columns and bilinear columns, with residual displacement by white dot

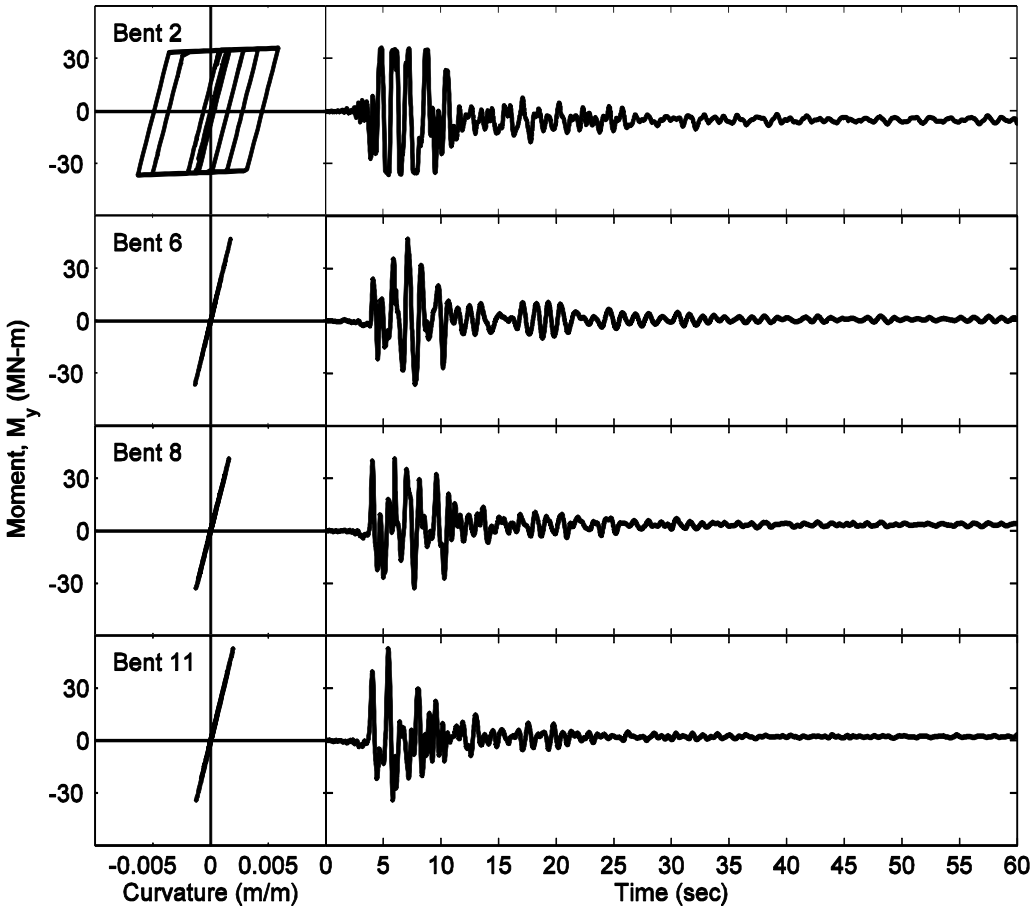

(a) Longitudinal direction

Figure 7.47: Moment-curvature response and moment time histories at the base of Bents 2, 6, 8, and 11

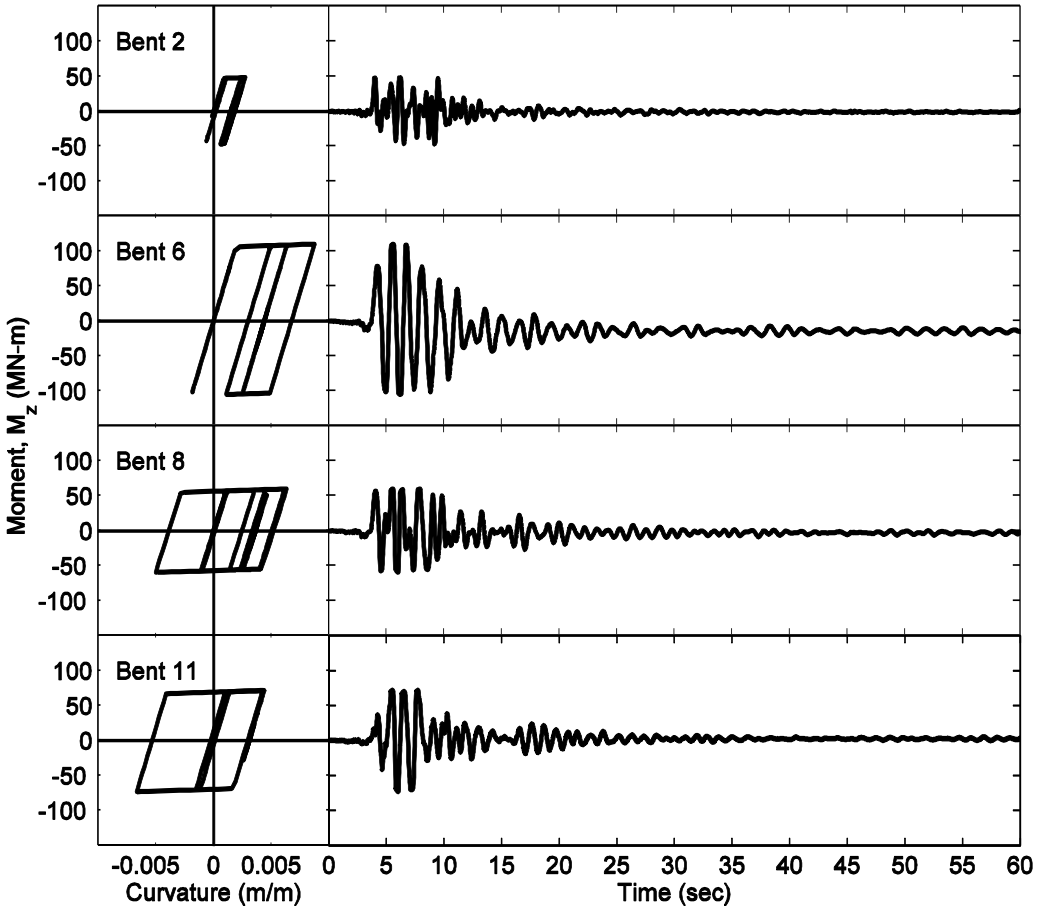

(b) Transverse direction

Figure 7.47: (continued) Moment-curvature response and moment time histories at the base of Bents 2, 6, 8, and 11

Chapter 8

Soil-Structure-Interaction for a Deeply Embedded Structure

This chapter presents seismic response results for a simple rectangular rigid structure embedded at a considerable depth in the linear soil domain using the Domain Reduction Method (DRM). Due to the limitation imposed by soil element size (20 m brick elements), the results only attempt to capture a partial picture of the overall response. Primarily, the results mainly reflect response characteristics resulting from the geometric configuration of such a relatively large rigid structure embedded within the surrounding soil domain (influence thereof on the low frequency response as represented by the employed mesh). Effects due to changes in soil elastic properties, depth of embedment, and characteristics of input excitation on the response of the structure are

discussed. An effort is made to isolate and study the effect of kinematic interaction, by looking at the response of a corresponding massless structural model.

8.1 Introduction

In a seismic analysis of massive embedded structures, an evaluation of dynamic interaction with surrounding soil is an important aspect. For this evaluation, embedment of the structure and the soil characteristics may play a major role in dictating the resulting dynamic response. In order to study effects of these issues, finite element (FE) analyses are performed and results are presented. In the FE model, a rigid rectangular structure with elastic material properties is employed. Simulation results are discussed and compared to a corresponding free-field scenario (i.e. without any structure in the soil deposit). Overall, the conducted numerical investigations addressed:

(1) Soil characteristics: stiff and soft soil layers, and

(2) Depth of embedment: no embedment (surface foundation), 20 m, 40, and 60 m embedment.

8.2 Description of the numerical model

8.2.1 Ground model

In order to study dynamic interaction for an embedded large rigid structure, the region of interest (ROI; Petropoulos 2008) is adopted for modeling (see Section 2.1). As discussed earlier in Chapter 5, the linear soil material properties are employed for the stiff

and the soft cases (Table 8.1). For these cases, the ground response (i.e. free-field) can be found in Section 5.2.1.

8.2.2 Structural model

A relatively rigid rectangular structure is considered (Figure 8.1). The size of the structure is 40 m by 40 m in the horizontal plane (square) with a height of 60 m. For this structure, elastic isotropic solid elements are used with rigid properties relative to the employed soil stiffness (modulus of elasticity of 170 GPa and Poisson's ratio of 0.2). The structure is composed of two parts (denoted as m1 and m2 in Figure 8.1) with mass of 30 and 13.5 tons, respectively. With two layers of soil, the structure base is embedded (Figure 8.1) in the relatively stiffer underlying material (Table 8.1).

In order to isolate the effect of kinematic interaction, a massless structure is employed in an additional numerical investigation. Figure 8.2 shows the finite element (FE) model excluding the buffer zone in which spurious reflections of waves are absorbed (Petropoulos 2008).

8.2.3 Input excitation

As discussed earlier in Chapter 2 (see Section 2.1.4), the low frequency input is specified along the exterior boundaries (except for the surface) of the ROI. This input results from the scenario of a magnitude 7.1 (moment magnitude) rupture of the Puente Hills fault as represented by the DRM (Bielak et al. 2003a).

8.3 Effect of soil characteristics

Analyses are presented to study effects of the soil characteristics in the following scenarios; 1) two types of soil layers are employed (stiff soil and the soft soil cases); 2) the rigid structure is fully embedded in the soil layers (60 m embedment); 3) the low-frequency input motion is used.

8.3.1 Results for the stiff soil case

Generally, the stiff soil condition did not allow for any significant amplification of seismic motions all along the depth (Figure 8.7). The peak base acceleration (X component) of the structure is almost identical to that at the top (Figure 8.8a and Figure 8.9a). In the Y direction, acceleration at the top of the structure is even lower than that at the base (Figure 8.8b and Figure 8.9b). Compared to the soft soil case, the soil zone affected by presence of the structure is significantly reduced (about one half). Rocking is also much less than the soft soil case (induce a drift of 0.02%).

8.3.2 Results for the soft soil case

Maximum accelerations along the base of the structure are very similar to the corresponding free-field response at the same location. However, the rigidity of the structure and embedment in the underlying stiff soil decrease the amplification of acceleration along its height. Consequently, the maximum acceleration at the top of the structure (level of the soil surface) is reduced (13% and 9% for the X and Y components, respectively), compared to the free-field response (Figure 8.3). This reduction also affects

ground response in the local region near the structure (up to 300 m away) in the X direction (Figure 8.4a). In the Y direction, the affected spatial extent is about 200 m (Figure 8.4b). In addition, it can be seen that base-slab averaging across the structure is an additional significant effect in this reduced response.

During the excitation, rigid body rotations are mostly observed in the structural response. Rocking at the base induces a top displacement of about 0.03 m (about 0.1% drift ratio) in both X and Y directions (Figure 8.5). On the other hand, it appears that displacement deviations between the structure base and the corresponding free-field response are negligible (less than 0.01 m; see Figure 8.6).

8.4 Effects of embedment

In this section, attention is focused on the soft soil case with the low-frequency input motion. The rigid structure is analyzed for the four different depths of 0 m (i.e. surface foundation), 20 m, 40 m, and 60 m.

8.4.1 Simulation results

Maximum accelerations at the levels of ground surface and structure base are shown in Figure 8.10 through Figure 8.12, corresponding to the employed embedment depths. As observed earlier in the 60 m scenario (Figure 8.4), all embedded cases show a reduction of accelerations in the zone around the structure, However, it can be seen that decreasing embedment reduces the spatial extent of this reduction (Figure 8.10 through Figure 8.12). Thus, this reduction can be attributed to embedment in the relatively soft

upper layer (depth of 0-40 m), unlike the 60 m case (where the base was located in the lower stiffer layer)

Due to higher amplification of acceleration near the ground surface, the maximum acceleration at the base increases as embedment decreases. Consequently, a larger acceleration is developed at the top of the structure. Overturning tendency of the structure founded directly on the ground surface (case of the 0 m embedment) also contributes to a higher acceleration at the base, compared to the corresponding free-field response at the same location (Figure 8.10).

8.5 Evaluation of kinematic interaction

In order to isolate and study effects of kinematic interaction, a massless structural model is employed in an additional analysis. Corresponding results are compared to the response (mass of the structure considered) in the previous cases (four different embedment depths from 0 m to 60 m in the soft and the stiff soil cases). The low-frequency input motion is used.

In the soft soil, Figure 8.13 shows a comparison of rotation (rocking) time histories at the structure base (with and without its mass) for the employed embedment depths. As embedment decreases, deviations of the angles with and without the structure mass tend to increase (Figure 8.13). In Figure 8.18, peak rotation (with the structural mass) is normalized by that resulting from the massless structure. Thus, increasing embedment decreases the effect of inertial interaction (Figure 8.14a), as the structure is constrained by a large area of the surrounding soil and lower accelerations at its base.

Meanwhile, in the stiff soil, the effect of kinematic interaction is dominant, with overall little dependence on embedment (Figure 8.14b).

As discussed earlier, the overturning tendency of the structure induces a larger base acceleration (compared to the free-field response), particularly in the surface foundation case. However, the massless structure base acceleration is very similar to the corresponding free-field response (Figure 8.10). Thus, this larger acceleration can be attributed to inertial interaction imposed by the structural mass. As embedment increases, differences of the base accelerations with and without mass of the structure tend to decrease. Consequently, acceleration and rocking at the structure base with and without its mass appear to be essentially identical for the 60 m embedment (induced by base-slab averaging interpreted as kinematic interaction). The same applies to torsion, spatially induced by the non-uniform DRM input excitation.

The schematics in Figure 8.15 might also be helpful in visualization the influence of inertial interaction. The displaced structural configuration (referenced to the free-field structure-base-center displacement), is shown for the different embedment depths (with and without structural mass) at the instant of peak free field surface acceleration. Rocking and out of phase responses may be visualized on this basis (Figure 8.15).

8.6 Summary and conclusions

Dynamic interaction for the rigid structure with different levels of embedment depths is investigated using the DRM. Effects of the soil characteristics with the elastic material properties and the seismic input characteristics in terms of the employed low

(narrow) frequency excitation are investigated. Imposed by the structure without its mass, kinematic interaction is isolated and evaluated. From the results of the present study, the main observations are:

1. For the fully embedded structure in the soft soil, rigidity of the structure and embedment in the underlying stiffer layer contributed to reduction of peak accelerations developed at the top. This reduction affected free-field accelerations in the local region near the structure. As embedment decreased, the affected spatial extent of the free-field response tended to be smaller.
2. As embedment decreased, a larger acceleration was observed in the soft soil due to amplification of the ground motion along the depth. At different embedment levels, the base acceleration of the structure was essentially dictated by the corresponding free-field response at the same location. Particularly for the surface foundation, overturning tendency of the structure increased the base acceleration.
3. In the stiff soil, no significant change was observed in base accelerations with different embedment depths (in this specific study). As observed in the soft soil, free-field response in the vicinity of the structure was affected by its presence. Compared to the soft soil, the affected spatial extent was about 50% less.
4. Through comparison of the structure with and without mass scenarios, out-of-phase response between top and base of the structure was induced by its mass in the surface foundation case (i.e. inertial interaction contributed to the structural response). As embedment decreased, this interaction tended to decrease and kinematic interaction became a more prominent parameter. On a similar note, kinematic interaction was more pronounced in the stiff soil, regardless of the embedment depth.

Table 8.1: Soil material properties for the soft soil profile

Layer	Density (t/m^3)	Vp (m/s)	Vs (m/s)	Thickness (m)	Region
1	1.5	1337.3	482.2	40	Region of Interest
2	1.714	1622.4	584.3	60	Region of Interest
3	1.714	1622.4	584.3	340	Buffer Zone
4	2.054	2372.9	651.3	60	Buffer Zone

Table 8.2: Soil material properties for the stiff soil profile

Layer	Density (t/m^3)	V_p (m/s)	V_s (m/s)	Thickness (m)	Region
1	1.5	668.7	241.1	40	Region of Interest
2	1.714	811.3	293.2	60	Region of Interest
3	1.714	811.2	292.2	340	Buffer Zone
4	2.054	1186.5	325.7	60	Buffer Zone

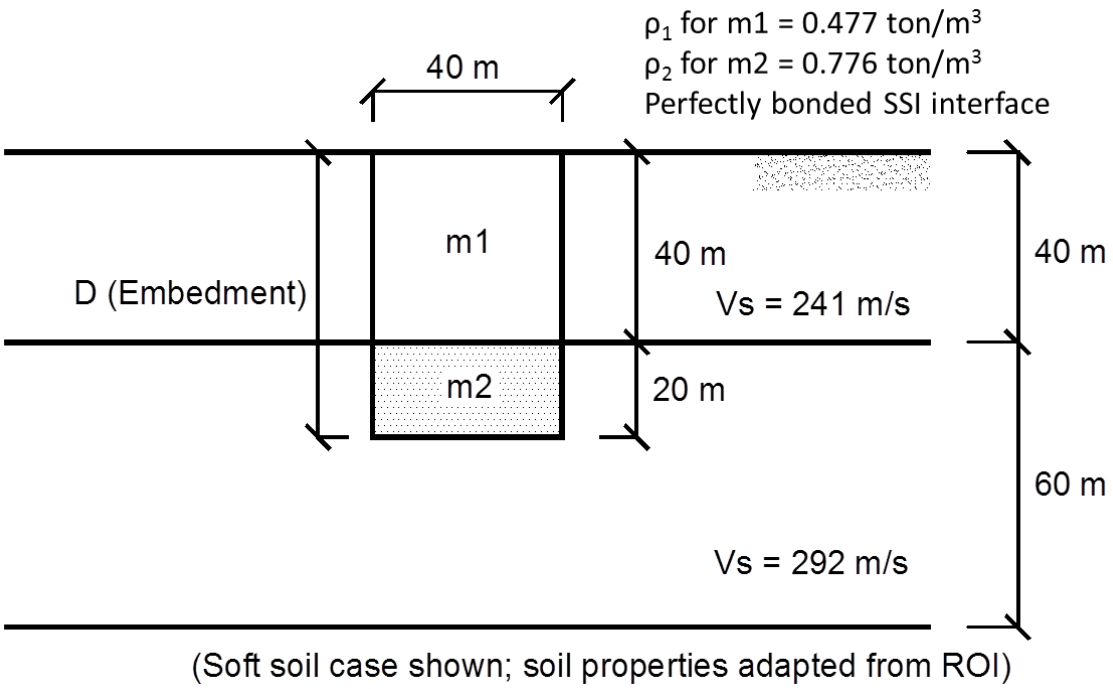

Figure 8.1: Schematic plan view of the fully embedded structure

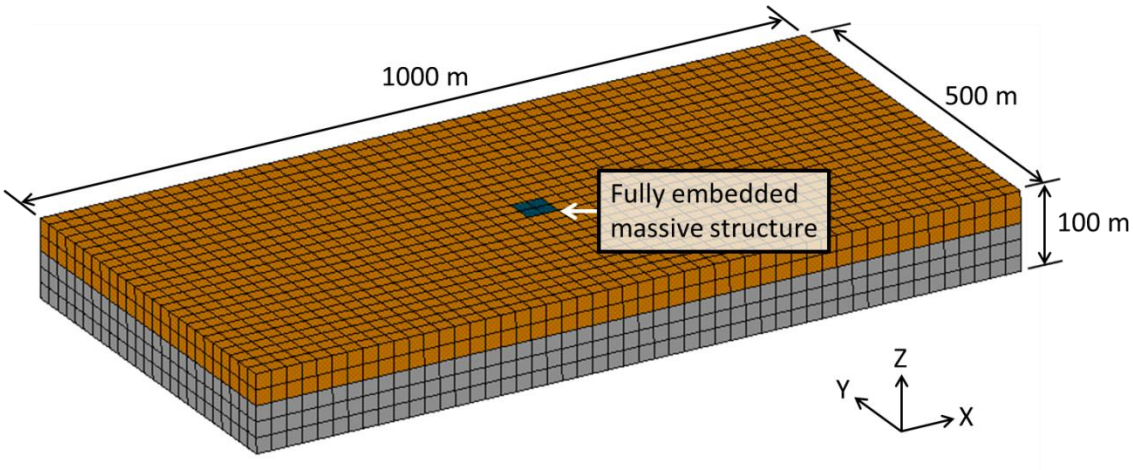

Figure 8.2: FE model for the fully embedded structure and ROI (i.e., excluding the buffer zone)

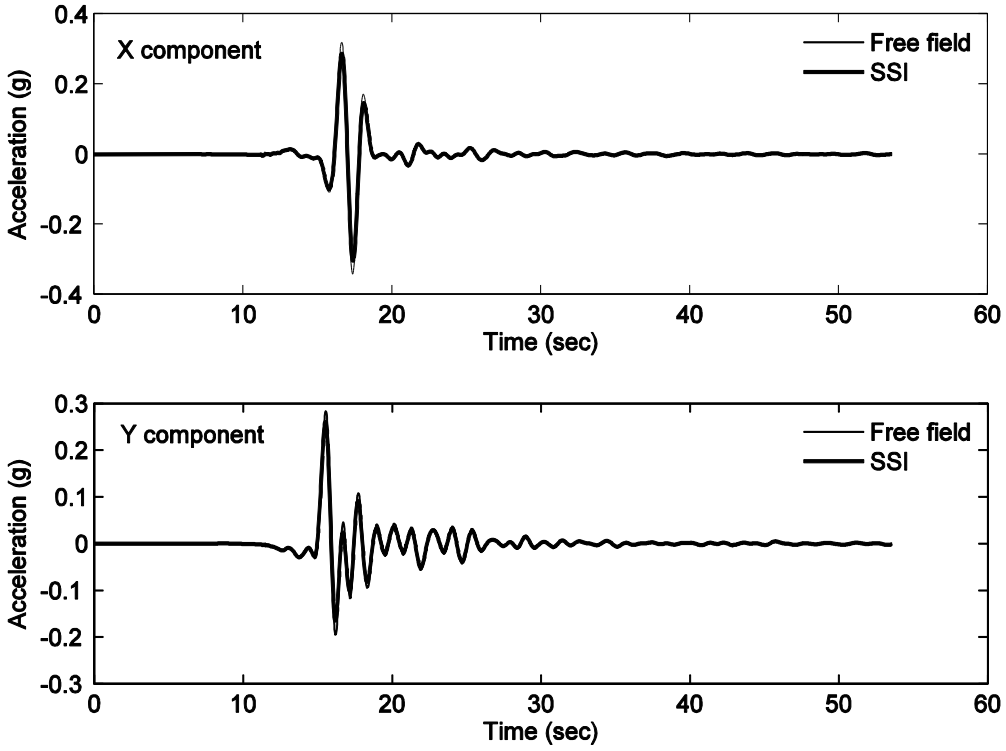

Figure 8.3: Total acceleration time histories at the center soil surface and top of the structure (60 m embedment)

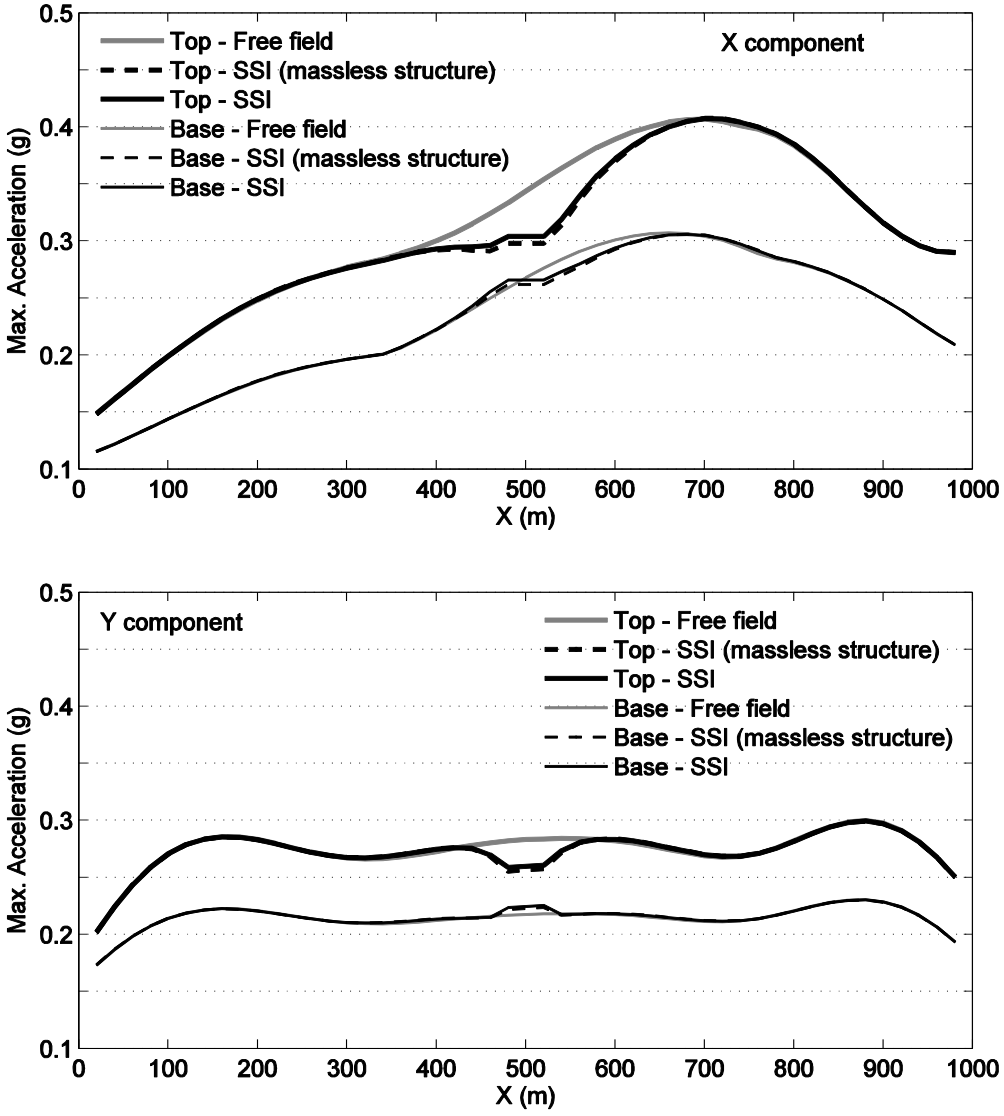

(a) Along the X center line

Figure 8.4: Peak ground acceleration distributions at the level of the top and base of the structure (case of the 60 m embedment)

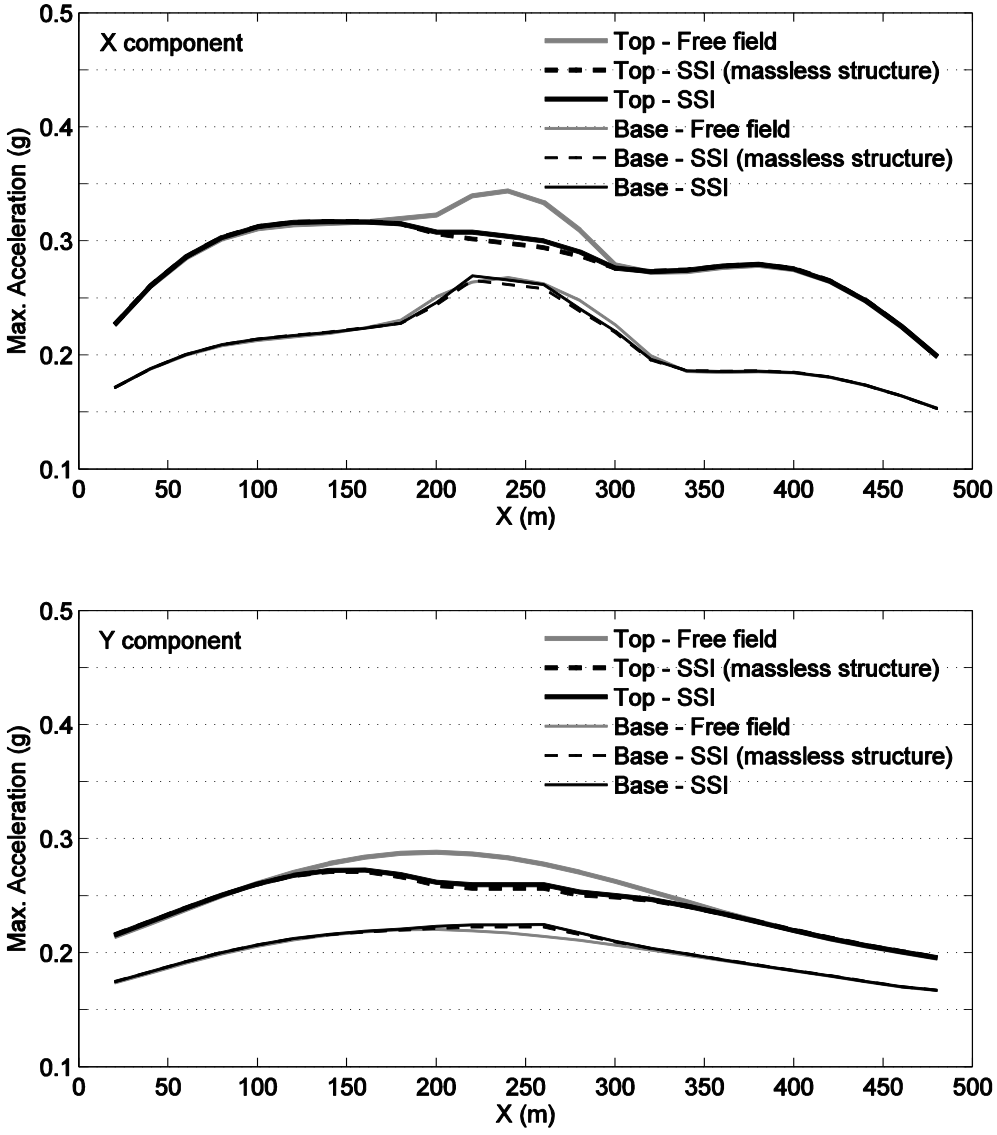

(b) Along the Y center line

Figure 8.4: (continued) Peak ground acceleration distributions at the level of the top and base of the structure (case of the 60 m embedment)

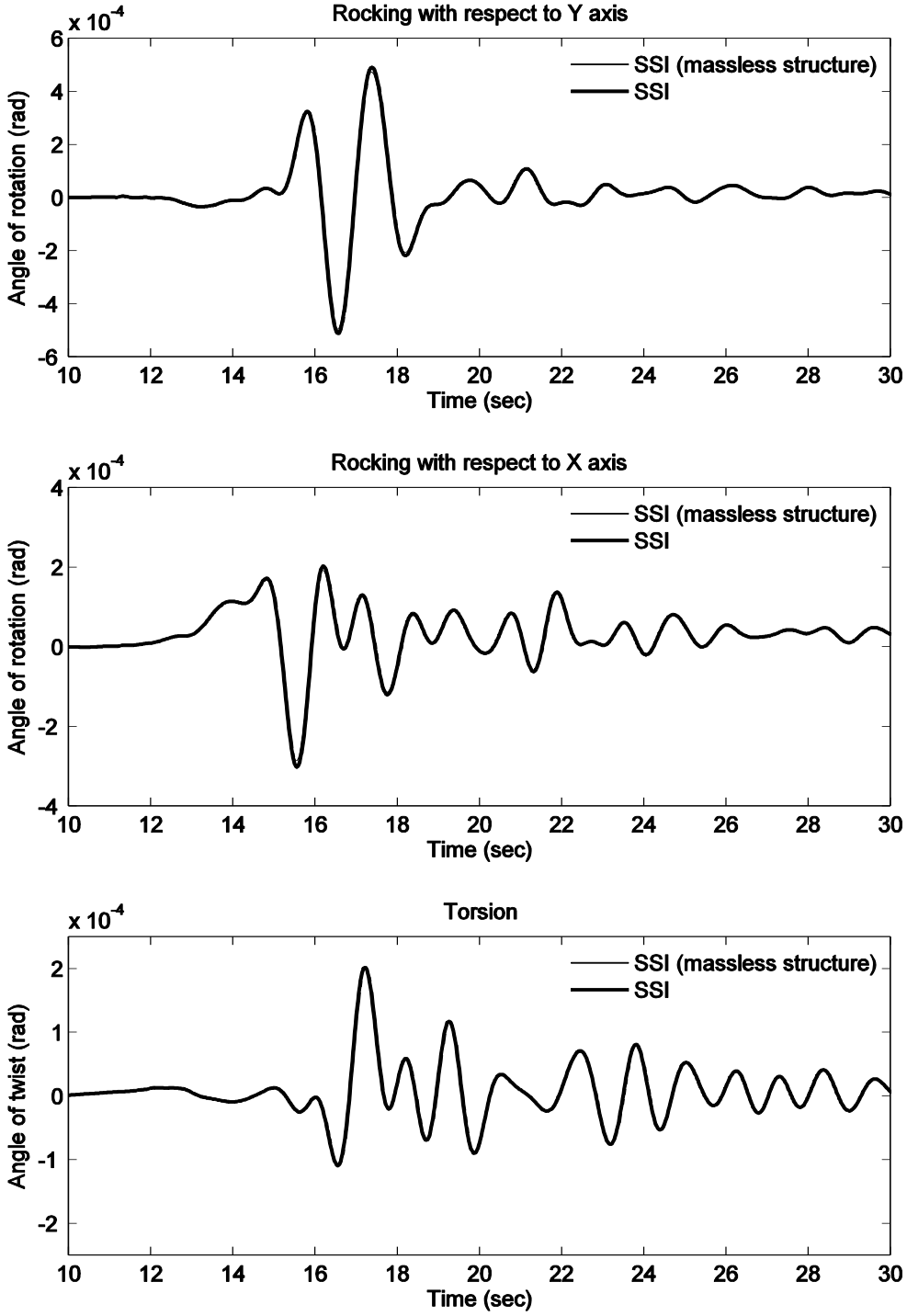

Figure 8.5: Angle of rotation and torsion time histories at the base

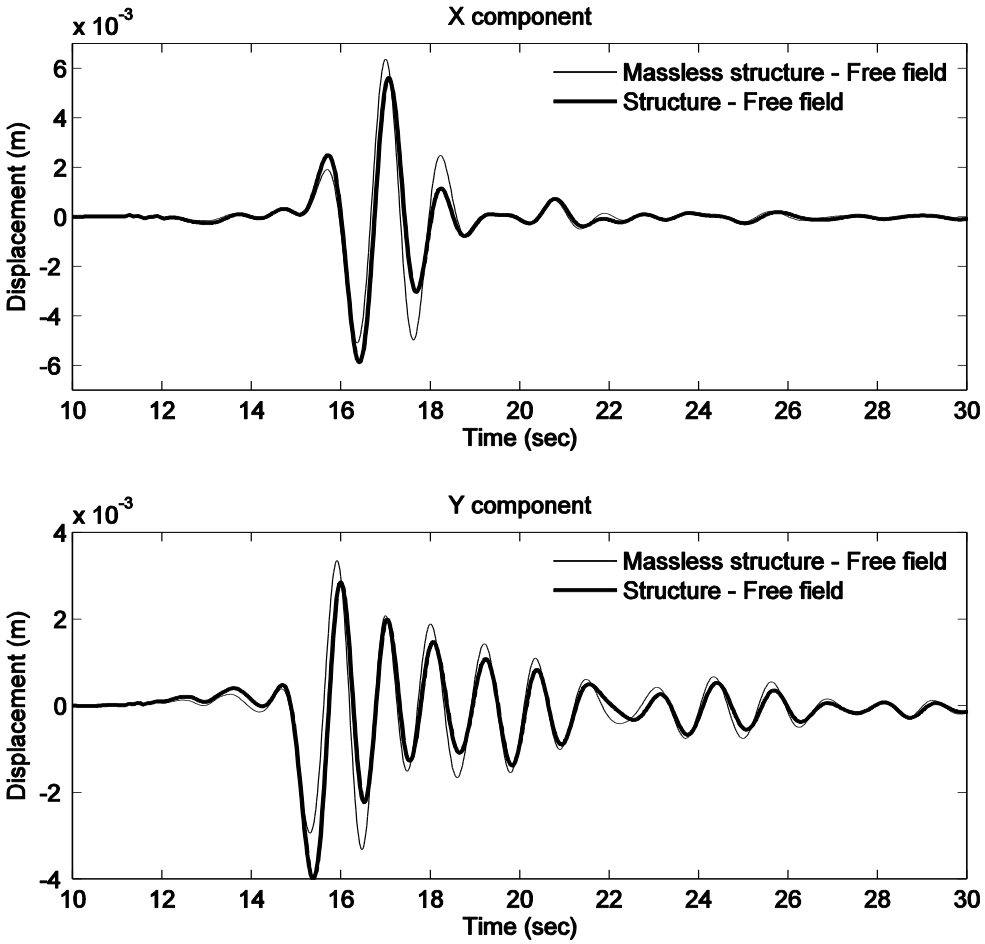

Figure 8.6: Displacement time histories at the base of the structure relative to the free-field

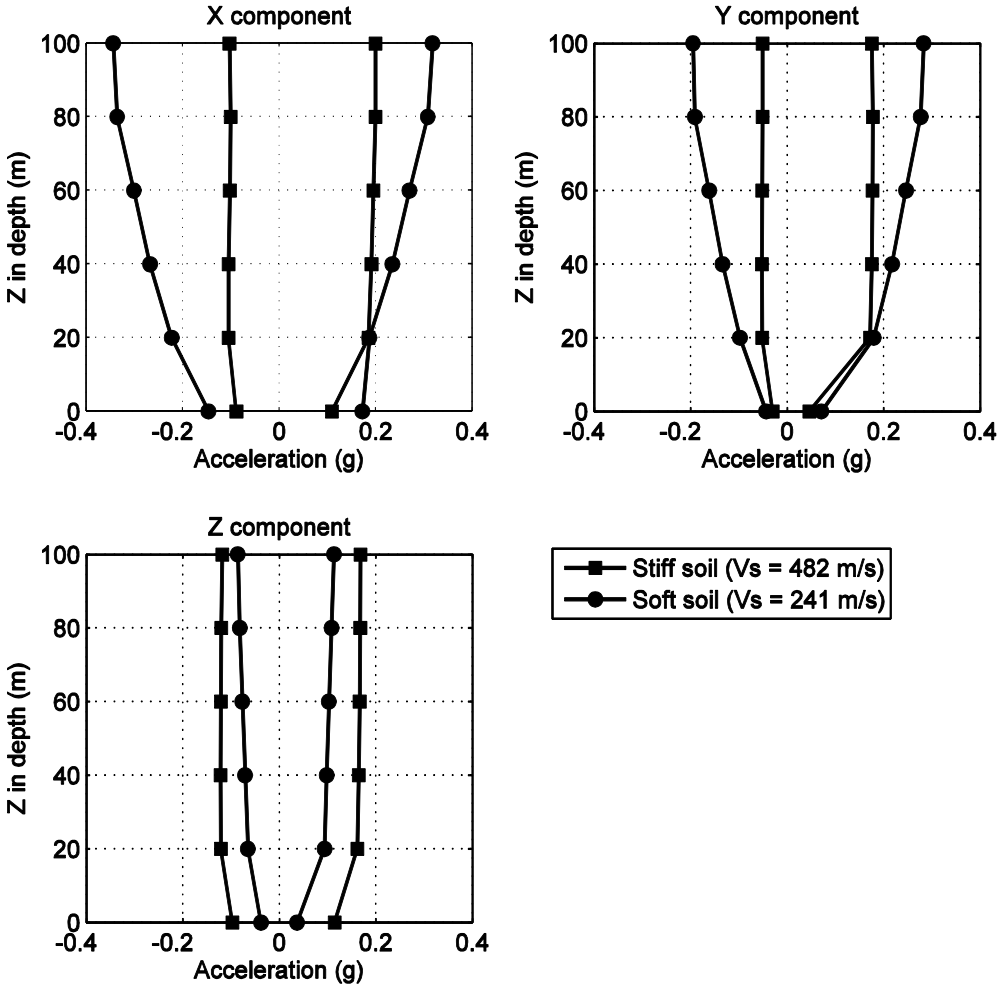

Figure 8.7: Comparison of the peak acceleration profiles along depth below the center node obtained from the stiff and soft soil

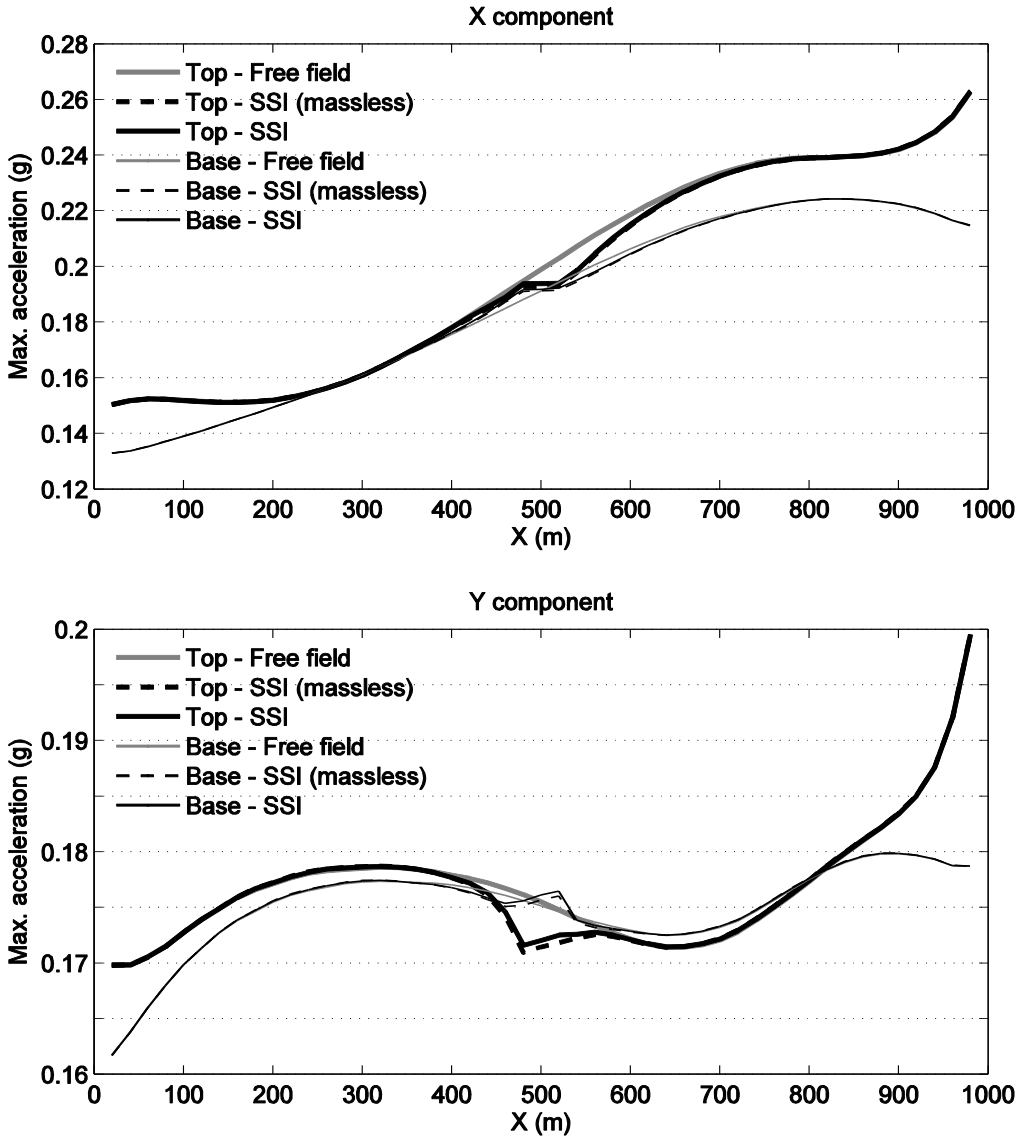

Figure 8.8: Peak ground acceleration (positive values for X and Y components) along the X center line at the level of soil surface and the base of the structure (60 m embedment) in the stiff soil

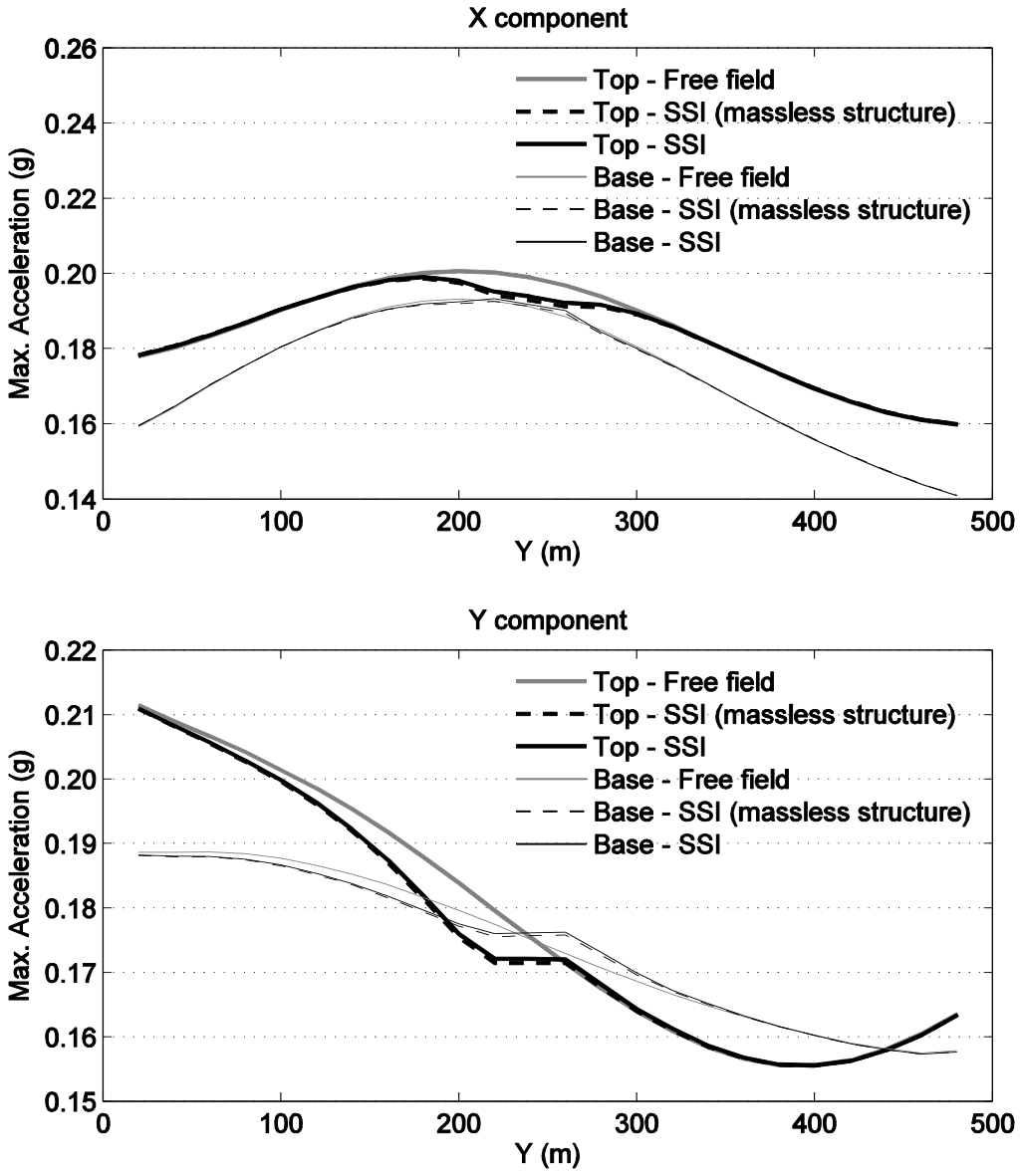

Figure 8.9: Peak ground acceleration (positive values for X and Y components) along the Y center line at the level of soil surface and the base of the structure (60 m embedment) in the stiff soil

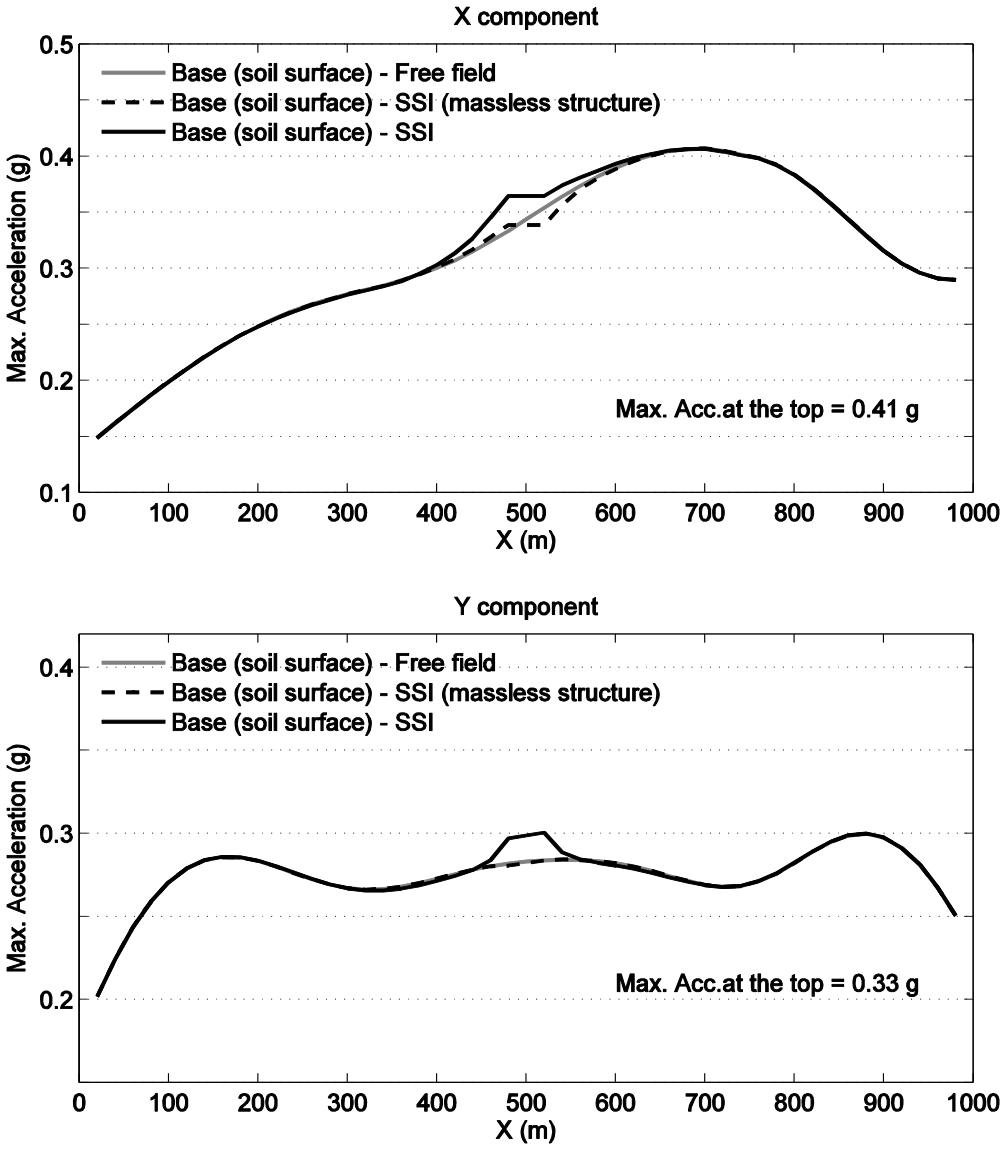

Figure 8.10: Peak ground acceleration along the center line at the level of the base of the structure (no embedment) in the X direction

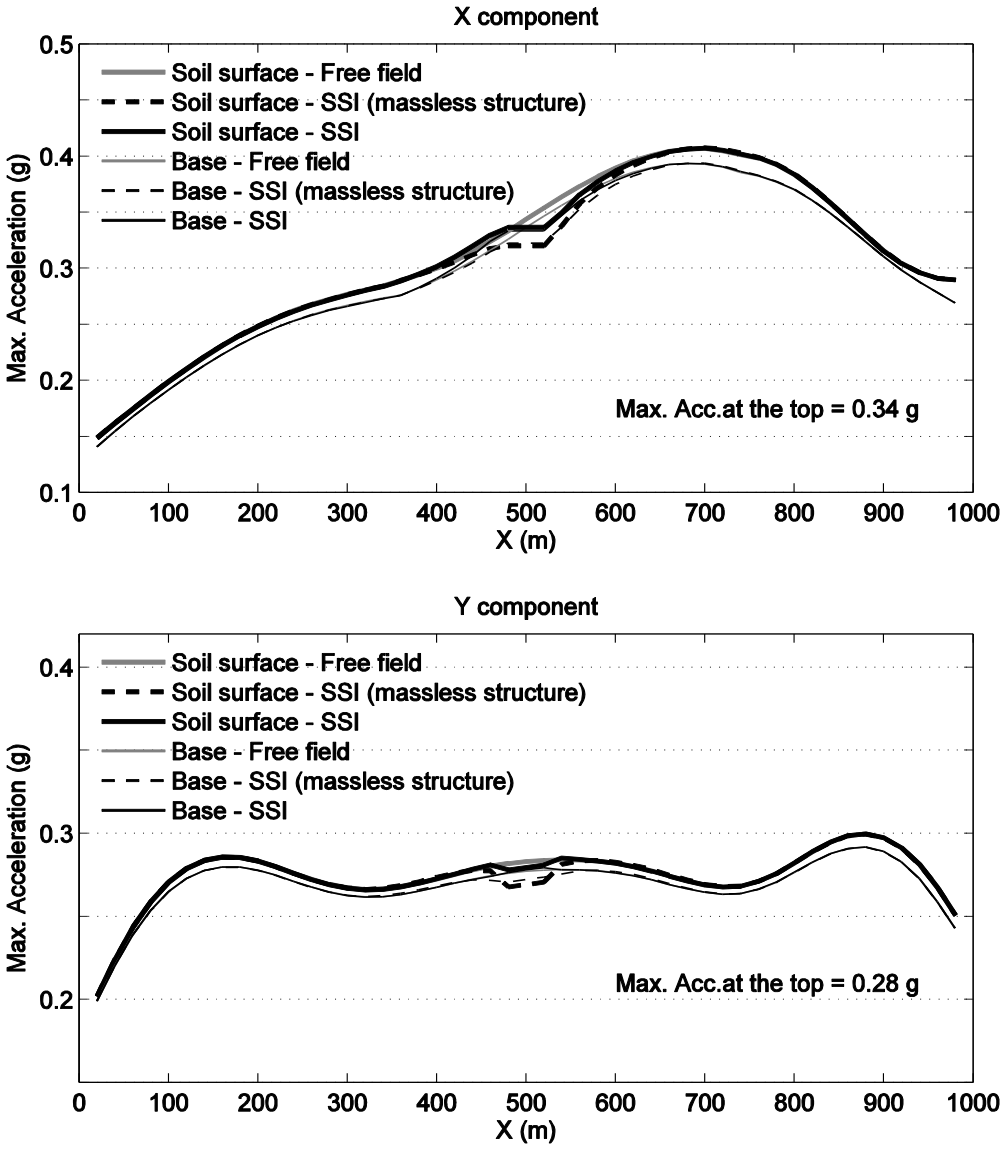

Figure 8.11: Peak ground acceleration along the center line at the level of soil surface and the base of the structure (20 m embedment) in the X direction

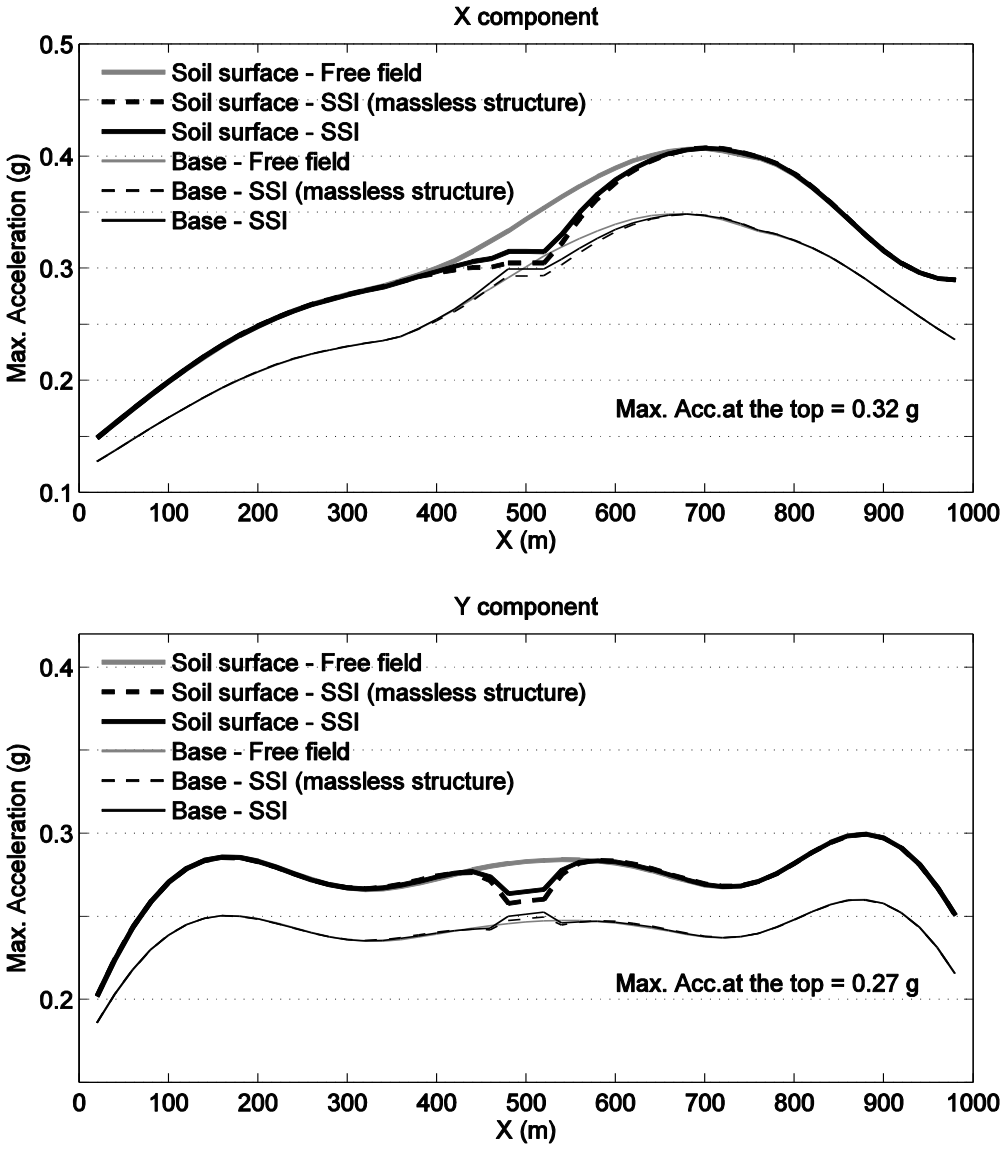

Figure 8.12: Peak ground acceleration along the center line at the level of soil surface and the base of the structure (40 m embedment) in the X direction

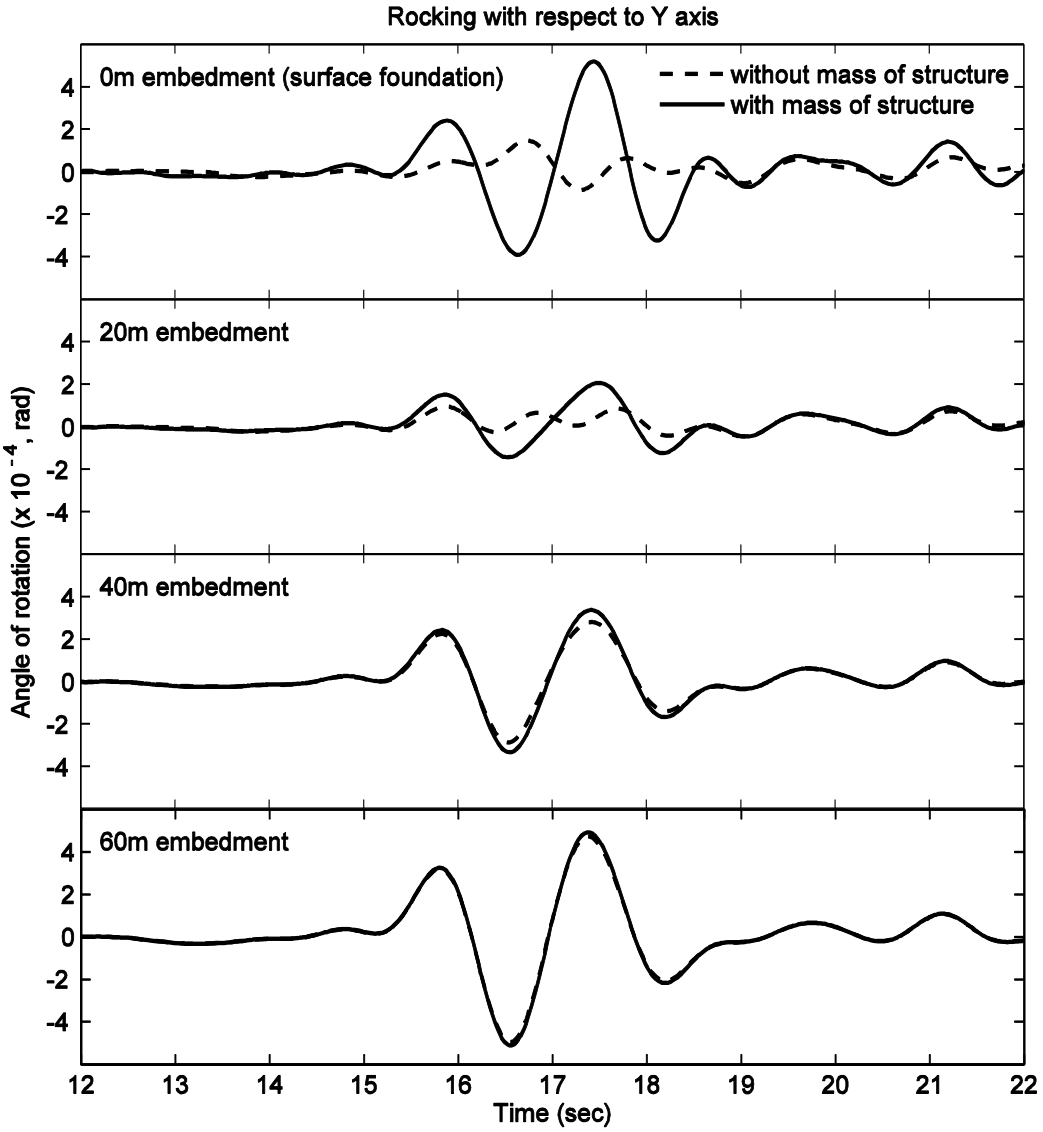

(a) with respect to the global Y axis (θ_Y)

Figure 8.13: Comparison of angle of rotation (rocking at the structure base) for different embedment levels

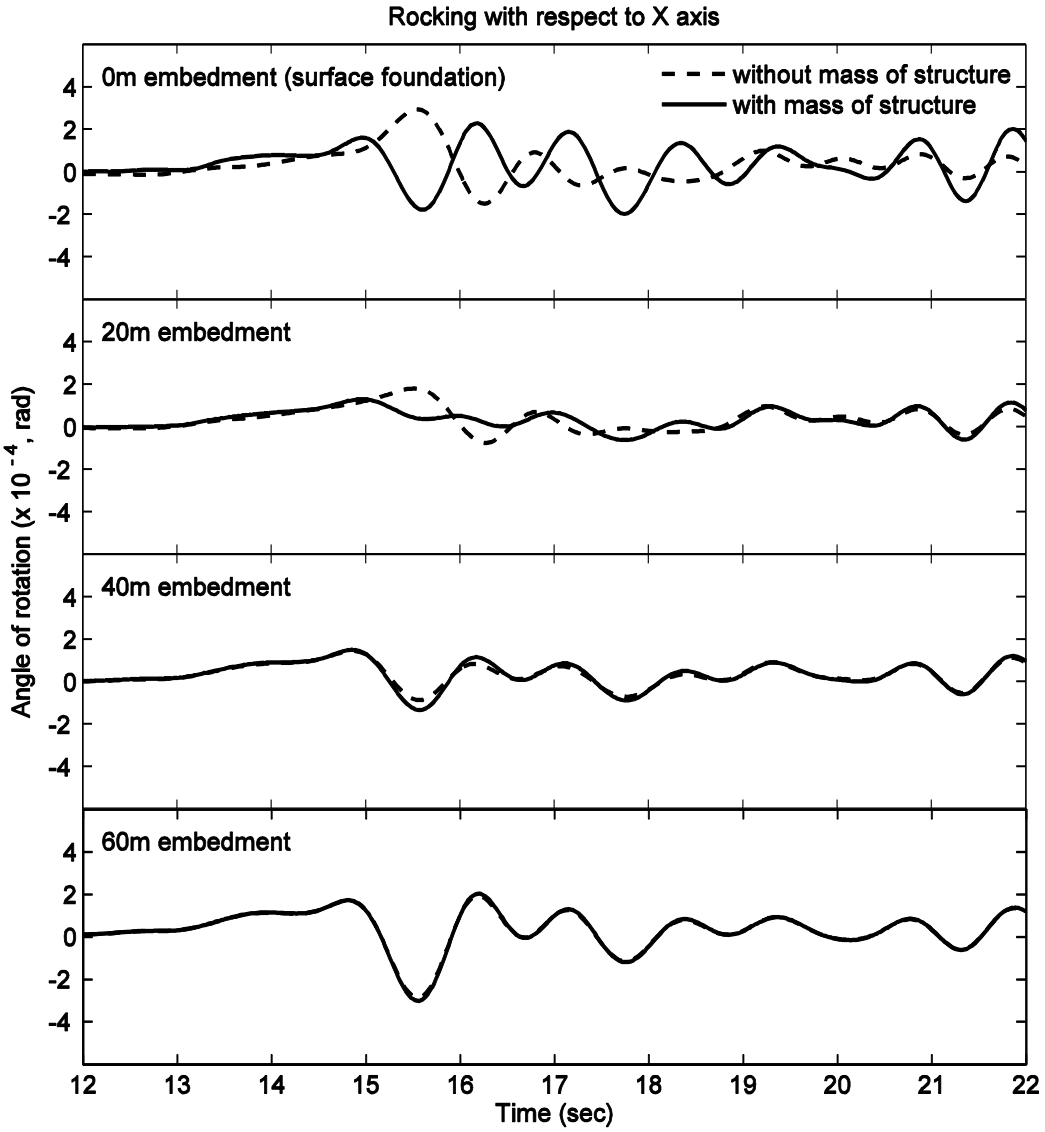

(b) with respect to the global Y axis ($\theta_{X)}$

Figure 8.13: (continued) Comparison of angle of rotation (rocking at the structure base) for different embedment levels

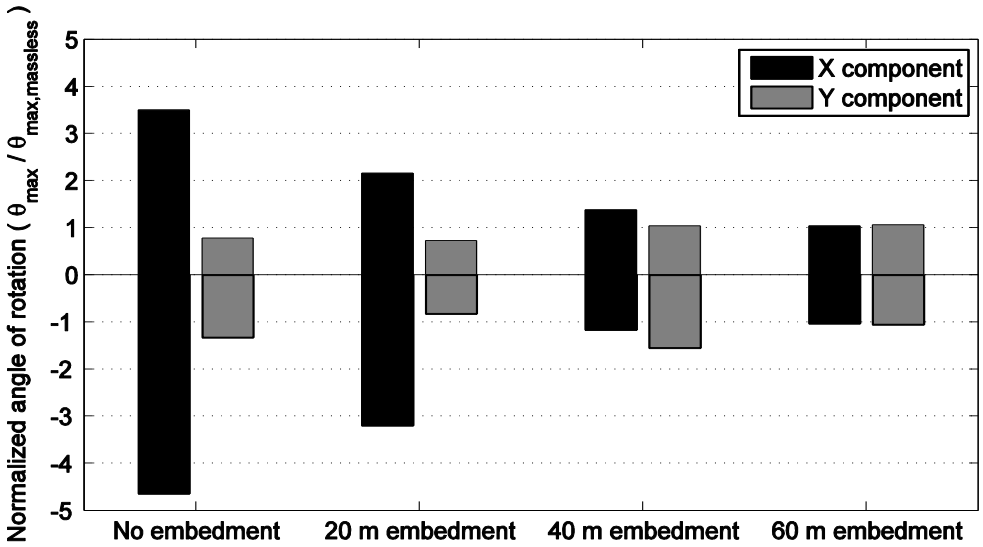

(a) In the soft soil case

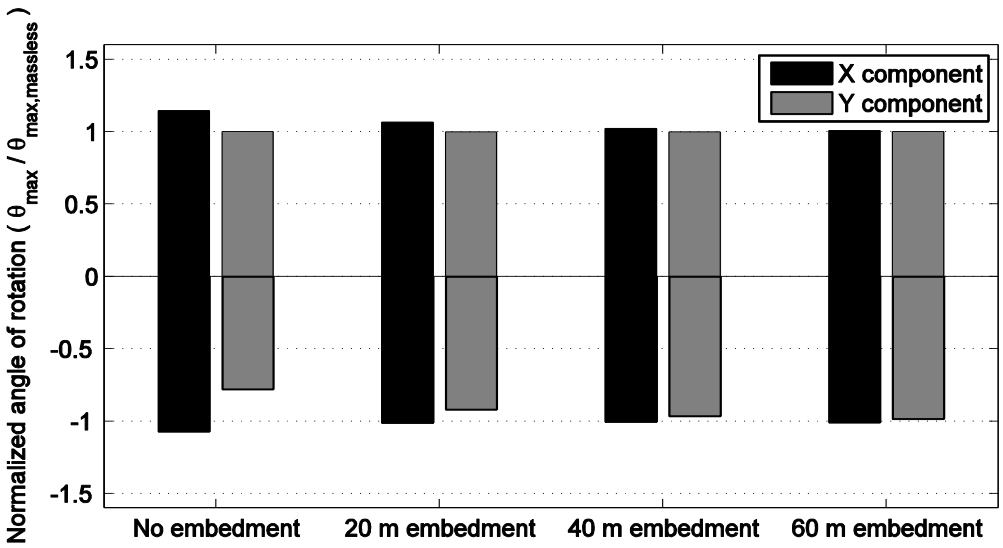

(b) In the stiff soil case

Figure 8.14: Normalized angle of rotation at the base of the structure for the different depths of the embedment

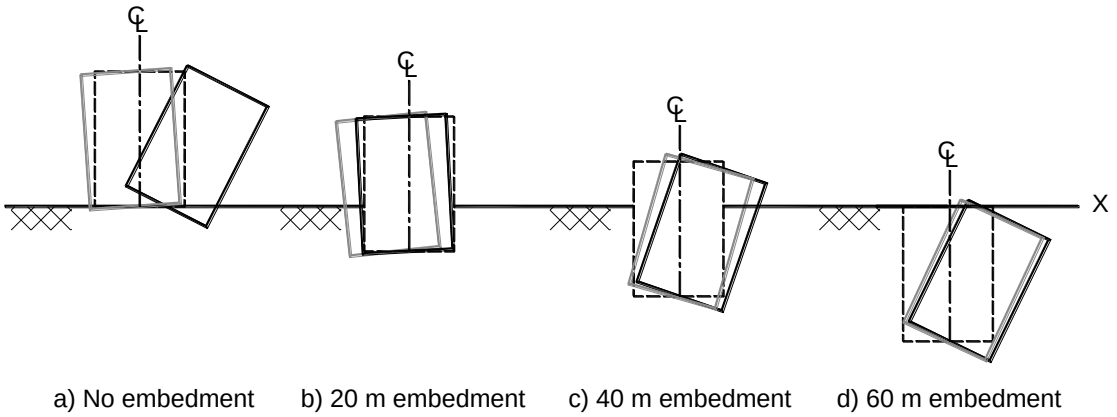

(a) In the X direction

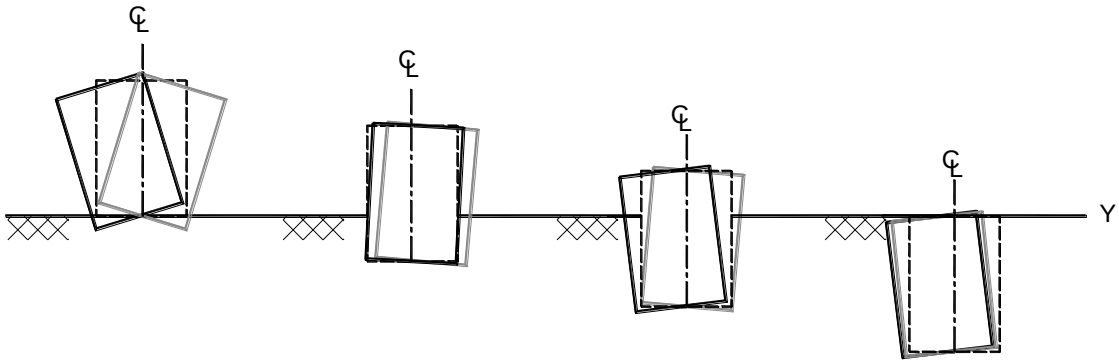

(b) In the Y direction

Figure 8.15: Schematic geometric deviation of the structure without mass (dashed line) and mass (solid line) from ground

Chapter 9

Soil-Structure-Interaction for a Fully Embedded Structure

9.1 Introduction

As discussed earlier in Chapter 2, the employed implementation of the Domain Reduction Method (DRM) region of interest was only possible for the 20 m brick element (in this report). The embedded structure of Chapter 8 was studied on this basis. In order to permit a more accurate representation of the response at higher frequencies for this modeling configuration, this chapter presents additional analyses using a finer mesh, without spatial variation of ground motion. Depending on soil stiffness, the following is discussed: 1) change of acceleration response along height of the structure compared to

the free-field, 2) lateral soil pressure profile along height of the structure, and 3) normal pressure developed along base of the structure.

9.2 Description of the numerical model

9.2.1 FE model and boundary conditions

The object-oriented open-source FE analysis framework, OpenSees, (McKenna 1997) is used. Figure 9.1 shows the computational FE model (half mesh for symmetry) with a size of 304.8 m by 152.4 m by 61.0 m in the longitudinal (X), transverse (Y), and vertical (Z) directions, respectively. At the center of the mesh, a cylindrical structure model with a height of 23 m is fully embedded in the soil domain.

In this study, elastic material properties were adopted as reported in an earlier study of soil-structure interaction for a large embedded structure (Seed and Idriss, 1973). For the soil deposit, shear wave velocity of 550 m/s is considered with mass density of 2.0 ton/m^3 and Poisson's ratio of 0.4. For comparison, two additional shear wave velocities of 300 m/s and 700 m/s are studied. Table 9.1 summarizes the employed soil material properties.

For material properties of the structure, Young's modulus of 5.4 GPa is used with mass density of 0.75 ton/m^3 and Poisson's ratio of 0.2. These properties are specified based on the earlier reported investigation (Seed and Idriss, 1973) as shown in Table 9.2.

At the interface between the structure and the soil, rigid links are deployed using zeroLength elements (connecting the structure to the surrounding soil). These rigid links

are included to merely to provide output force at the corresponding nodal locations, based on the earth pressure exerted on the sides of the structure and contact pressure under the base of the structure during dynamic excitation.

Along the base of the FE soil mesh, the Lysmer-Kuhlemeyer (1969) dashpot boundary is employed to avoid spurious wave reflections (as a simple effective numerical approach). For the imparted excitation only in the global X direction (Figure 9.1), the dashpots are activated only in this corresponding direction with fixity in the other directions. Coefficient of the employed dashpots is based on material properties of underlying base rock with an assumed shear wave velocity of 700 m/s and mass density of 2.0 ton/m^3. As such, the incident seismic wave is defined by dynamic equivalent base nodal forces. Details regarding the Lysmer-Kuhlemeyer boundary can be found in the earlier Section 7.2.1.

For the lateral boundaries, a shear beam idealization is adopted. In this regard, the longitudinal and transverse lateral boundaries are constrained to have the same longitudinal (X), transverse (Y), and vertical (Z) response (for each given depth). The lateral dimensions of the soil domain (X and Y directions) are chosen so as to have these boundaries relatively far from the structure (to decrease any effect of boundary conditions on response of the structure).

Rayleigh damping is employed for the structure and the soil. The corresponding coefficients for mass and stiffness proportional damping are chosen to result in 2% equivalent damping at the frequencies of 1 Hz and 6 Hz.

9.2.2 Earthquake input motion

Input motion at the base of soil domain is derived from the Taft 1952 Kern Country, CA earthquake record, as employed in the earlier study of Seed and Idriss (1973). In the N21E component, peak ground acceleration is 0.16 g as shown in Figure 9.2 (Fourier amplitude spectrum shown in Figure 9.3). For the Lysmer-Kuhlemeyer (1969) boundary, the acceleration is integrated to velocity that is used for deriving equivalent nodal forces. This input motion is applied in the global X direction at the base of the FE mesh (i.e., one directional excitation).

9.2.3 Computation

In this study, no gravity analysis is conducted prior to earthquake excitation. In the dynamic analysis phase, the Newmark-β time-stepping method is employed to integrate the matrix equation of motion with the integration parameters γ of 0.5 and β of 0.25. The total number of time steps of 2713 ($\Delta t = 0.02$ s) are executed to evaluate the system response during 54.26 seconds of earthquake excitation.

In addition to the above, a massless structure scenario is considered to shed more light on the inertial soil-structure interaction mechanism. A free-field analysis (i.e. site response analysis) is also performed for comparison (i.e., in the absence of the structure).

9.3 Results

9.3.1 Site response analysis

From the free-field analysis, Figure 9.4 shows total acceleration time histories at ground surface in the absence of the structure. As expected, motion amplification is observed in this relatively soft soil profile. The amplification is mainly observed at the site frequencies of 1.25, 2.25, and 2.86 Hz for the shear wave velocities (V_s) of 300, 548, and 700 m/s, respectively (Figure 9.5). Compared to V_s of 700 m/s, peak ground acceleration increases as much as 50% for V_s of 300 m/s. In addition, relative to base of the structure location, surface ground acceleration is amplified by 53%, 30%, and 34% for V_s of 300, 548, and 700 m/s, respectively (Figure 9.6).

9.3.2 Analysis of soil-structure interaction

9.3.2.1 Reduction of peak ground acceleration

Peak ground acceleration (PGA) at top (soil surface) and base of the structure along the excitation direction (global X direction) is shown in Figure 9.7 through Figure 9.9, for V_s of 300, 584, and 700 m/s, respectively. The presence of the structure decreases amplification of acceleration along its height. In the relative soft soil (V_s = 300 m/s), a marked reduction (about 35%) of the PGA (0.15g) developed at top of the structure is observed, compared to free-field response (0.21g). This reduction also affects ground response in the local region near the structure (about 100 m away as shown in Figure 9.7).

Meanwhile, PGA developed at base of the structure decreases about 20% (case of V_s = 300 m/s).

As soil becomes stiffer, the effects observed above tend to decrease. In the soil with V_s of 548 m/s, the reduction is about 20% (top of the structure) and 10% (base of the structure), compared to free-field response (soil surface). In the soil with V_s of 700 m/s, the reduction is about 10% at top of the structure. In this case, PGA at the base is very similar to the free-field response at the corresponding location (about 2% difference is observed).

Table 9.3 summarizes PGAs at top and base of the structure with and without its mass. Results from cases without mass of the structure show larger reductions of PGA (about 50% compared to 35% in case of V_s of 300 m/s). In other words, inertial interaction limits reduction of acceleration amplification developed along height of the structure. As soil becomes stiffer, the limitation tends to decrease and inertial interaction becomes of lower significance.

9.3.2.2 Lateral soil pressure

Figure 9.10 shows maximum compressive normal and tangential soil pressure profiles along height of the structure in the V_s of 300 m/s case. This maximum pressure occurs at the time instant of 6.86 seconds, shown along the cylindrical circumference from angle of 0 (aligned in the global X direction) to 90 degrees (aligned in the global Y direction) when free-field acceleration at the soil surface reached a peak in the positive direction. From 90 to 180 degrees, the time instant of 7.22 seconds was used for the maximum normal pressure when surface free-field acceleration reached a peak in the

negative direction. In the soft soil (V_s of 300 m/s), the maximum normal pressure of 50 kPa at the 0 degree orientation was reached at the depth of 7 m (i.e. height of 15 m out of 22 m). Compared to a postulated static pressure at rest using a friction angle of 30 degrees and mass density of 2 ton/m^3, the computed dynamic pressure is about 75%. In addition, the tangential (shear) pressure of 47 kPa was reached at the depth of 5 m at the 90 degrees.

As soil becomes stiffer, the maximum soil pressure decreases. In the soil with V_s of 548 m/s, a maximum normal pressure of 37 kPa was reached at the depth of 7 m (0 degree orientation) when free-field surface acceleration reached a peak at 6.78 seconds (Figure 9.11). A maximum tangential pressure of 26 kPa was developed at the depth of 5 m. In the stiff soil case (V_s of 700 m/s), the maximum normal and tangential pressures are 30 kPa at the depth of 7 m (0 degree orientation) and 20 kPa at the depth of 5 m (90 degrees orientation), respectively (Figure 9.12).

In addition, the maximum normal pressure can be compared with and without mass of the structure. It can be seen that out-of-phase response at top of the structure is imposed by the structural mass in the case of V_s of 300 m/s (Figure 9.13; a negative value indicates that the lateral normal pressure exerted on the structure was in compression). Meanwhile, as soil becomes stiff, out-of phase response tends to decrease (Figure 9.14 for V_s of 584 m/s and Figure 9.15 for V_s of 700 m/s). Due to this decreasing out-of-phase response, differences of the exerted soil pressures with and without mass of the structure are relatively larger in the stiffer soil (Figure 9.16). In other words, inertial interaction plays a more important role in determining lateral soil pressures in the relatively stiff soil considered in this study.

9.3.2.3 Base pressure

Figure 9.17 through Figure 9.19 show normal pressure distributions along the base of the structure for the cases of V_s of 300 m/s, 548 m/s, and 700 m, respectively. The normal maximum distribution is computed at the time instant time when lateral normal pressure reaches the maximum along height of the structure. The maximum compression pressure (indicated by negative pressures) is 72 kPa for Vs of 300 m/s. As soil becomes stiffer, the developed pressure decreases to about 40 kPa and 30 kPa for V_s of 548 m/s and 700 m/s, respectively. Finally, the effect of structural mass (i.e. inertial interaction) on the base normal pressure appears negligible in three cases considered.

9.4 Summary and conclusions

Dynamic interaction for the fully embedded structure was investigated under uniform spatial dynamic excitation. Effects of the employed elastic soil characteristics were investigated in terms of acceleration developed at top and base of the structure, lateral soil pressure along height of the structure, and normal pressure along the base. Imposed by the structure without its mass, inertial interaction was isolated and evaluated. From the results of the present study, the main observations are:

1. Rigidity of the structure contributed to reduction of peak accelerations developed at its top and base. The marked reduction of 35% at the top was observed in the soft soil (V_s of 300 m/s). This reduction affected free-field accelerations in the local region near the structure. As soil stiffness increases, the reduction decreases.

2. In the considered cases, maximum compressive normal pressure occurred at the depth of 7 m (i.e. structure height of 15 m) when free-field acceleration at the soil surface reached its peak. In the soft soil, the maximum normal pressure was 50 kPa (about 75% of an estimated static pressure at rest). As soil stiffness increases, the maximum pressure decreases.
3. In comparison of the response with and without mass of the structure, inertial interaction limited the reduction of acceleration amplification along height of the structure. In terms of lateral normal soil pressures, out-of-phase response imposed by inertial interaction tended to increase as soil stiffness decreased. Consequently, a lower reduction of normal pressure due to inertial interaction was observed in the softer soil. Meanwhile, differences of the normal pressure developed along the base were negligible with and without mass of the structure.

Table 9.1: Linear elastic material properties of the FE model

(a) Soil deposit

Case	Soil depth (m)	Shear wave velocity (m/s)	Mass density (ton/m^3)	Poisson's ratio
1	0 – 60.96	300	2.0	0.4
2	0 – 60.96	548.64	2.0	0.4
3	0 – 60.96	700	2.0	0.4

(b) Structure

Distance below the soil surface (m)	Mass density (ton/m^3)	Elastic modulus (kPa)	Poisson's ratio
0 – 22.86	0.754	5,400,000	0.2

Table 9.2: Original material properties of the structure (Seed and Idriss, 1973)

Distance below top of the structure (m)	Average unit weight (kN/m^3)	Average elastic modulus (kPa)	Poisson's ratio
0 – 13	0.3	23,940	0.2
13 - 21	15	2,538,000	0.2
21 – 28	10	7,134,000	0.2
28 - 36	11	3,734,000	0.2

Table 9.3: Comparison of peak ground acceleration (PGA) in units of (g) at top and base of structure with and without mass of structure (parenthesis indicates change of PGA compared to free-field response)

Level of the structure	**Case**	**V_s = 300 m/s**	**V_s = 548 m/s**	**V_s = 700 m/s**
At top	Free-field	0.208	0.156	0.140
	With mass	0.154 (-35%)	0.132 (-18%)	0.125 (-12%)
	Without mass	0.136 (-53%)	0.126 (-24%)	0.120 (-17%)
At base	Free-field	0.148	0.121	0.104
	With mass	0.126 (-17%)	0.110 (-10%)	0.107 (3%)
	Without mass	0.122 (-21%)	0.108 (-12%)	0.105 (2%)

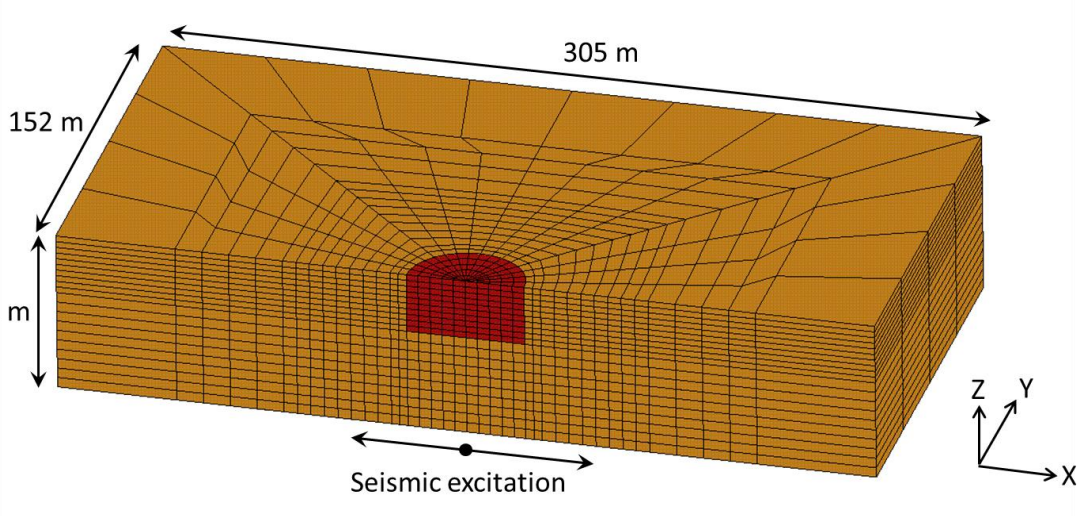

Figure 9.1: 3D finite element model (half mesh) of rigid structure with full embedment

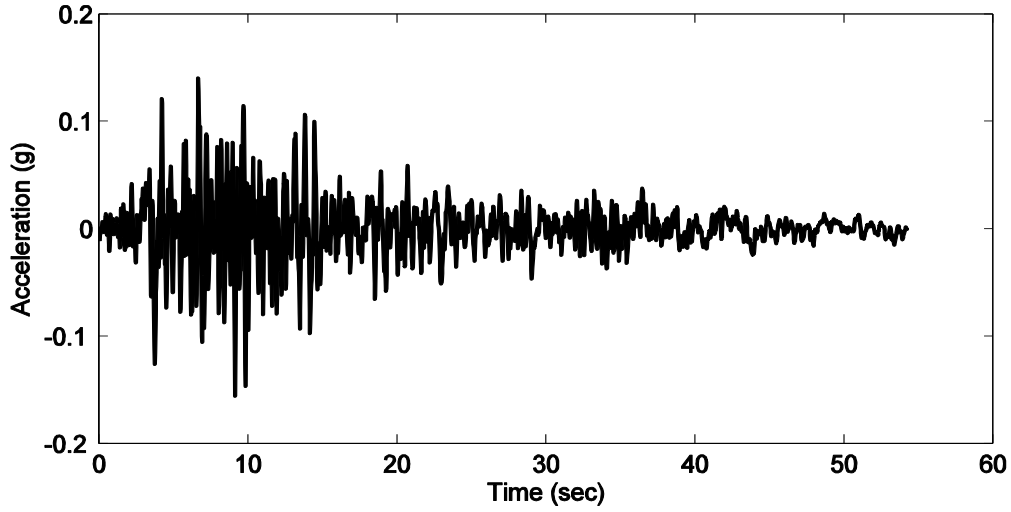

Figure 9.2: Input ground motion: N21E component of the Taft record (Kern County Earthquake 1952, USGS station 1095)

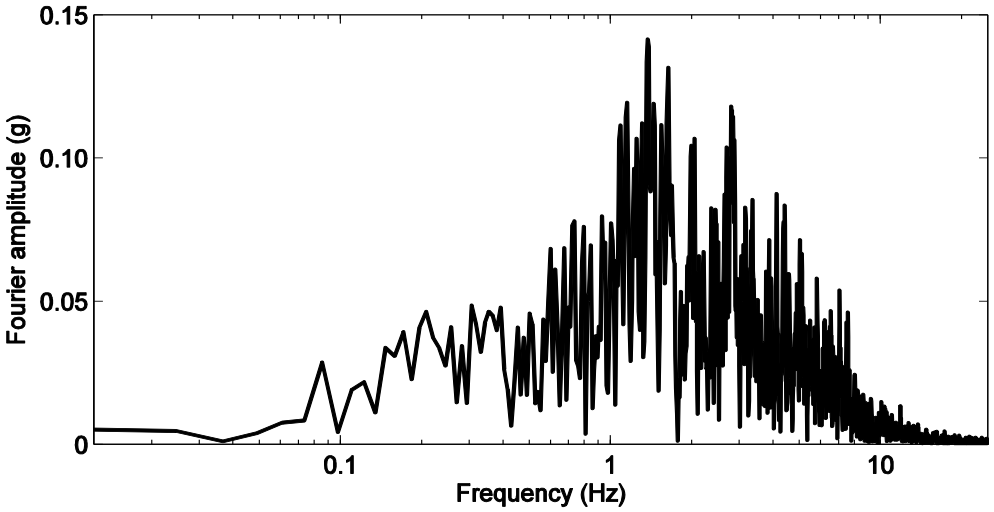

Figure 9.3: Fourier amplitude spectrum: N21E component of the Taft record (Kern County Earthquake 1952, USGS station 1095)

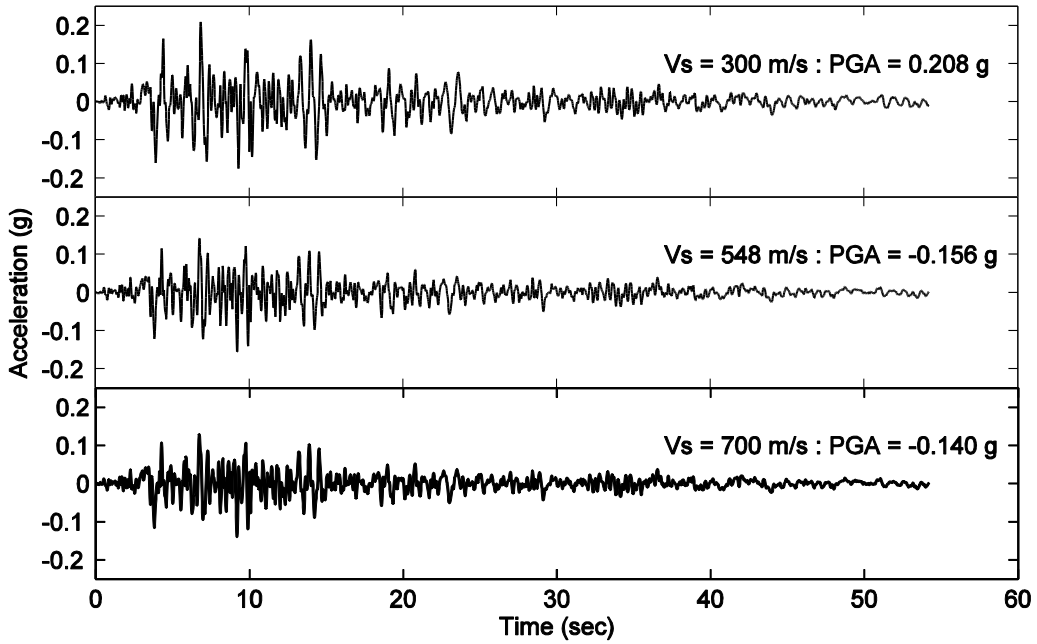

Figure 9.4: Comparison of free-field ground acceleration time histories at the soil surface for shear wave velocities of 300, 584, and 700 m/s

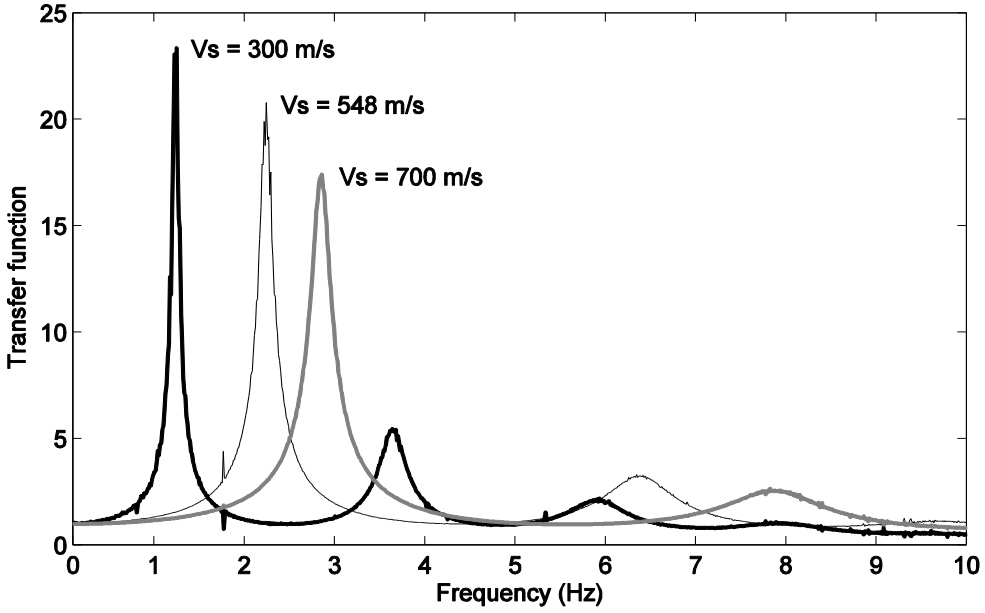

Figure 9.5: Comparison of transfer functions of free-field acceleration at the soil surface to base of the soil

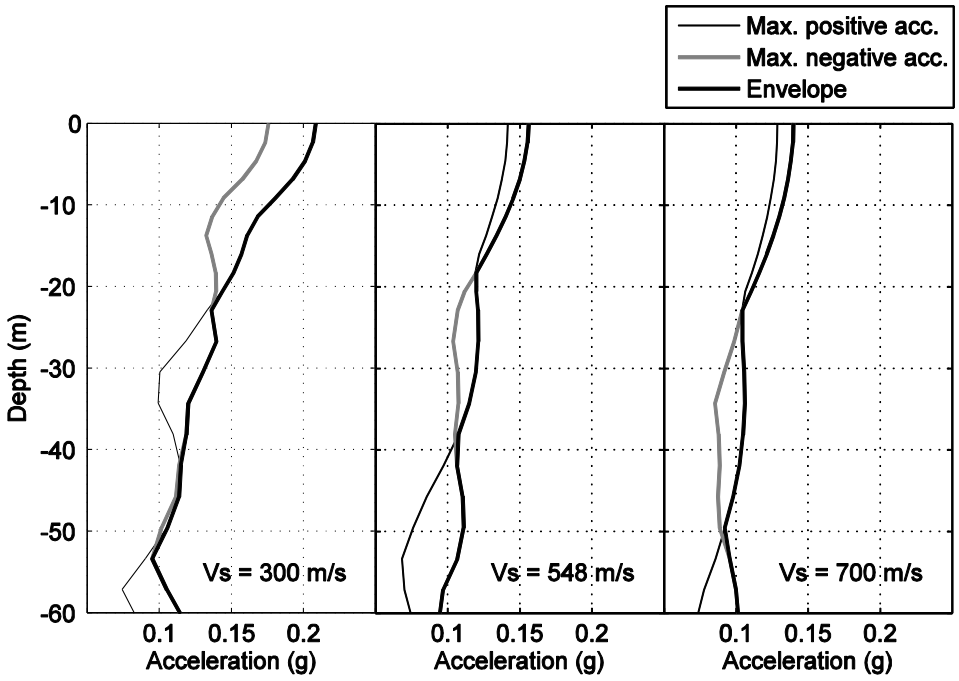

Figure 9.6: Free-field peak ground acceleration profile along the depth

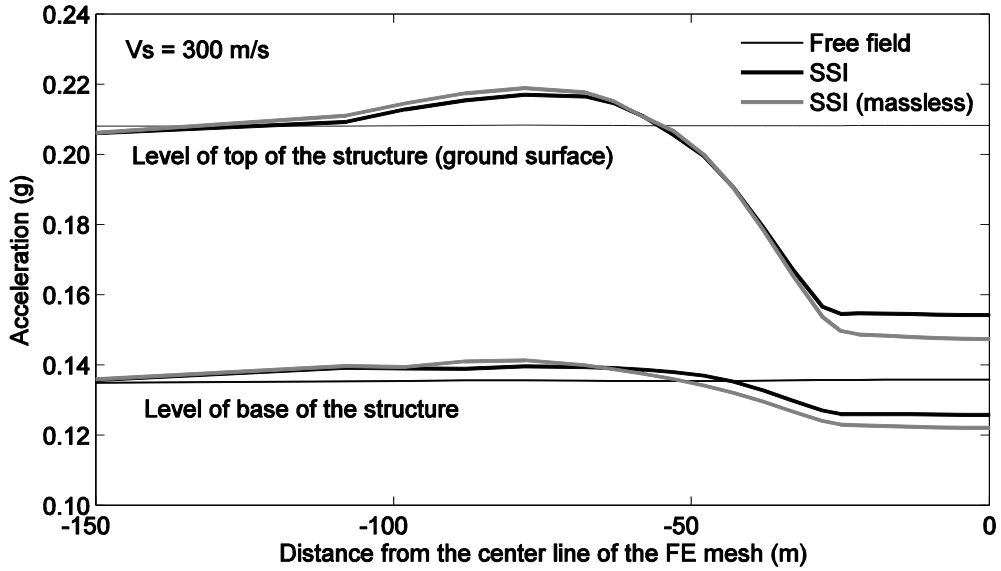

Figure 9.7: Case of Vs = 300 m/s: peak ground acceleration along the center line at the level of soil surface (top of the structure) and the base of the structure in the X direction

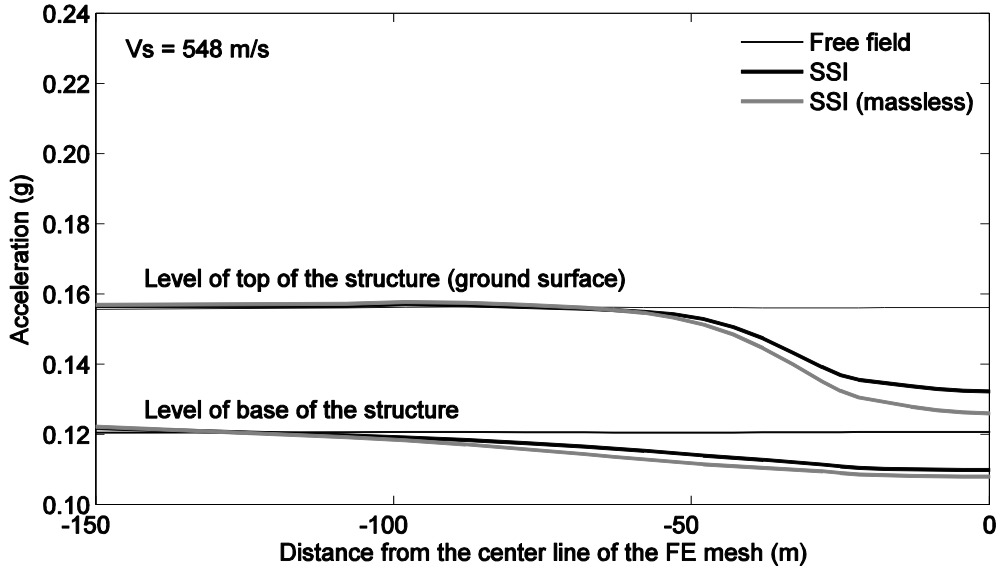

Figure 9.8: Case of Vs = 548 m/s: peak ground acceleration along the center line at the level of soil surface (top of the structure) and the base of the structure in the X direction

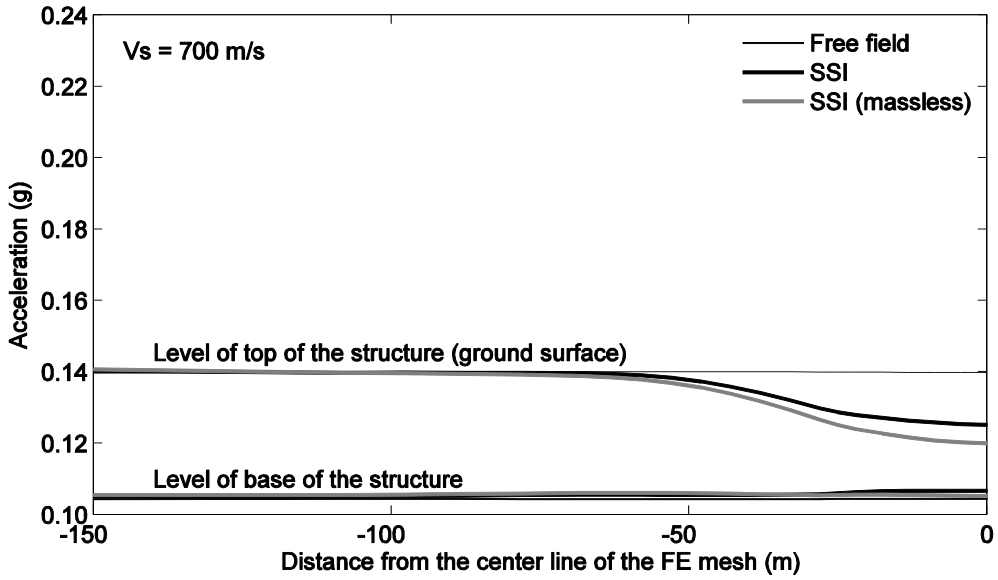

Figure 9.9: Case of Vs = 700 m/s: peak ground acceleration along the center line at the level of soil surface (top of the structure) and the base of the structure in the X direction

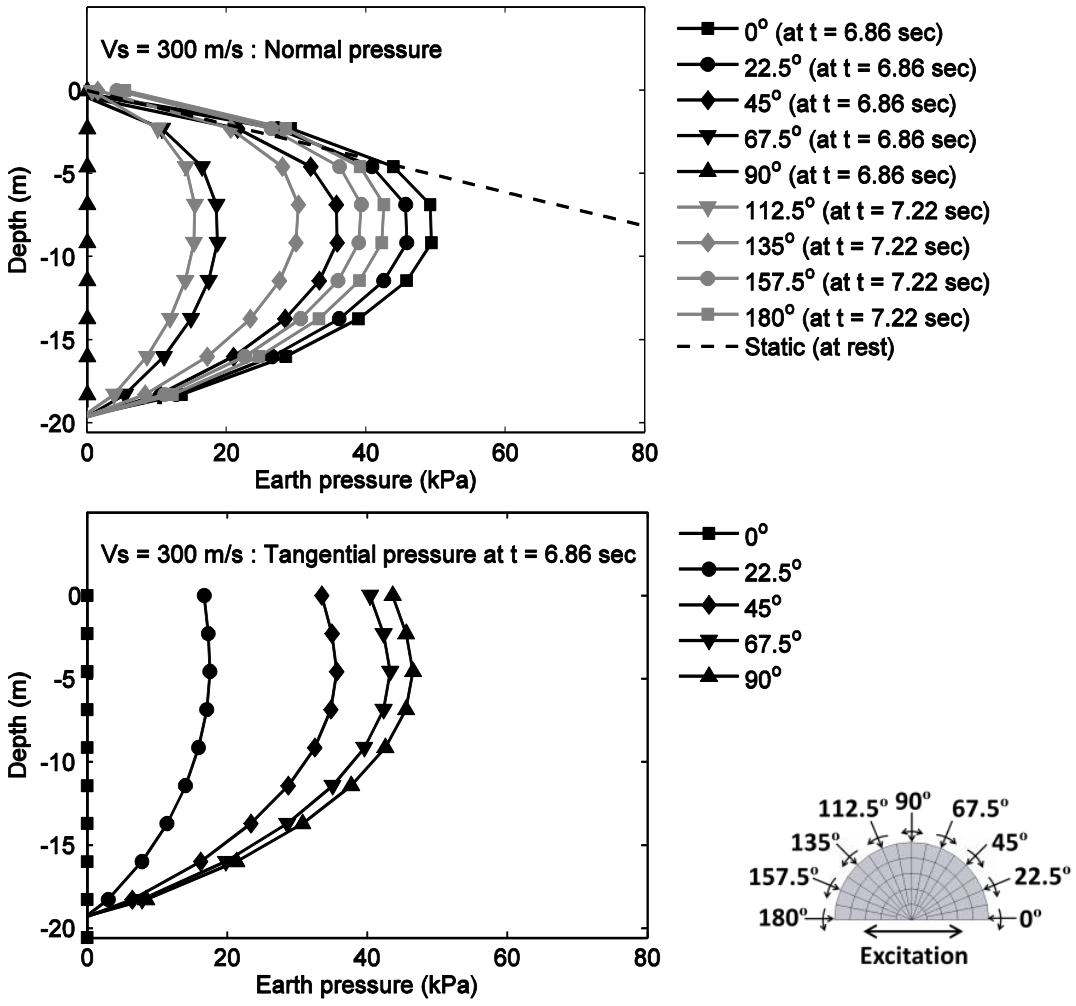

Figure 9.10: Case of Vs =300 m/s: earth pressure distribution along sides of the structure at t = 6.86 sec (0° - 90°) and at t = 7.22 sec (90°-180°)

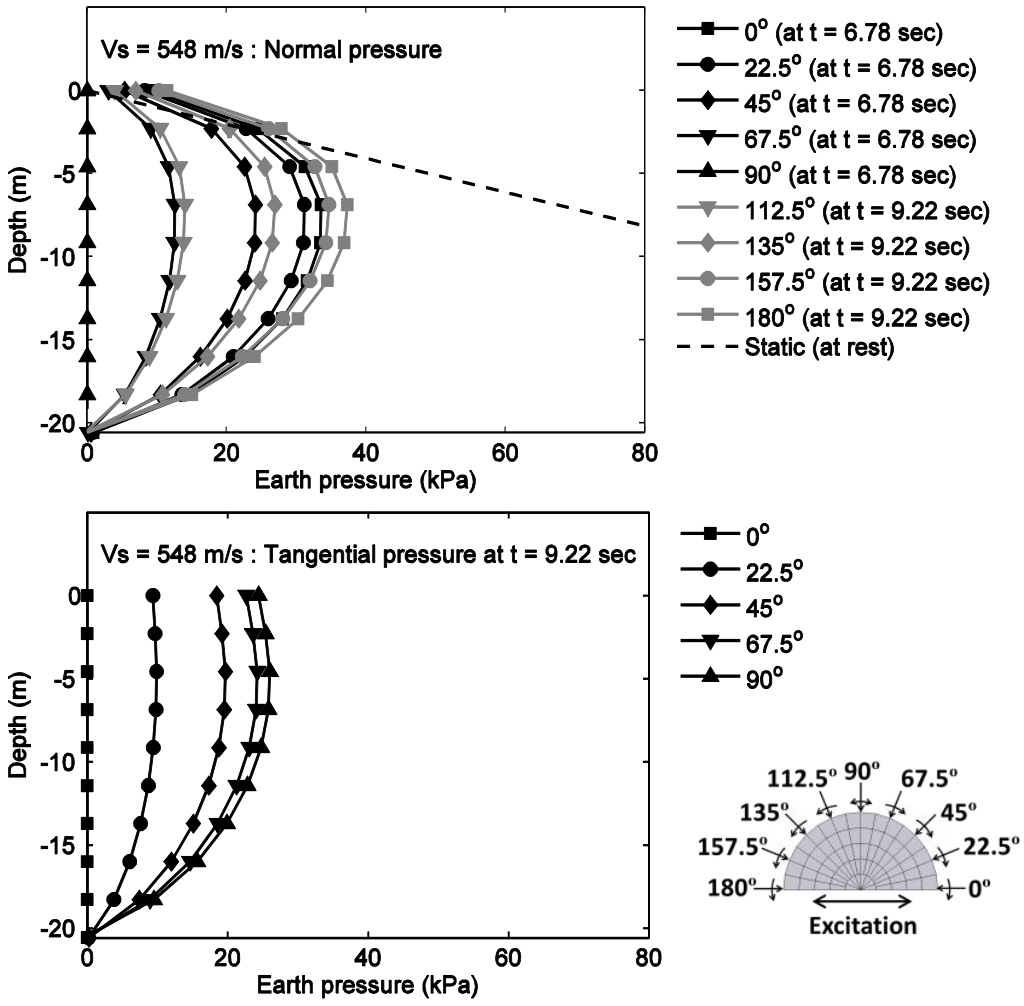

Figure 9.11: Case of Vs =548 m/s: earth pressure distribution along sides of the structure at t = 6.78 sec (0° - 90°) and at t = 9.22 sec (90°-180°)

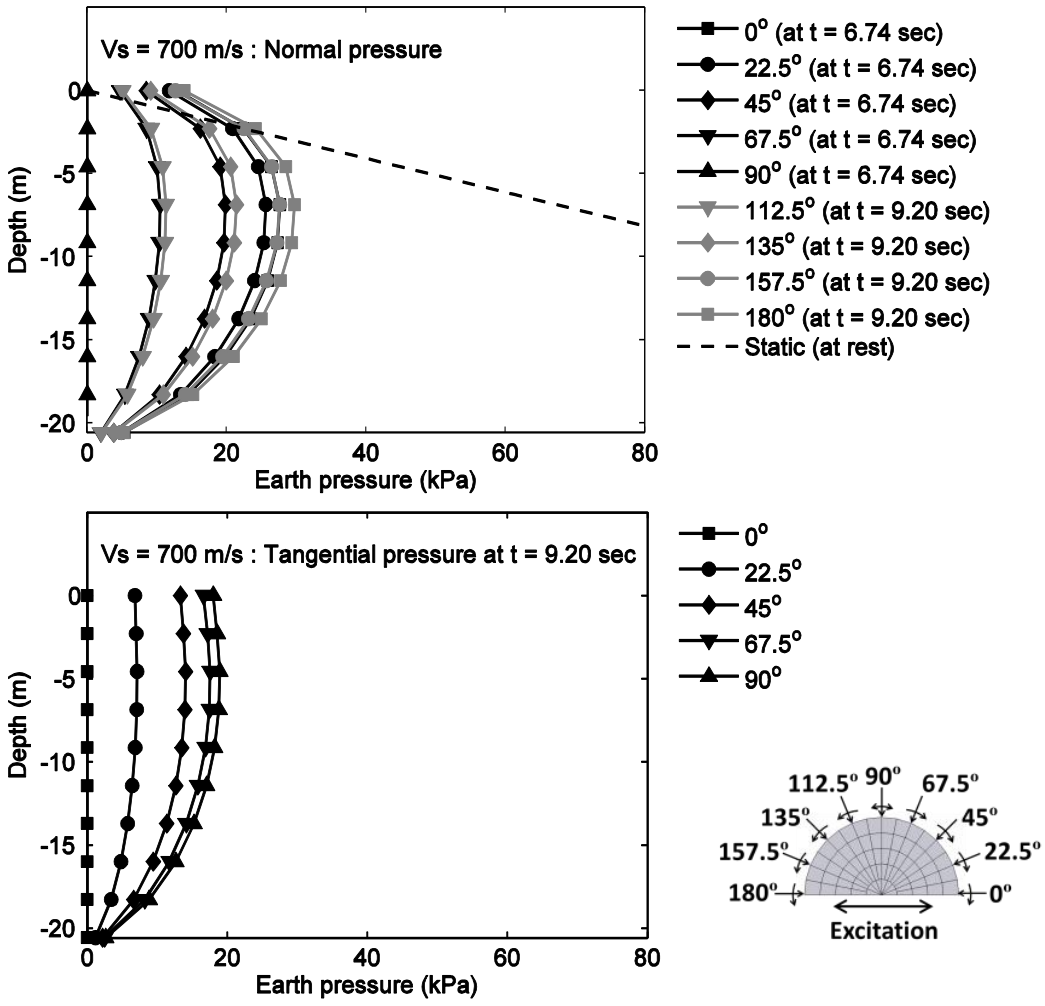

Figure 9.12: Case of Vs =700 m/s: earth pressure distribution along sides of the structure at t = 6.74 sec (0° - 90°) and at t = 9.2 sec (90°-180°)

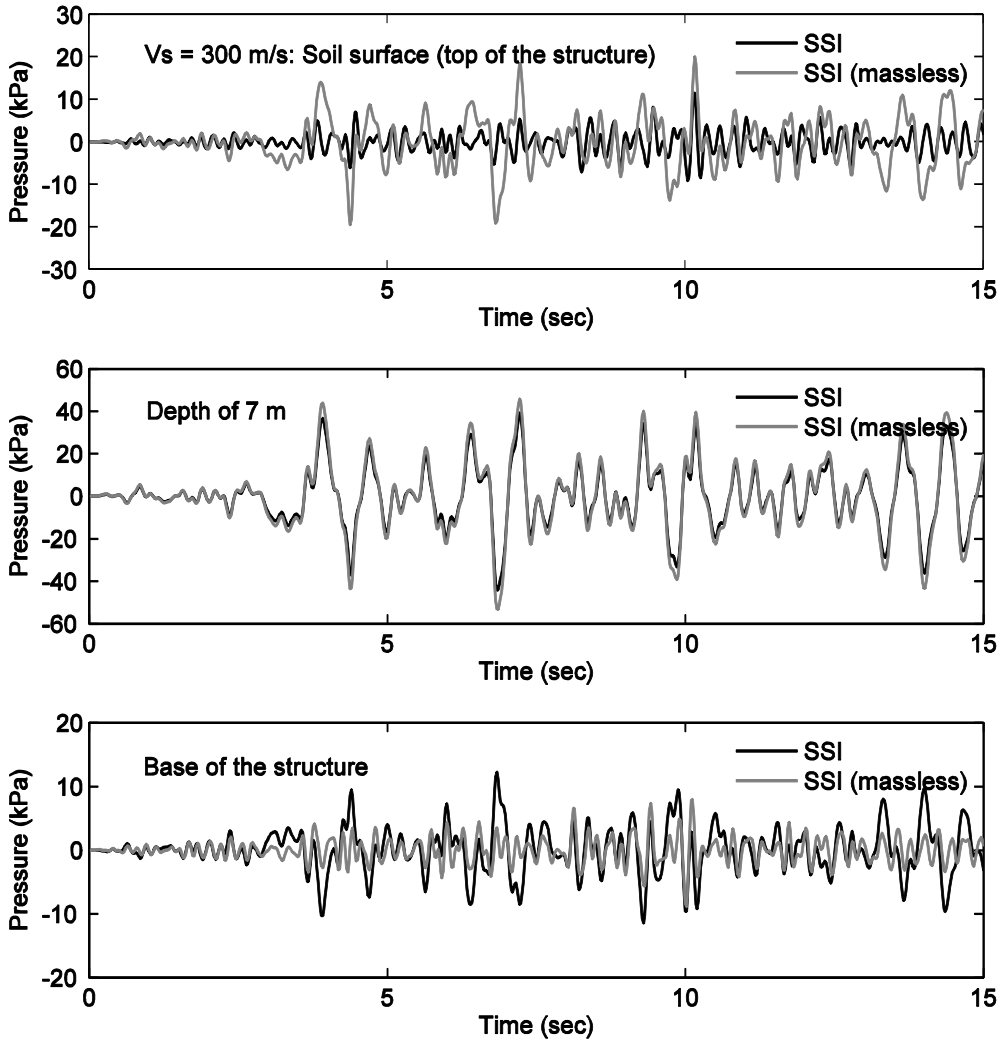

Figure 9.13: Case of Vs =300 m/s: normal pressure time histories at soil surface, depth of 7 m, and base of the structure at the center line (0 degree; negative value in compression and vice versa) of the model with and without mass of the structure

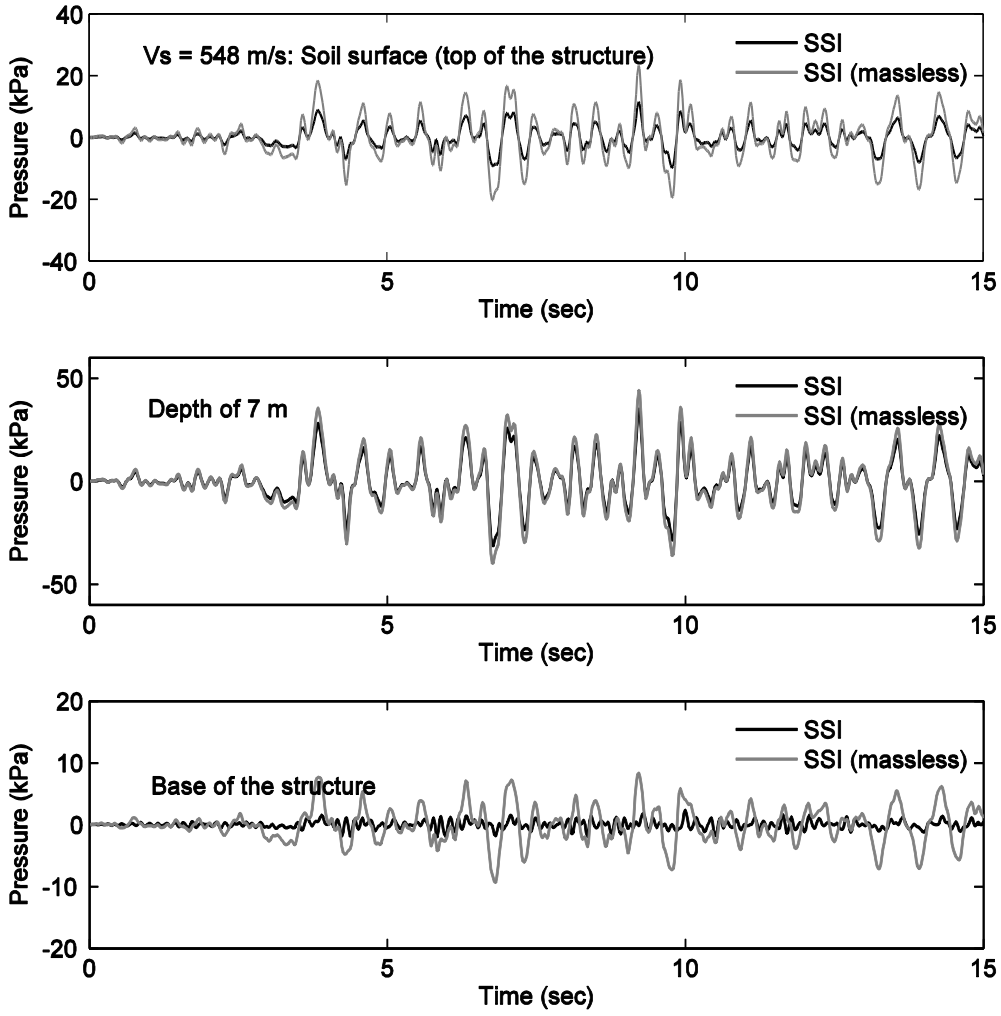

Figure 9.14: Case of Vs =548 m/s: normal pressure time histories at soil surface, depth of 7 m, and base of the structure at the center line (0 degree; negative value in compression and vice versa) of the model with and without mass of the structure

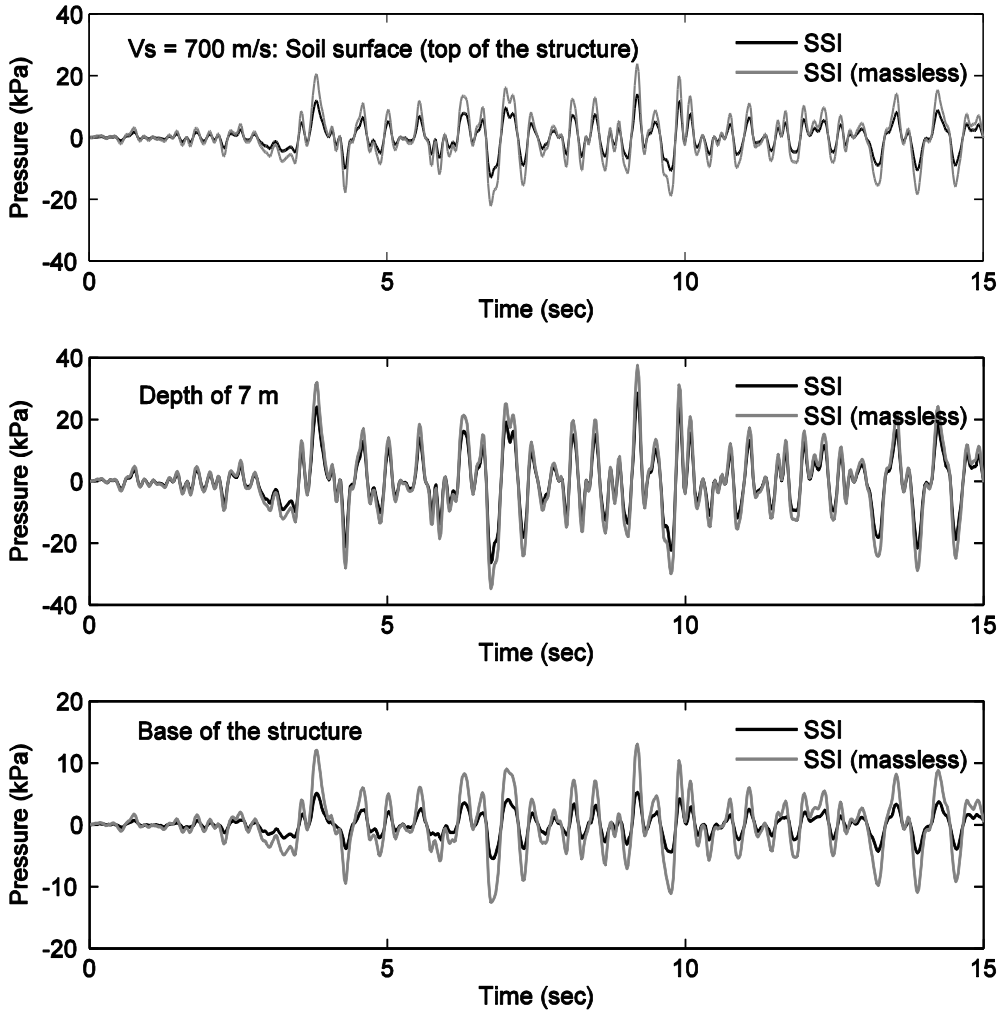

Figure 9.15: Case of Vs =700 m/s: normal pressure time histories at soil surface, depth of 7 m, and base of the structure at the center line (0 degree; negative value in compression and vice versa) of the model with and without mass of the structure

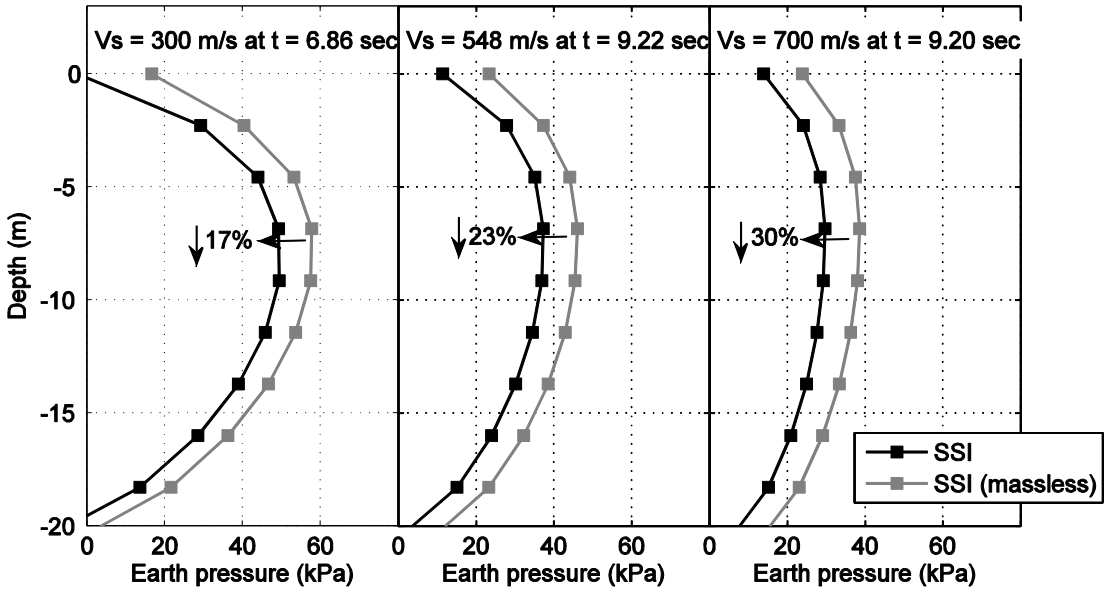

Figure 9.16: Comparison of lateral earth distribution with and without mass of the structure along the center line (X direction)

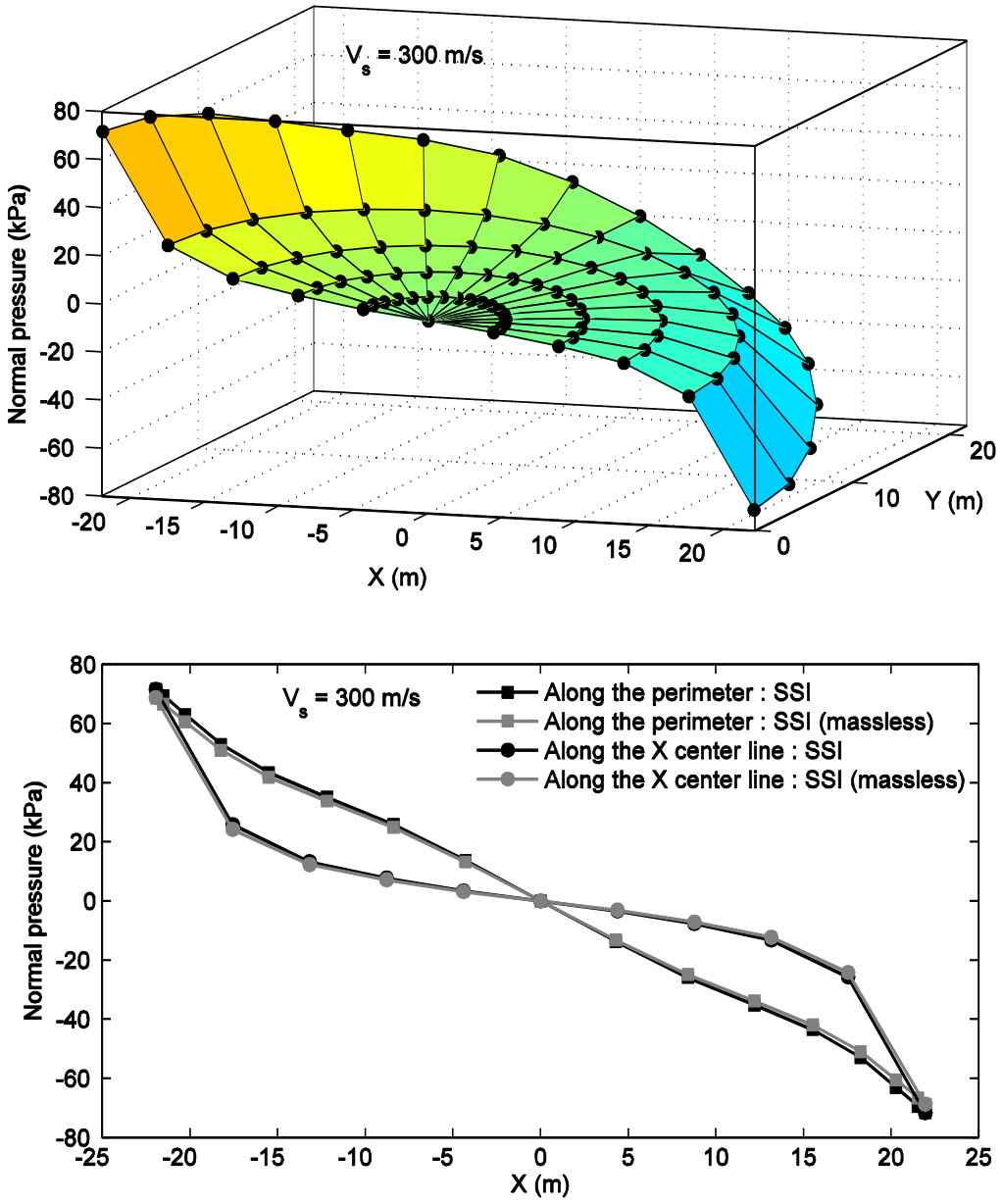

Figure 9.17: Case of Vs = 300 m/s: Normal pressure distributions (positive value in compression and vice versa) along the base of the structure at the instant time of 6.86 seconds

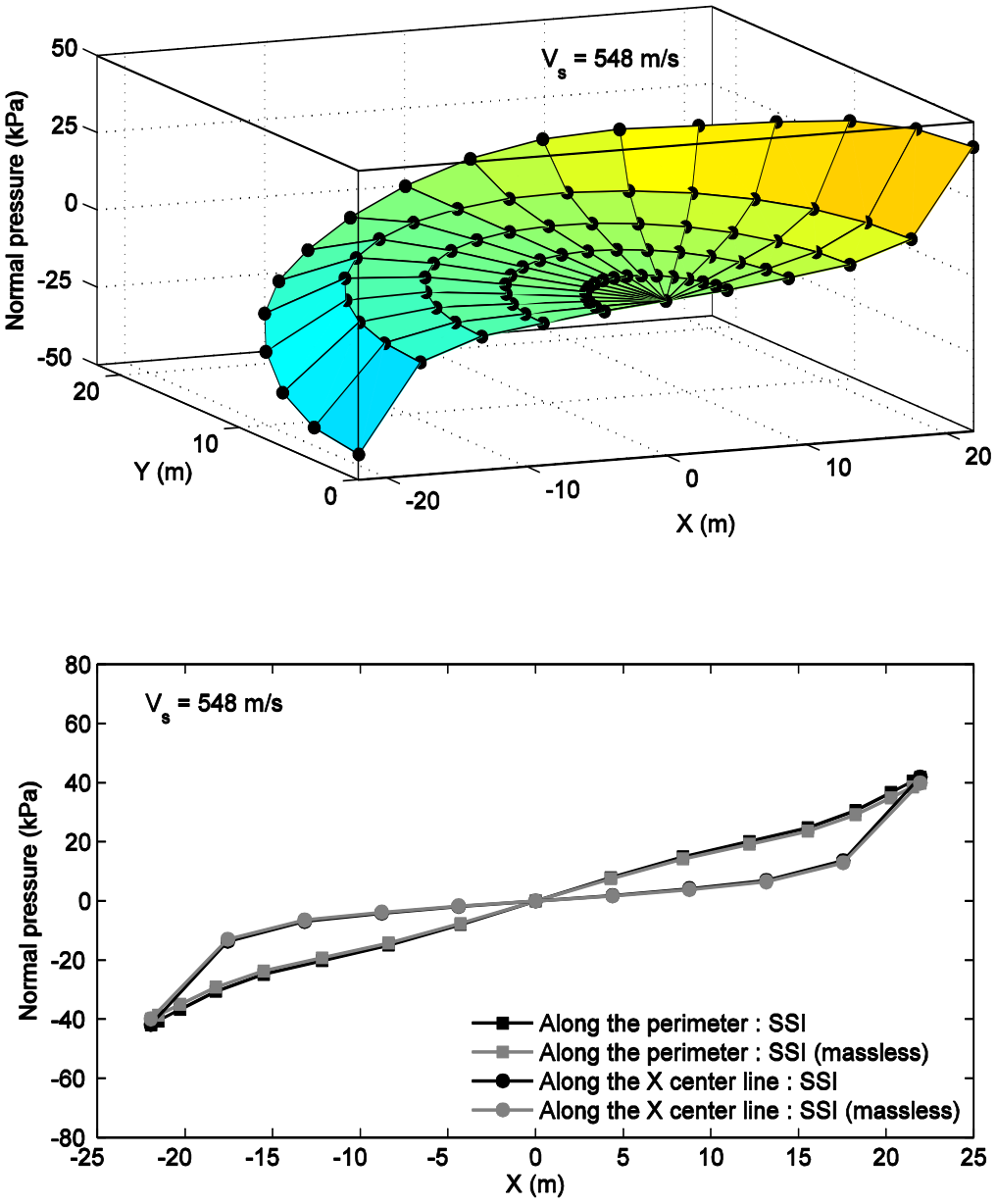

Figure 9.18: Case of Vs = 584 m/s: Normal pressure distributions (positive value in compression and vice versa) along the base of the structure at the instant time of 9.22 seconds

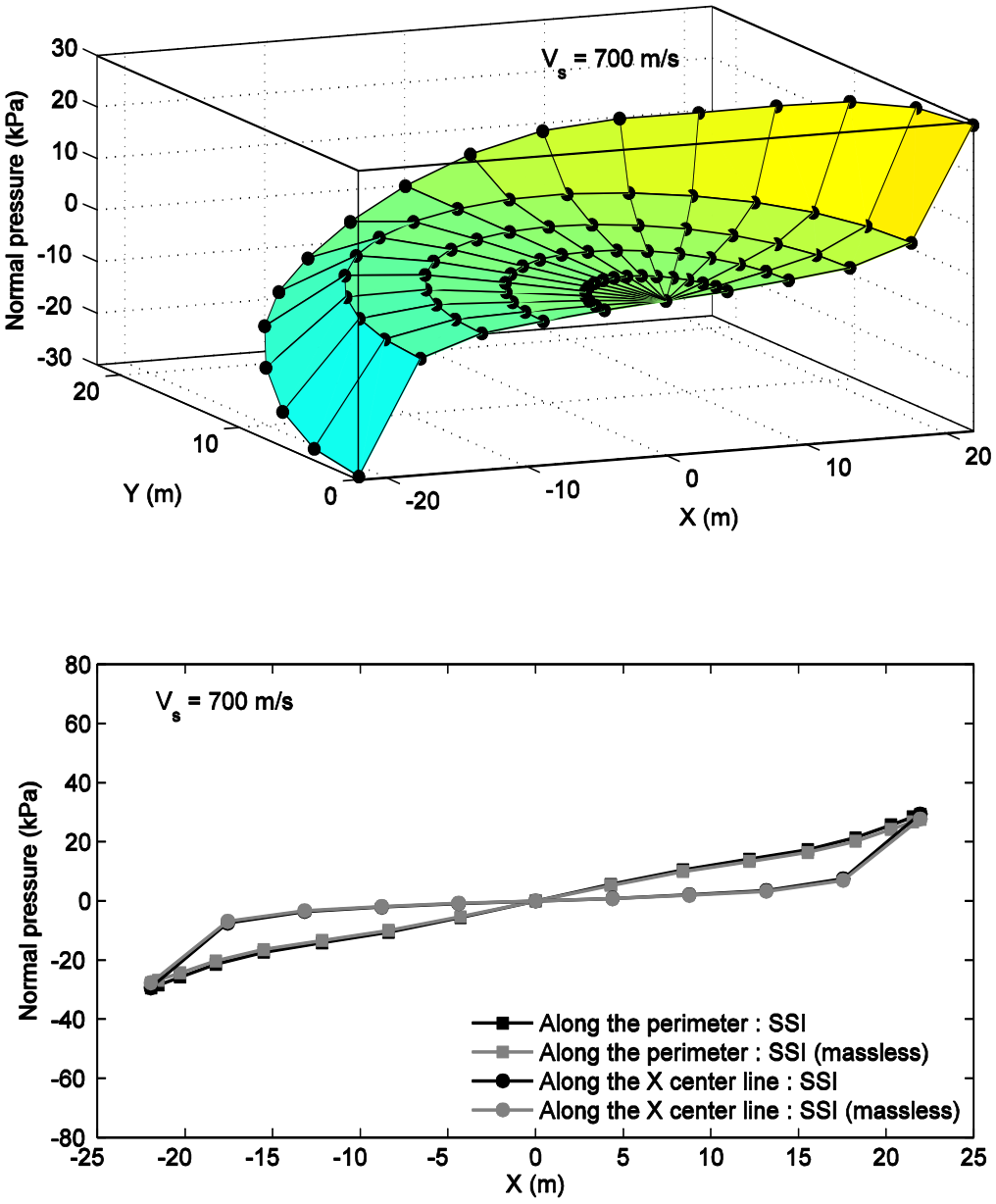

Figure 9.19: Case of Vs = 700 m/s: Normal pressure distributions (positive value in compression and vice versa) along the base of the structure at the instant time of 9.20 seconds

Chapter 10

Conclusion and Future Directions

10.1 Summary

The SSI contributions presented in this report are mainly motivated by availability of the DRM capability of modeling a ROI subjected to incident seismic waves resulting from a realistic fault rupture scenario. This capability provides a numerical platform to enable assessment of engineering aspects related to structural and/or geotechnical response within the ROI. It also offers the advantage of providing free-field ground motions at any desired location along the ground surface. Consequently, it enables one to analyze a fixed-base structure under multiple base excitations at the location of each column foundation, with possible comparison to uniform base excitation using a representative ground motion (e.g., surface motion at the center of the soil domain).

Based on this framework, this research can be classified and summarized into the following categories:

1) Modeling of the bridge-foundation-ground system (BFGS) based on the DRM ROI
2) Response characterizations in conjunction with characteristics of the DRM ROI
3) Assessment of the fixed-base structural response without the soil domain (ROI)
4) Analysis of an additional BFGS based on the actual local site
5) Study of soil-structure interaction for a rigid embedded structure

10.1.1 Modeling of a bridge-foundation ground system based on the DRM ROI (Chapters 3 and 4)

1. In the structural models (the three bridge connectors at the Interstates 10 and 215 interchange, I-10/215), the resonant response characteristics were investigated with and without the nonlinear hinge model. The employed hinge model was found to be a critical parameter to capture variation of the resonance as assessed from past earthquake records.
2. From validation using strong motion data recorded at the bridge (North-West connector, NW) during past earthquake excitation, the structural model (without the soil domain) provided a reasonable estimate of its recorded seismic response.
3. In order to couple the structural and soil models, the devised pile group foundation model reproduced by an essentially rigid solid element embedded in the ground was presented and efficiently enabled the reproduction of the corresponding translation and rocking characteristics.

4. Based on the conducted research scope, the BFGS enabled simultaneous analysis of multiple bridge structures and was found to be an efficient tool for assessment of seismic response of the structure and the ground.

10.1.2 Response characterizations in conjunction with characteristics of the ground model (Chapters 4, 5, and 6)

1. Numerical simulation of three bridges in the BFGS was presented. The relatively stiff soil domain (ROI) with elastic material properties were used to evaluate their seismic demands. Below is a list summarizing some of the major findings:

(1) Longitudinal structural response was generally dictated by the seismic ground motion (non-uniform support motions), while the transverse response mainly depended on flexibility of the structures (in the NW and the SE; the relatively flexible bridges). However, in the NE (relatively stiff bridge) with a different geometric configuration, the ground response was more significantly attributable to the structural response in both the longitudinal and transverse directions.

(2) Spatial variation of ground motions contributed to pounding between the bridge deck sections (frames). Consequently, intermittent spikes were observed in the structural response. Although the peak ground acceleration attained about 0.2g, the structural peak acceleration reached greater than 1g (because of the spikes).

(3) In the columns, larger shear forces were generally observed in the longitudinal direction, particularly near both abutments. The maximum bending moments were mostly developed at the base of the columns. In the relatively flexible frames (with

longer columns) of the NW and the SE, large transverse bending moments were observed due to the pronounced bridge flexibility in this direction.

(4) Excessive relative displacement (in the longitudinal direction) at the hinges induced significant gap opening instants between adjacent frames. The corresponding stresses at some of the hinges exceeded the actual yield stress of the restrainer cables in the NW and the SE.

(5) The backwall abutment forces in the longitudinal direction and the transverse forces transmitted to the wingwalls were mostly affected by the overall longitudinal structural behavior (due to the bridge curved configuration).

(6) Although presence of adjacent structures hardly affected response of the other bridge, it appeared that dynamic properties of the 3-bridge BFGS system slightly changed (stiffened) the system, and somewhat larger accelerations and displacements at the top of the relatively flexible columns were developed.

2. Numerical simulation of the NW separately was undertaken in the BFGS DRM ROI environment. In order to consider implications of soil stiffness on structural response, two types of soil domain properties (stiff and soft soil scenarios) were studied. Compared to the stiff soil scenario, the main differences in the soft soil case are summarized below:

(1) For the softer soil scenario, higher amplification of the ground response at the surface and larger support motions generally induced larger force/displacement demands (in terms of peak column shear and bending forces/column drift ratios). In addition, intermittent spikes induced by pounding in the longitudinal direction at the intermediate hinges were much more pronounced in the soft soil scenario.

(2) Displacements induced by base rocking generally increased.

(3) In comparison of the low-frequency (≤ 1 Hz) and the broadband (≤ 5 Hz) input motions, more prominent response of the bridge (natural frequency of 1.5 Hz) was observed for the latter scenario. The higher amplitude of the ground acceleration also induced larger force/displacement demands than those from the low frequency input scenario.

3. Possible contribution of nonlinearity emanating from presence of a soft soil stratum near the ground surface for the NW in the BFGS was studied as well. Main observations include:

(1) The presence of the soft material in the upper 40 m layer significantly limited amplification of ground acceleration, acting as a base-isolation mechanism. However, relative support motions induced by the spatially variable permanent ground deformation over the soil surface significantly affected the longitudinal response of the bridge (drift ratios in this direction, hinge opening/stresses in restrainer cables, abutment forces against bridge approach ramp).

(2) Despite the limited low acceleration at the ground surface, yielding of the soil in the vicinity of the column pile foundations was observed. However, the level of deformation in the columns was significantly reduced by rocking of the foundation. In addition, impacts between adjacent frames were observed due to the pronounced ground motion spatial variability.

10.1.3 Assessment of the fixed-base structural response without the soil domain (Chapters 5 and 6)

Compared to structural response in the BFGS (with the soil domain, ROI), results obtained from the fixed-base structure without the soil domain under multiple support excitation and uniform excitation were compared. Below is a list summarizing the main observed differences:

1. For the stiff soil with elastic material properties:

Due to the stiff material properties for the soil domain, both scenarios of multiple support excitation and uniform excitation without the soil domain (i.e. no effect of SSI) led to a reasonable estimate of the structural response. The following summarizes some differences from the results of the BFGS (with the soil domain):

1) Without rocking of the foundations, multiple support excitation slightly underestimated displacement demands and column forces, particularly in the relatively flexible columns (longer columns).
2) Uniform excitation overestimated or underestimated the displacement/force demands, depending on the particular column location.

2. For the soft soil with elastic material properties:

The flexible soil properties induced higher variation in ground motion over the soil surface. As input, dictated by the free-field motions, both scenarios of multiple support excitation and uniform excitation resulted in some extent of deviation from the BFGS response:

1) Under multiple support excitation, without the rocking observed in the BFGS, the resulting outcomes (e.g., deformation column drift ratios, shear/bending moments in the columns) were generally underestimated. In particular, more difference was observed in the longer columns, associated with transverse response. In the longitudinal direction, more deviation was observed in the middle of the bridge.
2) Under uniform excitation, the relatively high shaking level of the employed input excitation (at the mesh center), compared to the non-uniform support motion scenario, did not lead to a close estimate of the structural response. Over all the column locations, overestimation or underestimation of the response was observed (depending on location).

3. For the soft soil material in the upper 40 m layer (Chapter 6):

1) Presence of the soft soil layer limited the amplification of ground motions and induced permanent ground deformation at the soil surface. In the BFGS, the actual foundation inputs were significantly different compared to the corresponding free-field input motions for the fixed-base structure. Consequently, analysis of the fixed-base bridge did not lead to accurate prediction of structural response (e.g. drift ratios at the top of columns, internal columns forces, and gap opening at the intermediate hinges).
2) Depending on frequency content of the employed input motions (low-frequency and broadband frequency), the discrepancy of the structural response, compared to that in the BFGS, increased in the broadband frequency scenario (up to 5Hz in this study). Thus, for satisfactory prediction of the bridge response supported on a soft

soil layer, a detailed analysis that considers the full coupling between the structure and the underlying soil may become necessary.

10.1.4 Analysis of bridge-foundation-ground system based on an actual local site (Chapter 7)

Based on the actual local site at the I-10/215, a ground model was developed. Supported on this soil model, the BFGS was analyzed for a potential site specific strong earthquake. Computed ground and structural response (displacement/force demands in the linear column) were discussed. In order to compare the column demand to its capacity, an additional bridge model with bilinear behavior (based on the moment-curvature relation for the columns) was also developed and the corresponding results were discussed. On this basis, the following observations are presented:

(1) The developed BFGS model provided a satisfactory agreement with recorded seismic response (in terms of free-field and structural acceleration/displacement response) in the case of the Landers earthquake 1992 (San Bernardino – E & Hospitality, CSMIP Station No. 23542).

(2) During the potential site specific strong earthquake using the 1994 Northridge earthquake recorded at CSMIP Station 24279 (Newhall, Fire station), limitation of acceleration transferred to the ground surface was induced by relatively large inelastic deformation at depths from 5 m to 30 m in the ground.

(3) In the potential earthquake scenario, it was observed that rocking of the foundation (as a result of SSI) decreased the deformation drift ratio in most of the columns.

Nevertheless, the computed force demand exceeded the idealized strength in most of the columns.

(4) When the bilinear column model was employed, a larger reduction in the demand was observed due to yielding and energy dissipation in the moment-curvature response and change of the overall dynamic properties (i.e., the period lengthening).

10.1.5 Soil-structure interaction for a large rigid structure with considerable embedment in ROI (Chapter 8)

Dynamic interaction for a large rigid structure in the ROI (elastic material properties, and low-frequency input scenario) was investigated with different embedment depths and soil characteristics. Kinematic soil-structure interaction was isolated and evaluated by also analyzing the structure without its mass. The finding support the following conclusions:

1. In the soft soil case:

(1) For the fully embedded structure, rigidity of the structure and embedment in the underlying stiffer layer contributed to reduction of peak accelerations developed at the top. This reduction affected free-field accelerations in the local region near the structure. As embedment decreased, the affected spatial extent of surrounding free-field tended to be smaller.

(2) At different embedment levels, base acceleration of the structure was significantly dictated by the corresponding free-field response at the same depth. Particularly, for the surface foundation, overturning tendency of the structure was observed to increase the base acceleration.

2. In the stiff soil case:

(1) In this study, no significant change was observed in base accelerations at different embedment levels.

(2) Free-field response in the vicinity of the structure was less affected by its presence, compared to the soft soil case.

10.1.6 Soil-structure interaction of a fully embedded large rigid structure under uniform excitation (Chapter 9)

Dynamic interaction for a fully embedded large rigid cylindrical structure was investigated under uniform spatial dynamic excitation. Elastic soil characteristics were employed to investigate variation of the acceleration developed at top and base of the structure, lateral soil pressure along height of the structure, and normal pressure along the base. Kinematic soil-structure interaction was isolated and evaluated by also analyzing the structure without its mass. The finding support the following conclusions:

1. Rigidity of the structure contributed to reduction of peak accelerations developed at its top and base (a marked reduction of 35% at top of the structure (case of V_s= 300 m/s). This reduction affected free-field accelerations in the local region near the structure (as soil stiffness increased, the reduction decreased).
2. As free-field acceleration at the soil surface reached its peak in the studied cases, maximum compressive lateral pressure occurred at the depth of 7 m (structure height is 23 m) reaching 50 kPa (case of V_s = 300 m/s). As soil stiffness increased, the maximum pressure tended to decrease.

3. Inertial interaction limited the reduction of acceleration amplification along height of the structure. In view of the maximum compressive lateral pressure imposed by inertial interaction, out-of-phase response at top and base of the structure tended to increase as soil stiffness decreased.

10.2 Future research

In this research, the ROI provided an efficient tool to analyze a large-scale extended bridge interchange and a large embedded rigid structural configuration. The employed structural models are subjected to spatial variation of ground motion emanating from incident seismic waves based on the Puente Hills rupture scenario using the DRM (Bielak et al., 2003a). Several future extensions and research directions related to ROI implementation are presented as follows:

- Further verification of the computed DRM computed ROI spatial variability is needed on the basis of available ground motion records.
- Motions resulting from additional fault rupture scenarios are needed (similar to Puente Hills fault scenario motions employed herein).
- Finer meshes for the soil domain would be helpful in order to more accurately address higher frequency content. However the finer mesh will in turn lead to longer computation time on parallel processing systems.
- For the studied bridge interchange, formal inclusion of local topographical effects would add to the simulation fidelity.

- Generally, developing the ground-bridge model based on the actual local site characteristics can be enhanced based on:

    1. Consideration of actual ground surface topography, as mentioned above.

    2. More accurate foundation modeling:

In this study, the foundation comprised of a pile cap and pile group is simply modeled as a rigid solid element. While the employed foundation model crudely captures the involved foundation geometry, more insights into local behavior such as actual shear force /moment distribution along individual piles may be of importance.

3. Modeling of steel jacket retrofits in the bridge columns:

In order to investigate response of a retrofitted column with steel jackets, a more advanced modeling scheme is needed. For arbitrary column cross-sectional shapes, an appropriate formulation to represent the confinement produced by steel jacketing is needed.

REFERENCES

Aagard, B. T., Hall, J. F. and Heaton, T. (2001). “Characterization of near-source ground motions with earthquake simulations.” Earthquake Spectra, 17, 177-207.

Aviram, A., Mackie, K., and Stojadinovic, B. (2008). "Effect of abutment modeling on the seismic response of bridge structures." Earthquake Eng. and Engineering Vibration, Vol. 7, No. 4, 395-402.

Bao, H., Bielak, J. Ghattas, O., Kallivokas, L. F., O’Hallaron, D. R., Schewchuk, J., and Xu, J. (2001). “Large-scale simulation of elastic wave propagation in heterogeneous media on parallel computers.” Comput. Methods Appl. Mech. Eng., 152, 85-102.

Bielak, J. and Christiano, P. (1984). "On the effective seismic input for non-linear soil-structure interaction systems," Earthquake engineering & structural dynamics, 12 (1), 107-119.

Bielak, J., Loukakis, K., Hisada, Y., and Yoshimura, C. (2003a). "Domain reduction method for three-dimensional earthquake modeling in localized regions, Part I: Theory," Bulletin of the Seismological Society of America, 93 (2), 817-824.

Caltrans (2010). Caltrans Seismic Design Criteria version 1.6. California Department of Transportation, Sacramento, California.

CDMG (1977). Special studies zones, San Bernardino South Quadrangle. Sacramento, CA, California Division of Mines and Geology.

Conte, J. P., Elgamal, A., Yang, Z., Zhang, Y., Acero, G., and F., S. (2002). "Nonlinear seismic analysis of a bridge ground system." Proc., of 15th Engineering Mechanics Conf., ASCE, Reston, Va.

Cremonini, M. G., Christiano, P., and Bielak, J. (1988). "Implementation of effective seismic input for soil-structure interaction systems," Earthquake engineering & structural dynamics, 16 (4), 615-625.

Desroches, R. and Fenves, G. L. (1997). “Evaluation of recorded earthquake response of a curved highway bridge.” Earthquake Spectra, Vol. 13, No. 3, August.

Doser, D. I. (1992). "Historic earthquakes (1918 to 1923) and an assessment of source parameters along the San Jacinto fault system," Bulletin of the Seismological Society of America, 82 (4), 1786-1801.

Dryden, G. M. (2009). The integration of experimental and simulation data in the study of reinforced concrete bridge systems including soil-foundation-structure interaction, University of California, San Diego. Ph.D. dissertation, La Jolla, CA.

Elgamal, A., Yan, L., Yang, Z., and Conte, J.P. (2008). "Three-dimensional seismic response of bridge foundation-ground system." J. of Structural Engineering, ASCE, Vol. 134, No. 7, 1165-1176, July.

Elgamal, A., Yang, Z., and Lu, J., (2006). "Cyclic1D seismic ground response version 1.00 user's manual," Research report, SSRP-06/04, Department of Structural Engineering, University of California, San Diego.

Fenves, G. L. and DesRoches, R. (1994). "Response of the northwest connector in the Landers and Big Bear earthquakes," Report No. Report No. UCB/EERC-94/12, Earthquake Engineering Research Center, University of California, Berkeley.

Graves, R.W., and Pitarka, A. (2010). "Broadband ground-motion simulation using a hybrid approach," Bulletin of the Seismological Society of America, Vol. 100, No. 5A, 2095-2123, October.

Huang, M. and A. Shakal (1995). "CSMIP strong-motion instrumentation and records from the I10/215 interchange bridge near San Bernardino." Earthquake Spectra, Vo. 11, No. 2, 193-215.

Idriss, I. M., and Sun, J. I. (1993). "User's manual for SHAKE91: A computer program for conducting equivalent linear seismic response analyses of horizontally layered soil deposits," Center for Geotechnical Modeling, Dept. of Civil and Environmental Engineering, University of California Press, Davis, CA.

Iwan, W. D. (1967). "On a class of models for the yielding behavior of continuous and composite systems," Journal of Applied Mechanics, 34 612.

Jackura, K. A. (1991). "Study of liquefaction potential at the I-10/I-215 Interchange in San Bernardino County," Report No. California Department of Transportation

Jaremprasert, S., Bazan-Zurita, E., and Bielak, J. (2013). "Seismic soil-structure interaction response of inelastic structures." Soil Dynamics and Earthquake Engineering, 47, 132-43

Jennings, C.W., and Bryant, W.A., (2010). Fault activity map of California: California Geological Survey Geologic Data Map 6, scale 1:750,000.

Jeremić, B., Jie, G., Preisig, M., and Tafazzoli, N. (2009). "Time domain simulation of soil–foundation–structure interaction in non-uniform soils." Earthquake Engineering and Structural Dynamics, Vol. 38, No. 5, 699-718.

Jeremić, B., Kunnath, S., and Xiong, F. (2004). "Influence of soil–foundation–structure interaction on seismic response of the I-880 viaduct." Engineering Structures, Vol. 26, No. 3, 391-402.

Ju, S. H. (2004). "Three-dimensional analyses of wave barriers for reduction of train-induced vibrations," Journal of geotechnical and geoenvironmental engineering, 130 740.

Kramer, S., (1996). "Geotechnical Earthquake Engineering." Prentice Hall, Upper Saddle River, NJ, USA.

Kondner, R. (1963). "Hyperbolic stress-strain response: cohesive soils," Journal of the Soil Mechanics and Foundations Division, ASCE, 89 (1), 115-143.

Kubo, T. and Penzien, J. (1979). "Analysis of three-dimensional strong ground motions along principal axes, San Fernando Earthquake," Earthquake Engineering and Structural Dynamics 7, 265–278.

Kwon, O. S. and Elnashai, A. S. (2008). "Seismic analysis of Meloland road overcrossing using multiplatform simulation software including SSI," Journal of structural engineering, 134 651.

Liu, W. K. and Belytschko, T. (1982). "Mixed-time implicit-explicit finite elements for transient analysis," Journal of Computers and Structures, Vol. 15, 445-450.

Lysmer, J. and Kuhlemeyer, R. L. (1969). "Finite dynamic model for infinite media," Journal of the Engineering Mechanics Division, ASCE, 95(3) 859-877.

Mackie, K. R., Lu, J., and Elgamal, A. (2012). "Performance-based earthquake assessment of bridge systems including ground-foundation interaction," Soil Dynamics and Earthquake Engineering, 42, 184-196.

Malhotra, P. K., Huang, M. J., and Shakal, A. F. (1995). "Seismic interaction at separation joints of an instrumented concrete bridge," Earthquake engineering & structural dynamics, 24 (8), 1055-1067.

Maroney, B. and Chai, Y. (1994). "Seismic Design and retrofitting of reinforced concrete bridges." Proceedings of 2nd International Workshop, Earthquake Commission of New Zealand, Queenstown, New Zealand.

Maroney, B. H. (1995). Large scale bridge abutment tests to determine stiffness and ultimate strength under seismic loading, University of California, Davis. Ph.D. dissertation.

McKenna, F. T. (1997). Object-oriented finite element programming: Frameworks for analysis, algorithms and parallel computing, University of California, Berkeley, California. Ph.D. dissertation.

Mosquera, V., Smyth, A. W., and Betti, R. (2009). "Utilization of Strong-Motion Data for Assessment of Structural Integrity in Instrumented Highway Bridges," SMIP09, 65.

Mroz, Z. (1967). "On the description of anisotropic workhardening," Journal of the Mechanics and Physics of Solids, 15 (3), 163-175.

Olsen, K., Day, S., and Bradley, C. (2003). "Estimation of Q for long-period (> 2 sec) waves in the Los Angeles basin," Bulletin of the Seismological Society of America, 93 (2), 627-638.

Parra, E. (1996). Numerical modeling of liquefaction and lateral ground deformation including cyclic mobility and dilation response in soil systems. Department of Civil Engineering, Rensselaer Polytechnic Institute, Troy, NY, Rensselaer Polytechnic Institute, Troy, NY. Ph.D. dissertation.

Petropoulos, G. (2008). Soil-structure interaction analysis using high-performance parallel computation. Department of Civil and Environmental Engineering University of California, Berkeley, CA. Ph.D. dissertation.

Prevost, J. H. (1978). "Plasticity theory for soil stress-strain behavior," Journal of the Engineering Mechanics Division, 104 (5), 1177-1194.

Priestley, M., Seible, F., and Chai, Y. (1992). "Seismic retrofit of bridge columns using steel jackets."

Priestley, M. J. N., Seible, F., and Calvi, M. (1996). Seismic design and retrofit of bridges, Wiley-Interscience.

Seed, H. B. and Idriss, I. M. (1973), “Soil-structure interaction of massive embedded structures during earthquakes,” Proc. 5th World Conf. Earthq. Engng., Rome, Italy.

Sharp, R. V. and Survey, G. (1972). Map showing recently active breaks along the San Jacinto fault zone between the San Bernardino area and Borrego Valley, California, US Geological Survey.

Sieh, K., Cheatum, C., Dingus, L., Johnson, W., and McMurty, G. (1973). "Geological investigations of portions of the San Jacinto fault zone, San Bernardino Valley, California," Univ. Calif. Riverside Campus Museum Contrib, 3.

Trifunac, M. and Todorovska, M. (1998). "Nonlinear soil response as a natural passive isolation mechanism--the 1994 Northridge, California, earthquake," Soil Dynamics and Earthquake Engineering, 17 (1), 41-51.

Wesnousky, S. G., Prentice, C. S., and Sieh, K. E. (1991). "An offset Holocene stream channel and the rate of slip along the northern reach of the San Jacinto fault zone, San Bernardino Valley, California," Geological Society of America Bulletin, 103 (5), 700-709.

Zhang, Y., Conte, J. P., Yang, Z., Elgamal, A., Bielak, J., and Acero, G. (2008). “Two-dimensional nonlinear earthquake response analysis of a bridge-foundation-ground system,” Earthquake Spectra, Vol. 24, No. 2, 343–386, May.

Zhang, Y., Yang, Z., Bielak, J., Conte, J. P., and Elgamal, A., (2003). “Treatment of seismic input and boundary conditions in nonlinear seismic analysis of a bridge ground system.” Proc. 16th ASCE Engineering Mechanics Conf., ASCE, Reston, VA.

Appendix A

Additional results in the comparison of numerical results with the recorded strong motions

The numerical analysis of the fixed-base structure (North-West connect) is conducted using the strong motions recorded at the connector for Big Bear earthquake in 1992 and Northridge earthquake in 1994. Recorded accelerations at the base of Bent 8 (channel 22, 23, and 24; see Figure 5 for the instrumentation plan) are uniformly applied to the numerical model. The results are compared with the strong motions at the different superstructure elevations to validate the structural model.

A.1 Big Bear earthquake in 1992

The structural responses obtained from the numerical analysis during the Big Bear earthquake in 1992 are investigated. Acceleration time histories at the base of Bent 8 as the input for the uniform excitation are shown in Figure A. 1. The comparison of response in time domain with the recorded response of the bridge is shown in Figure A. 2 (total displacements), Figure A. 3 (displacement of deck relative to pile cap near hinges 3 and 7), and Figure A. 4 (the transverse acceleration near hinges 3, 7 and at the midspan between bents 5 and 6).

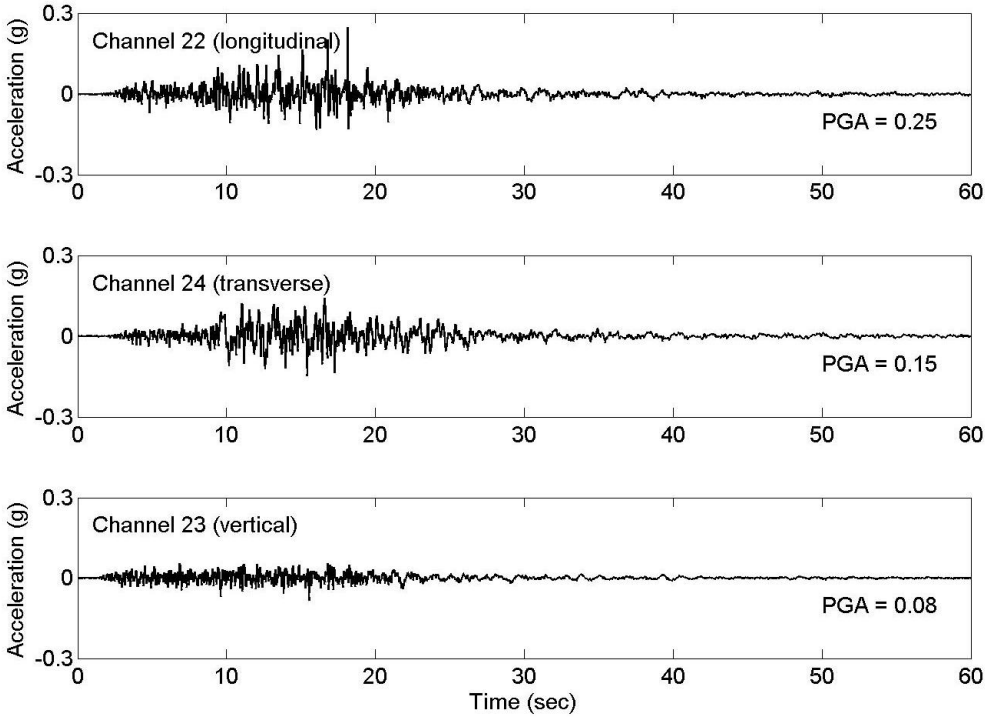

Figure A. 1: Acceleration time histories recorded at the base of Bent 8 during Big Bear earthquake in 1992

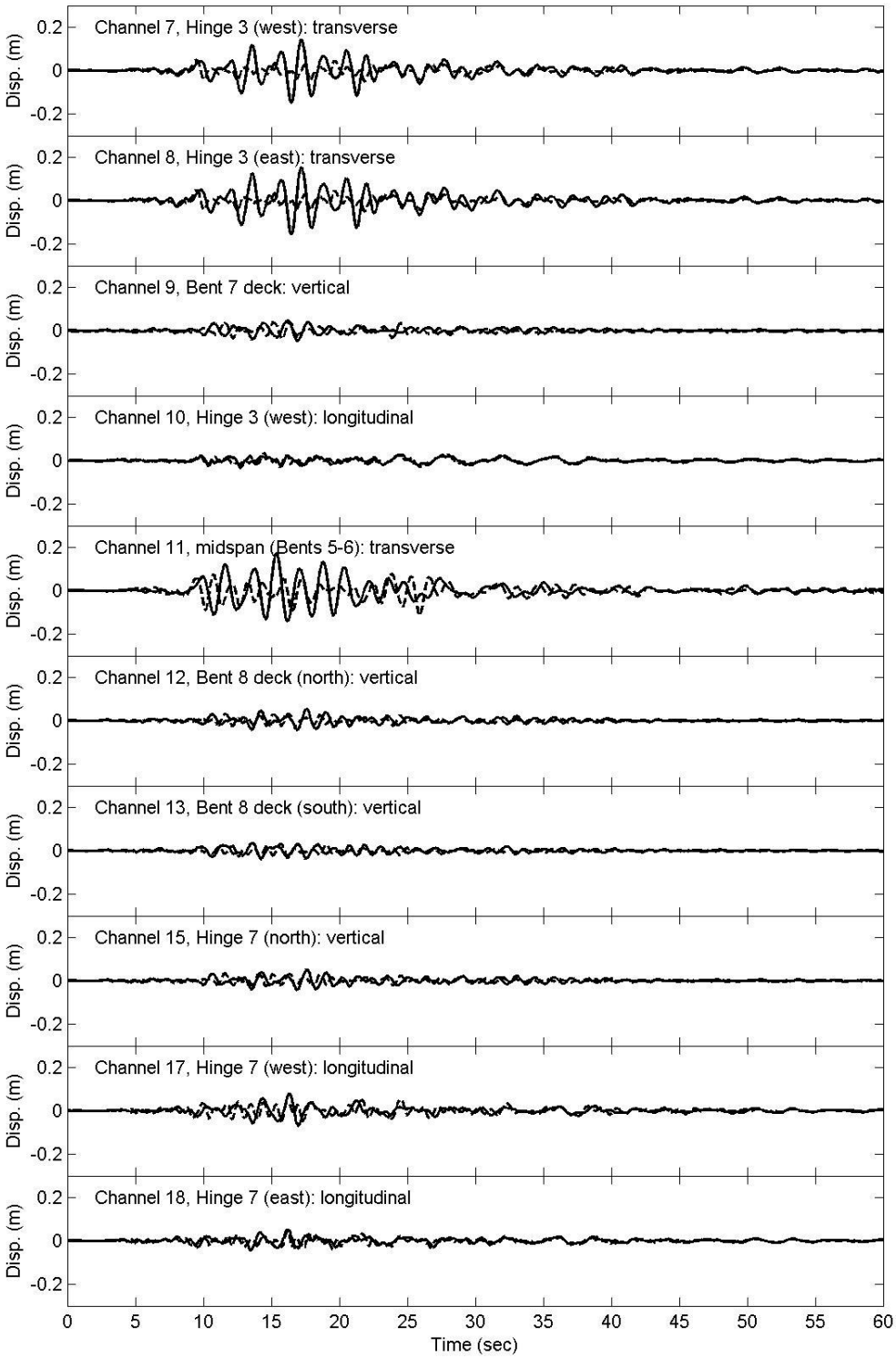

Figure A. 2: Comparison of recorded total displacement (solid line) with computed total displacement (dashed line) for Big Bear earthquake 1992

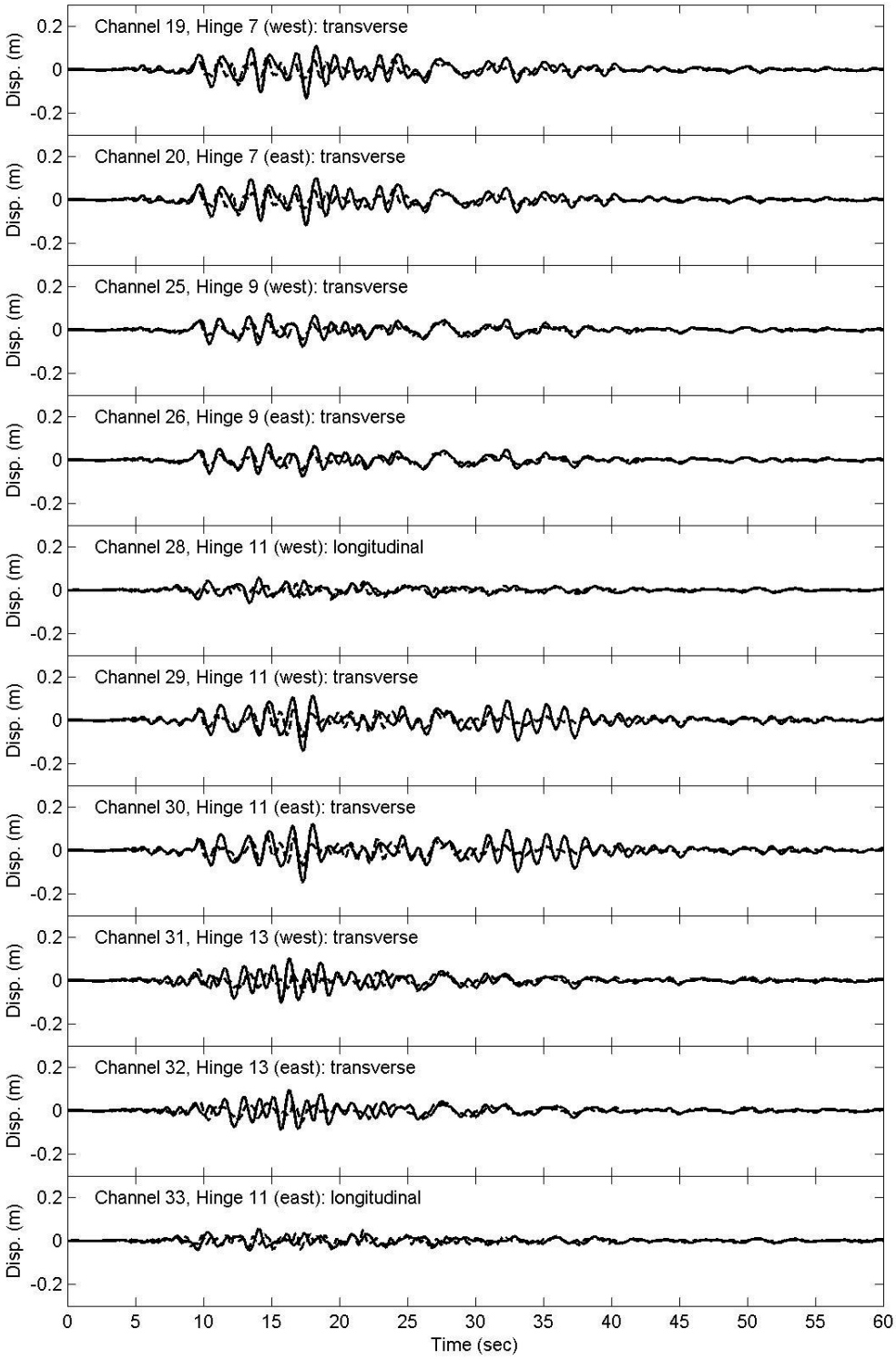

Figure A. 2: (continued) Comparison of recorded total displacement (solid line) with computed total displacement (dashed line) for Big Bear earthquake 1992

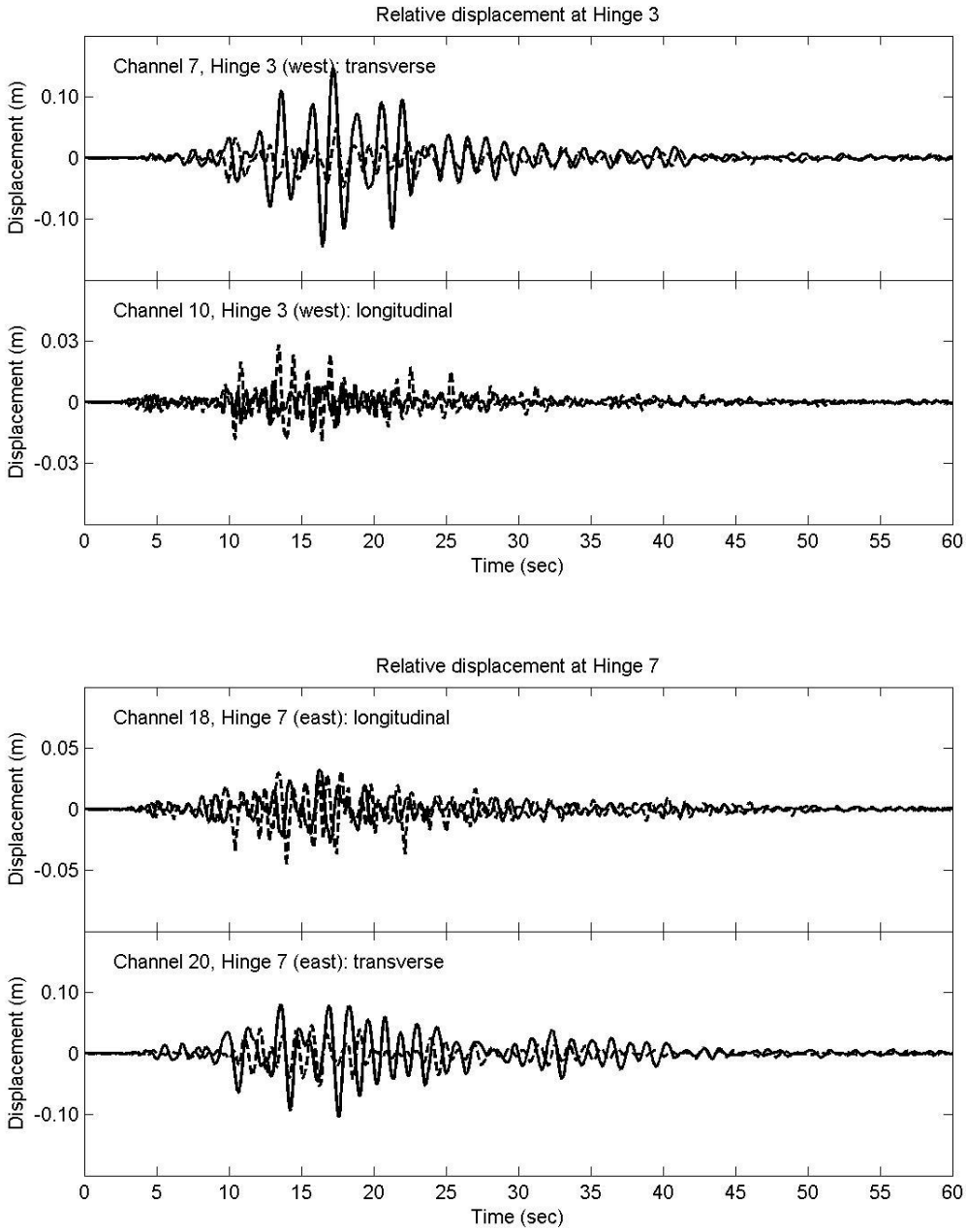

Figure A. 3: Comparison of displacement of deck relative to pile cap in Big Bear earthquake 1992 (solid-recorded, dashed-model)

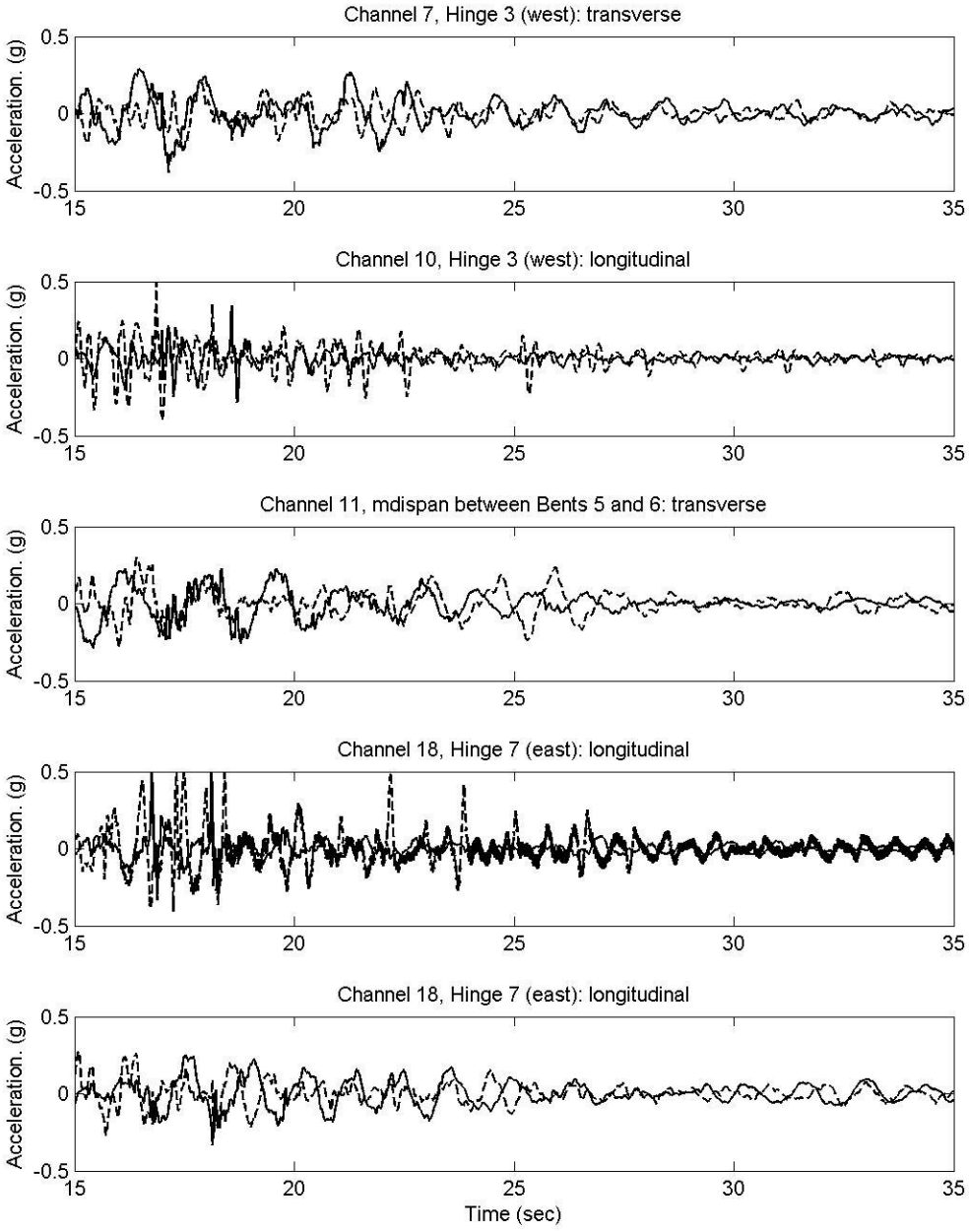

Figure A. 4: Comparison of recorded acceleration (solid line) with computed acceleration (dashed line) for Big Bear earthquake 1992

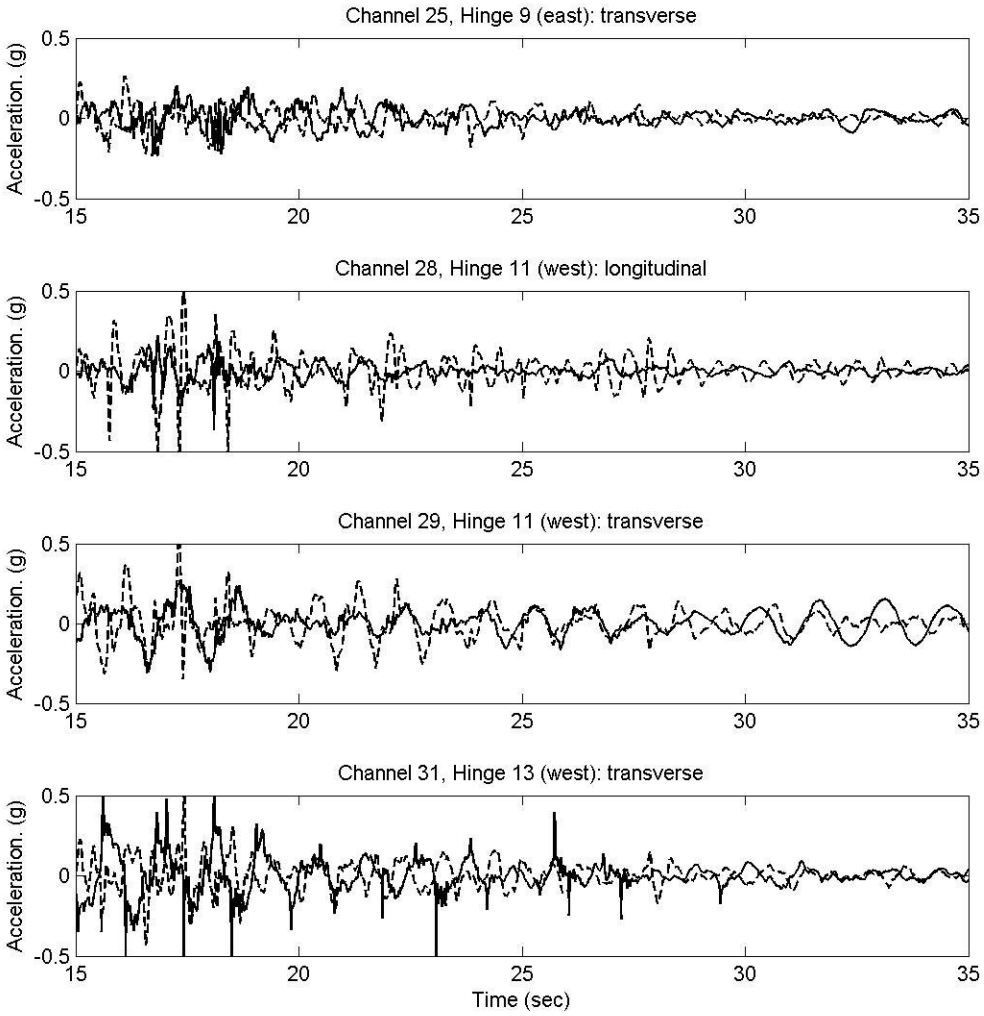

Figure A. 4: (continued) Comparison of recorded acceleration (solid line) with computed acceleration (dashed line) for Big Bear earthquake 1992

A.2 Northridge Earthquake in 1994

The structural responses obtained from the numerical analysis during the Northridge Earthquake in 1994 are investigated. Acceleration time histories at the base of Bent 8 as the input for the uniform excitation are shown in Figure A. 5. The comparison of the results in time domain with the recorded responses of the bridge are shown in Figure A. 6 (total displacements), Figure A. 7 (displacement of deck relative to pile cap near hinges 3 and 7), and Figure A. 8 (the transverse acceleration near hinges 3, 7 and at the midspan between bents 5 and 6).

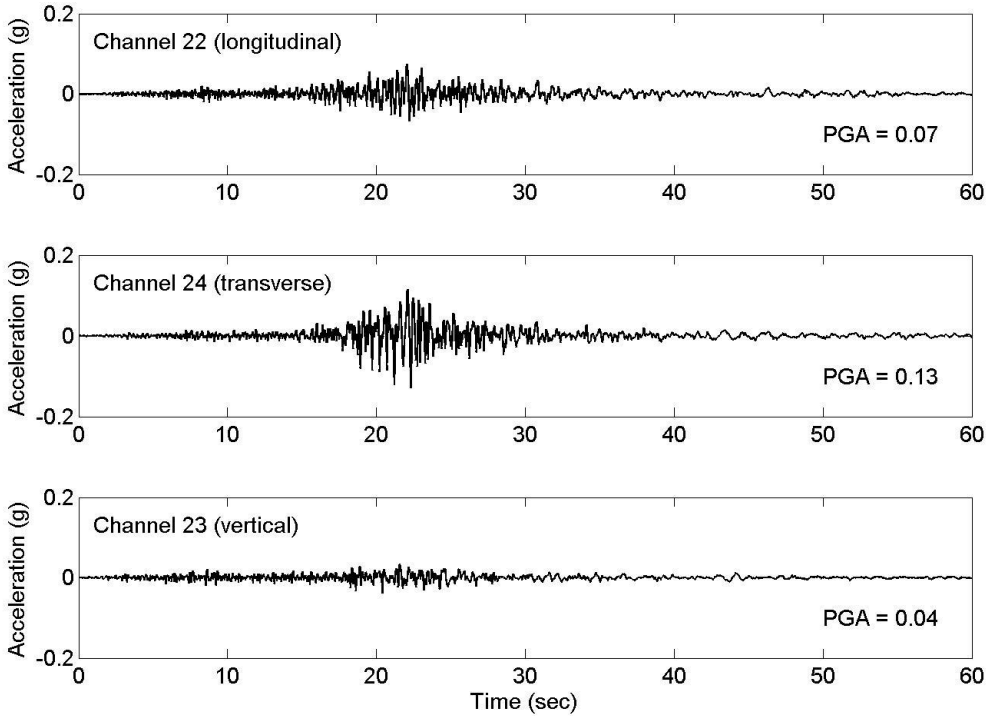

Figure A. 5: Acceleration time histories recorded at the base of Bent 8 during Northridge earthquake in 1994

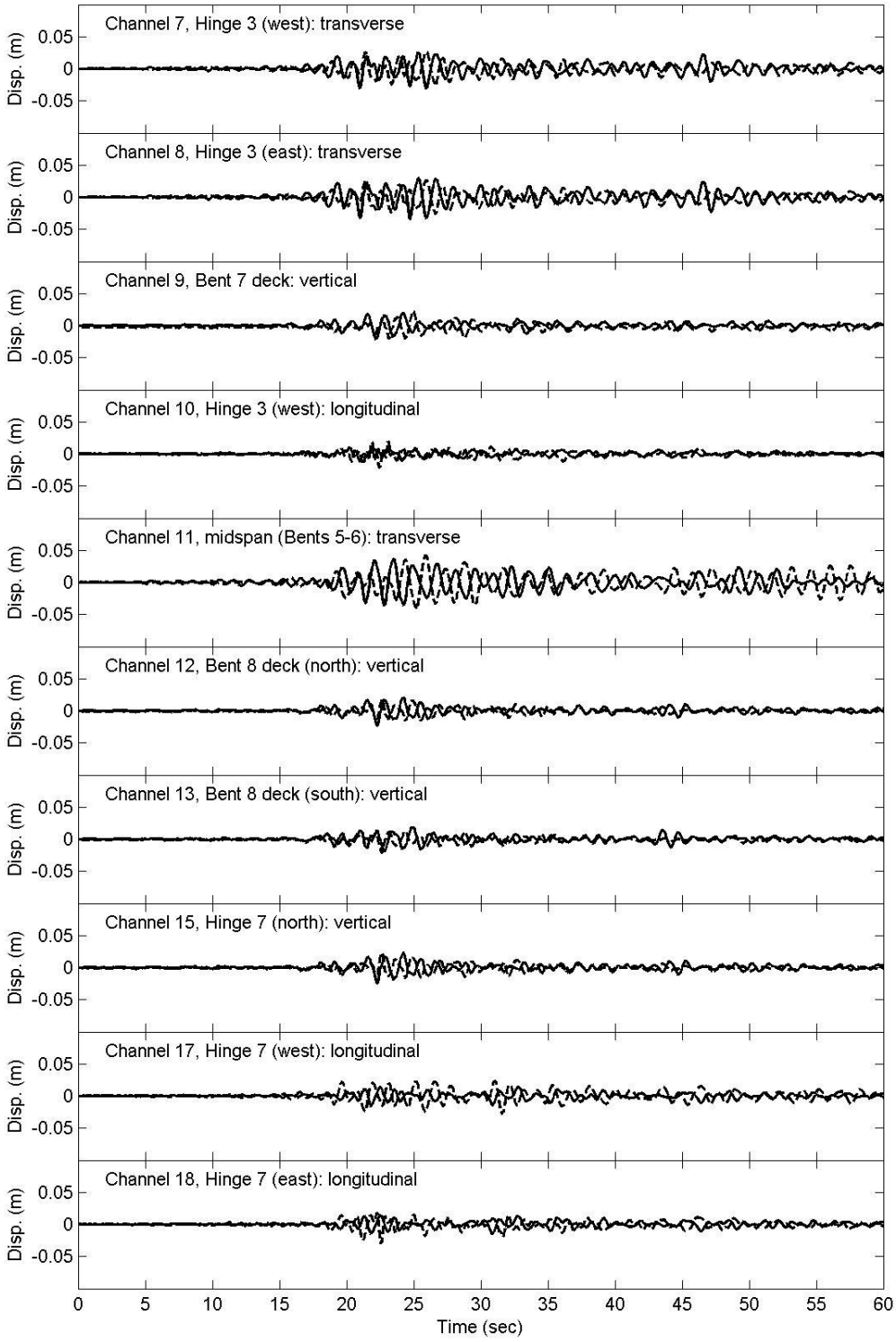

Figure A. 6: Comparison of recorded total displacement (solid line) with computed total displacement (dashed line) for Northridge Earthquake in 1994

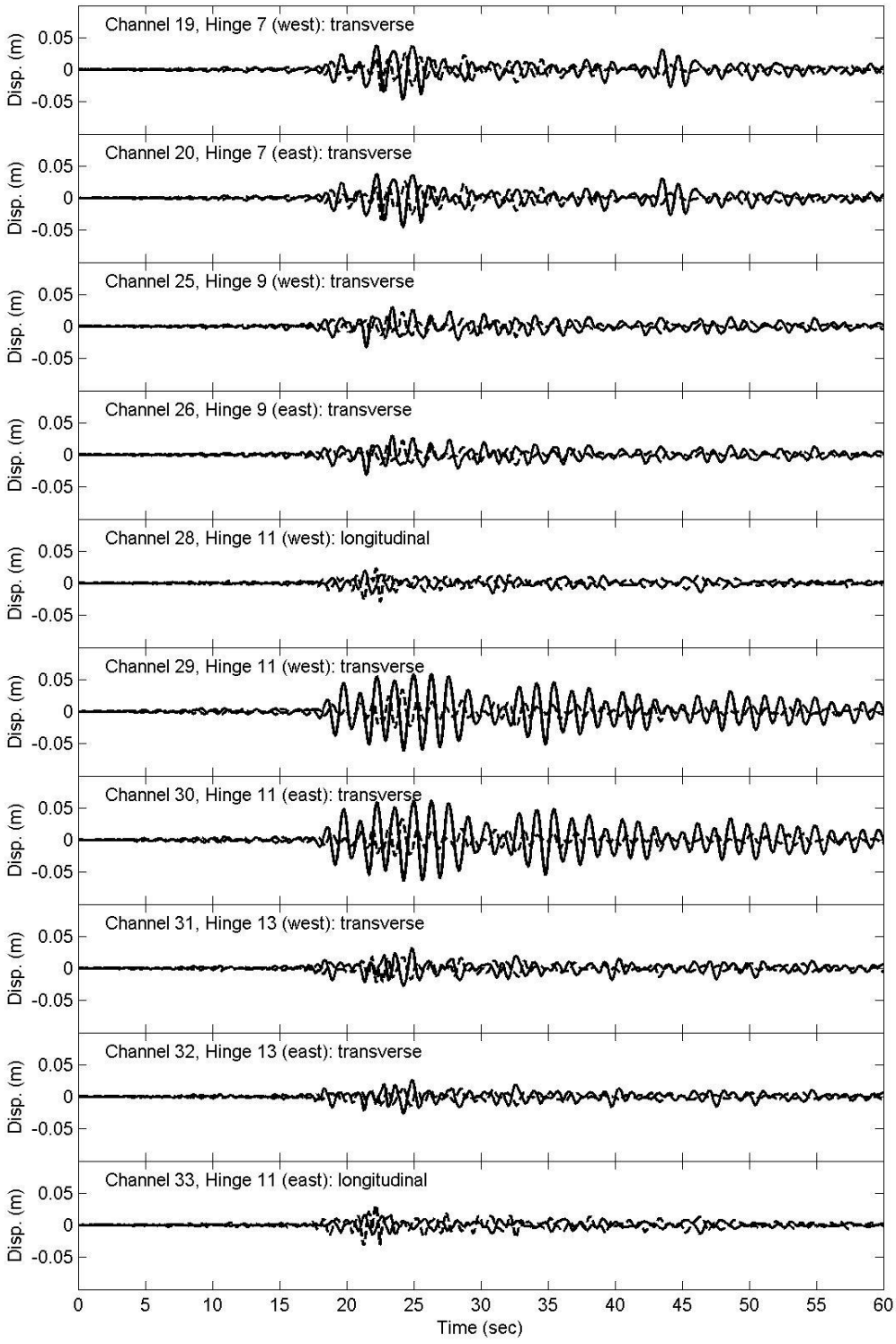

Figure A. 6: (continued) Comparison of recorded total displacement (solid line) with computed total displacement (dashed line) for Northridge Earthquake in 1994

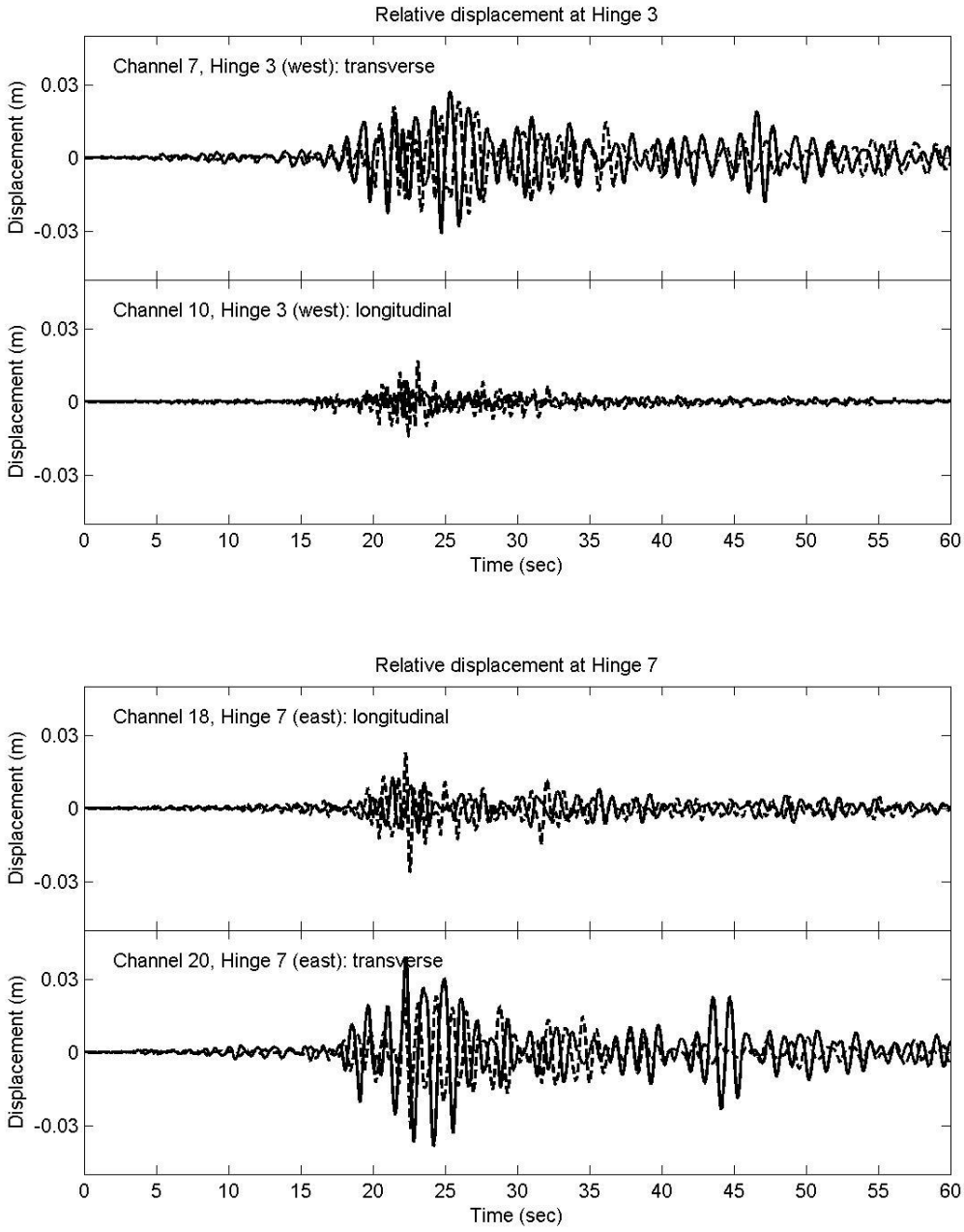

Figure A. 7 Comparison of relative displacement of deck relative to pile cap in Northridge earthquake 1994 (solid-recorded, dashed-model)

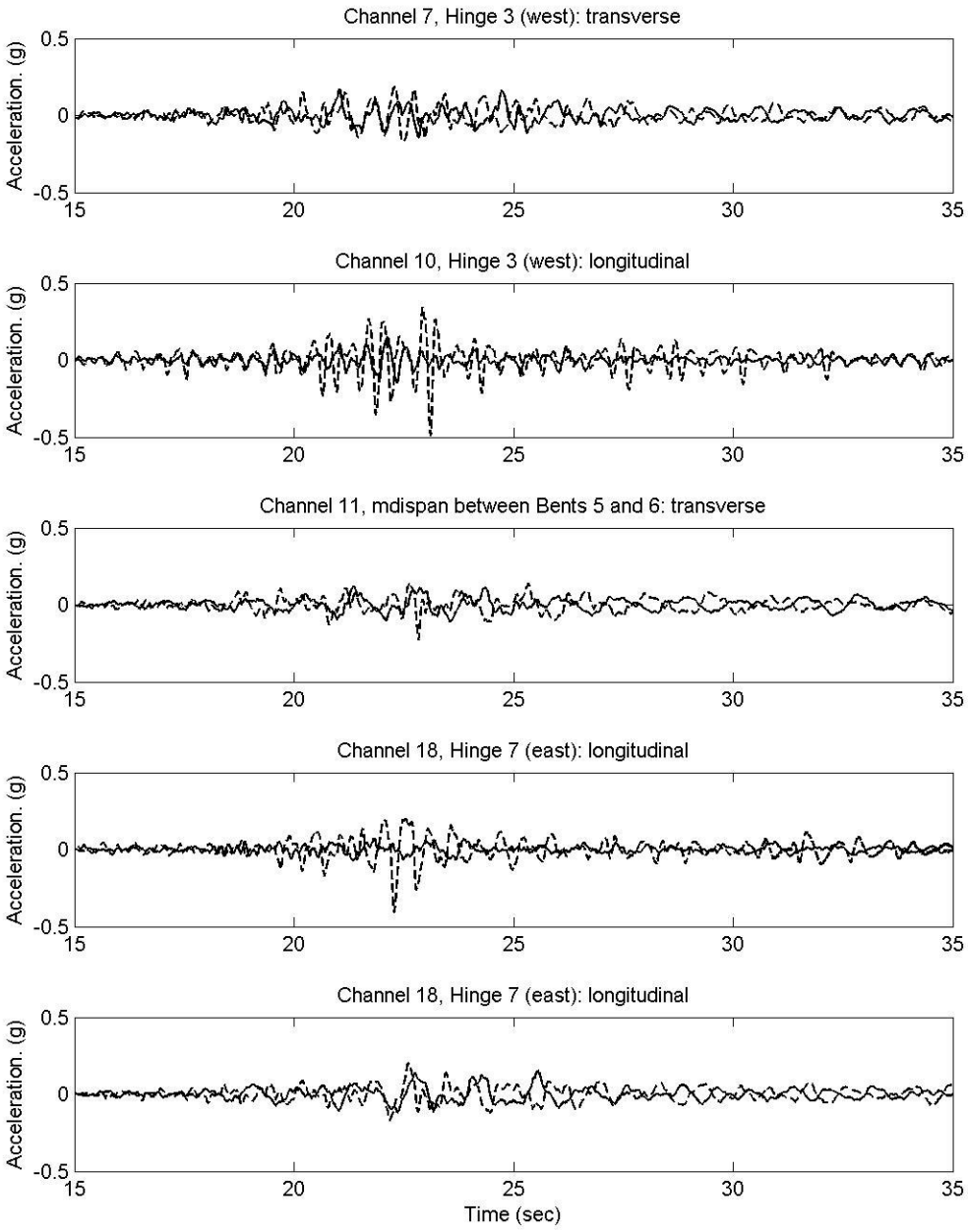

Figure A. 8: Comparison of recorded acceleration (solid line) with computed acceleration (dashed line) for Northridge Earthquake 1994

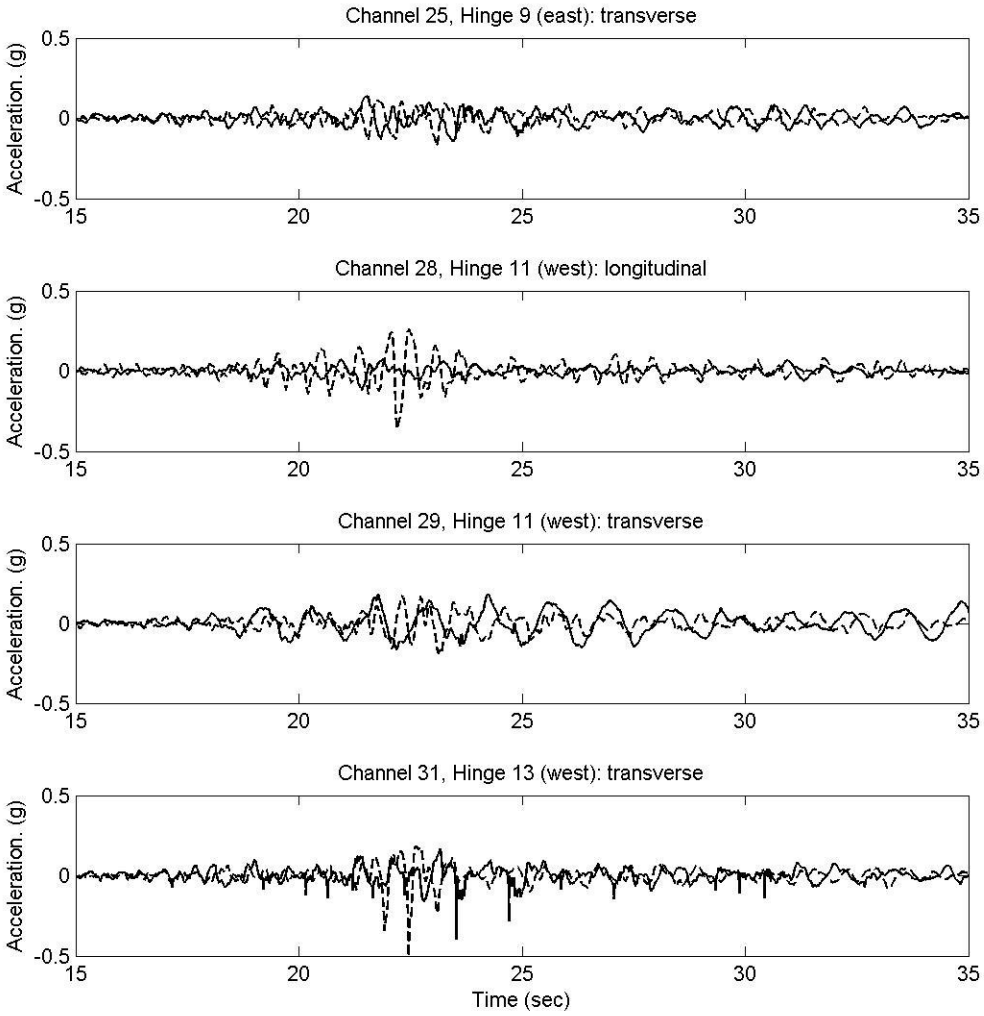

Figure A. 8: (continued) Comparison of recorded acceleration (solid line) with computed acceleration (dashed line) for Northridge Earthquake 1994

Appendix B

Ground response of region of interest obtained from linear and nonlinear soil profile

The ground motions at the center node of the free surface (called the centernode system) are examined obtained from linearly stiff/soft and nonlinear soil profile. In addition to the responses at the centernode system, ground surface responses are examined in one of centerlines along the X direction on the free surface of the region of interest

B.1 Stiff soil profile with linear material properties

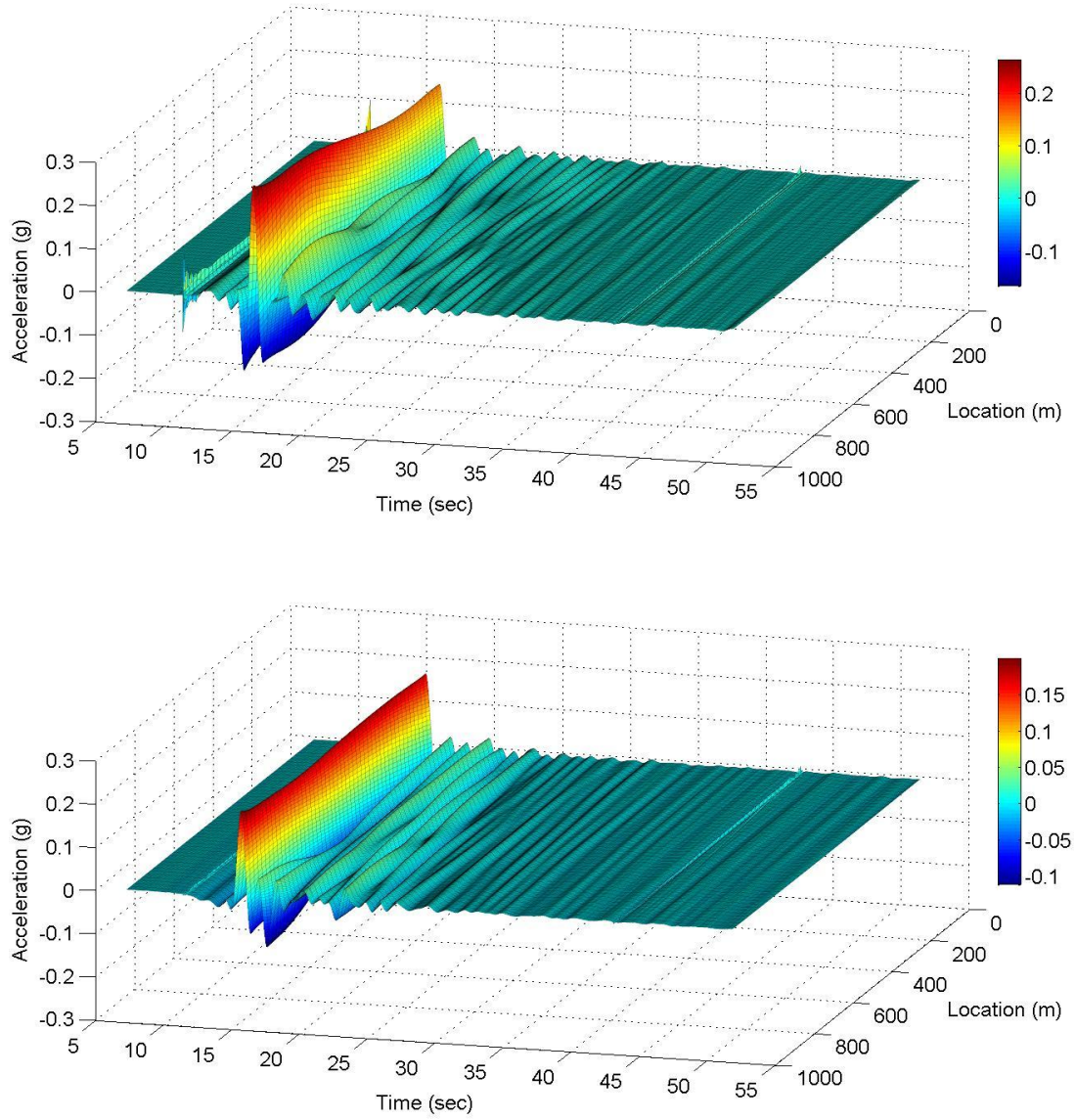

Figure B. 1: X (top) and Y (bottom) component of ground accelerations along X centerline of surface of region of interest with stiff soil profile

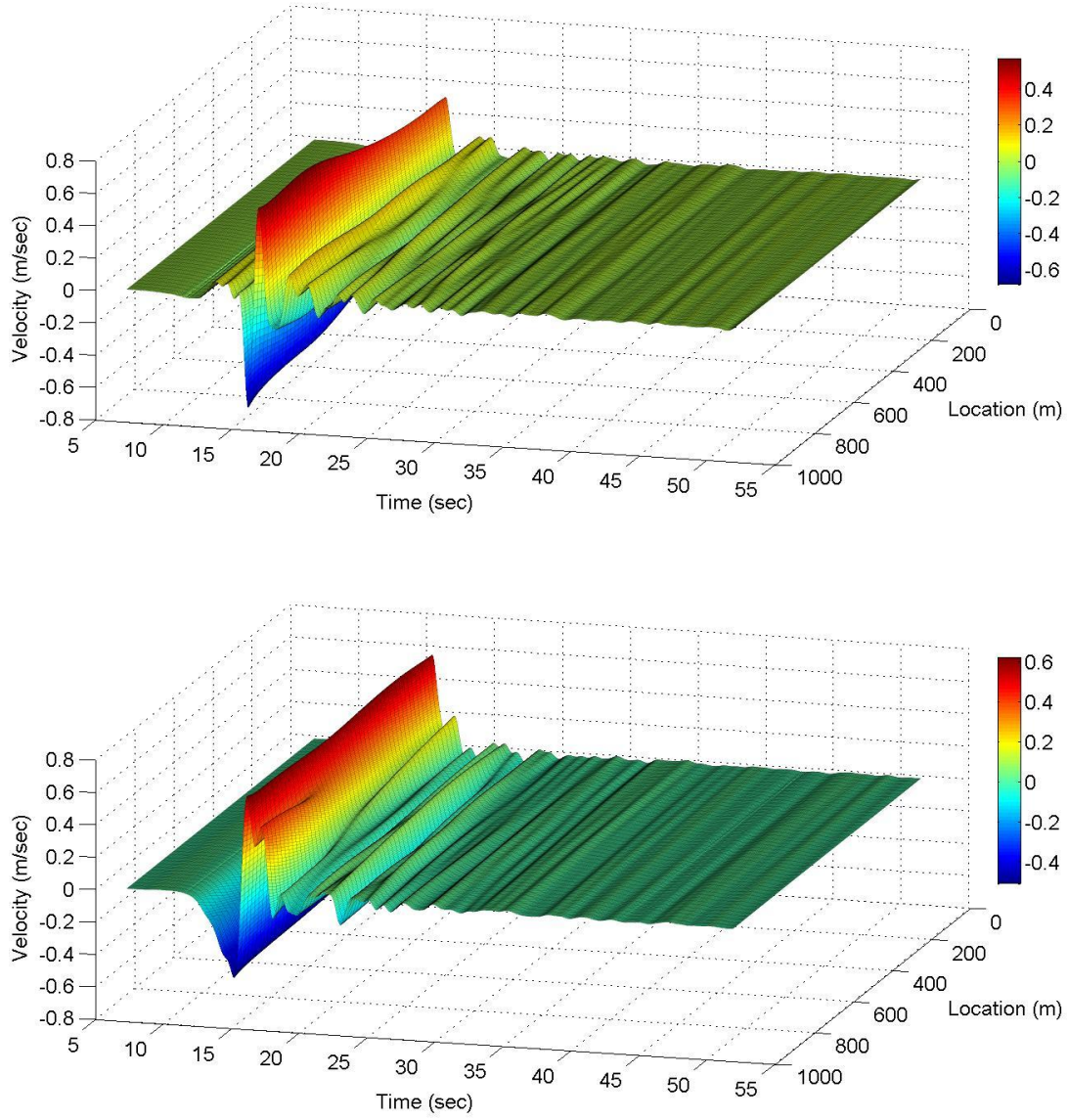

Figure B. 2: X (top) and Y (bottom) component of ground velocities along X centerline of surface of region of interest with stiff soil profile

B.2 Soft soil profile with linear properties

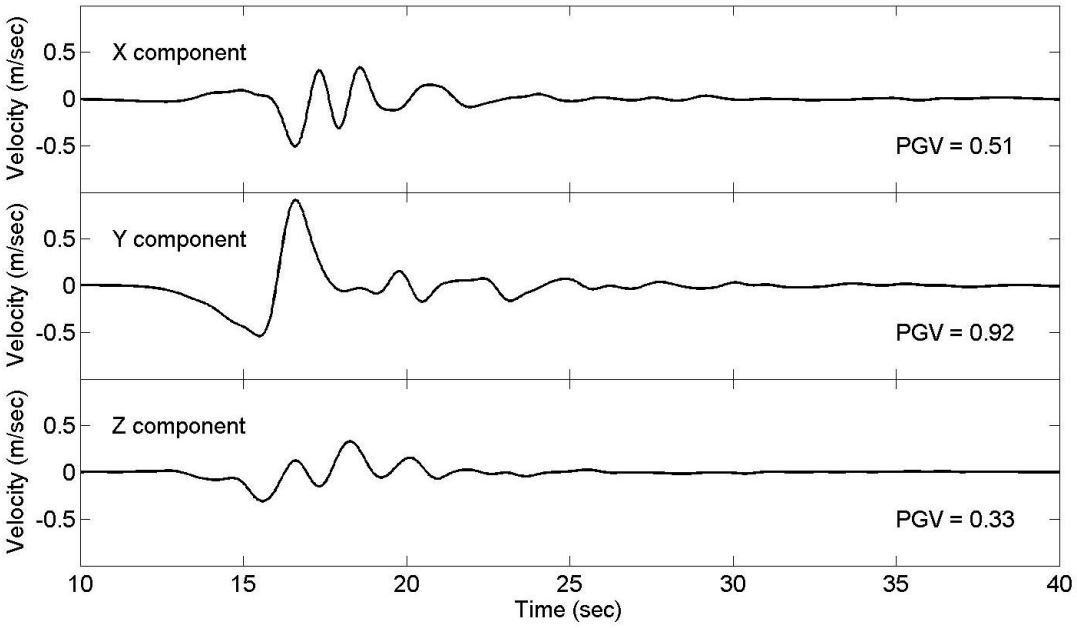

Figure B. 3: Velocity time histories at the centernode system at (Xcenternode, Ycenternode, Zcenternode) = (500 m, 240 m, 100 m)) in the soft soil profile

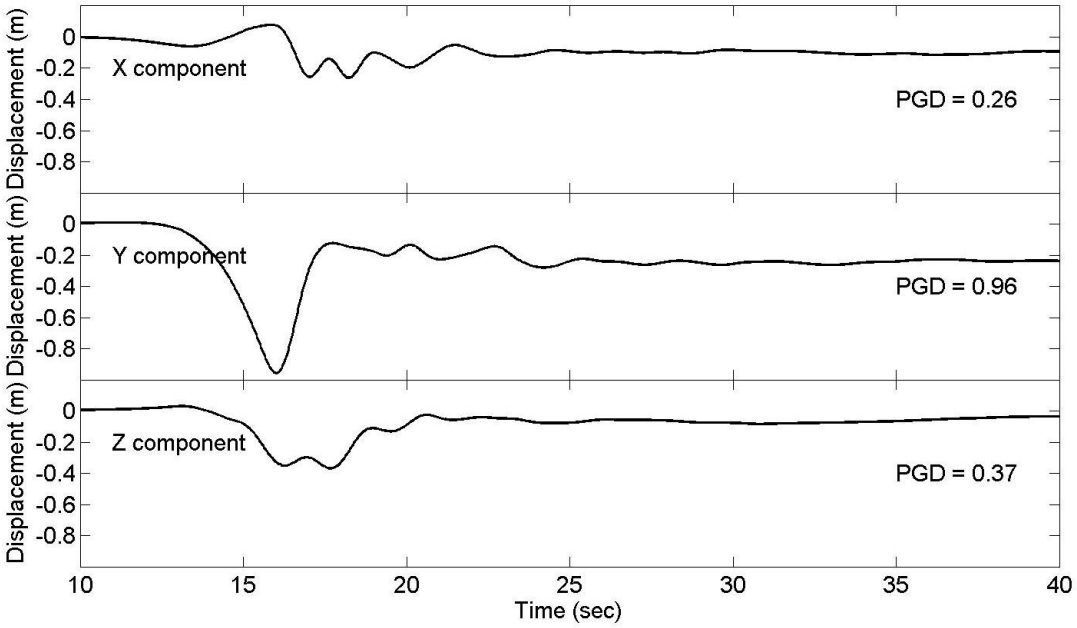

Figure B. 4: Displacement time histories at the centernode system at (Xcenternode, Ycenternode, Zcenternode) = (500 m, 240 m, 100 m)) in the soft soil profile

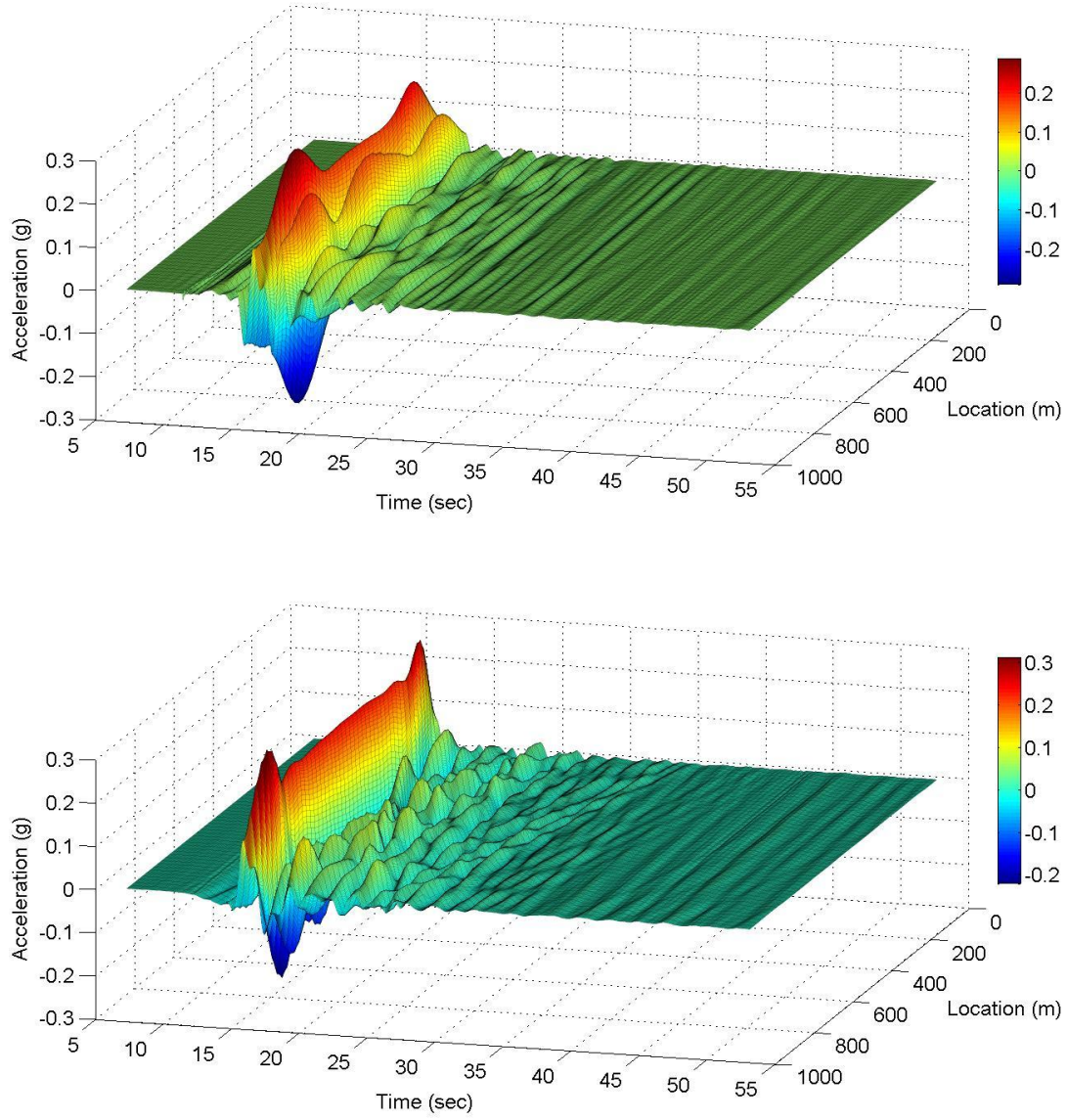

Figure B. 5: X (top) and Y (bottom) component of ground accelerations along X centerline of surface of region of interest with soft soil profile

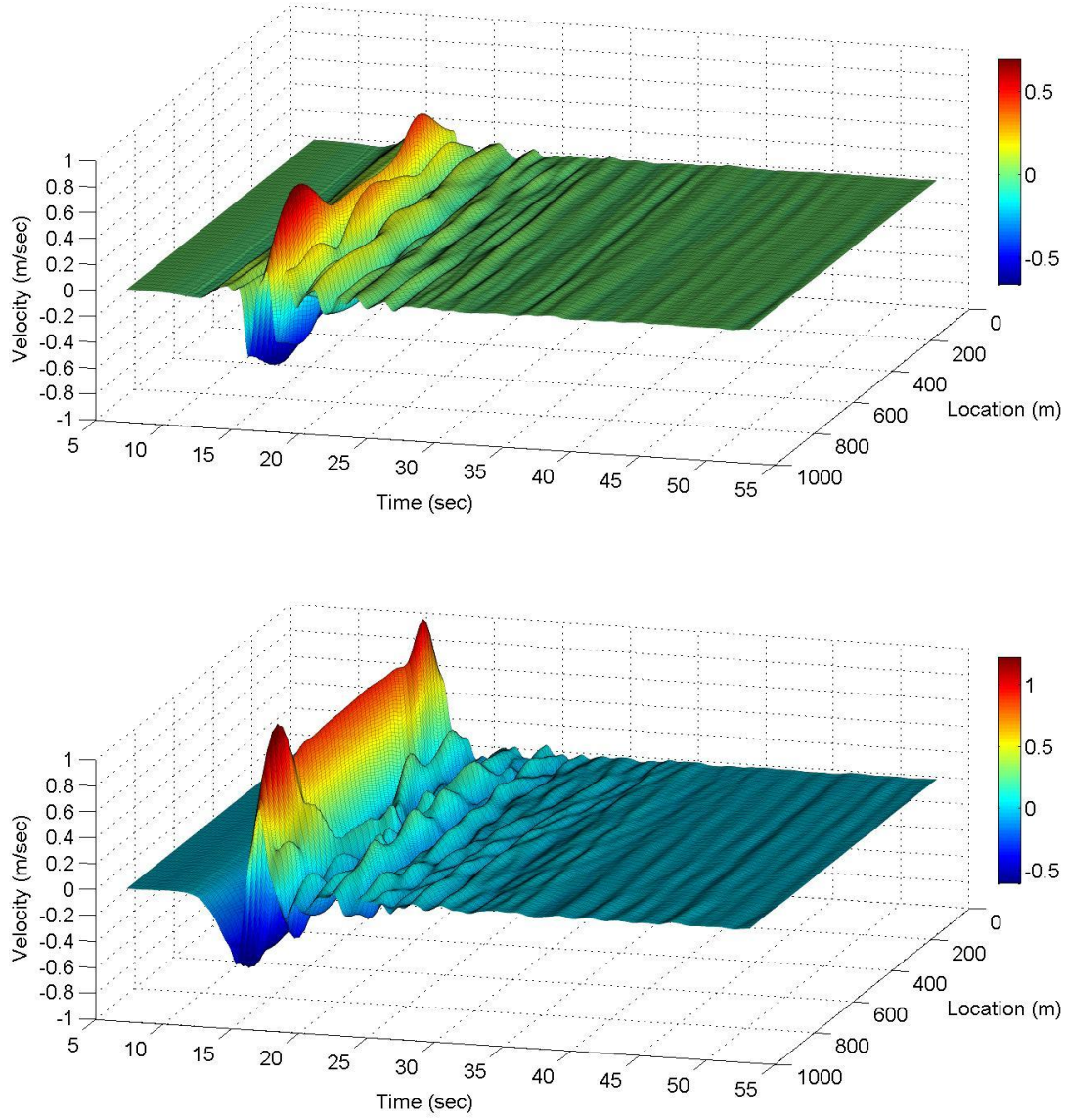

Figure B. 6: X (top) and Y (bottom) component of ground velocities along X centerline of surface of region of interest with soft soil profile

B.3 Nonlinear soil profile

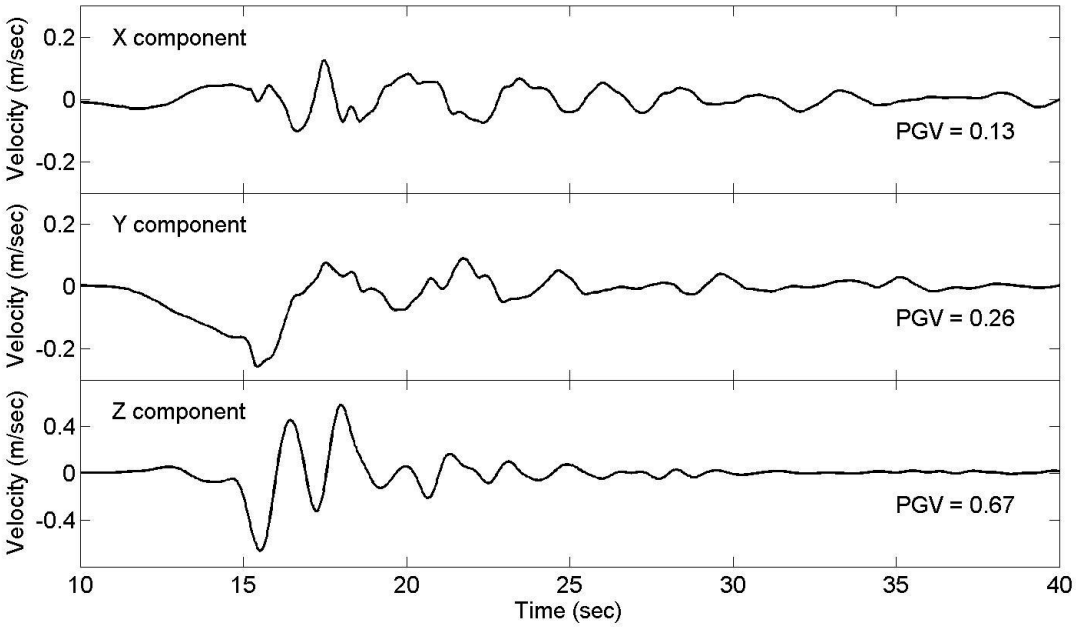

Figure B. 7: Velocity time histories at the centernode system in global directions

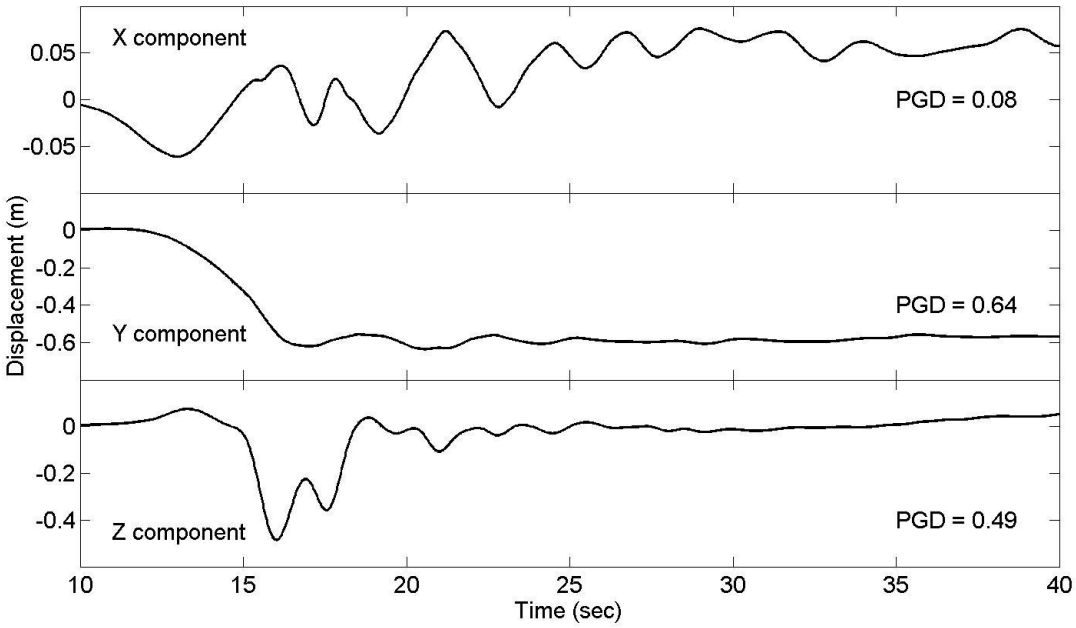

Figure B. 8: Displacement time histories at the centernode system in global directions

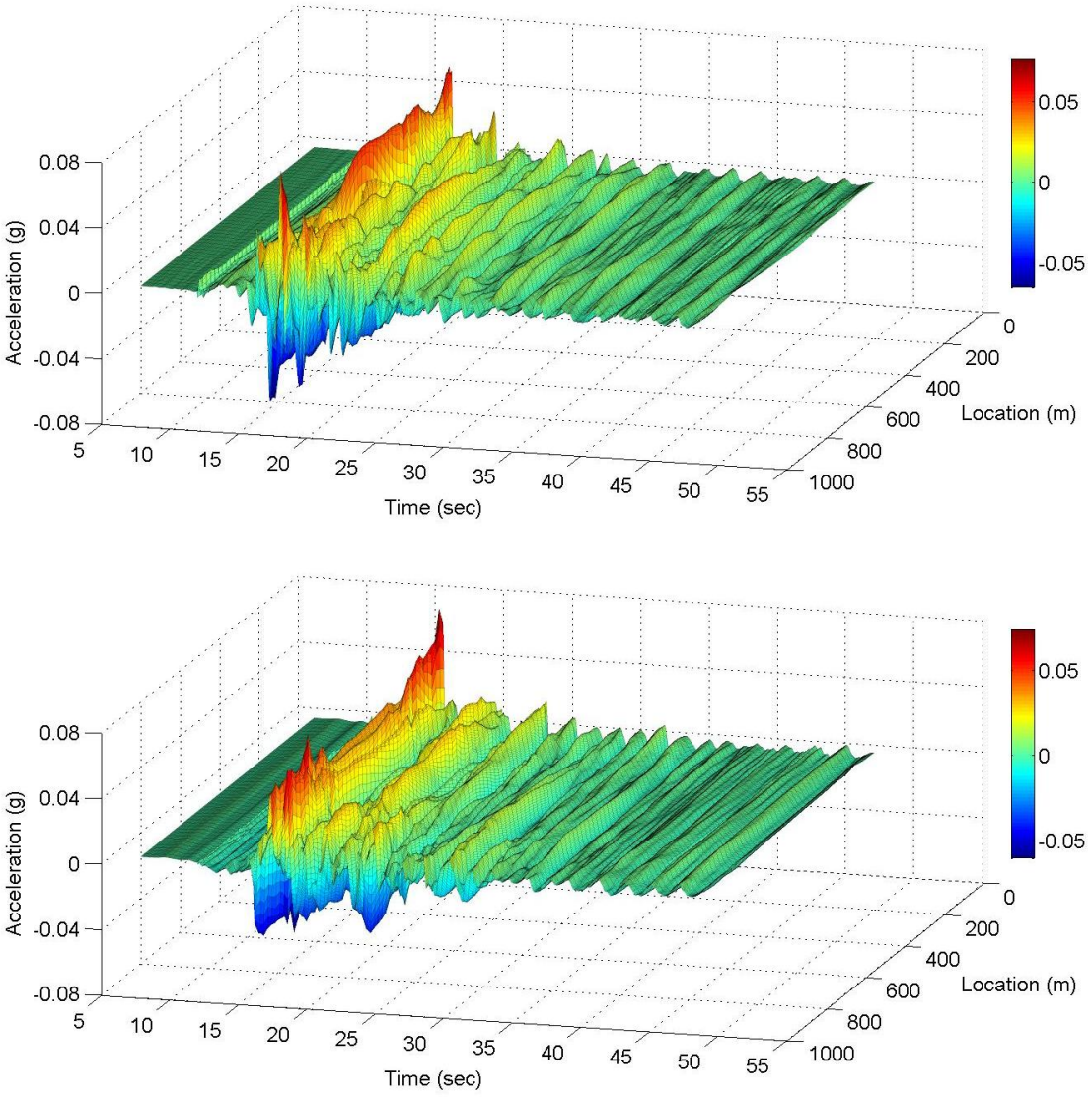

Figure B. 9: X (top) and Y (bottom) component of ground accelerations along X centerline of surface of region of interest with nonlinear soft soil profile

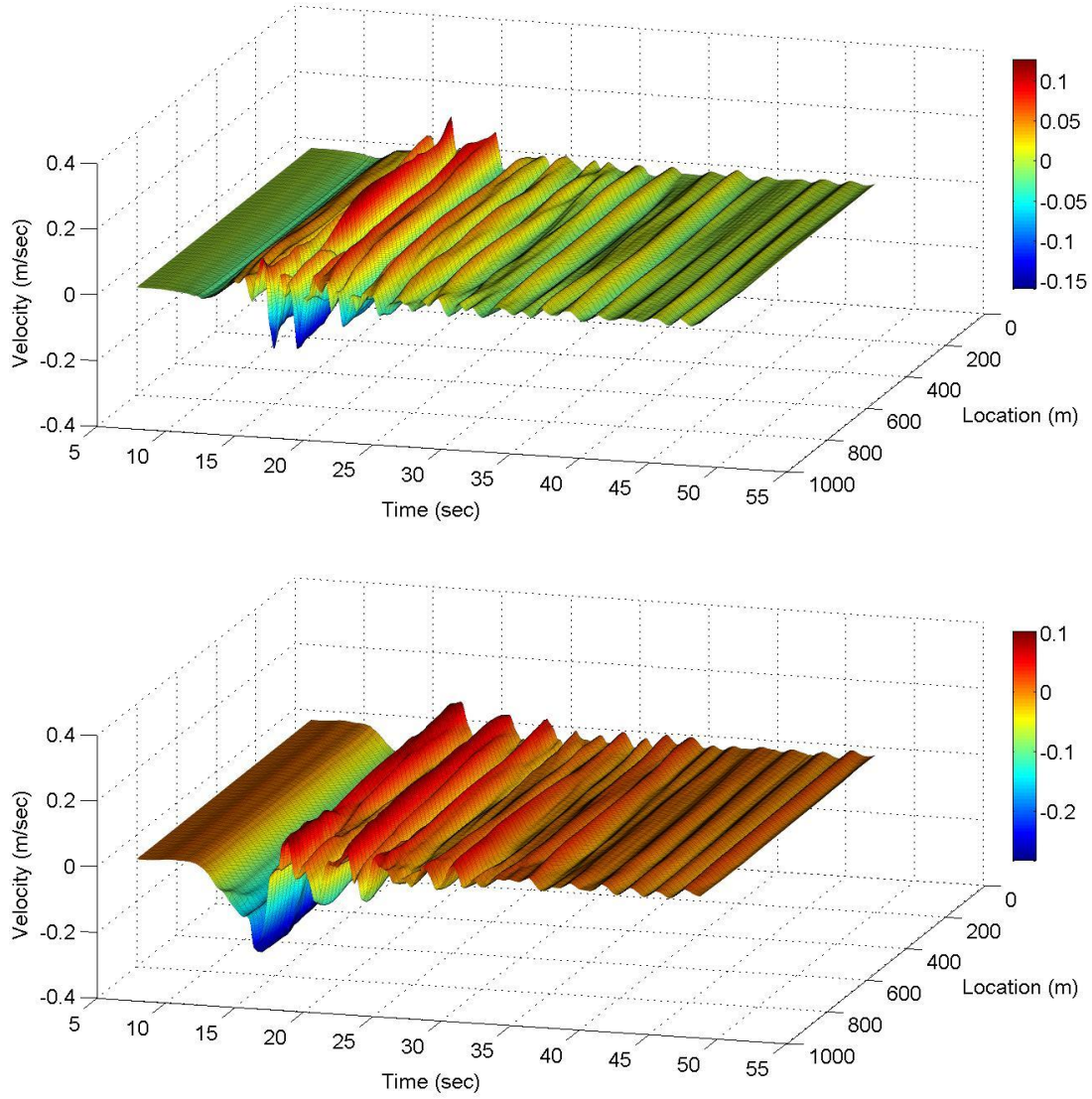

Figure B. 10: X (top) and Y (bottom) component of ground velocities along X centerline of surface of region of interest with nonlinear soft soil profile

Appendix C

Structural responses obtained from the large-scale bridge-foundation-ground system

In this appendix, additional results obtained from the simulation conducted in Chapter 4 are presented. In all the bridges (North-West connector, North-East connector, and South-East connector), the results are shown in terms of: 1) total acceleration at the top of bents and 2) bending moments and shear forces developed at the base of bents.

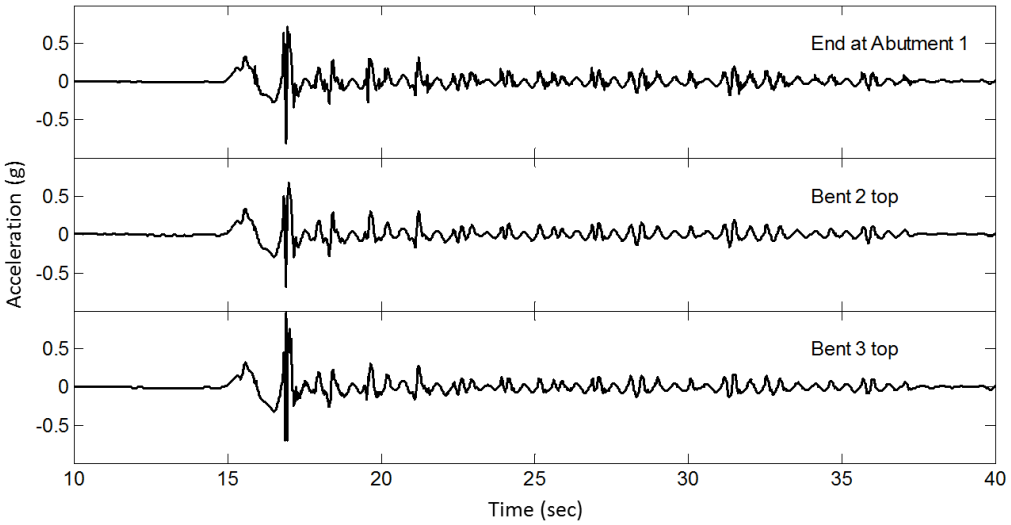

(a) Longitudinal direction

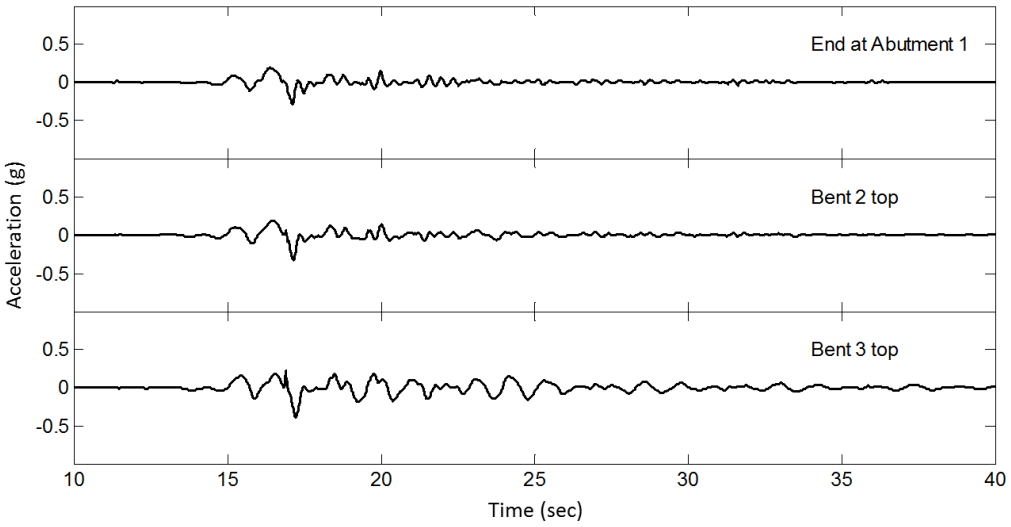

(b) Transversal direction

Figure C. 1: Acceleration time histories at deck locations in the frame 1of the North-West connector

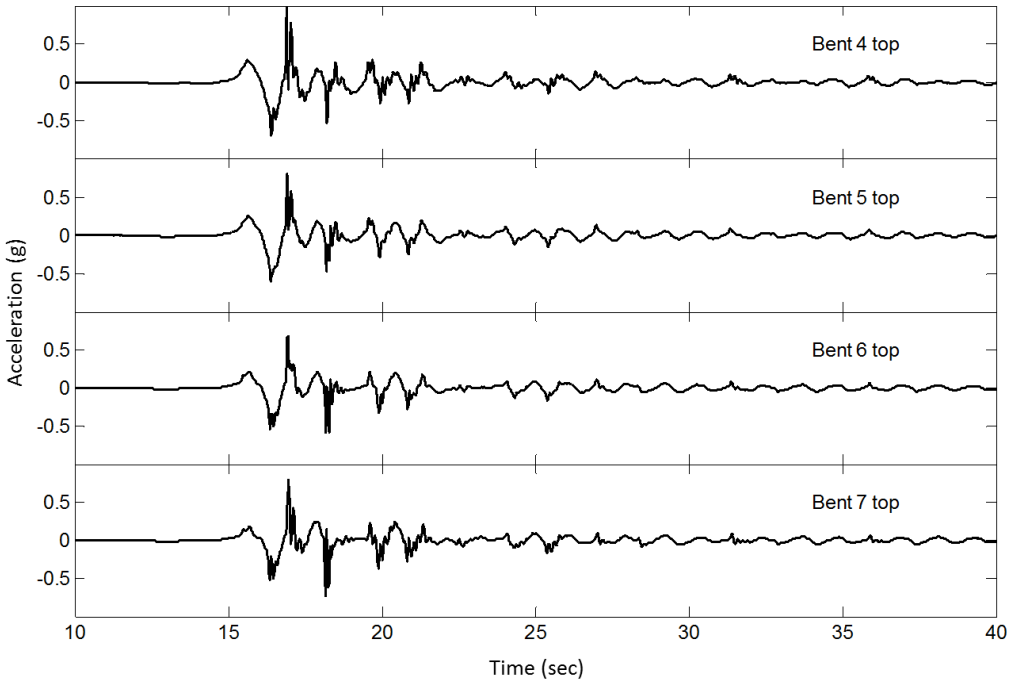

(a) Longitudinal direction

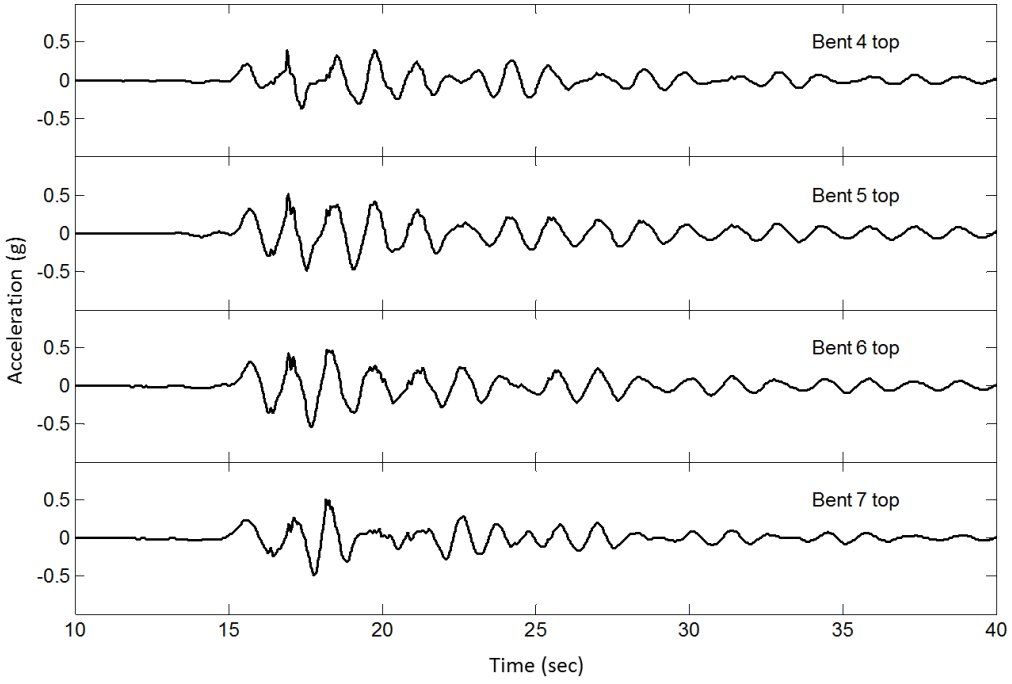

(b) Transversal direction

Figure C. 2: Acceleration time histories at deck locations in the frame 2 of the North-West connector

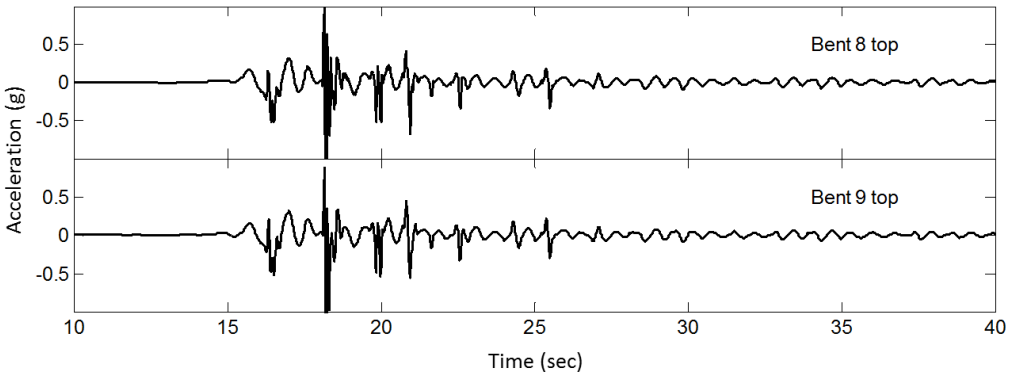

(a) Longitudinal direction

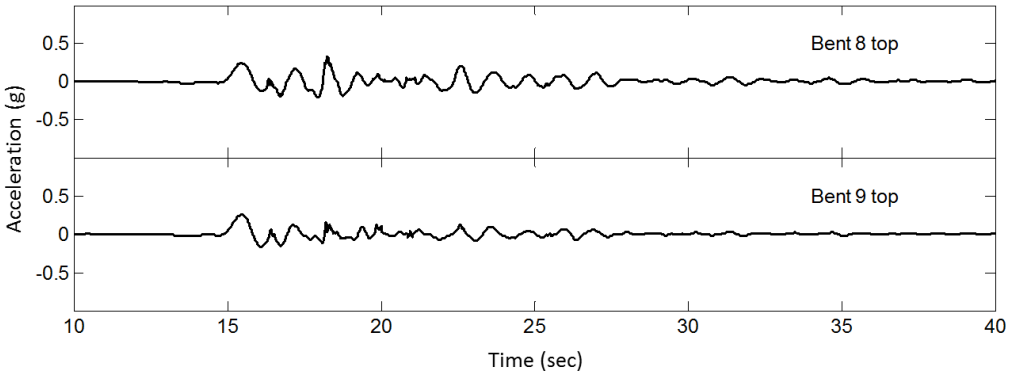

(b) Transversal direction

Figure C. 3: Acceleration time histories at deck locations in the frame 3 of the North-West connector

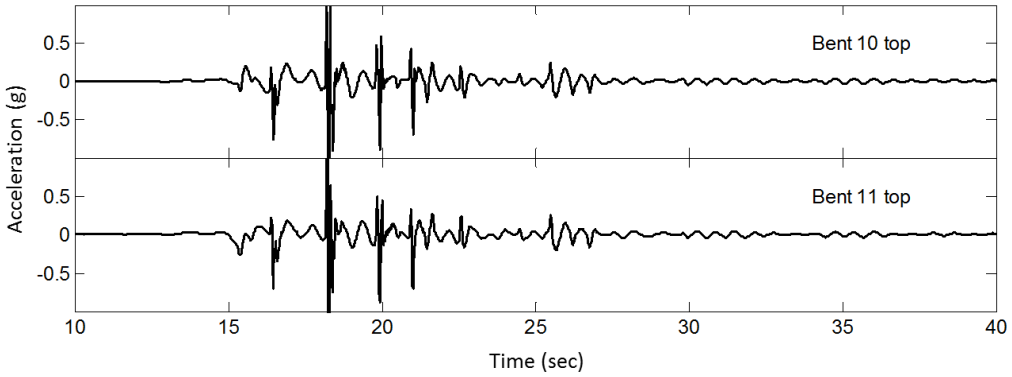

(a) Longitudinal direction

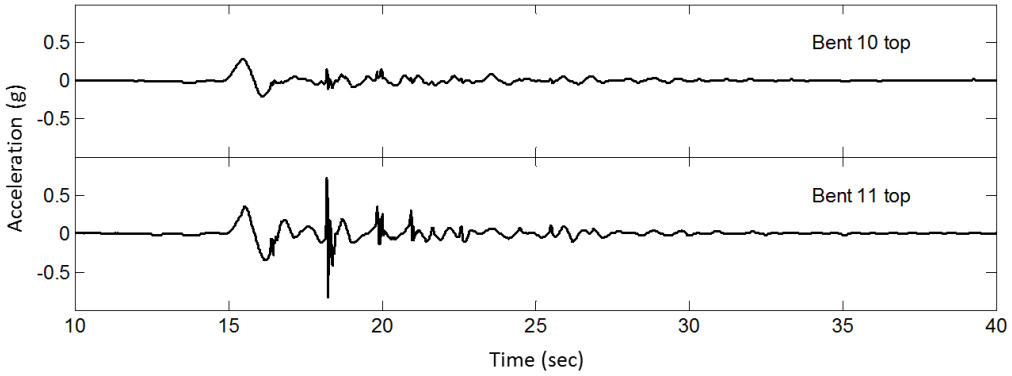

(b) Transversal direction

Figure C. 4: Acceleration time histories at deck locations in the frame 4 of the North-West connector

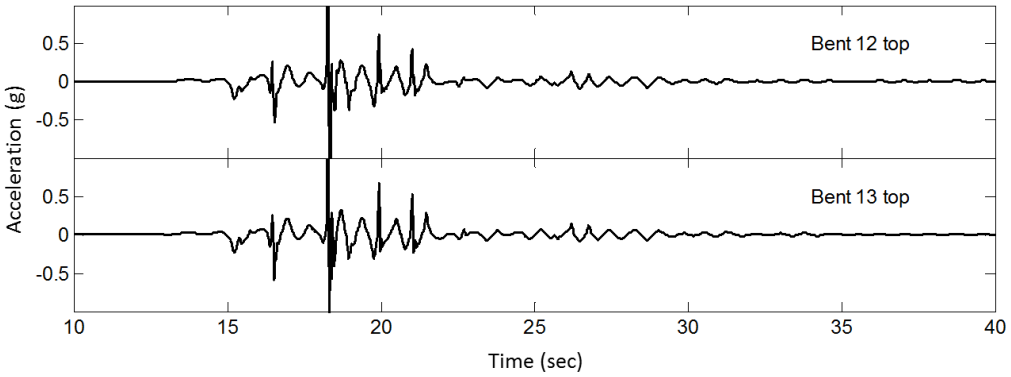

(a) Longitudinal direction

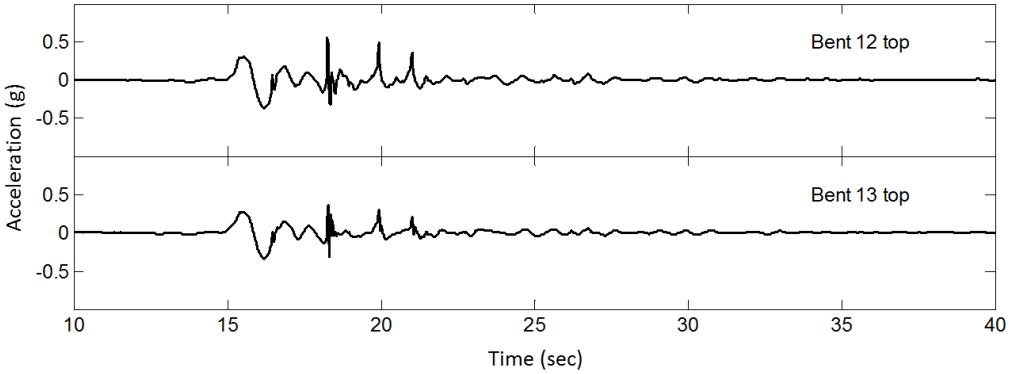

(b) Transversal direction

Figure C. 5: Acceleration time histories at deck locations in the frame 5 of the North-West connector

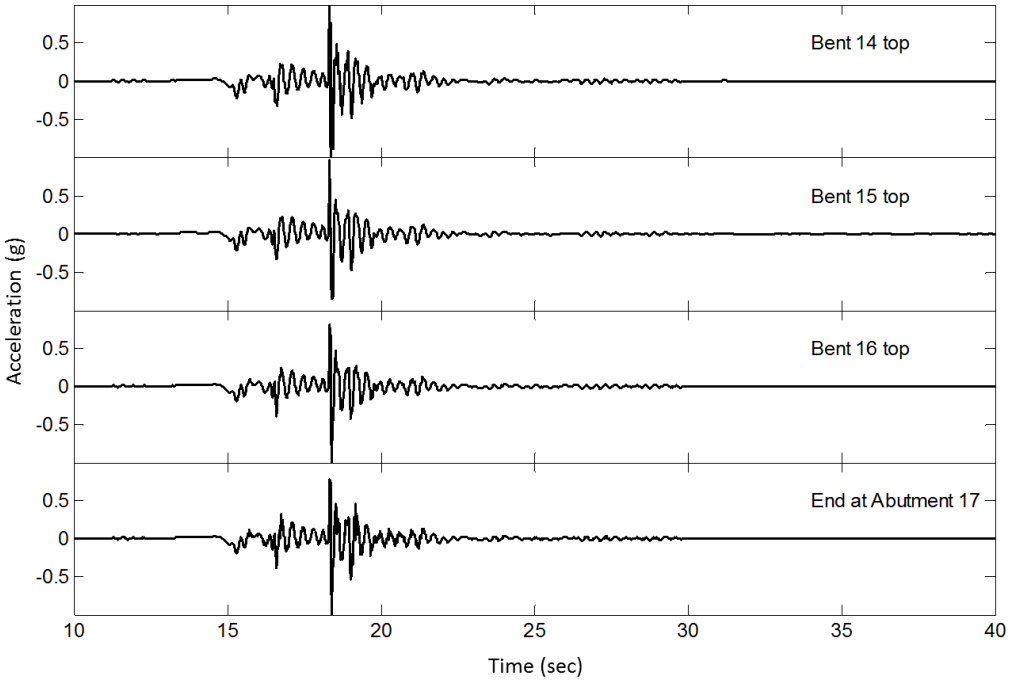

(a) Longitudinal direction

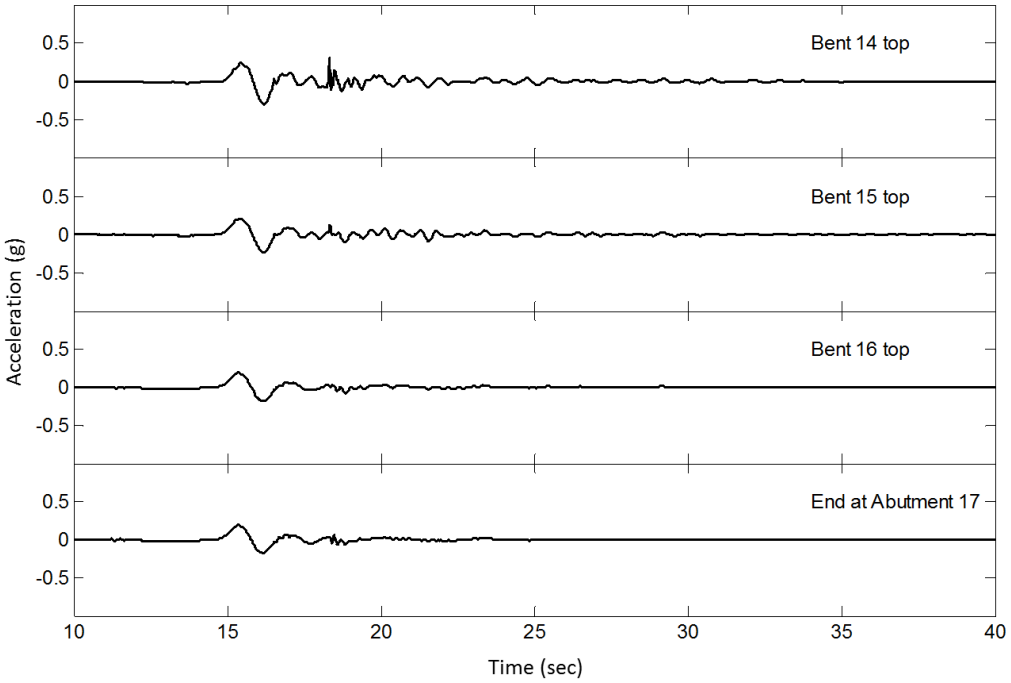

(b) Transversal direction

Figure C. 6: Acceleration time histories at deck locations in the frame 6 of the North-West connector

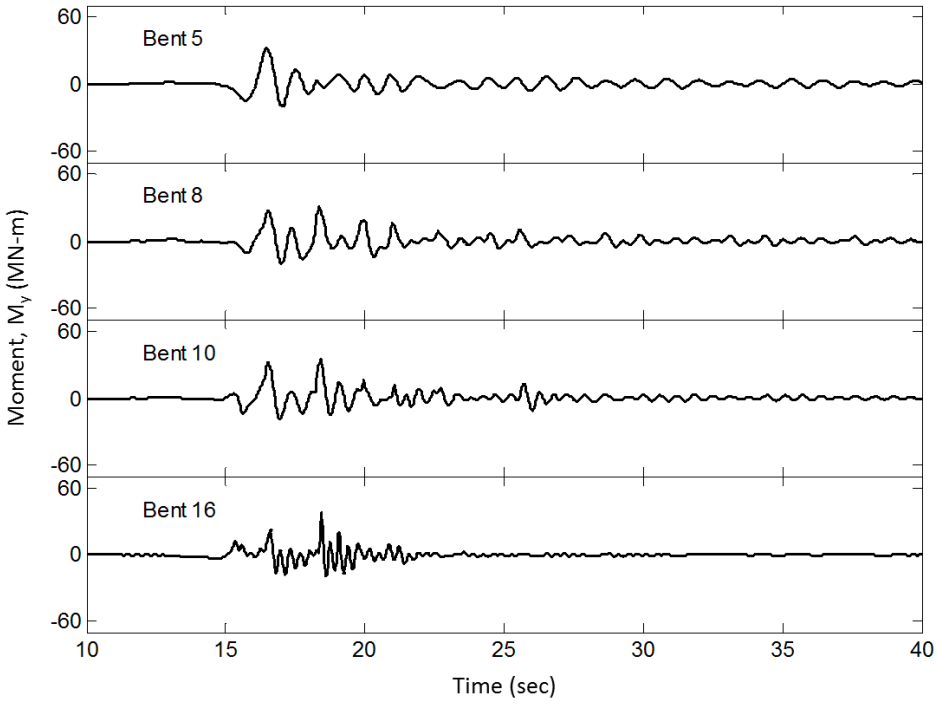

(a) Longitudinal direction

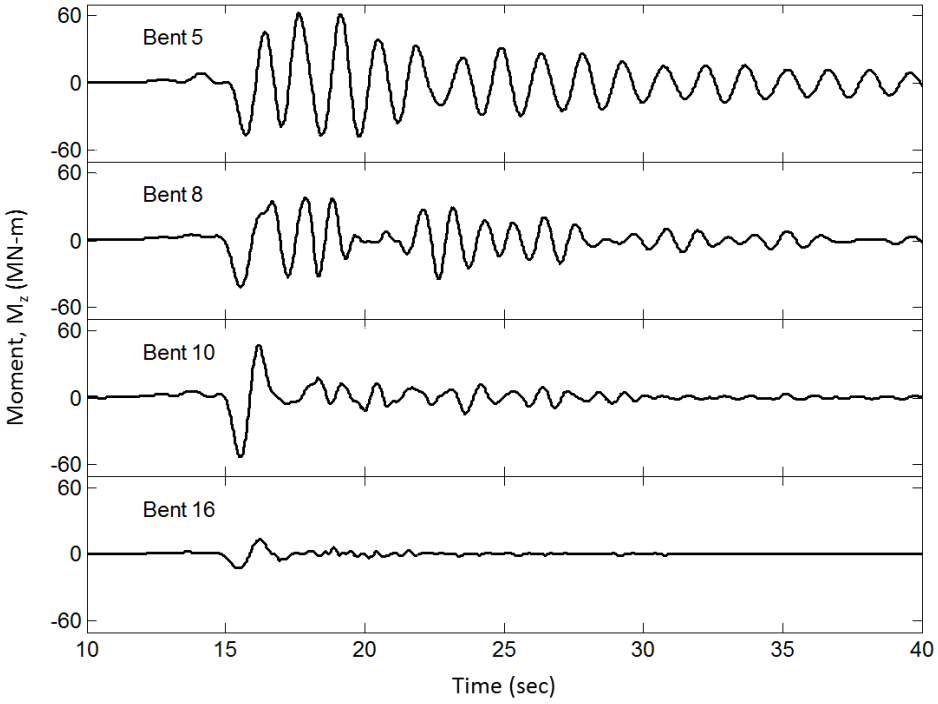

(b) Transversal direction

Figure C. 7: Moment time histories at the base of Bents 5, 8, 10, and 16 in the North-West connector

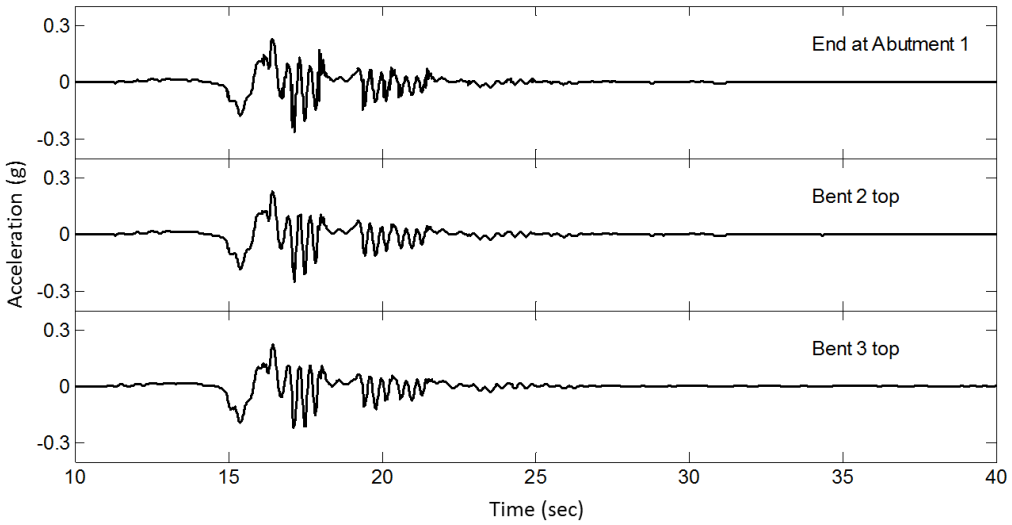

(a) Longitudinal direction

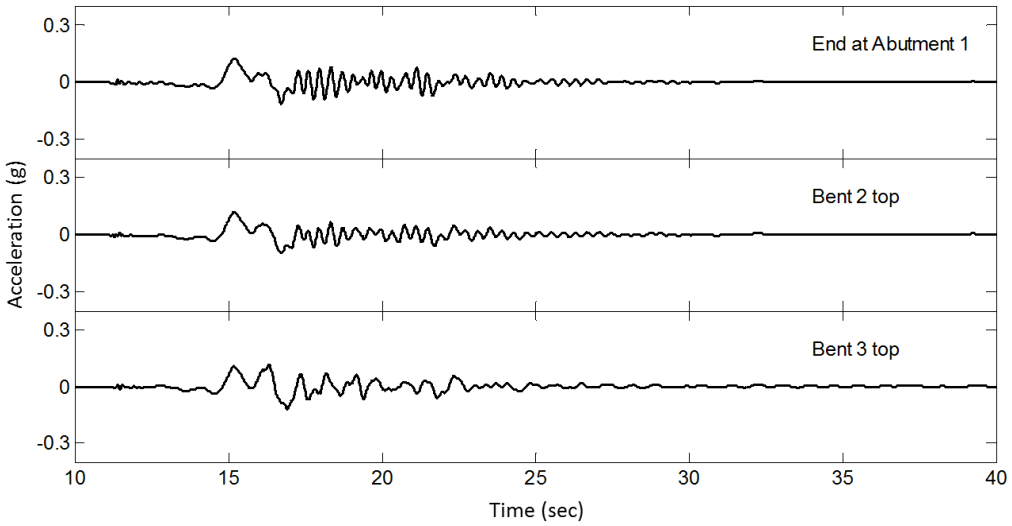

(b) Transversal direction

Figure C. 8: Acceleration time histories at deck locations in the frame 1 of the North-East connector

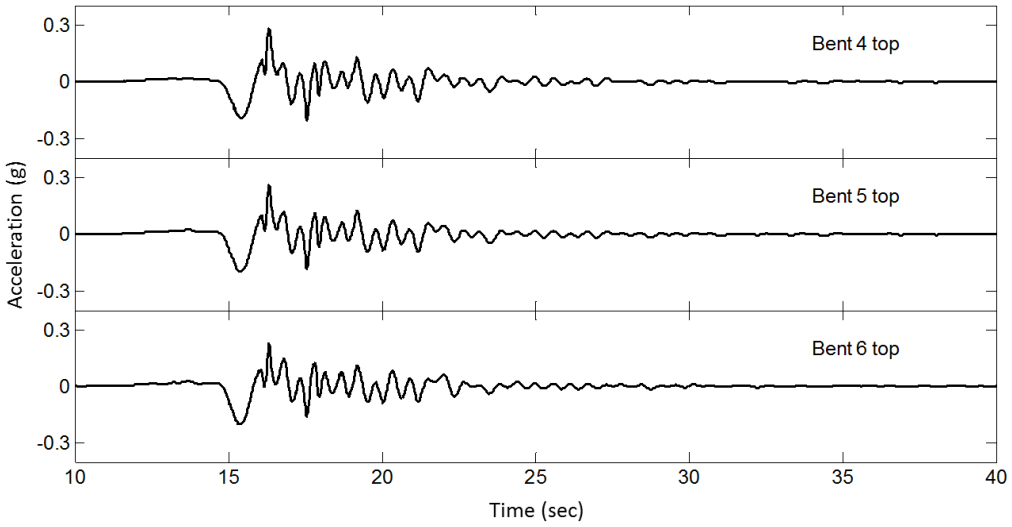

(a) Longitudinal direction

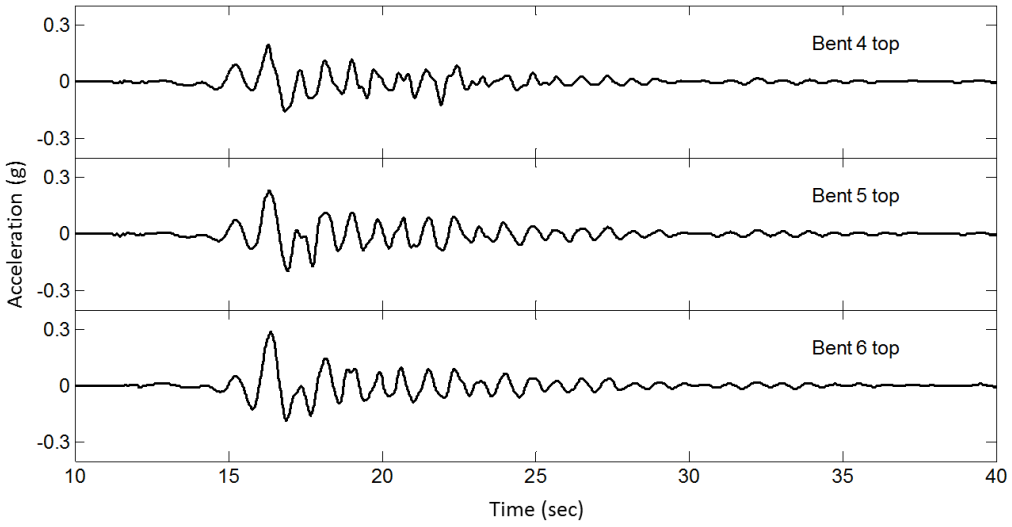

(b) Transversal direction

Figure C. 9: Acceleration time histories at deck locations in the frame 2 of the North-East connector

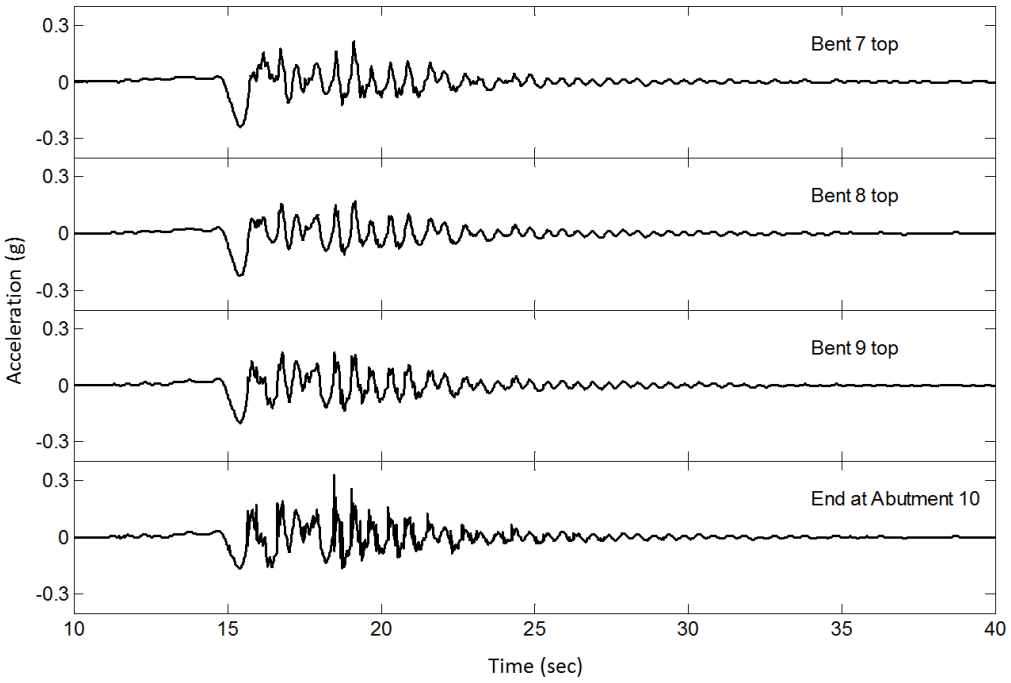

(a) Longitudinal direction

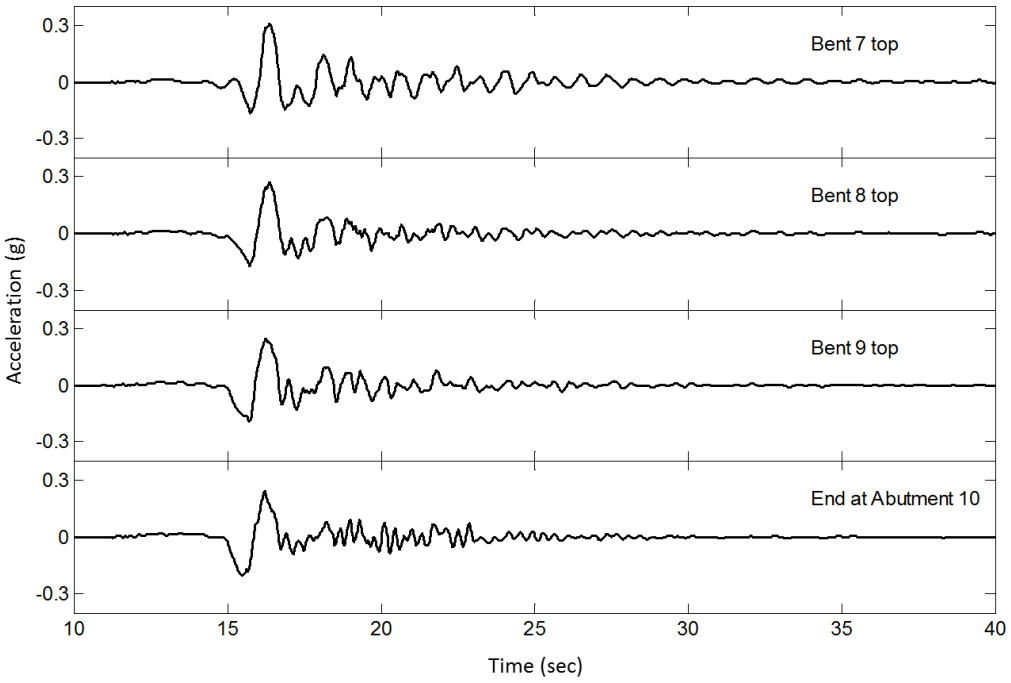

(b) Transversal direction

Figure C. 10: Acceleration time histories at deck locations in the frame 3 of the North-East connector

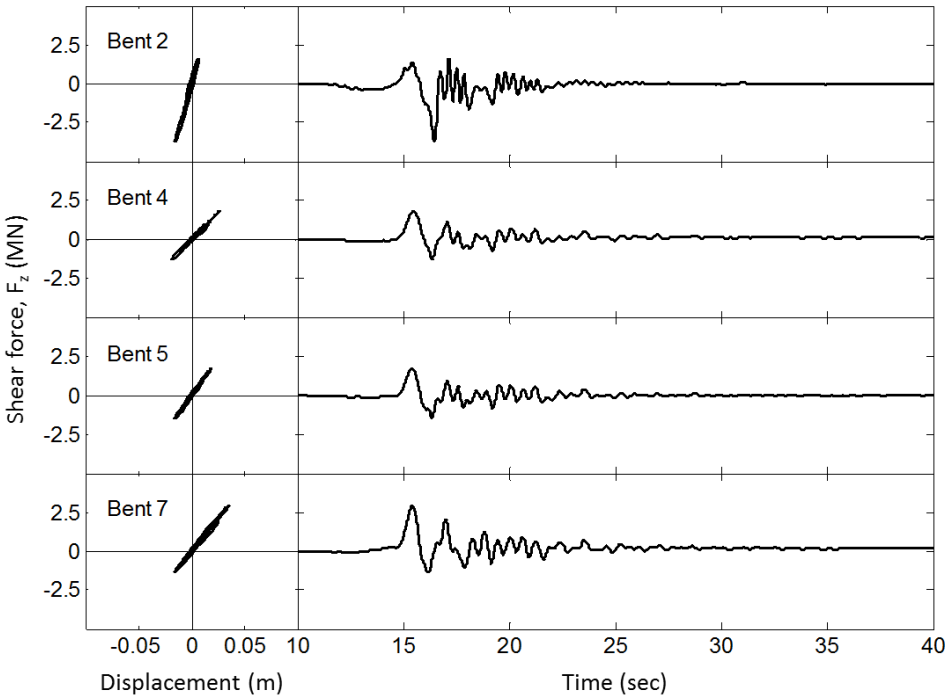

(a) Longitudinal direction

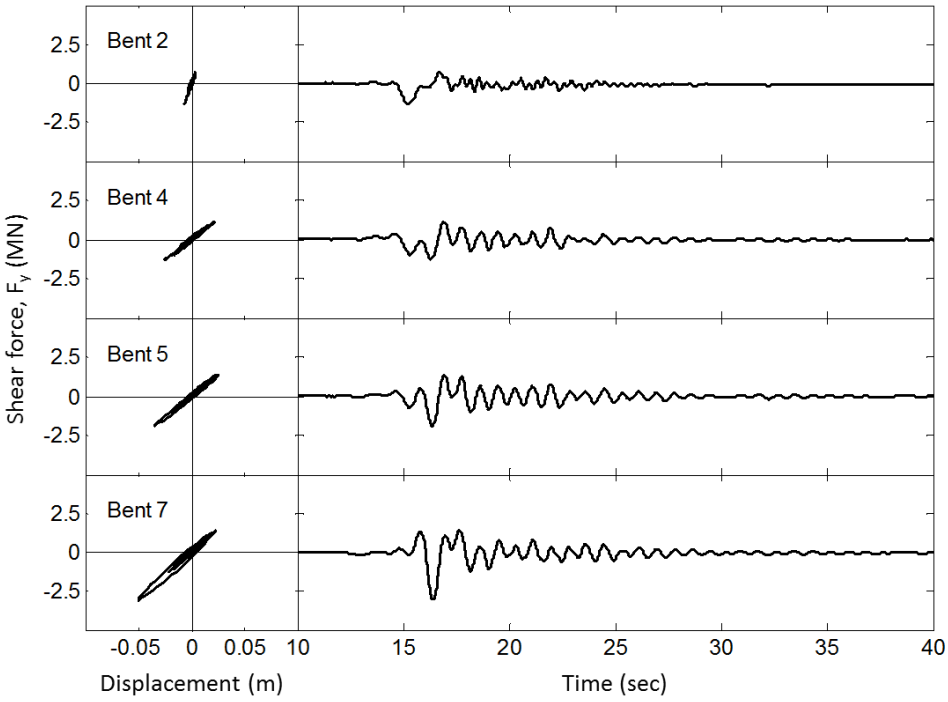

(b) Transversal direction

Figure C. 11: Relation of shear forces and relative displacements at the top to the base with shear force time histories in the North-East connector

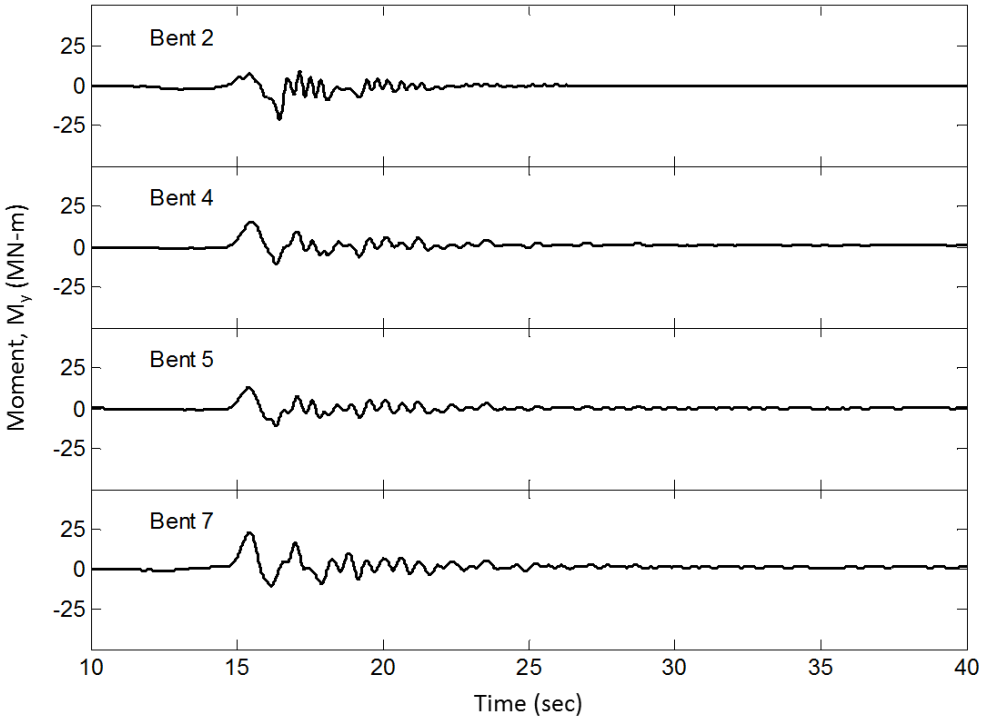

(a) Longitudinal direction

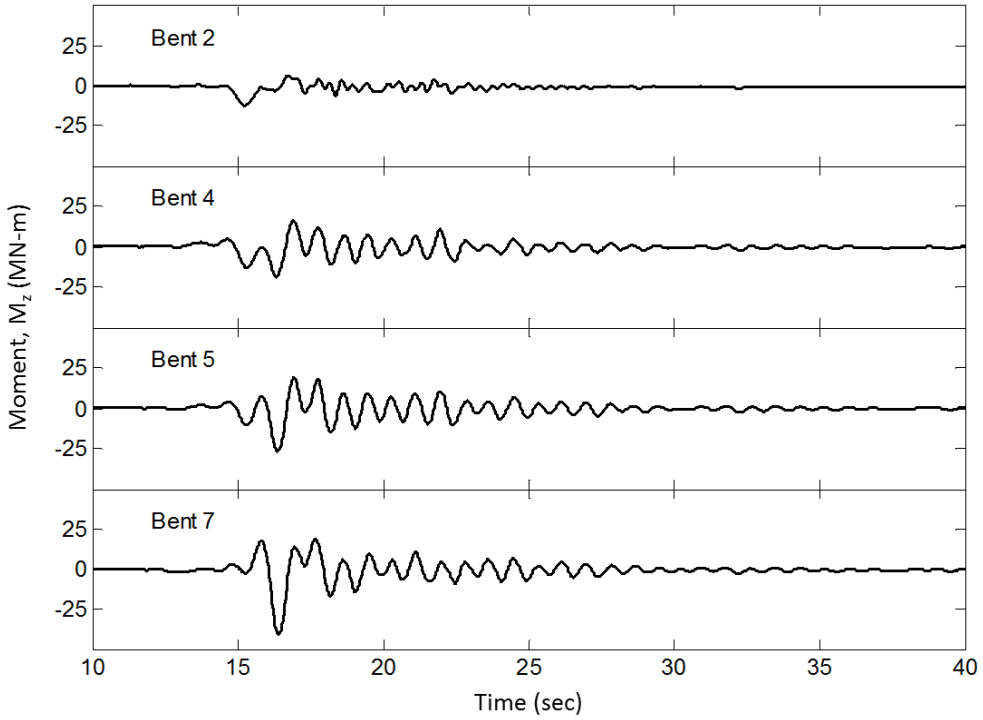

(b) Transversal direction

Figure C. 12: Moment time histories at the base of Bents 2, 4, 5, and 7 in the North-East connector

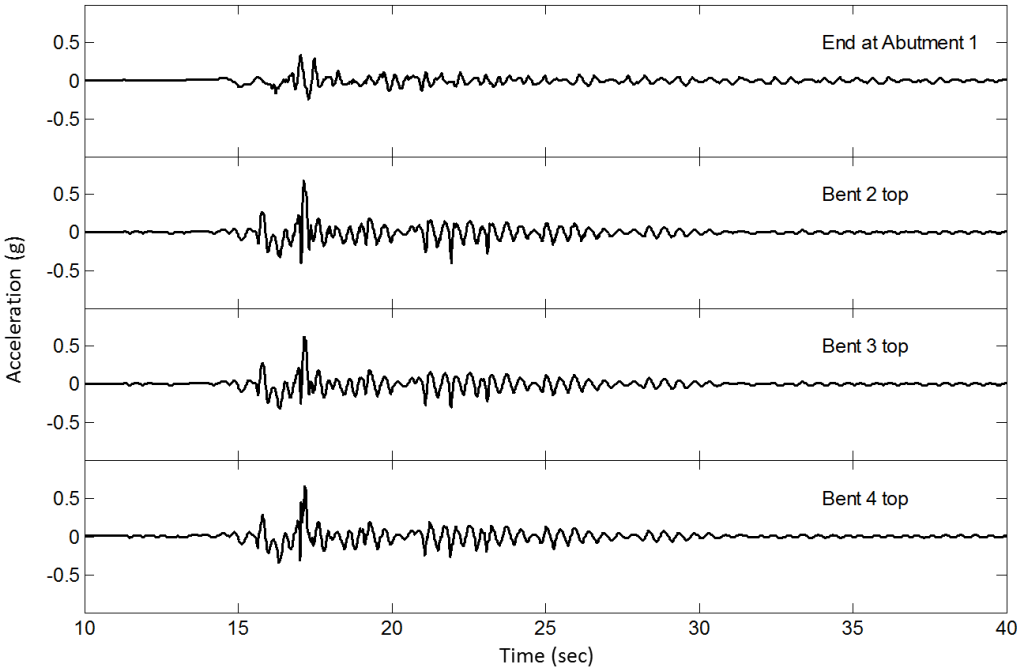

(a) Longitudinal direction

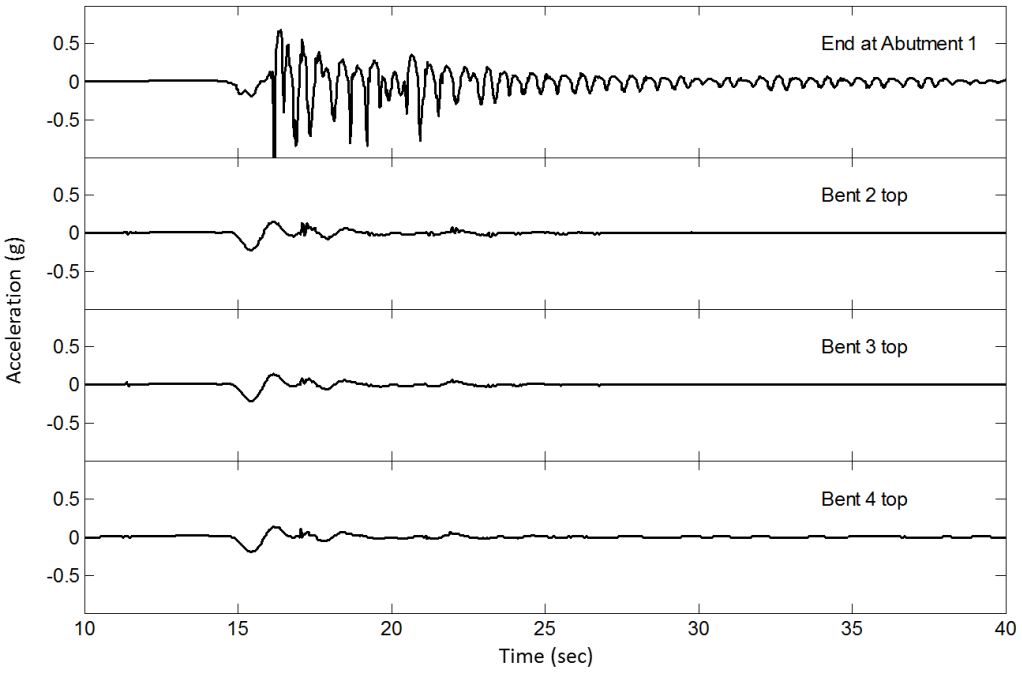

(b) Transversal direction

Figure C. 13: Acceleration time histories at deck locations in the frame 1 of the South-East connector

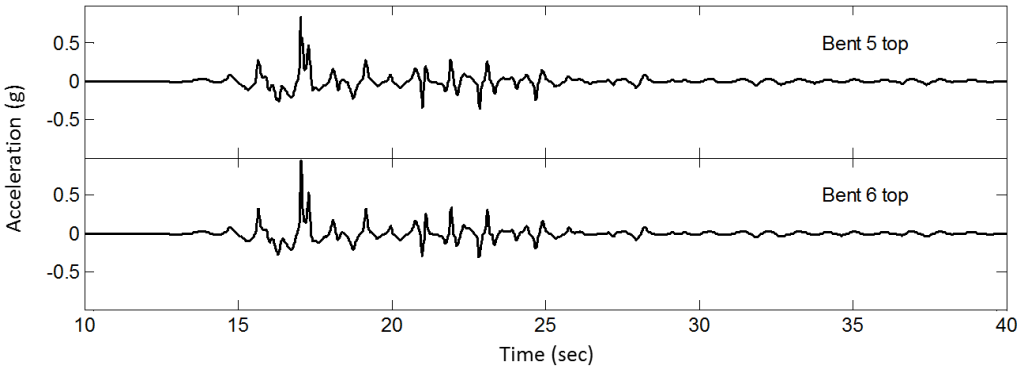

(a) Longitudinal direction

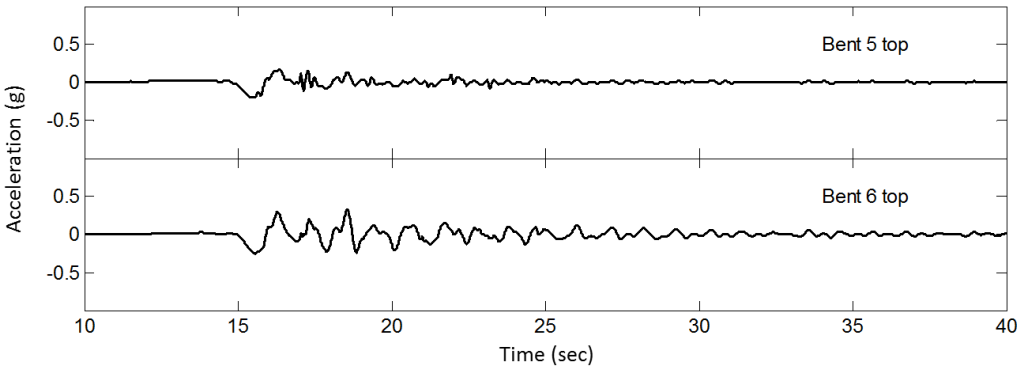

(b) Transversal direction

Figure C. 14: Acceleration time histories at deck locations in the frame 2 1 of the South-East connector

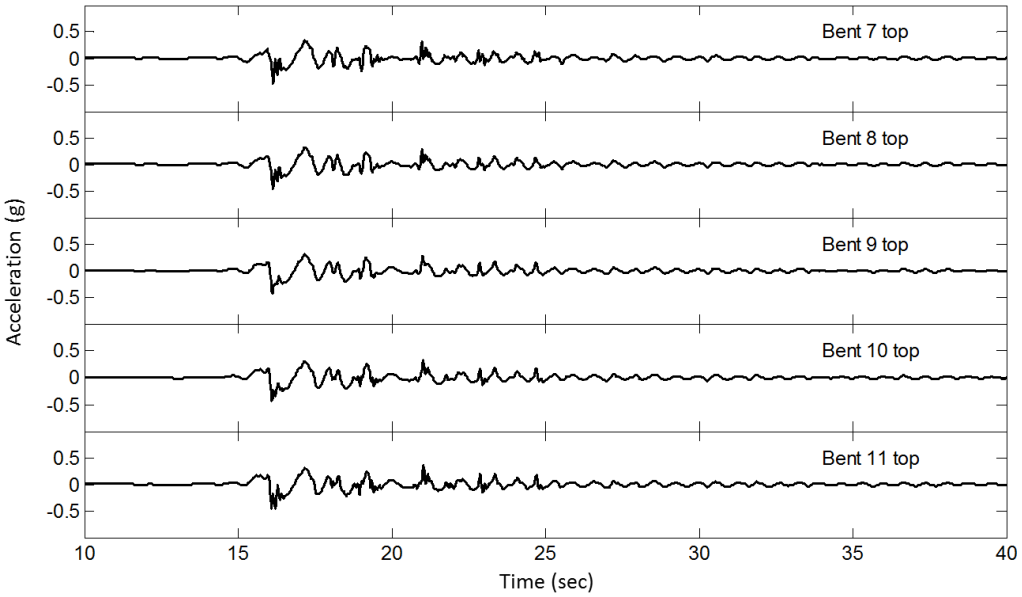

(a) Longitudinal direction

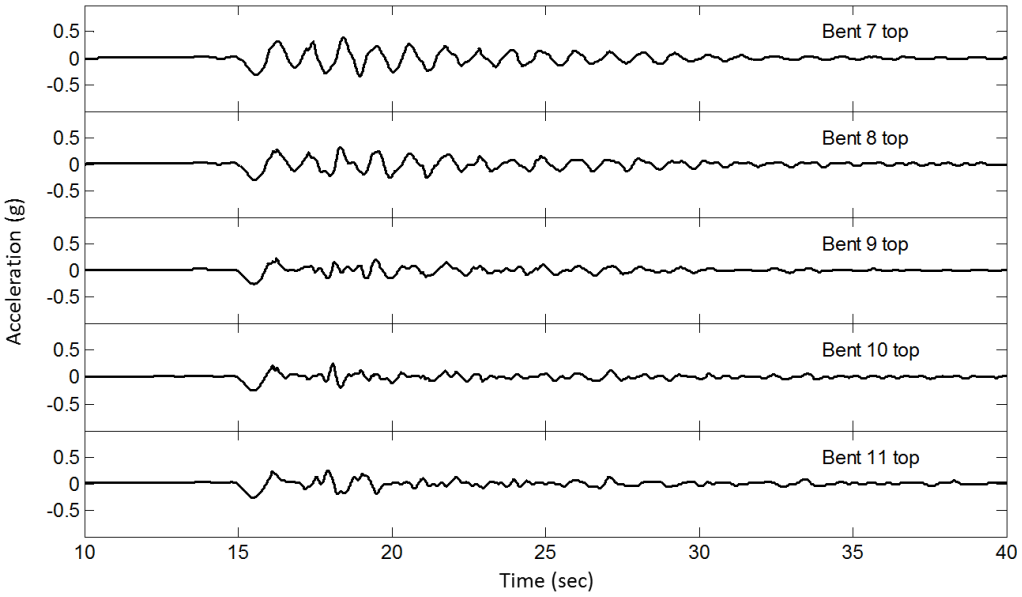

(b) Transversal direction

Figure C. 15: Acceleration time histories at deck locations in the frame 3 1 of the South-East connector

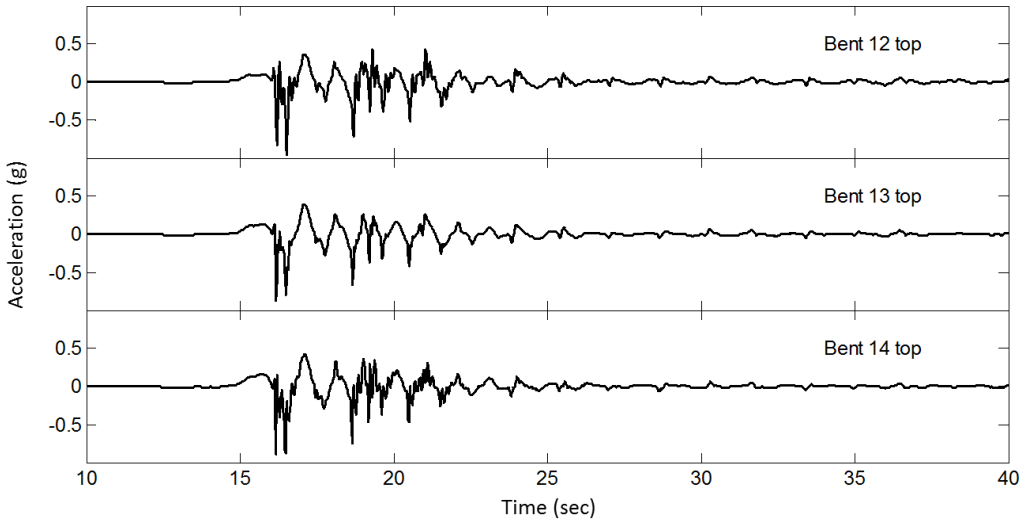

(a) Longitudinal direction

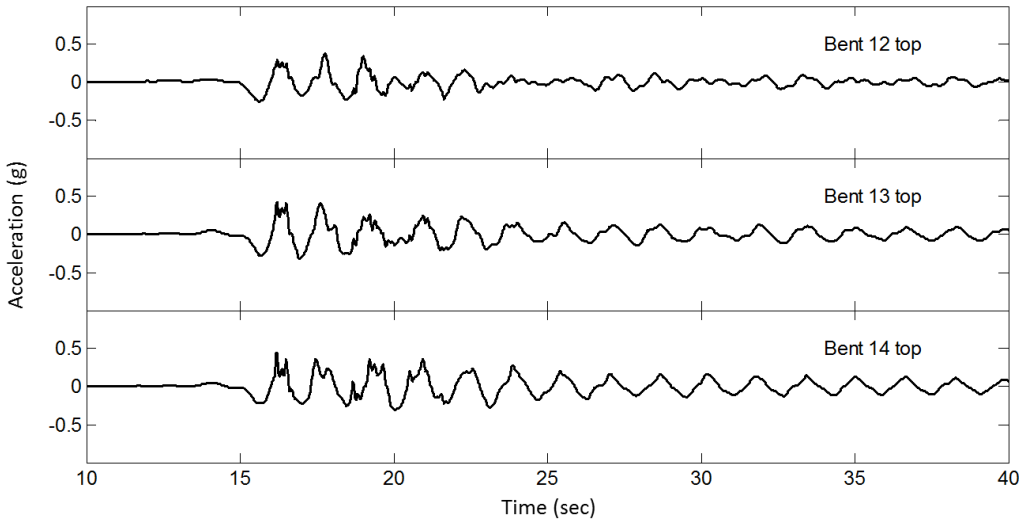

(b) Transversal direction

Figure C. 16: Acceleration time histories at deck locations in the frame 4 1 of the South-East connector

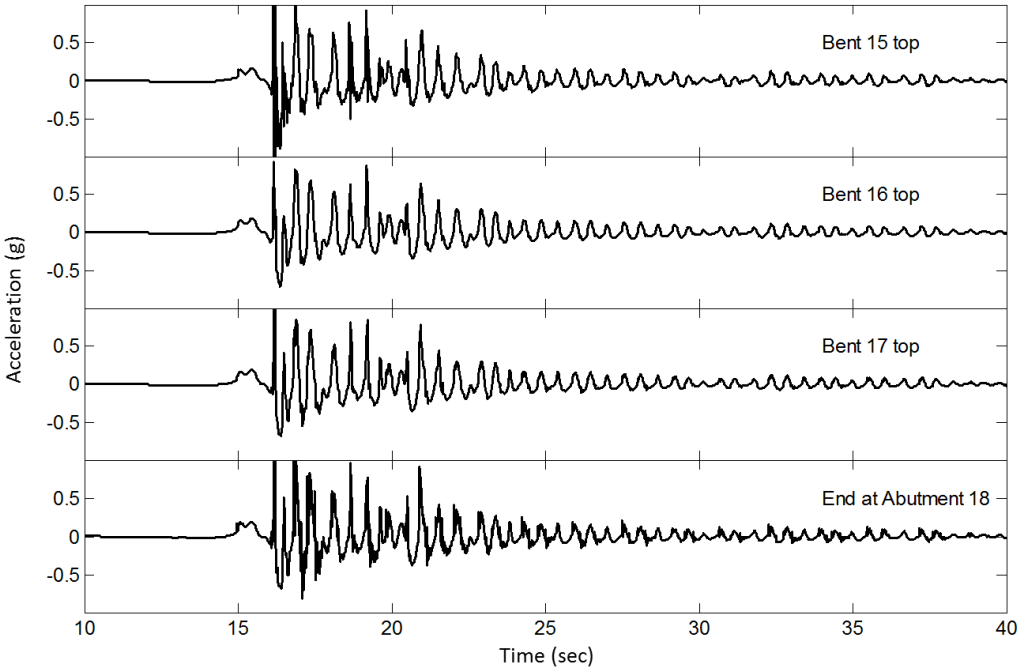

(a) Longitudinal direction

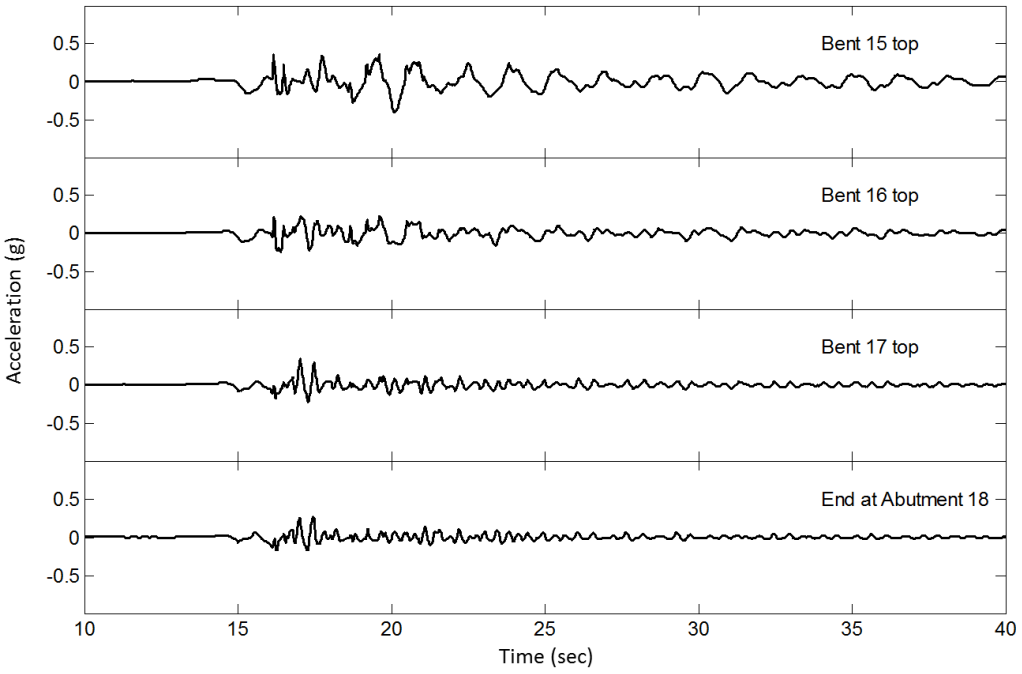

(b) Transversal direction

Figure C. 17: Acceleration time histories at deck locations in the frame 5 1 of the South-East connector

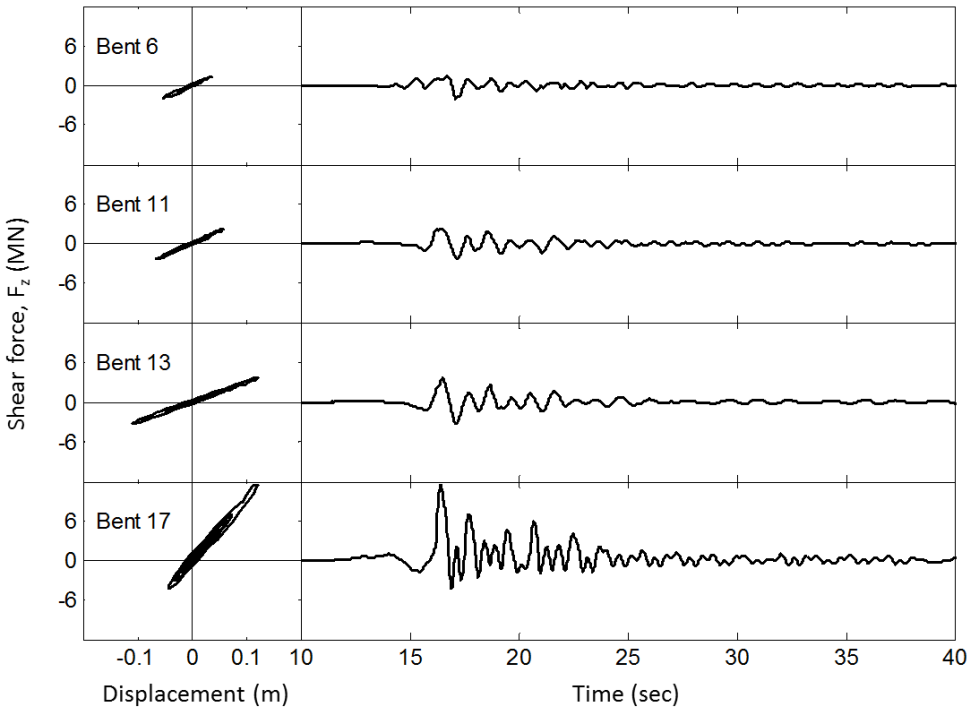

(a) Longitudinal direction

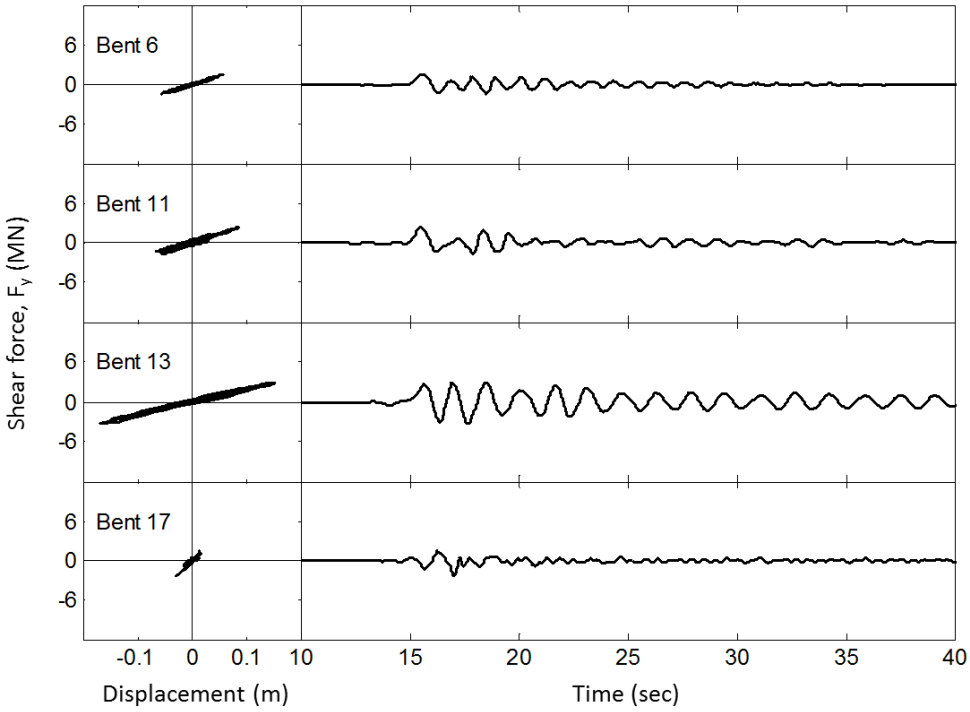

(b) Transversal direction

Figure C. 18: Relation of shear forces and relative displacements at the top to the base with shear force time histories bents in the South-East connector

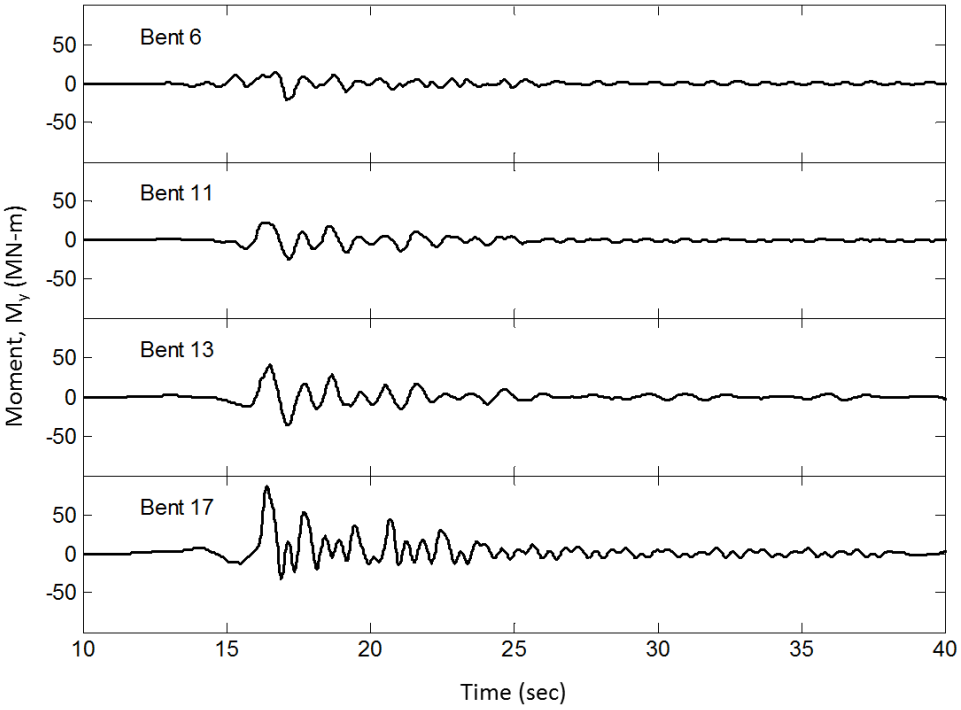

(a) Longitudinal direction

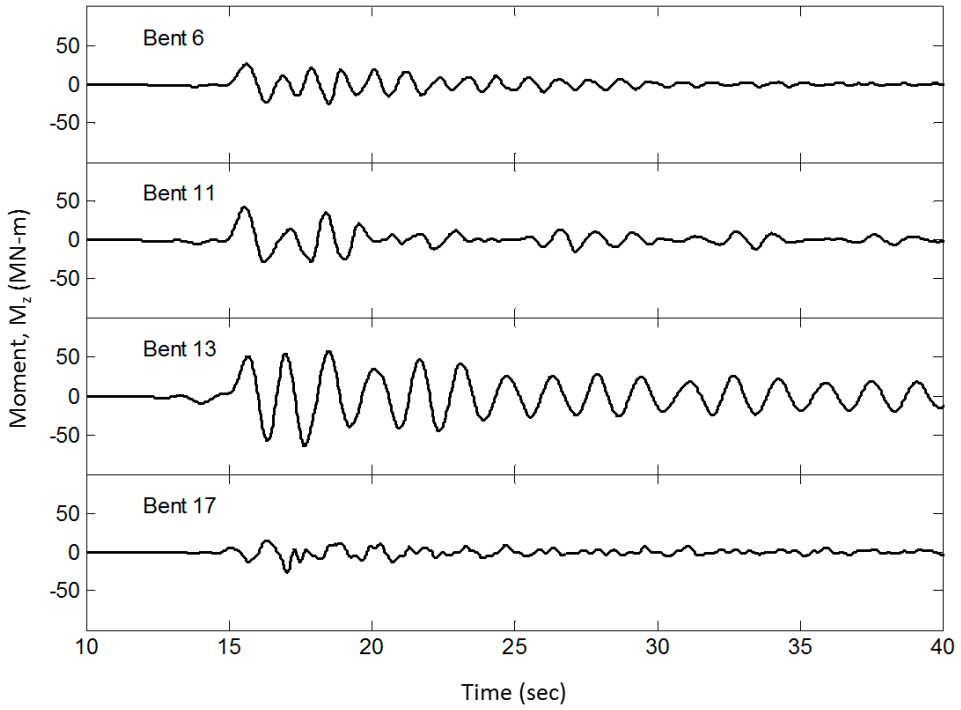

(b) Transversal direction

Figure C. 19 Moment time histories at the base of Bents 2, 4, 5, and 7 bents in the South-East connector

Appendix D

Structural response from the bridge-foundation-ground system

From the analysis conducted in Chapter 6, additional acceleration time histories are examined. Accelerations at the level of deck along the bridge superstructure are shown in the longitudinal and transversal directions, connected by five intermediate hinges from Abutment 1 to 17.

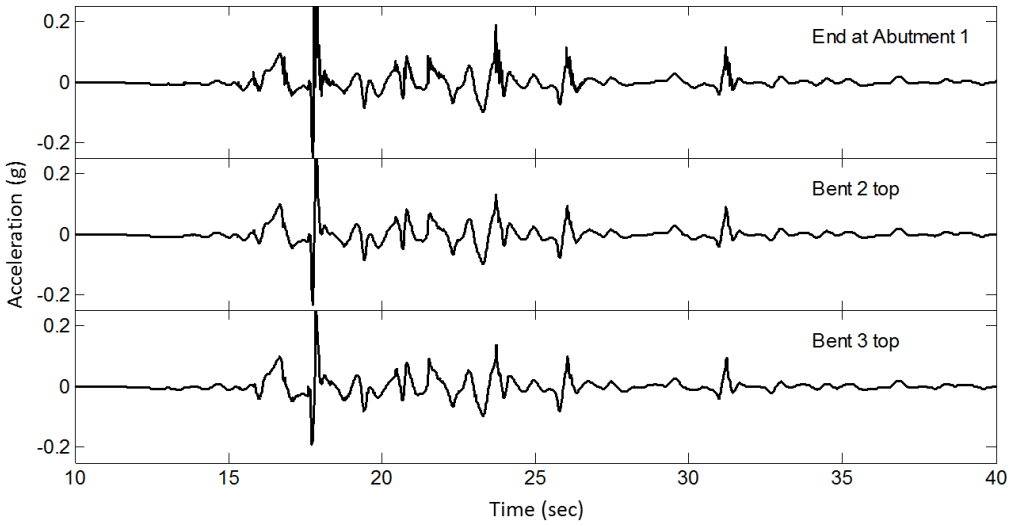

(a) Longitudinal direction

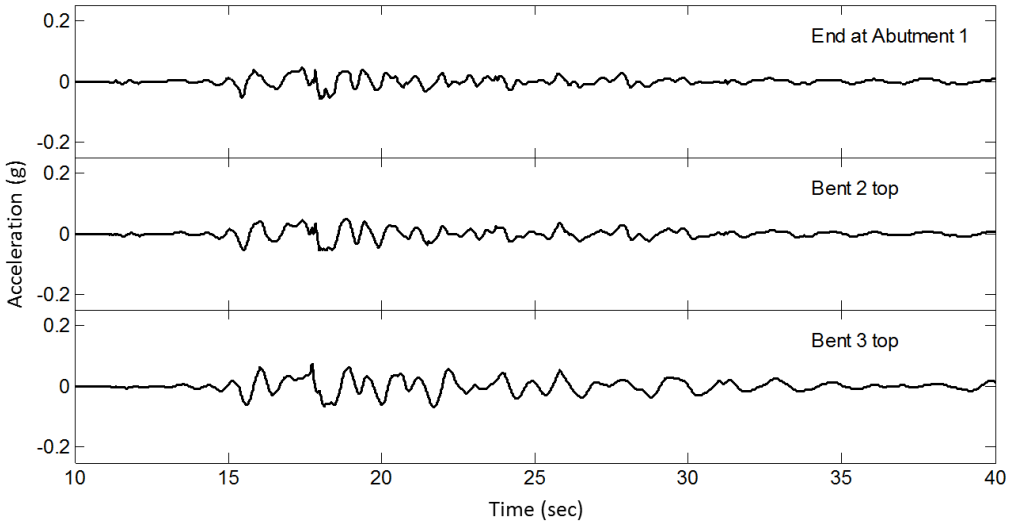

(b) Transversal direction

Figure D. 1: Acceleration time histories at deck locations in the frame 1

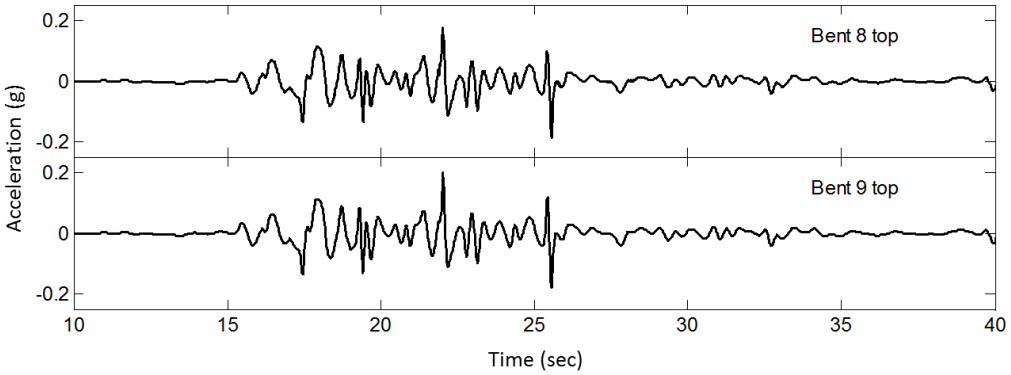

(a) Longitudinal direction

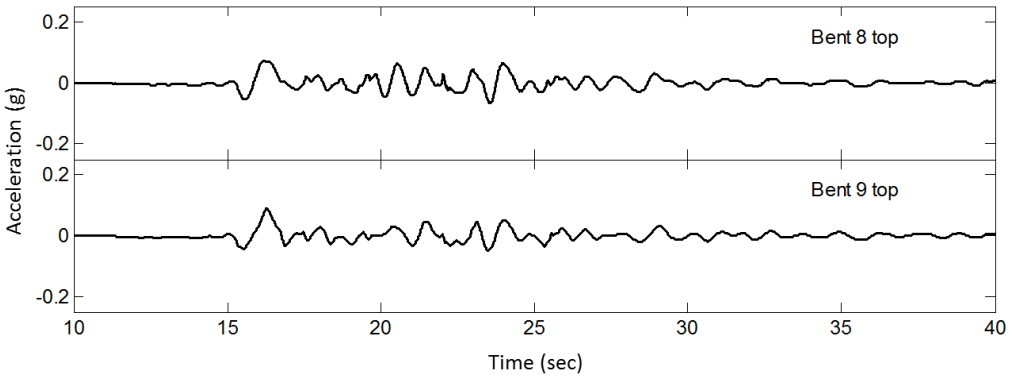

(b) Transversal direction

Figure D. 2: Acceleration time histories at deck locations in the frame 3

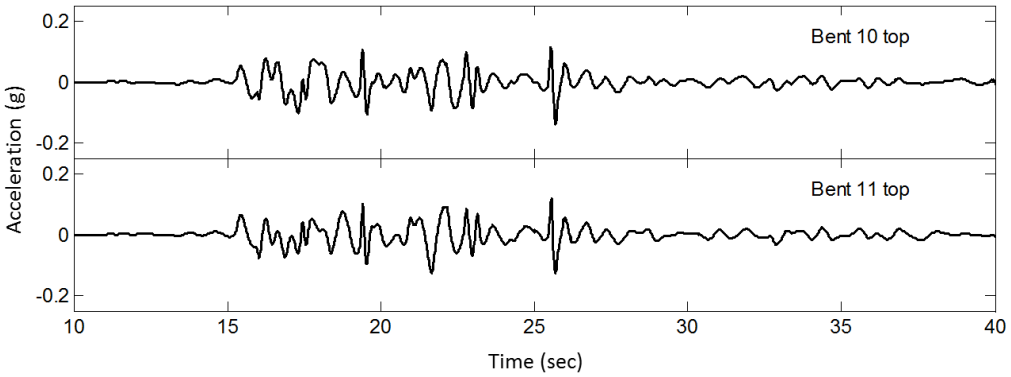

(a) Longitudinal direction

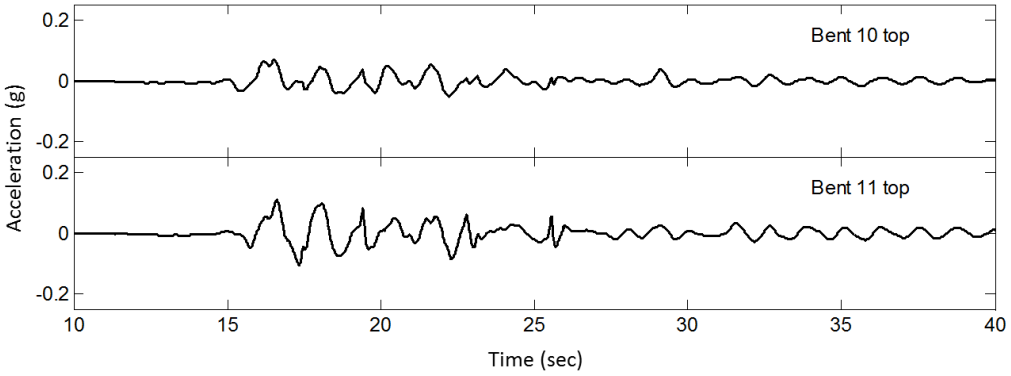

(b) Transversal direction

Figure D. 3: Acceleration time histories at deck locations in the frame 4

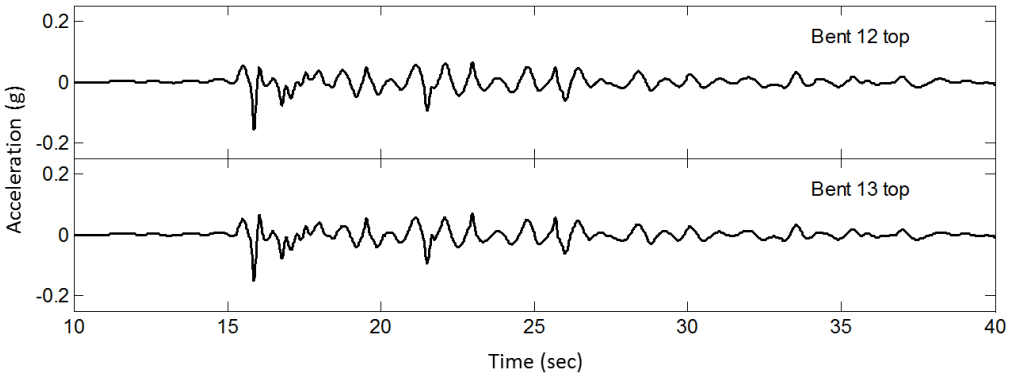

(a) Longitudinal direction

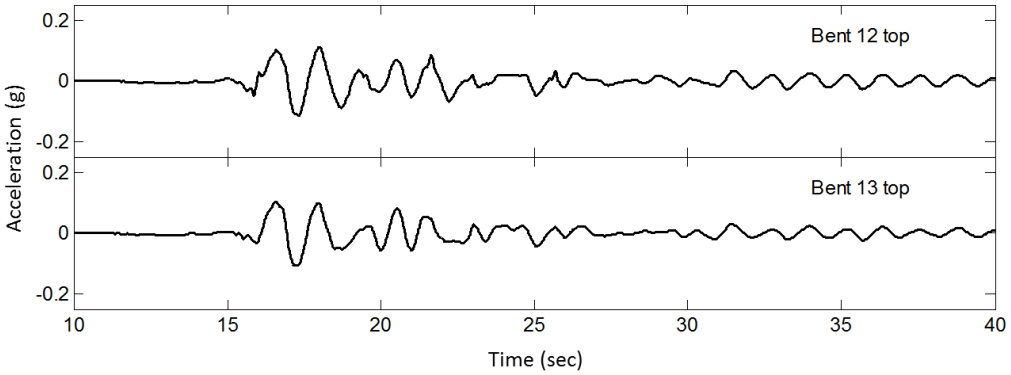

(b) Transversal direction

Figure D. 4: Acceleration time histories at deck locations in the frame 5

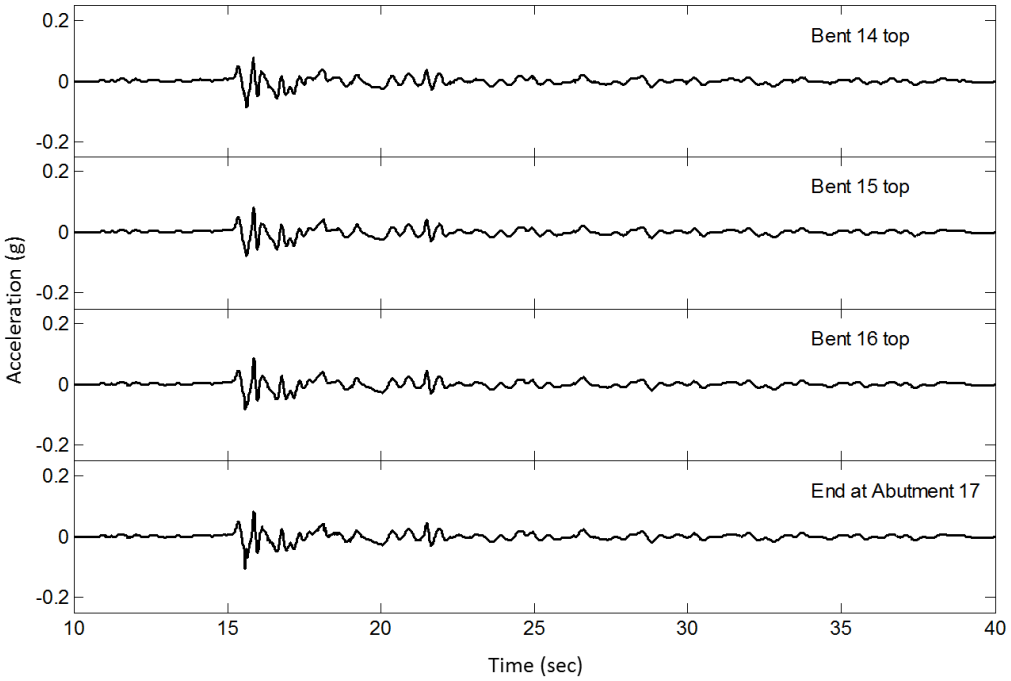

(a) Longitudinal direction

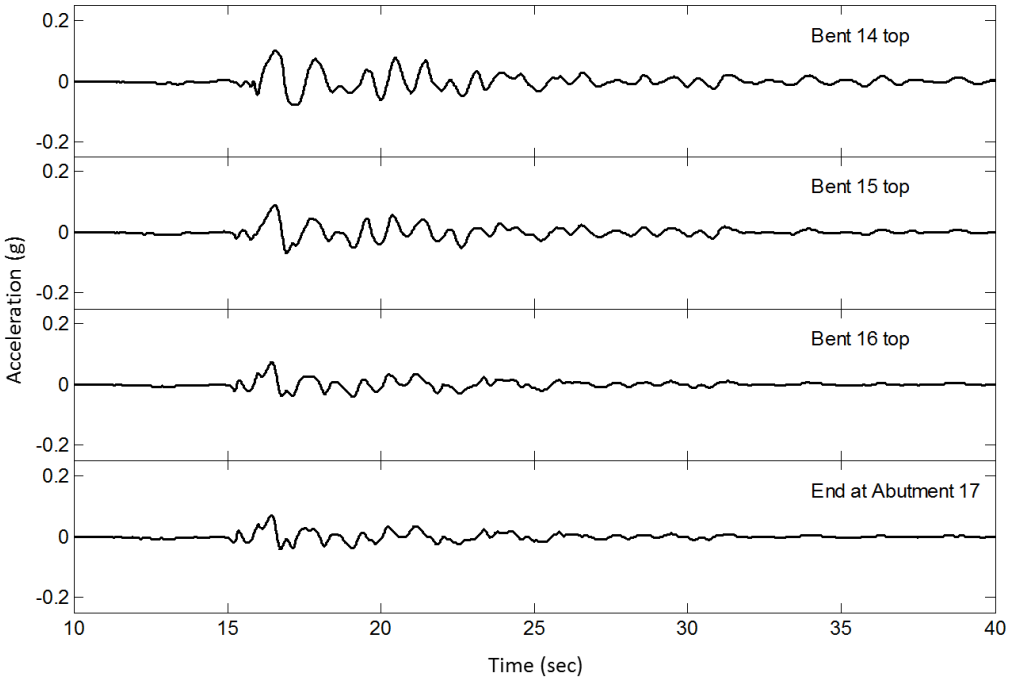

(b) Transversal direction

Figure D. 5: Acceleration time histories at deck locations in the frame 6

Appendix E

Additional results in the North-West Connector Bridge-Foundation-Ground System

As discussed earlier in Chapter 8, for the potential site specific strong ground motion (1994 Northridge earthquake recorded at recorded at CSMIP Station 24279-Newhall Fire station), additional results are shown. Accelerations at the level of deck along the bridge superstructure are shown in the longitudinal and transversal directions, connected by five intermediate hinges from Abutment 1 to 17.

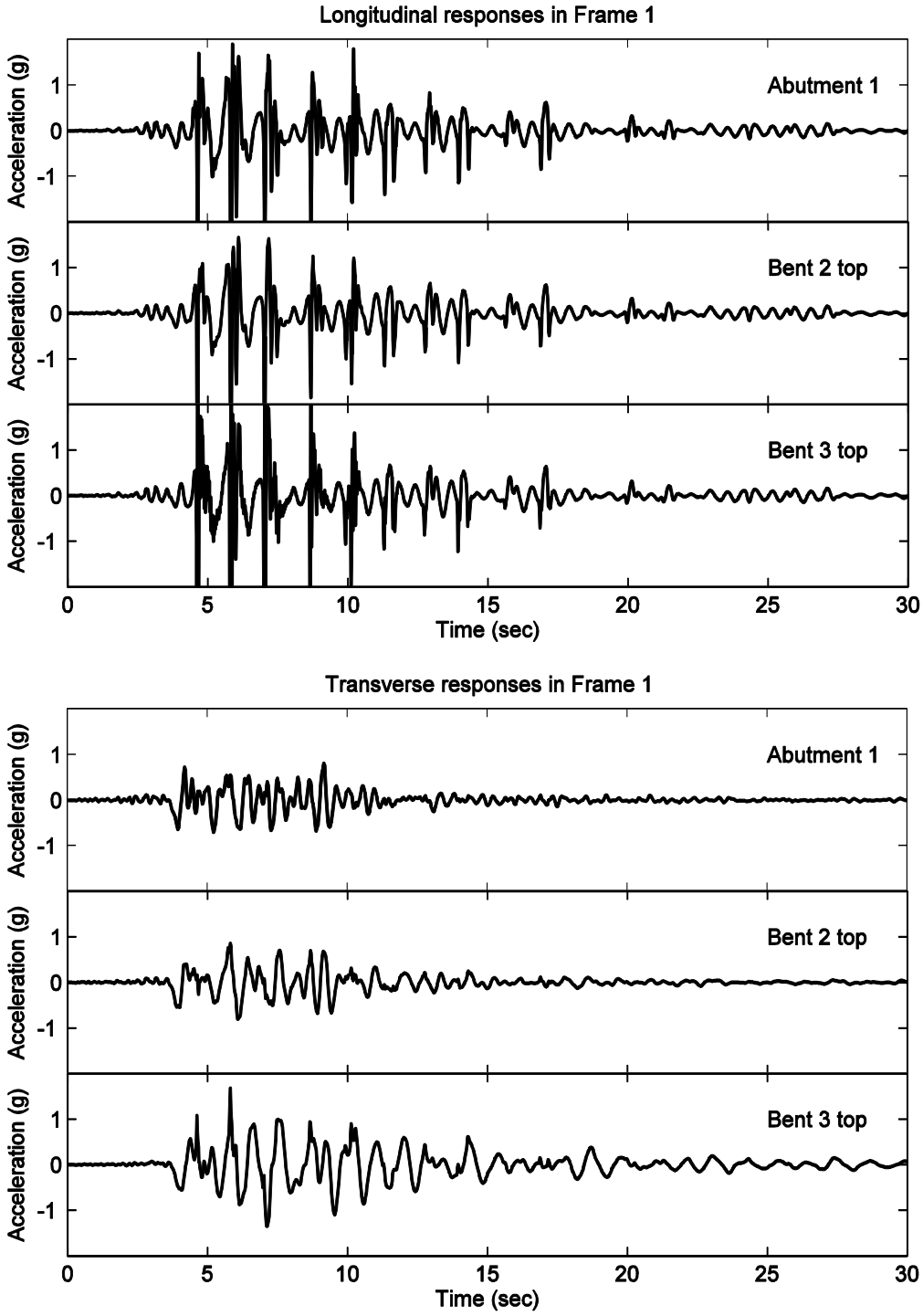

Figure E. 1: Acceleration time histories at deck locations in the frame 1 of the North-West connector

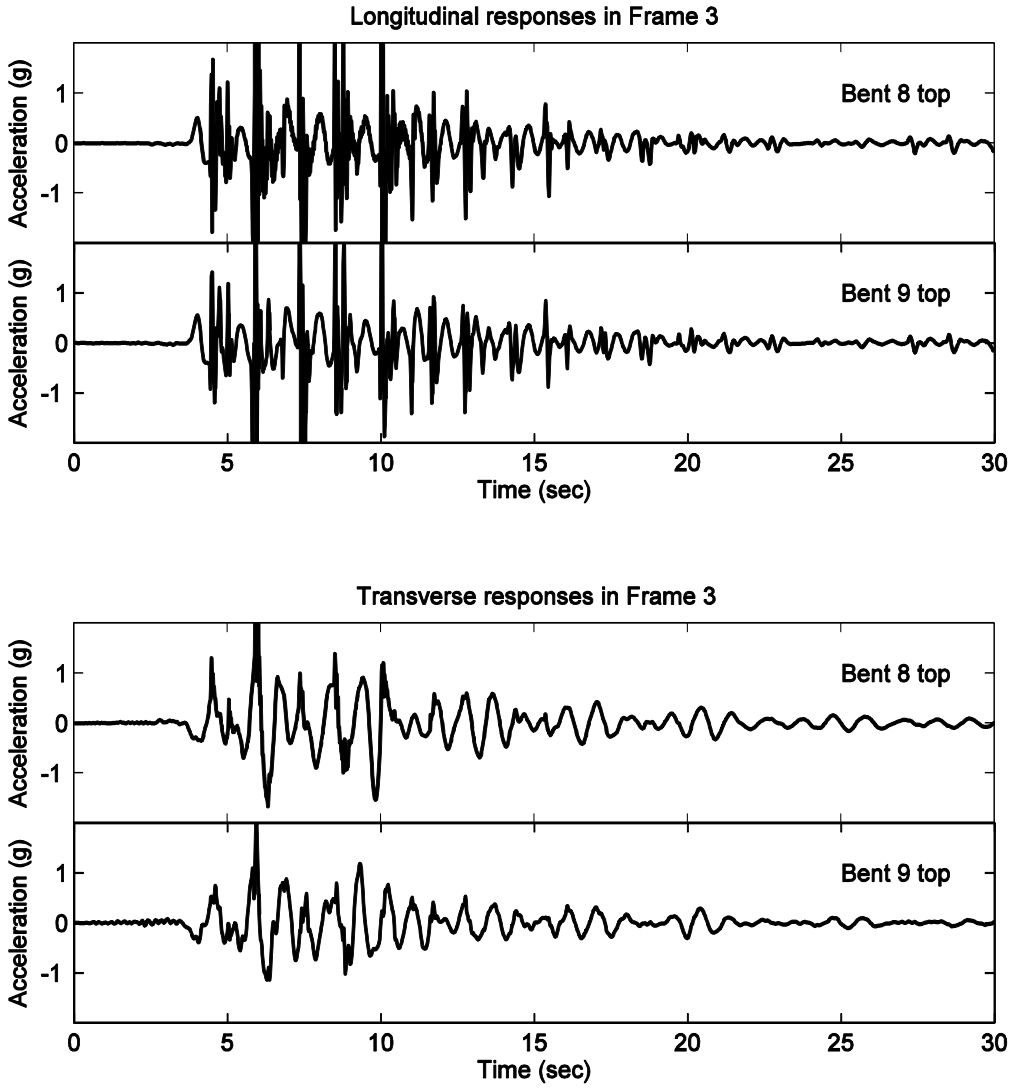

Figure E. 2: Acceleration time histories at deck locations in the frame 3 of the North-West connector

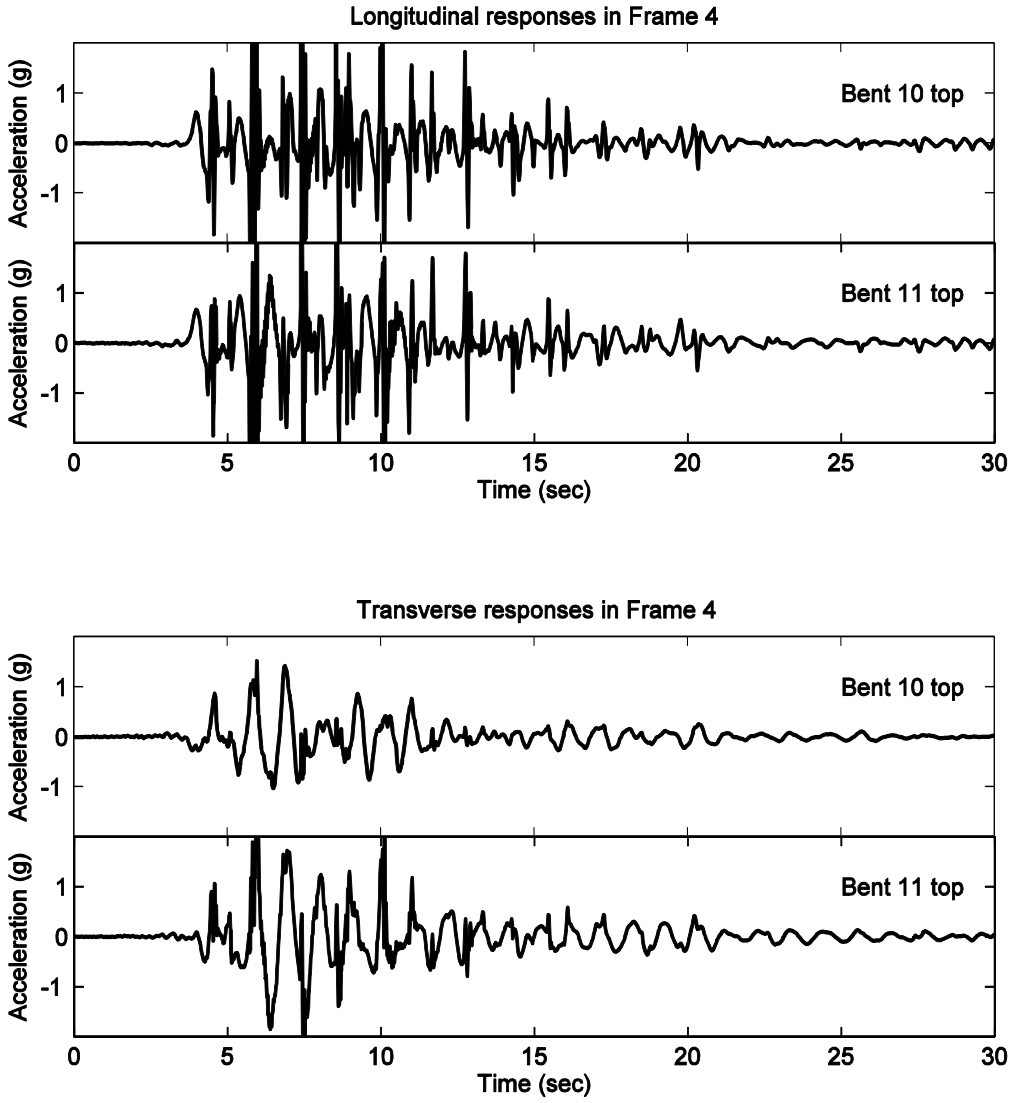

Figure E. 3: Acceleration time histories at deck locations in the frame 4 of the North-West connector

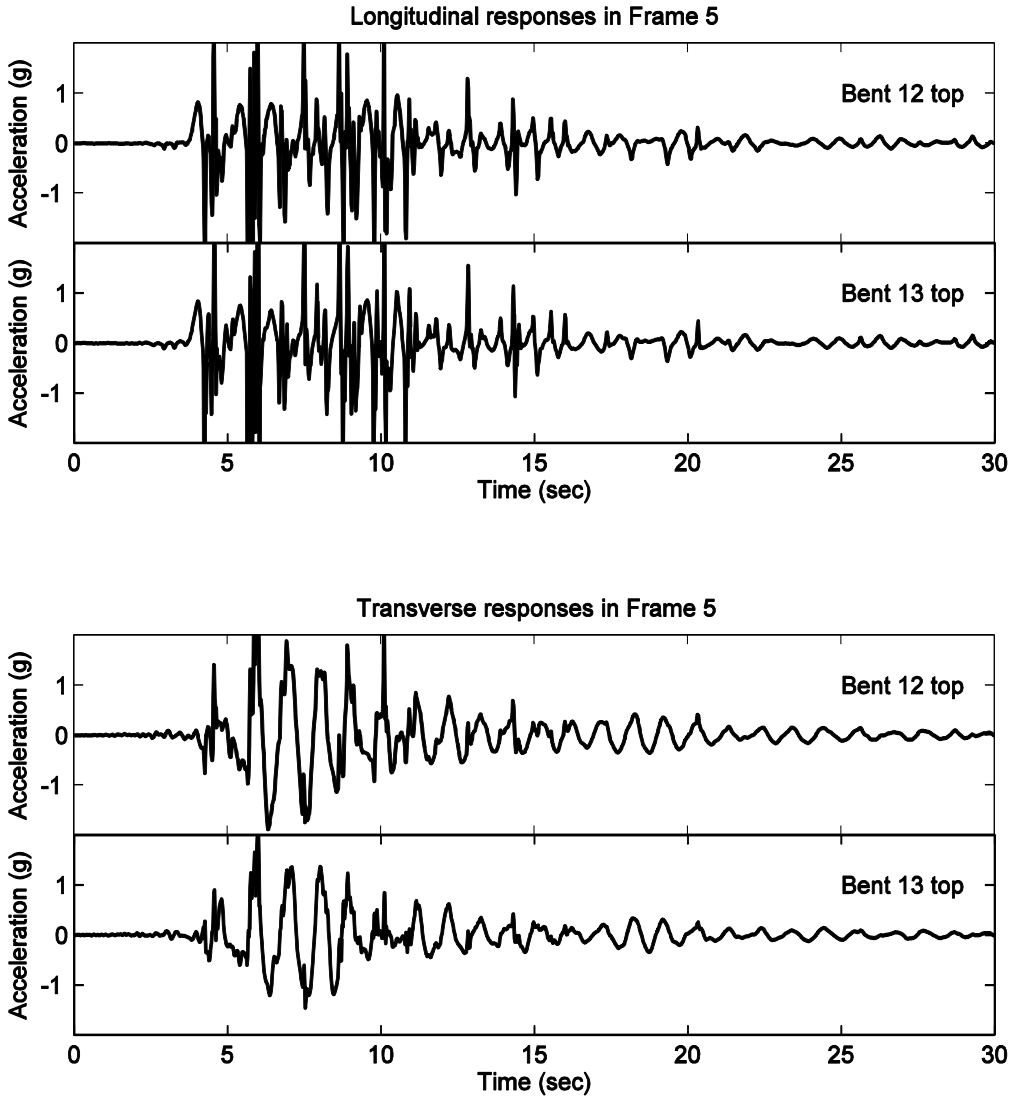

Figure E. 4: Acceleration time histories at deck locations in the frame 5 of the North-West connector

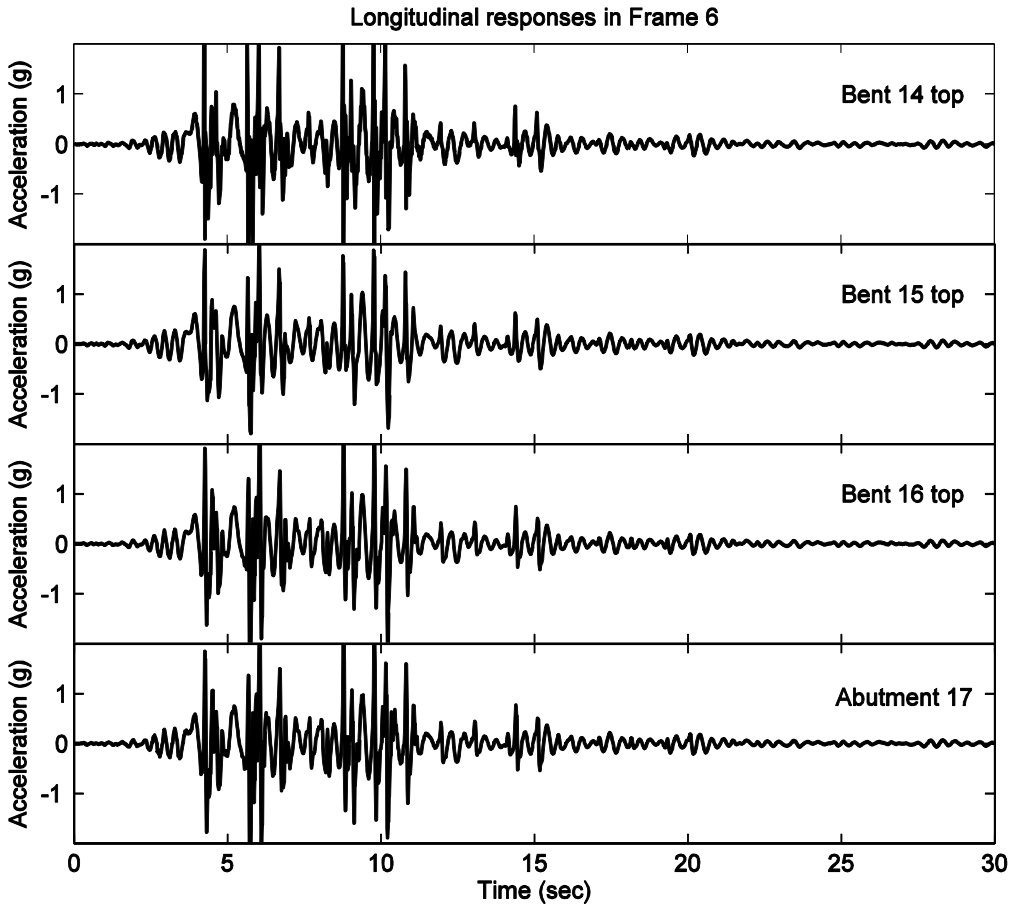

Figure E. 5: Acceleration time histories at deck locations in the frame 6 of the North-West connector

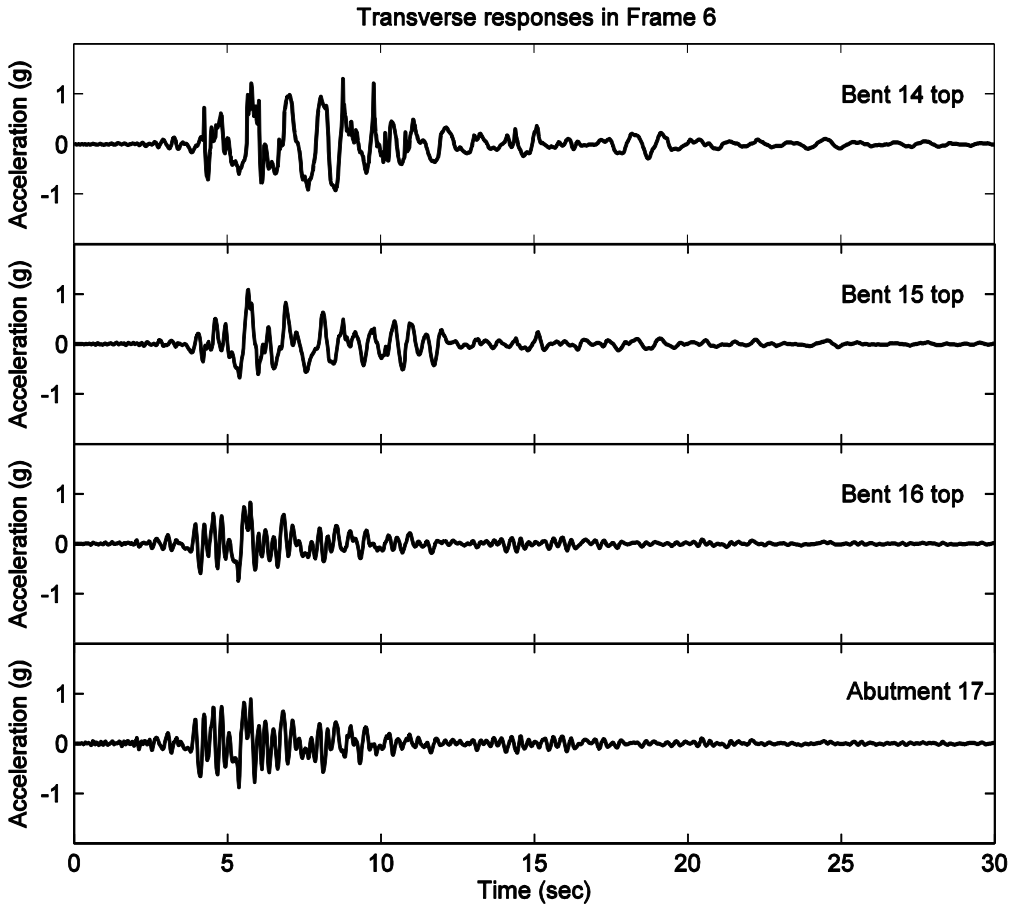

Figure E. 5: (continued) Acceleration time histories at deck locations in the frame 6 of the North-West connector